frontiers | Research Topics

Gas hydrate appearance accumulation, exploration and exploitation in continental margins

Edited by
Pibo Su, Wei Zhang, Zhifeng Wan, Lihua Zuo and Jinan Guan

Published in
Frontiers in Earth Science

ISSN 1664-8714
ISBN 978-2-8325-2487-9
DOI 10.3389/978-2-8325-2487-9

About Frontiers

Frontiers is more than just an open access publisher of scholarly articles: it is a pioneering approach to the world of academia, radically improving the way scholarly research is managed. The grand vision of Frontiers is a world where all people have an equal opportunity to seek, share and generate knowledge. Frontiers provides immediate and permanent online open access to all its publications, but this alone is not enough to realize our grand goals.

Frontiers journal series

The Frontiers journal series is a multi-tier and interdisciplinary set of open-access, online journals, promising a paradigm shift from the current review, selection and dissemination processes in academic publishing. All Frontiers journals are driven by researchers for researchers; therefore, they constitute a service to the scholarly community. At the same time, the *Frontiers journal series* operates on a revolutionary invention, the tiered publishing system, initially addressing specific communities of scholars, and gradually climbing up to broader public understanding, thus serving the interests of the lay society, too.

Dedication to quality

Each Frontiers article is a landmark of the highest quality, thanks to genuinely collaborative interactions between authors and review editors, who include some of the world's best academicians. Research must be certified by peers before entering a stream of knowledge that may eventually reach the public - and shape society; therefore, Frontiers only applies the most rigorous and unbiased reviews. Frontiers revolutionizes research publishing by freely delivering the most outstanding research, evaluated with no bias from both the academic and social point of view. By applying the most advanced information technologies, Frontiers is catapulting scholarly publishing into a new generation.

What are Frontiers Research Topics?

Frontiers Research Topics are very popular trademarks of the *Frontiers journals series*: they are collections of at least ten articles, all centered on a particular subject. With their unique mix of varied contributions from Original Research to Review Articles, Frontiers Research Topics unify the most influential researchers, the latest key findings and historical advances in a hot research area.

Find out more on how to host your own Frontiers Research Topic or contribute to one as an author by contacting the Frontiers editorial office: frontiersin.org/about/contact

Gas hydrate appearance accumulation, exploration and exploitation in continental margins

Topic editors

Pibo Su — Guangzhou Marine Geological Survey, China
Wei Zhang — Guangzhou Marine Geological Survey, China
Zhifeng Wan — Sun Yat-sen University, China
Lihua Zuo — Texas A&M University Kingsville, United States
Jinan Guan — Guangzhou Institute of Energy Conversion, Chinese Academy of Sciences (CAS), China

Citation

Su, P., Zhang, W., Wan, Z., Zuo, L., Guan, J., eds. (2023). *Gas hydrate appearance accumulation, exploration and exploitation in continental margins*. Lausanne: Frontiers Media SA. doi: 10.3389/978-2-8325-2487-9

Table of contents

frontiers in Earth Science

ORIGINAL RESEARCH
published: 24 February 2022
doi: 10.3389/feart.2022.831405

Hydrate Attenuation Characteristics Based on the Patchy-Saturation Model

Pengqi Liu[1,2], *Handong Huang*[1]*, *Liguo Hu*[2], *Shuang Mao*[2,3], *Zhongbin Tian*[4] *and Youyi Shen*[4]

[1]State Key Laboratory of Petroleum Resources and Prospecting, China University of Petroleum-Beijing, Beijing, China, [2]PetroChina Liaohe Oilfield Company, Panjin, China, [3]Yangtze University, Wuhan, China, [4]Shanxi Province Coal Geophysical Prospecting and Surveying and Mapping Institute, Jinzhong, China

At present, attenuation characteristics of hydrate applicable to the seismic frequency band are still controversial. In this study, the dispersion and attenuation characteristics of hydrate in different occurrence modes were defined from the mesoscale perspective, and the saturation of hydrate in the study area is estimated. Based on effective medium theory and cementation theory, the skeleton elastic modulus of the sedimentary layer was obtained in the present study. The variation of P-wave attenuation with hydrate saturation was obtained by the patchy-saturation theory. P-wave attenuation increased with saturation when hydrate occurred in the suspension mode. P-wave attenuation decreased with saturation when hydrate occurred in the particle-contact or cementation mode. The particle-contact mode and cementation mode hydrate made the P-wave attenuation peak shift to the right. The influence of the cementation mode on attenuation was greater than that of the particle-contact mode. The conclusions of this study are applicable to the frequency range of seismic exploration, thus solving the problems of hydrate saturation prediction and resource quantity calculation assessment in the study area.

Keywords: patchy-saturation model, hydrate saturation, dispersion, attenuation, mesoscale

OPEN ACCESS

Edited by:
Pibo Su,
Guangzhou Marine Geological Survey, China

Reviewed by:
Hua Ning Xu,
Qingdao Institute of Marine Geology (QIMG), China
Jing Ba,
Hohai University, China

***Correspondence:**
Handong Huang
757542363@qq.com

Specialty section:
This article was submitted to Marine Geoscience, a section of the journal Frontiers in Earth Science

Received: *08 December 2021*
Accepted: *13 January 2022*
Published: *24 February 2022*

Citation:
Liu P, Huang H, Hu L, Mao S, Tian Z and Shen Y (2022) Hydrate Attenuation Characteristics Based on the Patchy-Saturation Model. Front. Earth Sci. 10:831405. doi: 10.3389/feart.2022.831405

INTRODUCTION

Gas hydrate, also known as "combustible ice," is a kind of ice-like crystalline substance formed by natural gas and water under high pressure and low temperature, distributed in deep-sea sediments or permafrost soil. Gas hydrate has attracted much attention because of its great importance regarding energy, climate, environment, and disasters. The effect of gas hydrate on the velocity of seismic waves has been well understood. Various theoretical or experimental models have been proposed to estimate hydrate saturation by linking hydrate saturation with velocity (Wyllie et al., 1956; Wood et al., 1994; Lee et al., 1996; Helgerud et al., 1999). The common conclusion is that P-wave and S-wave velocities increase with hydrate saturation. Available theoretical formulae have different conditions of applicability. In areas without well data, it is not possible to calibrate theoretical formulae to guarantee the accuracy of hydrate saturation estimates. Therefore, alternative methods for hydrate saturation estimation are required.

Studies have shown that hydrate saturation is related to seismic wave attenuation. This study, therefore, aims to estimate hydrate saturation using attenuation. The dispersion and attenuation of the hydrate sediment layer have been studied with observational data, simulation experiments, and theoretical derivations. The conclusions obtained by these studies differ significantly. Some studies have concluded that attenuation decreases with hydrate saturation (Wood et al., 2000; Rossi et al., 2007; Jaiswal et al., 2012; Dewangan et al., 2014). Other studies have shown that attenuation increases with hydrate saturation (Sakai 1999; Guerin and Goldberg 2002; Dvorkin and Uden, 2004; Pratt et al.,

2005; Gerner et al., 2007; Zhang et al., 2016). However, it has also been argued that the relationship between attenuation and hydrate saturation is more complex than single positive or negative correlations (Priest et al., 2006; Lee and Waite 2007; Sun et al., 2014; Li 2015; Sahoo et al., 2018; Sahoo et al., 2019; Guo et al., 2021; Wang et al., 2021).

This study used existing attenuation theories to obtain the relationship between hydrate saturation and seismic wave attenuation. Dispersion and attenuation theories are mainly based on the mesoscale, microscopic, and macroscale perspective. Among them, only the mesoscale is applicable to the frequency domain range of seismic surveys (Pride and Berryman, 2003; Carcione José and Picotti, 2006; Rubino and Holliger, 2012). To date, the relationship between dispersion and attenuation and hydrate saturation on the mesoscale has rarely been studied. In this study, three hydrate models were developed for the first time based on the patchy saturation theory applicable to the mesoscale. The relationships between hydrate saturation and dispersion and attenuation were obtained for the suspension mode, particle-contact mode, and cementation mode. In addition, the dispersion and attenuation patterns of each mode were clarified (White, 1975).

The study area was conducted in a deep-water area on the continental slope of a sea, representing a new field of hydrate research. The geological characteristics, temperature and pressure conditions, gas source conditions, tectonic conditions, and sedimentation conditions met the requirements for gas hydrate formation and preservation. Accordingly, the area had good prospects for gas hydrate resources. However, the study area only had seismic data, and well data were absent, making the calculation of hydrate saturation and resources an urgent problem. In this study, hydrate saturation and resource calculations in the study area were realized, providing a theoretical basis for hydrate resource assessment.

PATCHY-SATURATION THEORY AND HYDRATE MODEL

White first used the patchy-saturation model to simulate velocity dispersion and attenuation caused by mesoscale heterogeneity (White, 1975). The patchy-saturation model assumes that a partially saturated water rock consists of several units, each consisting of a pair of concentric spheres. The concentric sphere is filled with a gas sphere of radius r_{in} and a water-saturated sphere of radius r_{out}. There is no interaction between the different units. Gas saturation is expressed as follows:

$$S_g = \frac{r_{in}^3}{r_{out}^3}. \tag{1}$$

The patchy-saturation model assumes that the inner sphere (denoted by subscript 1) has the same properties as the outer sphere shell (denoted by subscript 2). The complex moduli $K(\omega)$ and $G(\omega)$ of partially saturated pore rocks are corrected (Dutta and Seriff 1979) as follows:

$$K(\omega) = \frac{K_{HFL}}{1 - WK_{HFL}}, \tag{2}$$

$$W = \frac{3r_1(R_1 - R_2)(-Q_1 + Q_2)}{r_{out} i\omega (Z_1 + Z_2)}, \tag{3}$$

$$R_1 = \frac{K_{sat1} - K_{dry}}{1 - K_{dry}/K_g} \frac{3K_{sat2} + 4G_{dry}}{K_{sat2}\left(3K_{sat1} + 4G_{dry}\right) + 4G_{dry}(K_{sat1} - K_{sat2})S_g}, \tag{4}$$

$$R_2 = \frac{K_{sat2} - K_{dry}}{1 - K_{dry}/K_g} \frac{3K_{sat1} + 4G_{dry}}{K_{sat2}\left(3K_{sat1} + 4G_{dry}\right) + 4G_{dry}(K_{sat1} - K_{sat2})S_g}, \tag{5}$$

$$Z_1 = \frac{\eta_1 r_1}{\kappa_1} \frac{1 - e^{-2\gamma_1 r_{in}}}{(\gamma_1 r_{in} - 1) + (\gamma_1 r_{in} + 1)e^{-2\gamma_1 r_1}}, \tag{6}$$

$$Z_2 = -\frac{\eta_2 r_{in}}{\kappa_2} \frac{(\gamma_2 r_{out} + 1) + (\gamma_2 r_{out} - 1)e^{2\gamma_2 (r_{out} - r_{in})}}{(\gamma_2 r_{out} + 1)(\gamma_2 r_{in} - 1) - (\gamma_2 r_{out} - 1)(\gamma_2 r_{in} + 1)e^{2\gamma_2 (r_{out} - r_{in})}}, \tag{7}$$

$$\gamma_n = \sqrt{i\omega \eta_n / \kappa_n K_{En}}, \quad n = 1 \ or \ 2, \tag{8}$$

$$K_{En} = \left[1 - \frac{K_{fn}\left(1 - K_{satn}/K_g\right)\left(1 - K_{dry}/K_g\right)}{\varphi K_{satn}\left(1 - K_{fn}/K_g\right)}\right] K_{An}, \quad n = 1 \ or \ 2, \tag{9}$$

$$K_{An} = \left(\frac{\varphi}{K_{fn}} + \frac{1 - \varphi}{K_g} - \frac{K_{dry}}{K_g^2}\right)^{-1}, \quad n = 1 \ or \ 2, \tag{10}$$

$$Q_n = \frac{\left(1 - K_{dry}/K_g\right) K_{An}}{K_{satn}}, \quad n = 1 \ or \ 2, \tag{11}$$

$$K_{HFL} = \frac{K_{sat2}\left(3K_{sat1} + 4G_{dry}\right) + 4G_{dry}(K_{sat1} - K_{sat2})S_g}{\left(3K_{sat1} + 4G_{dry}\right) - 3(K_{sat1} - K_{sat2})S_g}, \tag{12}$$

$$G(\omega) = G_{dry}, \tag{13}$$

where K_{HFL} is the bulk modulus in the high-frequency limit; K_{dry} and G_{dry} are the bulk and shear moduli of the dry rock, respectively; K_f is the bulk modulus of the pore fluid; η_n is the viscosity of the pore fluid; κ_n is the permeability of the rock; and ϕ is the porosity. The saturated bulk modulus of region n K_{satn} (n = 1 or 2) is obtained by the Gassmann equation Gassmann (1951).

$$f_c \approx \frac{\kappa_2 K_{E2}}{\pi \eta_2 r_{out}^2}. \tag{14}$$

If the interaction force between the air pockets is not considered using the White model, it must be ensured that the air saturation S_g cannot exceed 0.52. If the value is higher, the units will interact and cause the gas plaques to collapse. When the gas saturation exceeds 0.52, the water-in-air mode should be adopted, that is, the inside of the concentric sphere is water, and the outside is air.

The patchy-saturation model discusses the attenuation caused by uneven fluid distribution in the pores. The suspension mode natural gas hydrate in the sediment also has uneven distribution. The gas can replace the gas hydrate in the patchy-saturation theory for attenuation calculation (see **Figure 1**). For the three models A, B, and C, the suspension mode hydrates exist in the

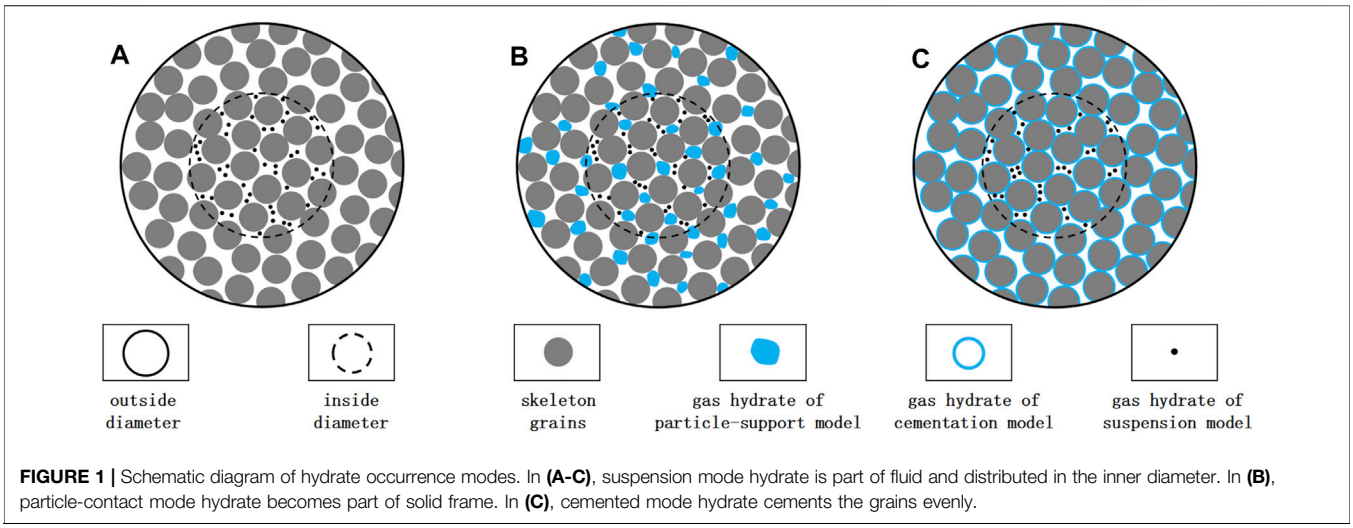

FIGURE 1 | Schematic diagram of hydrate occurrence modes. In **(A-C)**, suspension mode hydrate is part of fluid and distributed in the inner diameter. In **(B)**, particle-contact mode hydrate becomes part of solid frame. In **(C)**, cemented mode hydrate cements the grains evenly.

inner sphere. Model B represents the coexistence of the suspension and particle-support modes. The particle-support mode hydrate and skeleton grains form a new skeleton particle. Model C represents the coexistence of the suspension and cementation modes, and the cementation mode hydrate and skeleton grains form the new skeleton grains.

Model A

Based on Hertz–Mindlin theory Mindlin (1949), Dvorkin Helgerud et al. (1999) proposed a velocity model for non-cemented, high-porosity, hydrate-bearing deposits, and the equations are as follows:

$$K_{Dry}=\begin{cases}\left(\dfrac{\phi/\phi_0}{K_{HM}+\frac{4}{3}G_{HM}}+\dfrac{1-\phi/\phi_0}{K_0+\frac{4}{3}G_{HM}}\right)^{-1}-\dfrac{4}{3}G_{HM}, \phi<\phi_0\\ \left[\dfrac{(1-\phi)/(1-\phi_0)}{K_{HM}+\frac{4}{3}G_{HM}}+\dfrac{(\phi-\phi_0)/(1-\phi_0)}{\frac{4}{3}G_{HM}}\right]^{-1}-\dfrac{4}{3}G_{HM}, \phi\geq\phi_0,\end{cases} \tag{15}$$

$$G_{Dry}=\begin{cases}\left(\dfrac{\phi/\phi_0}{G_{HM}+Z}+\dfrac{1-\phi/\phi_0}{G_0+Z}\right)^{-1}-Z, \phi<\phi_0\\ \left[\dfrac{(1-\phi)/(1-\phi_0)}{G_{HM}+Z}+\dfrac{(\phi-\phi_0)/(1-\phi_0)}{Z}\right]^{-1}-Z, \phi\geq\phi_0,\end{cases} \tag{16}$$

$$Z=\frac{G_{HM}}{6}\left(\frac{9K_{HM}+8G_{HM}}{K_{HM}+2G_{HM}}\right), \tag{17}$$

$$K_{HM}=\left[\frac{n^2(1-\phi_0)^2G^2}{18\pi^2(1-\nu)^2}P\right]^{\frac{1}{3}},$$
$$G_{HM}=\frac{5-4\nu}{5(2-\nu)}\left[\frac{3n^2(1-\phi_0)^2G^2}{2\pi^2(1-\nu)^2}P\right]^{\frac{1}{3}}, \tag{18}$$

where ϕ_0 is the critical porosity (ϕ_0 = 0.36–0.40); K_{HM} and G_{HM} are the effective bulk modulus and shear modulus of dry rock when the rock porosity is at critical porosity, respectively; K_0, G_0, and υ_0 are the bulk modulus, shear modulus, and Poisson's ratio of the skeleton grains, respectively; n is the average number of particles in contact per unit volume, generally 8 or 9 (Dvorkin and Nur, 1996); and P is the effective pressure, which is generally calculated according to the following formula:

$$P=(1-\phi)(\rho_0-\rho_f)gh, \tag{19}$$

where ρ_0 and ρ_f are the density of skeleton grains and fluid, respectively; g is the acceleration due to gravity; and h is the depth below the seabed. $K_{Dry}=K_{HM}$; $G_{Dry}=G_{HM}$. When $\phi=\phi_0$, the bulk modulus and shear modulus of the dry rock were calculated by **Eq. 18**, that is, $K_{Dry}=K_{HM}$, $G_{Dry}=G_{HM}$. $\phi\neq\phi_0$, K_{Dry}, and G_{Dry}were calculated by **Eq. 15** to **Eq. 17**.

The bulk modulus of the fluid in the inner sphere is as follows:

$$K_{f1}=\left[\frac{(1-S_{h1})}{K_w}+\frac{S_{h1}}{K_h}\right]^{-1}. \tag{20}$$

K_w and K_h represent the bulk modulus of formation water and hydrate, respectively; and S_{h1} is the saturation of the hydrate in the suspension mode in the inner sphere.

The fluid viscosity in the internal region was calculated using Balakin's experimental data fitting (Balakin et al., 2010):

$$\eta_{f1}=\eta_w(1-S_{h1})^{-2.55}, \tag{21}$$

where η_w is the viscosity of formation water.

Model B

Compared with the suspension mode, the hydrate was considered part of the rock skeleton in the particle-contact mode, which had two effects: one was to change the bulk modulus and shear modulus of the skeleton, and the other was to reduce the formation's porosity. The skeleton's bulk modulus and shear modulus were calculated using the method mentioned in the study by Liu et al. (2019). The particle-contact mode hydrate saturation is S_{h2}.

The remaining porosity is as follows:

TABLE 1 | Parameters.

Parameter	Symbol	Value
Bulk modulus of skeleton particles/GPa	K_0	22.91
Shear modulus of skeleton particles/GPa	G_0	20.78
Density of skeleton particles/kg/m^3	ρ_0	2650
Bulk modulus of hydrate/GPa	K_h	6.41
Shear modulus of hydrate/GPa	G_h	2.55
Density of hydrate/kg/m^3	ρ_h	900
Bulk modulus of formation water/GPa	K_w	2.25
Shear modulus of formation water/GPa	G_w	0
Density of formation water/kg/m^3	ρ_w	1,000
Critical porosity/f	ϕ_0	0.36
Porosity/f	ϕ	0.4
Acceleration of gravity/m/s^2	g	9.8
Depth below the sea floor/m	h	300
Average number of particles in contact per unit volume	n	9
Particle diameter/ μm	d	20
Viscosity of formation water/cp	η_w	1
Permeability/mD	κ	500
Outer diameter/m	r_{out}	0.05
Inside diameter/m	r_{in}	0.03

$$\phi_r = \phi(1 - S_{h2}). \tag{22}$$

The hydrate saturation in the suspension mode in the remaining pores is S_{h1}。

The bulk modulus of the fluid in the inner sphere is expressed by **Eq. 20**. The fluid's viscosity in the inner sphere is expressed by **Eq. 21**.

Model C

When the coexistence of suspension and cementation modes of the hydrate occurs, the skeleton's bulk modulus and shear modulus were calculated using the method mentioned in the study by Liu et al. (2019). The hydrate saturation of the cementation mode is S_{h2}. The calculation method of residual porosity ϕ_r, fluid bulk modulus K_{f1}, and fluid viscosity η_{f1} in the inner sphere is the same as that of model B.

RESULTS

The Relationship Between Hydrate Saturation and Attenuation

At high hydrate concentrations (hydrate saturation exceeding 0.4), the hydrate greatly strengthens the skeleton of the sediments, bonds to adjacent porous medium particles, and causes sediments to solidify. Thus, the suspension mode hydrate changes into particle-contact mode or cemented mode hydrate (Yun et al., 2005; Yun et al., 2007; Xue 2016). Therefore, the upper limit of hydrate saturation for the suspension mode used in this study was 0.4. Attenuation is not only related to fluid distribution heterogeneity but also fabric heterogeneity (Ba et al., 2017; Zhang et al., 2021). In this study, uniform spherical particles were used as skeleton particles for simplicity. The parameters in **Table 1** are used to calculate the relationship between hydrate saturation and attenuation for the three models.

Figure 2 shows the variation in P-wave velocity and attenuation with frequency in model A. For different hydrate saturation, the P-wave velocity increased nonlinearly with frequency, and the P-wave velocity shifted upward overall with hydrate saturation. The P-wave velocity increased rapidly to a certain value near the characteristic frequency, and the increase was positively correlated with hydrate saturation (**Figure 2A**). **Figure 2B** shows the variation of the P-wave attenuation coefficient with frequency. The attenuation tended to increase and then decrease with hydrate saturation, reaching a peak at the characteristic frequency. The peak value of the attenuation versus the frequency curve gradually increased with saturation.

Figure 3 shows the variation of P-wave velocity and attenuation with frequency in model B. The P-wave velocity increased with saturation in both the suspension and particle-contact modes, assuming hydrate saturations of 0.1, 0.2, and 0.3 in the particle-contact mode and 0, 0.1, 0.2, 0.3, and 0.4 in the suspension mode. When the hydrate saturation in the

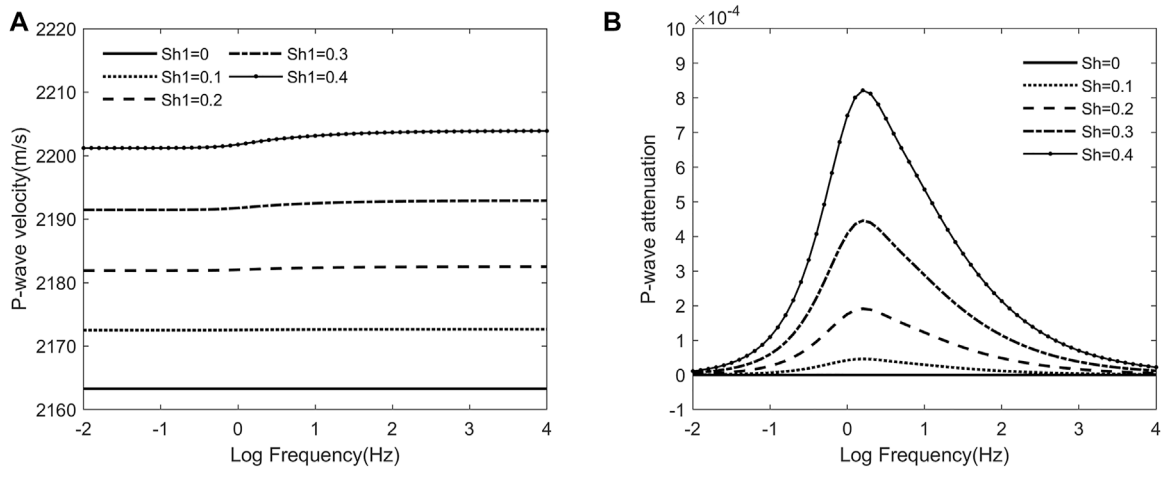

FIGURE 2 | P-wave velocity **(A)** and P-wave attenuation **(B)** vs. frequency curves at different hydrate contents in model A.

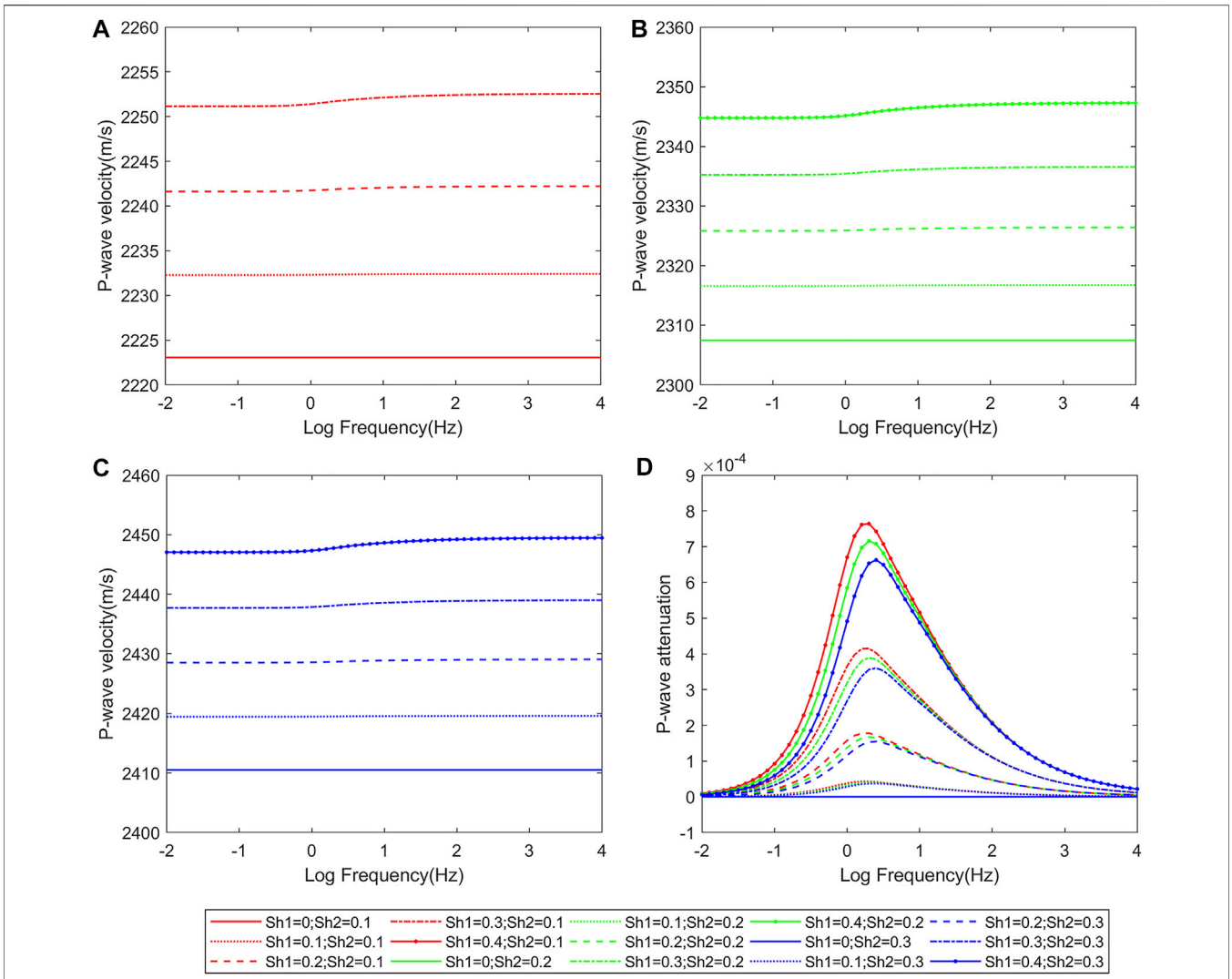

FIGURE 3 | P-wave velocity **(A-C)** and P-wave attenuation **(D)** vs. frequency curves at different hydrate contents in mode B.

suspension mode was 0, the P-wave velocity was constant, that is, it did not vary with frequency (**Figures 3A-C**). As shown in **Figure 3D**, attenuation increased with hydrate saturation in the suspension mode and decreased with hydrate saturation in the particle-contact mode. The peak of P-wave attenuation shifted to the right as hydrate saturation increased in the particle-contact mode.

Figure 4 shows the variation of P-wave velocity and attenuation with frequency in model C. The effects on velocity and dispersion were roughly the same for cemented and particle-contact hydrates. However, the effect of the cementation mode hydrate on P-wave velocity and P-wave attenuation was greater. When hydrate saturation was the same, the increase in velocity was greater for the cemented mode hydrates than for particle-contact mode hydrates. The decrease in attenuation was greater for cemented mode hydrates than for particle-contact mode hydrates.

Estimation of Hydrate Resources

The simulation experiment of the hydrate aggregation and dispersion process showed that the hydrate formed by free methane mainly occurred in sediment particles in the cemented mode. The hydrate particles formed by dissolved methane were relatively small and mainly occurred among the sediment particles in the suspension mode. The study area was located in the deep-water area of the continental slope. The analysis of seismic data and metallogenic conditions in the study area showed that the hydrate ore bodies in the study area were derived from dissolved methane.

The suspension mode hydrate model was also used to study saturation. Mode A was suitable for the study area. **Figure 5A** shows the seismic profile of the research area. The wave impedance between the peak (black axis) and trough (red axis) with strong energy in the black dotted line box should be high, which was the target layer of the research area. The attenuation data were calculated by the inversion technique (**Figure 5B**). The attenuation of the target layer showed a high value, which further

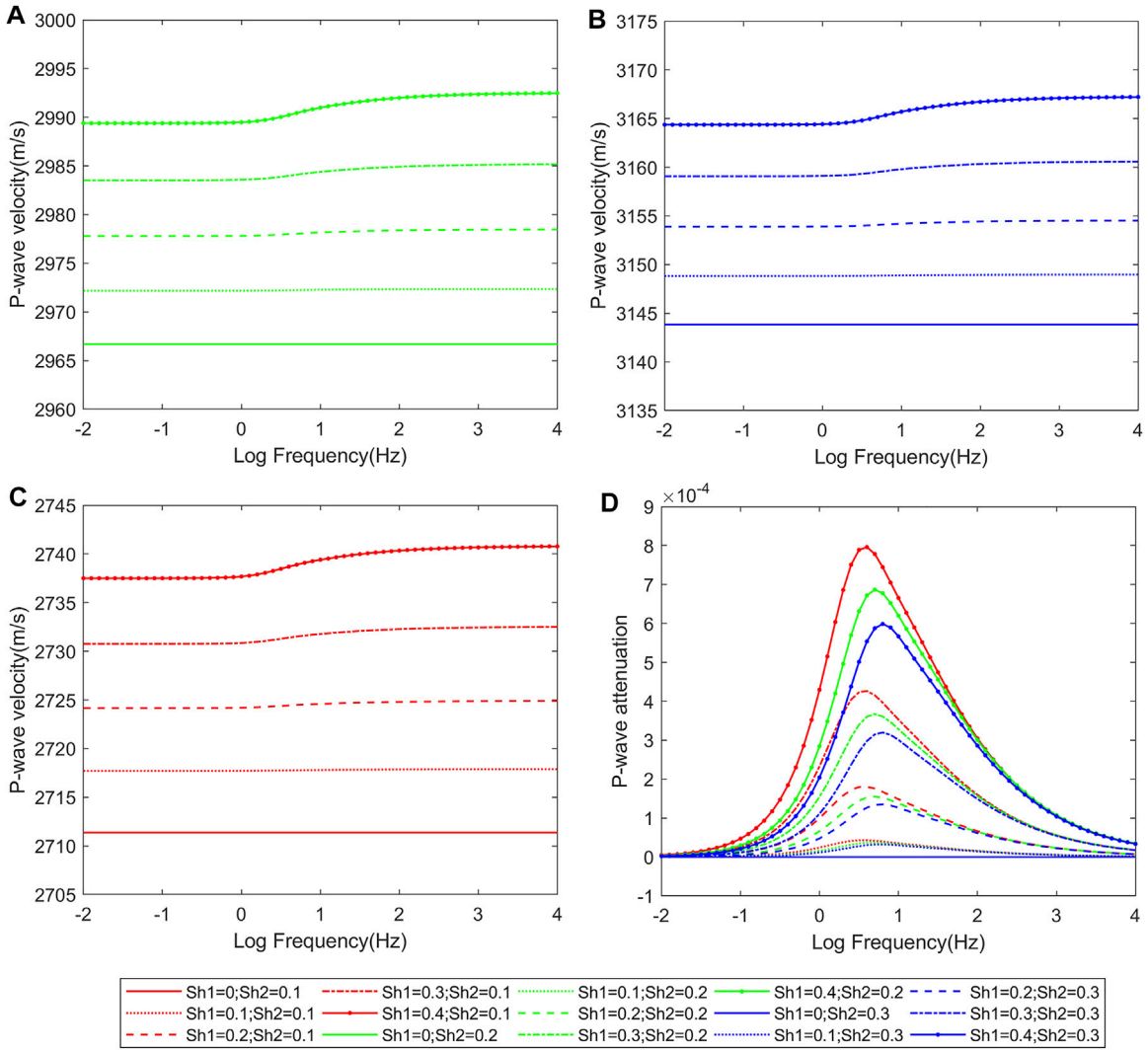

FIGURE 4 | P-wave velocity **(A-C)** and P-wave attenuation **(D)** vs. frequency curves at different hydrate contents in mode C.

showed that the target layer developed hydrate. The dominant frequency of the target layer in the study area was 35 Hz. The hydrate saturation data volume was calculated using the relationship between hydrate attenuation and saturation in Mode A (**Figure 5C**). The maximum value of the hydrate was 38%, and the average value was 28%. The area and the effective thickness of the hydrate in the target layer were determined. The formula for calculating hydrate resources is as follows:

$$Q = \phi \cdot S_h \cdot f \cdot A \cdot T, \tag{23}$$

where ϕ is the porosity, S_h is the hydrate saturation, f is the volume coefficient, A is the area, and T is the thickness.

According to the adjacent area data, the porosity of the target layer was 0.4. The target layer area was 1.96*107 m^2 square meters. The average thickness of the target layer was 14 m. The volume factor was 164; that is, one volume of hydrate released 164 volumes of methane gas. Based on this estimation, the hydrate resources in the study area were $5.05*10^9$ m^3.

DISCUSSION

In this study, three hydrate models were developed based on the patchy-saturation theory applicable at the mesoscale (White, 1975), and the relationships between hydrate saturation and dispersion and attenuation were obtained for different models. Furthermore, hydrate saturation and resource calculation in the study area were completed using attenuation inversion data. Three hydrate models were developed to assess the hydrate dispersion and attenuation characteristics under the patchy-saturation theory. Finally, hydrate saturation and resource estimates for the study area were presented.

The patchy-saturation model discusses attenuation due to the inhomogenous distribution of fluids within the pore space. Suspension mode hydrates in the sediment layer are in a flowing state and have a nonuniform distribution. For this reason, suspension mode hydrates are used instead of fluids in the patchy-saturation model. The three hydrate models developed

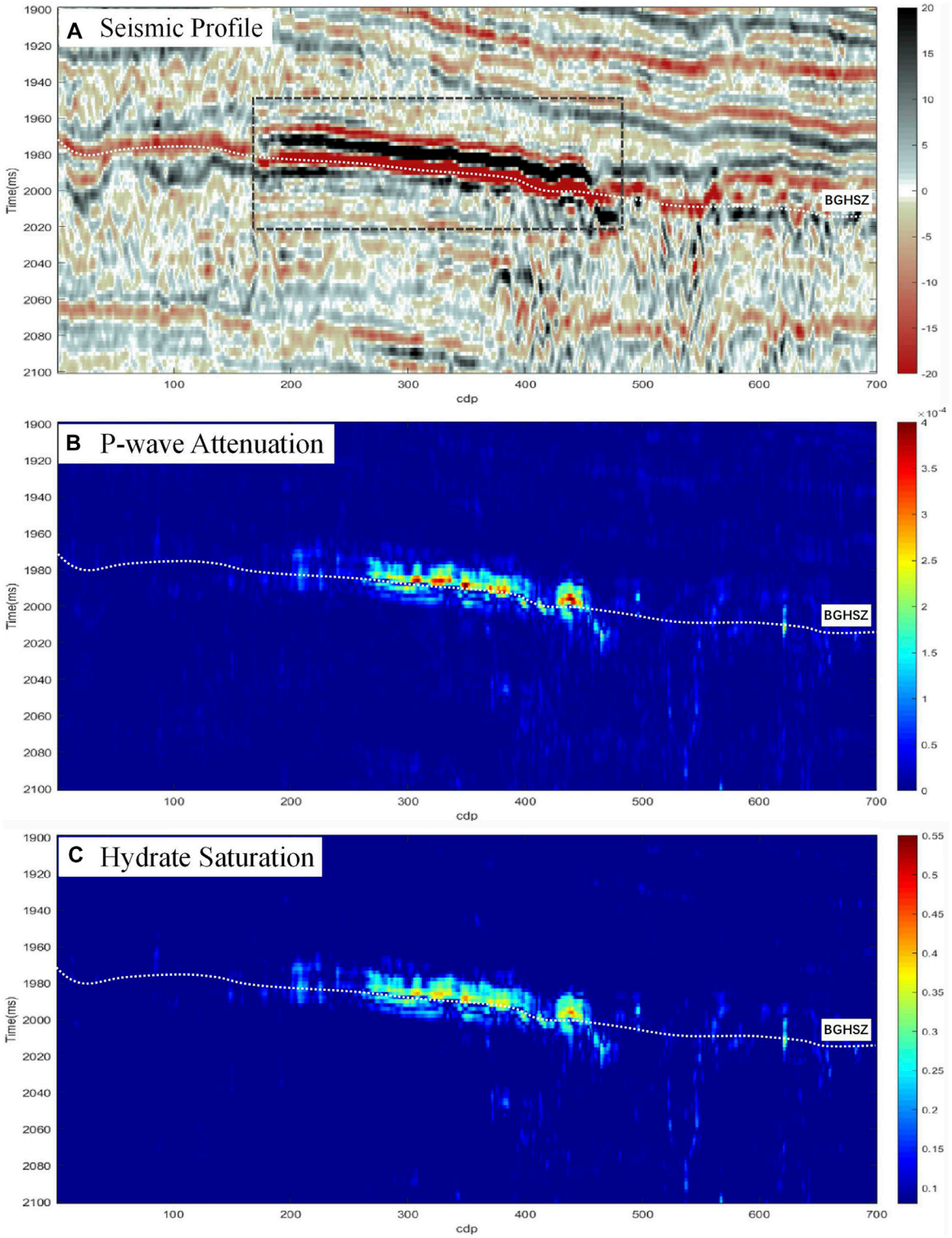

FIGURE 5 | Seismic **(A)**, attenuation **(B)**, and hydrate saturation **(C)** profiles of the study area. The white dotted line is the base of the gas hydrate stability zone (BGHSZ), above which hydrates usually develop. The black dotted line box is the boundary of the target layer. The target layer is between the peak (black axis) and trough (red axis) with strong energy in the black dotted line box.

for the first time in this study represent 1) the suspension mode, 2) coexistence of the suspension mode and particle-contact mode, and 3) coexistence of the suspension mode and cementation mode. The suspension-mode hydrate was distributed in the inner sphere, while the particle-contact and cementation-mode hydrates were uniformly distributed as part of the skeleton in both the inner sphere and the outer spherical shell. The skeleton properties were similar in both regions. The purpose of the three models was to clarify the effects on dispersion and attenuation caused by the suspension mode hydrate as a fluid and the particle-contact and cemented mode hydrates as a skeleton, respectively.

The results of our study support the view that the relationship between attenuation and hydrate saturation is more complex than single positive or negative correlations. Hydrate attenuation characteristics in the sediment layer depended on the hydrate reservoir state. P-wave attenuation increased with saturation when the hydrate reservoir was in the suspension mode because as hydrate saturation increased in the suspension mode, the nonequilibrium pore pressure between different fluid zones increased, causing an increase in pore fluid flow velocity, which in turn led to an increase in seismic attenuation. Conversely, P-wave attenuation decreased with saturation when the hydrate reservoir state in the sediment layer was in both particle-contact and cemented modes because the particle-contact and cemented-mode hydrates increased the cementation of the sediment layer, leading to an increase in its strength, which in turn led to a decrease in seismic attenuation. The cementation mode had a greater effect on attenuation than the particle-contact mode because increases in skeleton bulk modulus, shear modulus, and strength were greater for the cemented mode than for the particle-contact mode hydrates when hydrate saturation is the same.

Hydrates formed from dissolved methane are small and mainly suspended between the sediment particles. The analysis of seismic data and metallogenic conditions in the study area indicated that the hydrate in the study area originated from dissolved methane. Therefore, the suspension mode hydrate model (Model A) was used for the saturation study. An inversion of the study area was carried out to obtain attenuation data, and the model A relationship was used to calculate the hydrate saturation data body in the study area, which in turn led to the calculation of study area resources. The attenuation theory was chosen to predict hydrate saturation because it had the following advantages. First, attenuation data equivalent to seismic attributes were derived from seismic data, and the process of obtaining them was uninterrupted and reliable. Second, the method was less dependent on well data than the velocity method and did not require well data to be calibrated to obtain hydrate saturation. Third, the patchy-saturation theory used in this study was applicable to the exploration frequency domain and could solve practical problems in the study area. Finally, the method utilized was an effective solution for the currently available data in the study area and may provide insights into hydrate quantification in other similar areas.

This study used only seismic data and metallogenic conditions, combined with data from neighboring areas, to determine the hydrate reservoir model as a suspension model. There was no logging data in the study area to determine the specific hydrate storage state. It is also unlikely that there is a single model for the hydrate reservoir in the sediment layer. Therefore, there is insufficient evidence for the suspension model, and further drilling is required to confirm it. When the hydrate reservoir state in a sedimentary formation follows Model B or Model C, or when all three reservoir modes coexist, it is not possible to accurately calculate the hydrate saturation profile from the attenuation profile using the relational equation. This is because the suspension model hydrate increases the attenuation, and particle-contact and cementation mode hydrate saturation decreases the attenuation, making it impossible to calculate hydrate directly from the attenuation profile when the respective content is unknown.

The next step in this line of research is calculating hydrate saturation when the hydrate state follows either model B or model C. The core of this is to determine the respective contents of hydrate in the sediment layer for the suspension, particle-contact, and cementation models.

CONCLUSION

In this study, the theoretical relationships between the dispersion and attenuation of the three models and the hydrate saturation were derived from a mesoscale perspective for the first time. Moreover, the influence of hydrates with different occurrence modes on dispersion and attenuation was clarified. When the hydrate occurrence in the sedimentary layer was in the suspension mode, the P-wave attenuation increased with saturation. When the hydrate occurrence in the sedimentary layer was particle-contact and cementation mode, the P-wave attenuation decreased with saturation. The particle-contact mode and the cementation mode hydrate moved the attenuation peak of the P-wave to the right. The degree of influence of the cementation mode on attenuation was greater than that of the particle-contact mode. The conclusions obtained in this study are applicable to the frequency range of seismic exploration, thus solving the problems of hydrate saturation prediction and resource estimation in the study area. When the hydrate occurrence in the formation follows model B or C, or the three occurrence modes coexist, it is still impossible to accurately calculate hydrate saturation based on attenuation, and further research is needed.

DATA AVAILABILITY STATEMENT

The original contributions presented in the study are included in the article/Supplementary Material; further inquiries can be directed to the corresponding author.

AUTHOR CONTRIBUTIONS

PL: modeling and writing. HH: communication and guidance. SM: translation and suggestion. LH: guidance. ZT: suggestion and verification. YS: suggestion and verification. All authors contributed to the article and approved the submitted version.

FUNDING

The authors were grateful to the support of the Natural Science Foundation of China (No. 41974124).

ACKNOWLEDGMENTS

The authors would like to express their gratitude to EditSprings (https://www.editsprings.cn/) for the expert linguistic services provided.

REFERENCES

Ba, J., Xu, W., Fu, L., Carcione, J. M., and Zhang, L. (2017). Rock Anelasticity Due to Patchy-Saturation and Fabric Heterogeneity: A Double Double-Porosity Model of Wave Propagation. *J. Geophys. Research-solid earth.* 122 (3), 1949–1976. doi:10.1002/2016jb013882

Balakin, B. V., Hoffmann, A. C., Kosinski, P., and Høiland, S. (2010). Turbulent Flow of Hydrates in a Pipeline of Complex Configuration. *Chem. Eng. Sci.* 65 (17), 5007–5017. doi:10.1016/j.ces.2010.06.005

Carcione José, M., and Picotti, S. (2006). P-wave Seismic Attenuation by Slow-Wave Diffusion: Effects of Inhomogeneous Rock Properties. *Geophysics.* 71 (3), 11–21. doi:10.1190/1.2194512

Dewangan, P., Mandal, R., Jaiswal, P., Ramprasad, T., and Sriram, G. (2014). Estimation of Seismic Attenuation of Gas Hydrate Bearing Sediments from Multi-Channel Seismic Data: A Case Study from Krishna-Godavari Offshore basin. *Mar. Pet. Geology.* 58, 356–367. doi:10.1016/j.marpetgeo.2014.05.015

Dutta, N. C., and Seriff, A. J. (1979). On White's Model of Attenuation in Rocks With Partial Gas Saturation. *Geophysics.* 44 (11), 1806–1812. doi:10.1190/1.1440940

Dvorkin, J., and Nur, A. (1996). Elasticity of High-Porosity Sandstones: Theory for Two North Sea Data Sets. *Geophysics.* 61 (5), 1363–1370. doi:10.1190/1.1444059

Dvorkin, J., and Uden, R. (2004). Seismic Wave Attenuation in a Methane Hydrate Reservoir. *The Leading Edge.* 23 (8), 730–732. doi:10.1190/1.1786892

Gassmann, F. (1951). Über die Elastizität poröser Medien. *Gesellschaft in ZÜrich.* 90 (9), 1–23. doi:10.6038/cjg20160924

Gerner, A., Saenger, E. H., and Shapiro, S. A. (2007). Attenuation of P-Waves Due to Interlayer Fluid Flow in Hydrate-Bearing Sediments. *J. Geophys. Eng.* 4 (4), 394–403.

Guerin, G., and Goldberg, D. (2002). Sonic Waveform Attenuation in Gas Hydrate-Bearing Sediments from the Mallik 2L-38 Research Well, Mackenzie Delta, Canada. *J. Geophys. Res.* 107 (B5), 1–12. doi:10.1029/2001jb000556

Guo, Z., Wang, X., and Jiao, J. (2021). Rock Physics Model and Seismic Dispersion and Attenuation in Gas Hydrate-Bearing Sediments. *Front. Earth Sci.* 64 (9), 1–14. doi:10.3389/feart.2021.641606

Helgerud, M. B., Dvorkin, J., Nur, A., Sakai, A., and Collett, T. (1999). Elastic-Wave Velocity in Marine Sediments With Gas Hydrates: Effective Medium Modeling. *Geophys. Res. Lett.* 26 (13), 2021–2024. doi:10.1029/1999gl900421

Jaiswal, P., Dewangan, p., and Ramprasad, T. (2012). Seismic Characterization of Hydrates in Faulted, fine-grained Sediments of Krishna-Godavari Basin: Full Waveform Inversion. *Geophys. Res. Solid Earth.* 117 (B10), B10305. doi:10.1029/2012jb009201

Lee, M. W., Hutchinson, D. R., Collett, T. S., and Dillon, W. P. (1996). Seismic Velocities for Hydrate-Bearing Sediments Using Weighted Equation. *J. Geophys. Res.* 101 (B9), 20347–20358. doi:10.1029/96jb01886

Lee, M. W., and Waite, W. F. (2007). Amplitude Loss of Sonic Waveform Due to Source Coupling to the Medium. *Geophys. Res. Lett.* 34 (5), L05303. doi:10.1029/2006gl029015

Li, C. (2015). *Seismic Wave Attenuation in Hydrate-Bearing Sediments and the Estimates of Attenuation Coefficient.* Beijing: China University of Geosciences.

Liu, P., Sun, S. Z., and Hu, L. (2019). Estimation of Gas Hydrate Saturation at the Slope in the Northwest of South China Sea. *Pet. Sci. Technology.* 37 (15), 1777–1787. doi:10.1080/10916466.2019.1594289

Mindlin, R. D. (1949). Compliance of Elastic Bodies in Contact. *Appl. Mech.* 16, 259–268. doi:10.1115/1.4009973

Pratt, R. G., Hou, F., and Bauer, K. (2005). *Waveform Tomography Images of Velocity and Inelastic Attenuation from the Mallik 2002 Crosshole Seismic Surveys.* Vancouver: Geological Survey of Canada.

Pride, S. R., and Berryman, J. G. (2003). Linear Dynamics of Double-Porosity Dual-Permeability Materials. I. Governing Equations and Acoustic Attenuation. *Phys. Rev. E Stat. Nonlin Soft Matter Phys.* 68 (3), 036603. doi:10.1103/PhysRevE.68.036603

Priest, J. A., Best, A. I., and Clayton, C. R. I. (2006). Attenuation of Seismic Waves in Methane Gas Hydrate-Bearing Sand. *Geophys. J. Int.* 164 (1), 149–159. doi:10.1111/j.1365-246x.2005.02831.x

Rossi, G., Gei, D., Böhm, G., Madrussani, G., and Carcione, J. M. (2007). Attenuation Tomography: An Application to Gas-Hydrate and Free-Gas Detection. *Geophys. Prospect.* 55 (5), 655–669. doi:10.1111/j.1365-2478.2007.00646.x

Rubino, J. G., and Holliger, K. (2012). Seismic Attenuation and Velocity Dispersion in Heterogeneous Partially Saturated Porous Rocks. *Geophys. J. Int.* 188 (3), 1088–1102. doi:10.1111/j.1365-246x.2011.05291.x

Sahoo, S. K., Marín-Moreno, H., North, L. J., Falcon-Suarez, I., Madhusudhan, B. N., Best, A. I., et al. (2018). Presence and Consequences of Coexisting Methane Gas With Hydrate Under Two Phase Water-Hydrate Stability Conditions. *J. Geophys. Res. Solid Earth.* 123 (5), 3377–3390. doi:10.1029/2018jb015598

Sahoo, S. K., North, L. J., Marín-Moreno, H., Minshull, T. A., and Best, A. I. (2019). Laboratory Observations of Frequency-Dependent Ultrasonic P-Wave Velocity and Attenuation During Methane Hydrate Formation in Berea sandstone. *Geophys. J. Int.* 219 (1), 713–723. doi:10.1093/gji/ggz311

Sakai, A. (1999). Velocity Analysis of Vertical Seismic Profile (VSP) Survey at JAPEX/JNOC/GSC Mallik 2L-38 Gas Hydrate Research Well, and Related Problems for Estimating Gas Hydrate Concentration. *GSC Bull.* 544, 323–340. doi:10.4095/210775

Sun, W., Ba, J., Müller, T. M., Carcione, J. M., and Cao, H. (2014). Comparison of P-Wave Attenuation Models of Wave-Induced Flow. *Geophys. Prospecting.* 63, 378–390. doi:10.1111/1365-2478.12196

Wang, W., Ba, J., Carcione, J. M., Liu, X., and Zhang, L. (2021). Wave Properties of Gas-Hydrate Bearing Sediments Based on Poroelasticity. *Front. Earth Sci.* 9, 283. doi:10.3389/feart.2021.640424

White, J. E. (1975). Computed Seismic Speeds and Attenuation in Rocks with Partial Gas Saturation. *Geophysics.* 40 (2), 224–232. doi:10.1190/1.1440520

Wood, W. T., Holbrook, S. W., and Hoskins, H. (2000). *In Situ* measurements of P-Wave Attenuation in the Methane Hydrate- and Gas-Bearing Sediments of the Blake Ridge. *Proc. Ocean Drilling Program Scientific Results.* 164, 265–272. doi:10.2973/odp.proc.sr.164.246.2000

Wood, W. T., Stoffa, P. L., and Shipley, T. H. (1994). Quantitative Detection of Methane Hydrate through High-Resolution Seismic Velocity Analysis. *J. Geophys. Res.* 99 (B5), 9681–9695. doi:10.1029/94jb00238

Wyllie, M. R. J., Gregory, A. R., and Gardner, L. W. (1956). Elastic Wave Velocities in Heterogeneous and Porous Media. *Geophysics* 21, 41–70. doi:10.1190/1.1438217

Xue, K. (2016). *Study on Formation and Dissociation Characteristics of the Natural Gas Hydrate*. Dalian: Dalian University Of Technology.

Yun, T. S., Francisca, F. M., Santamarina, J. C., and Ruppel, C. (2005). Compressional and Shear Wave Velocities in Uncemented Sediment Containing Gas Hydrate. *Geophys. Res. Lett.* 32, L10609. doi:10.1029/2005gl022607

Yun, T. S., Santamarina, J. C., and Ruppel, C. (2007). Mechanical Properties of Sand, silt, and clay Containing Tetrahydrofuran Hydrate. *J. Geophys. Res. Solid Earth.* 112, B04106. doi:10.1029/2006jb004484

Zhang, L., Ba, J., and Carcione, J. M. (2021). Wave Propagation in Infinituple-Porosity Media. *J. Geophys. Res. - Solid earth.* 126 (4), e2020JB021266. doi:10.1029/2020jb021266

Zhang, R., Li, H., and Wen, P. (2016). The Velocity Dispersion and Attenuation of Marrine Hydrate-Bearing Sediments. *Chin. J. Geophys.* 59 (9), 3417–3427. doi:10.6038/cjg20160924

Conflict of Interest: Author PL was employed by the company PetroChina.

The remaining authors declare that the research was conducted in the absence of any commercial or financial relationships that could be construed as a potential conflict of interest.

frontiers in Earth Science

ORIGINAL RESEARCH
published: 02 March 2022
doi: 10.3389/feart.2022.843521

Numerical Simulations of Combined Brine Flooding With Electrical Heating–Assisted Depressurization for Exploitation of Natural Gas Hydrate in the Shenhu Area of the South China Sea

Qi Zhang[1,2,3] *and Yanfei Wang*[1,2,3]*

[1]*Key Laboratory of Petroleum Resources Research, Institute of Geology and Geophysics, Chinese Academy of Sciences, Beijing, China,* [2]*College of Earth and Planetary Sciences, University of Chinese Academy of Sciences, Beijing, China,* [3]*Innovation Academy for Earth Science, Chinese Academy of Sciences, Beijing, China*

OPEN ACCESS

Edited by:
Pibo Su,
Guangzhou Marine Geological Survey, China

Reviewed by:
Bo Li,
Chongqing University, China
Xianying Wang,
Guangzhou Marine Geological Survey, China
Cheng Lu,
China Geological Survey, China

***Correspondence:**
Yanfei Wang
yfwang@mail.iggcas.ac.cn

Specialty section:
This article was submitted to Economic Geology, a section of the journal Frontiers in Earth Science

Received: *04 January 2022*
Accepted: *07 February 2022*
Published: *02 March 2022*

Citation:
Zhang Q and Wang Y (2022) Numerical Simulations of Combined Brine Flooding With Electrical Heating–Assisted Depressurization for Exploitation of Natural Gas Hydrate in the Shenhu Area of the South China Sea. Front. Earth Sci. 10:843521. doi: 10.3389/feart.2022.843521

The Shenhu area of the South China Sea (SCS) is one of the most promising fields for natural gas hydrate (NGH) exploitation. However, previous studies conclude that using only depressurization is inefficient for this challenging hydrate deposits surrounded by permeable water zones, which requires assistance by thermal stimulation to promote hydrate decomposition and methane recovery. However, traditional thermal stimulation methods with hot water or steam injection induce massive heat loss along the wellbore. In addition, *in situ* electrical heating only results in a limited high temperature region due to low thermal conductivity of hydrate deposits. Therefore, we numerically investigate the performance of combined brine flooding with electrical heating–assisted depressurization in horizontal wells for exploitation of natural gas hydrate in the SCS, which simultaneously possesses the merits of low heat loss and enhanced heat transfer by convection. Our simulation results show that thermal stimulation by combined brine flooding with electrical heating can significantly enhance hydrate dissociation and methane recovery. After 20 years of production, the cumulative methane production of combined brine flooding with electrical heating–assisted depressurization is 1.41 times of that conducted by the only depressurization method. Moreover, the energy efficiency can be improved by reducing electrical heating time, and terminating electrical heating with 70% hydrate dissociation achieves the highest net energy gain. In addition, methane recovery and net energy gain increases with electrical heating power and brine injection pressure but with a decreasing rate. Therefore, the selection of electrical heating power and brine injection pressure should be performed carefully and comprehensively considering both the efficiency of gas production and risks of geological hazard. It is hoped that our research results will provide reference and guidance for the development of a similar NGH reservoir in order to promote the industrial development process of NGH.

Keywords: natural gas hydrate, numerical simulations, brine injection, electrical heating, depressurization, Shenhu area

INTRODUCTION

Natural gas hydrates are crystalline substances comprising water molecules and gas molecules, in which a solid water lattice accommodates gas molecules in a cage-like structure (Sloan, 2003; Wang et al., 2017; Wu et al., 2020). The most typical hydrate-forming gas is methane, and NGH mainly occurs in terrestrial permafrost and offshore sediments where low temperature and high-pressure conditions needed by hydrate stabilization are met (Collett, 2002; Koh, 2002; Chong et al., 2016). As a potential new unconventional energy, NGHs are currently attracting significant attention owing to their extensive distribution, great resource potential, high energy density, and low environmental pollution (Koh et al., 2012; Yang et al., 2018). Current estimations of the hydrate-containing hydrocarbon gas available at standard conditions ranges from 10^{15} to 10^{18} m^3, which is twice as much as the conventional fossil energy (Moridis et al., 2009a). If NGH can be exploited in a safe and efficient way to produce natural gas and replace traditional fossil fuels, the problem of global energy shortage and environmental pollution can be greatly alleviated (Liang et al., 2020; Yin et al., 2020).

The Shenhu area on the northern continental slope of the South China Sea (SCS) is one of the most promising fields for gas hydrate exploitation. In 2007, 2015, and 2016, three gas hydrate drilling expeditions (GMGS1, 3, and 4) were conducted in this area by the Guangzhou Marine Geological Survey (Wu and Wang, 2018). During the GMGS1, five sites were selected for deep drilling and sampling in the Shenhu area (**Figure 1**), among which three sites (SH2, SH3, and SH7) were verified with the existence of methane gas hydrates by depressurization experiments (Wu et al., 2011). Since then, many numerical simulations were carried out on hydrate production in the Shenhu area, including the SH2 site (Su et al., 2011; Su et al., 2012b; Su et al., 2013; Jin et al., 2016), SH3 site (Su et al., 2012a), and SH7 site (Li et al., 2010; Li et al., 2011; Li et al., 2013; Sun et al., 2015). These simulations include different production methods, such as depressurization and thermal stimulation, the use of vertical and horizontal wells, the effects of the underlying and overburden layer permeability, and other aspects related to hydrate production (Sun et al., 2019). Based on aforementioned numerical studies and many other laboratory experiments on the NGH in the SCS, the China Geological Survey successfully conducted the first and second production tests in the Shenhu area of the SCS in 2017 and 2020, respectively, using a vertical well and a horizontal well. The first production test lasted for 60 days with a cumulative gas production of 3.09×10^5 m^3 (Li et al., 2018b), and the second production test achieved 30 days of continuous gas production, with a cumulative gas production of 8.614×10^5 m^3, whose average daily gas production is 5.57 times as much as that obtained in the first production test (Ye et al., 2020). The two successful production tests proved the technical feasibility of gas production from the clayey silt NGH reservoir, which accounts for 90% of the total hydrate reservoirs but tend to be the most difficult to exploit owing to low permeability and high content of clay (Boswell and Collett, 2011).

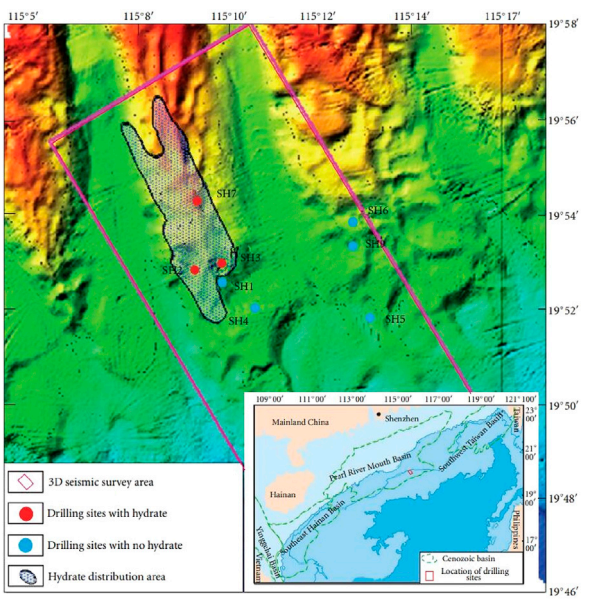

FIGURE 1 | Location of study area, drilling sites, and the confirmed gas hydrate distribution in the Shenhu area. Insert: General location of study area in the northern slope of the South China Sea (Wu et al., 2011).

To exploit the NGH, the equilibrium state of the reservoirs should be broken by certain mechanisms, leading to *in situ* dissociation of the NGH into gas and water; then the gas–water mixture can be extracted and gas–liquid separation can be conducted successively (Konno et al., 2016). According to the phase equilibrium curve of the NGH, those certain mechanisms include the following: depressurization (Moridis et al., 2007; Moridis et al., 2009b; Sun et al., 2015; Yang et al., 2019); thermal stimulation (Moridis et al., 2004; Wang et al., 2018; Liu et al., 2020); use of inhibitors (Sung et al., 2002); and gas molecule exchange (White et al., 2011; Koh et al., 2016; Zhang et al., 2017). Currently, depressurization is considered to be the most economical and efficient method for NGH exploitation (Oyama et al., 2012; Chong et al., 2017), which was used in the first and second production tests in the Shenhu area of the SCS. However, there are also problems attached to this method, such as small influence range and rapid drop of the gas production rate. Hydrate decomposition is an endothermic reaction, but the only heat sources of NGH exploitation by depressurization are the sensible heat of the hydrate deposit, the heat transferred from the surroundings, and the latent heat released by the phase transition from water to ice (Zhao et al., 2014). Due to insufficient heat supply, the reservoir temperature will significantly reduce which may lead to the formation of ice and secondary hydrate, hindering the recovery of methane (Wang et al., 2020). Therefore, thermal stimulation methods are usually used in company with depressurization to provide additional heat for the hydrate deposit and accelerate NGH dissociation (Wan et al., 2018).

Traditional thermal stimulation methods utilize hot water and steam injection, which can be implemented in the form of the huff and puff method, hot water/steam flooding, and hot water/steam-assisted gravity drainage (SAGD). Actually, these methods have

widely been used in the field of thermal enhanced oil recovery and provide a significant amount of oil in the overall global oil outlook (Mokheimer et al., 2019). Many authors also evaluated the potential of these methods in promoting methane production from the NGH by laboratory experiments and numerical simulations. Li et al. (2011) and Su et al. (2012b) numerically investigated the gas production performance by the huff and puff method in the Shenhu area, and the results showed that the gas production rate was very low and the secondary hydrate formation occurs during the injection stage. In addition, Feng et al. (2013) and Feng et al. (2014) compared the gas production potential of depressurization combined with warm brine injection by different dual horizontal well configurations, respectively, corresponding to the flooding method (dual horizontal wells in the same horizontal plane) and the SAGD method (dual horizontal wells in the same vertical plane). They concluded that the average gas production rate of the flooding method exceeds the commercially viable production rate in the Gulf of Mexico, which is more favorable than the SAGD method. In addition, Jin et al. (2016) also proved that gas recovery can be improved significantly by hot water flooding for the hydrate deposits in the Shenhu area, and the well spacing affects the methane production significantly when thermal stimulation starts. However, when hot water or steam is injected, the heat loss along the wellbore is considerable even with insulated tubing, after hundreds or even thousands of meter transportation from the surface or ocean to the hydrate-bearing layers (hereafter, referred to as HBL) (Li et al., 2018a).

To overcome the shortcoming of traditional hot water/steam flooding method, novel thermal stimulation methods of electrical or electromagnetic heating and methane *in situ* combustion have been proposed, which generate heat directly in the formation to avoid wellbore heat loss. In this study, we focus on electrical heating, and many laboratory experiments have been conducted to clarify the effects of electrical heating–assisted depressurization on hydrate dissociation and methane recovery (Falser et al., 2012; Li et al., 2018a; Liang et al., 2018; Minagawa et al., 2018; Wan et al., 2020a; Wan et al., 2020b; He et al., 2021). For example, Li et al. (2018b) found that the production efficiency of depressurization can be greatly enhanced by using the electrical heating simultaneously for the methane hydrate in a cuboid pressure vessel. In their experiment, a resistance heating wire is distributed uniformly in the inner surface of the well, and the whole well can be heated evenly when direct current is supplied to the wire. On the other hand, electrical heating was performed through the application of alternating current using two end caps as a pair of electrodes in the experiments by Minagawa et al. (2018), which suppressed the decrease in the temperature of NGH sediment core and enabled higher gas production when combined with depressurization. In addition, Wan et al. (2020b) proposed a novel tripartite strategy of electrical resistance heating, room temperature water flooding, and depressurization which combines the advantages of simultaneously reducing heat loss and enhanced heat transfer by convection and results in the best energy recovery efficiency among different thermal stimulation modes in a high-pressure reactor using two vertical wells. In addition to laboratory experiments, several numerical simulations were also conducted on the gas production of hydrate dissociation by electrical heating combined with depressurization (Wan et al., 2020a; Li et al., 2020; Zhao et al., 2021; Liu et al., 2022), but mainly performed in the laboratory scale. Wan et al. (2020a) conducted simulations of wellbore heating with depressurization for gas production from hydrate sediments in a rectangular cylinder model. Their results showed that a combination of depressurization and wellbore heating is more favorable for the enhancement of heat transfer and faster energy recovery. Similarly, in a laboratory-scale axisymmetric model, Liu et al. (2022) conducted simulations on the gas production behavior from the depressurization-induced dissociation of methane hydrate by electrical heating and on the optimization of the electrical heating scheme to achieve high-efficient utilization of electrical energy. However, the numerical simulations in the reservoir scale are rare, and recently Zhao et al. (2021) numerically evaluated the production performance of the low-frequency electrical heating–assisted depressurization (LF-EHAD) method for methane recovery from hydrate deposits in the Shenhu area of the SCS. In addition, the LF-EHAD method significantly enhances hydrate dissociation and gas production over the depressurization method and outperforms hot water flooding in higher energy utilization efficiency. Due to the large gap between laboratory and reservoir conditions, it is necessary to further numerically investigate the methane production from the NGH by electrical heating–assisted depressurization in field scale.

Therefore, the goal of this study is to numerically evaluate the performance of the combined brine flooding with electrical heating–assisted depressurization for hydrate exploitation in the Shenhu area of the SCS. The tripartite exploitation strategy with brine injection given by Wan et al. (2020b) is utilized because the simulation results of hydrate exploitation in field scale by *in situ* electrical heating show limitation of the high-temperature region and existing mainly near the heating wellbore due to the low thermal conductivity of hydrate deposits (Li et al., 2020). In consideration of the obvious advantages of horizontal wells over vertical wells, such as increasing single-well controlled reserves and gas production and reducing the risks of generating secondary hydrates and freezing (Feng et al., 2015; Ye et al., 2020), we adopt the same well configuration as done by Feng et al. (2014), that is, horizontal wells in the same horizontal plane. In addition, the pure depressurization method is also conducted as a comparison. In order to optimize the novel tripartite strategy, numerical results of methane recovery, water production and energy efficiency from different electrical heating times and power, and brine injection pressure are provided in detail and comprehensively analyzed. It is hoped that our numerical results in this study will provide reference and guidance for the development of similar low-permeability marine clayey–silt NGH with permeable surrounding water zones.

MATERIALS AND METHODS

Geological Setting of Study Area

The Shenhu area is near southeast of Shenhu Underwater Sandy Bench in the middle of the north slope of the SCS, between Xisha Trough and Dongsha Islands. Tectonically, the research area is

located in the Zhu II Depression, Pearl River Mouth Basin (**Figure 1**), which has been in the process of tectonic subsidence since the middle Miocene along with a high sedimentation rate, providing abundant organic matter (producing methane by pyrolysis or biological action) for the NGH (Wu et al., 2010). Large-scale mud diapirs, vertical fissure systems, and highly angled fractures were formed by tectonic movements, which can provide conduits for gas migration (Sun et al., 2019). The bottom temperature of the Shenhu area is 3.3–3.7°C with a geothermal gradient of 45–67°C/km, and the bottom pressure is more than 10 MPa (Yang et al., 2010; Sun et al., 2015), which meets the favorable temperature and pressure conditions for the formation of the hydrate reservoir. Therefore, this area becomes one of the most promising fields for gas hydrate exploitation.

In this study, we focused on the hydrate deposits that occur at the site SH2 drilled in GMGS1 because of high hydrate saturation and substantial amount of available data. The water depth at SH2 is 1,235 m. The HBL is 40 m thick overlain by a permeable overburden of 188 m thick and underlain by a permeable zone of mobile water. Based on the drilling and sampling data, the hydrate saturation ranges from 25 to 48%, and the porosity ranges from 0.33 to 0.48, which implies that a huge amount of natural gas is stored in the hydrate deposits. The hydrate disseminates in the sediments that mainly comprise silty clay and clay silt. In addition, it is detected that the gases contained in the hydrate in SH2 mainly consist of methane (96.10–99.91%) with minor quantities of ethane and propane (Wu et al., 2010).

Model Setup and Well Configuration

Based on the geological setting of SH2 of the Shenhu area in the SCS, the established conceptual model for numerical simulation and well configuration is shown in **Figure 2A**. The conceptual model consists of three horizontal layers including the 40-m-thick HBL and 30-m-thick permeable overburden and underburden water-bearing stratums (100 m in total), which are thought to be sufficient to accurately calculate the heat transfer to the HBL during the 20 years of production (Moridis and Reagan, 2011). The hydrate in the HBL is assumed to only comprise methane with a saturation of 0.4, and the remaining pore space is occupied by water with a saturation of 0.6. The porosity and intrinsic permeability of the HBL are, respectively, 0.38 and 10 millidarcy (mD). Due to lack of relevant information, the lithology of the surrounding water-bearing stratums is assumed to be same as the HBL but lacking hydrate. The values of simulation parameters used in our numerical model are summarized in **Table 1**.

As shown in **Figure 2A**, three horizontal wells are adopted in our study considering their obvious advantages over vertical wells, such as increasing single-well controlled reserves and gas production and reducing the risks of generating secondary hydrates and freezing (Feng et al., 2015; Ye et al., 2020). In order to avoid water and gas leakage, the vertical part of wells is sealed and the opened horizontal part with a length of 1,000 m is located at the middle of the HBL. Same as the study by Moridis et al. (2013), the interior of the wells is defined as pseudo porous media approximately, which has a high porosity of 1.0, a high permeability of 1.0×10^{-6} m^{2,} and a low capillary pressure of 0. Two side wells are conducted at a constant pressure to produce methane for the whole exploitation period (20 years). However, the middle well is first used to depressurize for 5 years in order to dissociate the hydrate and increase the permeability around the well. Then, thermal simulation starts by the flowing electric current through the resistance wire around the middle well. At the same time, a brine of 20°C (directly from sea) is also injected into hydrate formation at a constant pressure by the middle well, which can carry the electrical heat deep into the HBL.

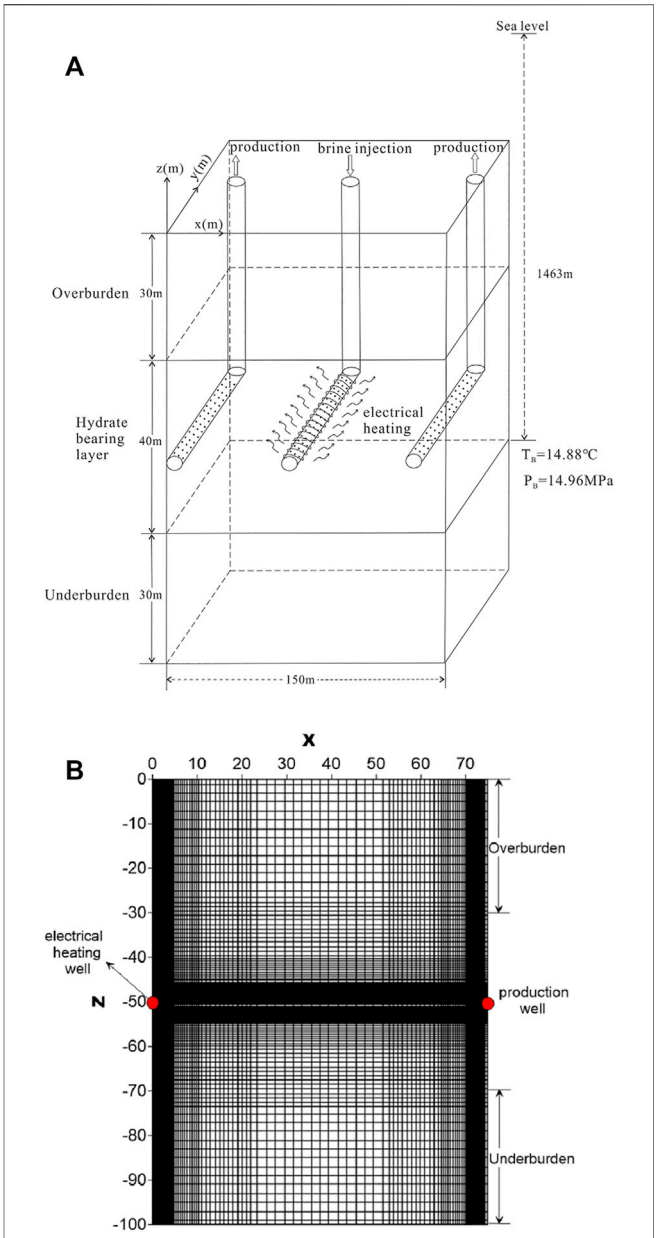

FIGURE 2 | Schematic diagrams of **(A)** the conceptual model and the well configuration and **(B)** domain discretization mesh used in our numerical simulations. The outside of the middle well is surrounded by the electric resistance wire which can release heat when current flows by.

TABLE 1 | Reference hydrate deposit properties and parameters in simulations.

Parameter	Value
The thickness of water-bearing stratums (m)	30
The thickness of the HBL (m)	40
Initial water and hydrate saturation of the HBL (S_A, S_H)	$S_A = 0.6$, $S_H = 0.4$
Gas composition	100% CH_4
Porosity of all layers	0.38
Permeability of all layers (mD)	10
The depth of the base of the HBL (m)	1,463
The average density of sea water (kg/m^3)	1,035
Initial pressure of the base of the HBL (MPa)	14.96
Initial temperature of the base of the HBL (°C)	14.88
Geothermal gradient (°C/m)	0.047
Pore water salinity (mass fraction)	0.03
Grain density of all layers (kg/m^3)	2,600
Compression coefficient of all layers (Pa^{-1})	1.0×10^{-8}
Wet formation thermal conductivity of all layers (W/m/°C)	3.1
Dry formation thermal conductivity of all layers (W/m/°C)	1.0
Rock grain specific heat of all layers (J/kg/°C)	1,000
Relative permeability model of liquid and gas phases (K_{rA}, K_{rG}) Moridis (2014)	$K_{rA} = [(S_A - S_{irA})/(1 - S_{irA})]^n, K_{rG} = [(S_G - S_{irG})/(1 - S_{irA})]^{n_G}$
n (index for aqueous phase)	5
n_G (index for gas phase)	3.5
S_{irA} (irreducible aqueous saturation)	0.30
S_{irG} (irreducible gas saturation)	0.03
Capillary pressure model (P_{cap}) Vangenuchten (1980)	$P_{cap} = -P_0[(S^*)^{-1/\lambda} - 1]^{1-\lambda}, S^* = (S_A - S_{irA})/(S_{mxA} - S_{irA})$
S_{mxA} (maximal aqueous saturation)	1
λ (index for pore structure)	0.45
P_0 (Pa) (the entry capillary pressure)	1.0×10^5

A unit width (1 m) in y direction is used without considering the pressure and temperature drop in the wellbore of the horizontal wells. In addition, a mild well spacing of 75 m is adopted, considering that small well spacing controls less reserves and big well spacing may go beyond the influence radius of the injected electrical heat (Jin et al., 2016). In addition, due to symmetric well configuration, only half of the hydrate deposits need to be simulated. Therefore, the size of the 2D numerical model is 75 m × 100 m in x and z directions, which is discretized into 101 × 114 = 11,514 grid blocks (**Figure 2B**). Because the vicinity of the wellbore had been shown to be critically important to production (Moridis et al., 2009b), a very fine discretization of 0.25 m was used around the horizontal wells. In addition, the spacing intervals increase with the distance to wells, which reaches a size of 2 m at the middle between the wells and at the top and bottom of the model.

The numerical simulator used for the simulation of the behavior of hydrate-bearing geologic systems in this study is TOUGH + HYDRATE, which was developed by the Lawrence Berkeley National Laboratory (Moridis, 2014). The initial distributions of pressure and temperature are, respectively, obtained by hydrostatic pressure distribution and a geothermal gradient of 0.047°C/m (Moridis et al., 2007; Su et al., 2012b). In addition, the base of the HBL initially lies in the hydrate equilibrium condition. As for boundary conditions, constant temperature and pressure boundary are applied to the top and the bottom of the model, and non-flow boundary is applied at x = 0 and x = 75 m during the whole exploitation period (Su et al., 2012a, 2012b; Li et al., 2013).

Simulation Scenarios

The factors that are related to gas production performance of a hydrate deposit can be divided into two classes: formation conditions and artificial operations. The most related formation condition is the permeability of the HBL, which can be improved by hydraulic fracturing, but not involved in our research. Therefore, we mainly consider optimizing artificial operations to promote the exploitation of the NGH, including electrical heating time and power and brine injection pressure, whose effects to gas production are investigated by different exploitation scenarios listed in **Table 2**. As the base case, A0 adopts a brine injection pressure of 17 MPa, which corresponds to the maximum of the wellbore pressure to avoid the overpressure of the HBL (Li et al., 2011). In addition, 2,000 W of electrical heating is applied to the same 2D-simulated hydrate deposit of 75 m × 100 m. In addition, the only depressurization method D1 is also included to verify the feasibility of the new exploitation method of combined brine flooding with electrical heating–assisted depressurization. The production pressures of all scenarios are set to be 8 MPa, which is larger than the pressure at the quadruple point to eliminate the possibility of ice formation.

The following criteria are used to compare the gas production performance of different exploitation scenarios: volumetric rate of total produced methane from wells (Q_P) and volumetric rate of produced methane in gas phase (Q_{PG}), volumetric rate of released methane by hydrate dissociation (Q_R), and volumetric rate of produced water (Q_W); cumulative volume of methane and water produced from wells (V_P and V_W, respectively), gas-to-water ratio (R_{GW}); energy efficiency ratio (η) and net energy gain (E_{net}).

TABLE 2 | Summary of simulation scenarios and part of the simulation results.

Run	Description	P_{pro} (MPa)	P_{inj} (MPa)	P_{ele} (W)	S_R	R_{GW}	η	V_P ($10^8 m^3$)	E_{net} (10^{15}J)
A0	Base case	8	17	2,000	1	6.32	2.33	1.37	2.93
A1	Sensitivity of electrical heating time	8	17	2,000	**0.5**	4.98	5.25	1.09	3.32
A2		8	17	2,000	**0.7**	6.05	3.86	1.30	3.62
B1	Sensitivity of electrical heating power	8	17	**1,000**	0.7	5.21	4.64	1.14	3.37
B2		8	17	**3,000**	0.7	6.38	3.31	1.37	3.61
C1	Sensitivity of brine injection pressure	8	**15**	2,000	0.7	4.54	2.40	1.03	2.25
C2		8	**19**	2,000	0.7	6.43	4.27	1.35	3.90
D1	Only depressurization	8	—	—	—	2.20	5.65	0.97	3.00

Note: P_{pro} is production pressure, P_{inj} is brine injection pressure, P_{ele} is electrical heating power, S_R is the rate of the dissociated hydrate to the initial hydrate when electrical heating stops, and S_R = 1 means electrical heating lasts until the end of simulation. All values in bold denote the investigated parameters needed to be optimized. Part of the simulation results are also given in order to make a comparison of different scenarios, including the gas-to-water ratio (R_{GW}), energy efficiency ratio (η), the cumulative volume of produced methane (V_P), and the net energy gain (E_{net}).

Among these criteria, four of them are particularly important, which can also be classified as relative criterion (R_{GW} and η) and absolute criterion (V_P and E_{net}), which are also listed in **Table 2**. R_{GW} is defined as the ratio of V_P and V_W, while η is the ratio of the recovered energy to the total consumed energy, which can be defined as

$$\boldsymbol{\eta} = \boldsymbol{n} \cdot \Delta \boldsymbol{H_c} \,/\, (\boldsymbol{W} + \boldsymbol{Q}), \tag{1}$$

where ΔH_c is the combustion enthalpy of methane (1 atm, 25°C, 889.6 kJ/mol); n is the amount of substance of the produced methane (mol); W is the energy used for pumping the produced fluids to the ground (kJ); and Q is the total electrical energy injected into the reservoir (kJ). High R_{GW} and η, respectively, indicate satisfying production efficiency and economic performance. Other than the relative criterion, the potential of a specific exploitation scenario can also be validated by a large V_P and E_{net} in the sense of absolute criteria. E_{net} is the difference of the recovered energy with consumed energy calculated as follows:

$$\boldsymbol{E_{net}} = \boldsymbol{n} \cdot \Delta \boldsymbol{H_c} \cdot \left(1 - 1/\boldsymbol{\eta}\right). \tag{2}$$

In order to simulate actual exploitation conditions, all of these criteria are scaled according to the length of the horizontal wells (1,000 m).

RESULTS AND DISCUSSION

Effects of Combined Brine Flooding With Electrical Heating

The exploitation scenario of pure depressurization is first simulated and evaluated, whose methane volumetric rate and water production are shown in **Figure 3**. As shown in **Figure 3A**, the hydrate is rapidly dissociated by depressurization in the initial stage due to the largest pressure difference between production wells and formation, known as pressure driving force. Therefore, Q_R and Q_P, respectively, reach a maximum of 260,000 m^3/day and 43,000 m^3/day in a short time. In addition, Q_R is larger than Q_P in the first 580 days, indicating that the released methane cannot be produced in time due to the low permeability of the HBL. With the reduction of pressure driving force and exhaustion of the hydrate around production wells, Q_R rapidly drops below Q_P, and the remaining methane is discharged from production wells. Then, Q_P and Q_R almost keep stable before a sudden decrease happening at 5 years. The reason is that the hydrate between the HBL and surrounding permeable water-bearing stratums is completely dissociated, resulting in rapid water invasion, proven by the sudden increase of the water-produced rate (Q_W) at 5 years in **Figure 3B**. Massive water production slows down the propagation of low pressure. Therefore, Q_P and Q_R keep decreasing with a similar trend and reach a value of 6,500 m^3/day at the end of simulation, which is much lower than the commercially viable production rate.

However, Q_W keeps increasing in the whole simulation process due to increase of formation permeability after hydrate dissociation and the influence of permeable water-bearing stratums. The different variations of Q_P and Q_W indicate that gas production is controlled by methane from hydrate dissociation rather than original methane dissolved in *in situ* water. In addition, the released methane can be produced in free gas or in dissolution. Initially, due to rapid release of methane from hydrate dissociation, free gas takes a large proportion of the total produced methane. However, Q_G gradually decreases with reduction of Q_R and becomes zero at 2,650 days, indicating that methane is produced completely in dissolution after then. The relative criterion (R_{GW} and η) and absolute criterion (V_P and E_{net}) to judge gas production performance are given in **Figure 4**. At the end of the simulation, the cumulative volume of the produced methane for only depressurization is 9.7×10^7 m^3, corresponding to an average production rate of 13,275 m^3/day. With the increase of the produced water rate and the decrease of produced methane rate, R_{GW} and η of only depressurization keeps descending, respectively, with a final value of 2.20 and 5.65.

From the previous analysis, only depressurization is inefficient for the challenging hydrate deposit with permeable overlying and underlying layers. The hydrate dissociation rate and methane production rate will rapidly decrease when the water from the surrounding permeable layers invades into the HBL. Therefore, thermal stimulation by combined brine flooding with electrical heating is conducted after 5 years of only depressurization in order to promote hydrate dissociation. For the base case, brine injection (20°C) at a constant pressure of 17 MPa and electrical

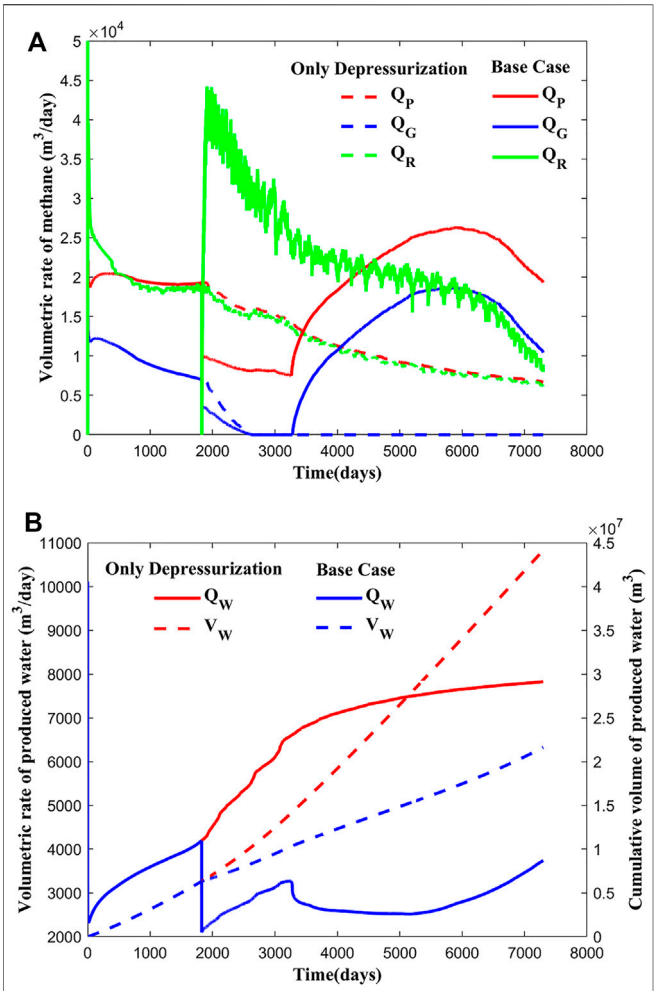

FIGURE 3 | Evolution of **(A)** methane production rate (Q_P), methane production rate in gaseous phase (Q_{PG}) and release rate (Q_R), **(B)** water production rate (Q_W) and water production volume (V_W) for the only depressurization method and combined brine flooding with electrical heating–assisted depressurization method (the base-case). The unit of the volumetric rate is measured at standard temperature and pressure.

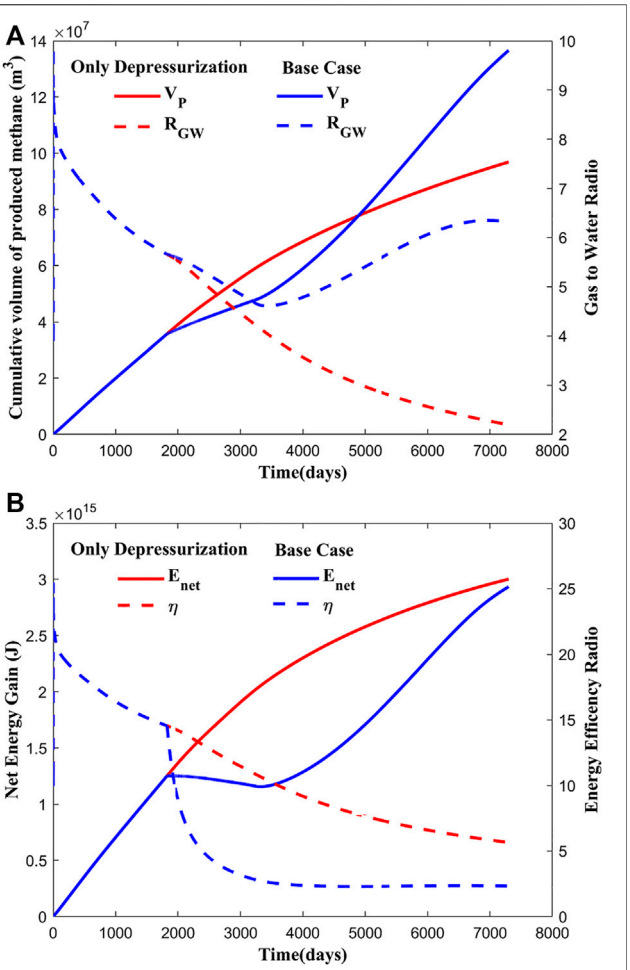

FIGURE 4 | Evolution of **(A)** methane production volume (V_P) and gas-to-water ratio (R_{GW}), **(B)** energy efficiency ratio (η) and net energy gain (E_{net}) for the only depressurization method and combined brine flooding with electrical heating–assisted depressurization method (the base-case).

heating with a power of 2,000 W are simultaneously applied to the left well, while the other well is still used for depressurization at a constant pressure of 8 MPa. For comparison with only depressurization, methane production, water production, and energy gain of the base case are also given in **Figures 3**, **4**. In addition, **Figures 5–8**, respectively, show the evolution of temperature (T), hydrate saturation (S_H), gas saturation (S_G) and salinity (X_{inh}) of the base case in order to figure out the variation of the system state over time under thermal stimulation.

When thermal stimulation starts at 5 years, Q_R of the base case rapidly increases and reaches a peak of 45,000 m^3/day, proving that hydrate dissociation is accelerated by the electrical heat, which is carried by the brine into the deep of the HBL. On the other hand, the vacated pore space after hydrate dissociation increases the permeability of formation, which is beneficial to the flow of the heated brine. As a result, hydrate complete dissociation area and high-temperature region around the injection well move rapidly toward the production well (**Figures 5**, **6**). Contrary to the immediate increase of Q_R, Q_P and Q_{PG} first drop by half after thermal stimulation due to the halving of production wells and then keep decreasing until 3,280 days. During this stage, the released methane is detained in the HBL due to the distance between the wells, which leads to the increase of gas saturation (**Figures 7A,B**). Therefore, further dissociation of the hydrate is suppressed, and Q_R gradually decreases.

When the released methane reaches the production well at 3,280 days (**Figure 7C**), Q_P and Q_G start rapidly increasing, which is 1,455 days later than the increase of Q_R. Then, Q_P exceeds Q_R at 4,420 days and reaches a peak of 6,140 m^3/day at around 6,000 days, indicating that the detained methane is gradually produced. After 6,000 days, a quick drop of Q_R (as well as Q_P and Q_{PG}) appears due to the exhaustion of the hydrate, validated by the small green part in **Figures 6E,F**. In addition, the similar variation between Q_P and Q_{PG} indicates that gaseous methane makes the main contribution of the increase of Q_P after

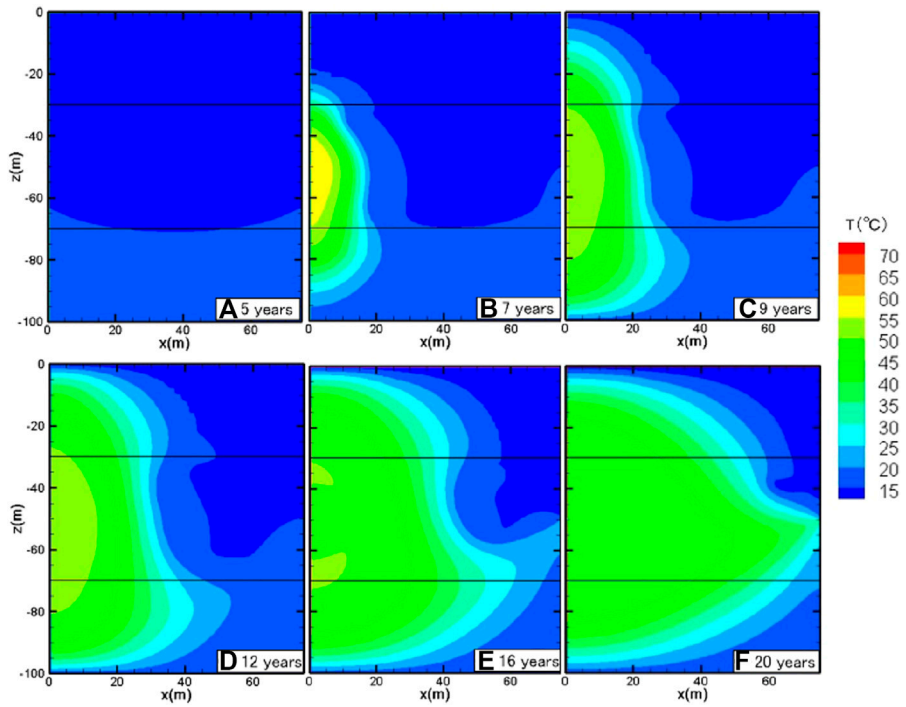

FIGURE 5 | Evolution of spatial distributions of temperature (T) over time: **(A)** 5 years, **(B)** 7 years, **(C)** 9 years, **(D)** 12 years, **(E)** 16 years, and **(F)** 20 years for the combined brine flooding with electrical heating–assisted depressurization method (the base-case).

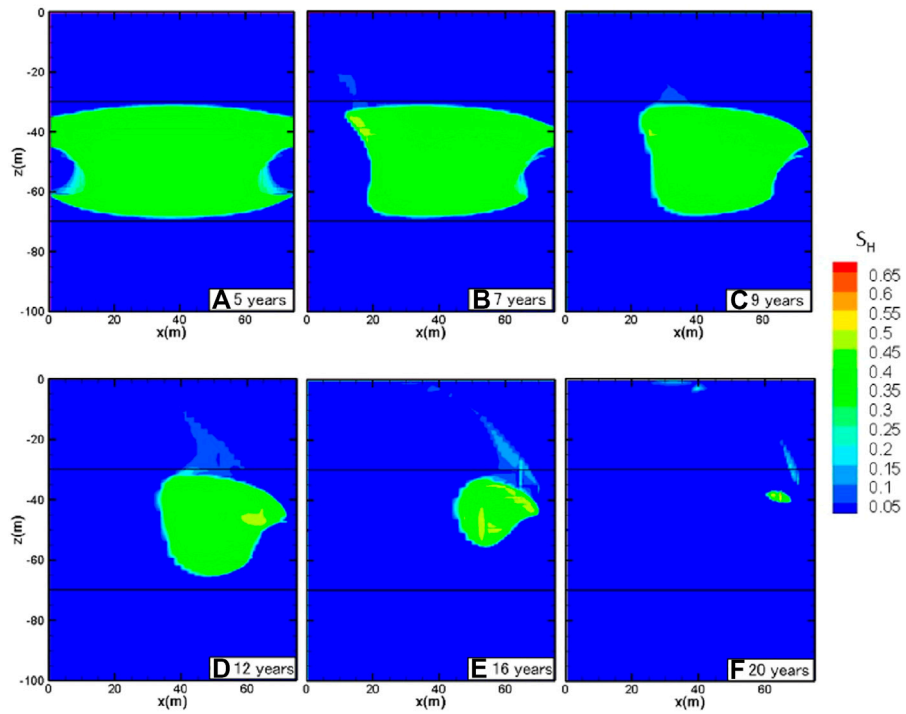

FIGURE 6 | Evolution of spatial distributions of hydrate saturation (S_H) over time: **(A)** 5 years, **(B)** 7 years, **(C)** 9 years, **(D)** 12 years, **(E)** 16 years, and **(F)** 20 years for the combined brine flooding with electrical heating–assisted depressurization method (the base-case).

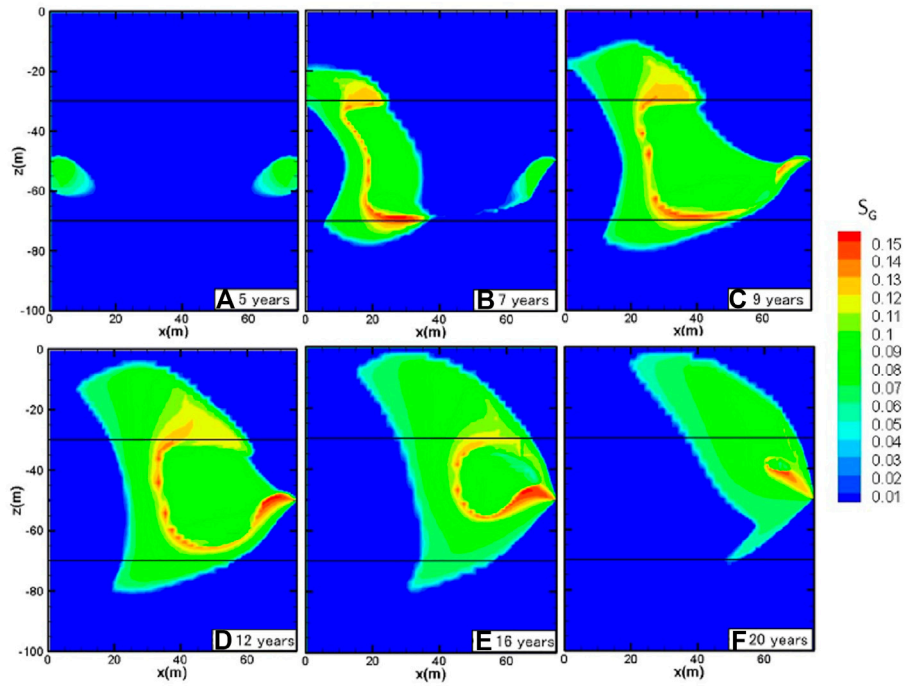

FIGURE 7 | Evolution of spatial distributions of gas saturation (S_G) over time: **(A)** 5 years, **(B)** 7 years, **(C)** 9 years, **(D)** 12 years, **(E)** 16 years, and **(F)** 20 years for the combined brine flooding with electrical heating–assisted depressurization method (the base-case).

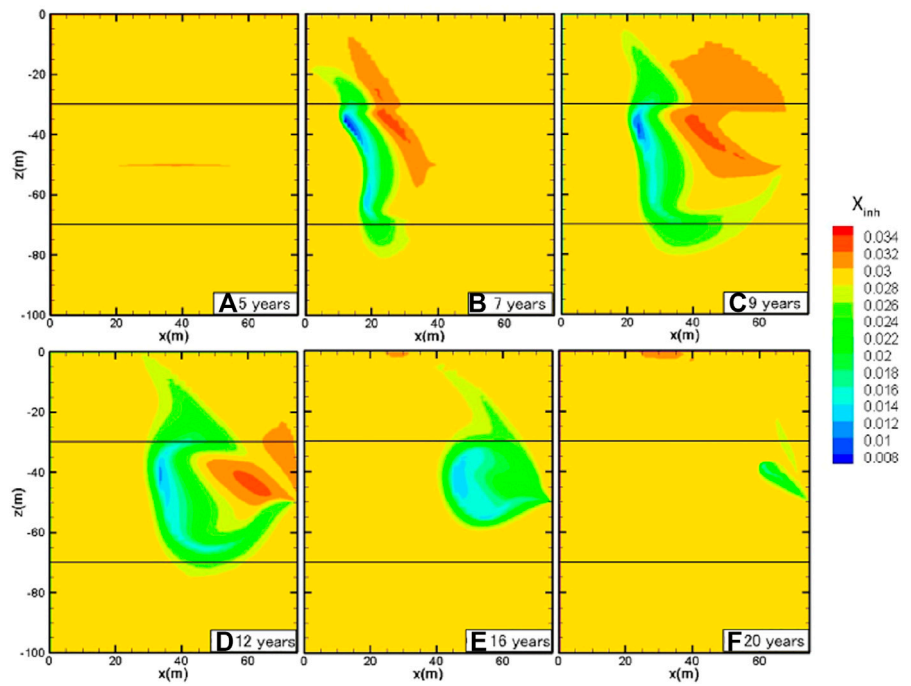

FIGURE 8 | Evolution of spatial distributions of salinity (X_{inh}) over time: **(A)** 5 years, **(B)** 7 years, **(C)** 9 years, (D) 12 years, **(E)** 16 years, and **(F)** 20 years for the combined brine flooding with electrical heating–assisted depressurization method (the base-case).

thermal stimulation. As shown in **Figure 8**, a high salinity abnormal forms at the behind of the dissociation interfaces around the injection well. This is a sign of secondary hydrate formation because that salt is excluded from the lattice of the hydrate, which originates from the pressure increment by brine injection and should be responsible for the fluctuations of Q_R after thermal stimulation. With the exhaustion of the hydrate, the high salinity abnormal gradually disappears.

Different from the continuous increase of the water production rate of only depressurization, water production of the base case is suppressed when the released methane reaches the production well, because the relative permeability of water is inversely proportional to gas saturation. With the discharge of methane and increase of absolute permeability of formation, Q_W increases again after 5,500 days but is still much lower than that of only depressurization. From **Figure 4A**, thermal stimulation by combined brine flooding with electrical heating can greatly increase methane recovery, with a higher V_P (except the period before methane reaches production well) and R_{GW} over only depressurization. At the end of the simulation, the cumulative volume of the produced methane is increased by 41% with thermal stimulation. However, the net energy gain of the base case shows no improvement over only depressurization because the additional methane recovery is offset by massive injected electrical heat, and a rather low energy efficiency ratio of 2.33 is obtained by thermal stimulation. Therefore, the energy efficiency of the combined brine flooding with electrical heating–assisted depressurization needs to be improved before field application.

Sensitivity Analysis of Electrical Heating Time

In order to save energy and gain a higher energy efficiency, electrical heating should be terminated at the later stage of the base case because there is only little hydrate left (**Figures 6E,F**). Therefore, another two runs of A1 and A2 are conducted to determine the effects of the electrical heating time, which, respectively, terminate electrical heating when the rate of the dissociated hydrate to the initial hydrate (S_R) reaches 0.5 (at 3,156 days) and 0.7 (at 4,579 days). The base case corresponds to an S_R of 1.0, which means that electrical heating lasts until the end of the simulation. Though electrical heating stops at an earlier time for A1 and A2, brine of 20°C is still injected into the HBL with an injection pressure of 17 MPa to assist the drainage of methane. As shown in **Figure 9A**, longer electrical heating time leads to a higher Q_P due to more hydrate dissociation. In addition, the termination of electrical heating results in the increase of Q_W on account of the alleviation of water production restriction by the reduction of gas saturation around the production well (**Figure 9B**). However, Q_W increases with increasing of S_R at the end of the simulation because more vacated pore space for a longer electrical heating time leads to higher formation permeability. In addition, the final V_W is almost equal for different electrical heating times.

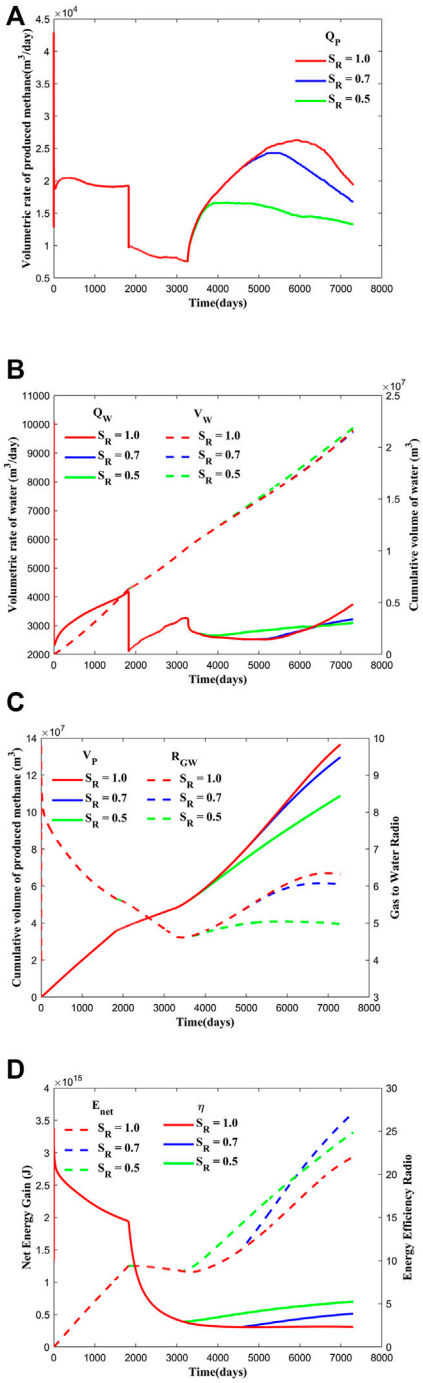

FIGURE 9 | Evolution of **(A)** methane production rate (Q_P), **(B)** water production rate (Q_W) and water production volume (V_W), **(C)** methane production volume (V_P) and gas-to-water ratio (R_{GW}), and **(D)** energy efficiency ratio (η) and net energy gain (E_{net}) under different electrical heating times.

The optimization of electrical heating time can be achieved by the criteria shown in **Figures 9C,D**. Compared with the base case, V_P only decreases by 5.1%, but the injected heat is reduced by 49.7% for terminating electrical heating when 70% hydrate has already been dissociated (SR = 0.7). Therefore, the energy

efficiency and net energy gain can be greatly improved by decreasing electrical heating time. However, further advancing the termination of electrical heating with an S_R of 0.5 decreases V_P by 16.1%, and the net energy gain is lower than that of terminating electrical heating with an S_R of 0.7, indicating that stopping electrical heating prematurely is disadvantageous to methane production due to insufficient hydrate dissociation, even though a higher energy efficiency ratio is obtained. Therefore, a medium electrical heating time is preferred for gas production from hydrate deposit in order to accelerate hydrate dissociation and gain satisfactory energy efficiency. Thus, the subsequent simulations all terminate electrical heating when 70% of hydrate is dissociated in order to avoid massive energy waste.

Sensitivity Analysis of Electrical Heating Power

Apparently, the gas production performance of the combined brine flooding with electrical heating–assisted depressurization is closely related to electrical heating power. Therefore, another two simulations with a power of 1,000 W (B1) and 3,000 W (B2) are conducted to explore the effects of electrical heating power. The two additional simulations adopt same parameters as A2 except the electrical heating power, which also terminate electrical heating when 70% hydrate has already been dissociated in order to save energy. As shown in **Figure 10A**, Q_P initially increases with electrical heating power because of the accelerated hydrate dissociation. Moreover, a larger power not only induces earlier increase of Q_P due to advanced breakthrough of released methane from the injection well to the production well but also induces earlier drop of Q_P due to the advanced termination of electrical heating. In addition, faster exhaustion of the hydrate induces that Q_P decreases with increasing of the electrical heating power at the end of the simulation. Contrary to Q_P, a larger power leads to a lower Q_W at an early time and a higher Q_W at a later time (**Figure 10B**). The different variation of methane production and water production is reasonable considering that the relative permeability of gas phase and aqueous phase change oppositely at all times. In addition, the final V_W is basically unchanged with electrical heating power.

The relative criteria and absolute criteria are also given in **Figures 10C,D** in order to optimize the electrical heating power. From **Figure 10C**, V_P and R_{GW} increase with the electrical heating power though with a decreasing rate. Compared with the electrical heating power of 2,000 W, V_P increases by 5.9% for the electrical heating power of 3,000 W, while V_P decreases by 12.0% for the electrical heating power of 1,000 W. Thus, a low electrical heating power of 1,000 W is inefficient for gas production from the hydrate deposit though with a high energy efficiency ratio (**Figure 10D**). In addition, the net energy gain of 2,000 and 3,000 W is basically the same, indicating that the additional recovered methane just catches up with the enlarged electrical heat injection. At the same time, increasing electrical heating power also enlarges the risks of wellbore failure due to thermal stress variation. Therefore, a mild electrical heating power is preferred for increasing methane recovery and reducing geological risks.

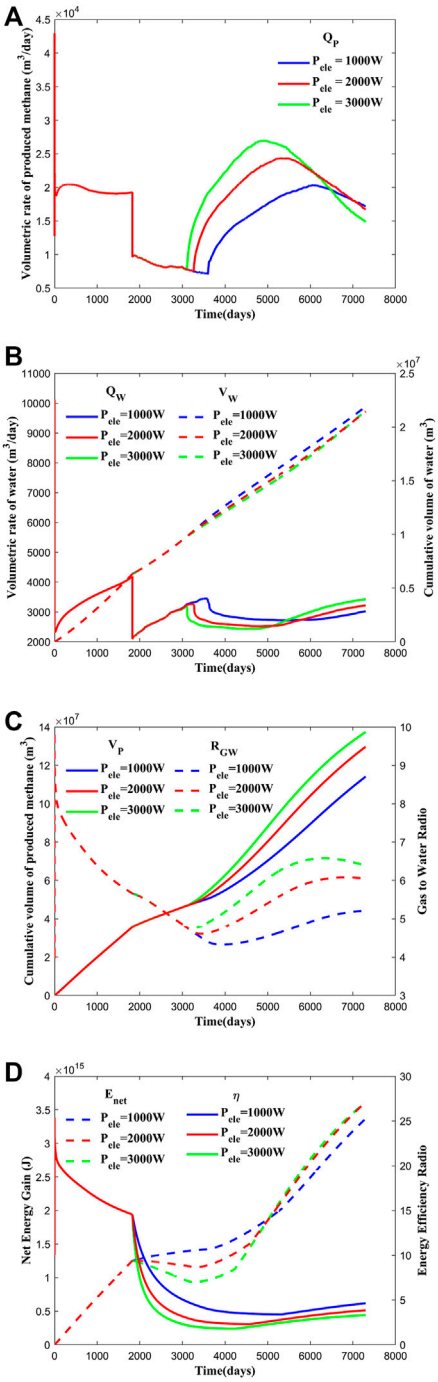

FIGURE 10 | Evolution of **(A)** methane production rate (Q_P), **(B)** water production rate (Q_W) and water production volume (V_W) under different electrical heating powers, **(C)** methane production volume (V_P) and gas-to-water ratio (R_{GW}), and **(D)** energy efficiency ratio (η) and net energy gain (E_{net}) under different electrical heating powers.

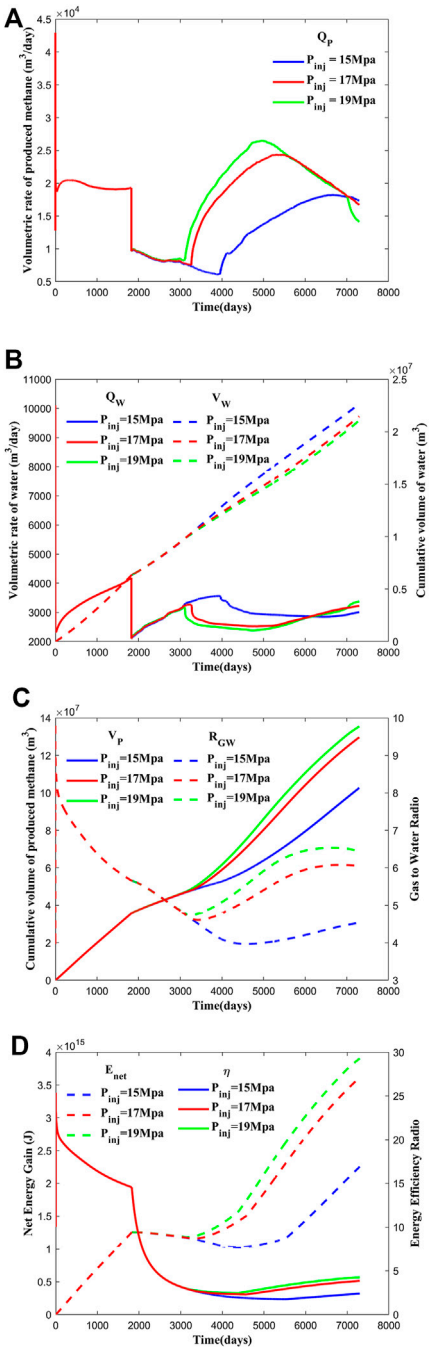

FIGURE 11 | Evolution of **(A)** methane production rate (Q_P), **(B)** water production rate (Q_W) and water production volume (V_W), **(C)** methane production volume (V_P) and gas-to-water ratio (R_{GW}), and **(D)** energy efficiency ratio (η) and net energy gain (E_{net}) under different brine injection pressures.

Sensitivity Analysis of Brine Injection Pressure

Other than electrical heating power, brine injection pressure is also a key parameter related to gas production performance, whose effects are determined by another two procedures with injection pressure of 15 MPa (C1) and 19 MPa (C2). Except brine injection pressure, other parameters of C1 and C2 are the same as A2. From the simulation results of methane and water production shown in **Figures 11A,B**, Q_P initially increases with injection pressure because of faster brine injection, leading to a larger heat diffusion rate. Driven by larger pressure gradient between wells, faster breakthrough of released methane is also realized by higher injection pressure. At the same time, the advanced termination of electrical heating after 70% of hydrate dissociation for higher injection pressure induces an earlier drop and a lower final value of Q_P. As clarified before, Q_W still varies oppositely with Q_P. However, a confusing phenomenon of water production is that larger injection pressure, instead, possesses a lower final V_W. This can be explained as more methane accumulation around the production well by higher injection pressure results in a stronger suppression of water production in the early stage of the thermal stimulation.

The superiority of higher brine injection pressure is adequately verified by higher methane recovery and gas-to-water ratio (**Figure 11C**), as well as the higher energy efficiency ratio and net energy gain (**Figure 11D**). Raising brine injection pressure from 15 to 17 MPa increases E_{net} by 60.4%, while further raising injection pressure to 19 MPa only increases E_{net} by 8.0%. On the other hand, higher injection pressure also enlarges the risks of geological hazards, such as reservoir instability and submarine landslide. Therefore, the selection of brine injection pressure should be carefully and comprehensively considered regarding the factors of gas production and geological risks.

CONCLUSION

This study numerically verifies the feasibility of combined brine flooding with electrical heating–assisted depressurization in horizontal wells to improve gas production from the natural gas hydrate in the Shenhu area of the South China Sea. By analyzing the simulation results of methane recovery, water production, and energy gain, the optimizations of electrical heating time and power and brine injection pressure are achieved, and the following conclusions can be drawn:

Thermal stimulation by combined brine flooding with electrical heating can greatly improve methane recovery. After 20 years of production, the cumulative methane production of combined brine injection with electrical heating–assisted depressurization is 1.41 times of that conducted by the only depressurization method. However, the rather low energy efficiency ratio of the thermal stimulation method results in a similar net energy gain with the only depressurization method.

In order to improve energy efficiency, the advanced termination of electrical heating is proposed and numerically evaluated. The simulation results of three different termination times indicate that stopping electrical heating prematurely is disadvantageous to methane production due to insufficient hydrate dissociation. At the same time, keeping on electrical heating after 70% of hydrate dissociation results in massive energy wastes. Therefore, a medium electrical heating time is preferred for gas production from the hydrate deposit, whose superiority is proven by the largest net energy gain and a satisfactory energy efficiency ratio.

Increasing electrical heating power and brine injection pressure leads to better exploitation performance with higher methane recovery and net energy gain. However, the degree of improvement is gradually weakened after a certain threshold; in the meantime, the risks of wellbore and reservoir failures increase with these factors. Therefore, the selection of electrical heating power and injection pressure should be performed carefully and comprehensively, considering both the efficiency of the gas recovery and the risks of geological hazard.

This study only optimized the artificial operations of the tripartite exploitation strategy, however, the effect of reservoir physical property, hydrate saturation, and fluid component on the gas recovery has not yet been well-revealed and will be our next stage of investigation. In addition, comprehensive comparison with other electrical heating methods, for example, low-frequency electrical heating and electromagnetic heating, remains to be conducted.

DATA AVAILABILITY STATEMENT

The raw data supporting the conclusion of this article will be made available by the authors, without undue reservation.

AUTHOR CONTRIBUTIONS

QZ: conceptualization, methodology, data curation, visualization, and writing—original draft. YW: conceptualization, methodology, visualization, writing—review and editing, and supervision.

FUNDING

The research is supported by the Original Innovation Research Program of the Chinese Academy of Sciences (CAS) under Grant number ZDBS-LY-DQC003, and the Key Research Program of the Institute of Geology and Geophysics, CAS under Grant numbers IGGCAS-2019031 and SZJJ-201901.

ACKNOWLEDGMENTS

We are grateful to editors and reviewers for important questions and suggestions.

REFERENCES

Boswell, R., and Collett, T. S. (2011). Current Perspectives on Gas Hydrate Resources. *Energy Environ. Sci.* 4 (4), 1206–1215. doi:10.1039/c0ee00203h

Chong, Z. R., Yang, S. H. B., Babu, P., Linga, P., and Li, X.-S. (2016). Review of Natural Gas Hydrates as an Energy Resource: Prospects and Challenges. *Appl. Energ.* 162, 1633–1652. doi:10.1016/j.apenergy.2014.12.061

Chong, Z. R., Yin, Z., Tan, J. H. C., and Linga, P. (2017). Experimental Investigations on Energy Recovery from Water-Saturated Hydrate Bearing Sediments via Depressurization Approach. *Appl. Energ.* 204, 1513–1525. doi:10.1016/j.apenergy.2017.04.031

Collett, T. S. (2002). Energy Resource Potential of Natural Gas Hydrates. *AAPG Bull.* 86 (11), 1971–1992. doi:10.1306/61eeddd2-173e-11d7-8645000102c1865d

Falser, S., Uchida, S., Palmer, A. C., Soga, K., and Tan, T. S. (2012). Increased Gas Production from Hydrates by Combining Depressurization with Heating of the Wellbore. *Energy Fuels* 26 (10), 6259–6267. doi:10.1021/ef3010652

Feng, J.-C., Li, G., Li, X.-S., Li, B., and Chen, Z.-Y. (2013). Evolution of Hydrate Dissociation by Warm Brine Stimulation Combined Depressurization in the South China Sea. *Energies* 6 (10), 5402–5425. doi:10.3390/en6105402

Feng, J.-C., Li, X.-S., Li, G., Li, B., Chen, Z.-Y., and Wang, Y. (2014). Numerical Investigation of Hydrate Dissociation Performance in the South China Sea with Different Horizontal Well Configurations. *Energies* 7 (8), 4813–4834. doi:10.3390/en7084813

Feng, J.-C., Wang, Y., Li, X.-S., Li, G., Zhang, Y., and Chen, Z.-Y. (2015). Effect of Horizontal and Vertical Well Patterns on Methane Hydrate Dissociation Behaviors in Pilot-Scale Hydrate Simulator. *Appl. Energ.* 145, 69–79. doi:10.1016/j.apenergy.2015.01.137

He, J., Li, X., Chen, Z., Li, Q., Zhang, Y., Wang, Y., et al. (2021). Combined Styles of Depressurization and Electrical Heating for Methane Hydrate Production. *Appl. Energ.* 282, 116112. doi:10.1016/j.apenergy.2020.116112

Jin, G., Xu, T., Xin, X., Wei, M., and Liu, C. (2016). Numerical Evaluation of the Methane Production from Unconfined Gas Hydrate-Bearing Sediment by thermal Stimulation and Depressurization in Shenhu Area, South China Sea. *J. Nat. Gas Sci. Eng.* 33, 497–508. doi:10.1016/j.jngse.2016.05.047

Koh, C. A., Sum, A. K., and Sloan, E. D. (2012). State of the Art: Natural Gas Hydrates as a Natural Resource. *J. Nat. Gas Sci. Eng.* 8, 132–138. doi:10.1016/j.jngse.2012.01.005

Koh, D.-Y., Kang, H., Lee, J.-W., Park, Y., Kim, S.-J., Lee, J., et al. (2016). Energy-Efficient Natural Gas Hydrate Production Using Gas Exchange. *Appl. Energ.* 162, 114–130. doi:10.1016/j.apenergy.2015.10.082

Koh, C. A. (2002). Towards a Fundamental Understanding of Natural Gas Hydrates. *Chem. Soc. Rev.* 31 (3), 157–167. doi:10.1039/b008672j

Konno, Y., Masuda, Y., Akamine, K., Naiki, M., and Nagao, J. (2016). Sustainable Gas Production from Methane Hydrate Reservoirs by the Cyclic Depressurization Method. *Energ. Convers. Manage.* 108, 439–445. doi:10.1016/j.enconman.2015.11.030

Li, G., Moridis, G. J., Zhang, K., and Li, X.-S. (2010). Evaluation of Gas Production Potential from Marine Gas Hydrate Deposits in Shenhu Area of South China Sea. *Energy Fuels* 24 (11), 6018–6033. doi:10.1021/ef100930m

Li, G., Moridis, G. J., Zhang, K., and Li, X.-s. (2011). The Use of Huff and Puff Method in a Single Horizontal Well in Gas Production from marine Gas Hydrate Deposits in the Shenhu Area of South China Sea. *J. Pet. Sci. Eng.* 77 (1), 49–68. doi:10.1016/j.petrol.2011.02.009

Li, G., Li, X.-S., Zhang, K., Li, B., and Zhang, Y. (2013). Effects of Impermeable Boundaries on Gas Production from Hydrate Accumulations in the Shenhu Area of the South China Sea. *Energies* 6 (8), 4078–4096. doi:10.3390/en6084078

Li, B., Liu, S.-D., Liang, Y.-P., and Liu, H. (2018a). The Use of Electrical Heating for the Enhancement of Gas Recovery from Methane Hydrate in Porous media. *Appl. Energ.* 227, 694–702. doi:10.1016/j.apenergy.2017.08.066

Li, J.-F., Ye, J. L., Ye, J.-L., Qin, X.-W., Qiu, H.-J., Wu, N.-Y., et al. (2018b). The First Offshore Natural Gas Hydrate Production Test in South China Sea. *China Geol.* 1 (1), 5–16. doi:10.31035/cg2018003

Li, L., Li, X., Wang, Y., Luo, Y., and Li, B. (2020). Analyzing the Applicability of *In Situ* Heating Methods in the Gas Production from Natural Gas Hydrate-Bearing Sediment with Field Scale Numerical Study. *Energ. Rep.* 6, 3291–3302. doi:10.1016/j.egyr.2020.11.208

Liang, Y.-P., Liu, S., Wan, Q.-C., Li, B., Liu, H., and Han, X. (2018). Comparison and Optimization of Methane Hydrate Production Process Using Different Methods in a Single Vertical Well. *Energies* 12 (1), 124. doi:10.3390/en12010124

Liang, Y., Tan, Y., Luo, Y., Zhang, Y., and Li, B. (2020). Progress and Challenges on Gas Production from Natural Gas Hydrate-Bearing Sediment. *J. Clean. Prod.* 261, 121061. doi:10.1016/j.jclepro.2020.121061

Liu, Y., Hou, J., Chen, Z., Su, H., Zhao, E., and Li, G. (2020). A Novel Natural Gas Hydrate Recovery Approach by Delivering Geothermal Energy through Dumpflooding. *Energ. Convers. Manage.* 209, 112623. doi:10.1016/j.enconman.2020.112623

Liu, S., Li, H., Wang, B., and Sun, B. (2022). Accelerating Gas Production of the Depressurization-Induced Natural Gas Hydrate by Electrical Heating. *J. Pet. Sci. Eng.* 208, 109735. doi:10.1016/j.petrol.2021.109735

Minagawa, H., Ito, T., Kimura, S., Kaneko, H., Noda, S., and Tenma, N. (2018). Depressurization and Electrical Heating of Methane Hydrate Sediment for Gas Production: Laboratory-Scale Experiments. *J. Nat. Gas Sci. Eng.* 50, 147–156. doi:10.1016/j.jngse.2017.10.024

Mokheimer, E. M. A., Hamdy, M., Abubakar, Z., Shakeel, M. R., Habib, M. A., and Mahmoud, M. (2019). A Comprehensive Review of Thermal Enhanced Oil Recovery: Techniques Evaluation. *J. Energ. Resour. Technol.-Trans. ASME* 141 (3), 030801. doi:10.1115/1.4041096

Moridis, G. J., and Reagan, M. T. (2011). Estimating the Upper Limit of Gas Production from Class 2 Hydrate Accumulations in the Permafrost: 1. Concepts, System Description, and the Production Base Case. *J. Pet. Sci. Eng.* 76 (3-4), 194–204. doi:10.1016/j.petrol.2010.11.023

Moridis, G. J., Collett, T. S., Dallimore, S. R., Satoh, T., Hancock, S., and Weatherill, B. (2004). Numerical Studies of Gas Production from Several CH4 Hydrate Zones at the Mallik Site, Mackenzie Delta, Canada. *J. Pet. Sci. Eng.* 43 (3-4), 219–238. doi:10.1016/j.petrol.2004.02.015

Moridis, G. J., Kowalsky, M. B., Pruess, K., and Lab, L. B. N. (2007). Depressurization-induced Gas Production from Class 1 Hydrate Deposits. *SPE Reserv. Eval. Eng.* 10 (5), 458–481. doi:10.2118/97266-Pa

Moridis, G. J., Collett, T. S., Boswell, R., Kurihara, M., Reagan, M. T., Koh, C., et al. (2009a). Toward Production from Gas Hydrates: Current Status, Assessment of Resources, and Simulation-Based Evaluation of Technology and Potential. *SPE Reserv. Eval. Eng.* 12 (5), 745–771. doi:10.2118/114163-Pa

Moridis, G. J., Reagan, M. T., Kim, S.-J., Seol, Y., and Zhang, K. (2009b). Evaluation of the Gas Production Potential of Marine Hydrate Deposits in the Ulleung Basin of the Korean East Sea. *SPE J.* 14 (4), 759–781. doi:10.2118/110859-Pa

Moridis, G. J., Kim, J., Reagan, M. T., and Kim, S.-J. (2013). Feasibility of Gas Production from a Gas Hydrate Accumulation at the UBGH2-6 Site of the Ulleung basin in the Korean East Sea. *J. Pet. Sci. Eng.* 108, 180–210. doi:10.1016/j.petrol.2013.03.002

Moridis, G. J. (2014). "User's Manual for the Hydrate v1.5 Option of TOUGH+V1.5: a Code for the Simulation of System Behavior in Hydrate-Bearing Geologic media," in *Earth Sciences Division* (Berkeley, CA 94720: Lawrence Berkeley National Laboratory).

Oyama, H., Konno, Y., Suzuki, K., and Nagao, J. (2012). Depressurized Dissociation of Methane-Hydrate-Bearing Natural Cores with Low Permeability. *Chem. Eng. Sci.* 68 (1), 595–605. doi:10.1016/j.ces.2011.10.029

Sloan, E. D. (2003). Fundamental Principles and Applications of Natural Gas Hydrates. *Nature* 426 (6964), 353–359. doi:10.1038/nature02135

Su, Z., Cao, Y., Wu, N., and He, Y. (2011). Numerical Analysis on Gas Production Efficiency from Hydrate Deposits by Thermal Stimulation: Application to the Shenhu Area, South China Sea. *Energies* 4 (2), 294–313. doi:10.3390/en4020294

Su, Z., He, Y., Wu, N., Zhang, K., and Moridis, G. J. (2012a). Evaluation on Gas Production Potential from Laminar Hydrate Deposits in Shenhu Area of South China Sea through Depressurization Using Vertical wells. *J. Pet. Sci. Eng.* 86-87, 87–98. doi:10.1016/j.petrol.2012.03.008

Su, Z., Moridis, G. J., Zhang, K., and Wu, N. (2012b). A Huff-And-Puff Production of Gas Hydrate Deposits in Shenhu Area of South China Sea through a Vertical Well. *J. Pet. Sci. Eng.* 86-87, 54–61. doi:10.1016/j.petrol.2012.03.020

Su, Z., Huang, L., Wu, N., and Yang, S. (2013). Effect of thermal Stimulation on Gas Production from Hydrate Deposits in Shenhu Area of the South China Sea. *Sci. China Earth Sci.* 56 (4), 601–610. doi:10.1007/s11430-013-4587-4

Sun, J., Ning, F., Li, S., Zhang, K., Liu, T., Zhang, L., et al. (2015). Numerical Simulation of Gas Production from Hydrate-Bearing Sediments in the Shenhu Area by Depressurising: The Effect of burden Permeability. *J. Unconventional Oil Gas Resour.* 12, 23–33. doi:10.1016/j.juogr.2015.08.003

Sun, Y., Ma, X., Guo, W., Jia, R., and Li, B. (2019). Numerical Simulation of the Short- and Long-Term Production Behavior of the First Offshore Gas Hydrate Production Test in the South China Sea. *J. Pet. Sci. Eng.* 181, 106196. doi:10.1016/j.petrol.2019.106196

Sung, W., Lee, H., Lee, H., and Lee, C. (2002). Numerical Study for Production Performances of a Methane Hydrate Reservoir Stimulated by Inhibitor Injection. *Energ. Sourc.* 24 (6), 499–512. doi:10.1080/00908310290086527

Vangenuchten, M. T. (1980). A Closed-form Equation for Predicting the Hydraulic Conductivity of Unsaturated Soils. *Soil Sci. Soc. Am. J.* 44 (5), 892–898. doi:10.2136/sssaj1980.03615995004400050002x

Wan, Q.-C., Si, H., Li, B., and Li, G. (2018). Heat Transfer Analysis of Methane Hydrate Dissociation by Depressurization and thermal Stimulation. *Int. J. Heat Mass Transfer* 127, 206–217. doi:10.1016/j.ijheatmasstransfer.2018.07.016

Wan, Q.-C., Chen, L.-L., Li, B., Peng, K., and Wu, Y.-Q. (2020a). Insights into the Control Mechanism of Heat Transfer on Methane Hydrate Dissociation via Depressurization and Wellbore Heating. *Ind. Eng. Chem. Res.* 59 (22), 10651–10663. doi:10.1021/acs.iecr.0c00705

Wan, Q.-C., Si, H., Li, B., Yin, Z.-Y., Gao, Q., Liu, S., et al. (2020b). Energy Recovery Enhancement from Gas Hydrate Based on the Optimization of thermal Stimulation Modes and Depressurization. *Appl. Energ.* 278, 115612. doi:10.1016/j.apenergy.2020.115612

Wang, P., Yang, M., Chen, B., Zhao, Y., Zhao, J., and Song, Y. (2017). Methane Hydrate Reformation in Porous media with Methane Migration. *Chem. Eng. Sci.* 168, 344–351. doi:10.1016/j.ces.2017.04.036

Wang, B., Dong, H., Liu, Y., Lv, X., Liu, Y., Zhao, J., et al. (2018). Evaluation of thermal Stimulation on Gas Production from Depressurized Methane Hydrate Deposits☆. *Appl. Energ.* 227, 710–718. doi:10.1016/j.apenergy.2017.08.005

Wang, B., Dong, H., Fan, Z., Liu, S., Lv, X., Li, Q., et al. (2020). Numerical Analysis of Microwave Stimulation for Enhancing Energy Recovery from Depressurized Methane Hydrate Sediments. *Appl. Energ.* 262, 114559. doi:10.1016/j.apenergy.2020.114559

White, M. D., Wurstner, S. K., and McGrail, B. P. (2011). Numerical Studies of Methane Production from Class 1 Gas Hydrate Accumulations Enhanced with Carbon Dioxide Injection. *Mar. Pet. Geology.* 28 (2), 546–560. doi:10.1016/j.marpetgeo.2009.06.008

Wu, S., and Wang, J. (2018). On the China′s Successful Gas Production Test from marine Gas Hydrate Reservoirs. *Chin. Sci. Bull.* 63 (1), 2–8. doi:10.1360/n972017-00645

Wu, N. Y., Yang, S. X., Zhang, H. Q., Liang, J. Q., Wang, H. B., and Lu, J. A. (2010). Gas Hydrate System of Shenhu Area, Northern South China Sea: Wire-Line Logging, Geochemical Results and Preliminary Resources Estimates. *2010 Offshore Technol. Conf.* 1 (1). (Houston, Texas, USA). doi:10.4043/20485-ms

Wu, N., Zhang, H., Yang, S., Zhang, G., Liang, J., Lu, J. a., et al. (2011). Gas Hydrate System of Shenhu Area, Northern South China Sea: Geochemical Results. *J. Geol. Res.* 2011, 1–10. doi:10.1155/2011/370298

Wu, P., Li, Y., Sun, X., Liu, W., and Song, Y. (2020). Mechanical Characteristics of Hydrate-Bearing Sediment: A Review. *Energy Fuels* 35 (2), 1041–1057. doi:10.1021/acs.energyfuels.0c03995

Yang, T., Jiang, S., Ge, L., Yang, J., Wu, N., Zhang, G., et al. (2010). Geochemical Characteristics of Pore Water in Shallow Sediments from Shenhu Area of South China Sea and Their Significance for Gas Hydrate Occurrence. *Chin. Sci. Bull.* 55 (8), 752–760. doi:10.1007/s11434-009-0312-2

Yang, L., Chen, C., Jia, R., Sun, Y., Guo, W., Pan, D., et al. (2018). Influence of Reservoir Stimulation on Marine Gas Hydrate Conversion Efficiency in Different Accumulation Conditions. *Energies* 11 (2), 339. doi:10.3390/en11020339

Yang, M., Gao, Y., Zhou, H., Chen, B., and Li, Y. (2019). Gas Production from Different Classes of Methane Hydrate Deposits by the Depressurization Method. *Int. J. Energ. Res.* 43 (10), 5493–5505. doi:10.1002/er.4669

Ye, J. L., Qin, X. W., Xie, W. W., Lu, H. L., Ma, B. J., Qiu, H. J., et al. (2020). The Second Natural Gas Hydrate Production Test in the South China Sea. *China Geol.* 2, 197–209. doi:10.31035/cg2020043

Yin, Z., Wan, Q.-C., Gao, Q., and Linga, P. (2020). Effect of Pressure Drawdown Rate on the Fluid Production Behaviour from Methane Hydrate-Bearing Sediments. *Appl. Energ.* 271, 115195. doi:10.1016/j.apenergy.2020.115195

Zhang, L., Yang, L., Wang, J., Zhao, J., Dong, H., Yang, M., et al. (2017). Enhanced CH4 Recovery and CO2 Storage via thermal Stimulation in the CH4/CO2 Replacement of Methane Hydrate. *Chem. Eng. J.* 308, 40–49. doi:10.1016/j.cej.2016.09.047

Zhao, J., Liu, D., Yang, M., and Song, Y. (2014). Analysis of Heat Transfer Effects on Gas Production from Methane Hydrate by Depressurization. *Int. J. Heat Mass Transfer* 77, 529–541. doi:10.1016/j.ijheatmasstransfer.2014.05.034

Zhao, E., Hou, J., Du, Q., Liu, Y., Ji, Y., and Bai, Y. (2021). Numerical Modeling of Gas Production from Methane Hydrate Deposits Using Low-Frequency Electrical Heating Assisted Depressurization Method. *Fuel* 290, 120075. doi:10.1016/j.fuel.2020.120075

Conflict of Interest: The authors declare that the research was conducted in the absence of any commercial or financial relationships that could be construed as a potential conflict of interest.

Publisher's Note: All claims expressed in this article are solely those of the authors and do not necessarily represent those of their affiliated organizations, or those of the publisher, the editors, and the reviewers. Any product that may be evaluated in this article, or claim that may be made by its manufacturer, is not guaranteed or endorsed by the publisher.

frontiers in Earth Science

ORIGINAL RESEARCH
published: 30 March 2022
doi: 10.3389/feart.2022.859111

A Thermodynamic Method for the Estimation of Free Gas Proportion in Depressurization Production of Natural Gas Hydrate

Shouding Li[1,2,3]*, *Yiming Sun*[1,2,3], *Cheng Lu*[4,5], *Weichang Chen*[1,2,3], *Shimin Liu*[6], *Lin Chen*[7,8] *and Xiao Li*[1,2,3]

[1]Key Laboratory of Shale Gas and Geoengineering, Institute of Geology and Geophysics, Chinese Academy of Sciences, Beijing, China, [2]Innovation Academy for Earth Science, Chinese Academy of Sciences, Beijing, China, [3]College of Earth and Planetary Sciences, University of Chinese Academy of Sciences, Beijing, China, [4]Guangzhou Marine Geological Survey, China Geological Survey, Guangzhou, China, [5]Center of Oil and Natural Gas Resource Exploration, China Geological Survey, Beijing, China, [6]Department of Energy and Mineral Engineering, G[3] Center and Energy Institute, The Pennsylvania State University, University Park, State College, PA, United States, [7]Institute of Engineering Thermophysics, Chinese Academy of Sciences, Beijing, China, [8]School of Aeronautics and Astronautics, University of Chinese Academy of Sciences, Beijing, China

OPEN ACCESS

Edited by:
Jinan Guan,
Guangzhou Institute of Energy Conversion (CAS), China

Reviewed by:
Lele Liu,
Qingdao Institute of Marine Geology (QIMG), China
Zhichao Liu,
China University of Geosciences Wuhan, China
Guangrong Jin,
Guangzhou Institute of Energy Conversion (CAS), China

***Correspondence:**
Shouding Li
lsdlyh@mail.iggcas.ac.cn

Specialty section:
This article was submitted to Marine Geoscience, a section of the journal Frontiers in Earth Science

Received: 20 January 2022
Accepted: 07 March 2022
Published: 30 March 2022

Citation:
Li S, Sun Y, Lu C, Chen W, Liu S, Chen L and Li X (2022) A Thermodynamic Method for the Estimation of Free Gas Proportion in Depressurization Production of Natural Gas Hydrate. Front. Earth Sci. 10:859111. doi: 10.3389/feart.2022.859111

Free gas saturation is one of the key factors that affect the overall production behaviors of hydrate reservoirs. For example, different free gas contents could alter the thermal response of hydrate reservoirs to the artificial stimulation and hence change the gas production performance. To investigate whether and how much the hydrate reservoir contains free gas, we proposed a thermodynamic method to calculate the total heat consumption of hydrate dissociation throughout gas production and assess the free gas proportion. Based on the monitoring data of the first offshore hydrate production in Japan, we calculated the total heat consumption and analyzed the contributions of heat convection, heat conduction, and sensible heat during the entire test. The calculation results showed that there is likely to be a certain amount of free gas in the hydrate reservoir in the Eastern Nankai Trough. In addition, the analysis of different heat sources revealed the critical thermodynamic phenomenon in which the reservoir sensible heat was the main source for enthalpy of hydrate dissociation, which consistently contributed more than 95% of the total heat supply during the 6-day production test. The results of this work may help upgrade the production strategy for natural gas hydrates.

Keywords: natural gas hydrate, free gas proportion, thermodynamic analysis, heat transfer, hydrate production

1 INTRODUCTION

Natural gas hydrates (NGHs), found in permafrost regions and marine continental margin sediments, are crystalline compounds formed by water and natural gas molecules (mainly methane) (Kvenvolden 1988; Sloan 2003; Boswell and Collett 2011). In an ideally saturated methane hydrate, the molar ratio of methane to water is nearly 1:6, that is, equal to a volumetric ratio of about 164 (Kvenvolden 1988). The methane concentration in hydrates is comparable to that of a highly compressed gas (Sloan 2003). Therefore, hydrates need to form in the condition in which hydrate-forming gas is sufficient and both pressure and temperature are conducive to hydrate stability. Otherwise, the hydrate crystal may break down and release methane into the

surrounding water. Whether the gas resource is sufficient or not directly affects the formation of NGH and the volume percentage of gas hydrate in hydrate-bearing sediments (HBSs). The presence of methane within the pressure–temperature stability field for methane gas hydrate is not sufficient to ensure the occurrence of gas hydrate, which tends to form when the mass fraction of methane dissolved in liquid exceeds methane solubility in seawater (Xu and Ruppel 1999) and there is free methane gas in the fluid system (Ben Clennell et al., 1999; Waite et al., 2009; Lu et al., 2019). Accordingly, fluid containing methane must rise to the depth at which the local solubility limit is less than the methane content in order for hydrate to precipitate (Waite et al., 2009).

NGH reservoirs can be divided into three main classes on the basis of geological features and initial conditions (Moridis et al., 2009), in which NGH indeed generally coexists with free gas (Makogon and Omelchenko 2013; Miyakawa et al., 2014; Li et al., 2016; Ye et al., 2020). Free gas saturation is a key factor that affects the overall production behaviors of marine hydrate deposit, for example, influencing the thermal response of hydrate reservoir to the artificial stimulation and hence altering the gas production performance (Moridis et al., 2007). Generally, when the gas content is lower than the local solubility, the gas dissolves in the pore water and migrates with it. If the gas exceeds the solubility and the amount is small, a small number of bubbles will migrate with the pore fluid in a discrete form. Accordingly, there are two main sources of free gas in the hydrate reservoir. In one case, methane is transported to the hydrate stability zone by dissolving in pore water. In the rising process, due to the gradual decrease of methane solubility, methane precipitates from water. In another case, methane is directly provided by the fluid containing saturated methane and free gas (Lu et al., 2019). These imply that there is supposed to be a certain proportion of free gas in the hydrate reservoir. Understanding the free gas content of a reservoir will help to establish a hydrate accumulation model and formulate the corresponding production strategy, such as heat-supply strategy and depressurization strategy. However, the evidence of whether and how much the hydrate reservoir contains free gas is scarce, and the method to assess the overall free gas content in a hydrate reservoir is deficient and needs to be developed.

In this article, we proposed a thermodynamic method using real-world production data to calculate the heat consumption of hydrate dissociation in gas production and ultimately evaluate the free gas content in a hydrate reservoir. Taking the first offshore hydrate production of Japan as an example, we conducted the estimation and analyses of free gas proportion in the test reservoir using the on-site monitoring data. Based on this work, we also analyzed the thermal responses of the reservoir and revealed the contributions of different thermal processes. This work will not only conduce to understanding the phase composition of methane gas in hydrate reservoirs but also help us better comprehend the effect of different heat sources in hydrate reservoirs to hydrate dissociation, all of which will better guide future hydrate production.

2 PRINCIPLE AND METHOD

The dissociation of methane hydrate is an endothermic process and can significantly change the temperature field in the reservoir (Song et al., 2015; Yamamoto et al., 2017). In contrast, the thermodynamic effect of the release of free gas originally existing in the hydrate reservoir can be ignored. Based on this, we can estimate the heat consumption during gas production according to the thermal response of the formation and then obtain the amount of hydrate-released gas by converting the heat consumption into gas volume. Furthermore, we can calculate the proportion of free gas in the total gas yield.

In the process of gas production, artificial stimulation, such as depressurization, triggers the dissociation, and immediately the hydrate dissociation will absorb heat from the surrounding environment. As the dissociation goes on, a disturbed zone, which can be defined as the zone in which the temperature diverges from the initial state, will expand over time. Consequently, convective water driven by the pressure gradient will be cooled due to heat transfer to the disturbed zone, heat conduction due to the temperature gradient will occur, and sensible heat of the disturbed zone will be released due to formation cooling. In the aforementioned processes, the heat consumption of hydrate dissociation Q_h, the heat loss of extracted formation water Q_w, the heat conduction through surrounding formation Q_c, and the sensible heat released by the disturbed zone Q_r are the main thermal factors influencing the temperature field (**Figure 1**). According to the conservation of energy, we can conclude the following relationship (**Eq. 1**) between these heat items: the heat needed or consumed by hydrate dissociation (Q_h) is ultimately derived from and compensated by heat released by formation water (Q_w), heat conduction through the disturbed zone (Q_c), and sensible heat released by the disturbed zone (Q_r). The method of energy balance enables us to ignore the intermediate processes and focus on the change of the thermal field in which the thermal effects of many aspects, such as ice formation and hydrate reformation, will submerge and be reflected in the ultimate temperature states.

$$Q_h = Q_w + Q_c + Q_r. \tag{1}$$

From this point of view, to estimate the free gas content, the first step is to calculate the right-hand members in **Eq. 1** and then convert the results into an equivalent volume of hydrate-released gas according to the enthalpy of hydrate dissociation.

In this work, the heat contributed by formation water convection (Q_w) in each temporal interval was regarded and calculated as the sensible heat associated with water cooling using **Eq. 2**:

$$Q_w = c_w \rho_w V_w \Delta t_w, \tag{2}$$

where c_w and ρ_w are the specific heat capacity and density of the water, respectively, V_w is the water production in an interval, and Δt_w is the temperature difference between the real-time temperature and the initial formation temperature.

The heat conduction through the disturbed zone (Q_c) is divided into two parts, i.e., the lateral heat conduction from

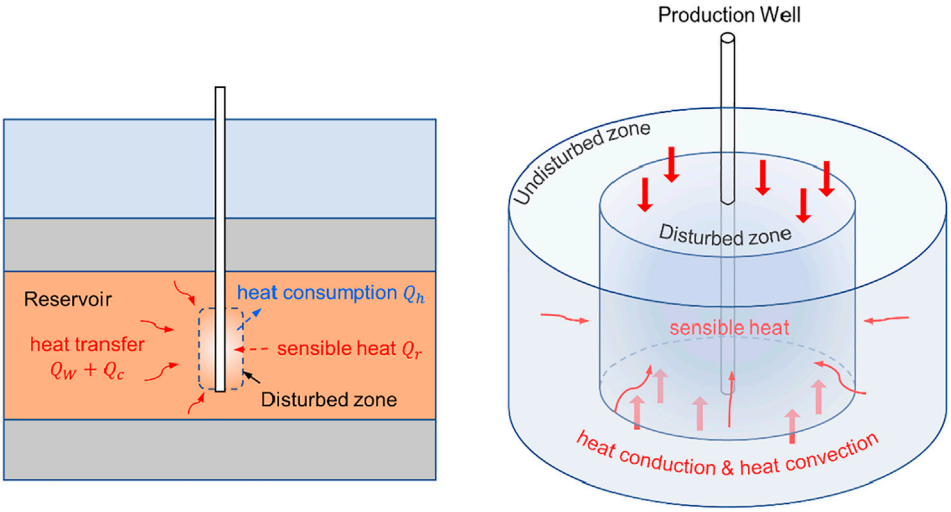

FIGURE 1 | Schematic diagram of the thermodynamic processes during hydrate production.

the undisturbed zone and the vertical heat conduction from the overburden and underlying layers. In this work, the lateral heat conduction was considered a one-dimension steady heat conduction problem in each temporal interval. As a conventional simplifying method (Li G. et al., 2012; Chen et al., 2018; Yu et al., 2019; Xu et al., 2021), we assumed that the expansion of the disturbed zone approximated to an axisymmetric process in a short-term production, and thus we calculated the corresponding heat using Fourier's law of heat conduction in cylindrical coordinates:

$$\Phi = 2\pi\lambda l \frac{t_1 - t_2}{\ln(r_2/r_1)}, \tag{3}$$

where Φ is the heat transfer rate, λ is the thermal conductivity of formation, l is the height of the cylindrical disturbed zone, r_1 and r_2 are the inner and outer radii of the cylinder, respectively, and t_1 and t_2 are the corresponding boundary temperature. In the geological model, r_1 and r_2 are the radius of wellbore and the radius of the disturbed zone, respectively. By ignoring the effect of the geothermal gradient, the vertical heat conduction was directly calculated using Fourier's law of heat conduction in Cartesian coordinates:

$$\Phi = -2A\lambda\nabla t, \tag{4}$$

where A is the area of the upper or lower surface of the disturbed zone, and ∇t is the temperature gradient in formation.

The sensible heat released by the disturbed zone (Q_r) can be estimated using the volume of the disturbed zone, the heat capacity of the reservoir, and the temperature difference between the initial and final states according to **Eq. 5**:

$$Q_r = c_r\rho_r V_r \Delta t_r, \tag{5}$$

where c_r and ρ_r are the specific heat capacity and density of formation, respectively, V_r is the volume of the disturbed zone, and Δt_r is the temperature change of formation. The equation and calculation will be further detailed later.

With heat consumption calculated, we can estimate the hydrate-released gas by attributing all the heat consumption to the hydrate dissociation. The enthalpy of methane hydrate dissociation ΔH can be set at 54 kJ mol^{-1} (Handa 1986; Sloan and Koh 2008); therefore, the dissociation equation of methane hydrate can be formulated as

$$1\ mol\ CH_4 \cdot 5.75H_2O + 54\ kJ \rightarrow 1\ mol\ CH_4 + 5.75\ mol\ H_2O. \tag{6}$$

The estimated hydrate-released gas according to **Eqs 1**,**6** is supposed to be less than the gross gas production because of the free gas in the reservoir. Comparing the hydrate-released gas with the gross gas production, we can determine the free gas content in the hydrate deposit. The values and calculations of physical parameters, especially the thermophysical properties will be detailed in the following section.

3 CALCULATION AND DISCUSSION

3.1 Data Acquisition and Processing

In March 2013, the world's first field trial of gas production from marine hydrate deposits was conducted in the Daini Atsumi Knoll area of the Eastern Nankai Trough off the Pacific coast of Japan (Yamamoto et al., 2014). One production well AT1-P with two monitoring boreholes, AT1-MC and AT1-MT1, was drilled in the test site. During the entire 6-day flow test, the gas production rate was stable at about 2.0 × 10^4 m^3 d^{-1}, with the highest rate of 2.5 × 10^4 m^3 d^{-1}. The water production rate was about 200 m^3 d^{-1}. The cumulative gas production was 11.9 × 10^4 m^3, and water production was 1,250 m^3 (Konno et al., 2017; Yamamoto et al., 2017). Along with the flow test, the intensive data acquisition program was implemented. DTS and RTD

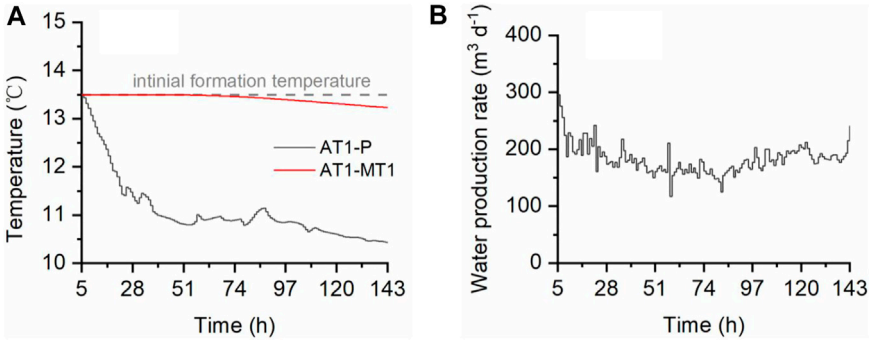

FIGURE 2 | Data used for calculation. **(A)** Processed downhole temperature data of production well AT1-P and monitoring well AT1-MT1 from the sensor installed 10 m below the top of the methane hydrate-concentrated zone. **(B)** Processed water production data from production well AT1-P.

temperature sensors installed along the production and two observation boreholes detected temperature variations caused by the endothermic dissociation process and heat transfer around the boreholes during gas production.

As the first offshore hydrate production test of Japan provided an integral dataset that recorded the production behavior and reservoir response during the entire depressurization production, in this work, we attempted to take this pilot production as an example and assess the free gas content in the test reservoir. To conduct the calculation in a unified geometry of the model, we simplified the temperature profile in the reservoir via average temperature in our calculations, which should be acceptable given the linear relationship between the heat items and temperature variation and the thermal independence of other parameters. According to the temperature monitoring data, we chose the data gathered by the sensor installed 10 m below the top of the methane hydrate-concentrated zone, which could typify the temperature variation of different formation intervals, as the average temperature to conduct the calculation. According to the timeline of the major events (Yamamoto et al., 2017), the calculated span was set at 138 h, i.e., from 5 to 143 h after the start of depressurization, when the downhole P-T state reached the phase equilibrium curve of methane hydrate and the depressurization operation terminated, respectively.

The fundamental calculation data, namely, temperature variation and water production, were gathered from the literature of Yamamoto et al. (2017) and processed by overall smoothing and hourly homogenizing, as shown in **Figure 2**.

3.2 Heat Consumption Calculation

3.2.1 Heat From Formation Water

In the process of hydrate production, hydrate dissociation will absorb heat from the surrounding environment. Therefore, the temperature of the final produced water, that is, the downhole monitoring temperature of the production well was lower than the initial formation temperature. According to energy conservation, the heat loss of produced water constituted a part of heat sources for hydrate dissociation. The produced water was composed of decomposed hydrate water, *in situ* formation water, and inflow formation water. We assume that

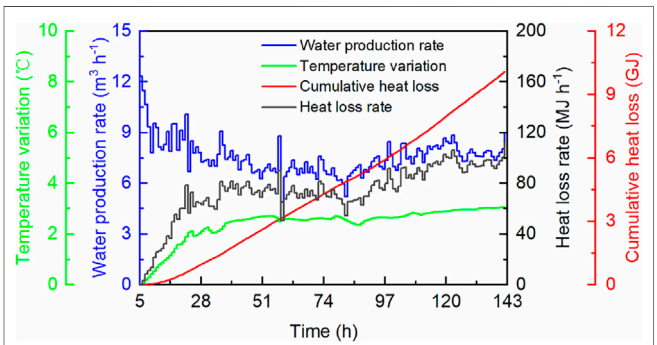

FIGURE 3 | Calculation results of the heat loss from produced formation water contributing to hydrate dissociation.

the extracted hydrate water and *in situ* water will be replaced by the inflow water, so it can be equivalently considered that they are stationary, and the produced water is equivalent to the inflow water. The heat convection calculation of this part only considers the heat loss of produced water, while the heat loss of hydrate water and *in situ* water is classified into the following sensible heat calculation.

Based on the real-time temperature difference (**Figure 2A**) and **Eq. 2**, the heat contributed by formation water can be calculated. The specific heat capacity of seawater was taken as 4.1 kJ kg^{-1} K^{-1} (Sharqawy et al., 2012; Haynes 2016). **Figure 3** gives the temperature variation quantity Δt_w and water production rate, whereby we calculated the item of Q_w, that is, the heat released by formation water on the hourly basis and obtained a total heat loss of about 10.08 GJ.

Given the discrepancy between the water flux through the boundary of the disturbed zone and the water production rate, for example, the production rate would be bigger than the influx at the beginning in order to decrease the downhole pressure, we carried out the following examination to determine the influence of this issue. Our calculation interval spanned from 5 to 143 h after the start of depressurization, in which the downhole pressure basically hovered between 4.5–5 MPa. The biggest pressure drop of about 6 MPa occurred in the period of

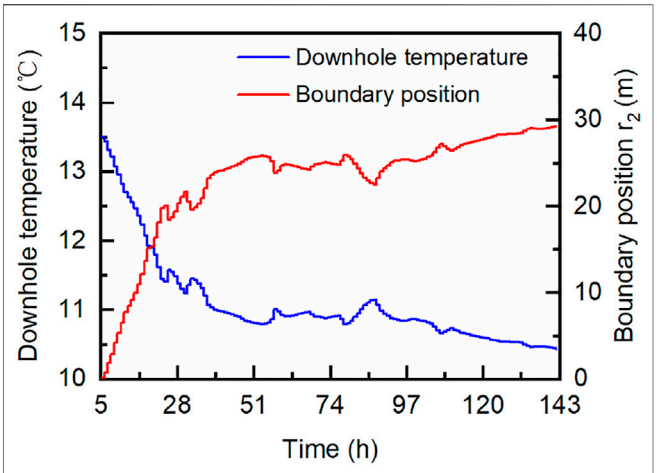

FIGURE 4 | Downhole temperature of the production well and corresponding extrapolated position of the lateral heat conduction boundary.

5–12 h. Taking the well diameter as 21.5 cm (8–1/2″ drill bit) (Yamamoto et al., 2014), the total introduced error of water volume is about 22 m^3. Given the temperature drop during this period was less than 1 K, the total corresponding energy error is believed to be about 0.1 GJ, which is 1% of the current calculation results. This shows that the error introduced by the altering of downhole pressure is minor and negligible.

3.2.2 Heat From Formation Conduction

The dissociation of hydrates can change the temperature field around the production well, and thus the heat conduction in formation will occur. In this work, the heat conduction through the disturbed zone was simply divided into two parts, that is, the heat from lateral conduction and vertical conduction. The lateral heat conduction was considered a one-dimension steady heat conduction problem in each hourly interval. According to numerical simulations of the short-term hydrate production employing the vertical production well (Yamamoto et al., 2017; Boswell et al., 2019; Feng et al., 2019; Yu et al., 2019), we assumed a cylindrical disturbed zone during the production to calculate the corresponding heat (Q_c) using Fourier's law of heat conduction in cylindrical coordinates (**Eq. 3**). By ignoring the effect of the geothermal gradient, the vertical heat conduction was directly calculated using Fourier's law of heat conduction in Cartesian coordinates (**Eq. 4**).

Although the calculation model has been simplified, the direct application of Fourier's law is still not feasible because the temperature and position of the internal and external heat conduction boundaries are needed. In the calculation, the temperature at the inner and outer boundaries is known. The former is the temperature data from the production well, and the latter is the initial formation temperature of 13.5°C. The location of the inner boundary, that is, the wellbore radius, is also known, which is 0.1 m (Yamamoto et al., 2017). The biggest obstacle to the calculation lies in the real-time position of the outer conduction boundary. In this hydrate production trial, no instrument could keep track of the boundary of the disturbed zone, that is, r_2 in **Eq. 3** was unknown. We tackled this problem in light of the information provided by the monitoring well AT1-MT1. We noted that the temperature in the AT1-MT1 well, which was 22 m away from the production well, started to manifest a divergence from the initial formation temperature about 30 h after pumping operation. In the meantime, the temperature in the production well was recorded as 11.2°C. Based on the temperature difference and distance between production and monitoring wells, we presumed a linear temperature gradient of 0.1°C m^{-1} in the formation in order to extrapolate the lateral position of the heat conduction boundary, as well as the disturbed zone boundary, using the downhole temperature of the production well. The calculation result is shown in **Figure 4**.

Having the position of the heat conduction boundary in each temporal interval, we can conduct the calculations of lateral conduction and vertical conduction. In **Eq. 3**, the height l of the cylindrical disturbed zone was taken as 30 m according to the spatial range of temperature change in the monitoring well during the production test (Yamamoto et al., 2017). The temperature gradient of formation ∇t in **Eq. 4** also used the value of 0.1°C m^{-1}. The thermal conductivity of formation λ was estimated as 1.76 W m^{-1} K^{-1} using the reservoir parameters (Fujii et al., 2015; Konno et al., 2017; Yamamoto et al., 2017) and the distribution model (Muraoka et al., 2014):

$$\lambda = \lambda_h^{S_h\varphi}\lambda_s^{(1-\varphi)}\lambda_w^{(1-S_h)\varphi}, \tag{7}$$

where λ_h, λ_s, and λ_w are the thermal conductivities of methane hydrate, sediment grain, and seawater, respectively, and S_h and φ are the hydrate saturation and porosity of HBS, respectively. This thermal conductivity of formation λ was considered constant irrespective of the temporal and spatial difference caused by the variation of the hydrate saturation in sediments because of the small extent of this difference (Cortes et al., 2009; Waite et al., 2009; Yang et al., 2015; Yang et al., 2016). **Figure 5** shows the results of the heat transfer rate in each interval and the cumulative heat contributed by conduction. The heat derived from lateral and vertical heat conduction through formation adds up to about 72.55 and 314.96 MJ, respectively, with a total value of 387.51 MJ.

It should be noted that the calculations of this part were simplified. For instance, the actual temperature profile in the reservoir is bound to be different from the one adopted in the calculation, and the actual geometry of the boundary must not be a simple cylinder. These deficiencies should be overcome in the further study via numerical calculation. But fortunately, the magnitude of the result indicates that the role of heat conduction in the hydrate production is astonishingly insignificant, as the equivalent gas volume of this amount of heat is merely 161 m^3 according to **Eq. 6**.

3.2.3 Sensible Heat Released by the Disturbed Zone

As defined previously and illustrated in **Figure 1**, the disturbed zone in this work refers to a cylindrical zone in which the temperature diverges from the initial state due to hydrate dissociation and related thermal effect. **Figure 4** shows the boundary position of the disturbed zone and the downhole temperature of the production well, whereby the sensible heat associated with the temperature

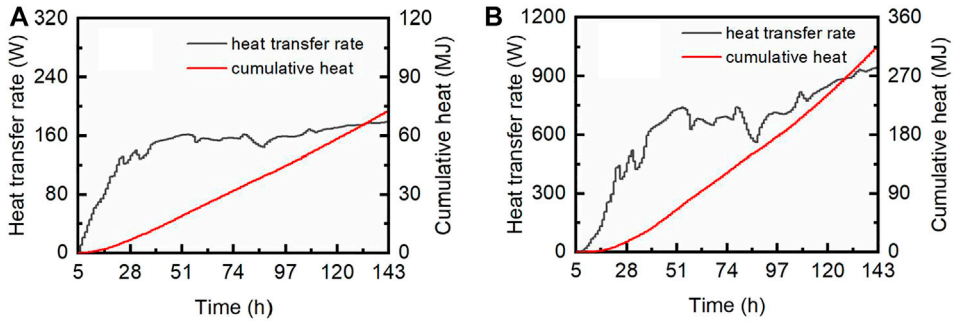

FIGURE 5 | Heat transfer rate and cumulative heat of lateral heat conduction **(A)** and vertical heat conduction **(B)**.

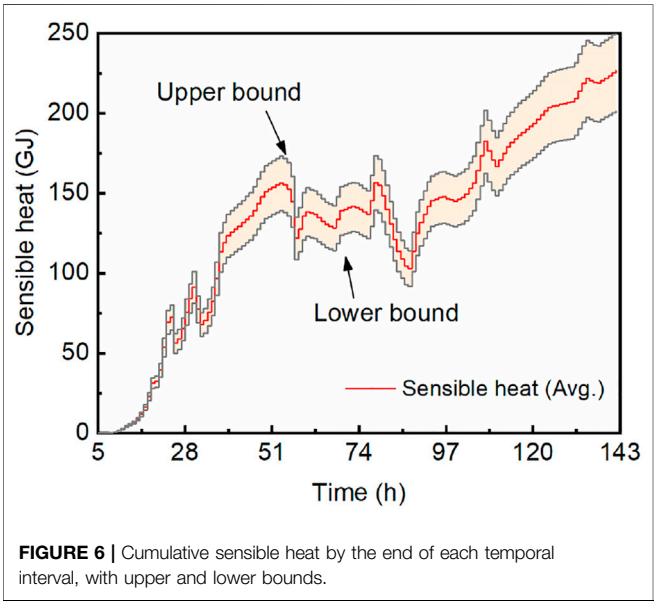

FIGURE 6 | Cumulative sensible heat by the end of each temporal interval, with upper and lower bounds.

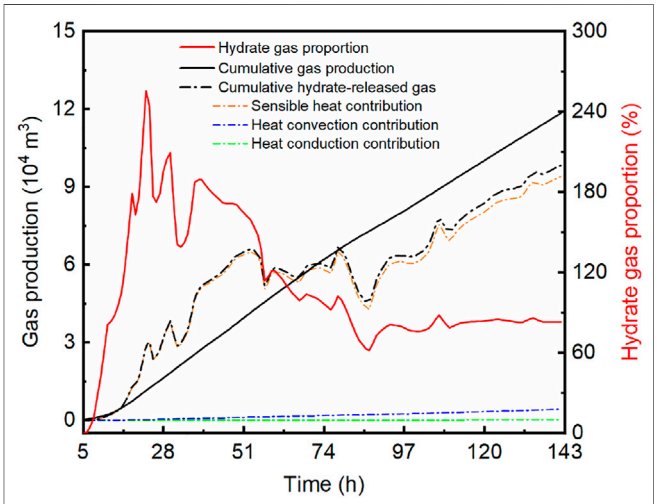

FIGURE 7 | Comparison of the total gas production (black solid line) and the calculated hydrate-released gas production (dashed-dotted lines) and the real-time ratio of hydrate-released gas to gas production (red solid line).

decrease of formation can be calculated based on **Eq. 5**. As in **Eq. 3**, the height l of the cylindrical disturbed zone was taken as 30 m according to the spatial range of temperature variation in the monitoring well throughout the test (Yamamoto et al., 2017). The volume specific heat $\rho_r c_r$ of formation is calculated using the arithmetic mean formula:

$$\rho_r c_r = \rho_h c_h S_h \varphi + \rho_s c_s (1-\varphi) + \rho_w c_w (1-S_h)\varphi, \tag{8}$$

where ρ_r, ρ_h, ρ_s, and ρ_w are the densities of HBS, methane hydrate, sediment grain, and seawater, respectively, and c_r, c_h, c_s, and c_w are the specific heat capacities of the same components. For this calculation, φ = 40% (Fujii et al., 2015), ρ_h = 0.92 g cm^{-3} (Waite et al., 2007; Muraoka et al., 2014), c_h = 2.01 kJ kg^{-1} K^{-1} (Waite et al., 2009; Konno et al., 2010), ρ_s = 2.65 g cm^{-3}, c_s = 0.73 kJ kg^{-1} K^{-1} (Muraoka et al., 2014), ρ_w = 1.00 g cm^{-3}, and c_w = 4.11 kJ kg^{-1} K^{-1} (3.5% salinity) (Sharqawy et al., 2012) were considered. The variable is the hydrate saturation S_h. With the expansion of the dissociation zone, hydrate dissociation may significantly raise the specific heat of HBS, as the specific heat of methane hydrate is less than that of half of seawater. However, a dynamic calculation with a specific heat varying with time and position is complicated and impracticable. As a compromise in the calculation, the volume-specific heat $\rho_r c_r$ adopted the mean value of its maximum case 2.80 MJ m^{-3} K^{-1}, where S_h = 0, and its minimum case 2.25 MJ m^{-3} K^{-1}, where S_h = 60%, the initial hydrate saturation in the reservoir (Fujii et al., 2015), and the mean value turned out to be 2.53 MJ m^{-3} K^{-1}, which was regarded as temporally and spatially constant. To calculate the value of Q_r, **Eq. 5** was specified as **Eq. 9**

$$Q_r = \int_{r_1}^{r_2} \rho_r c_r \, 2\pi r dr l \, (\Delta t_r - r\nabla t), \tag{9}$$

based on which the cumulative sensible heats by the end of each temporal interval were calculated. **Figure 6** shows the upper bound, average, and lower bound of the sensible heat released by the disturbed zone. The ultimate sensible heat was 226.64 GJ on average, and the upper and lower bounds were 251.25 and 201.75 GJ, respectively.

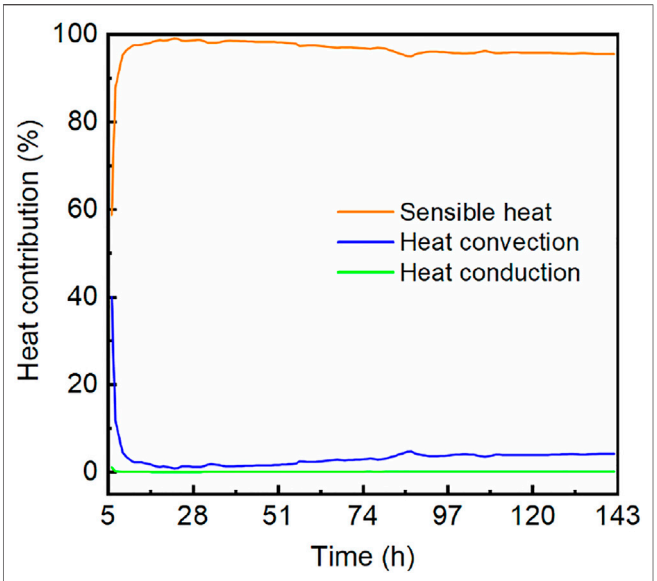

FIGURE 8 | Contributions of sensible heat, heat convection, and heat convection to hydrate dissociation.

3.3 Free Gas Proportion and Implication

Figure 7 summarizes the calculation results, based on which we can estimate the free gas proportion in the test reservoir using **Eqs 1**,**6**. The heat from formation water in total is 10.08 GJ. The heat derived from lateral and vertical heat conduction through the formation adds up to 72.55 and 314.96 MJ, respectively, with a total value of 387.51 MJ. The ultimate sensible heat released by the disturbed zone was 226.64 GJ. Corresponding to these heat items, the equivalent gas volumes are 4,181 m^3, 161 m^3, and 94014 m^3, respectively. These results mean that in 138-h gas production interval, 98356 m^3 of methane gas was generated due to hydrate dissociation. As the total extracted gas was 119000 m^3, the proportion of free gas in the gross gas yield, or in the test reservoir, was estimated as 17.35%. Considering the variation range of cumulative sensible heat, the maximum and minimum volumes of the total hydrate-released gas would be 108565 m^3 and 88031 m^3, respectively. The corresponding free gas proportion will be 8.77% and 26.02%, respectively. According to the results, there is likely to be a certain amount of free gas in the NGH deposit in the Eastern Nankai Trough.

In **Figure 7** the hydrate gas proportion, namely, the ratio of hydrate-released gas to actual extracted gas, indicates that free gas was first extracted in the beginning of few hours, and then the hydrate dissociation sprang up as the hydrate gas proportion surged in the following hours. The proportion exceeding 100% indicates a delay of gas extraction caused by the sluggish gas migration in low-permeability formation. However, after the delay period, the hydrate gas production represents a declining trend, which may imply a pause of hydrate dissociation and even a reformation phenomenon of hydrates. As the gas extraction went on, the hydrate gas proportion decreased continuously until it converged to a basically stable value of 82.65%.

As an endothermic process, hydrate dissociation will absorb heat from various sources. Our calculation demonstrated that hydrate gas generation was mainly contributed by sensible heat associated with the temperature decrease of formation. As shown in **Figure 7**, the gas production related to sensible heat accounts for 95.6% of the total hydrate-released gas. **Figure 8** shows the contributions of the three heat items to hydrate dissociation. In the first few hours, both the sensible heat and heat convection constituted the main heat source to hydrate dissociation, but then they evolved toward opposite directions. In the rest of the production time, the sensible heat consistently contributed more than 95% of the total heat supplement, while that proportion of heat convection was less than 5%. Meanwhile, the contribution of heat conduction was negligible because the proportion was not more than 0.2% in the entire production test. After a 24-h gas production, a noteworthy change occurred, and the heat proportion of sensible heat began to decline, while the heat convection and heat conduction exhibited an upward trend. As the hydrate dissociation absorbs heat immediately from the HBS, a moderate hydrate dissociation will bring about a moderate release of sensible heat. So, the change might result from the continuous temperature decline, which made hydrates dissociated less intensively (Kim et al., 1987; Song et al., 2015). This explanation is in agreement with the temperature records, which presented a rapid temperature decrease before 24 h and then had a relatively temperate descending trend.

To sum up, hydrate dissociation will mainly count on sensible heat of formation in a relatively long term; therefore, a hydrate reservoir with a high initial temperature is preferable for production. But with the formation temperature gradually declining to the equilibrium temperature, the spontaneous hydrate dissociation and corresponding heat absorption from HBS will become feeble. In this stage, heat convection may play an increasingly important role. As for the production strategy, these perceptions suggest that the formation temperature is the primary factor in terms of thermodynamics. It is reasonable to choose a reservoir with a higher temperature, even to artificially supply heat into the reservoir to facilitate and maintain hydrate dissociation. In addition, it is also a measure worthy of consideration to enhance heat convection in a certain stage to boost the hydrate dissociation and compensate for the degradation of formation heat release. There has been plenty of research investigating the techniques or schemes by implementing heat injection and hydraulic fracturing in the hydrate reservoir (Li X.-S. et al., 2012; Chen et al., 2014; Konno et al., 2016; Chen et al., 2017; Sun et al., 2021), by which we can carry out the enhanced recovery of hydrates. It is foreseeable that novel comprehensive and sophisticated production strategies or methods will emerge and come into play in the upcoming hydrate production.

4 CONCLUSION

In this study, we proposed a thermodynamic method for the estimation of free gas proportion in a hydrate reservoir using the field production and monitoring data. Based on this, we managed to approximately estimate the free gas content in the first test reservoir in the Nankai Trough. Considering the main contributing thermal processes for hydrate dissociation,

namely, heat convection of formation water, heat conduction in formation, and sensible heat releasing of the thermal disturbed zone, we calculated the total heat consumption due to hydrate dissociation during the entire production period. We converted this heat consumption into equivalent hydrate-released gas according to the enthalpy of hydrate dissociation and obtained the estimated gas volume of 98356 m^3, which means the proportion of free gas in total produced gas, or in total reservoir-trapped gas, may be 17.35%, as the actual total gas production was 119000 m^3. Given the variation range of sensible heat, the lower and upper free gas proportions were estimated as 8.77% and 26.02%, respectively.

Based on the calculation results, the hydrate gas proportion varying with time indicates that free gas accounted for a major part of gas generation in the first few hours, and then the hydrate dissociation sprang up. The proportion exceeding 100% implies a delay of gas extraction due to sluggish gas migration in low-permeability formation. The subsequent decline of hydrate gas proportion and generation may imply a pause of hydrate dissociation and even reformation of hydrates.

The heat analyses demonstrated that hydrate dissociation was mainly contributed by the sensible heat of the disturbed zone at least in this 6-day production. Gas production related to sensible heat accounted for 95% or so of the total hydrate-released gas, while that of heat convection was less than 5% and not more than 0.2% for heat conduction.

Through thermodynamic analysis and calculation, we revealed the gas composition in a hydrate reservoir, which is essential for understanding and predicting the gas production behavior of the hydrate reservoir. The analysis of thermal response unraveled the energy contribution of different heat sources to hydrate dissociation, which will guide the development of the production strategy in the future.

DATA AVAILABILITY STATEMENT

The raw data supporting the conclusion of this article will be made available by the authors, without undue reservation.

AUTHOR CONTRIBUTIONS

SL: conceptualization, methodology, formal analysis, investigation, supervision, project administration, and funding acquisition. YS: conceptualization, methodology, formal analysis, investigation, data curation, writing–original draft, and visualization. CL: investigation, review and editing, and funding acquisition. WC: formal analysis, investigation, and review and editing. LC: review and editing. SML: formal analysis and review and editing. XL: supervision, project administration, and funding acquisition. All authors contributed to manuscript revision and read and approved the submitted version.

FUNDING

This study was funded by the Guangdong Major Project of Basic and Applied Basic Research (No. 2020B0301030003), the National Natural Science Foundation of China (42090023 and 51991365), China Geological Survey Project (No. DD20211350), the IGGCAS Key Deployment Project (Nos. IGGCAS-201903 and SZJJ201901), the Key Deployment Program of Chinese Academy of Sciences (Nos. YJKYYQ20190043, ZDBS-LY-DQC003, XDA14040401, KFZD-SW-422, and ZDRW-ZS-2021-3-1), and the CAS Key Technology Talent Program.

REFERENCES

Boswell, R., and Collett, T. S. (2011). Current Perspectives on Gas Hydrate Resources. *Energy Environ. Sci.* 4 (4), 1206–1215. doi:10.1039/c0ee00203h

Boswell, R., Myshakin, E., Moridis, G., Konno, Y., Collett, T. S., Reagan, M., et al. (2019). India National Gas Hydrate Program Expedition 02 Summary of Scientific Results: Numerical Simulation of Reservoir Response to Depressurization. *Mar. Pet. Geology.* 108, 154–166. doi:10.1016/j.marpetgeo.2018.09.026

Chen, L., Feng, Y., Okajima, J., Komiya, A., and Maruyama, S. (2018). Production Behavior and Numerical Analysis for 2017 Methane Hydrate Extraction Test of Shenhu, South China Sea. *J. Nat. Gas Sci. Eng.* 53 (53), 55–66. doi:10.1016/j.jngse.2018.02.029

Chen, L., Sasaki, H., Watanabe, T., Okajima, J., Komiya, A., and Maruyama, S. (2017). Production Strategy for Oceanic Methane Hydrate Extraction and Power Generation with Carbon Capture and Storage (CCS). *Energy* 126, 256–272. doi:10.1016/j.energy.2017.03.029

Chen, Z., Feng, J., Li, X., Zhang, Y., Li, B., and Lv, Q. (2014). Preparation of Warm Brine *In Situ* Seafloor Based on the Hydrate Process for Marine Gas Hydrate Thermal Stimulation. *Ind. Eng. Chem. Res.* 53 (36), 14142–14157. doi:10.1021/ie501181r

Clennell, M. B., Hovland, M., Booth, J. S., Henry, P., and Winters, W. J. (1999). Formation of Natural Gas Hydrates in marine Sediments: 1. Conceptual Model of Gas Hydrate Growth Conditioned by Host Sediment Properties. *J. Geophys. Res.* 104 (B10), 22985–23003. doi:10.1029/1999jb900175

Cortes, D. D., Martin, A. I., Yun, T. S., Francisca, F. M., Santamarina, J. C., and Ruppel, C. (2009). Thermal Conductivity of Hydrate-Bearing Sediments. *J. Geophys. Res.* 114 (B11). doi:10.1029/2008jb006235

Feng, Y., Chen, L., Suzuki, A., Kogawa, T., Okajima, J., Komiya, A., et al. (2019). Enhancement of Gas Production from Methane Hydrate Reservoirs by the Combination of Hydraulic Fracturing and Depressurization Method. *Energ. Convers. Management* 184, 194–204. doi:10.1016/j.enconman.2019.01.050

Fujii, T., Suzuki, K., Takayama, T., Tamaki, M., Komatsu, Y., Konno, Y., et al. (2015). Geological Setting and Characterization of a Methane Hydrate Reservoir Distributed at the First Offshore Production Test Site on the Daini-Atsumi Knoll in the Eastern Nankai Trough, Japan. *Mar. Pet. Geology.* 66, 310–322. doi:10.1016/j.marpetgeo.2015.02.037

Handa, Y. P. (1986). Compositions, Enthalpies of Dissociation, and Heat Capacities in the Range 85 to 270 K for Clathrate Hydrates of Methane, Ethane, and Propane, and Enthalpy of Dissociation of Isobutane Hydrate, as Determined by a Heat-Flow Calorimeter. *The J. Chem. Thermodynamics* 18 (10), 915–921. doi:10.1016/0021-9614(86)90149-7

Haynes, W. M. (2016). *CRC Handbook of Chemistry and Physics*. 97th Edition. Boca Raton: Taylor and Francis;CRC Press.

Kim, H. C., Bishnoi, P. R., Heidemann, R. A., and Rizvi, S. S. H. (1987). Kinetics of Methane Hydrate Decomposition. *Chem. Eng. Sci.* 42 (7), 1645–1653. doi:10.1016/0009-2509(87)80169-0

Konno, Y., Fujii, T., Sato, A., Akamine, K., Naiki, M., Masuda, Y., et al. (2017). Key Findings of the World's First Offshore Methane Hydrate Production Test off the Coast of Japan: Toward Future Commercial Production. *Energy Fuels* 31 (3), 2607–2616. doi:10.1021/acs.energyfuels.6b03143

Konno, Y., Jin, Y., Yoneda, J., Uchiumi, T., Shinjou, K., and Nagao, J. (2016). Hydraulic Fracturing in Methane-Hydrate-Bearing Sand. *RSC Adv.* 6 (77), 73148–73155. doi:10.1039/c6ra15520k

Konno, Y., Masuda, Y., Hariguchi, Y., Kurihara, M., and Ouchi, H. (2010). Key Factors for Depressurization-Induced Gas Production from Oceanic Methane Hydrates. *Energy Fuels* 24 (3), 1736–1744. doi:10.1021/ef901115h

Kvenvolden, K. A. (1988). Methane Hydrate — A Major Reservoir of Carbon in the Shallow Geosphere? *Chem. Geology.* 71 (1), 41–51. doi:10.1016/0009-2541(88)90104-0

Li, G., Li, B., Li, X.-S., Zhang, Y., and Wang, Y. (2012a). Experimental and Numerical Studies on Gas Production from Methane Hydrate in Porous Media by Depressurization in Pilot-Scale Hydrate Simulator. *Energy Fuels* 26 (10), 6300–6310. doi:10.1021/ef301229k

Li, X.-S., Wang, Y., Duan, L.-P., Li, G., Zhang, Y., Huang, N.-S., et al. (2012b). Experimental Investigation into Methane Hydrate Production during Three-Dimensional thermal Huff and Puff. *Appl. Energ.* 94, 48–57. doi:10.1016/j.apenergy.2012.01.024

Li, X.-S., Xu, C.-G., Zhang, Y., Ruan, X.-K., Li, G., and Wang, Y. (2016). Investigation into Gas Production from Natural Gas Hydrate: A Review. *Appl. Energ.* 172, 286–322. doi:10.1016/j.apenergy.2016.03.101

Lu, X., Zhang, X., Wang, P., and Liang, Q. (2019). Advances of Formation Dynamics of Natural Gas Hydrate. *Sci. Sin.-Phys. Mech. Astron.* 49 (3), 034605. doi:10.1360/sspma2018-00362

Makogon, Y. F., and Omelchenko, R. Y. (2013). Commercial Gas Production from Messoyakha deposit in Hydrate Conditions. *J. Nat. Gas Sci. Eng.* 11, 1–6. doi:10.1016/j.jngse.2012.08.002

Miyakawa, A., Saito, S., Yamada, Y., Tomaru, H., Kinoshita, M., and Tsuji, T. (2014). Gas Hydrate Saturation at S Ite C 0002, IODP E Xpeditions 314 and 315, in the K Umano B Asin, N Ankai Trough. *Isl. Arc* 23 (2), 142–156. doi:10.1111/iar.12064

Moridis, G. J., Collett, T. S., Boswell, R., Kurihara, M., Reagan, M. T., Koh, C., et al. (2009). Toward Production from Gas Hydrates: Current Status, Assessment of Resources, and Simulation-Based Evaluation of Technology and Potential. *Spe Reservoir Eval. Eng.* 12 (5), 745–771. doi:10.2118/114163-pa

Moridis, G. J., Kowalsky, M. B., Pruess, K., and Lawrence Berkeley Nat, L. (2005). Depressurization-Induced Gas Production from Class-1 Hydrate Deposits. *Spe Reservoir Eval. Eng.* 10 (5), 458–481. doi:10.2118/97266-MS

Muraoka, M., Ohtake, M., Susuki, N., Yamamoto, Y., Suzuki, K., and Tsuji, T. (2014). Thermal Properties of Methane Hydrate-Bearing Sediments and Surrounding Mud Recovered from Nankai Trough wells. *J. Geophys. Res. Solid Earth* 119 (11), 8021–8033. doi:10.1002/2014jb011324

Sharqawy, M. H., Lienhard, J. H., and Zubair, S. M. (2012). Thermophysical Properties of Seawater: a Review of Existing Correlations and Data. *Desalination Water Treat.* 16 (1-3), 354–380. doi:10.5004/dwt.2010.1079

Sloan, E. D. (2003). Fundamental Principles and Applications of Natural Gas Hydrates. *Nature* 426 (6964), 353–359. doi:10.1038/nature02135

Sloan, E. D., and Koh, C. A. (2008). *Clathrate Hydrates of Natural Gases*. Boca Raton,FL: CRC Press.

Song, Y., Cheng, C., Zhao, J., Zhu, Z., Liu, W., Yang, M., et al. (2015). Evaluation of Gas Production from Methane Hydrates Using Depressurization, thermal Stimulation and Combined Methods. *Appl. Energ.* 145, 265–277. doi:10.1016/j.apenergy.2015.02.040

Sun, Y., Li, S., Lu, C., Liu, S., Chen, W., and Li, X. (2021). The Characteristics and its Implications of Hydraulic Fracturing in Hydrate-Bearing Clayey silt. *J. Nat. Gas Sci. Eng.* 95, 104189. doi:10.1016/j.jngse.2021.104189

Waite, W. F., Santamarina, J. C., Cortes, D. D., Dugan, B., Espinoza, D. N., Germaine, J., et al. (2009). Physical Properties of Hydrate-Bearing Sediments. *Rev. Geophys.* 47 (4). doi:10.1029/2008rg000279

Waite, W. F., Stern, L. A., Kirby, S. H., Winters, W. J., and Mason, D. H. (2007). Simultaneous Determination of thermal Conductivity, thermal Diffusivity and Specific Heat in sI Methane Hydrate. *Geophys. J. Int.* 169 (2), 767–774. doi:10.1111/j.1365-246X.2007.03382.x

Xu, T., Zhang, Z., Li, S., Li, X., and Lu, C. (2021). Numerical Evaluation of Gas Hydrate Production Performance of the Depressurization and Backfilling with an *In Situ* Supplemental Heat Method. *ACS Omega* 6 (18), 12274–12286. doi:10.1021/acsomega.1c01143

Xu, W., and Ruppel, C. (1999). Predicting the Occurrence, Distribution, and Evolution of Methane Gas Hydrate in Porous marine Sediments. *J. Geophys. Res.* 104 (B3), 5081–5095. doi:10.1029/1998jb900092

Yamamoto, K., Kanno, T., Wang, X.-X., Tamaki, M., Fujii, T., Chee, S.-S., et al. (2017). Thermal Responses of a Gas Hydrate-Bearing Sediment to a Depressurization Operation. *RSC Adv.* 7 (10), 5554–5577. doi:10.1039/C6RA26487E

Yamamoto, K., Terao, Y., Fujii, T., Ikawa, T., and Seki, M. (2014). "Operational Overview of the First Offshore Production Test of Methane Hydrates in the Eastern Nankai Trough," in *Offshore Technology Conference 2014* (Houston, Texas, USA: OnePetro). doi:10.4043/25243-ms

Yang, L., Zhao, J., Liu, W., Yang, M., and Song, Y. (2015). Experimental Study on the Effective thermal Conductivity of Hydrate-Bearing Sediments. *Energy* 79, 203–211. doi:10.1016/j.energy.2014.11.008

Yang, L., Zhao, J., Wang, B., Liu, W., Yang, M., and Song, Y. (2016). Effective thermal Conductivity of Methane Hydrate-Bearing Sediments: Experiments and Correlations. *Fuel* 179, 87–96. doi:10.1016/j.fuel.2016.03.075

Ye, J.-l., Qin, X.-w., Xie, W.-w., Lu, H.-l., Ma, B.-j., Qiu, H.-j., et al. (2020). The Second Natural Gas Hydrate Production Test in the South China Sea. *China Geology.* 3, 197–209. doi:10.31035/cg2020043

Yu, T., Guan, G., and Abudula, A. (2019). Production Performance and Numerical Investigation of the 2017 Offshore Methane Hydrate Production Test in the Nankai Trough of Japan. *Appl. Energ.* 251, 113338. doi:10.1016/j.apenergy.2019.113338

Conflict of Interest: The authors declare that the research was conducted in the absence of any commercial or financial relationships that could be construed as a potential conflict of interest.

Publisher's Note: All claims expressed in this article are solely those of the authors and do not necessarily represent those of their affiliated organizations, or those of the publisher, the editors and the reviewers. Any product that may be evaluated in this article, or claim that may be made by its manufacturer, is not guaranteed or endorsed by the publisher.

frontiers | Frontiers in Earth Science

ORIGINAL RESEARCH
published: 25 April 2022
doi: 10.3389/feart.2022.880471

Source-Reservoir Characteristics and Accumulation of Gas Chimney-Type Gas Hydrates in Qiongdongnan Basin, Northern South China Sea

Qi Fan[1,2]*, *Qingping Li*[1,2], *Shouwei Zhou*[2,3], *Lixia Li*[1,2], *Zhenyu Zhu*[1,2] and *Xin Lv*[1,2]

[1]CNOOC Research Institute Company Limited, Beijing, China, [2]State Key Laboratory of Natural Gas Hydrates, Beijing, China, [3]China National Offshore Oil Company, Beijing, China

The Qiongdongnan Basin is an important gas hydrate exploration area in the South China Sea, but the gas hydrate accumulation process is poorly understood. By selecting an Lingshui (LS) target area and using first-hand geochemical data, three-dimensional seismic data, and an independent thermal insulation and pressure maintaining shipborne core analysis system, in this study, comprehensive geological evaluation was carefully conducted around the gas source and reservoir of the gas chimney hydrates, and the accumulation process was investigated. Geochemical data for a total of 47 sets of gas samples revealed that the gas source of the hydrates in the study area was mainly thermogenic gas supplemented by mixed gas. It was predicted that the contribution of the thermogenic gas to the hydrate accumulation was up to 70%. Using the independent shipborne core analysis system, the characteristics of the low-temperature combustible gas hydrates were determined, and the reservoir in the study area was characterized as non-diagenetic to weakly diagenetic, rich in clay and silt (D50 = 15.1–34.1 μm), weakly self-sustaining, and strongly heterogeneous. Based on the differentiated seismic response of the hydrate layer-gas bearing hydrate layer-shallow gas layer at the top of the gas chimney, the accumulation process in the target area was determined to be as follows: remote thermogenic gas transportation, local microbial genetic gas accumulation, episodic dynamic gas chimney reservoir formation, and source-reservoir control. In addition, the exploration ideas of an effective supply from a gas source and a shallow large-scale sand body are emphasized. The results of this study provide an important reference for the trial production of natural gas hydrates in the South China Sea.

Keywords: Qiongdongnan Basin, gas hydrates, gas chimney, gas source, reservoir, accumulation process

OPEN ACCESS

Edited by:
Pibo Su,
Guangzhou Marine Geological Survey, China

Reviewed by:
Zhifeng Wan,
Sun Yat-sen University, China
Qing Li,
Qingdao Institute of Marine Geology (QIMG), China

***Correspondence:**
Qi Fan
fanqi@cnooc.com.cn

Specialty section:
This article was submitted to Sedimentology, Stratigraphy and Diagenesis, a section of the journal Frontiers in Earth Science

Received: *21 February 2022*
Accepted: *01 April 2022*
Published: *25 April 2022*

Citation:
Fan Q, Li Q, Zhou S, Li L, Zhu Z and Lv X (2022) Source-Reservoir Characteristics and Accumulation of Gas Chimney-Type Gas Hydrates in Qiongdongnan Basin, Northern South China Sea. Front. Earth Sci. 10:880471. doi: 10.3389/feart.2022.880471

1 INTRODUCTION

Natural Gas Hydrates (NGHs) are a type of ice-like cage structure formed by water and natural gas molecules under low temperature and high pressure conditions. They mainly occur in dispersed, nucleated, vein-like, and massive forms in the seabed and at depths of >300 m in terrestrial permafrost regions in passive continental margins. Countries continue to pay attention to and invest in the research and development of natural gas hydrates, which are a strategic clean energy source. Gas hydrates have been found in 240 locations around the world. Hydrate pilot production has been

completed in Mackenzie in Canada, the north slope of Alaska, the Nankai trough in Japan, and the South China Sea (Paganoni et al., 2019; Wei et al., 2019; Deng et al., 2021; Lai et al., 2021).

Chinese gas hydrate surveying began in 1999. After long-term exploration and sea trials, NGHs have been identified as the 173rd new mineral. The Qiongdongnan Basin and the Pearl River Basin are delineated as two pilot test areas for natural gas hydrate exploration and production (Zhu et al., 2009; Zhang et al., 2019a). The research on exploration technology, reservoir formation mechanisms, and basic physical properties has reached or approaches the international advanced level, but the overall exploration degree is low. At present, the most important work is to establish reliable natural gas hydrate resource evaluation and exploration techniques. Since 2017, China has completed several rounds of offshore gas hydrate drilling, logging while drilling, and coring operations in the deep water area of the Qiongdongnan Sea area using the drilling and logging system on the independent offshore oil 708 deep water engineering survey ship and independently developed coring technology. Comprehensive domestic technologies and a complete operation process of the ship exploration drilling, logging, and coring evaluation sea test have been developed, making China the third country in the world to independently master this type of technology. After three rounds of voyage, Qiongdongnan Sea Area containing the hydrate formation of "strong BSR seismic reflection, high resistivity and low acoustic time" features, can be divided into "type gas chimney that are rich in thermogenic gas hydrate, polygons that are rich in thermogenic gas fracture—silt composite hydrate and the causes of thermogenic gas and mixed gas hydrate sliding body at the bottom of the" three kinds of hydrates. But the study on the geological process of accumulation is not enough.

The Qiongdongnan Basin is an important oil- and gas-producing area and hydrate-rich region in the South China Sea. The X17-2, X25-1, and X18-1 gas fields and the Haima active cold seep have been discovered successively along the channel of the central canyon of the basin, indicating that the deep gas source supply is sufficient and there are good transport channels and a favorable reservoir formation environment (Xu et al., 2016; Wang et al., 2018; Yang et al., 2018; Zhang et al., 2019b; Wan et al., 2020; Wei et al., 2020; Zhang et al., 2021; Chen et al., 2022). In particular, leaky gas hydrates, represented by gas chimney hydrates, have become one of the research objects in trial production projects (Zhang et al., 2016; Paganoni et al., 2019; Wei et al., 2019; Zhang et al., 2020a; Zhang et al., 2020b; Deng et al., 2021; Lai et al., 2021; Wan et al., 2021). However, gas chimney hydrates are characterized by multi-stage dynamic accumulation, multi-solution of logging seismic responses, strong reservoir heterogeneity, and low saturation of the ore body, which restrict our geological understanding and exploration techniques (Zhu et al., 2009; Wang et al., 2015; Wan et al., 2017; Wang et al., 2018; Wan et al., 2022).

In this study, the gas source, reservoir, and accumulation process of gas hydrates in the selected gas chimney hydrate enrichment area in the Lingshui(LS) sea area in the Qiongdongnan Basin were systematically and carefully investigated using first-hand geochemical and geophysical data. In terms of gas source, this is the first time that China's independent coring technology is used to collect and analyze the gas data of hydrate formation in hydrate well and conventional gas layer in gas well, which is of practical significance to the co-production of hydrate and conventional gas and the correlation analysis of hydrate and conventional gas. In terms of reservoir, the infrared imaging characteristics, scanning electron microscopy and remolding characteristics of hydrate reservoir in previous studies are supplemented, and the fine grain characteristics and physical properties of hydrate reservoir are reported. A quantitative understanding of the gas source (70% thermogenic gas and 30% mixed gas) was obtained; two main reservoir types (rich silt shale (clay) reservoir and microfracture reservoir), were identified; and the "remote thermogenic gas filling gas chimney, local microbial origin supplementation, episodic dynamic accumulation, and source-reservoir control" accumulation mechanism was identified. The exploration idea of a gas source and sand body was determined to have a great potential. The results of this study provide an important scientific reference for the trial production of natural gas hydrates in the South China Sea.

2 GEOLOGIC BACKGROUND

The Qiongdongnan Basin is located at the west end of the continental shelf of the South China Sea, north of Hainan Island, south of the Yongle uplift of the Paracel Islands, west of the Yinggehai Basin, and adjacent to the Shenhu uplift and the Zhu III and Zhu II depressions. It is a NE-trending extensional rift sedimentary basin with a basin area of 8.3×10^4 km^2. It consists of five secondary structural units: the Hainan uplift, northern depression, central uplift, central depression, and southern uplift. Because the Mesozoic, the Qiongdongnan Basin has experienced the Shenhu movement, the South China Sea movement, and the Dongsha movement successively, the sedimentary strata are characterized by three stages of differentiation: the Late Cretaceous-Late Oligocene multi-episode rifting period, the Early Miocene-Middle Miocene thermal subsidence period, and the Neotectonic period since the Late Miocene (Liang et al., 2019; Paganoni et al., 2019; Wei et al., 2019; Ye et al., 2019; Deng et al., 2021; Lai et al., 2021).

At present, the Qiongdongnan deep water area has become a key area for conventional oil and gas exploration and hydrate trial production, with a deep water area of about 5.3×10^4 km^2 and a maximum water depth of 3,000 m, including the central depression, the Songnan low uplift, and the Lingnan low uplift. The faults in the deep water area of the Qiongdongnan Basin are mainly developed in Paleogene strata, and the faults mainly trend NE-SW, E-W, and NW-SE. Among them, the large-scale NE-SW faults run through the central depression, with a length of about 300 km in the deep water area; and they divide the central Canyon waterway into the Ledong section, Lingshui section, Songnan section, and Baodao section. The deep water area of the basin exhibits a structural pattern characterized by north-south zoning and east-west partitioning (**Figure 1**) (Huang et al., 2016; Huang et al., 2017).

The study area is located in the Songnan low uplift area and is surrounded by the Lingshui Sag and the Beijiao Sag, with water

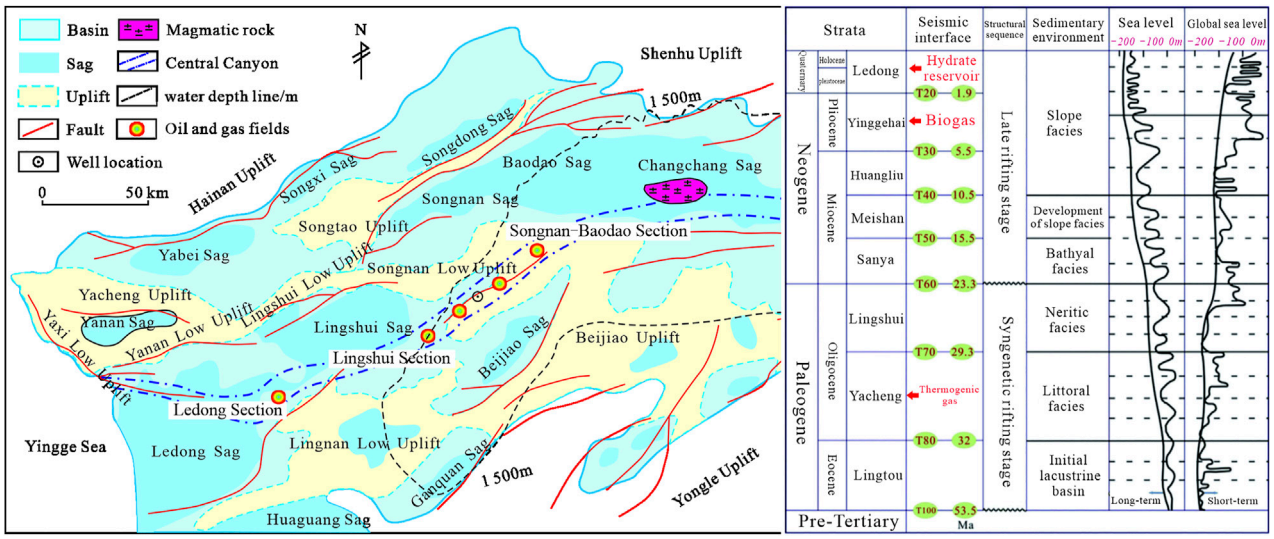

FIGURE 1 | Regional tectonic position and stratigraphic histogram of Qiongdongnan Basin.

depths of 1,650 m–1800 m. The focus of the exploration is the gas chimney group in the Songnan low uplift. The 3D seismic data and general survey reveal that this area has geological characteristics indicative of gas hydrate accumulation. 1) High production gas flow has been obtained from an exploration well adjacent to the X17-2 gas field in the submarine fan sandstone reservoir of the Neogene Yinggehai Formation, with a daily gas output of 110×10^4 m^3, which is the first large deep water gas field covering over 100 billion cubic meters discovered by CNOOC. 2) Multiple gas chimneys are distributed in the Ne-trending belt; a typical blank zone reflection and BSR distribution can be seen in the structure. The geothermal gradient of the gas chimneys is high (113°C/km), the transport system is well developed, and the fluid circulation is active. 3) The hydrates are mainly developed in the submarine fan silt-sand reservoir in the Quaternary Ledong Formation, the provenance of which includes the Kunsong Block, Red River in India, and Hainan Island. 4) Remotely Operated Vehicle (ROV) observations revealed that the terrain of the seafloor is flat, with a small number of pock marks and deep-sea organisms. Crustacean fragments were observed around the pocks.

3 METHODS

In this study, 47 representative samples were systematically collected from hydrate wells and conventional exploration wells in the study area, and they were subjected to gas source analysis, including data on the gas components and carbon isotope compositions of the methane in the deep, medium, and shallow strata in the gas chimney development areas, such as areas X18-H5 and X17-2. The gas composition was analyzed by gas chromatography mass spectrometer. The carbon isotope was analyzed by stable isotope mass spectrometer. The water depth of the sampling well is 1720 m, and the hydrate occurrence depth is 24–172 mbsf. The well is located above the core of the gas chimney. Based on the identification chart for hydrocarbon gas genetic types in marine sediments, the genetic discrimination was conducted using the samples' gas humidity values, k = C1/(C2+C3), the carbon isotope compositions of the methane and ethane in the gas samples.

The reservoir in the Qiongdongnan Sea Area has been carefully analyzed using an independent ship-borne thermal insulation and pressure preserving core analysis and testing system developed in China. To confirm the low temperature and flammability of the methane hydrates, a portable infrared thermal imager was used to core the hydrate enrichment intervals from 127 to 153 mbsf. The sediment particle sizes of 15 samples from different depths (0–173 mbsf) were analyzed using a shipboard laser particle size analyzer (BT-9300ST, Dandong Bettersize Instruments Co., Ltd., Dandong, China). According to the national standard (GB/T19077.1-2008), sediment samples weighing 0.5 g were added to 1,000 ml of deionized water, and then 0.5 M sodium hexametaphosphate was added as the dispersant. After that, the samples were stirred for at least 1 min to evenly disperse the particles. Finally, the samples were dried and tested. The rock and mineral analysis of the sediment samples from 151.7 mbsf was conducted using a shipboard X-ray diffractometer. In addition, the samples were observed using a scanning electron microscope (SEM) (Nova NanoSEM 450, FEI Co.,, United States of America). Ten grams of the sample was weighed and dried, and then, a small spoonful of dry sample was smeared on tape for field emission SEM measurements. *In situ* X-ray Computed Tomography (CT) scans (SMX-225CTX-SV, Shimadzu Co.,, Japan) were performed on samples from depths of 120 and 123.5 mbsf under pressure with a resolution of 40 μm.

4 RESULTS

4.1 Characteristics of the Gas Source of the Natural Gas Hydrates

4.1.1 Gas Composition and Isotopic Characteristics

It can be seen from the test results of the samples from the deep, medium, and shallow strata that the main components of the gas include hydrocarbon gases, such as methane, ethane, and propane, and non-hydrocarbon gases, such as carbon dioxide, sulfur dioxide, and nitrogen. The methane content is the highest (97.7%, average of 89.21%, excluding four shallow samples from area X25-1), and the ethane content is also high(17.01%, average of 7.88%, excluding four shallow samples from area X25-1). The average carbon dioxide content was 1% (**Table 1**) (Huang et al., 2016; Huang et al., 2017; Cong et al., 2018; Liang et al., 2019; Paganoni et al., 2019; Wei et al., 2019; Ye et al., 2019; Deng et al., 2021; Lai et al., 2021). Therefore, the gas composition shows that Type I and II methane hydrates are developed and occur in the study area (**Figure 2**). The carbon isotope values of the methane are −59.5‰ to −35.4‰, with an average of −46.26‰. The carbon isotope values of the ethane are −20.67‰ to −27.6‰, with an average of −25.22‰. The humidity values of the samples are

TABLE 1 | Gas composition and isotope data of gas chimney type hydrate in Qiongdongnan Basin (Huang et al., 2016; Huang et al., 2017; Cong et al., 2018; Liang et al., 2019; Paganoni et al., 2019; Wei et al., 2019; Ye et al., 2019; Deng et al., 2021; Lai et al., 2021)

No.	Sample	Sample type	Deepth/mbsf	C_1/%	C_2/%	CO_2/%	δC_1/‰	δC_2‰	C_1/(C2+C3)	Maker	Source
1	X18-H5-1	Hydrate gas	27.2	83.08	13.54	3.38	−58.7	−23.07	6	CNOOC	This study
2	X18-H5-2	Hydrate gas	67.2	95.83	4.17	0	−58.47	−22.95	23	CNOOC	This study
3	X18-H5-3	Hydrate gas	129.7	86.64	11.5	1.86	/	/	8	CNOOC	This study
4	X18-H5-4	Hydrate gas	147.2	92.93	6.3	0.77	/	/	15	CNOOC	This study
5	X18-H5-5	Hydrate gas	151.7	81.85	15.8	2.35	/	/	5	CNOOC	This study
6	X18-H5-6	Hydrate gas	172	86.17	13.51	0.32	−48.08	−20.67	6	CNOOC	This study
7	X25-1-1	Deposits	37	10.22	0.46	0.02	−46.2	−27.6	22	CNOOC	This study
8	X25-1-2	Deposits	37.2	3.55	0.18	0.04	−45.9	−24.3	20	CNOOC	This study
9	X25-1-3	Deposits	37.4	8.12	0.16	0.05	−46.5	−25.5	51	CNOOC	This study
10	X25-1-4	Deposits	37.6	2.64	0.12	0.06	−46.7	−26.9	22	CNOOC	This study
11	X25-1	Natural gas	Huangliu	83.66	7.2	5.98	−38.3	−24.8	13	CNOOC	Gan et al., 2018
12	X25-2	Natural gas	Huangliu	77.81	6.84	4.29	−35.4	−25.2	14	CNOOC	Gan et al., 2018
13	X25-5	Natural gas	Huangliu	79.93	8.23	2.6	−41.6	−26.1	15	CNOOC	Gan et al., 2018
14	X17-2-1	Natural gas	3,306	92.51	6.14	0.45	−36.8	−23.5	15	CNOOC	Huang et al. (2016)
15	X17-2-2	Natural gas	3,329	91.68	5.9	0.7	−38.2	−23.7	16	CNOOC	Huang et al. (2016)
16	X17-2-3	Natural gas	3,407	89.45	7.21	0.53	−38.0	−25.3	12	CNOOC	Huang et al. (2016)
17	X17-2-4	Natural gas	3,251	90.97	7.68	0.2	−39	−25.4	12	CNOOC	Huang et al. (2016)
18	X18A-1	Natural gas	Huangliu	88.01	6.89	0.06	−40.1	−26.4	16	CNOOC	Gan et al., 2018
19	X18A-2	Natural gas	Huangliu	89.30	5.95	0.05	−40.4	−25.2	17	CNOOC	Gan et al., 2018
20	X18B-1	Natural gas	Huangliu	94.15	3.67	0.05	−40.4	−25.2	18	CNOOC	Gan et al., 2018
21	X22-1-1	Natural gas	3,339	91.16	7.48	0.31	−39.2	−26.2	19	CNOOC	Liang et al., 2016
22	X22-1-2	Natural gas	3,352	91.37	7.28	0.32	−38.8	−26	20	CNOOC	Liang et al., 2016
23	X22-1-3	Natural gas	3,391	91.53	7.20	0.32	−39.2	−26	21	CNOOC	Liang et al., 2015
24	W08-2018-1	Hydrate gas	8	97.69	2.05	/	−59.5	−26.0	46	CGS	Lai et al. (2021)
25	W08-2018-2	Hydrate gas	62.93	81.21	12.88	/	−56.3	−26.9	5	CGS	Lai et al. (2021)
26	W08-2018-3	Hydrate gas	148.4	79.16	14.4	/	−50.4	−26.5	4	CGS	Lai et al. (2021)
27	W08-2018-4	PCS	32.88	94.94	4.23	/	−54.4	−25.5	19.7	CGS	Lai et al. (2021)
28	W08-2018-5	PCS	79	95.75	3.69	/	−58.6	−25.1	23.5	CGS	Lai et al. (2021)
29	W08-2018-6	PCS	80.9	95.73	3.68	/	−48.8	−22.4	23.7	CGS	Lai et al. (2021)
30	W08-2018-7	PCS	112.3	96.46	2.99	/	−53.8	−23.3	29.1	CGS	Lai et al. (2021)
31	W08-2018-8	PCS	145.65	83.49	11.61	/	-49.3	−27.5	5.4	CGS	Lai et al. (2021)
32	W08-2018-9	PCS	158	84.17	10.99	/	−50.4	−26.9	5.7	CGS	Lai et al. (2021)
33	W08-2018-10	PCS	187.1	92.82	4.56	/	−50.4	−26.7	14	CGS	Lai et al. (2021)
34	W9B-2018–1	Void gas	18.55	95.2	4.22	/	/	/	22	CGS	Liang et al. (2019)
35	W9B-2018–2	Void gas	42	88.3	9.71	/	/	/	8	CGS	Liang et al. (2019)
36	W9B-2018–3	Void gas	43.98	90.4	7.98	2978 ppm	/	/	10	CGS	Liang et al. (2019)
37	W9B-2018–4	Void gas	59.12	98.3	1.33	1687 ppm	/	/	68	CGS	Liang et al. (2019)
38	W9B-2018–5	Void gas	59.9	98.3	1.31	1776 ppm	/	/	70	CGS	Liang et al. (2019)
39	W9B-2018–6	Void gas	73.18	95.1	4.50	/	/	/	20	CGS	Liang et al. (2019)
40	W9C-2018–1	Void gas	106	97.3	2.40	/	/	/	40	CGS	Liang et al. (2019)
41	W9C-2018–2	Void gas	107	97.7	2.07	1088 ppm	/	/	46	CGS	Liang et al. (2019)
42	W9C-2018–3	Void gas	131.81	81.6	15.04	700 ppm	/	/	5	CGS	Liang et al. (2019)
43	W9C-2018–4	Void gas	133.61	86.9	11.31	/	/	/	7	CGS	Liang et al. (2019)
44	W9C-2018–5	Void gas	152.29	79.1	16.56	2339 ppm	/	/	4	CGS	Liang et al. (2019)
45	W9C-2018–6	Void gas	152.69	78.5	17.01	2216 ppm	/	/	4	CGS	Liang et al. (2019)
46	W9C-2018–7	Void gas	155.14	84.5	11.38	2142 ppm	/	/	6	CGS	Liang et al. (2019)
47	W9C-2018–8	Void gas	156.21	85.6	10.51	1880 ppm	/	/	6	CGS	Liang et al. (2019)

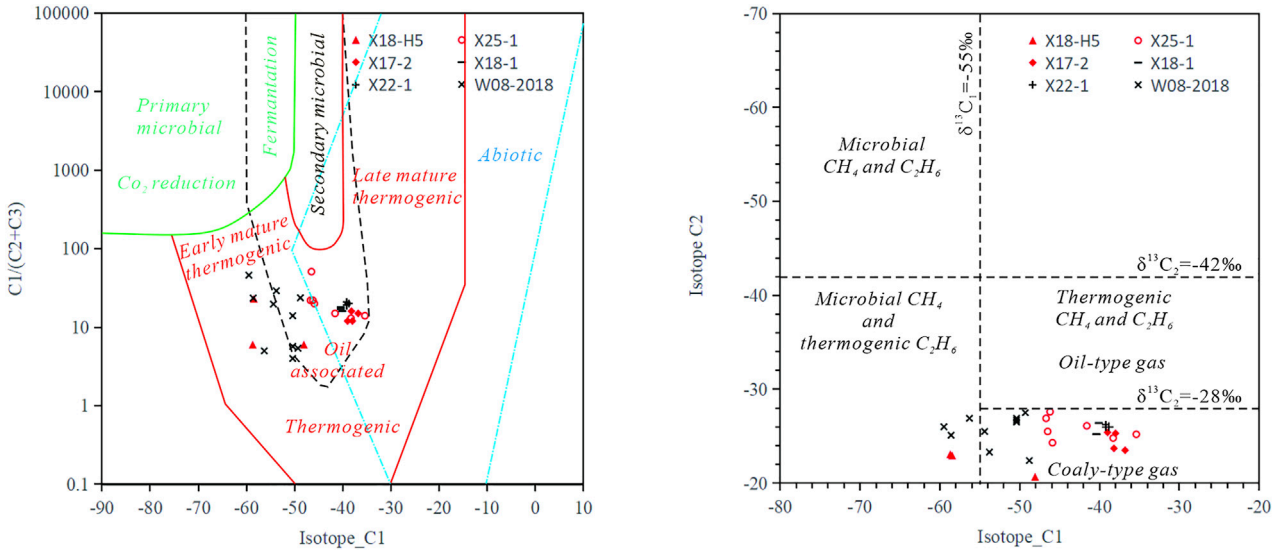

FIGURE 2 | Identification plate of gas source types of gas chimney hydrate in Qiongdongnan Basin.

4–51, with an average of 17.8. From the relationship between the gas composition and depth, it can be seen that the methane contents of the shallow samples are higher than those of the deep samples, and the ethane contents of the deep samples are higher than those of the shallow samples. The contributions of the deep thermogenic gas and shallow microbial gas to the gas components are shown in **Figure 3**.

4.1.2 Gas Source Types and Contributions

The isotopic error analysis revealed that the original signal is clearly retained in the isotopic data for the collected samples. The first gas origin chart (Milkov and Etiop, 2018) divides the gas into primary microbial origin, low microbial origin, thermal origin, and abiotic origin. The majority of the gas samples plot in the oil-type thermal origin gas and early maturation thermal origin gas fields (**Figure 2**). On the second gas origin chart (Huang et al., 2016; Huang et al., 2017; Cong et al., 2018; Liang et al., 2019; Paganoni et al., 2019; Wei et al., 2019; Ye et al., 2019; Deng et al., 2021; Lai et al., 2021; Zhang et al., 2020), the majority of the gas samples plot in the coal-derived thermogenic methane and ethane fields, and only four samples plot in the microbiological methane and thermogenic ethane fields (mixed gas) (**Figure 2**). Both of these results confirm a thermogenic gas origin, but there are limitations to the coal type pyrolysis gas and oil type pyrolysis gas (i.e., they are significantly different in terms of the chemical composition and structure of the gas forming parent material). Combined with the sample properties and identification results, it is concluded that the hydrate gas in the study area is mainly thermogenic gas, supplemented by mixed genetic gas, and the contribution of the thermogenic gas is 70%.

4.1.3 Gas Resource Potential

The comparison of the gas source revealed that the source rocks of the biogenic gas in the study area are the marine siltstone and argillaceous siltstone of the local Yinggehai Formation-Quaternary system. The carbon isotope compositions of the methane range from −87‰ to −62‰, and the organic carbon contents of the source rocks of the gas range from 0.28 to 0.49%. The thermogenic gas in the study area is derived from the source rocks of the Yacheng Formation to Sanya Formation in the Lingshui Sag and Beijiao Sag. The organic matter is Type II and III kerogen and is in the mature to highly mature (Ro = 1.6–3.5%) gas-generation stage. It is concluded that the gas source in this area is sufficient and can serve as the basis for mineralization.

4.2 Characteristics of Gas Hydrate Reservoir

The reservoir in the study area is composed of the clayey silty and silty clay deposits of the Quaternary Ledong Formation (~1.9 Ma), which is a non-diagenetic fine-grained reservoir in the abyssal plain facies. The natural gamma ray values of the hydrate formation are 30–50 API higher than those of the adjacent formation. The content of silty sand is high, but it is still in the clay-silty sand grade for weak diagenetic-non-diagenetic and quartz-rich feldspar. It was found that the hydrate reservoir is weakly diagenetic to non-diagenetic, is rich in clay and silt, is weakly self-sustaining, and is strongly heterogeneous.

4.2.1 Thermal Imaging Characteristics of Hydrate Cores

At room temperature (about 27°C), the temperature range of the core samples is −3.1 to 30°C, and the temperatures of the columnar thermal insulation and pressure retaining reservoir samples are 23–25°C. The block hydrate samples have

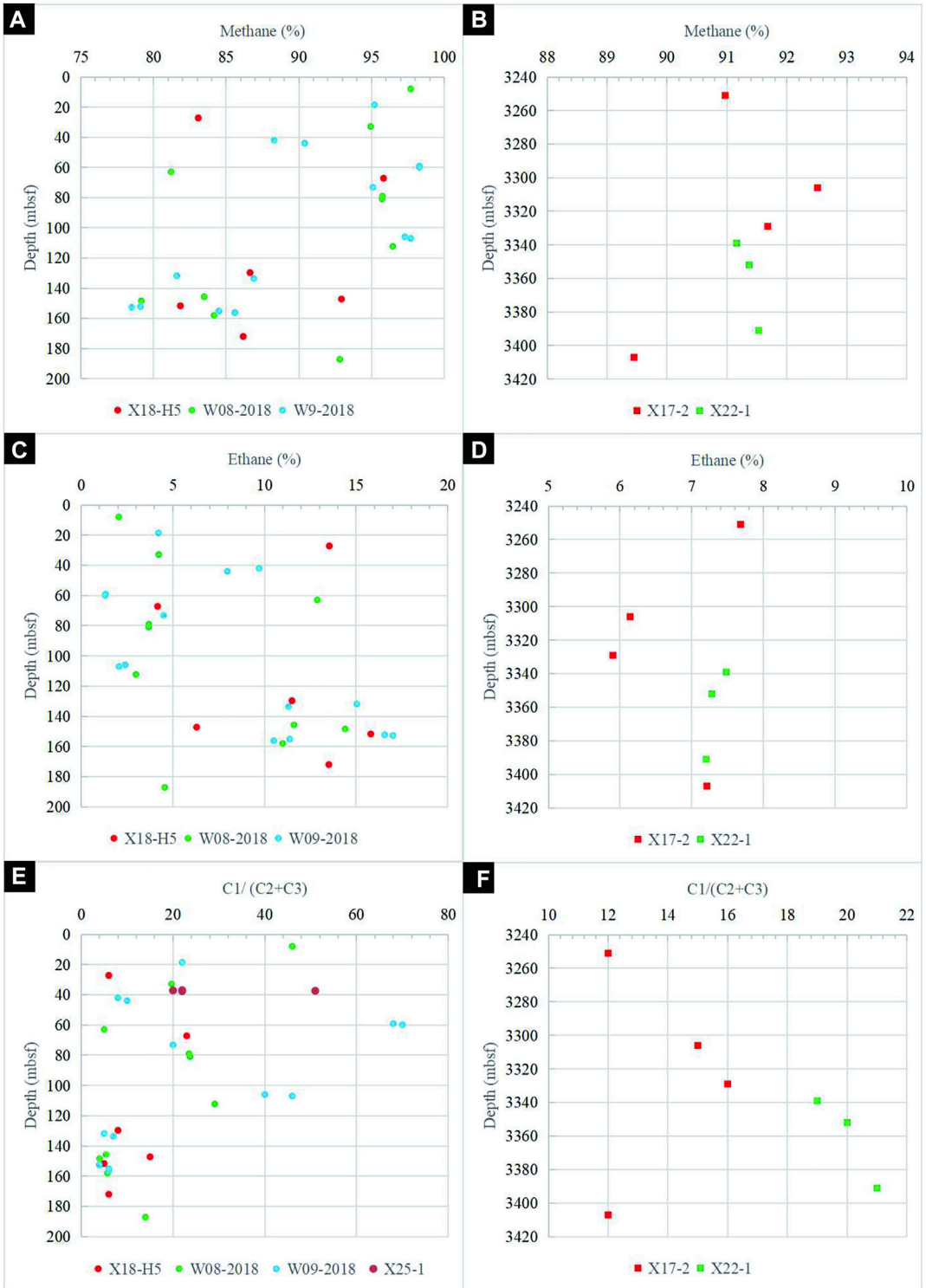

FIGURE 3 | Gas content at different depths at different sites **(A,B)** Methane; **(C,D)** Ethane; **(E,F)** C1/(C2+C3))

significant low temperature characteristics (−3.1–0°C), and they were compared with the flame temperature of the hydrate after ignition (89°C), which proves that the hydrates are characterized by low-temperature flammability. The overall shape of the reservoir is cylindrical (purple, about 25–26°C), and the hydrate ore body has a low temperature (black, about 1.6°C) and is distributed in patches and masses, indicating that the coring harvest was basically complete (**Figure 4**).

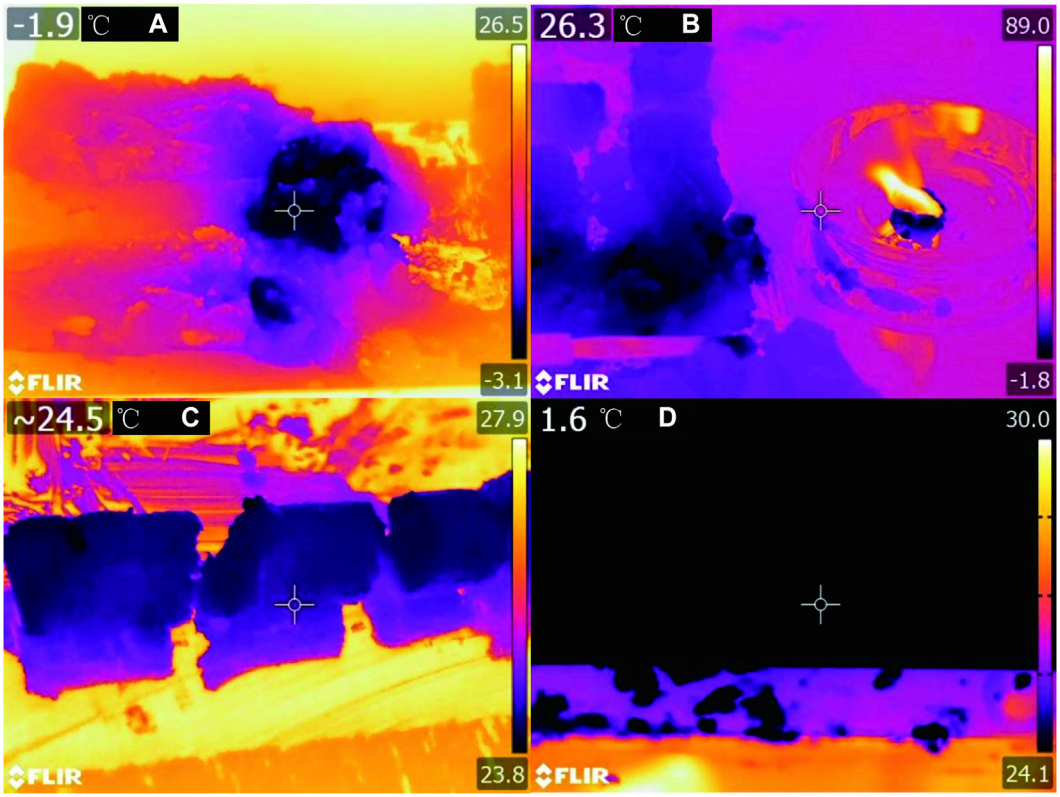

FIGURE 4 | Core thermal imaging characteristics **(A)** hydrate measurement; **(B)** flame measurement; **(C)** Columnar core measurement; **(D)** ore body measurement).

During the process of transferring the sample from the temperature and pressure environment, 1) in the initial stage of core removal, the reservoir exhibited a good cylindrical shape, but the cylindrical samples gradually collapsed during the subsequent testing process, with scattered and porridge-like characteristics. This indicates that the reservoir is non–diagenetic to weakly diagenetic and is poorly self-sustaining. The hydrates play an important role in supporting the stable consolidation of the reservoir's framework. 2) Several independent and dispersed hydrate ore bodies were observed in the obtained multi-section rock core, indicating the poor connectivity and strong heterogeneity of the hydrate reservoir. 3) During the core placement, the temperature of the reservoir continued to increase, which is speculated to have been caused by the decomposition and heat absorption of the dispersed hydrates in the reservoir's pores.

4.2.2 Particle Size Analysis

The particle size analysis results are presented in **Table 2**. The results show that 1) the median grain size of the sediments ranges from 15.1 to 34.1 μm, and the median grain size is concentrated in the range of 21.3–28.9 μm (9/15), indicating that the reservoirs are composed of silty sediments. 2) At sampling depths of 0.8 mbsf and 123 mbsf, the median grain size of the reservoir is 30–34 μm. Combined with the Cone Penetration Test (CPT) stress characteristics at the corresponding depth, the analysis results indicate that the reservoir is composed of carbonate crust or a small amount of silty deposits, reflecting ancient cold seep activity. 3) The grain size of the sediments varies little with depth, indicating that the sedimentary environment is Quaternary deep-sea suspended sediments, and large-scale silty and sandy deposits are not present.

4.2.3 Mineral Composition and Electron Microscopic Characteristics

The main mineral composition of the samples included quartz (23%), plagioclase (17%), sericite (15%), albite (14%), calcium carbonate (10%), illite (10%), potassium microcline (3%), pyrite (1%), and amphibole (1%). The corresponding major element compositions of the samples included silicon dioxide (54%), aluminum oxide (15%), calcium oxide (5%), ferric oxide (5%), potassium oxide (4%), magnesium oxide (3%), sodium oxide (2%), sulfur oxide (2%), and titanium dioxide (1%). The above results show that the main minerals in the samples were quartz, chlorite, mica, and feldspar, indicating that the reservoir is a clay-rich silty deposit.

A large number of lamellar clay minerals were observed under the electron microscope, but the mineralization and

TABLE 2 | Sample depth and median grain size of gas chimney type gas hydrate reservoir in Qiongdongnan Sea Area.

Depth(m)	median grain size(μm)
0.1	24.856
0.5	27.641
0.8	34.112
0.95	24.600
11.2	24.760
12.3	21.312
27.2	15.055
87.2	16.710
100.7	17.946
123.7	30.642
127.2	27.784
129.7	28.944
137.2	21.804
151.7	15.962
172	25.555

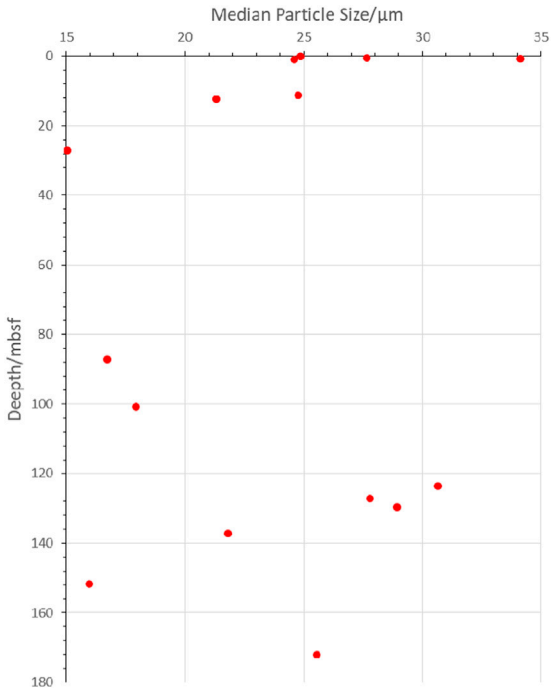

diagenetic characteristics of the minerals were weak, indicating that the reservoir is weakly diagenetic to non-diagenetic (**Figure 5**).

4.2.4 Pore Structure and CT Scans

In situ X-ray CT analysis yielded two typical reservoir structural features that were consistent with the predicted major reservoir types (**Figure 6**). **Figure 6A** shows the clay-rich silty reservoir lacking fractures, and it is fine grained and homogeneous overall (gray). The inferred hydrate ore body (black) is massive and porphyritic and is independently dispersed within the core, lacking a continuous veined core. **Figure 6B** shows the clay-rich silty reservoir with well-developed fractures. Overall, the fractures (dark brown) are well developed and have inconsistent strikes. A small amount of granular hydrate (black) can be seen in the core fractures, but

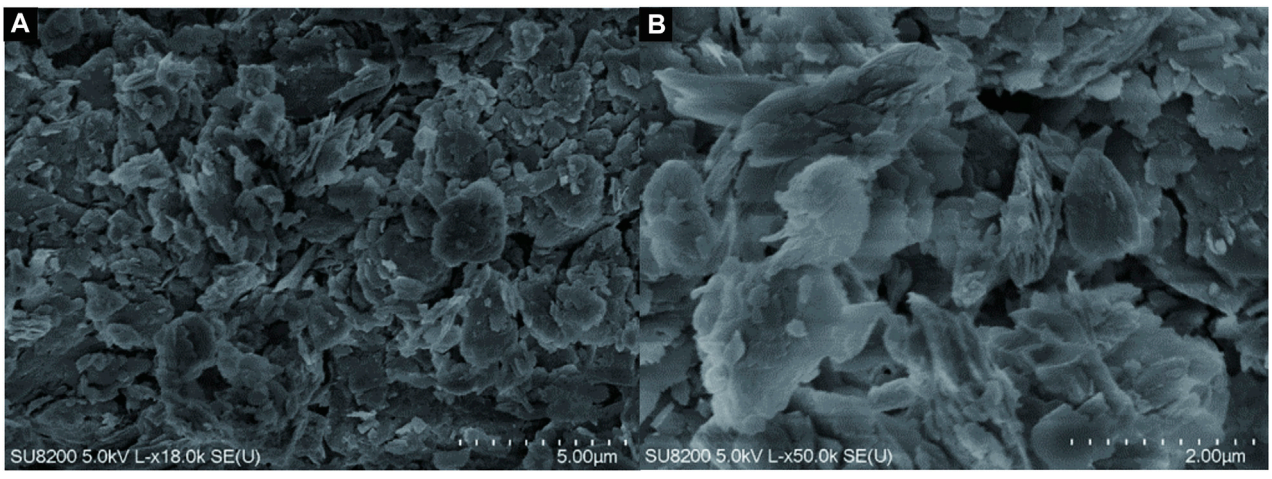

FIGURE 5 | Electron microscopic characteristics **(A)** reservoir sample**I**; **(B)** reservoir sample**II**).

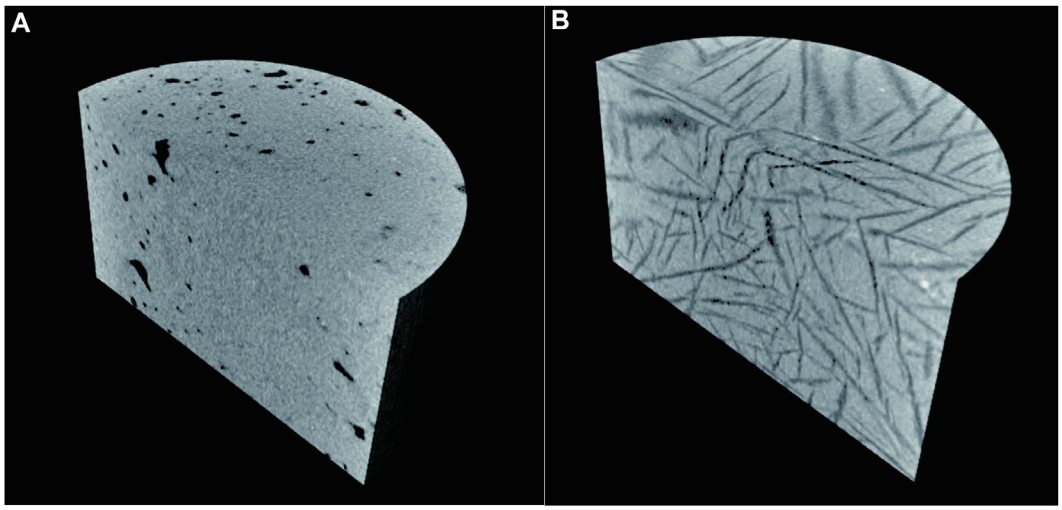

FIGURE 6 | 3D simulated images of two types of reservoirs by X-ray CT scanning **(A)** reservoir sample**I**; **(B)** reservoir sample**II**).

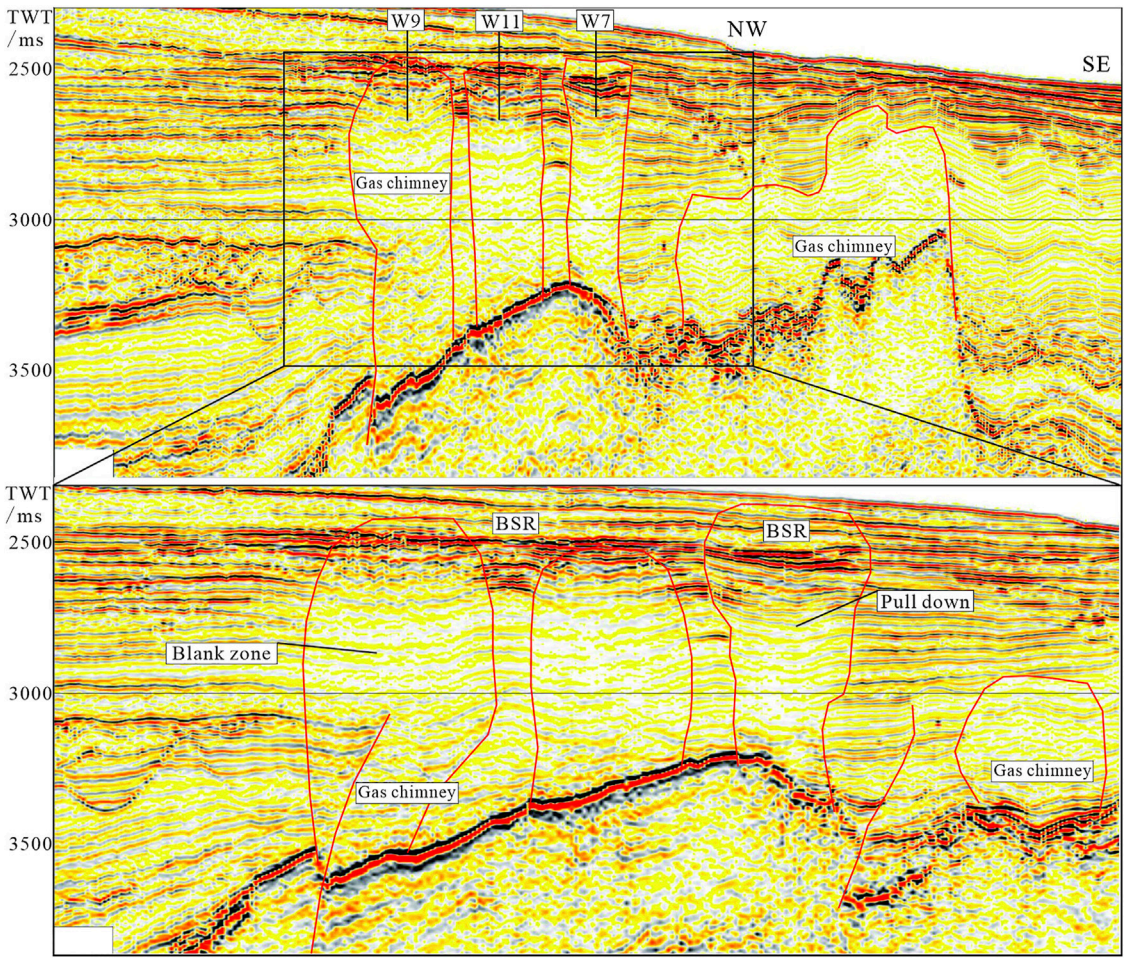

FIGURE 7 | Seismic reflection of gas chimney structure in H area of Qiongdongnan Basin.

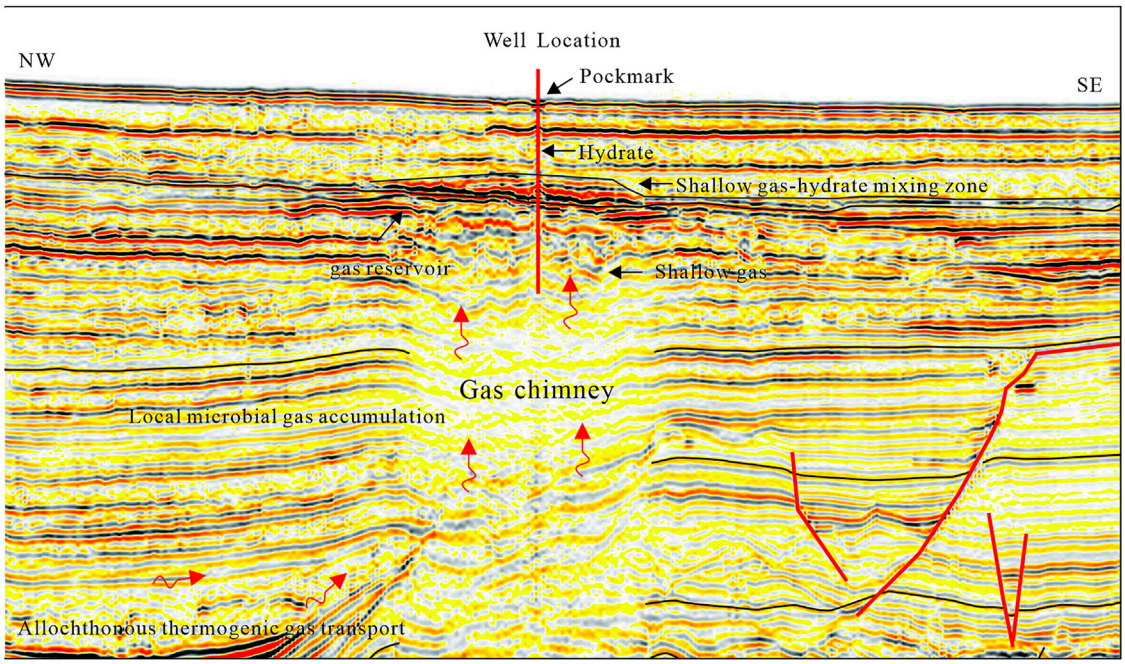

FIGURE 8 | Gas hydrate accumulation model in H area, Qiongdongnan Basin.

the amount of nucleation is limited. It was found that the microfracture reservoir is the main reservoir type in the gas chimney, and the fractures improve the hydrate storage space, which suggests that research on fractured reservoirs in fine-grained sediments should be strengthened.

5 DISCUSSION

5.1 Gas Chimney Conductor

Gas chimney-type hydrates are the main occurrence structure of the gas hydrates in the Qiongdongnan Sea Area. Gas chimneys are often formed by overpressure of the gas reservoir, low structural stress, and mud shale isolation. In fact, they are microfracture groups formed by abnormal formation pressure that appear as oval or upright chimneys on the seismic profile. They are characterized by abnormal velocities, in-phase axis pull down, and chaotic blank reflections due to the gas they contain (**Figure 7**) (He et al., 2015; Zhang et al., 2019). Theory and exploration have revealed that the evolution of mud diapirs, gas chimneys, and pocks is continuous, and these structural groups have a high fluid transport efficiency. The characteristics of gas chimneys can reflect the tectonic evolution stage of the gas chimneys, the fluid flux, and the migration path.

The gas chimneys in the LS region are concentrated in the ridges of the Songnan low uplift. The diameters of the individual gas chimneys are 3–7 km, and four consecutive gas chimneys form a group along the NEE direction. The tops of the gas chimneys are wide and low and are covered by Quaternary argillaceous deposits and silt-rich slump bodies. The bottom simulating reflector (BSR) phenomenon is obvious in the submarine fan of 3rd Ledong Formation and the 4th Ledong Formation. The acoustic Blank Zone (BZ) in the core of the gas chimney is long and elliptic and exhibits a wave impedance difference with the surrounding rock. The core is often connected with the sand body, and the root narrows, and it is in unconformable contact with the underlying strata (**Figure 8**).

Based on the geological and geophysical analysis, the gas chimneys are considered to be the most efficient known transport channels in this area. The study area has a high geothermal gradient (65°C/km in the wing and 113°C/km in the core). A large number of craters and biological remains of shellfish were observed on the seafloor, and carbonate crusts and bioclasts were repeatedly returned with the rock debris, indicating that fluid channels developed in the tops of the gas chimneys and there is upwelling and paleo-cold seep activity. In addition, a large number of fractures were observed in the remolded cores, indicating that abnormal fluid pressure played an important role in the formation of the large-scale fractured reservoirs.

In particular, combined with the logging data, the seismic profile can be divided into a hydrate layer (top), a hydrate and shallow gas mixed layer (middle), and a shallow gas layer (bottom). The gas hydrates in the upper member of the Ledong Formation at the top of the gas chimneys exhibit a scattered, patchy, strong amplitude and in-phase axial thickening, and the BSR is more obvious. The gas-water transition zone in the middle part of the Ledong Formation is characterized by multiple sets of external wedge-shaped filling deposits and a strong internal amplitude. Based on the core of the lower member of the Ledong Formation, the larger the free gas content is, the more obvious the pull-down amplitude of the isophase axis is. This three-section characteristic and the logging

interpretation indicate that deep and local gas accumulated at the top after convergence and spilled down after saturation. The gas boundary is controlled by the temperature and pressure conditions, indicating that the scope of the gas charging and the reservoir configuration affect the scale of the hydrate occurrence.

5.2 Accumulation and Main Controlling Factors

Based on the above understanding, the geological process and a model of the gas hydrate accumulation in the study area were determined: remote thermogenic gas transportation, local microbial genetic gas accumulation, episodic dynamic gas chimney reservoir formation, and source-reservoir control. The analysis of the source of the gas revealed that multiple gas sources are the material basis of the gas chimneys. The gas source of the NGHs in the Songnan low uplift is mainly thermogenic gas from the remote Lingshui Sag, Lingshui Subsag, and Beijiao Sag. Based on the geothermal gradient and basin model, the Yacheng, Lingshui, and Sanya formations are in the oil-generation window (3,150–5,000 m, RO = 0.5–1.3%), and they have a thermogenic gas generation and hydrocarbon expulsion capacity (Zhang et al., 2019). Allochthonous thermogenic gas can be transported into the mud diapir through the sand channels, sheet sands, unconformity interface, and faults around the gas chimney, and the gas continuously accumulates in the weak zone of the mud diapir. The deep-sea argillaceous gas source rocks of the Meishan Formation, Huangliu Formation, Yinggehai Formation, and Quaternary Formation have entered the stage of microbial gas generation and also have hydrocarbon generation and expulsion capabilities.

Because the hydrocarbon expulsion time of the deep geothermal gas is much earlier than that of the shallow microbial gas (Zuo et al., 2016; Li et al., 2017; Song et al., 2021), the two types of gas and their mixture migrate, charge, and converge in stages. First, the thermogenic gas in the remote Yacheng Formation migrated over a long distance into the mud diapirs-gas chimneys along the sand body, unconformity interface, and faults under the action of overpressure, and the continuous charging of a large amount of thermogenic gas led to the development of microcracks in the mud diapirs-gas chimneys. Then, the local microbial gas preferentially migrated from the high fluid potential area to the low fluid potential area along the existing fracture groups and sand bodies in the hydrocarbon expulsion stage, and the gas chimneys continued to evolve under the sufficient gas supply conditions. Finally, the gas accumulated at the top of the gas chimney and was charged down and on the weak side, forming different types of hydrates under the favorable temperature and pressure conditions in the trap.

Episodic and dynamic reservoir formation is a new understanding of gas chimney gas hydrate exploration, which is mainly manifested as dynamic reservoir formation and the strong heterogeneity of the hydrates. In the longitudinal direction, the thermogenic gas and microbial gas experience episodic hydrocarbon expulsion migration and accumulation processes. The gas can break through the surface and form an active cold seep (such as the Haima Cold Seep) during the peak of the hydrocarbon expulsion stage, and a migration channel is opened, which is conducive to the continuous development and enrichment of gas hydrates. In the low valley of the hydrocarbon expulsion stage, the migration channel is closed, and the cold seep can evolve into an ancient cold seep (a pock relic), resulting in the continuous decomposition and local diffusion of the hydrates. Such episodic reservoir formation is always in dynamic evolution and has been verified by multiple types of well data. The episodic and dynamic accumulation characteristics strengthen the contribution to the reservoir heterogeneity, which is beneficial to understanding the accumulation process.

In summary, the geological process of hydrate accumulation in the study area involves remote thermogenic gas transportation, local microbial genetic gas accumulation, gas chimney episodic dynamic reservoir formation, and source-reservoir control. Among them, the gas source determines the material basis of the hydrate accumulation, and the continuous charging and effective supply range of the gas are conducive to the stable development and accumulation of hydrates. The favorable reservoir determines the filling effect of the hydrate accumulation and the size and state of the ore body. Sand-rich reservoirs and fracture-rich reservoirs are favorable to the formation of a concentrated, high saturation ore body. The influences of the cap layer, conduction system, and temperature and pressure conditions are limited. Based on the above research results, we believe that the next step should be to strengthen research on the multi-source effective gas supply and deep-sea shallow sand body distribution to improve our geological understanding and exploration ideas.

6 CONCLUSION

1) Based on newly obtained geochemical data for 47 oil and gas wells and hydrate wells, it was found that the gas source of the gas chimney-type natural gas hydrates in the Qiongdongnan Basin is mainly thermogenic gas supplemented by mixed gas. Based on the samples, it was estimated that the contribution of the thermogenic gas to the hydrate accumulation was 70%.
2) The reservoirs in Qiongdongnan Basin were determined to be non-diagenetic to weakly diagenetic, rich in clay and silt (median grain size of 15.1–34.1 μm), weakly self-sustaining, and strongly heterogeneous. There are two main types of reservoirs: silty and argillaceous (clay) reservoirs and microfracture reservoirs.
3) Based on the seismic characteristics of the top of the gas chimney, i.e., a hydrate layer, gas hydrate-containing layer, and shallow gas layer, it was determined that the geological processes were as follows: remote thermogenic gas transportation, local microbial genetic gas accumulation, episodic dynamic gas chimney reservoir formation, and source-reservoir control. This suggests that the geological understanding and exploration ideas of an effective supply from a gas source and the distribution of deep-sea shallow sand bodies should be strengthened.

DATA AVAILABILITY STATEMENT

The original contributions presented in the study are included in the article/Supplementary Material, further inquiries can be directed to the corresponding author.

AUTHOR CONTRIBUTIONS

QF: main idea, writing-original draft, experimental analysis, and data analysis. QL: methodology, writing—review and editing, project administration, and funding acquisition. SZ: main idea, project administration. LL: experimental analysis. ZZ: data analysis. XL: experimental analysis and data analysis. All authors contributed to the article and approved the submitted version.

FUNDING

The research is sponsored by the National Key Research and Development Plan of China (Grant Nos. 2016YFC0304000, and 2021YFC2800046), Special fund support of CNOOC, and National Natural Science Foundation of China (Grant Nos. U19B2005, and U20B6005).

ACKNOWLEDGMENTS

The authors wish to thank all personnel of the drilling and logging technology trial of gas hydrate in the South China Sea in 2019 and 2021 led by CNOOC, for their field assistance and stimulating insights. Special thanks should be given to two reviewers, who have improved the manuscript thoroughly, and significantly.

REFERENCES

Chen, C. M., Zhong, L. F., Wan, Z. F., Cheng, C. Y., Zhou, W., and Xu, X. (2022). Geochemical Characteristics of Cold-Seep Carbonates in Shenhu Area, South China Sea. *J. Oceanology Limnology*. 2022. doi:10.1007/s00343-021-1112-z

Cong, X. R., Su, M., Wu, N. Y., Qiao, S. H., Sha, Z. B., Lu, H. L., et al. (2018). Contribution of Thermogenic Gases to Hydrate Accumulation under the marine Hydrocarbon-Rich Depression Setting. *Acta Geologica Sinica* 92 (1), 170–183.

Deng, W., Liang, J. Q., Zhang, W., Kuang, Z. G., Tong, Z., and He, Y. L. (2021). Typical Characteristics of Fracture-Filling Hydrate-Charged Reservoirs Caused by Heterogeneous Fluid Flow in the Qiongdongnan Basin, Northern south China Sea. *Mar. Pet. Geology*. 124, 104810. doi:10.1016/j.marpetgeo.2020.104810

Gan, J., Zhang, Y. Z., Liang, G., Yang, X. B., Yang, J. H., Li, X., et al. (2018). On Accumulation Process and Dynamic Mechanism of Natural Gas in the Deep Water Area of Central Canyon, Qiongdongnan Basin. *Acta Geologica Sinica* 92, 2359–2367. doi:10.1016/j.orggeochem.2018.09.002

He, J. X., Su, P. B., Lu, Z. Q., Zhang, W., Liu, Z. J., and Li, X. T. (2015). Prediction of Gas Sources of Natural Gas Hydrate in the Qiongdongnan Basin, Northern South China Sea, and its Migration, Accumulation and Reservoir Formation Pattern. *Nat. Gas Industry* 35 (8), 19–29.

Huang, B., Tian, H., Li, X., Wang, Z., and Xiao, X. (2016). Geochemistry, Origin and Accumulation of Natural Gases in the deepwater Area of the Qiongdongnan Basin, South China Sea. *Mar. Pet. Geology*. 72, 254–267. doi:10.1016/j.marpetgeo.2016.02.007

Huang, H. T., Huang, B. J., Huang, Y. W., Li, X., and Tian, H. (2017). Condensate Origin and Hydrocarbon Accumulation Mechanism of the deepwater Giant Gas Field in Western South China Sea: A Case Study of Lingshui 17-2 Gas Field in Qiongdongnan Basin, South China Sea. *Pet. Exploration Development* 44 (3), 380–388. doi:10.1016/s1876-3804(17)30047-2

Lai, H. F., Fang, Y. X., Kuang, Z. G., Ren, J. F., Liang, J. Q., LuWang, J. A. G. L., et al. (2021). Geochemistry, Origin and Accumulation of Natural Gas Hydrates in the Qiongdongnan Basin, South China Sea: Implications from Site GMGS5-W08. *Mar. Pet. Geology*. 123, 1–14. doi:10.1016/j.marpetgeo.2020.104774

Li, X. S., Zhang, Y. Z., Yang, X. B., Xu, X. F., Zhang, J. X., and Man, X. (2017). New Understandings and Achievements of Natural Gas Exploration in Yinggehai-Qiongdongnan basin,South China Sea. *China Offshore Oil and Gas* 29 (6), 1–11.

Liang, J. Q., Zhang, G. X., Lu, J. A., Su, P. B., Sha, Z. B., Gong, Y. H., et al. (2016). Accumulation Characteristics and Genetic Models of Natural Gas Hydrate Reservoirs in the NE Slope of the South China Sea (in Chinese). 36, 157–162.

Liang, J., Zhang, W., Lu, J. A., Wei, J., Kuang, Z., and He, Y. (2019). Geological Occurrence and Accumulation Mechanism of Natural Gas Hydrates in the Eastern Qiongdongnan Basin of the South China Sea: Insights from Site GMGS5-W9-2018. *Mar. Geology*. 418, 106042. doi:10.1016/j.margeo.2019.106042

Milkov, A. V., and Etiope, G. (2018). Revised genetic diagrams fornatural gases based on global dataset of ƀ20,000 samples. *Org. Geochem.* 125, 109–120. doi:10.1016/j.orggeochem.2018.09.002

Paganoni, M., King, J. J., Foschi, M., Mellor-Jones, K., and Cartwright, J. A. (2019). A Natural Gas Hydrate System on the Exmouth Plateau (NW Shelf of Australia) Sourced by Thermogenic Hydrocarbon Leakage. *Mar. Pet. Geology*. 99, 370–392. doi:10.1016/j.marpetgeo.2018.10.029

Song, R. Y., Chen, K., Li, A. Q., Mao, H., and Liu, Y. Z. (2021). Representation of Gas Hydrate Fracture Migration System by Seismic. *Pet. Geology. Exp.* 43 (1), 136–143. doi:10.11781/sysydz202101136

Wan, Z.-F., Zhang, W., Ma, C., Liang, J.-Q., Li, A., Meng, D.-J., et al. (2022). Dissociation of Gas Hydrates by Hydrocarbon Migration and Accumulation-Derived Slope Failures: An Example from the south china Sea. *Geosci. Front.* 13 (2), 101345. doi:10.1016/j.gsf.2021.101345

Wan, Z., Chen, C., Liang, J., Zhang, W., Huang, W., and Su, P. (2020). Hydrochemical Characteristics and Evolution Mode of Cold Seeps in the Qiongdongnan Basin, South China Sea. *Geofluids* 2020 (6), 1–16. doi:10.1155/2020/4578967

Wan, Z., Xu, X., Wang, X., Xia, B., and Sun, Y. (2017). Geothermal Analysis of Boreholes in the Shenhu Gas Hydrate Drilling Area, Northern South China Sea: Influence of Mud Diapirs on Hydrate Occurrence. *J. Pet. Sci. Eng.* 158, 424–432. doi:10.1016/j.petrol.2017.08.053

Wan, Z., Zhang, J., Lin, G., Zhong, S., Li, Q., Wei, J., et al. (2021). Formation Mechanism of Mud Volcanoes/Mud Diapirs Based on Physical Simulation. *Geofluids* 2021, 1–16. doi:10.1155/2021/5531957

Wang, J., Wu, S., Kong, X., Ma, B., Li, W., Wang, D., et al. (2018). Subsurface Fluid Flow at an Active Cold Seep Area in the Qiongdongnan Basin, Northern South China Sea. *J. Asian Earth Sci.* 168, 17–26. doi:10.1016/j.jseaes.2018.06.001

Wang, Z., Sun, Z., Zhu, J., Guo, M., and Jiang, R. (2015). Natural Gas Geological Characteristics and Great Discovery of Large Gas fields in Deep-Water Area of the Western South China Sea. *Nat. Gas Industry B* 2 (6), 489–498. doi:10.1016/j.ngib.2016.03.001

Wei, J. G., Li, J. W., Wu, T. T., Zhang, W., Li, J. T., Wang, J. L., et al. (2020). Geologically Controlled Intermittent Gas Eruption and its Impact on Bottom Water Temperature and Chemosynthetic Communities—A Case Study in the "HaiMa" Cold Seeps, South China Sea. *Geol. J.* 50, 1–13. doi:10.1002/gj.3780

Wei, J., Liang, J., Lu, J., Zhang, W., and He, Y. (2019). Characteristics and Dynamics of Gas Hydrate Systems in the Northwestern South China Sea - Results of the Fifth Gas Hydrate Drilling Expedition. *Mar. Pet. Geology*. 110, 287–298. doi:10.1016/j.marpetgeo.2019.07.028

Xu, X. D., Zhang, Y. Z., Liang, G., Xiong, X. F., Li, X., Guo, X. X., et al. (2016). Hydrocarbon Source Condition and Accumulation Mechanism of Natural Gasin deepwater Area of Qiongdongnan Basin, Northern South China Sea. *Nat. Gas Geosci.* 27 (11), 1985–1992.

Yang, L., Liu, B., Xu, M., Liu, S., Guan, Y., and Gu, Y. (2018). Characteristics of Active Cold Seepages in Qiongdongnan Sea Area of the Northern South China Sea. *Acta Geophysica Sinica* 61 (7), 2905–2914. doi:10.6038/cjg2018L0374

Ye, J., Wei, J., Liang, J., Lu, J., Lu, H., and Zhang, W. (2019). Complex Gas Hydrate System in a Gas Chimney, South China Sea. *Mar. Pet. Geology*. 104, 29–39. doi:10.1016/j.marpetgeo.2019.03.023

Zhang, G. C., Zeng, Q. B., Su, L., Yang, H. Z., Chen, Y., Yang, D. S., et al. (2016). Accumulation Mechanism of LS17-2 Deep Water Gaint Gas Field in Qiongdongnan Basin. *Acta Pet. Sin.* 37 (S1), 34–46.

Zhang, K., Song, H., Wang, H., Tao, J., Guan, Y., Gong, Y., et al. (2020). A Preliminary Study on the Active Cold Seeps Flow Field in the Qiongdongnan Sea Area, the Northern South China Sea. *Chin. Sci. Bull.* 65, 1130–1140. doi:10.1360/tb-2019-0582

Zhang, W., Liang, J., Liang, Q., Wei, J., Wan, Z., Feng, J., et al. (2021). Gas Hydrate Accumulation and Occurrence Associated with Cold Seep Systems in the Northern South China Sea: An Overview. *Geofluids* 2021, 1–24. doi:10.1155/2021/5571150

Zhang, W., Liang, J. Q., Wei, J. G., Lu, J. A., Su, P. B., Lin, L., et al. (2019a). Geological and Geophysical Features of and Controls on Occurrence and Accumulation of Gas Hydrates in the First Offshore Gas-Hydrate Production Test Region in the Shenhu Area, Northern South China Sea. *Mar. Pet. Geology.* 114, 104191. doi:10.1016/j.marpetgeo.2019.104191

Zhang, W., Liang, J., Su, P., Wei, J., Gong, Y., Lin, L., et al. (2019b). Distribution and Characteristics of Mud Diapirs, Gas Chimneys, and Bottom Simulating Reflectors Associated with Hydrocarbon Migration and Gas Hydrate Accumulation in the Qiongdongnan Basin , Northern Slope of the South China Sea. *Geol. J.* 54, 3556–3573. doi:10.1002/gj.3351

Zhang, W., Liang, J., Wan, Z., Su, P., Huang, W., Wang, L., et al. (2020a). Dynamic Accumulation of Gas Hydrates Associated with the Channel-Levee System in the Shenhu Area, Northern South China Sea. *Mar. Pet. Geology.* 117, 104354. doi:10.1016/j.marpetgeo.2020.104354

Zhang, W., Liang, J., Yang, X., Su, P., and Wan, Z. (2020b). The Formation Mechanism of Mud Diapirs and Gas Chimneys and Their Relationship with Natural Gas Hydrates: Insights from the Deep-Water Area of Qiongdongnan Basin, Northern South China Sea. *Int. Geology. Rev.* 62, 789–810. doi:10.1080/00206814.2018.1491014

Zhang, Y. Z., Gan, J., Xu, X. D., Liang, G., and Li, X. (2019). The Source and Natural Gas Lateral Migration Accumulation Model of Y 8-1 Gas Bearing Structure,East Deep Water in the Qiongdongnan Basin. *Earth Sci.* 44 (08), 2609–2618.

Zhu, W., Huang, B., Mi, L., Wilkins, R. W. T., Fu, N., and Xiao, X. (2009). Geochemistry, Origin, and Deep-Water Exploration Potential of Natural Gases in the Pearl River Mouth and Qiongdongnan Basins, South China Sea. *Bulletin* 93, 741–761. doi:10.1306/02170908099

Zuo, Q. M., Zhang, D. J., Wang, Y. H., Li, W., Chen, Y., He, X. H., et al. (2016). Sedimentary Characteristics and Exploration Potential of Neogene Submarine Fan in the deepwater Area of the Qiongdongnan Basin[J]. *Acta Oceanologica Sinica* 38 (11), 105–116.

Conflict of Interest: Author QF was employed by the company CNOOC Research Institute, Beijing, China.
The remaining authors declare that the research was conducted in the absence of any commercial or financial relationships that could be construed as a potential conflict of interest.

Publisher's Note: All claims expressed in this article are solely those of the authors and do not necessarily represent those of their affiliated organizations, or those of the publisher, the editors, and the reviewers. Any product that may be evaluated in this article, or any claim that may be made by its manufacturer, is not guaranteed or endorsed by the publisher.

frontiers | Frontiers in Earth Science

ORIGINAL RESEARCH
published: 26 April 2022
doi: 10.3389/feart.2022.861162

Characteristics of High Saturation Hydrate Reservoirs in the Low-Angle Subduction Area of the Makran Accretionary Prism

Jing Liao[1,2], Xinxin Liu[1,2], Qingfang Zhao[1,2], Jianming Gong[1,2], Weihan Yin[3,4], Sen Li[1,2], Baohua Lei[1,2], Jie Liang[1,2], Khalid Muhammad[5] and Waseem Haider Syed[6]*

[1]Qingdao Institute of Marine Geology, China Geological Survey, Qingdao, China, [2]Laboratory for Marine Mineral Resources, Pilot National Laboratory for Marine Science and Technology, Qingdao, China, [3]North China Sea Environmental Monitoring Center, SOA, Qingdao, China, [4]Key Laboratory of Ecological Prewarning, Protection and Restoration of Bohai Sea, MNR, Qingdao, China, [5]Pakistan Hydrographic Department, Liaquat Barracks Shahrae Faisal, Karachi, Pakistan, [6]National Institute of Oceanography, Karachi, Pakistan

OPEN ACCESS

Edited by:
Pibo Su,
Guangzhou Marine Geological Survey, China

Reviewed by:
Zhenquan Lu,
China Geological Survey, China
Jiasheng Wang,
China University of Geosciences Wuhan, China
Xin Su,
China University of Geosciences, China

***Correspondence:**
Qingfang Zhao
zqingfang@mail.cgs.gov.cn

Specialty section:
This article was submitted to Marine Geoscience, a section of the journal Frontiers in Earth Science

Received: 24 January 2022
Accepted: 28 March 2022
Published: 26 April 2022

Citation:
Liao J, Liu X, Zhao Q, Gong J, Yin W, Li S, Lei B, Liang J, Muhammad K and Syed WH (2022) Characteristics of High Saturation Hydrate Reservoirs in the Low-Angle Subduction Area of the Makran Accretionary Prism. Front. Earth Sci. 10:861162. doi: 10.3389/feart.2022.861162

To delineate the spatial distribution of high saturation gas hydrate reservoirs in the low-angle subduction areas of the Makran Accretionary Prism, we conducted seismic data interpretation and impedance inversion of gas hydrates in the Makran Accretionary Prism and comprehensively analyzed the characteristics of the high saturation gas hydrate reservoirs in the Nankai Trough in Japan and the Shenhu Area in the South China Sea. The results show that the Makran Accretionary Prism features thick sediments, developed transport systems of "two-way gas supply" (i.e., thrust fault and normal fault, thrust fault and high permeable strata), and clear and continuous bottom simulating reflector (BSR). Meanwhile, strong-amplitude reflectors and strong-impedance anomalies coexist in the anticline wing above the BSR. Combined with the proven characteristics of high saturation gas hydrate reservoir, the high saturation gas hydrate reservoirs in the Makran Accretionary Prism are probably mainly distributed in the anticline wings immediately above the BSR. These results provide useful information for the exploration and development of gas hydrate in the low-angle subduction area of the Makran Accretionary Prism.

Keywords: high saturation hydrate deposit, reservoir characteristic comparison, impedance anomalies, low-angle subduction area, Makran Accretionary Prism

1 GEOLOGICAL SETTING

At present, the accumulation mechanism of gas hydrate in the high-angle subduction area of the active continental margin is relatively clear (Hyndman and Spence, 1992; Baba and Yamada, 2004; Zhang et al., 2006; Riedel et al., 2010; Hu et al., 2020), however the accumulation mechanism of gas hydrate in the low-angle subduction area is rarely reported (Gong et al., 2018a). Makran Accretionary Prism is located in the active continental margin with the lowest subduction angle worldwide, in which has complex thrust structure and widely distributed BSRs in the slope area, indicating that gas hydrate has a great potential in this area. Therefore, Makran Accretionary Prism can be viewed as a natural laboratory to study hydrate accumulation mechanisms in the low-angle subduction margins.

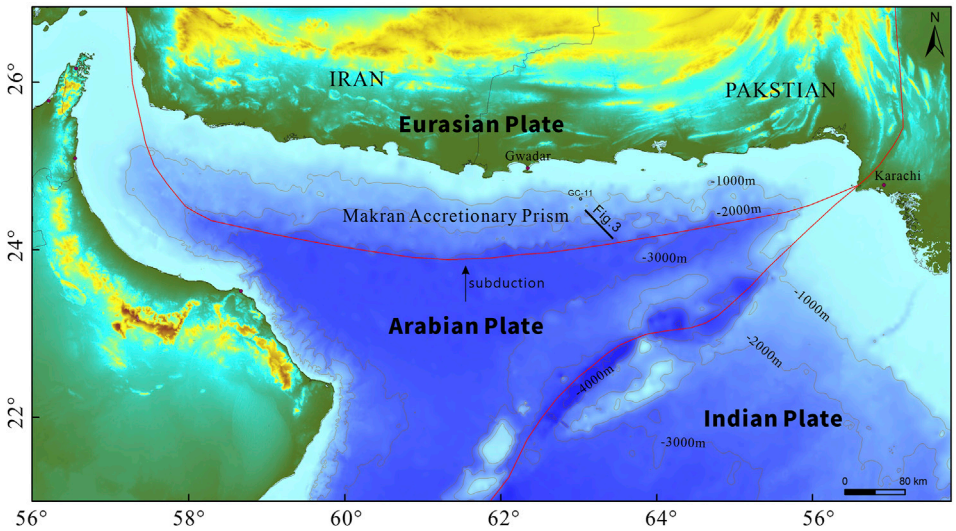

FIGURE 1 | Locations of the study area and seismic profile.

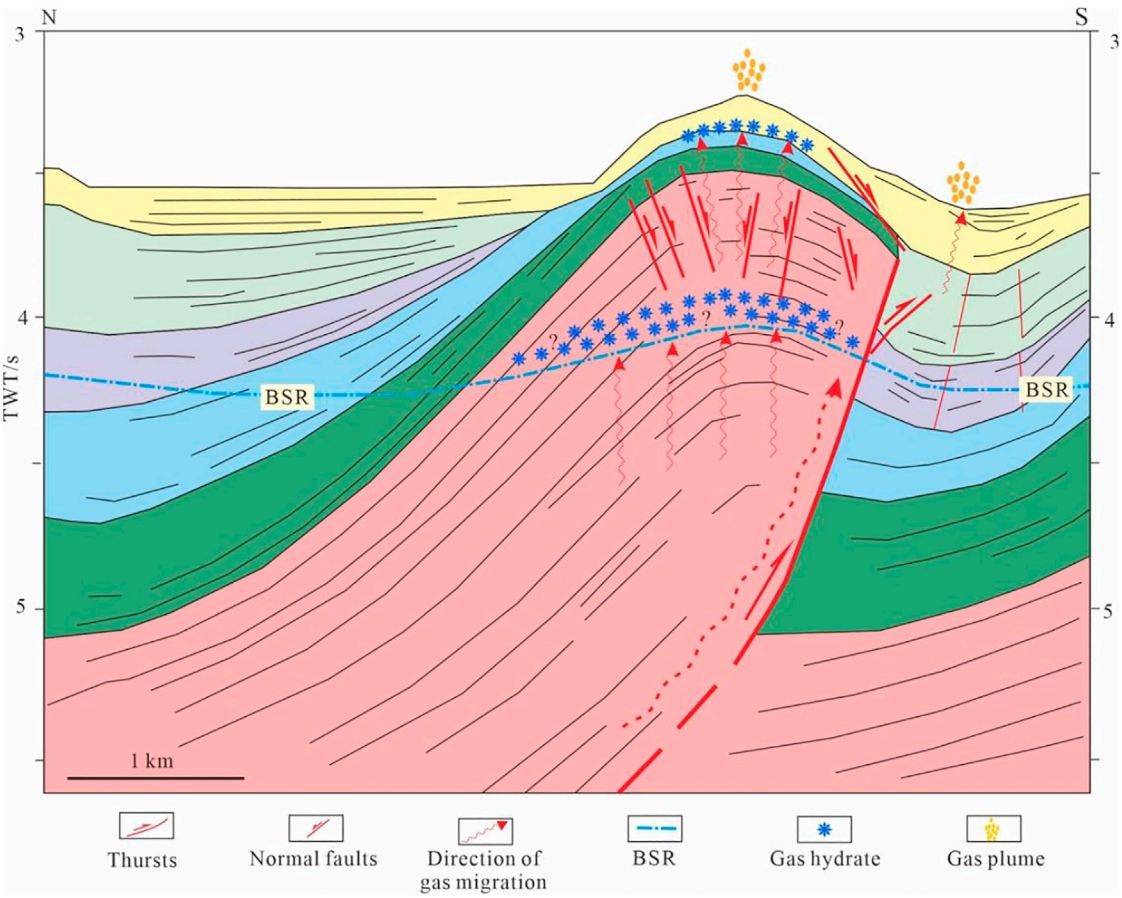

FIGURE 2 | Gas hydrate accumulation model of a two-story structure in the Makran Accretionary Prism (modified after Grando and McCla, 2007; Gong et al., 2018a).

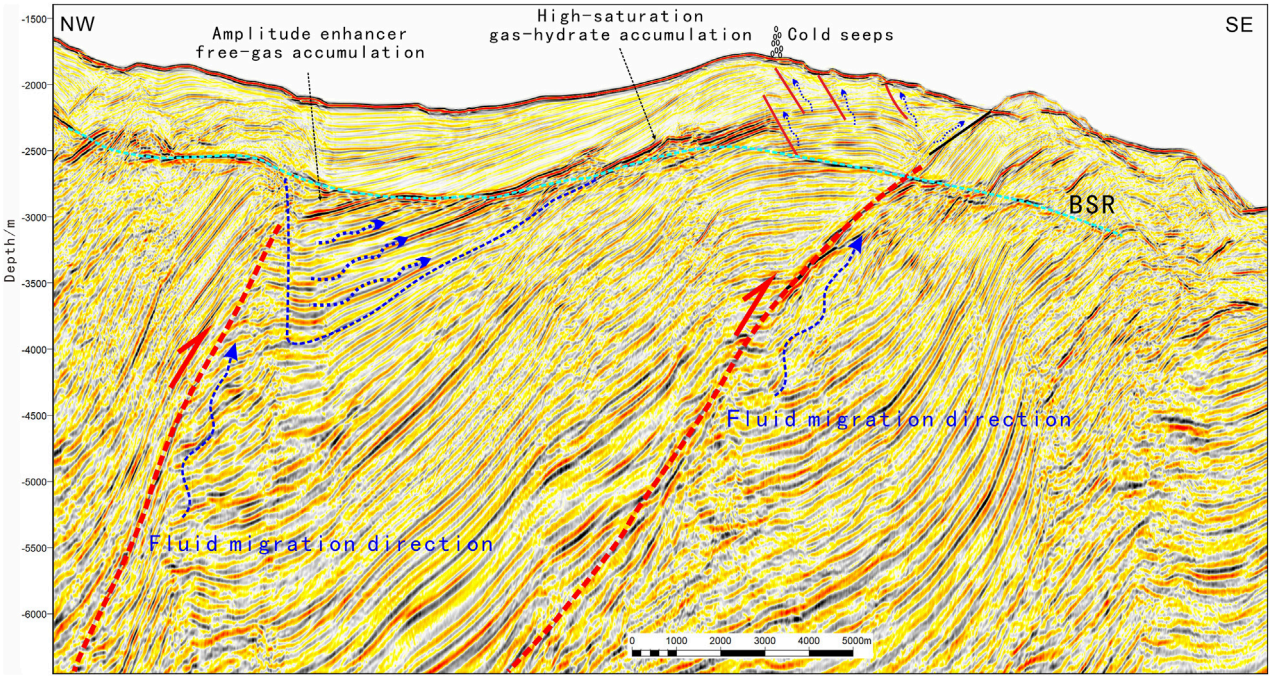

FIGURE 3 | Schematic diagram of the amplitude-enhanced reflectors above and below the BSRs and the highly permeable strata for fluid transport in the Makran Accretionary Prism (the section position shown in **Figure 1**).

The Makran Accretionary Prism in the northwest Indian Ocean was formed by the low-angle subduction of the Arabian Plate beneath the Eurasian Plate (**Figure 1**) Owing to the low subduction angle (less than 3°) and abundant sediments from the Eurasian Plate, the sediments of the Makran Accretionary Prism are over 7,000 m thick (Kopp et al., 2000; Grando and McCla, 2007). These sediments serve as the source rock for the formation of gas hydrates in the area. According to drilling and seismic data, the Makran Accretionary Prism is mainly composed of Cenozoic strata (Hussain et al., 2015; Gong et al., 2018b). Our findings suggest that Paleogene abyssal-facies mudstones and Miocene bathyal-facies mudstones are primary source rocks of gas hydrates in this area. According to the calculations using temperature and pressure fields under which gas hydrates remain stable, the gas hydrates in the Makran Accretionary Prism have developed in areas with a water depth of over 800 m, and distributed in sediments 300–700 m below the seafloor. The sediments are Pliocene-Quaternary strata and primarily consist of pelagic and hemipelagic mudstones interbedded with turbidites.

During surveys of several cruises in 1997, 1998 and 2007 (SO-122, SO-123, SO-124, SO-130 and (M74/3), gas seepage and a number of microbial mats were found (Von Rad et al., 2000). Previous studies have identified the distribution of BSR from 2D seismic data offshore Makran (Von Rad et al., 2000; Grevemeyer et al., 2000; Smith, 2013; Liao et al., 2019). Full wave-form inversion suggests that gas hydrate concentrations above the BSR as low as 10%, and most free-gas below BSR (Sain et al., 2000). Hydrate samples are porous and tubular, cold springs and plumes highly rise (Bohrmann and Ohling, 2008). Meanwhile, burnable methane is spewed out of near-shore mud volcanoes (Von Rad et al., 2000; Delisle et al., 2002, Delisle, 2004; Zhang et al., 2020). Therefore, the Makran Accretionary Prism has sufficient gas sources and favorable accumulation conditions for gas hydrates. Compared with other active continental margins, Makran Accretionary Prism has thicker free gas under the BSR (Sain et al., 2000; Smith, 2013). According to seismic data interpretation, fluids are mainly transported by deep thrust faults and highly permeable strata, followed by superficial small normal faults, and gas hydrates are mainly distributed in seafloor surface anticlinal ridges and strata immediately above the BSR (**Figure 2**) (Gong et al., 2016; Gong et al., 2018b).

2 DATA AND METHODOLOGY

2.1 Data Acquisition

The seismic data acquired in late 2019. Due to the increase of the record time and length of seismic cable (**Supplementary Table S1**), the resolution of seismic data has been greatly improved. This study incorporates the seismic and logging data from gas hydrate drilling holes in the Nankai Trough, Japan and the Shenhu Area, South China Sea to compare the characteristics of high saturation gas hydrate reservoirs by impedance inversion.

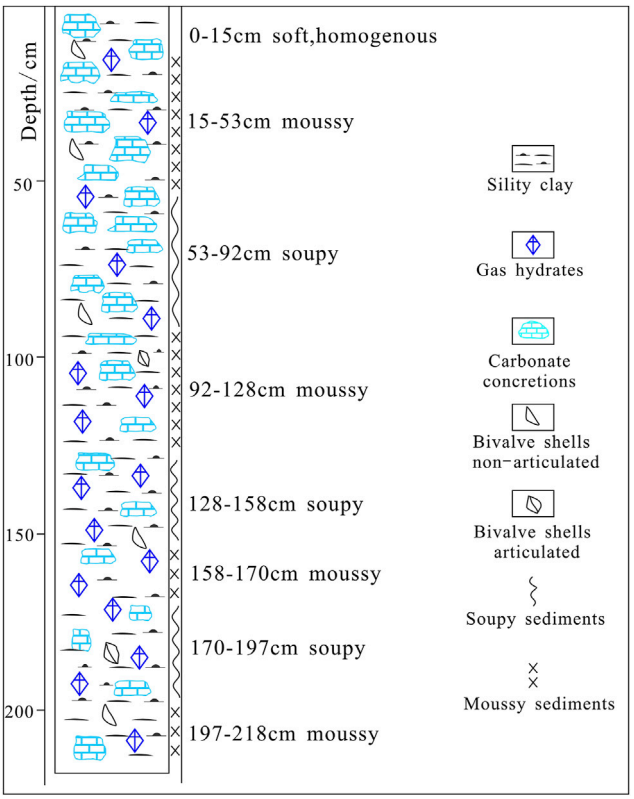

FIGURE 4 | Gravity core GC-11 from the Makran Accretionary Prism shows sporadically distributed hydrates in silty clay (Modified after Bohrmann and Ohling, 2008; Gong et al., 2017, site position shown in **Figure 1**).

2.2 Methodology

2.2.1 Seismic Interpretation and Impedance Inversion

Synthetic seismic records of gas hydrate-bearing layers were obtained using the reflection characteristics of seismic wave groups (i.e., external geometrical morphology, internal reflection structure, continuity, amplitude, frequency, and layer velocity), as well as regional geological data. Gas hydrate-bearing strata generally show strong amplitude anomalies in the synthetic seismic records (Riedel et al., 2010). Seismic impedance can well reflect the characteristics of gas hydrates (such as BSRs), and the applications of wave impedance in the identification of gas hydrate and the study of the concentration assessments have achieved good results (Riedel and Shankar, 2012; Wan et al., 2016; Xue et al., 2016; Li et al., 2019). In this study on the characteristics of hydrate-bearing reservoirs, we performed well-free acoustic impedance inversion using seismic data because there is no logging data in the study area. The low-frequency impedance model was obtained by seismic velocity data.

Most of the strata at the target location have large dip angle, which imposes higher requirements for the low-frequency model. It is necessary to improve the accuracy of seismic interpretation in the early stage to ensure the accuracy of horizon information. In order to ensure the rationality of the low-frequency impedance model, we extracted wavelets at multiple locations and obtained the optimal wavelet. Then, we used the inversion results to correct the initial model iteratively and finally obtained the final impedance inversion results. The high saturation hydrate reservoirs on the impedance inversion profile can be characterized by high impedance anomalies.

2.2.2 Hydrate Reservoir Correlation

A comparative analysis was conducted on the characteristics (e.g., lithology, thickness, and sedimentary facies) of high saturation hydrate layers using the seismic and logging data of high saturation hydrate concentrated areas confirmed by drilling in Nankai Trough and Shenhu area in South China Sea. In this way, the characteristics of the seismic reflections and inversed impedance anomalies of high saturation hydrate concentrated areas were determined. Based on this information, the authors can predict high saturation hydrate concentrated zones in the Makran Accretionary Prism.

3 RESULTS AND DISCUSSION

3.1 Seismic Interpretation and Impedance Inversion of the Makran Accretionary Prism

3.1.1 Amplitude-Enhanced Reflectors

According to the interpretation of newly acquired high-resolution seismic data, the BSR in the study area shows noticeable reflection characteristics and is continuously distributed, and fluids are transported by massive highly permeable strata (indicated with blue arrows in **Figure 3**) as well as deep thrust faults and shallow normal faults. Most of the highly permeable strata are located in the piggyback basin under the BSR. They correspond to the negative topography of the seafloor and are present as inclined amplitude-enhanced reflectors in the seismic profile (**Figure 3**). As revealed by previous studies, the amplitude-enhanced reflectors above the BSR are generally the high saturation hydrate concentrated zones (Guo et al., 2017), whereas those below the BSR are usually free gas concentrated zones (Riedel et al., 2010). Analysis shows that the free gas layers under the BSR in the Makran Accretionary Prism are 200–300 m thick (Grevemeyer et al., 2000; Sain et al., 2000; Ojha and Sain, 2008), indicating that the Makran Accretionary Prism has abundant gas sources. However, there are no apparent amplitude-enhanced reflectors in the shallow depth strata near seafloor of the Makran Accretionary Prism. This may be related to the small particle size of surface sediments (mainly including silty clay) and the low saturation hydrates with sporadic distribution (**Figure 4**) (Bohrmann and Ohling, 2008; Gong et al., 2017).

3.1.2 Impedance Inversion

Seismic data interpretation has revealed that the gas hydrates in the Makran Accretionary Prism are mainly concentrated in the anticlinal ridge and have a two-story structure (Gong et al., 2016; Gong et al., 2018a). To date, surface hydrate samples have been obtained from gravity cores (**Figure 4**), but the deep hydrate layers close to the BSR have not been drilled. Shallow hydrate-bearing sediments show weak amplitude or blank reflections in the seismic profile (**Figure 3**). By contrast, the unconfirmed deep hydrate layers above the BSR are

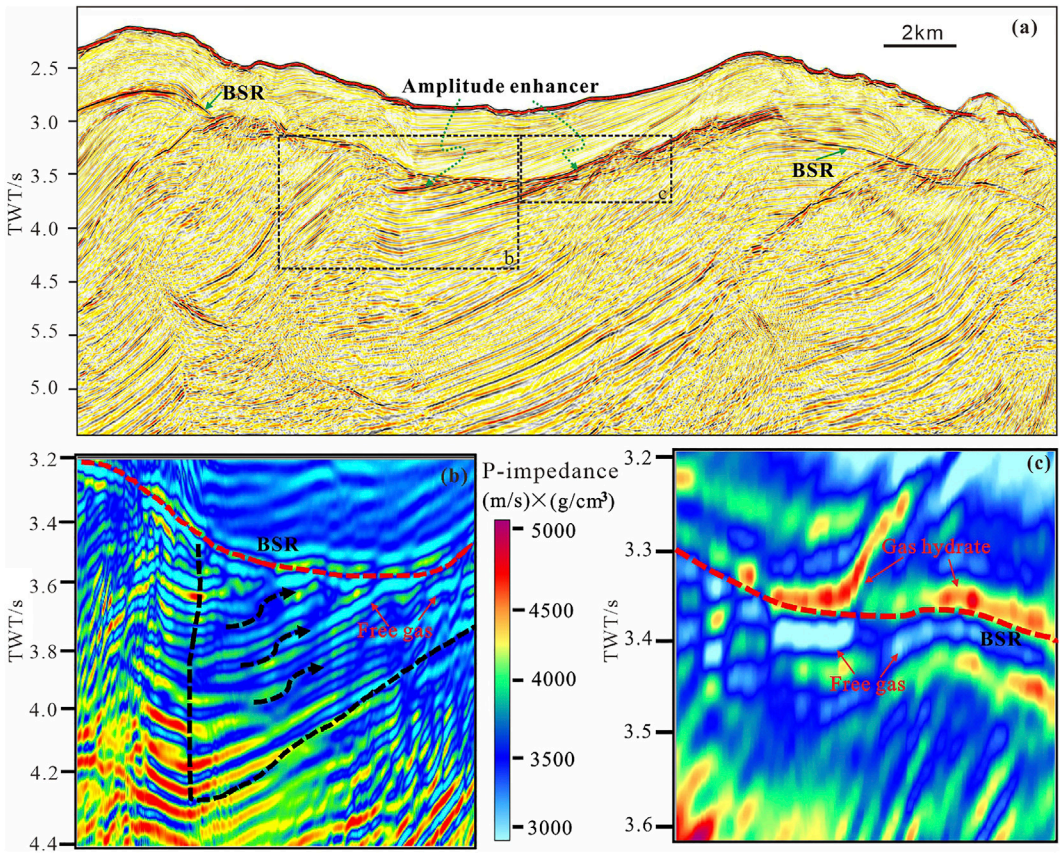

FIGURE 5 | Seismic profile (time domain) and detailed views of impedance inversion results (time domain). **(A)** Seismic profile; **(B)** impedance inversion results of the left part; **(C)** impedance inversion results of the right part.

present as amplitude-enhanced reflectors in the seismic profile (**Figures 3**, **5**) and show high impedance anomalies in the impedance inversion profile (**Figure 5**). Seismic data interpretation and the analysis of sedimentary conditions indicate that deep hydrate reservoirs may consist of coarse-grained turbidites. Comprehensive analysis suggests that the strong amplitude and high impedance above the BSR in the study area probably indicate high saturation hydrate concentrated zones as well as coarse-grained sediments (Guo et al., 2017). By contrast, the strong amplitude and low impedance under the BSR reflect free gas concentrated zones (**Figure 5**). It should be noted that the piggyback basin under the BSR show the interbeds of slightly higher and low impedance, reflecting both the low impedance of free gas and the slightly higher impedance of turbidite sands.

3.2 Comparison of Characteristics of High Saturation Hydrate Reservoirs

3.2.1 Characteristics of Hydrate Reservoirs in the Nankai Trough, Japan

Two hydrate production tests have been conducted in 2012 in the Nankai Trough offshore Japan, which is a typical example of the exploration and production tests of gas hydrates in active continental margins. According to Zhao, 2019, the high saturation hydrate reservoirs in the Nankai Trough were identified mainly based on the clear and continuous BSR, the existence of amplitude-enhanced reflectors above the BSR, high P-wave velocity, and sand-rich turbidites. The logging interpretation results show that the hydrates discovered in the first well (AT1-C) for coring and hydrate production tests in Japan are mainly concentrated in the wing of anticlinal ridges and show two layers of strong reflections above the BSR on the seismic profile (**Figure 6**) (Fujii et al., 2015). The upper layer of strong reflections is mainly composed of sheeted turbidite sands with high lateral continuity. By contrast, the lower layer of strong reflections consists of thick channel sands with poor lateral continuity, both sand layers have almost the same hydrate saturation of 50–80%. In addition, Komatsu et al. (2015) divided the 60 m thick hydrate concentrated zone of well AT1-C into four sedimentary facies zones based on logging curves (**Figure 6**). Analysis of sedimentary facies associations shows that the hydrate concentrated zone can be divided vertically into three portions, namely bottom turbidity channels, middle sheeted turbidity sands, and top basin-bottom sediments. Among them, the bottom and middle portions have the gas hydrates at the highest concentrated level (Ito et al., 2015).

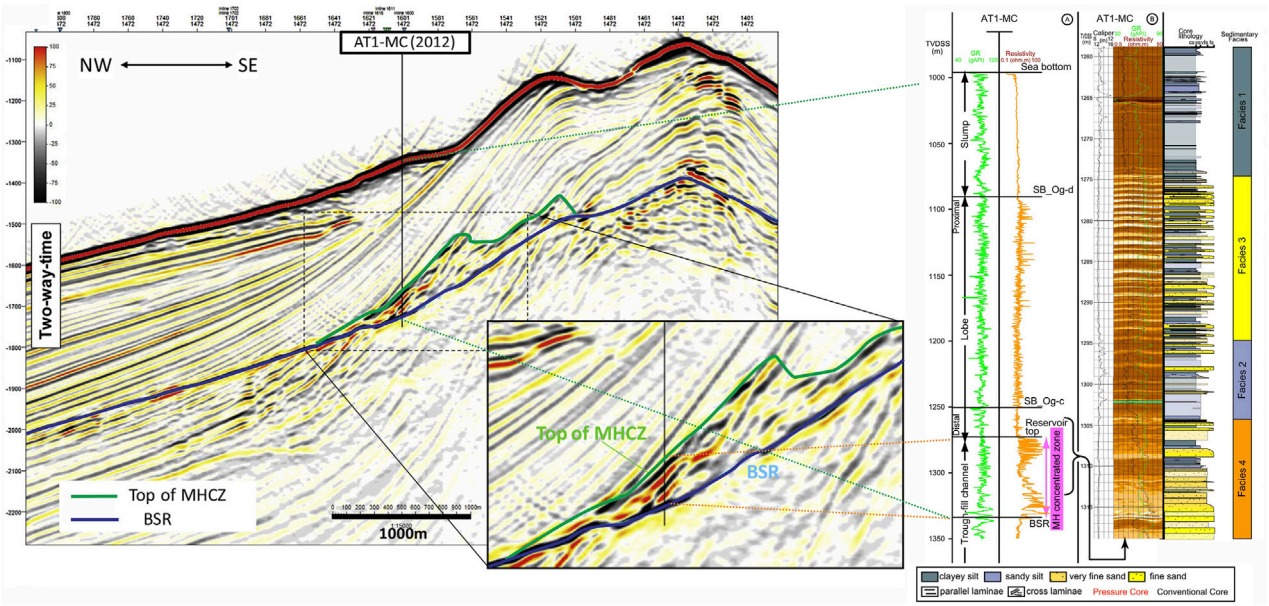

FIGURE 6 | Seismic reflection characteristics and sedimentary facies of high saturation hydrate deposits discovered during drilling in the Nankai Trough, Japan (Modified after Fujii et al., 2015; Komatsu et al., 2015). Note: High saturation hydrate deposits are located in the sand-rich turbidites with strong reflections above the BSR. MHCZ: methane hydrate concentrated zone.

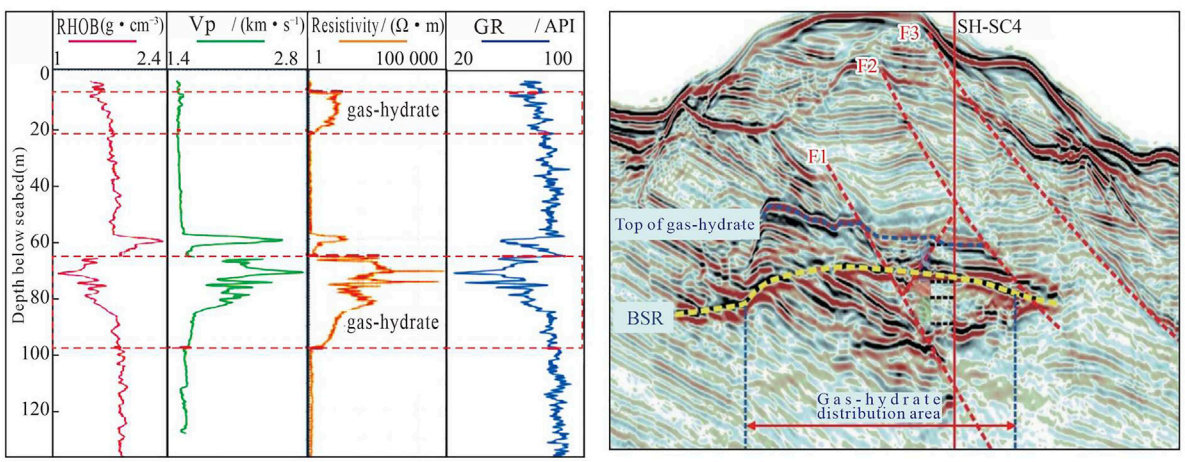

FIGURE 7 | Geophysical response of hydrate reservoirs in the Shenhu Area in the South China Sea (Modified after Li et al., 2018; Ning et al., 2020).

Therefore, the relatively continuous strong-amplitude reflections above the BSR indicate high-saturation hydrate deposits and highly permeable turbidites are high-saturation hydrate concentrated zones in the Nankai Trough.

3.2.2 Characteristics of Hydrate Reservoirs in the Shenhu Area, South China Sea

Three hydrate production tests have been conducted in the Shenhu Area in the South China Sea. Therefore, the Shenhu Area is also a model for the exploration and production tests of gas hydrates of passive continental margins. According to comprehensive analyses (Zhang et al., 2014; Li et al., 2018; Su et al., 2020; Ning et al., 2020), the conditions for the concentration of high saturation hydrate deposits in the Shenhu Area are similar to those in the Nankai Trough, Japan (**Figure 7**), despite they are in different tectonic backgrounds. The logging curves show that the average P-wave velocity of hydrate concentrated zones in the Shenhu Area is about 2.03 km/s, while that of non-hydrate layers under the BSR is only 1.1–1.7 km/s (Ye et al., 2020).

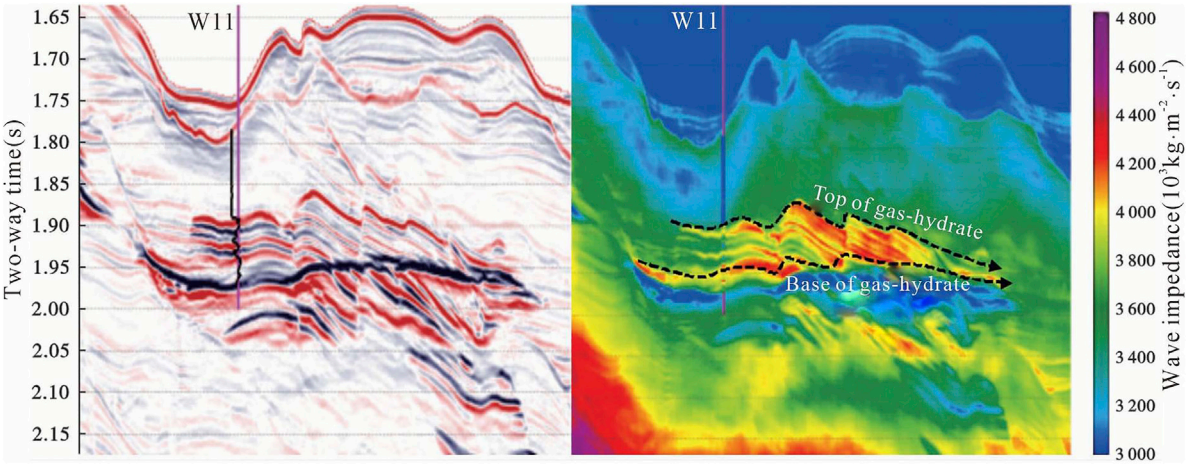

FIGURE 8 | Broadband seismic data of Well W11 (left) and well-free broadband seismic inversion results (Modified after Li et al., 2019).

In 2015, logging-while-drilling was conducted at 23 sites in the Shenhu Area carried out by the Guangzhou Marine Geological Survey. The logging data obtained during this expedition showed a hydrate saturation of up to 64%. Several sets of hydrate layers are vertically developed along Well W11, with a total thickness of over 70 m and a maximum hydrate saturation of up to 53%. By analyzing the seismic profile and synthetic seismic records of this well, Guo et al. (2017) found that the hydrate horizons are present as three strong reflections in the seismic profile and show strong impedance in the profile of synthetic seismic records. Li et al. (2019) obtained a detailed description of hydrate deposits passing through Well W11 using the well-free broadband seismic inversion technology (**Figure 8**). The inversion results clearly showed the top boundary, bottom boundary, and internal characteristics of the hydrate deposits in the Shenhu Area. Hydrate deposits in the Shenhu Area are located above the BSR and are manifested as three strong reflection axes (left, **Figure 8**), while the free gas under the BSR show weak impedance anomalies.

According to the above comparison, although there are different tectonic geological backgrounds, the corresponding relationship between strong reflection and gas hydrate is the same. We believe that the strong amplitude reflectors above BSR represents the existence of high saturation hydrate in both active and passive continental margins.

3.2.3 Analysis of Gas Hydrate Saturation by Comparison With ODP204

The seismic reflection characteristics of Makran Accretionary Prism are similar to those of Nankai Trough, and also can be compared with ODP204 drilling results (Tréhu et al., 2004). The drilling results of ODP204 show that gas hydrate is mainly distributed in three zones (**Figure 9**): 1. It is a high saturation accumulation area related to cold seeps, and its saturation can usually reach 30–40% (**Figure 9B**). The cold seep organisms found in the anticline ridge of Makran and the clear vertical channel on the seismic profile indicate that this type of hydrate distribution exists in the Makran area, However, its distribution range and thickness are relatively small, and the amount of resources is relatively small; 2. The weak reflections between seafloor and BSR, which is thicker than the cold seeps zones, and the saturation is generally 2–8% (**Figure 9A**), but its distribution area is relatively large and its thickness is also large, so the amount of hydrate resources should be relatively large; 3. Strong reflection above BSR, with saturation of about 15–20% (**Figure 9C**), distribution zone between 1 and 2, thickness of about 100m, and contains large hydrate resources. In addition, it is strongly reflected under the BSR, which can be determined as free gas can be considered as a part of the gas hydrate system, with a thickness of up to 1000m, which contains a great amount of resources (**Figure 9C**).

3.3 Discussion of Characteristics of High Saturation Hydrate Reservoirs

1) Drilling results from the gas hydrate reservoirs in the Nankai Trough, Japan confirmed that the amplitude-enhanced reflectors above the BSR are high saturation hydrate concentrated zones and that aquifers lacking amplitude-enhanced reflectors exist under the BSR. According to the logging curves of the gas hydrate reservoirs in the Nankai Trough, the sedimentary strata under the BSR show low resistivity and high gamma ray intensity (**Figure 6**). This indicates that the content of argillaceous materials increases and that the storage space decreases under the BSR accordingly. These conditions are unfavorable for the accumulation of free gas.
2) Drilling and impedance inversion results from the gas hydrate reservoirs in the Shenhu Area show that amplitude-enhanced reflectors coexisting with high impedance anomalies above the BSR are also high saturation hydrate concentrated zones. By contrast, the amplitude-enhanced reflectors below the BSR show low resistivity, high gamma ray intensity, and low impedance (**Figures 7**, **8**). Therefore, it can be inferred that the free gas under the BSR has low saturation.
3) The results of seismic interpretation and wave impedance inversion from the hydrate reservoirs in the Makran

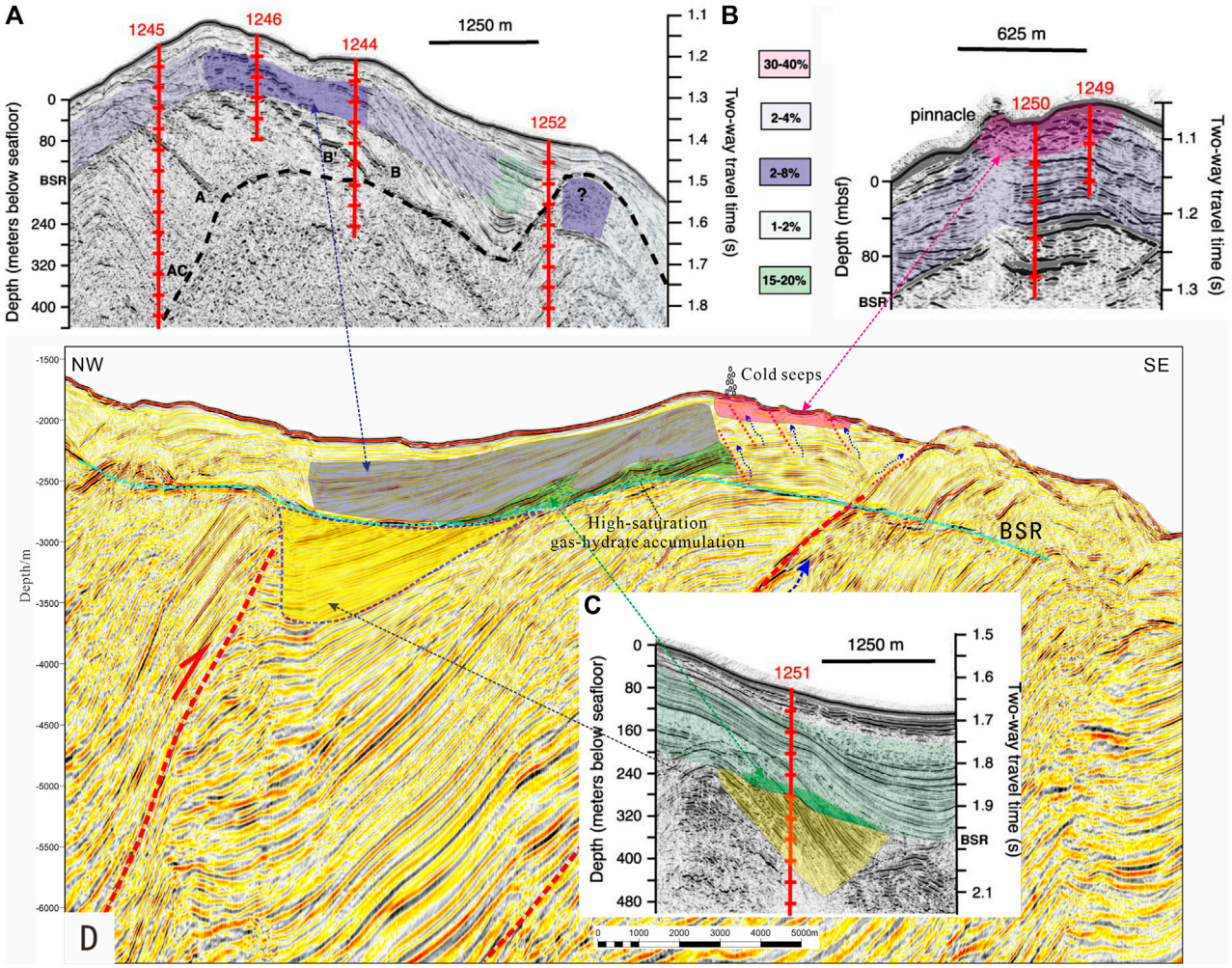

FIGURE 9 | Compared with ODP204 drilling results to speculate the gas hydrate saturation of Makran Accretionary Prism (modified after Tréhu et al., 2004). **(A)** seismic profile across the site 1245, 1246, 1244 and 1252 of ODP204. **(B)** seismic profile across the site 1250, 1249 of ODP204. **(C)** seismic profile across the site 1251 of ODP204. The transparent color areas of profile A, B, C represent different gas hydrate saturation calculated from the ODP204 drilling results. **(D)** seismic profile and inferred different concentration zones of gas hydrate in Makran Accretionary Prism.

Accretionary Prism indicate that amplitude-enhanced reflectors exist in the anticline wing above the BSR and the syncline area of the piggyback basin under the BSR. Given these results and the comparative analysis of characteristics of hydrate reservoirs in the Nankai Trough and the Shenhu Area, it can be inferred that the amplitude-enhanced reflectors above the BSR that coexist with high impedance anomalies are possibly high saturation hydrate concentrated zones.

4) The amplitude-enhanced reflectors below the BSR in the hydrate reservoirs in the Makran Accretionary Prism may be free gas concentrated zones. The slightly higher impedance anomalies coexisting with the amplitude-enhanced reflectors are related to the distribution state of the free gas in the strata or the coexistence of free gas and hydrates. In fact, the free gas below the BSR in the study area primarily occurs in coarse-grained turbidite sand layers and constitutes oblique interlayers together with mud layers. Such inclined layered distribution of free gas will change the velocity of gas-bearing sediments (Ojha and Sain, 2008). In addition, transition zones consisting of hydrates, free gas, and water exist below the hydrate deposits in the areas of production tests in the Shenhu Area (Qin et al., 2020). The degree of mixing of the substances of different phases in the transition zones changes the velocity of gas-bearing sediments, for which the specific reasons require further investigation.

4 CONCLUSION

1) According to the comprehensive analyses, the conditions for the formation of high saturation hydrate reservoirs should be characterized by a clear and continuous BSR, the coexistence

of amplitude-enhanced reflectors and high impedance anomalies above the BSR, high P-wave velocity, and relatively coarse-grained sediments.

2) The Makran Accretionary Prism has thick sediments, developed transport systems of "two-way gas supply" (i.e., thrust fault and normal fault, thrust fault and high permeable strata), and a clear and continuous BSR. Meanwhile, apparent amplitude-enhanced reflectors exist above and below the BSR. According to the impedance inversion results, the anticline wings above the BSR and the syncline area of the piggyback basin below the BSR show strong and a little strong impedance anomalies, respectively.
3) As inferred from the drilling results of high saturation hydrate reservoirs in the world, high saturation hydrate reservoirs in the Makran Accretionary Prism are mainly probably distributed in the anticline wings immediately above the BSR. Moreover, these reservoirs are characterized by coarse-grained sediments and the coexistence of amplitude-enhanced reflectors and high impedance anomalies.
4) The saturation of gas hydrate near cold seeps can reach 30–40%. However, its distribution range and thickness are relatively small, and the resources is relatively small. The saturation of gas hydrate of weak reflections between seafloor and BSR is generally 2–8%, the amount of hydrate resources should be relatively large. Strong reflection above BSR, with saturation of about 15–20% contains large hydrate resources. The free gas under the BSR with a thickness of up to 1000 m contains a great amount of gas.

DATA AVAILABILITY STATEMENT

The raw data supporting the conclusions of this article will be made available by the authors, without undue reservation.

AUTHOR CONTRIBUTIONS

JL is responsible for the interpretation of seismic data and compilation of the paper; XL is responsible for the inversion of gas hydrate seismic data; ZQ is responsible for the comparison of the characteristics of gas hydrate deposits with high saturation, JG is responsible for the analysis of the characteristics of gas hydrate deposits, WY is responsible for the collection of gas hydrate deposits in the Nankai Trough, SL, BL and JL are responsible for collecting the accumulation conditions of the gas hydrate deposits in the Shenhu area, KM and SW are responsible for collecting the relevant data on the accretion prism gas hydrate offshore Makran.

FUNDING

This study was funded by Marine S&T Fund of Shandong Province for Pilot National Laboratory for Marine Science and Technology (Qingdao) (2021QNLM020001-1) and the National Natural Science Foundation projects of China (42076069, 41706072), China Geological Survey project (DD20190581).

ACKNOWLEDGMENTS

The authors would like to express their gratitude to all members of R/V Haiyangdizhi 9, who assisted in the collection of field data for this project. Thanks also go to the reviewers and editors of this manuscript for their suggestions.

SUPPLEMENTARY MATERIAL

The Supplementary Material for this article can be found online at: https://www.frontiersin.org/articles/10.3389/feart.2022.861162/full#supplementary-material

REFERENCES

Baba, K., and Yamada, Y. (2004). BSRs and Associated Reflections as an Indicator of Gas Hydrate and Free Gas Accumulation: an Example of Accretionary Prism and Forearc basin System along the Nankai Trough, off central Japan. *Resource Geology*. 54, 11–24. doi:10.1111/j.1751-3928.2004.tb00183.x

Bohrmann, G., and Ohling, G. (2008). *Cold Seeps of the Makran Subduction Zone (Continental Margin of Pakistan): R/V Meteor Cruise Report M74/3:M74, Leg3, Fujairah-Male 30 October-28 November, 2007*. Fachbereich Geowissenschaften, Universitat Bremen, 1–120.

Delisle, G. (2004). The Mud Volcanoes of Pakistan. *Env Geol.* 46, 1024–1029. doi:10.1007/s00254-004-1089-x

Delisle, G., von Rad, U., Andruleit, H., Von Daniels, C., Tabrez, A., and Inam, A. (2002). Active Mud Volcanoes on- and Offshore Eastern Makran, Pakistan. *Int. J. Earth Sci.* 91, 93–110. doi:10.1007/s005310100203

Fujii, T., Suzuki, K., Takayama, T., Tamaki, M., Komatsu, Y., Konno, Y., et al. (2015). Geological Setting and Characterization of a Methane Hydrate Reservoir Distributed at the First Offshore Production Test Site on the Daini-Atsumi Knoll in the Eastern Nankai Trough, Japan. *Mar. Pet. Geology.* 66, 310–322. doi:10.1016/j.marpetgeo.2015.02.037

Gong, J. M., Liao, J., Sun, J., Yang, C. S., Wang, J. Q., He, Y. J., et al. (2016). Main Controlling Factors of Natural Gas Hydrate in Makran Accretionary Prism Pakistan. *Mar. Geology. Frontier* 32, 10–15. (in Chinese with English abstract).

Gong, J. M., Liao, J., Yang, C. S., Cheng, H. Y., Sun, J., Wang, J. Q., et al. (2017). The Relationship between Authigenic Carbonate and Gas Hydrates in Makran Accretionary Wedge: on the Basis of M 74/3 Cruise Report of "R/V Meteor" in 2007. *Mar. Geology. Front.* 33, 20–26. (in Chinese with English abstract).

Gong, J. M., Liao, J., Yin, W. H., Zhang, L., He, Y. J., Sun, Z. L., et al. (2018a). Gas Hydrate Accumulation Models of Makran Accretionary Prism, Northern Indian Ocean. *Mar. Geology. Quat. Geology.* 38, 148–155. (in Chinese with English abstract).

Gong, J. M., Liao, J., Zhang, L., He, Y. J., Zhai, B., Meng, M., et al. (2018b). Discussion on the Distribution and Main Controlling Factors of Mud Volcanoes in Makran Accretionary prism,Northern Indian Ocean. *Geoscience* 32, 1025–1030. (in Chinese with English abstract).

Grando, G., and McClay, K. (2007). Morphotectonics Domains and Structural Styles in the Makran Accretionary Prism, Offshore Iran. *Sediment. Geology.* 196, 157–179. doi:10.1016/j.sedgeo.2006.05.030

Grevemeyer, I., Rosenberger, A., and Villinger, H. (2000). Natural Gas Hydrates on the continental Slope off Pakistan: Constraints from Seismic Techniques. *Geophys. J. Int.* 140, 295–310. doi:10.1046/j.1365-246x.2000.00009.x

Guo, Y. Q., Yang, S. X., Liang, J. Q., Lu, J. A., Lin, L., and Kuang, Z. G. (2017). Characteristics of High Gas Hydrate Distribution in the Shenhu Area on the Northern Slope of the South China Sea. *Earth Sci. Front.* 24, 24–31. (in Chinese with English abstract).

Hu, G. W., Bu, Q. T., Lu, W. J., Wang, J. S., Chen, J., Li, Q., et al. (2020). A Comparative Study on Natural Gas Hydrate Accumulation Models at Active and Passive continental Margins. *Nat. Gas Industry* 40, 45–58.

Hussain, A., Khan, M. R., Ahmad, N., and Javed, T. (2015). *Mud-diapirism Induced Structuration and Implications for the Definition and Mapping of Hydrocarbon Traps in Makran Accretionary Prism*. Melbourne.Melbourne,Australia: Pakistan//AAPG/SEG International Conference&Exhibition, 13–16.

Hyndman, R., and Spence, G. (1992). A Seismic Study of Methane Hydrate marine Bottom Simulation Reflectors. *Geophys. Res.* 97, 6638–6698. doi:10.1029/92jb00234

Ito, T., Komatsu, Y., Fujii, T., Suzuki, K., Egawa, K., Nakatsuka, Y., et al. (2015). Lithological Features of Hydrate-Bearing Sediments and Their Relationship with Gas Hydrate Saturation in the Eastern Nankai Trough, Japan. *Mar. Pet. Geology.* 66, 368–378. doi:10.1016/j.marpetgeo.2015.02.022

Komatsu, Y., Suzuki, K., and Fujii, T. (2015). Sedimentary Facies and Paleoenvironments of a Gas-Hydrate-Bearing Sediment Core in the Eastern Nankai Trough, Japan. *Mar. Pet. Geology.* 66, 358–367. doi:10.1016/j.marpetgeo.2015.02.038

Kopp, C., Fruehn, J., Flueh, E. R., Reichert, C., Kukowski, N., Bialas, J., et al. (2000). Structure of the Makran Subduction Zone from Wide-Angle and Reflection Seismic Data. *Tectonophysics* 329, 171–191. doi:10.1016/s0040-1951(00)00195-5

Li, J.-f., Ye, J. L., Ye, J.-l., Qin, X.-w., Qiu, H.-j., Wu, N.-y., et al. (2018). The First Offshore Natural Gas Hydrate Production Test in South China Sea. *China Geology.* 1, 5–16. doi:10.31035/cg2018003

Li, Y. P., Yan, C. Z., Li, J., Shi, W. Y., and Chen, L. (2019). Application of Well-free Broadband Seismic Inversion Technology on the Description of Gas Hydrate Ore Body in Shenhu Waters, South China Sea. *China Offshore Oil and Gas* 31, 51–60. (in Chinese with English abstract).

Liao, J., Gong, J. M., He, Y. J., Yue, B. J., and Meng, M. (2019). Stratigraphic Sequence and Development Process of Makran Accretionary Prism. *Mar. Geology. Frontier* 35, 69–72. (in Chinese with English abstract).

Ning, F. L., Liang, J. Q., Wu, N. Y., Zhu, Y. H., Wu, S. G., Liu, C. L., et al. (2020). Reservoir Characteristics of Natural Gas Hydrates in China. *Nat. Gas Industry* 40, 1–24. (in Chinese with English abstract).

Ojha, M., and Sain, K. (2008). Appraisal of Gas-Hydrate/free-Gas from Vp/Vs Ratio in the Makran Acceretionary Prism. *Mar. Pet. Geology.* 25, 637–644. doi:10.1016/j.marpetgeo.2007.10.007

Qin, X. W., Lu, J. A., Lu, H. L., Qiu, H. J., Liang, J. Q., Kang, D. J., et al. (2020). Coexistence of Natural Gas Hydrate, Free Gas and Water in the Gas Hydrate System in the Shenhu Area, South China Sea. *China Geology.* 2, 210–220.

Riedel, M., Collett, T. S., and Malone, M. J. (2010). *Expedition 311 Synthesis: Scientific findings//Proceedings of the Integrated Ocean Drilling Program*, 311. Washington, DC: Integrated Ocean Drilling Program Management International Inc.

Riedel, M., and Shankar, U. (20122012). Combining Impedance Inversion and Seismic Similarity for Robust Gas Hydrate Concentration Assessments-A Case Study from the Krishna-Godavari basin. *East. Coast India Mar. Pet. Geology.* 36, 35–49. doi:10.1016/j.marpetgeo.2012.06.006

Riedel, M., Willoughby, E. C., and Chopra, S. (2010). *Geophysical Charaterization of Gas Hydrate*, 14. USA: SEG Geophysical Developments.

Sain, K., Minshull, T. A., Singh, S. C., and Hobbs, R. W. (2000). Evidence for a Thick Free Gas Layer beneath the Bottom Simulating Reflector in the Makran Accretionary Prism. *Mar. Geology.* 164, 3–12. doi:10.1016/s0025-3227(99)00122-x

Smith, G. L. (2013). *The Structure, Fluid Distribution and Earthquake Potential of the Makran Subduction Zone, Pakistan*. Southampton: Great Britain University of Southampton.

Su, P. B., Liang, J. Q., Zhang, W., Liu, F., Wang, F. F., Li, T. W., et al. (2020). Natural Gas Hydrate Accumulation System in the Shenhu Sea Area of the Northern South China Sea. *Nat. Gas Industry* 40, 77–89.

Tréhu, A. M., Long, P. E., Torres, M. E., Bohrmann, G., Rack, F. R., Collett, T. S., et al. (2004). Hree-Dimensional Distribution of Gas Hydrate beneath Southern Hydrate Ridge: Constraints from ODP Leg 204. *Earth Planet. Sci. Lett.* 222 (3-4), 845–862.

Von Rad, U., Berner, U., Delisle, G., Doose-Rolinski, H., Fechner, N., Linke, P., et al. (2000). Sonne 122/130 Scientific PartiesGas and Fluid Venting at the Makran Accretionary Prism off Pakistan. *Geo-Marine Lett.* 20, 10–19. doi:10.1007/s003670000033

Wan, X. M., Liang, J., Liang, J. Q., Lin, L., Sha, Z. B., Chai, Y., et al. (2016). The Application of post-stack Impedance Inversion without Well to the Prediction of Gas Hydrate Distribution in T Study Area. *Geophys. Geochemical Exploration* 40, 438–444. (in Chinese with English abstract).

Xue, H., Zhang, B. J., Xu, Y. X., Wen, P. F., and Zhang, R. W. (20162016). Application of Wave Impedance Inversion to Gas Hydrates Prediction in Southeast Hainan basin. *Mar. Geology. Quat. Geology.* 36, 173–180. (in Chinese with English abstract).

Ye, J. L., Qin, X. W., Xie, W. W., Lu, H. L., Ma, B. J., Qiu, H. J., et al. (2020). Main Progress of the Second Gas Hydrate Trial Production in the South China Sea. *Geology. China* 47, 557–568. (in Chinese with English abstract).

Zhang, G. X., Liang, J. Q., Lu, J. Q., Yang, J. G., Lu, J. A., Yang, S. X., et al. (2014). Characteristics of Natural Gas Hydrate Reservoirs on the Northeastern Slope of the South China Sea. *Nat. Gas Industry* 34, 1–10. (in Chinese with English abstract).

Zhang, G. X., Zhu, Y. H., Liang, J. Q., Wu, S. G., Yang, M. Z., and Sha, Z. B. (2006). Tectonic Controls on Gas Hydrate Deposits and Their Characteristics. *Geosciece* 20, 605–612.

Zhang, Z., He, G. W., Yao, H. Q., Deng, X. G., Yu, M., Huang, W., et al. (2020). Diapir Structure and its Constraint on Gas Hydrate Accumulation in the Makran Accretionary Prism, Offshore Pakistan. *China Geology.* 3, 611–622. doi:10.31035/cg2020049

Zhao, K. B. (2019). Occurrence and Accumulation Characteristics of Natural Gas Hydrate in the Eastern Nankai Trough, Japan. *Pet. Geology. Exp.* 41, 831–837. (in Chinese with English abstract).

Conflict of Interest: The authors declare that the research was conducted in the absence of any commercial or financial relationships that could be construed as a potential conflict of interest.

Publisher's Note: All claims expressed in this article are solely those of the authors and do not necessarily represent those of their affiliated organizations, or those of the publisher, the editors and the reviewers. Any product that may be evaluated in this article, or claim that may be made by its manufacturer, is not guaranteed or endorsed by the publisher.

frontiers | Frontiers in Earth Science

ORIGINAL RESEARCH
published: 28 April 2022
doi: 10.3389/feart.2022.880933

Spatial-Temporal Evolution of the Gas Hydrate Stability Zone and Accumulation Patterns of Double BSRs Formation in the Shenhu Area

Yingrui Song[1,2,3], *Yuhong Lei*[1,2]*, *Likuan Zhang*[1,2], *Ming Cheng*[1,2], *Chao Li*[1,2] *and Naigui Liu*[1,2]

[1]Key Laboratory of Petroleum Resources Research, Institute of Geology and Geophysics, Chinese Academy of Sciences, Beijing, China, [2]Innovation Academy for Earth Science, Chinese Academy of Sciences, Beijing, China, [3]University of Chinese Academy of Sciences, Beijing, China

OPEN ACCESS

Edited by:
Wei Zhang,
Guangzhou Marine Geological Survey, China

Reviewed by:
Jiapeng Jin,
Qingdao National Laboratory for Marine Science and Technology, China
Michael Riedel,
Helmholtz Association of German Research Centres (HZ), Germany
Jinxiu Yang,
China University of Petroleum, China
Chao Fu,
China National Offshore Oil Corporation, China

***Correspondence:**
Yuhong Lei
leiyh@mail.iggcas.ac.cn

Specialty section:
This article was submitted to Marine Geoscience, a section of the journal Frontiers in Earth Science

Received: 22 February 2022
Accepted: 06 April 2022
Published: 28 April 2022

Citation:
Song Y, Lei Y, Zhang L, Cheng M, Li C and Liu N (2022) Spatial-Temporal Evolution of the Gas Hydrate Stability Zone and Accumulation Patterns of Double BSRs Formation in the Shenhu Area. Front. Earth Sci. 10:880933. doi: 10.3389/feart.2022.880933

The current study examines the methane gas hydrate stability zone (GHSZ) in the Shenhu area in the northern South China Sea (SCS) as an example to calculate the thickness of the GHSZ and reconstruct its evolution since 8.2 Ma. Two mechanisms for typical double BSRs in the Shenhu area are shown, and the relationship between the evolving thickness of the GHSZ and the dynamic accumulation of NGHs at typical stations in the Shenhu area is clarified. The results show that the thickness of the GHSZ varies over time with overall thickening in the Shenhu area. The current thickness of the GHSZ is between 160.98 and 267.94 m. Two mechanisms of double BSRs in the Shenhu area are summarized: the double BSRs pattern based on changes in formation temperature, pressure and other conditions and the double BSRs pattern based on differences in gas source and composition. The formation process and occurrence characteristics of double BSRs and hydrate at site SH-W07-2016 in the Shenhu area are also closely related to the changes in thickness of the GHSZ. In addition, the age when gas source first enters the GHSZ has a considerable influence on the dynamic accumulation process of hydrate. Since the formation of hydrate above the BSR at site SH-W07-2016, the GHSZ has experienced up to two periods of thickening and two periods of thinning at this site. With the changes in the thickness of the GHSZ, up to two stages of hydrate formation and at most two stages of hydrate decomposition have occurred. This paper is of great value for understanding the formation of multiple bottom-simulating reflectors (BSRs) as well as the migration, accumulation and dissipation of natural gas hydrate (NGH) during the dynamic accumulation process.

Keywords: gas hydrate, gas hydrate stability zone, double BSRs, dynamic accumulation process, the Shenhu area

1 INTRODUCTION

The gas hydrate stability zone (GHSZ) is the zone of thermodynamic equilibrium of three-phase compounds composed of natural gas hydrate (NGH), water, and gas (Rempel and Buffett, 1997). The thickness of the GHSZ not only determines the maximum possible range of hydrates but is also an important index for NGH exploration and resource evaluation, and it has received extensive attention in recent decades (Kvenvolden, 1993; Sloan and Koh, 2008; Collett, 2009).

The spatial-temporal variability of GSHZ is important for understanding the dynamic accumulation process of hydrate The thickness and spatial distribution characteristics of the GHSZ are very sensitive to temperature and pressure and are also affected by gas composition and pore water salinity (Holder et al., 1987; Collett, 2009). Factors such as geothermal gradient, bottom water temperature (BWT), and climate cause changes in temperature and pressure conditions (Foucher et al., 2000; Zander et al., 2017; Lei et al., 2021); tectonic uplift and folding cause changes in seawater depth (Bangs et al., 2005; Haacke et al., 2007); and differences in hydrate gas source components (Posewang and Mienert, 1999; Andreassen et al., 2000; Lei et al., 2021) may lead to changes in the thickness and spatial distribution of the GHSZ. These changes will lead to a change in GHSZ, which affects the decomposition, migration, and accumulation or dissipation of hydrate, that is the dynamic accumulation process of hydrate (Foucher et al., 2000; Auguy et al., 2017; Pecher et al., 2017; Zander et al., 2017).

Bottom-simulating reflectors (BSRs) are strong impedance contrasts in seismic sections caused by upper hydrate-bearing sediments and lower water- or gas-bearing sediments (Ecker et al., 2000). BSRs are often used as a marker of the lowest formation of hydrate to search for marine gas hydrate (Ruppel et al., 2008; Mosher, 2011; Boswell et al., 2012; Phrampus and Hornbach, 2012). The dynamic accumulation process of hydrate will cause double/multiple BSRs. Clarifying the relationship between multiple BSRs and hydrate is of great significance for improving the success rate of marine hydrate exploration based on BSRs. However, there is not a one-to-one correspondence between the BSR and NGHs (Majumdar et al., 2016; Liu et al., 2017). NGHs were encountered in only 12 out of 35 sites with significant BSRs from 788 sites in the Gulf of Mexico (Majumdar et al., 2016). Moreover, BSR still lacks accuracy in identifying high-saturation hydrates (Majumdar et al., 2016; Liu et al., 2017); NGHs were discovered in 104 (14%) of 753 sites in the Gulf of Mexico without a BSR (Majumdar et al., 2016). The phenomenon of double BSRs or multiple BSRs is found in many hydrate occurrence areas. These include the Storegga Slide area west of Norway (Posewang and Mienert, 1999), the Nankai trough of Japan (Foucher et al., 2000; Baba and Yamada, 2004), the accretionary wedge of the Manila subduction zone (Wu et al., 2005), the southern Hydrate ridge offshore of Oregon (Bangs et al., 2005), the Danube deep-sea fan of the Black Sea (Popescu et al., 2006; Zander et al., 2017), the Kutei Basin offshore of Indonesia (Zhang and Wright, 2017), the Shenhu area on the northern slope of the South China Sea (SCS) (Liang et al., 2017; Wei et al., 2018) and the Dongsha area of the SCS (Li et al., 2015; Jin et al., 2020b). In these previous studies, double/multiple BSRs can be caused by differences in gas components (Posewang and Mienert, 1999; Andreassen et al., 2000; Liang et al., 2017), changes in stratigraphic lithology or mineral composition (Foucher et al., 2000; Martin et al., 2004; Musgrave et al., 2006), or an increased BWT, the pressure drop when the sea level drops, tectonic uplift, seafloor erosion and other factors leading to the change in the GHSZ (Foucher et al., 2000; Bangs et al., 2005; Haacke et al., 2007; Pecher et al., 2017; Zander et al., 2017; Jin et al., 2020b).

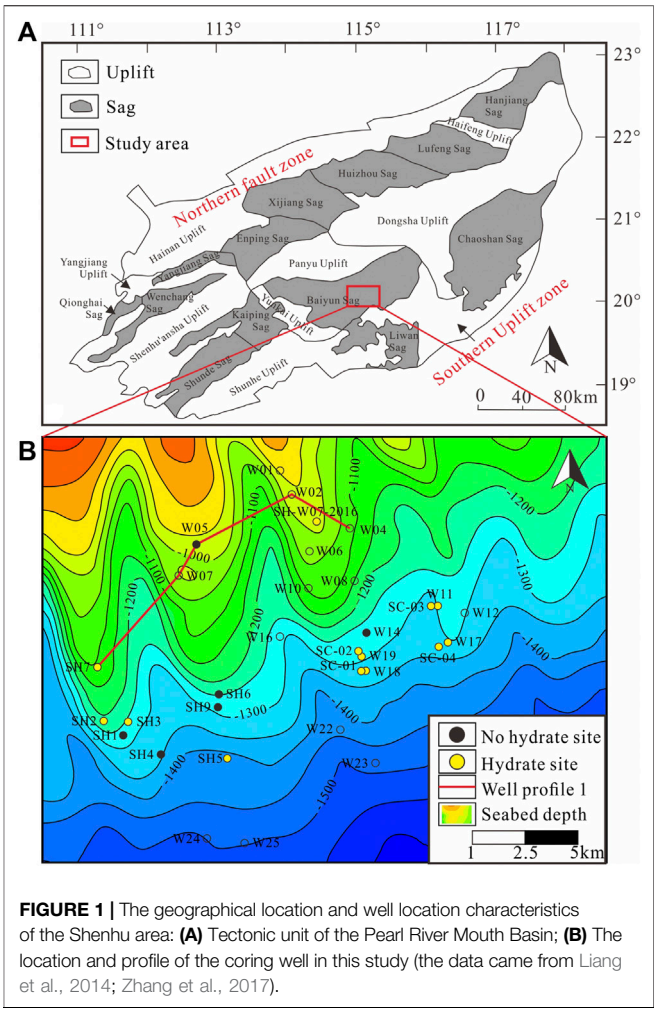

FIGURE 1 | The geographical location and well location characteristics of the Shenhu area: **(A)** Tectonic unit of the Pearl River Mouth Basin; **(B)** The location and profile of the coring well in this study (the data came from Liang et al., 2014; Zhang et al., 2017).

The South China Sea (SCS) is rich in NGH resources (Wu et al., 2010; Liang et al., 2014; Zhang et al., 2017). Geophysical exploration and drilling results reveal that double BSRs are common in the SCS, such as at sites SH7, SH-W07-2016 and W17 in the Shenhu area of the Pearl River Mouth Basin (Liang et al., 2017; Qian et al., 2018; Sun et al., 2018; Zhang et al., 2020b). The phenomenon of double BSRs may be related to the dynamic accumulation of hydrate, but is essentially caused by changes in the GHSZ. However, the existing studies on the spatial-temporal evolution of the GHSZ and its relationships with the formation of double BSRs and the dynamic migration, accumulation and dissipation of hydrate are not comprehensive.

The spatial-temporal evolution of the GHSZ can be used to better understand the dynamic decomposition, migration, accumulation and dissipation of gas hydrates and to analyse the formation mechanism of double and multiple BSRs. In view of this, this paper selected the Shenhu area on the northern continental slope of the SCS as the research object, where geophysical and logging while drilling (LWD) data are abundant. In this paper, the evolution and spatial distribution characteristics of the GHSZ in the Shenhu area are simulated, and the relationships between the evolution of the GHSZ and the

formation of double BSRs and the dynamic accumulation of hydrates in the Shenhu area are discussed. This work can provide a reference and insights for understanding the distribution of gas hydrate accumulation and clarifying the relationship between BSRs and NGHs in the Shenhu area.

2 GEOLOGICAL BACKGROUND

The Shenhu area is located in the middle of the Baiyun Sag of the Pearl River Mouth Basin in the northern SCS, which is located in a passive continental margin zone (**Figure 1**). The Pearl River Mouth Basin has experienced two tectonic evolution stages: Eocene–Oligocene rifting and Neogene-Quaternary postrift depression (He et al., 2017). Cenozoic marine and continental transitional sediments dominated by clay and silt have been deposited from bottom to top (Pang et al., 2007; Zhang et al., 2014). The present depth of the Shenhu area is approximately 800–1700 m (Liang et al., 2014; Zhang et al., 2017, Zhang et al., 2020a; ETOPO1 data), the seabed pressure ranges from approximately 11–14 MPa, the heat flow value ranges from 74 mW/m^2 to 78 mW/m^2, the geothermal gradient is 45°C/km to 67°C/km, and the temperature of the seawater at the seabed is between 2 and 6°C; thus, these temperature and pressure conditions are suitable for the generation of gas hydrates (Zhang et al., 2017).

Three sets of source rocks are developed in the Shenhu area. The Eocene–Oligocene Wenchang and Enping Formations are the main source rocks of thermogenic gas in the Baiyun Sag (Li et al., 2015). The total organic carbon (TOC) of the Wenchang Formation ranges from 0.53% to 6.10%, with an average of 2.63%, and the TOC of the Enping Formation ranges from 0.46% to 1.57%, with an average of 0.89% (Niu et al., 2019). The source rocks of the Wenchang Formation and Enping Formation are in the mature to high-maturity stage, the Ro of the Wenchang Formation ranges from 0.52% to 0.69%, and the Ro of the Enping Formation ranges from 0.55% to 0.88% (Niu et al., 2019). Pliocene and Quaternary marine sedimentary strata are the main source rocks of biogenic gas in the Baiyun sag. Although the abundance of organic matter in Pliocene and Quaternary marine sediments is low, with a TOC ranging from 0.51% to 1.83%, at the immature to low-maturity stage, the organic matter in these strata can also generate a large amount of biogenic gas (He et al., 2013), which provides a sufficient gas source for hydrate formation in the Shenhu area. Faults, fluid diapirs and microfractures are well developed in the Shenhu area. Some faults and diapir structures connect the deep source rocks of the Wenchang and Enping Formations, and a large number of small faults and diapir structures are also developed in the shallow strata (He et al., 2013). These faults, diapirs and fractures are important channels allowing thermal gas from deep strata and biogenic gas from shallow source rocks to move to the GHSZ and provide enough natural gas for the formation of gas hydrate (Su et al., 2017; Zhang et al., 2018). The sufficient gas sources, widely distributed gas migration channels and suitable temperature and pressure conditions all indicate that the Shenhu area is a favourable exploration area for NGHs (Wu et al., 2010; Liang et al., 2014; Su et al., 2016; Zhang et al., 2017).

Starting in the 21st century, China has carried out a series of scientific research and exploration activities for gas hydrates in the SCS and obtained a series of drilling data, including data from a large number of 2D and 3D seismic explorations (Yang et al., 2015, Yang et al., 2017 J.; Zhang et al., 2017; Qian et al., 2018; Sun et al., 2018; Zhang et al., 2020a; Zhang et al., 2020b), hydrate LWD data (Li et al., 2018; Ye et al., 2018, 2020) and data from massive pore-filling gas hydrate-bearing cores (Wang et al., 2014; Su et al., 2016; Yang S. X. et al., 2017; Zhang et al., 2017; Su et al., 2018; Wei et al., 2018; Zhang et al., 2019; Zhang et al., 2020a; Zhang et al., 2020b). From 2007 to 2016, a total of 31 hydrate sites were drilled in the Shenhu area, of which 12 operations encountered hydrate layers. The thickness of the hydrate layer was between 10 and 47 m (Zhang et al., 2007; Wu et al., 2011; Wang et al., 2014; Zhang et al., 2020a; Zhang et al., 2020b), and the porosity of the sediments was between 55% and 65%. Hydrate saturation was approximately 220%–80% (Wang et al., 2014; Yang et al., 2015; Su et al., 2016; Yang J. et al., 2017; Yang S. X. et al., 2017; Zhang et al., 2017; Zhang et al., 2020a; Zhang et al., 2020b). In 2017 and 2020, the Guangzhou Marine Geological Survey (GMGS) carried out hydrate mining experiments in the Shenhu area twice and achieved great success in the 60-day production test (Li et al., 2018; Ye et al., 2018; Ye et al., 2020). The geological and geophysical data and drilling and gas hydrate exploration results all show that the Shenhu area has great gas hydrate exploration and development prospects (Zhang et al., 2007; Wang et al., 2014; Yang et al., 2015; Su et al., 2016; Zhang et al., 2017; Su et al., 2018; Zhang et al., 2019; Zhang et al., 2020a; Zhang et al., 2020b).

3 METHODOLOGY AND DATA

3.1 Method

The GHSZ is the interval in which the three phases of NGH, water and gas reach thermodynamic equilibrium under certain temperature and pressure conditions. NGH in this range is thermodynamically stable (Kvenvolden, 1993; Rempel and Buffett, 1997). The intersection point of the geothermal gradient and the temperature-pressure phase equilibrium boundary below the sea bottom is the bottom boundary of the GHSZ, the seafloor is the top boundary of the GHSZ, and the vertical distance between the top boundary and the bottom boundary is the thickness of the GHSZ. Therefore, the thickness of the GHSZ can be calculated by using the temperature and pressure phase equilibrium equation of gas hydrate combined with the geothermal gradient curve (Dickens and Quinby-Hunt, 1994; Miles, 1995; Brown et al., 1996; Bishnoi and Dholabhai, 1999; Peltzer and Brewer, 2003; Sloan, 2008). The upper BSR usually represents the bottom boundary of the methane GHSZ. To verify the rationality of the simulation results, methane GHSZ was selected for

calculation in this research. The calculation method of the theoretical model is as follows:

The methane hydrate phase diagram shows the methane GHSZ as a function of pressure and temperature. By measuring the temperature (T) and pressure (P) of the stability field of methane hydrate in seawater in the laboratory, Miles's (1995) fourth-order polynomial phase equilibrium equation of temperature (T) and pressure (P) **Eq. 1** is more suitable for the calculation of GHSZ thickness in continental margin areas:

$$P = C + m_1(T-273.15) + m_2(T-273.15)^2 + m_3(T-273.15)^3 + m_4(T-273.15)^4 \quad (1)$$

where P is the pressure, MPa; T is temperature, K; C is the constant term of the fitting relation, with a value of 2.8074023. m_1, m_2, m_3 and m_4 denote fitting coefficients of polynomials under different conditions, with values of $m_1 = 1.559474 \times 10^{-1}$, $m_2 = 4.8275 \times 10^{-2}$, $m_3 = -2.78083 \times 10^{-3}$, and $m_4 = 1.5922 \times 10^{-4}$.

In the calculation, the range of the GHSZ is calculated by assuming that the gas consists entirely of methane. The transformation relationship between pressure (P) and depth ($h + D$) is shown in the equation:

$$P = P_{atm} + \rho g(h + D) \quad (2)$$

where P_{atm} is atmospheric pressure, with a value of 0.101325 MPa; ρ is seawater density, with a value of 1035 kg/m^3; g is gravity, with a value of 9.81 m/s^2; h is the vertical distance of the GHSZ bottom to seabed, km; and D is the present seawater depth, km.

The calculation equation of the geothermal gradient (G) is as follows:

$$G = \frac{(T - 273.15) - (T_i - 273.15)}{h - h_i} \quad (3)$$

where T_i is the sediment temperature at point I, K; h_i is the vertical distance to the seabed at point i, km; and G is the geothermal gradient, ˚C/km.

When temperature is taken as the varied parameter, the functional relations (4) and (5) with temperature as the independent variable and h as the dependent variable can be obtained by using **Eqs 1**–**3**.

$$h = \frac{[C + m_1(T-273.15) + m_2(T-273.15)^2 + m_3(T-273.15)^3 + m_4(T-273.15)^4 - P_{atm}] \times 10^9}{\rho g} - D \quad (4)$$

$$h = \frac{(T - 273.15) - (T_i - 273.15)}{G} + h_i \quad (5)$$

When **Eqs 4**, **5** are equal, the value of h is the thickness of the GHSZ.

3.2 Data

3.2.1 Seawater Depth Data

The present seawater depth (D) is an important parameter in calculating the thickness of the present GHSZ. The present seawater depth in the Shenhu area varies from 730 m in the northwest to 1,650 m in the southeast (**Figure 1**).

The paleo-seawater depth is the main parameter involved in calculating the paleo-GHSZ, and the paleo-seawater depth (D_p) is a function **Eq. 6** of the present seawater depth (D), the history of relative sea level fluctuation (ΔH_1), the history of sea floor subsidence (ΔH_2), and the history of depositional thickness (ΔH_3):

$$D_p = D + \Delta H_1 + \Delta H_2 - \Delta H_3 \quad (6)$$

where D_p is the paleo-seawater depth, km; ΔH_1 is the history of relative sea level fluctuation, km; ΔH_2 is the history of seafloor subsidence, km; and ΔH_3 is the history of depositional thickness, km.

Pang et al. (2007) studied the deep-water fan system of the Pearl River Mouth Basin in the SCS. The history of relative sea level change in the Pearl River Mouth Basin was established by analysing the coupled relationship between the large continental shelf delta and the Pearl River Mouth Basin deep-water fan system on the slope. The relative sea level change data over time in this study ($\triangle H_1$) refer to the research results of Pang et al. (2007) (**Figure 2A**).

The seafloor subsidence history (ΔH_2) and the history of depositional thickness (ΔH_3) in the Shenhu area are based on the burial history in the Shenhu area (**Figure 2B**), and the data of this burial history come from Su et al. (2018). The erosional events, timing of erosion, and eroded thickness in the Shenhu area are based on the studies of Li (2010), Zhang (2011), Zhao (2012), and He et al. (2019).

3.2.2 BWT

Zhu, 2007 established a fitting calculation equation for the present bottom water temperature (BWT) (T_s) and seawater depth (D) based on BWT and seawater depth data from the continental margin basins of the northern SCS. The results show that there is a certain deviation between the calculated BWT data and the measured BWT data. However, it can be seen from the World Ocean Atlas 2013 that the annual variability in the BWT in the Shenhu area is approximately ±2˚C, so this error is within the normal range of ±2˚C. According to **Formula 3**, the increase in BWT is accompanied by a decrease in GHSZ. The corrected value in **Formula 7** is larger than the average value, and the thickness of the GHSZ is correspondingly thinner. Although the BWT changes naturally within a year, it does not affect the change within the minimum range of the GHSZ. The change in BWT had little influence on subsequent analysis.

The measured temperature data of 10 wells, such as SH1 in the Shenhu area, were used as the benchmark to calibrate the equation, and the temperature-depth equation after correction is shown in **Eq. 7**. After numerical correction, the relative error between the measured and corrected BWT is between ±0.38% and 13.35% (**Table 1**), which is within the error range. Therefore, the equation of Zhu, 2007 was adopted in this study to calculate the present seabed temperature in the Shenhu area by correcting the measured BWT (**Figure 2C**).

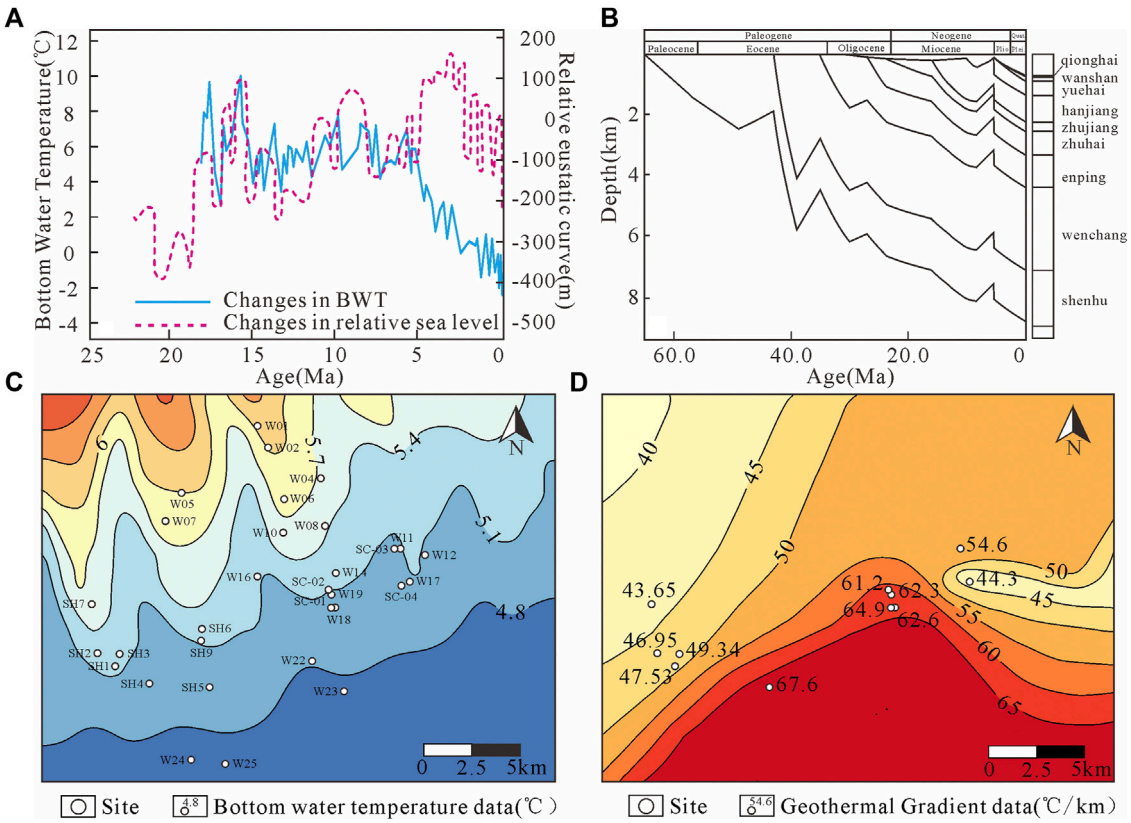

FIGURE 2 | (A) Changes in relative sea level and BWT at ODP 806 in the Pearl River Mouth Basin in the northern SCS (modified from Pang et al., 2007 and Lear et al., 2015); **(B)** Burial history of a single well in the Shenhu area, northern SCS; **(C)** The BWT characteristics in the Shenhu area, northern SCS; **(D)** The geothermal gradient characteristics in the Shenhu area, northern South China Sea (the data come from Su et al., 2016; Zhang et al., 2020a; Jin et al., 2020b).

TABLE 1 | Calculation parameters of the BWT (Zhu et al., 2013; Zhang et al., 2020a; Zhang et al., 2020b).

Site	Measured BWT (°C)	Calculated BWT (°C)	Relative error (%)
SH1	5.20	5.18	−0.38
SH2	4.84	5.25	8.47
SH3	5.53	5.22	−5.61
SH7	6.44	5.58	−13.35
W11	4.84	5.07	4.75
W17	4.74	5.19	9.49
W18	4.63	5.12	10.58
W19	5.64	5.16	−8.51
SC-01	4.94	5.12	3.64
SC-02	4.95	5.13	3.64

$$\begin{cases} T_s = -8.7946\ln(D\times 1000) + 337.4369 & 0.1km < D \le 0.8km \\ \ln(T_s - 274.4789) = -0.7485\times(\ln D - 2.0339) & 0.8km < D \le 2.8km \\ T_s = 276.6789 & D > 2.8km \end{cases} \quad (7)$$

where T_s is the present BWT, K.

Lear et al. (2015) used $\delta^{18}O$ and Mg/Ca records of the infaunal benthic foraminifer *O. umbonatus* from Ocean Drilling Program (ODP) Site 806 (equatorial Pacific; ~2,500 m) since 17 Ma in an adjacent research area (**Figure 2A**).

According to the present BWT and the research results of Lear et al. (2015), paleo-BWT (T_P) is a function of the present BWT (T_s) and the relative change in BWT (ΔT) by **Eq. 8**:

$$T_p = T_s + \Delta T \quad (8)$$

where T_p is the paleo-BWT, K, and ΔT is the relative change in BWT, K.

In addition, when the temperature changes, heat transfer occurs inside the model. The model should follow the basic theory of heat transfer and consider the calculation process of heat transfer. However, the process of temperature conduction and the change in hydrate phase state usually does not exceed several decades, which is far less than the time unit studied in this model (millions of years, Ma) (Zander et al., 2017). It is considered that temperature changes in the model will be rapidly converted to GHSZ changes. The possible changes caused by the thermal conductivity process are ignored.

3.2.3 Pressure

The measured drilling pressure in the Shenhu area shows that the present shallow formation pressure is at a normal pressure. Therefore, the formation pressure used to calculate the GHSZ in the Shenhu area is hydrostatic pressure, which can be obtained

TABLE 2 | Calculation parameters and results of the GHSZ (BWT data are from Zhu et al., 2013; Zhang et al., 2020a, Zhang et al., 2020b. Geothermal gradient data are from Su et al., 2016; Zhang et al., 2020a, Zhang et al., 2020b; Jin et al., 2020a. Seawater depth data are from Wang et al., 2014; Zhang et al., 2019; WOA13 V2. Seawater density data are from Wang et al., 2013. BSR data are from Wu et al., 2011; Wang et al., 2014; Su et al., 2016; Liang et al., 2017; Jin et al., 2020a).

Site	BWT (°C)	Geothermal gradient (°C/km)	Seawater depth (m)	Calculated thickness (m)	BSR (mbsf)	Relative error (%)
SH1	5.20	47.53	1,262.00	210.60	219.00	−3.84
SH2	4.84	46.95	1,230.00	218.10	221.00	−1.31
SH3	5.53	49.34	1,245.00	192.34	204.00	−5.72
SH7	6.44	43.65	1,105.00	175.95	181.00	−2.79
W11	4.84	54.60	1,309.75	192.67	200.00	−3.67
W17	4.74	44.30	1,259.00	239.28	237.00	0.96
W18	4.84	61.70	1,288.00	166.45	172.00	−3.23
W19	4.95	62.30	1,272.00	161.32	171.00	−5.66
SC-01	4.94	64.90	1,288.00	155.78	175.00	−10.98
SC-02	4.95	61.20	1,285.00	165.69	172.00	−3.67
SH-W07-2016	4.04	58.70	914.00	145.66	154.00	5.42

by **Eq. 2**. Sea level rise and fall directly cause changes in hydrostatic pressure, which affects the thickness of the GHSZ. As sea level rises, hydrostatic pressure increases. As sea level falls, hydrostatic pressure decreases. The paleo-seawater depth in different periods can be obtained by **Eq. 7**, and the paleo-formation pressure can be calculated by **Eq. 8**. The seawater density (ρ) of the Shenhu area is approximately 1.035 g/m^3 (Wang et al., 2013). The atmospheric pressure value (P_{atm}) was set to 0.101325 mPa, and the gravitational acceleration (g) was 9.81 m/s^2.

3.2.4 Geothermal Gradient

According to the measured geothermal gradients of 11 wells in the Shenhu area (Su et al., 2016; Jin et al., 2020a; Zhang et al., 2020a; Zhang et al., 2020b) and the geothermal gradient trend of the Pearl River Mouth Basin at a shallow depth of 3,000 m observed by Hu et al. (2019), the present distribution of geothermal gradient values in the Shenhu area is drawn in **Figure 2D**. The geothermal gradient in the Shenhu area varies between 39.44°C/km and 70.20°C/km and is generally low in the northwest and high in the southeast (**Figure 2D**).

Liu et al. (2018) studied the geothermal gradient evolution history of the Baiyun Sag, and the relationship between the geothermal gradient (G) and time (t) in this study was based on the research results of Liu et al. (2018) **Eq. 9**:

$$G = 0.0359t^2 + 0.567t + 0.0155 \quad (t < 10\ Ma) \quad R^2 = 0.9996 \tag{9}$$

where t is time, Ma.

4 RESULTS

Using the above methods and parameters, the evolution process of the GHSZ since 8.2 Ma in the Shenhu area was simulated.

4.1 The Calibration Results

Using the method described above, the present GHSZ thickness in 10 wells, such as SH1, was calculated and compared with the actual drilled GHSZ thickness (**Table 2**). The relative errors for all wells ranged from ±0.96% to 10.98%, indicating that the calculated results were generally reliable.

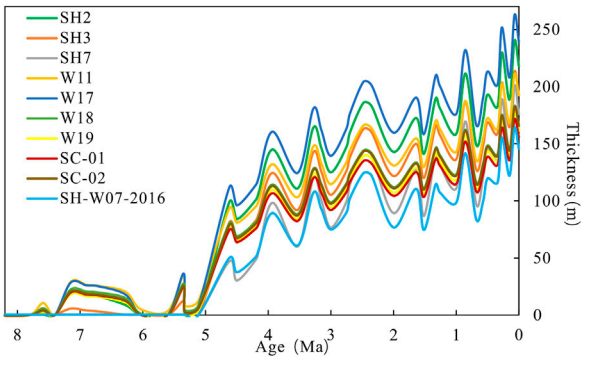

FIGURE 3 | The thickness change in the GHSZ at different single sites since 8.2 Ma.

4.2 Evolution of the GHSZ

The evolution characteristics of the GHSZ thickness in nine wells since 8.2 Ma show that the GHSZ in these nine wells was very thin before 5.33 Ma, generally less than 40 m. From 4.62 Ma to 0 Ma, overall, the GHSZ thickness gradually increased. However, due to the influence of sea level rise and fall, temperature change and other factors, the GHSZ underwent several cycles of thickening and thinning during this period. The overall variation trend of the thickness of the GHSZ in each well is similar, but the amplitudes of thickening and thinning of the GHSZ differ (**Figure 3**).

The evolution characteristics of the thickness of the GHSZ in **Section 1** spanning five wells (i.e., SH7, W07, W05, W02, and W04) in the Shenhu area (section location is shown in **Figure 1**) show that the evolution trend of the section is consistent with that of individual wells (**Figure 4**). At 5.33 Ma, the overall thickness of the GHSZ was less than 30 m or did not exist. The thickness of the GHSZ at 3.93 Ma was significantly thicker than that at 5.33 Ma, ranging from 80 to 140 m. The thickness of the GHSZ in wells SH7 and W07 was approximately 140 m. At 3.53 Ma, the GHSZ

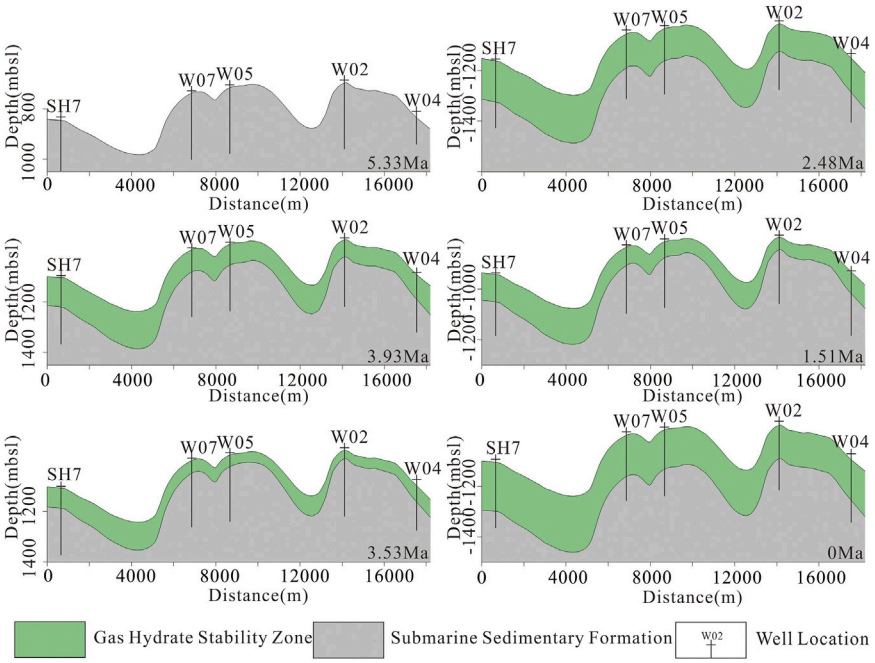

FIGURE 4 | Thickness variation in the GHSZ in **Section 1** since 5.33 Ma.

thinned to approximately 40–100 m, and the thickest GHSZ was approximately 100 m. The thickness of the GHSZ at 1.51 Ma was also reduced and was approximately 60–140 m thick. By 0 Ma, the thickness of the GHSZ had increased to 140–220 m.

The thickness evolution characteristics of the GHSZ in the Shenhu area show (**Figure 5**) that the overall trend of the study area is in line with the evolution trend of the profile and individual wells. At 5.33 Ma, the thickness of the GHSZ in the Shenhu area was relatively thin, ranging from 0.31 to 45.52 m, and the thickness gradually increased from NW to SE. The thickness of the GHSZ at 3.93 Ma was significantly different from that at 5.33 Ma. The thickness of the GHSZ increased significantly, and the thickness varied between 24.94 and 184.24 m. At 3.53 Ma, the thickness distribution of the GHSZ was similar to that at 3.93 Ma, but the thickness was generally thinner, ranging from 0.44 to 149.65 m. At 2.48 Ma, the GHSZ became thicker as a whole, with a thickness between 79.03 and 229.22 m. The thickness of the GHSZ at 1.51 Ma was generally thinner, ranging from 0.46 to 187.50 m. At present, the thickness of the GHSZ in the Shenhu area is significantly greater. The thickness of the GHSZ is between 106.98 and 267.94 m, with thicknesses being generally higher in the east and west (generally greater than 200 m) and lower in the south and north (generally less than 180 m).

5 DISCUSSION

5.1 The Relationship Between GHSZ Evolution and Double BSRs

Seismic facies and LWD results indicate that the GHSZ in the Shenhu area has obvious double BSRs, such as those found at sites SH7, W07 and W17 (Liang et al., 2017; Qian et al., 2018; Zhang et al., 2020a; Zhang et al., 2020b). Previous studies have analysed the origin of double/multiple BSRs and proposed changes in temperature and pressure conditions (Posewang and Mienert, 1999; Zander et al., 2017), tectonic uplift and subsidence (Bangs et al., 2005), multiple gas sources (Liang et al., 2017), and changes in formation lithology or mineral composition (Kuramoto et al., 1991; Langseth and Tamaki, 1992). In this study, the formation mechanism of double BSRs is discussed based on LWD results, hydrate types, gas sources of hydrate, and the thickness and evolutionary characteristics of the GHSZ in the Shenhu area.

Site SH7 has a notable double BSRs (**Figure 6A**). The upper BSR (BSR-1) is displayed at 181 mbsf (Sun et al., 2018). A hydrate approximately 25 m thick is drilled at 152 mbsf to 177 mbsf above BSR-1. The hydrate saturation ranges from 15% to 43.8%, with an average saturation of 23.1% (Wang et al., 2011). The underlying BSR (BSR-2) developed at 238 mbsf and was not drilled at the site but was clearly indicated in the seismic profile (Sun et al., 2018) (**Figure 6A**). The methane content of the BSR-1 hydrate at site SH7 is between 99.21% and 99.89%, and the ethane content is between 0.10% and 0.76%. Propane, butane and nitrogen are rare (Wu et al., 2011). The carbon isotope content of methane in this hydrate gas is −65.1‰, and $C_1/(C_2+C_3)$ is 160. Pure biogenic gases consist mainly of a large amount of methane and trace amounts of ethane (<1%) (Schoell, 1980; Dudley et al., 1981; Schoell, 1983), and their isotopic characteristics include a low $\delta^{13}C$ (δ13C < -55‰), low δD (δD < −200‰), and $C_1/C_2+<1000$ (Whiticar and Faber., 1986; Cicerone, 1988; Kirschke et al., 2013). The gas composition and isotopic characteristics of site SH7 indicate that the gas in the hydrates at this site is within the error range of biogenic gas (Liu et al., 2012). The analysis of gas composition and isotope characteristics of sites

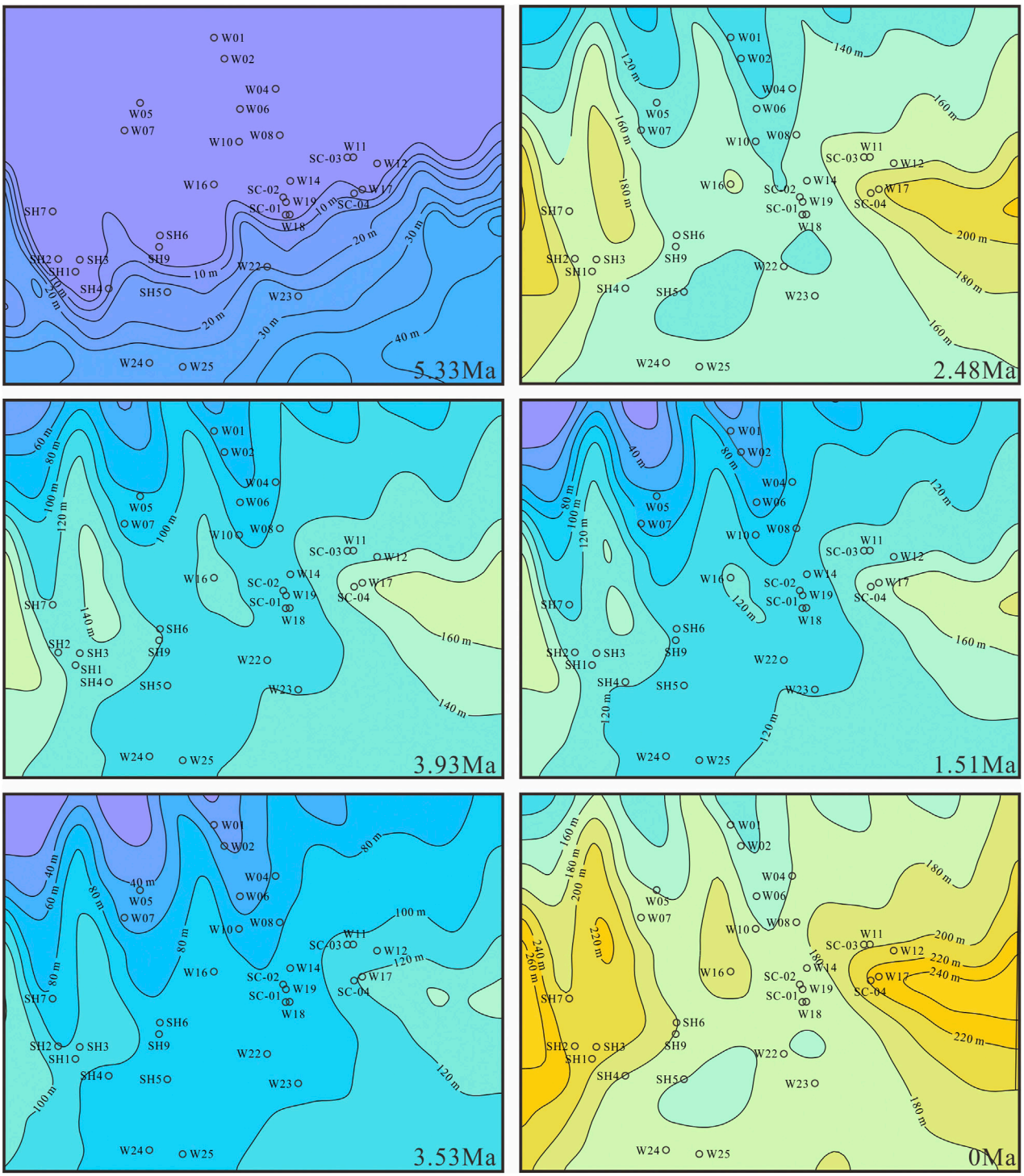

FIGURE 5 | Thickness variation in the GHSZ in the Shenhu area since 5.33 Ma.

SH2, SH3 and SH5 near SH7 also indicates that the gas in hydrates in these sites is biogenic gas (Wu et al., 2011; Liu et al., 2012; Zhu et al., 2013; Liu et al., 2015). The maximum thickness of the GHSZ at site SH7 is calculated by using the actual gas composition. The calculation results show that the maximum thickness of the GHSZ is 192.04 m when the gas composition is 99.21% CH_4+0.76% C_2H_6+0.03% C_3H_8. The GHSZ is much thinner here than in the location where BSR-2 occurs, indicating that the double BSRs composition at site SH7 is not caused by differences in gas composition.

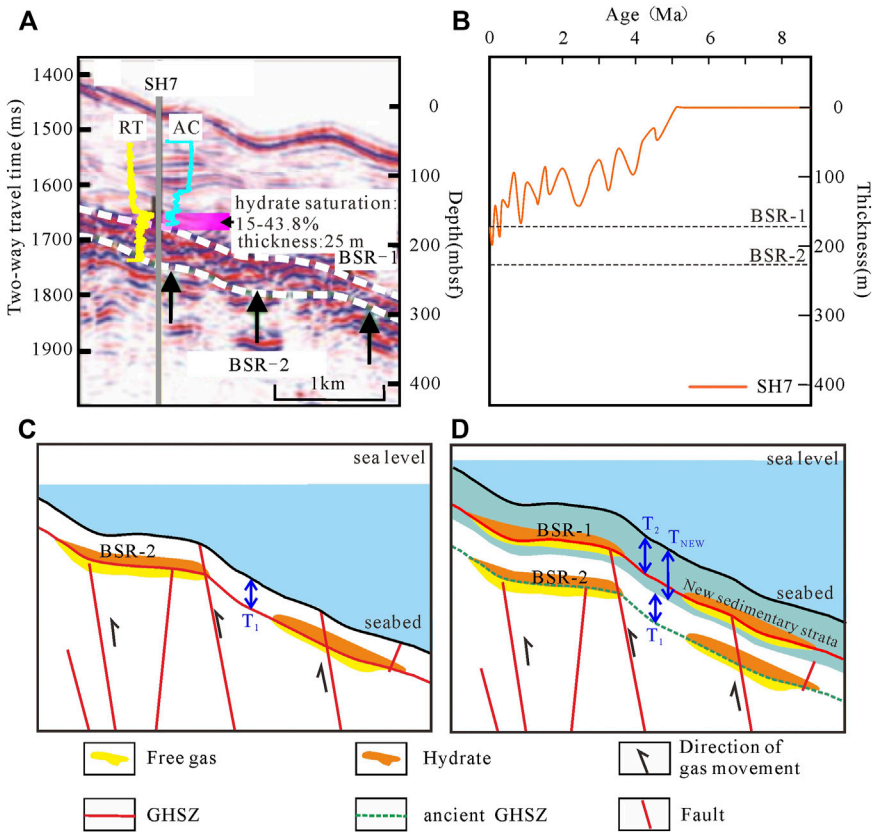

FIGURE 6 | (A) Seismic reflection characteristics of double BSRs across site SH7 (modified from Sun et al., 2018). **(B)** The thickness evolution process of the GHSZ at W17 since 8.2 Ma **(C),(D)** Double BSRs pattern based on changes in formation temperature, pressure and other conditions (taking site SH7 as an example).

According to the evolution of the thickness of the GHSZ since 8.2 Ma at site SH7 (**Figure 6B**), the thickness of the GHSZ varies over time. Since 10.5 Ma, the maximum deposition rate is 94 m/Ma, and the maximum deposition thickness is 985 m in the Baiyun Sag (Zhou et al., 2009). At one point, the thickness of the GHSZ is T_1, and a BSR display (BSR-2) is formed on the bottom (**Figure 6C**). After a period of deposition, the thickness of the new sedimentary strata is T_{new}, and the thickness of the GHSZ is T_2. The BSR display (BSR-1) is formed on the bottom (**Figure 6D**). When the thickness of T_1 plus T_{new} is greater than the thickness of T_2, the depth of the stratigraphic deposit burial increases is much greater than the thickness of the GHSZ. This finding indicates that the gas hydrates formed earlier may have been removed from the GHSZ during the process of formation deposition and burial. The gas hydrate outside the GHSZ is decomposed. The saturation of gas from decomposing hydrate is low enough to inhibit buoyancy-driven upwards migration, but enough to cause an impedance contrast in seismic data. It is the same principle as multiple BSRs in the Danube deep-sea fan, Black Sea (Zander et al., 2017).

Based on the above understanding, this paper speculated that the BSR-2 of site SH7 is an ancient BSR formed by hydrate decomposition due to the thinning of the GHSZ caused by a temperature rise and pressure decrease or by deposition and burial. The formation process of double BSRs at site SH7 in the Shenhu area is divided into two stages. In the first stage, biogenic gas migrated into GHSZ-1 along faults and diapirs and formed hydrates (**Figure 6C**). In the second stage, the hydrates formed earlier migrated out of the GHSZ (GHSZ-1) due to thinning of the GHSZ or with formation deposition. The early residual hydrates and free gas settled to form BSR-2 at 238 mbsf (**Figure 6D**). The late biogenic gas moved to GHSZ-2 to form new hydrates and formed BSR-1 together with free gas. BSR-1 together with residual paleo-BSR-2 formed double BSRs at site SH7.

Site W17 also has a double BSRs in seismic characteristics (**Figure 7A**). The upper BSR (BSR-1) is 237 mbsf, and the lower BSR (BSR-2) is 330 mbsf (Liang et al., 2017; Qian et al., 2018). Above BSR-1, hydrate approximately 16 m thick is developed at 207 mbsf-223 mbsf. Three thin hydrate layers are developed from below BSR-1 to above BSR-2, at 250 m, 253 and 261 m. Hydrate saturation at site W17 is 0%–76%, with an average of 33% (Zhang et al., 2020a). Based on the gas composition and isotope data of core samples, Liang et al. (2017) and Zhang et al. (2019), Zhang et al. (2020a) concluded that the gas hydrate of 207 mbsf to 223 mbsf in the upper part of BSR-1 is type I, and the gas of this hydrate is biogenic gas. The hydrate at 250 mbsf, 253 mbsf and 261 mbsf below BSR-1 is type II, and the gas is a mixture of

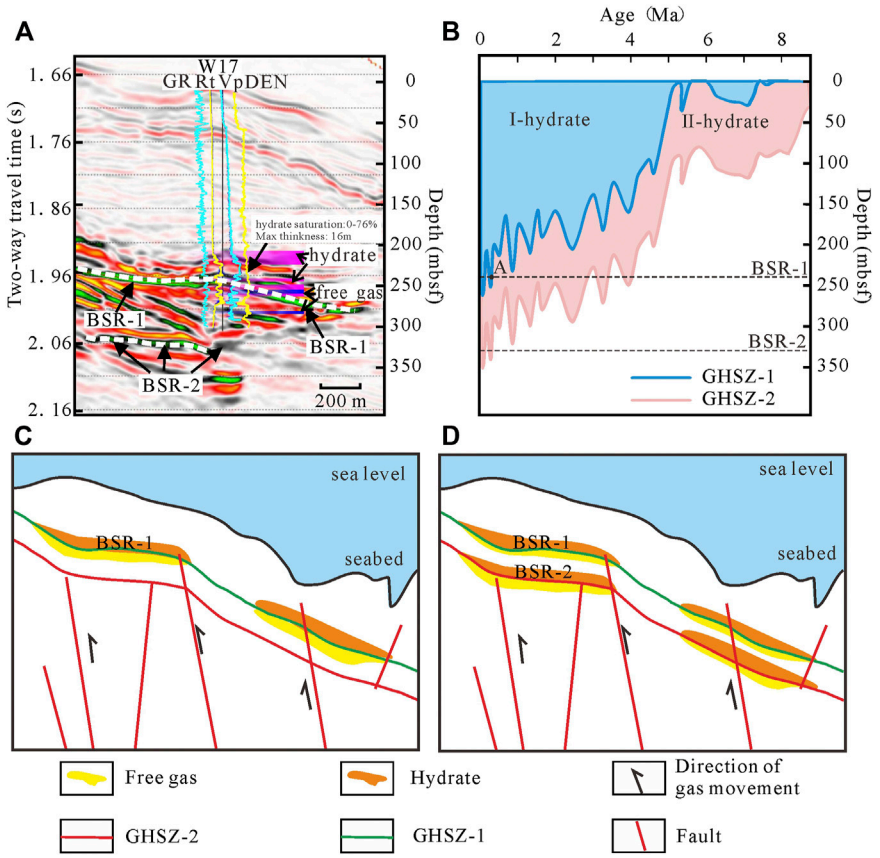

FIGURE 7 | (A) Seismic reflection characteristics of double BSRs across site W17 (modified from Qian et al., 2018). **(B)** The thickness evolution of the GHSZ at W17 and the possible depth range of type I and type II hydrate formation since 8.2 Ma **(C),(D)** Double BSRs pattern based on differences in gas source and composition (taking site W17 as an example).

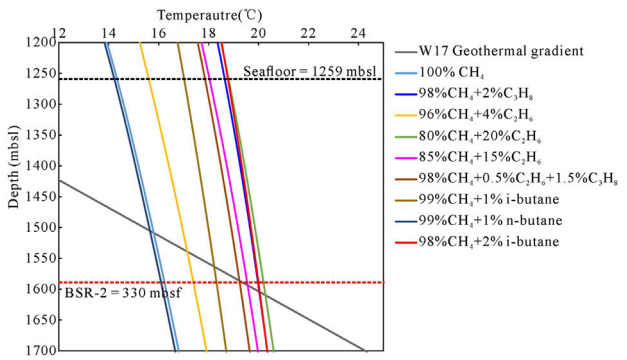

FIGURE 8 | The thickness of the GHSZ with different gas components at site W17.

biogenic and thermogenic gas, suggesting that the hydrate at site W17 has a deep thermogenic origin (Liang et al., 2017; Zhang et al., 2020a). The gas in the lower part of BSR-1 is at 250 mbsf. Hydrates at 253 mbsf and 261 mbsf are type II, and the gas is a mixture of biogenic and thermogenic gas, suggesting that the hydrate at site W17 is derived from deep thermogenic gas (Liang et al., 2017; Zhang et al., 2020a) (**Figure 7B**). By analysing the seismic reflection characteristics and geochemical characteristics of analytical gas in the core, Qian et al. (2018) concluded that type II hydrate is developed above the BSR (BSR-2) in the lower 330 mbsf. As shown in **Figure 8**, when the gas composition above BSR-2 is 98% CH_4+0.5% C_2H_6+1.5% C_3H_8, 85% CH_4+15% C_2H_6, or 98% CH_4+2% C_3H_8, or when the isobutane content is in the range of 1%–2% and the rest is CH4, the pore water salinity is 32.36‰, and the thickness of the GHSZ is approximately 330 m.

Therefore, the double BSRs at site W17 may have been caused by the difference in natural gas components from different sources or different periods. The formation process of the double BSRs at site W17 in the Shenhu Sea area is divided into two stages. In the first stage, the biogenic gas with high methane content migrated into GHSZ-1 along migration channels such as faults and diapirs and formed hydrates. GHSZ-1 was approximately 237 mbsf, and the hydrate and its free gas beneath formed BSR-1 (**Figure 7C**). In the second stage, the deep thermogenic gas migrated to the shallow area along migration channels such as faults and diapirs, and along with the shallow biogenic gas, it entered GHSZ-2 and formed hydrate (**Figure 7D**). GHSZ-2 was approximately 330 m thick, and the hydrate and the free gas beneath it formed BSR-2.

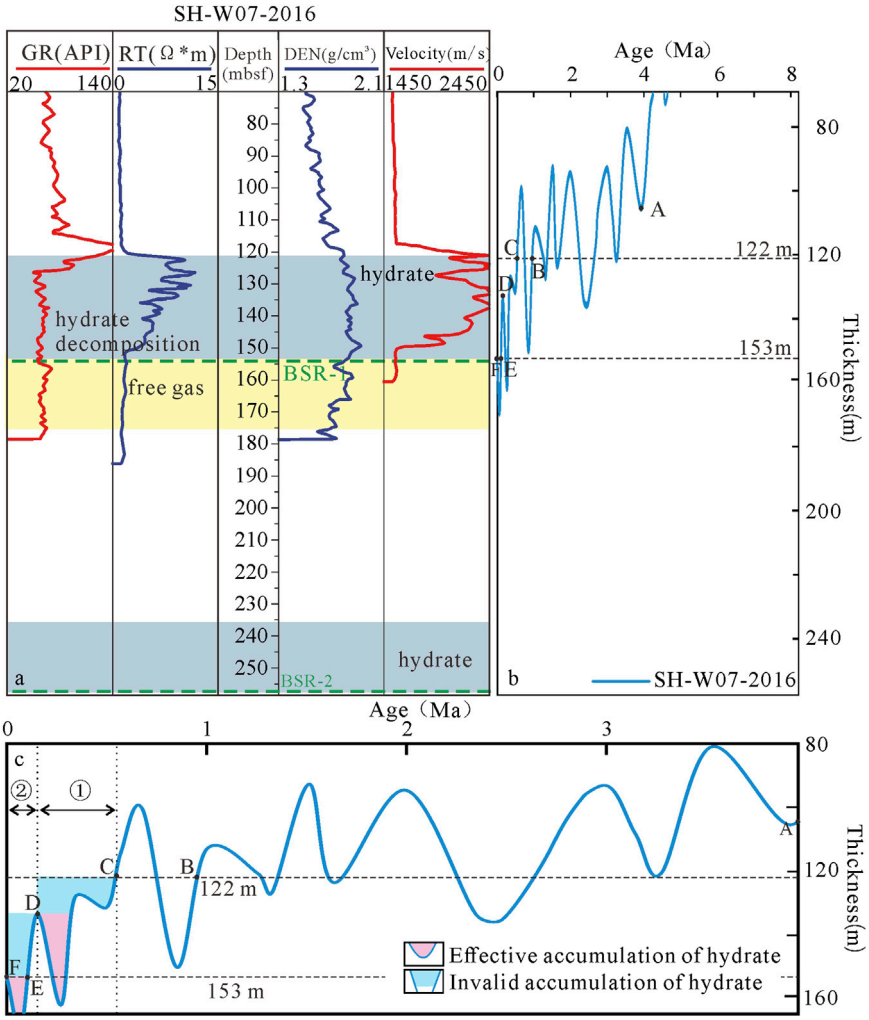

FIGURE 9 | (A) The LWD response characteristics of site SH-W07-2016 between 70 mbsf and 260 mbsf (data source: Zhang et al., 2020b). **(B)** The thickness evolution of the GHSZ at site SH-W07-2016 since 8.2 Ma. **(C)** The thickness evolution of the GHSZ at site SH-W07-2016 since 4 Ma (blue/pink parts in the figure correspond to the possible formation/decomposition times of decomposed hydrate at 132–137 m and 146–151 m).

5.2 Relationship Between the Evolution of the GHSZ and the Dynamic Decomposition, Migration, Accumulation and Dissipation of Gas Hydrate

Due to the changes in sea level, BWT, geothermal gradient, formation pressure and other factors in the Shenhu area, the thickness of the GHSZ has varied since 5.33 Ma, with a trend of overall thickening. In the evolution of the GHSZ, due to factors such as formation subsidence and a thin GHSZ, hydrates formed in the early stage, which developed at the bottom of the paleo-GHSZ and moved out of the GHSZ with the new formation deposition, which would lead to the decomposition of hydrate. The decomposed natural gas and/or the later migrated natural gas migrated upward to the GHSZ to form new hydrates or escaped.

Site SH-W07-2016 has two obvious BSRs in the seismic profile (Zhang et al., 2020b), and the upper BSR (BSR-1) is displayed at 154 mbsf. The lower BSR (BSR-2) develops at 259 mbsf (Zhang et al., 2020b) (**Figure 9A**). The 122 mbsf-153 mbsf well above BSR-1 encountered 31 m thick gas hydrates with hydrate saturations ranging from 39% to 62% (Zhang et al., 2020b). Core observations show that inflation cracks have been formed at 132 mbsf-137 mbsf (see **Figure 9** in Zhang et al., 2020b). A porridge structure has been found in cores at 146 mbsf-151 mbsf (see **Figure 6** in Zhang et al., 2020b). This is brief evidence for the existence of hydrate at 122 mbsf–153 mbsf. Based on Zhang et al. (2020b), we believe that BSR-2 was the paleo-BSR which formed from the decomposition of gas hydrates. BSR-2 was formed a long time ago and moved out of the GHSZ after formation deposition (see the double BSRs pattern based on changes in formation temperature, pressure and other conditions in 5.1). The hydrate at 122 mbsf -153 mbsf formed at relatively recent ages. As shown in **Figure 9B,C**, the hydrate began to form after 0.55 Ma (**Figure 9B,C**, point C). The hydrate starts to form in 0.55 Ma to 0.15 Ma (**Figure 9C**, ①), in

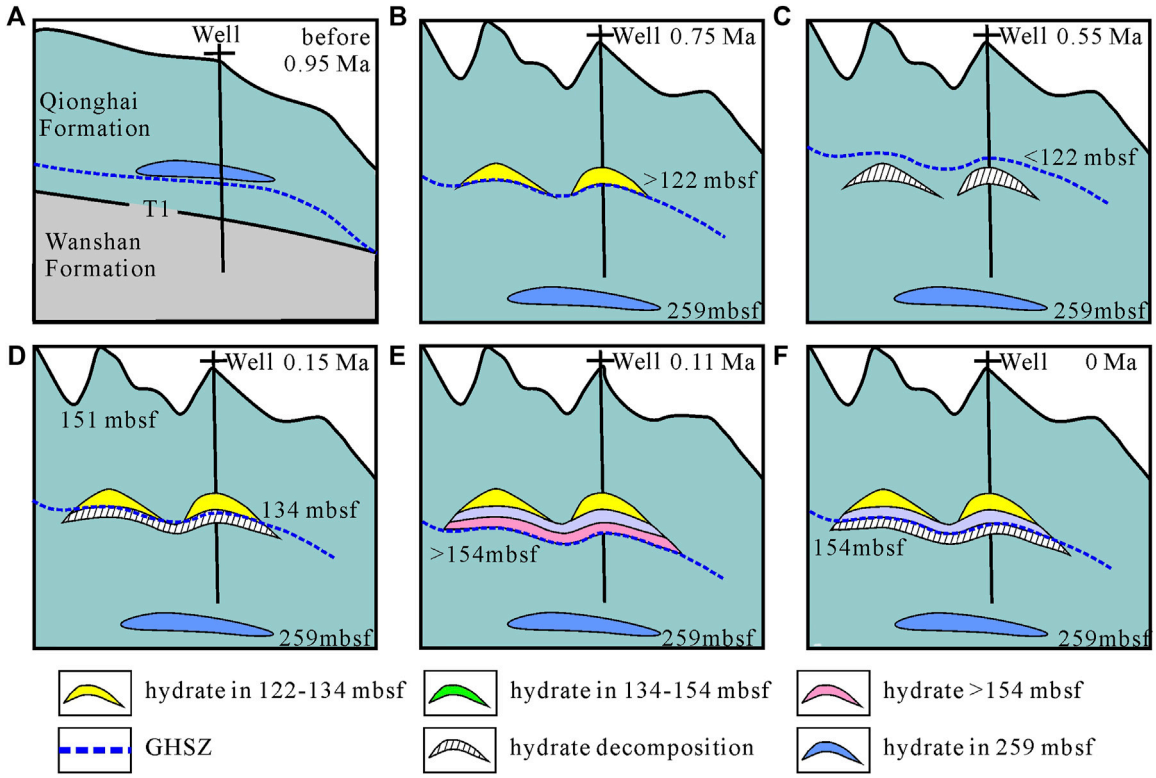

FIGURE 10 | Schematic diagram of the dynamic hydrate accumulation process at 122–151 m at site SH-W07-2016. **(A)** before 0.95 Ma. **(B)** 0.75 Ma. **(C)** 0.55 Ma. **(D)** 0.15 Ma. **(E)** 0.11 Ma. **(F)** 0 Ma.

which the GHSZ thinned after hydrate formation, and 0.15 Ma to 0 Ma (**Figure 9C**, ②), in which the hydrate is always in a suitable temperature and pressure condition after formation. The process of hydrate accumulation in these two cases is completely different. The possible accumulation process of hydrates that start to form in 0.55 Ma to 0.15 Ma are shown in **Figure 10** with at most two stages of hydrate formation and at most two stages of hydrate decomposition.

1) Before 0.95 Ma (before point B in **Figures 9B,C**), the hydrate at 259 mbsf at site SH-W07-2016 was formed in the GHSZ (**Figure 10A**).
2) During the period from hydrate formation at 259 mbsf to 0.75 Ma (before point C in **Figures 9B,C**), the bottom boundary of the GHSZ formed in the early stage changed to 259 mbsf due to changes in formation temperature, pressure and other conditions or formation subsidence. The gas from decomposed hydrate formed BSR-2 (**Figure 10B**).
3) From 0.95 Ma to 0.75 Ma, the bottom boundary of the GHSZ was deeper than 122 mbsf, and the free gas below entered the GHSZ and formed hydrates below 122 mbsf (**Figure 10B**).
4) From 0.75 Ma to 0.55 Ma (**Figures 9B,C**, point B-C), the GHSZ was thinned, the bottom boundary of the GHSZ moved to within 122 m, and the hydrates formed below 122 mbsf decomposed (**Figure 10C**).
5) From 0.55 Ma to 0.15 Ma (**Figures 9B,C**, point C-D), the GHSZ thickened and thinned from 122 mbsf to 134 mbsf, and the bottom boundary of the GHSZ migrated from 122 mbsf to 134 mbsf. If the hydrate is formed deeper than 134 mbsf, the hydrate will decompose (**Figure 10D**).
6) From 0.15 Ma to 0.11 Ma (**Figures 9B,C**, point D-E), the GHSZ thickened, and the bottom boundary of the GHSZ migrated from 134 mbsf to deeper than 154 mbsf. The hydrate formed within the bottom boundary of the GHSZ but was deeper than 154 mbsf (**Figure 10E**).
7) From 0.11 Ma to 0 Ma (**Figures 9B,C**, point E-F), the GHSZ thinned, and the bottom boundary of the GHSZ migrated to 154 mbsf. The hydrate below 154 mbsf decomposes into gas (**Figure 10F**). The hydrates at 122 mbsf-151 mbsf with free gas below in the upper layer formed BSR-1, and the residual hydrates at 259 mbsf with free gas formed BSR-2.

In another case, the hydrate above 154 mbsf may also form during 0.15 Ma to 0 Ma. The situation is shown in **Figures 10A, B, E, F** with at most one stage of hydrate formation and at most one stage of hydrate decomposition.

1) Before 0.15 Ma (before point B in **Figures 9B,C**), the hydrate at 259 mbsf at site SH-W07-2016 was formed in the GHSZ (**Figure 10A**).

2) During the period from hydrate formation at 259 mbsf to 0.15 Ma (before point C in **Figures 9B,C**), the bottom boundary of the GHSZ formed in the early stage changed to 259 mbsf due to changes in formation temperature, pressure and other conditions or formation subsidence. The gas from decomposed hydrate formed BSR-2 (**Figure 10B**).
3) From 0.15 Ma to 0.11 Ma (**Figures 9B,C**, point D-F), and the bottom boundary of the GHSZ is deeper than 154 mbsf (**Figures 10B,C**). The hydrate formed within the bottom boundary of the GHSZ but was deeper than 154 mbsf (**Figure 10E**).
4) From 0.11 Ma to 0 Ma (**Figures 9B,C**, point E-F), the GHSZ thinned, and the bottom boundary of the GHSZ migrated to 154 mbsf. The hydrate below 154 mbsf decomposes into gas (**Figure 10F**). The hydrates at 122 mbsf-151 mbsf with free gas below in the upper layer formed BSR-1, and the residual hydrates at 259 mbsf with free gas formed BSR-2.

From the above analysis, in the case of hydrate starting to formed at 0.55 Ma–0.15 Ma, at most two stages of hydrate formation and at most two stages of hydrate decomposition have occurred. In the case of hydrate starting from in 0.55 Ma–0.15 Ma, at most one stage of hydrate formation and at most one stage of hydrate decomposition have occurred. Of course, hydrate may also form before 0.55 Ma. As the GHSZ thinned, the hydrate decomposed into gas. When entering the GHSZ again, new hydrates will be formed.

According to the above analysis, the process of hydrate dynamic accumulation can be inferred by determining the spatial-temporal evolution of the GHSZ. The changes in the GHSZ and the changes in the dynamic accumulation process of hydrate. The formation mechanism of double/multiple BSRs and the dynamic accumulation process of hydrate can be better understood by clarifying the evolution of the GHSZ combined with the geological age and gas source. More details of the dynamic accumulation process require more geological, geochemical and seismic data for support.

6 CONCLUSION

Based on the variation in seawater depth, BWT, geothermal gradient and other parameters, the evolution of the thickness of the GHSZ in the Shenhu area of the SCS is calculated. Two formation modes of double BSRs in the Shenhu area are summarized, and the evolution of the thickness of the GHSZ and the dynamic accumulation of hydrates are discussed. The main conclusions are as follows:

There are two formation mechanisms of double BSRs in the Shenhu area. The first type is the double BSRs pattern based on changes in formation temperature, pressure and other conditions. In this pattern, the lower BSR is the residual BSR after the decomposition of the early hydrate that migrated out of the GHSZ, and the upper BSR is the BSR formed by hydrate re-enrichment in the new GHSZ in the late period, represented by sites SH7 and SH-W07-2016. The other is the double BSRs pattern based on differences in gas source and composition. The upper BSR is type I hydrate, and the lower BSR is type II hydrate, represented by site W17.

The relationship between the evolution of the thickness of the GHSZ and the dynamic evolution of gas hydrate migration, accumulation and dispersion at site SH-W07-2016 in the Shenhu area is preliminarily recognized. According to the different ages of hydrate formation, hydrates have undergone different dynamic accumulation processes. Since the formation of hydrates above the BSR at site SH-W07-2016, the GHSZ at this site has undergone at most two thickening and two thinning periods. With the change in thickness of the GHSZ at site SH-W07-2016, hydrate formation occurred at up two stages from0.55 Ma to 0.15 Ma and occurred at up to one stage from 0.15 Ma to 0 Ma.

SYMBOL ANNOTATIONS

T—temperature,K.
P—pressure, mPa.
C—the constant term of the fitting relation, with a value of 2.8074023.
m_1, m_2, m_3 and m_4—fitting coefficients of polynomials under different conditions, with values of $m_1 = 1.559474 \times 10^{-1}$, $m_2 = 4.8275 \times 10^{-2}$, $m_3 = -2.78083 \times 10^{-3}$, and $m_4 = 1.5922 \times 10^{-4}$.
P_{atm}—atmospheric pressure, with a value of 0.101325 mPa.
ρ—seawater density, with a value of 1.035 g/m^3.
g—gravity, with a value of 9.81 m/s^2.
h—the vertical distance to seabed, km.
D—the present seawater depth, km.
T_i—sediment temperature at point i, K.
h_i—the vertical distance to the seabed at point i, km.
G—geothermal gradient, ˚C/km.
D_p— paleo-seawater depth, km.
ΔH_1— the history of relative sea level fluctuation, km.
ΔH_2 — the history of sea floor subsidence, km.
ΔH_3 — the history of depositional thickness, km.
T_s—the present BWT, K.
T_p—the paleo-BWT, K.
ΔT—the relative change in BWT, K.
t—time, Ma.

DATA AVAILABILITY STATEMENT

The original contributions presented in the study are included in the article/Supplementary Material, further inquiries can be directed to the corresponding author.

AUTHOR CONTRIBUTIONS

YS: Writing—review and editing., Visualization. YL: Make important revisions to the paper, Investigation, Supervision. LZ: Investigation, Supervision. MC: Conceptualization, Visualization, Investigation. CL: Methodology, Investigation. NL: Formal analysis, Resources.

FUNDING

This work was supported by the Key Research Program of the Institute of Geology and Geophysics, CAS (IGGCAS-201903), Strategic priority Research Program of the Chinese Academy of Sciences (XDA14010202), National Natural Science Foundation of China (42030808), National major science and technology projects of China (2017ZX05008-004).

REFERENCES

Andreassen, K., Mienert, J., Bryn, P., and Singh, S. C. (2000). A Double Gas-Hydrate Related Bottom Simulating Reflector at the Norwegian continental Margin. *Ann. N. Y. Acad. Sci.* 912, 126–135. doi:10.1111/j.1749-6632.2000.tb06766.x

Auguy, C., Calvès, G., Calderon, Y., and Brusset, S. (2017). Seismic Evidence of Gas Hydrates, Multiple BSRs and Fluid Flow Offshore Tumbes Basin, Peru. *Mar. Geophys. Res.* 38, 409–423. doi:10.1007/s11001-017-9319-2

Baba, K., and Yamada, Y. (2004). BSRs and Associated Reflections as an Indicator of Gas Hydrate and Free Gas Accumulation: an Example of Accretionary Prism and Forearc basin System along the Nankai Trough, off Central Japan. *Resource Geology.* 54 (1), 11–24. doi:10.1111/j.1751-3928.2004.tb00183.x

Bangs, N. L. B., Musgrave, R. J., and Tréhu, A. M. (2005). Upward Shifts in the Southern Hydrate ridge Gas Hydrate Stability Zone Following Postglacial Warming, Offshore Oregon. *J. Geophys. Res.* 110 (3), 1–13. doi:10.1029/2004JB003293

Bishnoi, P. R., and Dholabhai, P. D. (1999). Equilibrium Conditions for Hydrate Formation for a Ternary Mixture of Methane, Propane and Carbon Dioxide, and a Natural Gas Mixture in the Presence of Electrolytes and Methanol. *Fluid phase equilibria* 158-160 (5), 821–827. doi:10.1016/S0378-3812(99)00103-X

Boswell, R., Collett, T. S., Frye, M., Shedd, W., McConnell, D. R., and Shelander, D. (2012). Subsurface Gas Hydrates in the Northern Gulf of Mexico. *Mar. Pet. Geology.* 34 (1), 4–30. doi:10.1016/j.marpetgeo.2011.10.003

Brown, K. M., Bangs, N. L., Froelich, P. N., and Kvenvolden, K. A. (1996). The Nature, Distribution, and Origin of Gas Hydrate in the Chile Triple Junction Region. *Earth Planet. Sci. Lett.* 139 (3-4), 471–483. doi:10.1016/0012-821X(95)00243-6

Cicerone, R. J. (1988). Methane Linked to Warming. *Nature* 334 (6179), 198. doi:10.1038/334198a0

Collett, T. S. (2009). *Unconventional Energy Resources: Making the Unconventional Conventional: 29th Annual GCSSEPM Proceedings*. Houston, Texas: Gulf Coast Section of the Society of Economic Paleontologists and Mineralogists Foundation, 6–30. doi:10.5724/gcs.09.29.0006Gas Hydrate Petroleum Systems in marine and Arctic Permafrost Environments

Dickens, G. R., and Quinby-Hunt, M. S. (1994). Methane Hydrate Stability in Seawater. *Geophys. Res. Lett.* 21 (19), 2115–2118. doi:10.1029/94GL01858

Dudley, D. R., George, E., Claypool, D. D., and Claypool, G. E. (1981). Generation, Accumulation, and Resource Potential of Biogenic Gas. *Bulletin* 65, 5–25. doi:10.1306/2F919765-16CE-11D7-8645000102C1865D

Ecker, C., Dvorkin, J., and Nur, A. M. (2000). Estimating the Amount of Gas Hydrate and Free Gas from marine Seismic Data. *Geophysics* 65, 565–573. doi:10.1190/1.1444752

Foucher, J. P., Nouzé, H., and Henry, P. (2000). Observation and Tentative Interpretation of a Double BSR on the Nankai Slope. *Mar. Geology.* 187, 161–175. doi:10.1016/S0025-3227(02)00264-5

Haacke, R. R., Westbrook, G. K., and Hyndman, R. D. (2007). Gas Hydrate, Fluid Flow and Free Gas: Formation of the Bottom-Simulating Reflector. *Earth Planet. Sci. Lett.* 261, 407–420. doi:10.1016/j.epsl.2007.07.008

He, J. X., Yan, W., Zhu, Y. H., Zhang, W., Gong, F. X., Liu, S. L., et al. (2013). Biogenetic and Sub-biogenetic Gas Resource Potential and Genetic Types of Natural Gas Hydrates in the Northern Marginal Basins of south China Sea. *Nat. Gas industry* 33 (6), 121–134. doi:10.3787/j.issn.1000-0976.2013.06.023

He, M., Zhong, G., Liu, X., Liu, L., Shen, X., Wu, Z., et al. (2017). Rapid post-rift Tectonic Subsidence Events in the Pearl River Mouth Basin, Northern south China Sea Margin. *J. Asian Earth Sci.* 147, 271–283. doi:10.1016/j.jseaes.2017.07.024

He, M., Zhu, W. L., Wu, Z., Zhong, G. F., Ren, J. Y., Liu, L. H., et al. (2019). Neotectonic Movement Characteristics and Hydrocarbon Accumulation of the Pearl River Mouth basin. *China offshore oil and gas* 31 (5), 9–20.

Holder, G. D., Malone, R. D., and Lawson, W. F. (1987). Effects of Gas Composition and Geothermal Properties on the Thickness and Depth of Natural-Gas-Hydrate Zones. *J. Pet. Techn.* 39, 1147–1152. doi:10.2118/13595-PA

Hu, S. B., Long, Z. L., Zhu, J. Z., Hu, D., Huang, Y. P., Shi, Y. L., et al. (2019). Characteristics of Geothermal Field and the Tectonic-thermal Evolution in Pearl River Mouth Basin. *Acta Petrol. Sin* 40 (S1), 178–187. doi:10.7623/syxb2019S1015

Jin, J., Wang, X., Guo, Y., Li, J., Li, Y., Zhang, X., et al. (2020a). Geological Controls on the Occurrence of Recently Formed Highly Concentrated Gas Hydrate Accumulations in the Shenhu Area, South China Sea. *Mar. Pet. Geology.* 116, 104294. doi:10.1016/j.marpetgeo.2020.104294

Jin, J., Wang, X., He, M., Li, J., Yan, C., Li, Y., et al. (2020b). Downward Shift of Gas Hydrate Stability Zone Due to Seafloor Erosion in the Eastern Dongsha Island, South China Sea. *J. Ocean. Limnol.* 38 (4), 1188–1200. doi:10.1007/s00343-020-0064-z

Kirschke, S., Bousquet, P., Ciais, P., Saunois, M., Canadell, J. G., Dlugokencky, E. J., et al. (2013). Three Decades of Global Methane Sources and Sinks. *Nat. Geosci* 6 (10), 813–823. doi:10.1038/NGEO1955

Kuramoto, S., Tamaki, K., Langseth, M. G., Nobes, D. C., Tokuyama, H., Pisciotto, K. A., et al. (1991). Can Opal-A/opal-CT BSR Be an Indicator of the thermal Structure of the Yamato Basin, Japan Sea? *Proc. ODP Sci. Results.* 127, 1145–1156. doi:10.2973/odp.proc.sr.127128-2.235.1992

Kvenvolden, K. A. (1993). Gas Hydrates-Geological Perspective and Global Change. *Rev. Geophys.* 31 (2), 173–187. doi:10.1029/93RG00268

Langseth, M. G., and Tamaki, K. (1992). Geothermal Measurements: Thermal Evolution of the Japan Sea Basins and Sediments. *Proc. Ocean Drilling Program Scientific Results* 127/128, 2. doi:10.2973/odp.proc.sr.127128-2.227.1992

Lear, C. H., Coxall, H. K., Foster, G. L., Lunt, D. J., Mawbey, E. M., Rosenthal, Y., et al. (2015). Neogene Ice Volume and Ocean Temperatures: Insights from Infaunal Foraminiferal Mg/Ca Paleothermometry. *Paleoceanography* 30, 1437–1454. doi:10.1002/2015PA002833

Lei, Y. H., Song, Y. R., Zhang, L. K., Miao, L. C., Cheng, M., and Liu, N. G. (2021). Research Progress and Development Direction of Reservoir-Forming System of marine Gas Hydrates. *Acta Petrolei Sinica* 42 (06), 801–820. doi:10.7623/syxb202106009

Li, H. B. (2010). *The Features of Construct and Structure and the Discussion of Relationship between Evolution with Hydrocarbon Reservoiring in Huizhou Depression and Dongsha Massif of Pearl River Mouth basin*. Wuhan P.R.China: China University of Geosciences.

Li, J.-f., Ye, J. L., Ye, J.-l., Qin, X.-w., Qiu, H.-j., Wu, N.-y., et al. (2018). The First Offshore Natural Gas Hydrate Production Test in South China Sea. *China Geol.* 1 (1), 5–16. doi:10.31035/cg2018003

Li, L., Liu, H., Zhang, X., Lei, X., and Sha, Z. (2015). BSRs, Estimated Heat Flow, Hydrate-Related Gas Volume and Their Implications for Methane Seepage and Gas Hydrate in the Dongsha Region, Northern South China Sea. *Mar. Pet. Geology.* 67, 785–794. doi:10.1016/j.marpetgeo.2015.07.008

Liang, J. Q., Wang, H. B., Su, X., Fu, S. Y., Wang, L. F., Guo, Y. Q., et al. (2014). Natural Gas Hydrate Formation Conditions and the Associated Controlling Factors in the Northern Slope of the South China Sea. *Nat. Gas Industry* 34 (7), 128–135. doi:10.3787/j.issn.1000-0976.2014.07.022

Liang, J., Zhang, Z., Su, P., Sha, Z., and Yang, S. (2017). Evaluation of Gas Hydrate-Bearing Sediments below the Conventional Bottom-Simulating Reflection on the Northern Slope of the South China Sea. *Interpretation* 5 (3), SM61–SM74. doi:10.1190/int-2016-0219.1

Liu, C. L., Ye, Y. G., Meng, Q. G., He, X. L., Lu, H. L., Zhang, J., et al. (2012). The Characteristics of Gas Hydrates Recovered from Shenhu Area in the South China Sea. *Mar. Geology.* 22-27, 307–310. doi:10.1016/j.margeo.2012.03.004

Liu, C., Meng, Q., He, X., Li, C., Ye, Y., Zhang, G., et al. (2015). Characterization of Natural Gas Hydrate Recovered from Pearl River Mouth basin in South China Sea. *Mar. Pet. Geology.* 61, 14–21. doi:10.1016/j.margeo.2012.03.004

Liu, J., Zhang, J., Ma, F., Wang, M., and Sun, Y. (2017). Estimation of Seismic Velocities and Gas Hydrate Concentrations: A Case Study from the Shenhu Area, Northern South China Sea. *Mar. Pet. Geology.* 88, 225–234. doi:10.1016/j.marpetgeo.2017.08.014

Liu, P., Zhang, X. T., Du, J. Y., Cheng, W., Tao, W. F., and Tao, Y. (2018). Tectonic-Thermal Evolution Process and the Petroleum Geological Significance of Relatively Low Geothermal Gradient in a Rift Basin: An Example from Xijiang Main Sag in pearl River Mouth Basin. *Geol. Sci. Techn. Inf.* 37 (2), 146–156.

Majumdar, U., Cook, A. E., Shedd, W., and Frye, M. (2016). The Connection between Natural Gas Hydrate and Bottom-simulating Reflectors. *Geophys. Res. Lett.* 43 (13), 7044–7051. doi:10.1002/2016GL069443

Martin Schoell, M. (1983). Genetic Characterization of Natural Gases. *Bulletin* 67, 2225–2238. doi:10.1306/AD46094A-16F7-11D7-8645000102C1865D

Martin, V., Henry, P., Nouzé, H., Noble, M., Ashi, J., and Pascal, G. (2004). Erosion and Sedimentation as Processes Controlling the BSR-Derived Heat Flow on the Eastern Nankai Margin. *Earth Planet. Sci. Lett.* 222 (1), 131–144. doi:10.1016/j.epsl.2004.02.020

Miles, P. R. (1995). Potential Distribution of Methane Hydrate beneath the European continental Margins. *Geophys. Res. Lett.* 22 (23), 3179–3182. doi:10.1029/95GL03013

Mosher, D. C. (2011). A Margin-wide BSR Gas Hydrate Assessment: Canada's Atlantic Margin. *Mar. Pet. Geology.* 28 (8), 1540–1553. doi:10.1029/95GL0301310.1016/j.marpetgeo.2011.06.007

Musgrave, R. J., Bangs, N. L., Larrasoaña, J. C., Gràcia, E., Hollamby, J. A., and Vega, M. E. (2006). Rise of the Base of the Gas Hydrate Zone since the Last Glacial Recorded by Rock Magnetism. *Geol* 34 (2), 117–120. doi:10.1130/G22008.1

Niu, Z., Liu, G., Ge, J., Zhang, X., Cao, Z., Lei, Y., et al. (2019). Geochemical Characteristics and Depositional Environment of Paleogene Lacustrine Source Rocks in the Lufeng Sag, Pearl River Mouth basin, South China Sea. *J. Asian Earth Sci.* 171, 60–77. doi:10.1016/j.jseaes.2018.01.004

Pang, X., Chen, C., Peng, D., Zhu, M., Shu, Y., He, M., et al. (2007). Sequence Stratigraphy of Deep-Water Fan System of Pearl River, South China Sea. *Earth Sci. Front.* 14 (1), 220–229. doi:10.1016/S1872-5791(07)60010-4

Pecher, I. A., Villinger, H., Kaul, N., Crutchley, G. J., Mountjoy, J. J., Huhn, K., et al. (2017). A Fluid Pulse on the Hikurangi Subduction Margin: Evidence from a Heat Flux Transect across the Upper Limit of Gas Hydrate Stability. *Geophys. Res. Lett.* 44 (12), 385–395. doi:10.1002/2017GL076368

Peltzer, E. T., and Brewer, P. G. (2003). Practical Physical Chemistry and Empirical Predictions of Methane Hydrate Stability. *Nat. Gas Hydrate Ocean Permafrost Environments* 5, 17–28. doi:10.1007/978-94-011-4387-5_3

Phrampus, B. J., and Hornbach, M. J. (2012). Recent Changes to the Gulf Stream Causing Widespread Gas Hydrate Destabilization. *Nature* 490, 527–530. doi:10.1038/nature11528

Popescu, I., De Batist, M., Lericolais, G., Nouzé, H., Poort, J., Panin, N., et al. (2006). Multiple Bottom-Simulating Reflections in the Black Sea: Potential Proxies of Past Climate Conditions. *Mar. Geology.* 227 (3/4), 163–176. doi:10.1016/j.margeo.2005.12.006

Posewang, J., and Mienert, J. (1999). The enigma of Double BSRs: Indicators for Changes in the Hydrate Stability Field? *Geo-Marine Lett.* 19, 157–163. doi:10.1007/s003670050103

Qian, J., Wang, X., Collett, T. S., Guo, Y., Kang, D., and Jin, J. (2018). Downhole Log Evidence for the Coexistence of Structure II Gas Hydrate and Free Gas below the Bottom Simulating Reflector in the South China Sea. *Mar. Pet. Geology.* 98, 662–674. doi:10.1016/j.marpetgeo.2018.09.024

Rempel, A. W., and Buffett, B. A. (1997). Formation and Accumulation of Gas Hydrate in Porous media. *J. Geophys. Res.* 102, 10151–10164. doi:10.1029/97JB00392

Ruppel, C., Boswell, R., and Jones, E. (2008). Scientific Results from Gulf of Mexico Gas Hydrates Joint Industry Project Leg 1 Drilling: Introduction and Overview. *Mar. Pet. Geology.* 25, 819–829. doi:10.1016/j.marpetgeo.2008.02.007

Schoell, M. (1980). The Hydrogen and Carbon Isotopic Composition of Methane from Natural Gases of Various Origins. *Geochimica et Cosmochimica Acta* 44, 649–661. doi:10.1016/0016-7037(80)90155-6

Sloan, E. D., and Koh, C. A. (2008). *Clathrate Hydrates of the Natural Gases*. 3rd ed. Boca Raton, FL: CRC Press.

Su, M., Sha, Z., Zhang, C., Wang, H., Wu, N., Yang, R., et al. (2017). Types, Characteristics and Significances of Migrating Pathways of Gas-Bearing Fluids in the Shenhu Area, Northern Continental Slope of the South China Sea. *Acta Geologica Sinica - English Edition* 91 (1), 219–231. doi:10.1111/1755-6724.13073

Su, M., Yang, R., Wang, H. B., Sha, Z. B., Liang, J. Q., Wu, N. Y., et al. (2016). Gas Hydrates Distribution in the Shenhu Area, Northern South China Sea: Comparisons between the Eight Drilling Sites with Gas Hydrate Petroleum System. *Geol. Acta* 14 (2), 79–100. doi:10.1344/GeologicaActa2016.14.2.1

Su, P., Liang, J., Peng, J., Zhang, W., and Xu, J. (2018). Petroleum Systems Modeling on Gas Hydrate of the First Experimental Exploitation Region in the Shenhu Area, Northern South China Sea. *J. Asian Earth Sci.* 168 (DEC), 57–76. doi:10.1016/j.jseaes.2018.08.001

Sun, Y., Zhang, X., Wu, S., Wang, L., and Yang, S. (2018). Relation of Submarine Landslide to Hydrate Occurrences in Baiyun Depression, South China Sea. *J. Ocean Univ. China* 17 (1), 129–138. doi:10.1007/s11802-018-3458-1

Wang, C., Lu, J. H., Zhu, R., and Yu, W. T. (2013). Validation on the Applicability of TEOS-10 Equation in the SCS Based on WOA09 Thermohaline Data. *Water Conservancy Sci. Techn. Economy* 19 (11), 1–6. doi:10.3969/j.issn.1006-7175.2013.11.001

Wang, X., Lee, M., Collett, T., Yang, S., Guo, Y., and Wu, S. (2014). Gas Hydrate Identified in Sand-Rich Inferred Sedimentary Section Using Downhole Logging and Seismic Data in Shenhu Area, South China Sea. *Mar. Pet. Geology.* 51, 298–306. doi:10.1016/j.marpetgeo.2014.01.002

Wang, X., Wu, S., Lee, M., Guo, Y., Yang, S., and Liang, J. (2011). Gas Hydrate Saturation from Acoustic Impedance and Resistivity Logs in the Shenhu Area, South China Sea. *Mar. Pet. Geology.* 28, 1625–1633. doi:10.1016/j.marpetgeo.2011.07.002

Wei, J., Fang, Y., Lu, H., Lu, H., Lu, J., Liang, J., et al. (2018). Distribution and Characteristics of Natural Gas Hydrates in the Shenhu Sea Area, South China Sea. *Mar. Pet. Geology.* 98, 622–628. doi:10.1016/j.marpetgeo.2018.07.028

Whiticar, M. J., and Faber, E. (1986). Methane Oxidation in Sediment and Water Column Environments-Isotope Evidence. *Org. Geochem.* 10 (4-6), 759–768. doi:10.1016/S0146-6380(86)80013-4

Wu, N., Yang, S., Zhang, H., Liang, J., Wang, H., and Lu, J. a. (2010). Gas Hydrate System of Shenhu Area, Northern South China Sea:Wire-Line Logging, Geochemical Results and Preliminary Resources Estimates. *Proc. Annu. Offshore Techn. Conf.* 1 (1). doi:10.4043/20485-MS

Wu, N., Zhang, H., Yang, S., Zhang, G., Liang, J., Lu, J. a., et al. (2011). Gas Hydrate System of Shenhu Area, Northern South China Sea: Geochemical Results. *J. Geol. Res.* 2011, 1–10. doi:10.1155/2011/370298

Wu, S., Zhang, G., Huang, Y., Liang, J., and Wong, H. K. (2005). Gas Hydrate Occurrence on the continental Slope of the Northern South China Sea. *Mar. Pet. Geology.* 22, 403–412. doi:10.1016/j.marpetgeo.2004.11.006

Yang, J., Wang, X., Jin, J., Li, Y., Li, J., Qian, J., et al. (2017a). The Role of Fluid Migration in the Occurrence of Shallow Gas and Gas Hydrates in the South of the Pearl River Mouth Basin, South China Sea. *Interpretation* 5 (3), SM1–SM11. doi:10.1190/INT-2016-0197.1

Yang, S. X., Lei, Y., Liang, J. Q., Holland, M., Schultheiss, P., Lu, J. A., et al. (2017b). "Concentrated Gas Hydrate in the Shenhu Area, south China Sea: Results from Drilling Expeditions GMGS3 & GMGS4," in Proceedings of 9th International Conference on Gas Hydrates, Denver, June, 25–30.

Yang, S. X., Zhang, M., Liang, J. Q., Lu, J. A., Zhang, Z. J., Melanie, H., et al. (2015). Preliminary Results of China's Third Gas Hydrate Drilling Expedition: a Critical Step from Discovery to Development in the south China Sea. *Fire and Ice* 15 (2), 1–5.

Ye, J. L., Qin, X. W., Xie, W. W., Lu, H. L., Ma, B. J., Qiu, H. J., et al. (2020). The Second Natural Gas Hydrate Production Test in the South China Sea. *China Geol.* 3 (2), 197–209. doi:10.31035/cg2020043

Ye, J., Qin, X., Qiu, H., Xie, W., Lu, H., Lu, C., et al. (2018). Data Report: Molecular and Isotopic Compositions of the Extracted Gas from China's First Offshore Natural Gas Hydrate Production Test in South China Sea. *Energies* 11 (10), 2793. doi:10.3390/en11102793

Zander, T., Haeckel, M., Berndt, C., Chi, W.-C., Klaucke, I., Bialas, J., et al. (2017). On the Origin of Multiple BSRs in the Danube Deep-Sea Fan, Black Sea. *Earth Planet. Sci. Lett.* 462, 15–25. doi:10.1016/j.epsl.2017.01.006

Zhang, G. C., Yang, H. Z., Chen, Y., Ji, M., Wang, K., Yang, D. S., et al. (2014). The Baiyun Sag: A Giant Rich Gas-Generation Sag in the deepwater Area of the Pearl River Mouth Basin. *Nat. Gas Industry* 34 (11), 11–25. doi:10.3787/j.issn.1000-0976.2014.11.002

Zhang, H. Q., Yang, S. X., and Wu, N. Y. (2007). GMGS-1 Science Team: China's First Gas Hydrate Expedition Successful (No.1). *Fire in the Ice: Methane Hydrate Newsletter* 7 (2), 4–8.

Zhang, R.-w., Lu, J. A., Lu, J.-a., Wen, P.-f., Kuang, Z.-g., Zhang, B.-j., et al. (2018). Distribution of Gas Hydrate Reservoir in the First Production Test Region of the Shenhu Area, South China Sea. *China Geology.* 1, 493–504. doi:10.31035/cg2018049

Zhang, W., Liang, J., Lu, J. a., Wei, J., Su, P., Fang, Y., et al. (2017). Accumulation Features and Mechanisms of High Saturation Natural Gas Hydrate in Shenhu Area, Northern South China Sea. *Pet. Exploration Develop.* 44 (5), 708–719. doi:10.1016/s1876-3804(17)30082-4

Zhang, W., Liang, J., Wan, Z., Su, P., Huang, W., Wang, L., et al. (2020b2020b). Dynamic Accumulation of Gas Hydrates Associated with the Channel-Levee System in the Shenhu Area, Northern South China Sea. *Mar. Pet. Geology.* 117, 104354. doi:10.1016/j.marpetgeo.2020.104354

Zhang, W., Liang, J., Wei, J., Lu, J. a., Su, P., Lin, L., et al. (2020a). Geological and Geophysical Features of and Controls on Occurrence and Accumulation of Gas Hydrates in the First Offshore Gas-Hydrate Production Test Region in the Shenhu Area, Northern South China Sea. *Mar. Pet. Geology.* 114, 104191. doi:10.1016/j.marpetgeo.2019.104191

Zhang, W., Liang, J., Wei, J., Su, P., Lin, L., and Huang, W. (2019). Origin of Natural Gases and Associated Gas Hydrates in the Shenhu Area, Northern South China Sea: Results from the China Gas Hydrate Drilling Expeditions. *J. Asian Earth Sci.* 183 (1), 103953. doi:10.1016/j.jseaes.2019.103953

Zhang, Y. (2011). *Characteristics and Main Controlling Factors of Hydrocarbon Accumulation in the Eogene of Huizhou Depression*. Wuhan P.R.China: Master's degree of China University of Geosciences.

Zhang, Z., and Wright, C. S. (2017). Quantitative Interpretations and Assessments of a Fractured Gas Hydrate Reservoir Using Three-Dimensional Seismic and LWD Data in Kutei basin, East Kalimantan, Offshore Indonesia. *Mar. Pet. Geology.* 84, 257–273. doi:10.1016/j.marpetgeo.2017.03.019

Zhao, S. J. (2012). *Structures of the Dongsha Movement at the Northern Margin of the south China Sea: Implications for the Evolution of the Passive continental Margins*. Qindao P.R.China: Master's degree of Institute of oceanology.

Zhou, D., Sun, Z., Liao, J., Zhao, Z., He, M., Wu, X., et al. (2009). Filling History and post-Breakup Acceleration of Sedimentation in Baiyun Sag, Deepwater Northern South China Sea. *J. Earth Sci.* 20 (1), 160–171. doi:10.1007/s12583-009-0015-2

Zhu, W. L. (2007). *Natural Gas Geology in the continental Margin basin of the Northern South China Sea*. Beijing: Petroleum Industry Press, 3–22.

Zhu, Y. H., Huang, X., Fu, S. Y., and Su, P. B. (2013). Gas Sources of Natural Gas Hydrates in the Shenhu Drilling Area, South China Sea. *Geochemical Evid. Geol. Anal.* 87 (3), 767–776.

Conflict of Interest: The authors declare that the research was conducted in the absence of any commercial or financial relationships that could be construed as a potential conflict of interest.

Publisher's Note: All claims expressed in this article are solely those of the authors and do not necessarily represent those of their affiliated organizations, or those of the publisher, the editors and the reviewers. Any product that may be evaluated in this article, or claim that may be made by its manufacturer, is not guaranteed or endorsed by the publisher.

frontiers | Frontiers in Earth Science

METHODS
published: 29 April 2022
doi: 10.3389/feart.2022.870582

Enhancement of Gas Production From Clayey Silt Hydrate Reservoirs Based on Near Wellbore Artificial Fractures Constructed Using High-Pressure Rotating Water Jets Technology

Zhanzhao Li[1], Tinghui Wan[1], Yanjiang Yu[1,2], Qianyong Liang[1,2], Hongfeng Lu[1,2], Jingli Wang[1], Lieyu Tian[1], Huice He[1], Keliang Li[1,2] and Haijun Qiu[1,2]**

[1]Guangzhou Marine Geological Survey, Guangzhou, China, [2]Southern Marine Science and Engineering Guangdong Laboratory, Guangzhou, China

OPEN ACCESS

Edited by:
Jinan Guan,
Guangzhou Institute of Energy Conversion (CAS), China

Reviewed by:
Ye Chen,
China University of Petroleum, Huadong, China
Yilong Yuan,
Jilin University, China
Guangrong Jin,
Guangzhou Institute of Energy Conversion (CAS), China

***Correspondence:**
Tinghui Wan
825848651@qq.com
Haijun Qiu
849238423@qq.com

Specialty section:
This article was submitted to Economic Geology, a section of the journal Frontiers in Earth Science

Received: 07 February 2022
Accepted: 21 March 2022
Published: 29 April 2022

Citation:
Li Z, Wan T, Yu Y, Liang Q, Lu H, Wang J, Tian L, He H, Li K and Qiu H (2022) Enhancement of Gas Production From Clayey Silt Hydrate Reservoirs Based on Near Wellbore Artificial Fractures Constructed Using High-Pressure Rotating Water Jets Technology. Front. Earth Sci. 10:870582. doi: 10.3389/feart.2022.870582

Over 90% of the global hydrate resources are stored in very-low-permeability clayey silt reservoirs. The low permeability significantly restricts the efficiency of gas and water flow into the production well. To enhance gas production efficiency in low-permeability hydrate reservoirs, the high-pressure rotating water jets (HPRWJ) technology is proposed to construct near wellbore artificial fractures (NWAFs) in hydrate reservoirs. The HPRWJ avoid the risks of hydraulic fracturing as well as large-scale reservoir damage, which makes it more suitable for constructing fractures in hydrate-bearing sediments (HBS). In this article, the site SH7 in the South China Sea is studied to evaluate the feasibility of this technology for enhancing gas production of low-permeability hydrate reservoirs by numerical simulation. The results show that the gas productivity is increased by approximately three times by using the HPRWJ technology to construct NWAFs with a depth of 3 m. It is suggested that the proposed technology is a promising method for improving gas production from the low-permeability hydrate reservoirs. Furthermore, the gas production performance is closely related to NWAF depth, NWAF permeability, and NWAF spacing. For the site SH7 in the South China Sea, the NWAF depth, permeability, and spacing are recommended as 3 m, 3D, and 3 m, respectively.

Keywords: natural gas hydrate, high-pressure rotating water jets, near wellbore artificial fractures, low-permeability reservoirs, production enhancement

INTRODUCTION

The energy demand is growing continually with the development of a global economy (Aydin et al., 2016). According to the International Energy Outlook et al., 2011 of the U.S. Energy Information Administration, the global energy demand will increase by 50% by 2050 and the most energy demand must be satisfied by renewable energy and natural gas (The U.S. Energy Information Administration, 2019). Natural gas hydrates (NGHs) are white, cage-shaped, crystalline solids composed of water and gas molecules, mainly methane, that widely occur in the permafrost and deep oceanic sediments at high pressure and low temperature (Sloan et al.,

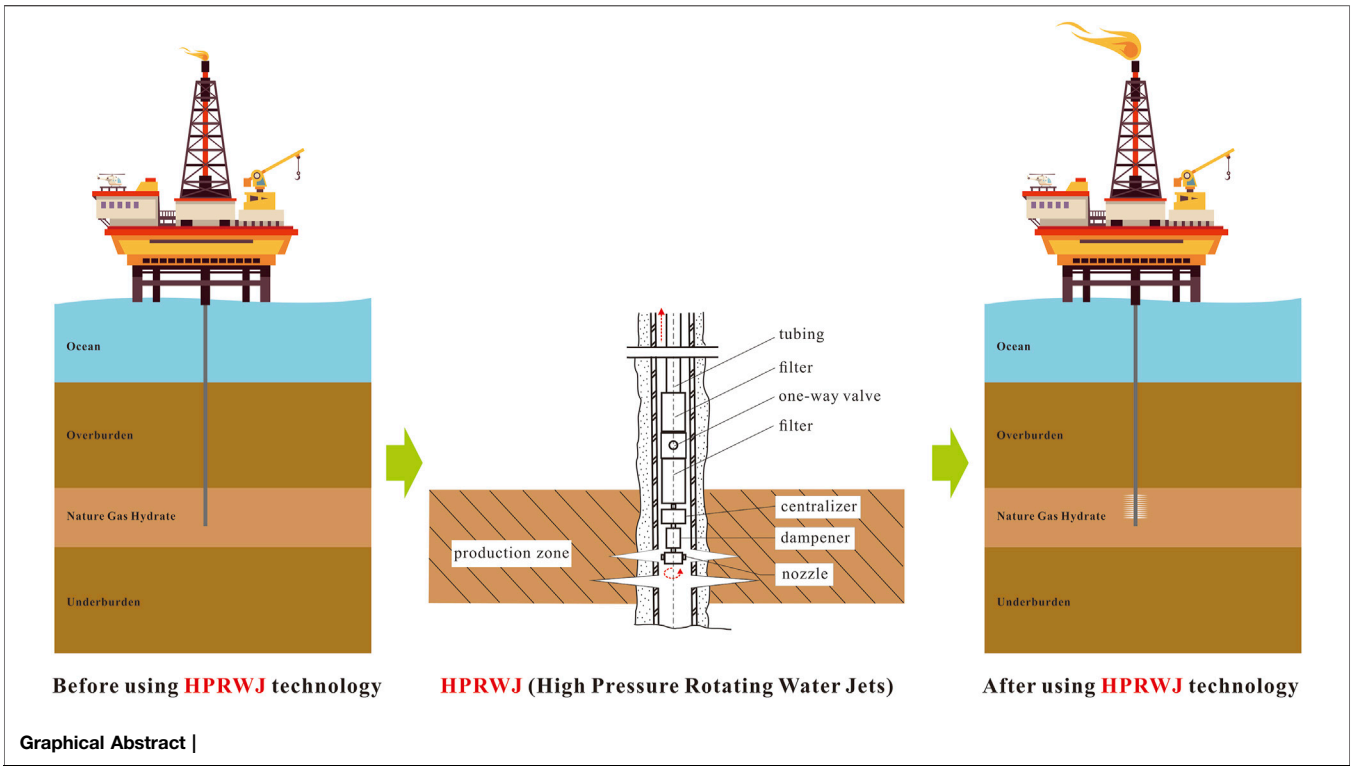

Graphical Abstract |

2008; Su et al., 2011; Sun et al., 2012; Qorbani et al., 2017). The global survey has proved that there is a large quantity of hydrate-bound natural gas that is mainly stored in marine sediments (Moridis and Sloan, 2007c). As a kind of clean and high-energy density resources, the NGHs are considered as a potential resource to meet the rapidly escalating global energy demand.

To harvest natural gas, NGHs have to be converted *in situ* to free gas. Several production methods have been proposed, such as depressurization (Yuan et al., 2017; Myshakin et al., 2018; Lei et al., 2022), thermal injection (Chong et al., 2016; Yu et al., 2019), gas replacement (Koh et al., 2016; Rossi et al., 2018), and inhibitor injection (Sun Y. et al., 2019; Mu and von solms, 2020). All these methods have been successfully conducted in field trial tests. For example, inhibitor injection was tried in the development of the Messoyakha gas hydrate field (Makogon and Omelchenko, 2013). The test results showed that depressurization is the most economical and effective method for exploiting gas from NGH reservoirs (Hancock et al., 2005; Yamamoto and Dallimore, 2008a; The Ignik Sikumi Gas Hydrate Exchange Trial Project Team, 2012). Therefore, four offshore gas production tests have been conducted using the depressurization method in the Eastern Nankai Trough and the South China Sea. However, the highest daily gas production was only 2.87×10^4 m^3. (Li et al., 2018; Ye et al., 2020). Therefore, the improvement of gas production efficiency is still a challenge for NGH exploitation because of the current low efficiency.

The key factors affecting gas production efficiency have been widely investigated. Wang et al. (2013) and Konno et al. (2014) analyzed the effect of production pressure on gas production and concluded that a larger volume of gas could be produced at a lower well pressure. Moridis et al. (2007b) investigated formation property factors affecting gas production and revealed that reservoir permeability was a very important factor controlling hydrate dissociation and gas production and that a lower reservoir permeability was associated with a lower gas production efficiency. However, oceanic NGH in clayey silt sediments with a potential development value have low porosity and poor original effective permeability because the pores are filled with solid hydrates (Fujii et al., 2015; Huang et al., 2015; Yoneda et al., 2017). Although the initial permeability of sediments at site SH7 of the Shenhu area in the South China Sea is 7.5–10^{-14} m^2, the effective permeability is only approximately 1.0×10^{-14} m^2 when the NGH pore fill is 40%, according to the relationship between porosity and permeability (Moridis et al., 2008). This will greatly restrict the transfer of pressure and heat between the production wells and the strata, which decreases the production efficiency of the decomposed gas and the dissociation continuity of NGH. Unfortunately, more than 90% of the global NGH is located in the clayey silt sediments with very low permeability (Boswell and Collett, 2011). Therefore, it is important to improve the gas production efficiency from low-permeability clayey silt sediments.

To promote the hydrate production performance, various methods have been investigated through numerical simulation, including well heating and hot water injection combined with depressurization, but the enhancement of gas production is limited (Su et al., 2012; Su et al., 2013). For example, using the well heating method, via heating a production well can only

affect the dissociation reaction in the vicinity of the production well. In addition, the hot water injection method cannot transfer injected hot water very far from the well due to the low permeability of reservoirs (Feng et al., 2019b). Although, the horizontal well can dramatically increase the gas production rates, the high operating costs and technical difficulty restrict its large-scale application (Feng et al., 2019a; Yuan et al., 2021b).

In recent years, the enhancement of gas production based on large-scale fractures constructed by hydraulic fracturing technology has been investigated through numerical simulations. For example, Chen et al. carried out the study on depressurization efficiency of a hydraulic fractured NGH reservoir, in which the fracture depth was 40 m (Chen et al., 2017). Feng et al. evaluated the efficacy of the combination of hydraulic fractures and depressurization and constructed an elliptic hydraulic fractured zone in an NGH reservoir, and the corresponding semi-major axis and semi-mini axis were 50 and 20 m respectively (Feng et al., 2019b). The simulation results indicated that the large-scale hydraulic fractures can greatly improve the CH_4 gas production rates during the depressurization process in the hydrate reservoir.

However, there are some challenges for the practical application of hydraulic fracturing technology in marine NGH reservoirs. The main challenges are as follows: (1) Marine NGH reservoirs are normally buried in the shallow seabed and the unconsolidated hydrate-bearing sediments exhibiting limited shear strength, especially after the hydrates have dissociated. (2) The NGH reservoirs are significantly thin. (3) There are distinct differences in the breakdown pressure between hydrate-bearing sediments and non-hydrate-bearing sediments, which are more than 10 MPa and less than 1 MPa, respectively (Too J. L. et al., 2018; Too J. L. et al., 2018). (4) The directivity, depth, and height of the fractures constructed by hydraulic fracturing are hard to control in unconsolidated sediments. As a result, high-pressure fracturing fluids (10 MPa) are liable to move through the non-hydrate-bearing overburden once the fluids break through hydrate-bearing sediments during hydraulic fracturing. Therefore, fractures that cut-through hydrate-bearing sediments and the seafloor are liable to form, causing environmental unfriendly gas seepages, uncontrolled dissociations, or blowouts (Koh et al., 2016). Moreover, the large-scale deep (tens, even hundreds of meters) fractures constructed by hydraulic fracturing technology destroy the structural stability of hydrate-bearing sediments (HBS), which is adverse to the long-term economic and feasible gas production from marine NGH reservoirs (Goto et al., 2016; Kim et al., 2016).

To solve the aforementioned challenges when exploiting gas from low-permeability clayey silt NGH reservoirs, the authors proposed the strategy of adopting the HPRWJ technology to construct NWAFs in order to improve the permeability of near wellbore reservoirs. The HPRWJ technology is widely used in conventional oil and gas reservoirs to enhance production. When constructing fractures using this method, high-pressure water (or water with added sand, expansion inhibitor, or clay stabilizers) is injected through a rotating nozzle to generate jets to penetrate into reservoirs, ultimately forming cylindrical jet artificial fractures around the wellbore (Li et al., 2002). As a result, NWAFs, whose depth is an order lower than that of the large-scale deep hydraulic fracturing fractures, are formed and the permeability of near wellbore reservoirs is distinctly improved. While constructing fractures, the jet pressure, rotary speed, processing interval, and processing time can be selected and controlled according to geological conditions, which means the fracture position, depth, and spacing are easy to control. While avoiding the risks of hydraulic fracturing, the NWAFs constructed by the HPRWJ technology have the following advantages: (1) The fracture position, spacing, and depth are easy to control. (2) The fractures are not likely to create large-scale reservoir damage. (3) Compared with hydraulic fractures, NWAFs can extremely maintain the stability of the hydrate reservoir. These advantages are beneficial to the long-term stable and economic exploitation of marine NGH reservoirs. Creating NWAFs using the HPRWJ technology is more feasible than the hydraulic fracturing fractures in marine NGH reservoirs. Moreover, the formation of hydrates in a sediment-hosted pore space increases the mechanical strength of the host sediments, making some of its physical and mechanical properties close to those of semi-consolidated marine sediments and increasing the feasibility of creating artificial fractures in NGH reservoirs. The feasibility has been reported by Konno et al. (2016) who found that the permeability of NGH-bearing sand was increased by fracturing and was maintained even after re-confining and closing the fractures. In addition, Too J. L. et al. (2018) and Too J. L. et al. (2018) examined the susceptibility of HBS with high saturation to fracture, and constructed artificial fractures. Therefore, creating NWAFs using the HPRWJ technology before gas production by depressurization is feasible and this work provides an alternative approach to produce gas more effectively from low-permeability clayey silt NGH reservoirs.

Based on low-permeability clayey silt NGH reservoirs in the South China Sea, the authors constructed a series of reservoir models with NWAFs to investigate the feasibility of the proposed strategy. Specifically, a depressurization vertical well was used to conduct our study, because it is the most practical and economical method for large-scale and long-term exploitation of marine NGH reservoirs. Furthermore, the effects of the factors of NWAFs such as depth, permeability, and spacing on the gas production performance were also tested in detail. This work may suggest an advantage reference for improving gas production efficiency from low-permeability clayey silt NGH reservoirs in the future.

MATERIALS AND EQUIPMENT

Completion of NWAFs in HBS

As shown in **Figure 1**, the HPRWJ tool consists of filters, a one-way valve, centralizer, rotation controller, and self-oscillation nozzles. While constructing NWAFs using the HPRWJ technology, the tool is lowered into the borehole at the perforation intervals using the connecting tubing. Then,

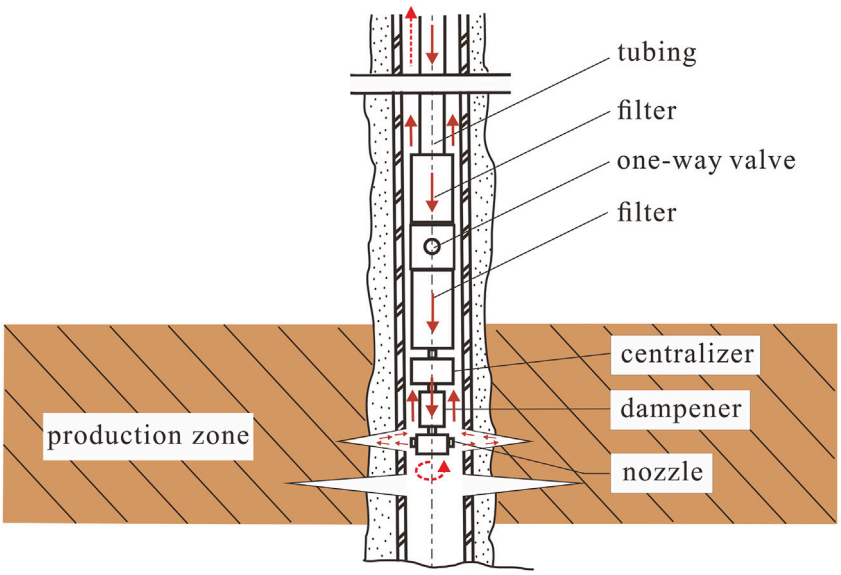

FIGURE 1 | Schematic of bottomhole assembly of the high-pressure rotating water jets tool.

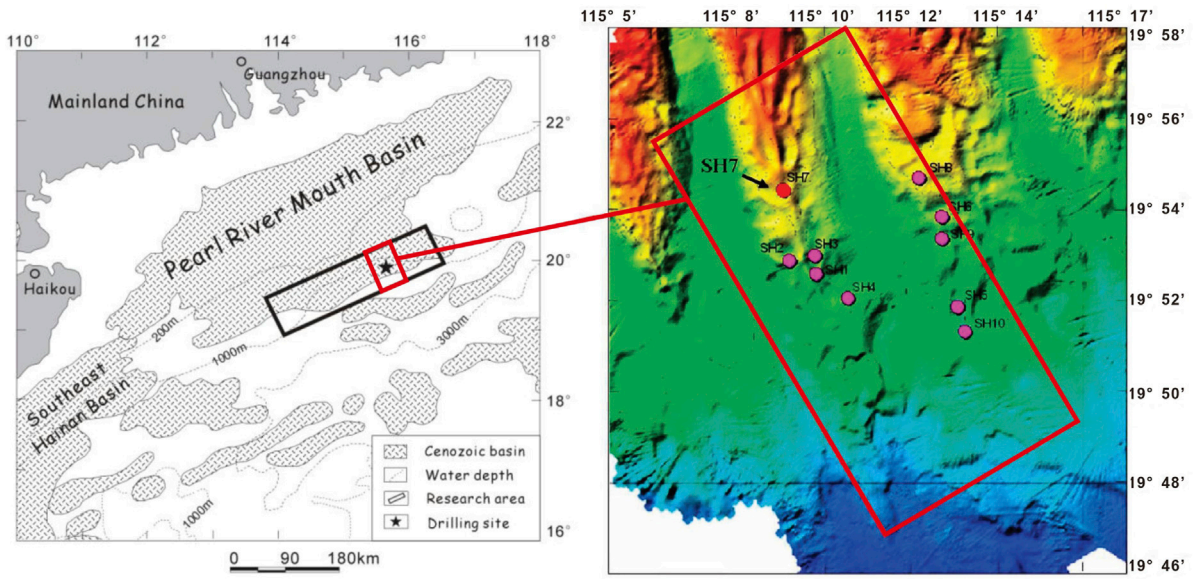

FIGURE 2 | Location of the Shenhu area, South China Sea (Wu et al., 2011).

high-pressure clean water (or water with added sands, expansion inhibitor, or clay stabilizers) is pumped through the tubing, filters, one-way valve, and nozzles to generate jets. Simultaneously, the nozzles are rotated by the rotation controller and the rotary speed is adjusted by the dampener. The impurities in the perforations become loose and will be removed with the back flow under repeated jet impacts. Then axisymmetric cylindrical artificial fractures are obtained near the wellbore in the selected position. The tool is able to move up and down to the next position by the draw work of the tubing. Therefore, a series of axisymmetric cylindrical artificial fractures are obtained very easily. Furthermore, fracture shapes can be kept by adding sand to the jet water or replacing the jet water with coagulable and permeable grouting mixtures (Yuan et al., 2021a; Li et al., 2021). This article focuses on the impacts of NWAFs on the hydrate production performance, the geomechanical effect on fractures' permeability, and the geomechanical response

associated with the fractures that are not considered during gas production. However, the geomechanical effect and response will be further investigated.

METHODS

Background

The Shenhu Area is the first NGH reservoir exploited in China. It is located in the middle part of the northern slope between the Xisha Trough and the Dongsha Islands in the South China Sea (**Figure 2**) (Wu et al., 2011). During GMGS-1 in 2007, three of the five sites (sites: SH2, SH3, and SH7) cored in this area were detected of having high concentrations of NGH. The thickness of the hydrate-bearing sediments (HBS) is 10–43 m and the bottom of the HBS is situated directly above the base of the gas hydrate stability zone, which is suitable for exploitation (Wang et al., 2011). Core sampling and well logging analysis of the SH7 site indicated that the NGH exist at depths of 155–177 m below the seabed, with a water depth of 1,108 m. The sediment porosity and NGH saturation are 33–48% and 20–44%, respectively (Li et al., 2011a). The overburden and underburden layers are similar to HBS but lack of hydrates sedimentary. *In situ* measurements show that the bottom temperature is approximately 3.7°C with a geothermal gradient of 43.3°C·km^{-1}. The main component of the gas is methane (96.10%–99.91%), with other gases mainly consisting of C_2H_6 and C_3H_8. In addition, the sediments are mainly composed of silty clay and clay silt with a millidarcy-range intrinsic permeability.

Numerical Simulation Code

In this study, the TOUGH + HYDRATE V1.5 software was used to investigate the effects of NWAFs on the gas production of NGH reservoirs (Moridis, 2014). The accuracy of this software has been tested by massive studies at different hydrate sites around the world. The following assumptions were made when using this simulator (Moridis, 2014): (1) Darcy's law is valid in the model domain, (2) the mechanical dispersion of dissolved gases and inhibitors is ignored, (3) the movement of the geologic medium is not described, (4) the aqueous phase is not allowed to disappear when salts are present, (5) the dissolved inhibitors do not affect the thermophysical properties of the aqueous phase, and (6) the inhibitor is a non-volatile component. The governing equations for its multiphase flow and heat convection and conduction processes are given as follows.

1) Components and phases:

Four phases, namely, solid-hydrate (H), aqueous (A), gaseous (G), and ice (I) phases are continuously distributed in the pore of HBS. The four components, including water (w), methane (m), hydrate (h), and salt (i), are partitioned among four possible phases. For simplicity, the κ and β indicators are used in the subsequent equations to define these components and phases, respectively.

According to the thermodynamic state of HBS, the quantity of formed hydrate or the quantity of released methane gas is determined by the following reaction:

$$CH_4 + N_H H_2O = CH_4 \cdot N_H H_2O, \tag{1}$$

2) Mass balance:

The governing equation for the flow of multicomponent fluid mixtures determined based on the mass balance is as follows:

$$\frac{d}{dt}\int_{V_n} M^\kappa dV = \int_{\Gamma_n} \mathbf{F}^\kappa \cdot \mathbf{n} d\Gamma + \int_{V_n} q^\kappa dV, \tag{2}$$

where M^κ, F^κ, and q^κ are the mass accumulation, flux, and source/sink ratio of component κ, respectively.

The mass accumulation term M^κ is determined by

$$M^\kappa = \sum\nolimits_{\beta=A,G,H,I} \varphi S_\beta \rho_\beta X_\beta^\kappa, \tag{3}$$

The mass flux term F^κ includes the contribution from the aqueous and gaseous phases and the equation is as follows:

$$\mathbf{F}^\kappa = \sum\nolimits_{\beta=A,G} \left(\mathbf{F}_\beta^\kappa + \mathbf{J}_\beta^\kappa\right), \tag{4}$$

For the aqueous phase, $\boldsymbol{F}_A^\kappa$ is calculated by multiphase Darcy's law using the following equations:

$$\mathbf{F}_A^\kappa = X_A^\kappa \mathbf{F}_A, \mathbf{F}_A = -k\frac{k_{rA}\rho_A}{\mu_A}\left(\nabla P_A - \rho_A \mathbf{g}\right), \tag{5}$$

For the gaseous phase, $\mathbf{F}_G^\kappa$ is affected by the Klinkenberg function and is determined by

$$\mathbf{F}_G^\kappa = X_G^\kappa \mathbf{F}_G, \mathbf{F}_G = -k\left(1 + \frac{b}{P_G}\right)\frac{k_{rG}\rho_G}{\mu_G}\left(\nabla P_G - \rho_G \mathbf{g}\right), \tag{6}$$

The diffusive mass flux of component κ *(κ = m,i)* is calculated using Fick's law. It is defined as

$$\mathbf{J}_\beta^\kappa = -\varphi S_\beta \tau_\beta D_\beta^\kappa \rho_\beta \nabla X_\beta^\kappa, \tag{7}$$

3) Energy balance:

The governing equation for the heat flow determined based on the energy balance is as follows:

$$\frac{d}{dt}\int_{V_n} M^\theta dV = \int_{\Gamma_n} \mathbf{F}^\theta \cdot \mathbf{n} d\Gamma + \int_{V_n} q^\theta dV, \tag{8}$$

where θ denotes the heat component and M^θ, F^θ, and q^θ are the heat accumulation, flux, and source/sink ratio, respectively.

The heat accumulation term includes contributions from the rock matrix and all the phases, and the equation is as follows:

$$M^\theta = (1-\varphi)\rho_R C_R T + \sum\nolimits_{\beta=A,G,H,I} \varphi S_\beta \rho_\beta U_\beta + Q_d, \tag{9}$$

The heat flux term includes conduction and advection, and the equation is as follows:

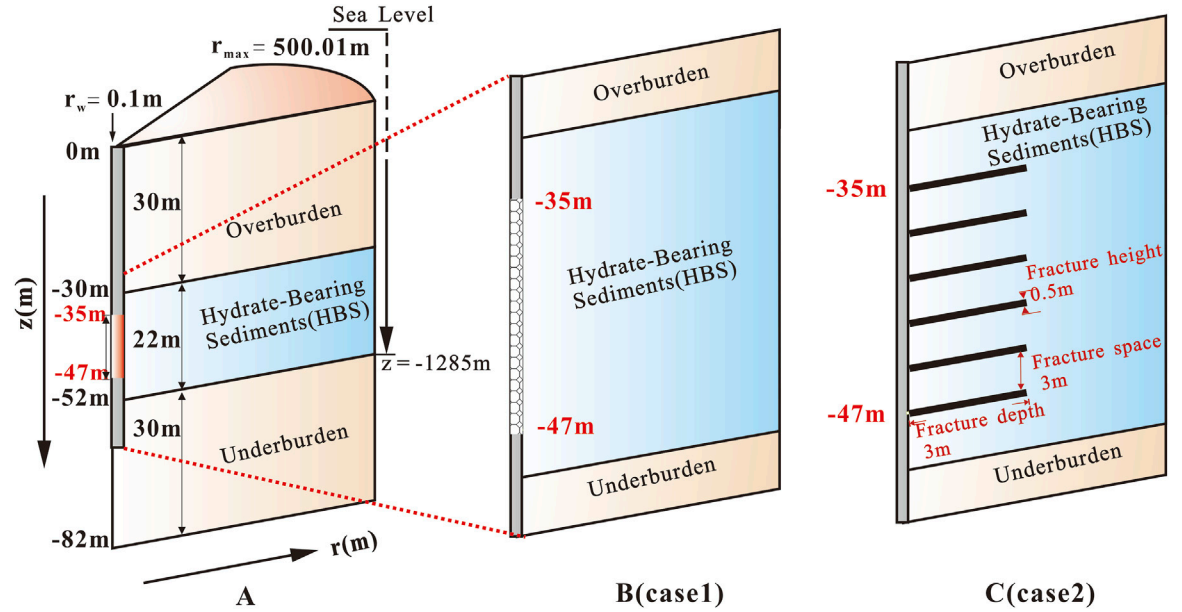

FIGURE 3 | Schematic of hydrate reservoir at site SH-7, schematic of hydrate reservoir **(A)**, conventional vertical well **(B)**, vertical well with NWAFs **(C)**.

$$\mathbf{F}^{\theta} = -\lambda_{\theta}\nabla T + \sum_{\beta=A,G} h_{\beta}\mathbf{F}_{\beta}, \tag{10}$$

Reaction heat Q_d of hydrate dissociation is calculated by

$$Q_d = \begin{cases} \Delta(\varphi\rho_H S_H \Delta U_H) \, for \, equilibrium \, dissociation \\ \Delta Q_H \cdot U_H \, for \, kinetic \, dissociation \end{cases}, \tag{11}$$

Model Construction

This study investigated the stimulated production performance with special emphasis placed on NWAFs and compared these results with the production potential determined using a conventional vertical well. To this end, two different cases were defined as follows:

1) Case 1: gas production using conventional vertical well design, as shown in **Figure 3B**.
2) Case 2: gas extraction using a vertical well with NWAFs, as shown in **Figure 3C**.

According to Li et al. (2002), when using the HPRWJ technology to construct NWAFs, the impact pressure, which is the pressure that the jet impacts at the sediment surface, will increase linearly with the increase of pump pressure, and the impact pressure is about 80–90% of pump pressure. Under the pump pressure of 20 MPa, the fracture's depth and height in the consolidated sediment can be up to 1 m, 500 mm respectively and the impact pressures still reach 3.0 MPa when the radial distance increases up to 1 m. Moreover, the maximum pump pressure can reach 50 MPa, which means the jet impacting distance can reaches far more than 1 m. Otherwise, according to the study conducted by Burland (1990) and Wei et al. (2021), the shear strength of hydrate-bearing sediments and consolidated

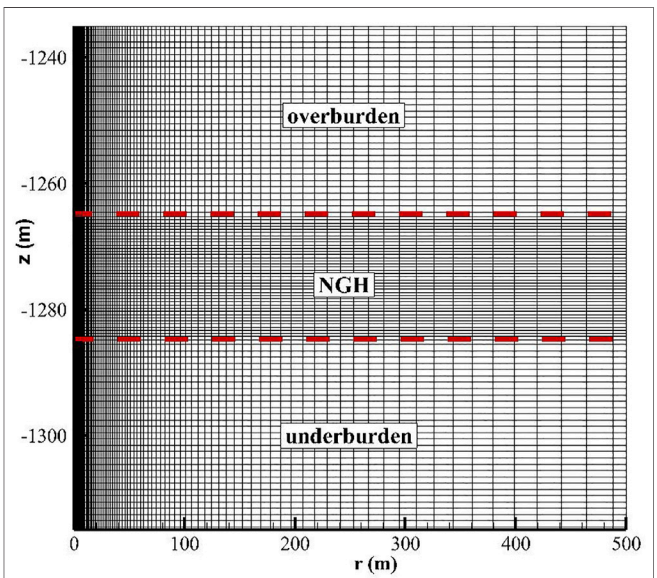

FIGURE 4 | Schematic of model discretization.

sediments is 0.5 MPa and more than 5 MPa, respectively. The bulk modulus and mechanical strength of HBS are both much lower than those of the consolidated sediment. Therefore, it is easier to create NWAFs in HBS. In this article, the fracture depth, height, and spacing in HBS is assumed to be 3 m, 500 mm, and 3 m, respectively, as shown in **Figure 3C**.

Figure 3A shows the schematic of the NGH reservoir model used in this study, which was established based on the SH7 site in the Shenhu area. According to the previous research results from

TABLE 1 | Main properties and parameters used in the hydrate reservoir model.

Parameter type	Parameter	Value
Reservoir	Overburden thickness	30 m
	Underburden thickness	30 m
	Thickness of hydrate reservoir	22 m
	Initial pressure, P_B	13.83 MPa
	Initial temperature, T_B	14.15°C
	Initial saturation	S_H = 0.44, S_A = 0.56
	Gas composition	100% CH_4
	Water salinity	30.5‰
	Permeability of the hydrate reservoir, k	75 mD
	Grain density, ρ_R	2,600 kg m^{-3}
	Porosity, φ	0.40
	Thermal conductivity of dry rocks, $k_{\Theta RD}$	1.0 W m^{-1}·K^{-1}
	Thermal conductivity of moist rocks, $k_{\Theta RW}$	3.1 W m^{-1}·K^{-1}
Multiphase flow	Composite thermal conductivity model	$K_{\theta C} = k_{\Theta RD}+(S_A^{1/2} + S_H^{1/2})\,(k_{\Theta RW}-k_{\Theta RD}) + \Phi D k_{\Theta D}$
	Capillary pressure model	$P_{cap} = -P_0\,[(S^*)^{-1/\lambda} - 1]^{1-\lambda}$
		$S^* = \frac{(S_A - S_{irA})}{(S_{mxA} - S_{irA})}$
		S_{mxA} = 1
		λ = 0.45
		$P_0 = 10^4$ Pa
	Relative permeability model	$K_{rA} = [(S_A - S_{irA})/(1 - S_{irA})]^n$, $k_{rG} = [(S_G - S_{irG})/(1 - S_{irA})]^{nG}$
		n = 3.75
		n_G = 2.5
		S_{irG} = 0.05
		S_{irA} = 0.30
Fractures	Permeability	*3D*
	Porosity	*1.0*

Li Gang et al. at this site, an axisymmetric cylinder with a radius of 500.1 m and a thickness of 82 m was employed to denote the model domain, which consisted of one HBS area, one permeable top layer (the overburden), and one permeable bottom layer (the underburden), whose thickness was 22, 30 and 30 m along the vertical direction, respectively (Li et al., 2011b). According to previous studies of Moridis and Kowalsky (2007a) and Moridis et al. (2007b), the overburden and underburden layers with a thickness of 30 m each were sufficient to simulate the heat and pressure transfer during gas production.

Additionally, the inner and outer boundaries are also very important for gas production prediction (Sun X. et al., 2019). The production well with a radius of r_w = 0.1 m was located in the center of the cylinder. The perforated interval was 12 m long and located in the middle part of the HBS which can prevent free water in the overburden and underburden layers from entering into the wellbore at the beginning of the simulation (Su et al., 2010). The bottomhole pressure was set to 4.5 MPa which is similar to the field test condition in the Nankai Trough (Yamamoto and Dallimore, 2008b; Fujii et al., 2013). The top and bottom boundaries were set to boundaries with constant temperature and pressure. Meanwhile, the outside of the model (r_{max} = 500.01 m, the thinkness of 0.01 m improves the boundary definition accurate) was treated as a boundary where no exchange of heat and flow occurred. The wellbore porosity, permeability, and capillary pressure are assumed to be 1.0, 5.0 × 10^{-9} m^2 and 0 respectively, treated as a pseudo-medium (Moridis and Reagan, 2011). Meanwhile, fractures were all assigned the same values except for the permeability. Based on the experiments performed by Liu et al. (2012) to analyze the effects of the width, generation method, and filled material of an artificial fracture on its permeability, the authors obtained the permeability of the fractures (≈3.0 × 10^{-12} m^2). While constructing NWAF using the HPRWJ technology, the tool is able to move up and down very slowly at a constant speed with a unaltered nozzle rotate speed at a fixed pump pressure,

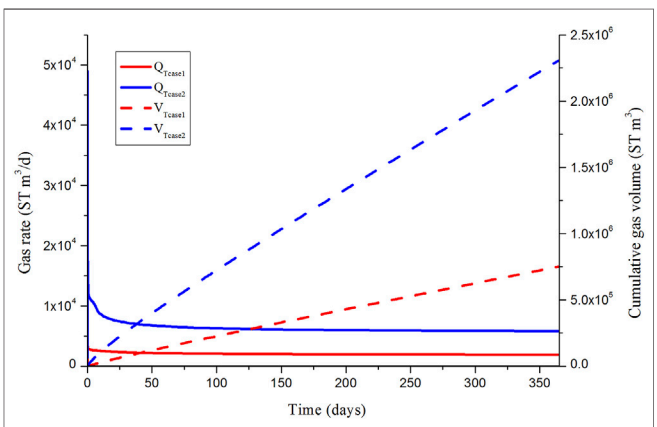

FIGURE 5 | Time-varying curve of Q_{Tcase1}, Q_{Tcase2}, V_{Tcase1}, and V_{Tcase2}.

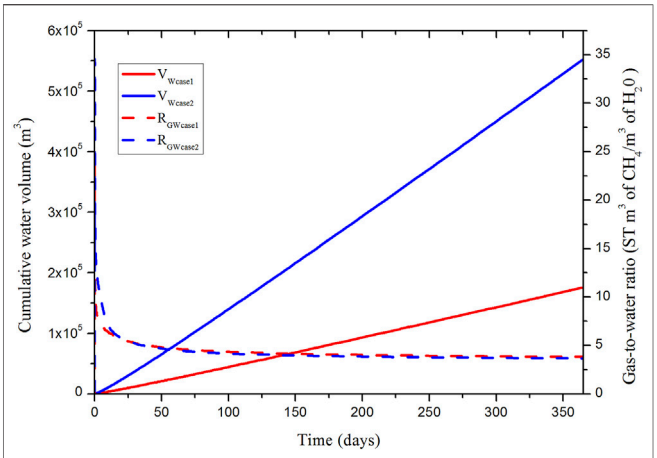

FIGURE 6 | Time-varying curve of V_{Wcase1}, V_{Wcase2}, $R_{GWcase1}$, and $R_{GWcase2}$.

and thus, the fracture is assumed to be a thin rectangular-shape as show in **Figure 3C**.

Domain Discretization

Figure 4 shows the schematic of the meshes used to predict the gas production from the HBS under two different conditions (i.e., cases 1 and 2). The model domain was discretized using a cylindrical coordinate system, producing 99 (in r direction) × 102 (in *z*-direction) = 10098 grids, including 9,876 active elements and 222 boundary elements located on the top, bottom, and inner portion of the model. In the r direction, the first grid (Δr = 0.10 m) represents the wellbore; a fine discretization (Δr = 0.25 m) was applied from the second to sixth grid; the grid size increases exponentially from the 7th to 98th grid; and the 99th grid acts as the outermost boundary. Since hydrate exploitation is a complicated process with heat and mass transfer, the grid blocks near the wellbore are relatively dense in order to accurately describe the change in the physical properties of the hydrates (Moridis and Sloan, 2007c). In the *z* direction, two thin layers (Δz = 0.01 m) are used to define the uppermost and lowermost boundaries; a sparse discretization (Δz = 1 m) was applied to the overburden and the underburden to improve the computational efficiency owing to the lack of hydrates in these layers; a fine discretization (Δz = 0.5 m) was applied in the HBS in order to accurately describe the physical properties of the hydrates during exploitation. Since four equations were calculated for each grid block, 39,504 (= 9876 × 4) equations were calculated in the whole simulation system in total.

Initial Conditions

The main parameters of the model were set based on the core samples' analyses and well logs in this region (Li et al., 2013; Liang et al., 2014). The sediment porosity and permeability were set to 0.4 and 7.5×10^{-14} m^2, respectively. The overburden and the underburden were fully saturated with water and the hydrate saturation of the HBS was set to 0.44. The capillary pressure model (e.g., the van Genuchten function) and the three-phase relative permeability model (e.g., the modified version of Stone's function) were employed. They are commonly used in numerical simulations and have been validated by field hydrate production tests (Anderson et al., 2011; Moridis and Reagan, 2011). The corresponding parameters of these multiphase flow models were determined using the accessible data in the literature. The lateral-to-vertical permeability ratio (k_R/k_Z) of HBS and the overburden and underburden layers were set to 4.0 according to the latest pressure core flood test (Yoneda et al., 2019). The system parameters and physical properties of the simulation are given in **Table 1**. It should be noted that the initial conditions in the whole reservoir would remain stable unless there was a disturbance from outside, such as depressurization or thermal injection.

RESULTS

Gas and Water Production Behaviors

The production performance of the two cases, including gas production rate (Q_T), cumulative gas production (V_T), cumulative water production (V_W), and gas-water ratio (R_{GW}), in 1 year are shown in **Figures 5**, **6**, respectively.

In case 2, the gas production rate and cumulative gas production (Q_T and V_T) were consistently over 6000 ST m^3/d and up to 230×10^4 ST m^3 respectively. In case 1, they were 2000 ST m^3/d and 75×10^4 ST m^3, respectively. These findings indicate that the hydrate reservoir productivity increased by about three times when NWAFs were constructed by the HPRWJ technology. Therefore, this technology is a promising method for improving the gas production of low-permeability hydrate reservoirs.

There are three main reasons that the HPRWJ technology promotes hydrate productivity. Firstly, high-conductivity fractures with certain morphologies can be created near the production well, thus increasing reservoir permeability and dramatically decreasing flow resistance around the production well. As a result, the efficiency of gas and water flow towards the production well can be improved. Secondly, the effective surface area for the discharge of water and gas can be increased. The effective surface area only includes the surface area of the wellbore in case 1, while it includes the surface area of the wellbore and the artificial fractures and thus increased by several times in case 2; as a result, in case 2, there was more flux at the same production pressure. Thirdly, NWAFs can enlarge the transfer distance of pressure drops, as shown in **Figure 7A**, and can correspondingly accelerate hydrate dissociation, as shown in **Figure 7B**, thus increasing the gas production rate of hydrate reservoirs.

During the simulated 1-year production period, the cumulative water production (V_W) and the gas–water ratio (R_{GW}) in case 2 were 55×10^4 m^3 and 3.7 respectively, and those in case 1 were 17.5×10^4 m^3 and 3.7 respectively. These numbers indicate that, in case 2, not only gas production, but also water production increased, whereas the gas–water ratio was hardly affected. Therefore, it is necessary to optimize the perforated interval before NWAFs are constructed in order to achieve the optimal gas–water ratio.

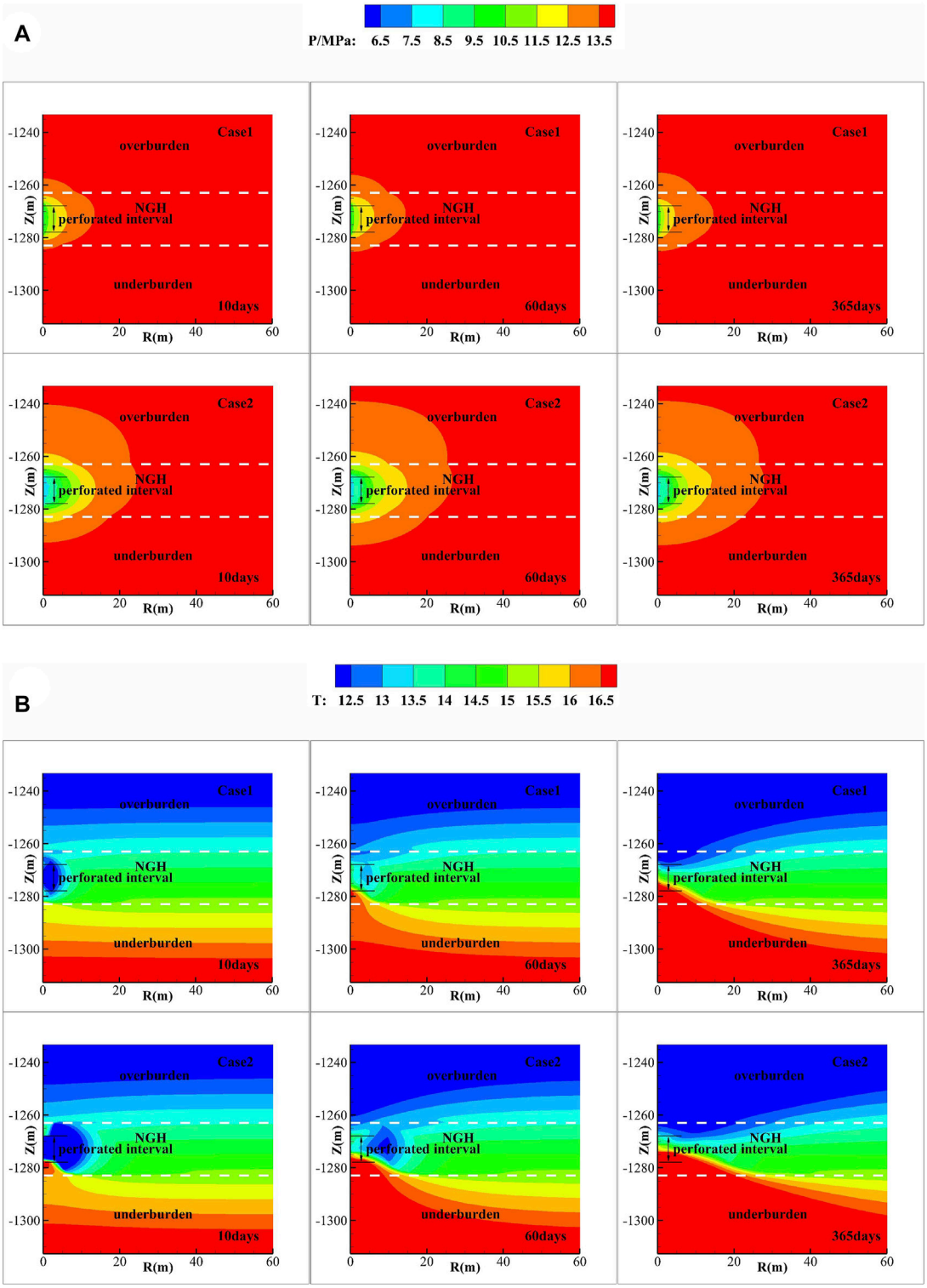

FIGURE 7 | Spatial distribution of pressure MPa **(A)**, temperature °C **(B)**, hydrate saturation **(C)**, and gas saturation **(D)** after 10, 60, and 365 days after and before reservoir stimulation.

Law of Change in Physical Properties

Analyzing the changes in the main physical properties of hydrate reservoirs helps to understand the characteristics of hydrate dissociation and the processes of gas and water production during NGH exploitation. The spatial distributions of the pressure, temperature, hydrate saturation, and gas saturation in

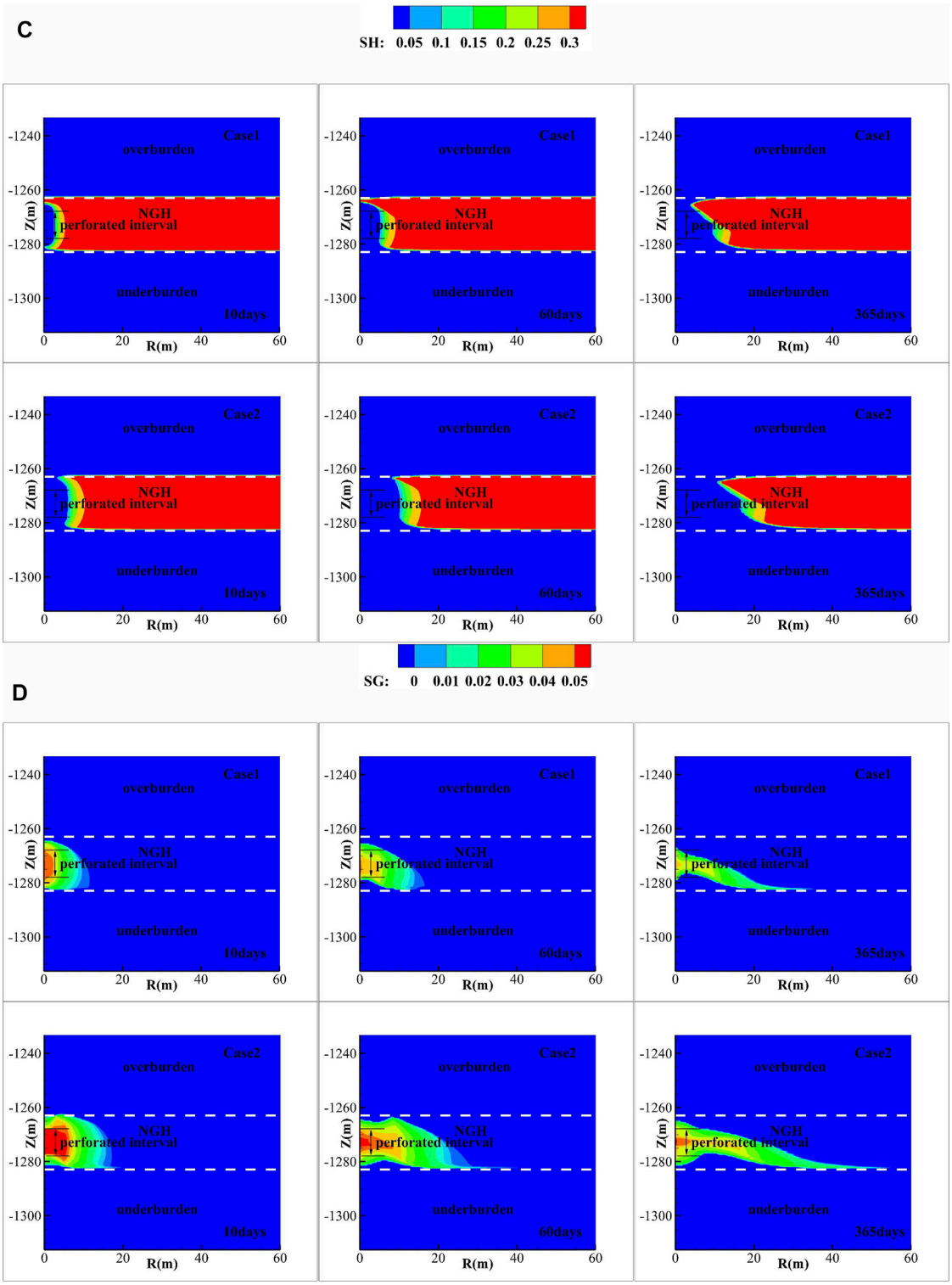

FIGURE 7 | (Continued).

TABLE 2 | Fracture depth and corresponding calculation case.

Case	Fracture depth (m)
D1	1
D2	2
D3	3
D4	4
D5	5

TABLE 3 | Fracture permeability and corresponding calculation case.

Case	Fracture permeability
P1	1 D
P2	2 D
P3	3 D
P4	4 D
P5	5 D

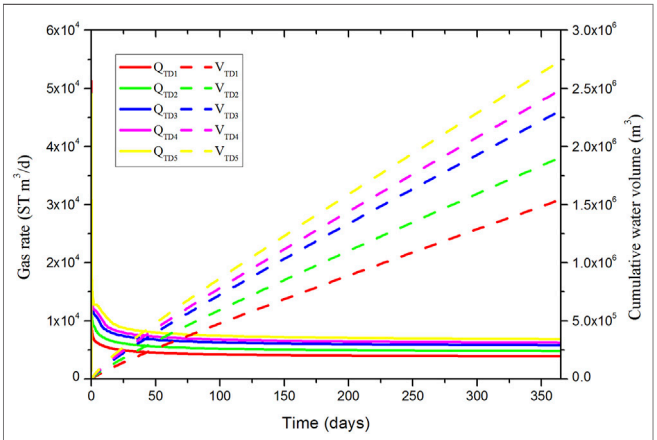

FIGURE 8 | Time-varying curve of gas production rate (Q_{TD}) and cumulative gas production (V_{TD}) in case of different fracture depths.

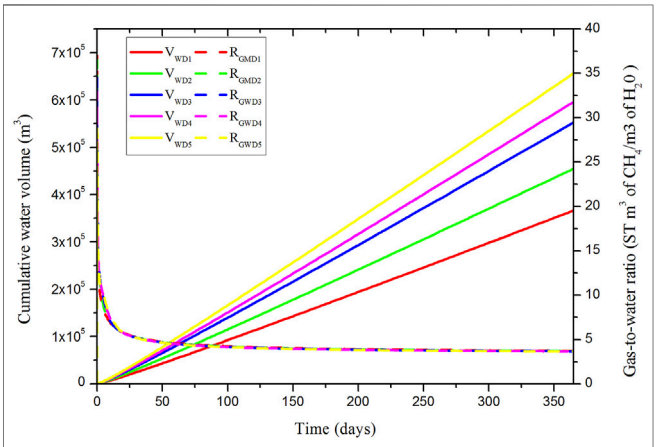

FIGURE 9 | Time-varying curve of cumulative water production (V_{WD}) and gas–water ratio (R_{GWD}) in case of different fracture depths.

case 1 and 2 after 10, 60, and 365 days are shown in **Figures 7A–D**, respectively.

As shown in **Figures 7A,C**, in case 2, the transfer distance of the pressure drop during the whole exploitation was about 30 m, which was two-fold larger than that in case 1. The hydrate dissociation range was also distinctly larger in case 2, which is the major reason why the gas production rate in case 2 was three times that of case 1 as shown in **Figure 5**. However, in both cases, there was no significant changes in the transfer range of the pressure drop in the early (60th day) and later stages (365th day) of gas production. This consistency was mainly due to the fact that both the overburden and the underburden layers were composed of permeable sediments, and the water in these sediments can flow into the production well after a certain period of time. As a result, the pressure drop failed to be transferred into the deep reservoir, which restricted the hydrate dissociation to some extent. Therefore, to improve the recovery of the entire hydrate reservoir, well spacing should be properly controlled when vertical wells are employed to exploit hydrate deposits with permeable boundaries.

As an endothermic reaction, hydrate dissociation consumes the heat of the surrounding areas while producing gas and water, thus affecting the temperature distribution of the hydrate reservoir. **Figure 7B** clearly shows that there was an obvious low-temperature area near the production well at the start stage of NGH exploitation (10 days) and that the low-temperature area in case 2 was significantly greater than that in case 1. These findings are consistent with the hydrate dissociation ranges shown in **Figure 7C**. **Figure 7B** also demonstrates that, in both cases, the low-temperature area gradually shrunk at the early and later stages of NGH exploitation (the 60th and 365th day, respectively). This occurred mainly because the water from the overburden and the underburden flowed into the production well, changing the temperature distribution of the hydrate reservoir around the well. In particular, the hot water in the underburden significantly heated the hydrate reservoir and promoted hydrate dissociation. This phenomenon is consistent with the morphology of the hydrate dissociation front illustrated in **Figure 7C**.

The gas released from the hydrate dissociation was either extracted from the hydrate reservoir or remained in it as free hydrocarbon gas. **Figure 7D** shows that the gas-bearing area in case 2 was significantly larger than that in case 1, which indirectly proves that NWAFs can effectively promote the dissociation of hydrates into gas and water.

DISCUSSION

Effects of Fracture Parameters on the Gas Productivity of the Hydrate Reservoir

This article aims to apply the HPRWJ technology to vertical wells. The parameters used in this technology (e.g., jet pressure, rotary speed, processing time, and the moving distance of the tubing) determine the key fracture parameters, such as fracture depth,

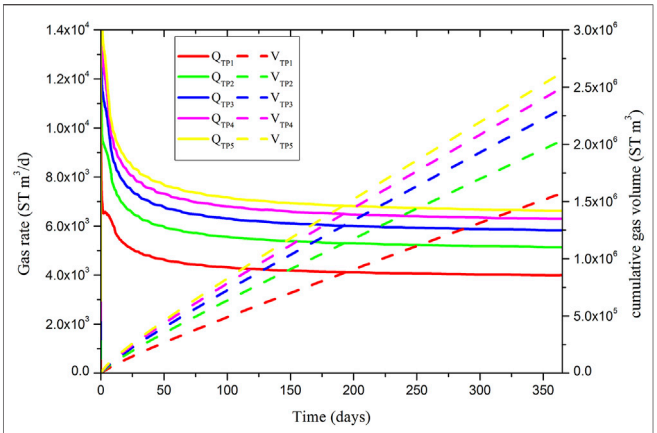

FIGURE 10 | Time-varying curve of gas production rate (Q_{TD}) and cumulative gas production (V_{TD}) in case of different fracture permeabilities.

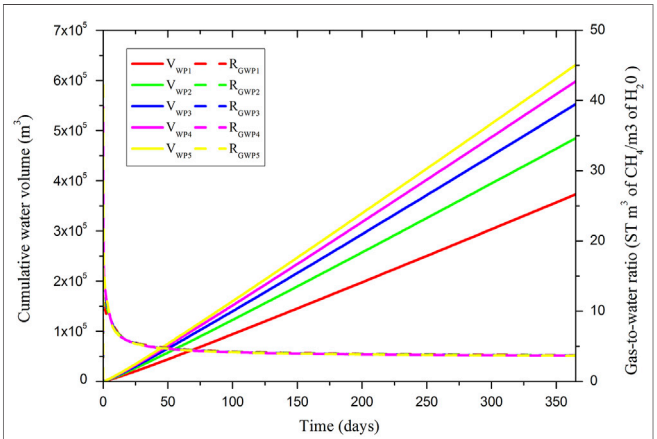

FIGURE 11 | Time-varying curve of cumulative water production (V_{WD}) and gas–water ratio (R_{GWD}) in case of different fracture permeabilities.

permeability, and spacing. Therefore, the effects of the key parameters of NWAFs on gas productivity were discussed, which is very important for parameter selection when using the HPRWJ technology for constructing NWAFs. The relationships between HPRWJ parameters and NWAF parameters will be further investigated through a laboratory and numerical study.

Effects of Fracture Depth on Gas Productivity

Fractures' depth is mainly controlled by jet pressure, rotary speed, and processing time. To compare the effects of different NWAF depths on the gas productivity of hydrate deposits, NWAF depths were set to 1, 2, 3, 4, and 5 m, as shown in **Table 2**. The authors assumed that fracture permeability, fracture spacing, fracture height, and the length of the completion interval were 3 D, 3, 0.5, and 12 m, respectively.

TABLE 4 | Fracture spacing and corresponding calculation case.

Case	Fracture spacing (m)	Fractures number
S1	1	13
S2	2	7
S3	3	5
S4	4	4
S5	5	2

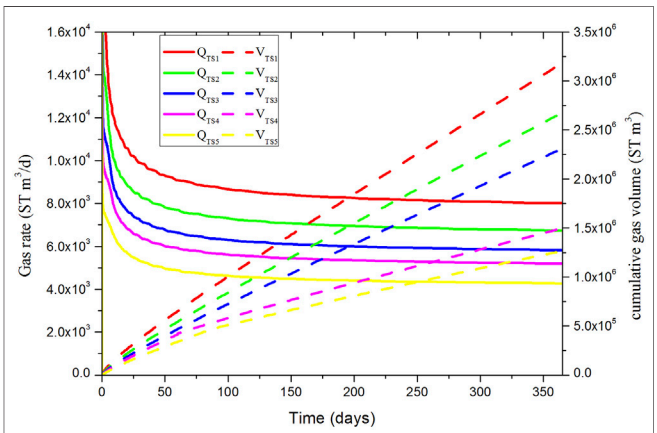

FIGURE 12 | Time-varying gas production rate (Q_{TS}) and cumulative gas production (V_{TS}) in case of different fracture spacings.

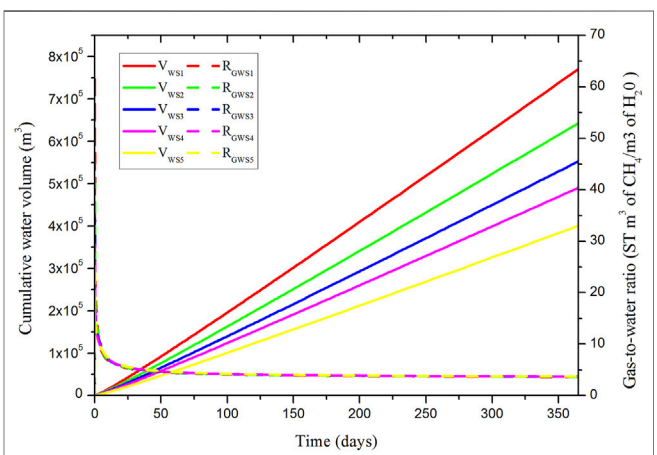

FIGURE 13 | Time-varying cumulative water production (V_{WS}) and gas–water ratio (R_{GWS}) in case of different fracture spacings.

Figures 8, **9** present the gas production rate (Q_{TD}), cumulative gas production (V_{TD}), cumulative water production (V_{WD}), and gas–water ratio (R_{GWD}) at different NWAF depths. When the fracture depth increased from 1 to 2, 3, 4, and 5 m, the V_{TD} increased from 1.54×10^6 ST m^3 to 1.91×10^6 ST m^3, 2.30×10^6 ST m^3, 2.49×10^6 ST m^3, and 2.73×10^6 ST m^3 respectively, increasing by 24.0, 49.3, 61.7, and 77.3%. The results indicate that the gas production rate increases with an increase in the NWAF depth. However, V_{TD}

increased by 8.3% when the fracture depth increased from 3 to 4 m, and by 20.4% when the fracture depth increased from 2 to 3 m. This indicates that the increase in fracture depth corresponds with the decrease in the magnitude of gas production efficiency. Therefore, a fracture depth of 3 m is recommended for the low-permeability hydrate reservoirs at site SH7. Moreover, it has been observed that cumulative water production increases as the NWAF depth increases, and that fracture depth has no effect on the gas–water ratio.

Effects of Fracture Permeability on Gas Productivity

According to laboratory test results, fracture permeability is closely related to the materials added to jet water and can reach 7.45×10^2 D during NWAF construction (Xu et al., 2016). To compare the effects of different NWAF permeability values on the productivity of hydrate deposits, NWAF permeability was set to 1 D, 2 D, 3 D, 4 D, and 5 D, as shown in **Table 3**. The authors assumed that fracture depth, fracture spacing, fracture height, and the length of the completion interval were 3, 3, 0.5, and 12 m, respectively.

Figures 10, **11** present the gas production rate (Q_{TP}), cumulative gas production (V_{TP}), cumulative water production (V_{WP}), and gas–water ratio (R_{GWP}) in cases of different NWAF permeability values. When fracture permeability increased from 1 D to 2 D, 3 D, 4 D, and 5 D, V_{TP} increased from 1.57×10^6 ST m^3 to 2.03×10^6 ST m^3, 2.30×10^6 ST m^3, 2.49×10^6 ST m^3, and 2.62×10^6 ST m^3, respectively, increasing by 29.3, 46.5, 58.6, and 66.9%, respectively. The results indicate that the gas production rate increases with an increase in the NWAF permeability. However, V_{TP} increased by 8.3% when fracture permeability increased from 3 D to 4 D, and by 13.3% when the fracture permeability increased from 2 D to 3 D. This illustrates that the increase in fracture permeability corresponds with the decrease in the magnitude of gas production efficiency. Therefore, fracture permeability of 3 D is recommended for the low-permeability hydrate reservoirs at site SH7. Moreover, cumulative water production increases as the NWAF permeability increases, and fracture permeability has no effect on the gas–water ratio.

Effects of Fracture Spacing on Gas Productivity

Fracture spacing can be controlled by lifting or lowering the tubing. To compare the effects of different NWAF spacing values on the productivity of hydrate deposits, the NWAF spacing was set to 1, 2, 3, 4, and 5 m, as shown in **Table 4**. The authors assumed that fracture depth, fracture permeability, fracture height, and the length of the completion interval were 3 m, 3 D, 0.5, and 12 m respectively.

Figures 12, **13** show the gas production rate (Q_{TS}), cumulative gas production (V_{TS}), cumulative water production (V_{WS}), and gas–water ratio (R_{GWS}) at different NWAF spacing values. **Figure 12** clearly demonstrates that NWAF spacing has significant effects on gas production rate (Q_{TS}). The stable gas production rate was 8,100 ST m^3/day when the fracture spacing was 1 m, whereas it was only 4,300 ST m^3/day when the NWAF spacing increased to 5 m. These findings show that the gas production rate increases with a decrease in the NWAF spacing. However, V_{TS} increased by 53.3% when fracture spacing decreased from 4 to 3 m, and by 16.1% when fracture spacing decreased from 3 to 2 m. This means that the decrease in fracture spacing corresponds with the decrease in the magnitude of gas production efficiency. Therefore, a fracture spacing of 3 m is recommended for the low-permeability hydrate reservoirs at site SH7. NWAF spacing has no effect on the gas–water ratio.

Discussion of the Effects of Key Parameters of NWAF on Gas Productivity

This study's investigation of the effects of the key parameters of NWAFs, such as depth, permeability, and spacing on gas productivity during 1 year of simulated mining led to important findings. As the fracture depth increases from 1 to 5 m, cumulative gas production can increase from 154×10^4 to 273×10^4 ST m^3. As the fracture permeability increases from 1 D to 5 D, the cumulative gas production can increase from 157×10^4 to 262×10^4 ST m^3. As fracture spacing increases from 1 to 5 m, cumulative gas production can decrease from 318×10^4 to 126×10^4 ST m^3. Gas production efficiency can be significantly increased by increasing fracture depth and permeability or by reducing fracture spacing. As mentioned previously, however, marine NGH deposits often involve unconsolidated sediments that exhibit limited shear strength, especially when the hydrates are dissociated. Under these conditions, the fractures can reduce the structural stability of NGH sediments. Therefore, when using NWAFs to increase gas production, the shear strength and structural stability of NGH sediments need to be considered in the determination of fracture depth and spacing, which will be researched by the authors in the future. After fracture depth and spacing are determined, fracture permeability, which hardly affects the structural stability of HBS, should be increased as much as possible. By comparing growth gaps between gradients under variable control, the recommended NWAF depth, permeability, and spacing are 3 m, 3 D, and 3 m, respectively for the clayey silt reservoirs at site SH7, and more detailed discussions will be investigated in a later study.

CONCLUSION

Low permeability significantly restricts the efficiency of gas and water flow into production wells. To enhance the gas production efficiency from low-permeability hydrate reservoirs, the high-pressure rotating water jets (HPRWJ) technology is proposed to construct near wellbore artificial fractures (NWAFs) in hydrate reservoirs. The HPRWJ can avoid the risks of hydraulic fracturing as well as large-scale reservoir damage. It is more suitable for constructing fractures in hydrate-bearing sediments (HBS). Taking site SH7 in the

South China Sea as a case study, this work used numerical simulations to evaluate the feasibility of this technology for enhancing gas production of low-permeability hydrate reservoirs. The following conclusions were obtained.

(1) NWAFs constructed by the HPRWJ technology can effectively increase the gas and water production efficiency of low-permeability hydrate reservoirs. The gas productivity can be increased by about three times by constructing fractures with a depth, spacing, and height of 3 m, 3, and 0.5 m respectively based on low-permeability hydrate reservoirs at site SH7. This is mainly because high-conductivity fractures are formed near the production well, which provide rapid flow channels for gas and water, thus contributing to pressure propagation.
(2) The water in permeable boundaries can flow into production wells after a certain period of production, thereby restricting the pressure drop from being transferred into deep reservoirs and limiting hydrate dissociation to some extent. Therefore, well spacing should be properly controlled when vertical wells are employed to exploit hydrate deposits at site SH7 in the South China Sea to improve the recovery of the entire hydrate reservoir.
(3) Fracture depth, fracture permeability, and fracture spacing have significant effects on the gas productivity of hydrate reservoirs. Production efficiency increases as fracture depth, and permeability increase, and as fracture spacing decreases. However, these fracture parameters can hardly affect the gas–water ratio.

The proposed HPRWJ technology may be an efficient stimulation method for gas recovery from low-permeability hydrate reservoirs in the foreseeable future. Therefore, there is an urgent need for conducting laboratory and numerical studies related to the high-pressure rotating water jet technology and the geomechanical responses associated with fractures in the future.

DATA AVAILABILITY STATEMENT

The original contributions presented in this study are included in the article/Supplementary Material, further inquiries can be directed to the corresponding authors.

AUTHOR CONTRIBUTIONS

ZL: modeling and writing. TW: communication and guidance. YY: translation and suggestion. QL: guidance. HL: suggestion and verification. JW: suggestion and verification. LT: guidance. HH: translation. KL: suggestion. HQ: communication and guidance. All authors contributed to the article and approved the submitted version.

FUNDING

This paper was supported by Key Special Project for Introduced Talents Team of Southern Marine Science and Engineering Guangdong Laboratory (Guangzhou) (No. GML2019ZD0506), MNR Key Laboratory of Marine Mineral Resources Fund (KLMMR-2018-A-05), Guangdong MEPP Fund [GDOE (2019) A39], Key Special Project for Introduced Talents Team of Southern Marine Science and Engineering Guangdong Laboratory (Guangzhou) (No. GML2019ZD0307) and Guangdong Major project of Basic and Applied Basic Research (No. 2020B0301030003).

ACKNOWLEDGMENTS

The authors would like to extend their sincere appreciation to Kewei Zhang from the Guangzhou Marine Geological Survey for editing this paper.

REFERENCES

Anderson, B. J., Kurihara, M., White, M. D., Moridis, G. J., Wilson, S. J., Pooladi-Darvish, M., et al. (2011). Regional Long-Term Production Modeling from a Single Well Test, Mount elbert Gas Hydrate Stratigraphic Test Well, Alaska north Slope. *Mar. Pet. Geology.* 28, 493–501. doi:10.1016/j.marpetgeo.2010.01.015

Aydin, G., Jang, H., and Topal, E. (2016). Energy Consumption Modeling Using Artificial Neural Networks: The Case of the World's Highest Consumers. *Energ. Sourc. B: Econ. Plann. Pol.* 11, 212–219. doi:10.1080/15567249.2015.1075086

Boswell, R., and Collett, T. S. (2011). Current Perspectives on Gas Hydrate Resources. *Energy Environ. Sci.* 4, 1206–1215. doi:10.1039/c0ee00203h

Burland, J. B. (1990). On the Compressibility and Shear Strength of Natural Clays. *Géotechnique* 40, 329–378. FEng. doi:10.1680/geot.1990.40.3.329

Chen, C., Yang, L., Jia, R., Sun, Y., Guo, W., Chen, Y., et al. (2017). Simulation Study on the Effect of Fracturing Technology on the Production Efficiency of Natural Gas Hydrate. *Energies* 10, 1241. doi:10.3390/en10081241

Chong, Z. R., Pujar, G. A., Yang, M., and Linga, P. (2016). Methane Hydrate Formation in Excess Water Simulating marine Locations and the Impact of thermal Stimulation on Energy Recovery. *Appl. Energ.* 177, 409–421. doi:10.1016/j.apenergy.2016.05.077

Feng, Y., Chen, L., Suzuki, A., Kogawa, T., Okajima, J., Komiya, A., et al. (2019b). Enhancement of Gas Production from Methane Hydrate Reservoirs by the Combination of Hydraulic Fracturing and Depressurization Method. *Energ. Convers. Manag.* 184, 194–204. doi:10.1016/j.enconman.2019.01.050

Feng, Y., Chen, L., Suzuki, A., Kogawa, T., Okajima, J., Komiya, A., et al. (2019a). Numerical Analysis of Gas Production from Layered Methane Hydrate Reservoirs by Depressurization. *Energy* 166, 1106–1119. doi:10.1016/j.energy.2018.10.184

Fujii, T., Noguchi, S., Takayama, T., Suzuki, T., Yamamoto, K., and Saeki, T. (2013). "Site Selection and Formation Evaluation at the 1st Offshore Methane Hydrate Production Test Site in the Eastern Nankai Trough, Japan," in Proceedings of the 75th EAGE Conference & Exhibition-Workshops (London, UK. doi:10.3997/2214-4609.20131159

Fujii, T., Suzuki, K., Takayama, T., Tamaki, M., Komatsu, Y., Konno, Y., et al. (2015). Geological Setting and Characterization of a Methane Hydrate Reservoir Distributed at the First Offshore Production Test Site on the Daini-Atsumi Knoll in the Eastern Nankai Trough, Japan. *Mar. Pet. Geology.* 66, 310–322. doi:10.1016/j.marpetgeo.2015.02.037

Goto, S., Matsubayashi, O., and Nagakubo, S. (2016). Simulation of Gas Hydrate Dissociation Caused by Repeated Tectonic Uplift Events. *J. Geophys. Res. Solid Earth* 121, 3200–3219. doi:10.1002/2015JB012711

Hancock, S. H., Carle, D., Weatheroll, B., Dallimore, S. R., Collett, T. S., Satoh, T., et al. (2005). *Overview of pressure –drawdown production-test results for the JAPEX/JNOC/GSC et al. Mallik 5L-38 gas hydrate production research well.* Canada: N. P. Web.

Huang, L., Su, Z., and Wu, N.-Y. (2015). Evaluation on the Gas Production Potential of Different Lithological Hydrate Accumulations in marine Environment. *Energy* 91, 782–798. doi:10.1016/j.energy.2015.08.092

International Energy Outlook, Boswell, R., and Collett, T. S. (2011). Current Perspectives on Gas Hydrate Resources. *Energ. Environ. Sci.* 4 (4), 1206–1215. doi:10.1039/c0ee00203h

Kim, A. R., Cho, G. C., Lee, J. Y., and Kim, S. J. (2016). "May). Numerical Simulation on Geomechanical Stability during Gas Hydrate Production by Depressurization," in 11th International Symposium on Cold Regions Development (ISCORD) (Incheon, Korea: International Association for Cold Region Development Studies (IACORDS).

Koh, D.-Y., Kang, H., Lee, J.-W., Park, Y., Kim, S.-J., Lee, J., et al. (2016). Energy-efficient Natural Gas Hydrate Production Using Gas Exchange. *Appl. Energ.* 162, 114–130. doi:10.1016/j.apenergy.2015.10.082

Konno, Y., Jin, Y., Shinjou, K., and Nagao, J. (2014). Experimental Evaluation of the Gas Recovery Factor of Methane Hydrate in sandy Sediment. *RSC Adv.* 4, 51666–51675. doi:10.1039/c4ra08822k

Konno, Y., Jin, Y., Yoneda, J., Uchiumi, T., Shinjou, K., and Nagao, J. (2016). Hydraulic Fracturing in Methane-Hydrate-Bearing Sand. *RSC Adv.* 6, 73148–73155. doi:10.1039/C6RA15520K

Lei, H., Yang, Z., Xia, Y., and Yuan, Y. (2022). Prospects of Gas Production from the Vertically Heterogeneous Hydrate Reservoirs through Depressurization in the Mallik Site of Canada. *Energ. Rep.* 8, 2273–2287. doi:10.1016/j.egyr.2022.01.170

Li, G., Huang, Z., Zhang, D., Ma, J., Shen, Z., and Niu, J. (2002). Study of Treatment of Near Well-Bore Formation Processed with High Pressure Rotating Water Jets. *Pet. Sci. Tech.* 20, 961–972. doi:10.1081/LFT-120003689

Li, G., Li, X.-S., Zhang, K., Li, B., and Zhang, Y. (2013). Effects of Impermeable Boundaries on Gas Production from Hydrate Accumulations in the Shenhu Area of the south China Sea. *Energies* 6, 4078–4096. doi:10.3390/en6084078

Li, G., Li, X. S., and Zhang, K. (2011b). Numerical Simulation of Gas Production from Hydrate Accumulations Using a Single Horizontal Well in Shenhu Area, South China Sea. *Chin. J. Geophys.* 54, 2325–2337. doi:10.3969/j.issn.0001-5733.2011.09.016

Li, G., Moridis, G. J., Zhang, K., and Li, X.-s. (2011a). The Use of Huff and Puff Method in a Single Horizontal Well in Gas Production from marine Gas Hydrate Deposits in the Shenhu Area of South China Sea. *J. Pet. Sci. Eng.* 77, 49–68. doi:10.1016/j.petrol.2011.02.009

Li, J.-f., Ye, J. L., Ye, J.-l., Qin, X.-w., Qiu, H.-j., Wu, N.-y., et al. (2018). The First Offshore Natural Gas Hydrate Production Test in South China Sea. *China Geology*. 1, 5–16. doi:10.31035/cg2018003

Liang, J., Wang, H., Su, X., Wang, L., Guo, Y., Chen, F., et al. (2014). Natural Gas Hydrate Formation Conditions and the Associated Controlling Factors in the Northern Slope of the South China Sea. *Nat. Gas Ind.* 34, 128–135. doi:10.3787/j.issn.1000-0976.2014.07.022

Liu, C. Z., Pu, W. F., Zhou, F. Y., and Yu, Q. L. (2012). The Influence of Different Artificial Cracks on Permeability by experiment. *Spec. Oil Gas Reserve* 19, 117–121. doi:10.3969/j.issn.1006-6535.2012.04.030

Ma, X., Sun, Y., Guo, W., Jia, R., Li, B., Yuang, Y., et al. (2021). Numerical Simulation of Horizontal Well Hydraulic Fracturing Technology for Gas Production from Hydrate Reservoir. *Appl. Ocean Res.* 112, 102674. in press. doi:10.1016/j.apor.2021.102674

Makogon, Y. F., and Omelchenko, R. Y. (2013). Commercial Gas Production from Messoyakha deposit in Hydrate Conditions. *J. Nat. Gas Sci. Eng.* 11, 1–6. doi:10.1016/j.jngse.2012.08.002

Moridis, G. J., Kim, S-J., and Seol, Y. (2007b). "Evaluation of the Gas Production Potential of Oceanic Hydrate Deposits in the Ulleung Basin of the Korean East Sea," in Asia Pacific Oil and Gas Conference and Exhibition (Jakarta, Indonesia: OnePetro). doi:10.2118/110859-ms

Moridis, G. J., Kowalsky, M. B., and Pruess, K. (2008). *TOUGH + HYDRATE V1.0 User's Manual: A Code for the Simulation of System Behavior in Hydrate-Bearing Geologic Media*.

Moridis, G. J., and Kowalsky, M. B. (2007a). Response of Oceanic Hydrate-Bearing Sediments to thermal Stresses. *SPE J.* 12, 253–268. doi:10.2118/111572-pa

Moridis, G. J., and Reagan, M. T. (2011). Estimating the Upper Limit of Gas Production from Class 2 Hydrate Accumulations in the Permafrost: 2. Alternative Well Designs and Sensitivity Analysis. *J. Pet. Sci. Eng.* 76, 124–137. doi:10.1016/j.petrol.2010.12.001

Moridis, G. J., and Sloan, E. D. (2007c). Gas Production Potential of Disperse Low-Saturation Hydrate Accumulations in Oceanic Sediments. *Energ. Convers. Manag.* 48, 1834–1849. doi:10.1016/j.enconman.2007.01.023

Moridis, G. J. (2014). *User's Manual for the Hydrate v1.5 Option of TOUGH+ v1.5: A Code for the Simulation of System Behavior in Hydrate-Bearing Geologic Media*.

Mu, L., and von Solms, N. (2020). Inhibition of Natural Gas Hydrate in the System Containing Salts and Crude Oil. *J. Pet. Sci. Eng.* 188, 106940. doi:10.1016/j.petrol.2020.106940

Myshakin, E. M., Seol, Y., Lin, J. S., Uchida, S., Collett, T. S., and Boswell, R. (2018). Numerical Simulations of Depressurization-Induced Gas Production from an Interbedded Turbidite Gas Hydrate-Bearing Sedimentary Section in the Offshore India: Site NGHP-02-16 (Area-B). *Mar. Petrol. Geol.* 108, 619–638. doi:10.1016/j.marpetgeo.2018.10.047

Qorbani, K., Kvamme, B., and Kuznetsova, T. (2017). Using a Reactive Transport Simulator to Simulate CH4 Production from Bear Island Basin in the Barents Sea Utilizing the Depressurization Method†. *Energies* 10, 187. doi:10.3390/en10020187

Rossi, F., Gambelli, A. M., Sharma, D. K., Castellani, B., Nicolini, A., and Castaldi, M. J. (2018). Experiments on Methane Hydrates Formation in Seabed Deposits and Gas Recovery Adopting Carbon Dioxide Replacement Strategies. *Appl. Therm. Eng.* 148, 371–381. doi:10.1016/j.applthermaleng.2018.11.053

Sloan, E. D., Jr., Koh, C. A., and Koh, C. A. (2008). "Clathrate Hydrates of Natural Gases," in *Clathrate Hydrates of Natural Gases* (Boca Raton, FL: CRC Press). 3re. doi:10.1201/9781420008494

Su, Z., Cao, Y. C., Yang, R., Zhang, K. N., and Wu, N. Y. (2011). Feasibility of Gas Production from Hydrate Reservoir Considering Heat Conduction: Taking Shen Hu Area in the South China Sea as an Example. *Geoscience* 25, 608–616. doi:10.1007/s12182-011-0118-0

Su, Z., Huang, L., Wu, N., and Yang, S. (2013). Effect of thermal Stimulation on Gas Production from Hydrate Deposits in Shenhu Area of the South China Sea. *Sci. China Earth Sci.* 56, 601–610. doi:10.1007/s11430-013-4587-4

Su, Z., Moridis, G. J., Zhang, K., and Wu, N. (2012). A Huff-And-Puff Production of Gas Hydrate Deposits in Shenhu Area of South China Sea through a Vertical Well. *J. Pet. Sci. Eng.* 86-87, 54–61. doi:10.1016/j.petrol.2012.03.020

Su, Z., Moridis, G., Zhang, K., Yang, R., and Wu, N. (2010). "Numerical Investigation of Gas Production Strategy for the Hydrate Deposits in the Shenhu Area, OTC 20551," in Proceedings of the Offshore Technology Conference (Houston, Texas, USA.

Sun, X., Luo, H., Luo, T., Song, Y., and Li, Y. (2019a). Numerical Study of Gas Production from marine Hydrate Formations Considering Soil Compression and Hydrate Dissociation Due to Depressurization. *Mar. Pet. Geology.* 102, 759–774. doi:10.1016/j.marpetgeo.2019.01.035

Sun, Y.-h., Jia, R., Guo, W., Zhang, Y.-q., Zhu, Y.-h., Li, B., et al. (2012). Design and Experimental Study of the Steam Mining System for Natural Gas Hydrates. *Energy Fuels* 26, 7280–7287. doi:10.1021/ef3014019

Sun, Y., Zhong, J., Chen, G., and Sun, C. (2019b). Enhanced Depressurization for Methane Recovery from Hydrate-Bearing Sediments by Ethylene Glycol Pre-injection. *Energ. Proced.* 158, 5207–5212. doi:10.1016/j.egypro.2019.01.674

The Ignik Sikumi gas hydrate exchange trial project team (2012). Ignik Sikumi Gas Hydrate Field Trial Completed. *Fire in the Ice* 12, 1–24.

The U.S. Energy Information Administration, 2019. *International Energy Outlook*.

Too, J. L., Cheng, A., Khoo, B. C., Palmer, A., and Linga, P. (2018a). Hydraulic Fracturing in a Penny-Shaped Crack. Part II: Testing the Frackability of Methane Hydrate-Bearing Sand. *J. Nat. Gas Sci. Eng.* 52, 619–628. doi:10.1016/j.jngse.2018.01.046

Too, J. L., Cheng, A., and Linga, P. (2018b). "Fracturing Methane Hydrate in Sand: a Review of the Current Status," in Proceedings of the Offshore Technology Conference Asia (Malaysia: Kuala Lumpur). doi:10.4043/28292-ms

Wang, X., Hutchinson, D. R., Wu, S., Yang, S., and Guo, Y. (2011). Elevated Gas Hydrate Saturation within silt and Silty clay Sediments in the Shenhu Area, South China Sea. *J. Geophys. Res. Solid Earth* 116, B05102. doi:10.1029/2010JB007944

Wang, Y., Li, X.-S., Li, G., Zhang, Y., Li, B., and Feng, J.-C. (2013). A Three-Dimensional Study on Methane Hydrate Decomposition with Different Methods Using Five-Spot Well. *Appl. Energ.* 112, 83–92. doi:10.1016/j.apenergy.2013.05.079

Wei, J., Yang, L., Liang, Q., Liang, J., Lu, J., Zhang, w., et al. (2021). Geomechanical Properties of Gas Hydrate-Bearing Sediments in Shenhu Area of the South China Sea. *Energy Rep. press*. doi:10.1016/j.egyr.2021.05.063

Wu, N., Zhang, S., Zhang, G., Liang, J., and Lu, J. (20112011). Gas Hydrate System of Shenhu Area, Northern South China Sea: Geochemical Results. *J. Geol. Res.*, 370298. doi:10.1155/2011/370298

Xu, Y. C., Xi, Y. T., and Lin, Y. C. (2016). The Experimental Analysis on Permeable Performance of Foamed concrete. *Low Temperature Architecture Tech.* 38, 8–11. doi:10.13905/j.cnki.dwjz.2016.10.004

Yamamoto, K., and Dallimore, S. (2008b). *Aurora-JOGMEC-NRCan Mallik 2006-2008 Gas Hydrate Research Project Progress*. Pittsburgh, PA: U.S. Department of Energy, Office of Fossil Energy. National Energy Technology Laboratory Fire In the Ice Newsletter.

Yamamoto, K., and Dallimore, S. (2008a). Aurora-JOGMEC-NRCanan Mallik 2006–2008 Gas Hydrate Research Project Progress. *Fire in the Ice* 8, 1–5.

Ye, J., Qin, X., Xie, W., Lu, H., Ma, B., Qiu, H., et al. (2020). Main Progress of the Second Gas Hydrate Trial Production in the South China Sea. *Geology. China* 47, 557–568. doi:10.12029/gc20200301

Yoneda, J., Masui, A., Konno, Y., Jin, Y., Kida, M., Katagiri, J., et al. (2017). Pressure-core-based Reservoir Characterization for Geomechanics: Insights from Gas Hydrate Drilling during 2012-2013 at the Eastern Nankai Trough. *Mar. Pet. Geology.* 86, 1–16. doi:10.1016/j.marpetgeo.2017.05.024

Yoneda, J., Oshima, M., Kida, M., Kato, A., Konno, Y., Jin, Y., et al. (2019). Permeability Variation and Anisotropy of Gas Hydrate-Bearing Pressure-Core Sediments Recovered from the Krishna-Godavari Basin, Offshore India. *Mar. Pet. Geology.* 108, 524–536. doi:10.1016/j.marpetgeo.2018.07.006

Yu, T., Guan, G., Abudula, A., Yoshida, A., Wang, D., and Song, Y. (2019). Heat-assisted Production Strategy for Oceanic Methane Hydrate Development in the Nankai Trough, Japan. *J. Pet. Sci. Eng.* 174, 649–662. doi:10.1016/j.petrol.2018.11.085

Yuan, Y., Xu, T., Jin, C., Zhu, H., Gong, Y., and Wang, F. (2021b). Multiphase Flow and Mechanical Behaviors Induced by Gas Production from Clayey-silt Hydrate Reservoirs Using Horizontal Well. *J. Clean. Prod.* 328, 129578. doi:10.1016/j.jclepro.2021.129578

Yuan, Y., Xu, T., Xin, X., Gong, Y., and Li, B. (2021a). Enhanced Gas Production from Clayey-silt Hydrate Reservoirs Based on Near-Well Reservoir Reconstruction Using the High-Pressure Jet Grouting Technology. *J. Nat. Gas Sci. Eng.* 94, 4121. doi:10.1016/j.jngse.2021.104121

Yuan, Y., Xu, T., Xin, X., and Xia, Y. (2017). Multiphase Flow Behavior of Layered Methane Hydrate Reservoir Induced by Gas Production. *Geofluids* 2017, 1–15. doi:10.1155/2017/7851031

Conflict of Interest: Authors ZL, TW, YY, QL, HL, JW, LT, HH, KL, and HQ were employed by the Guangzhou Marine Geological Survey.

Publisher's Note: All claims expressed in this article are solely those of the authors and do not necessarily represent those of their affiliated organizations, or those of the publisher, the editors, and the reviewers. Any product that may be evaluated in this article, or claim that may be made by its manufacturer, is not guaranteed or endorsed by the publisher.

NOMENCLATURE

M^{κ} Mass accumulation of component κ, kg/m^3

F^{κ} Mass flux of component κ, $kg/(m^2 \cdot s)$

q^{κ} Sink/source of component κ, $kg/(m^3 \cdot s)$

M^{θ} Energy accumulation, J/m^3

$\boldsymbol{F}^{\theta}$ Energy flux, $J/(m^2 \cdot s)$

q^{θ} Sink/source of heat, J/(m3·s)

V Volume, m^3

Γ Surface area, m^2

t Time, s

φ Porosity

S_{β} Saturation of phase β

ρ_{β} Density of phase β, kg/m3

X_{β}^{κ} Mass fraction of component κ in phase β

$\boldsymbol{k}$ Permeability, m^2

$k_{r\beta}$ Relative permeability of phase β

$\mu_{r\beta}$ Viscosity of phase β, $Pa \cdot s$

P_{β} Pressure of phase β, Pa

$\boldsymbol{g}$ Gravitational acceleration vector, m/s^2

$\boldsymbol{b}$ Klinkenberg factor, Pa

τ_{β} Medium tortuosity of phase β

D_{β}^{κ} Molecular diffusion coefficient of component κ in phase β, m^2/s

ρ_R Density of rock grain, kg/m^3

C_R Specific heat of rock grain, $J/(kg \cdot ^{\circ}C)$

$\boldsymbol{T}$ Temperature, $^{\circ}C$

U_{β} Internal energy of phase β, J/kg

$\boldsymbol{\lambda}$ Average thermal conductivity, $W/(m \cdot K)$

h_{β} Specific enthalpy of phase β, J/kg

$\boldsymbol{J}_{\beta}^{\kappa}$ Mass diffusion of component κ in phase β, $kg/(m^2 \cdot s)$

ρ_H Hydrate density, kg/m^3

S_H Hydrate saturation

$\boldsymbol{\nabla} U_H$ Specific enthalpy of hydrate dissociation/formation, j/kg

Q_H Mass change of hydrate component under kinetic dissociation, kg

N_H Hydration number

$\boldsymbol{\nabla}$ Gradient operator

$\boldsymbol{\beta}$ Phase, $\beta = A,G,H,I$ is aqueous, gas, hydrate, and ice, respectively

$\boldsymbol{\kappa}$ Component, $\kappa = w,m,i,h$ is water, methane, salt, and hydrate, respectively

frontiers | Frontiers in Earth Science

ORIGINAL RESEARCH
published: 03 May 2022
doi: 10.3389/feart.2022.876134

Sediment Microstructure in Gas Hydrate Reservoirs and its Association With Gas Hydrate Accumulation: A Case Study From the Northern South China Sea

Chenyang Bai[1,2], *Pibo Su*[3,4,5]*, *Xin Su*[1,2], *Jujie Guo*[6], *Hongpeng Cui*[1,2], *Shujun Han*[7,8] and *Guangxue Zhang*[3]

[1]School of Ocean Sciences, China University of Geosciences, Beijing, China, [2]Marine and Polar Research Center, China University of Geosciences, Beijing, China, [3]Guangzhou Marine Geological Survey, China Geological Survey, Guangzhou, China, [4]Academy of South China Sea Geological Science, China Geological Survey, Sanya, China, [5]Hubei Key Laboratory of Marine Geological Resources, China University of Geosciences, Wuhan, China, [6]Institute of Geology and Geophysics, Chinese Academy of Sciences, Beijing, China, [7]School of Geosciences and Resources, China University of Geosciences, Beijing, China, [8]Department of Earth and Environment Sciences, Macquarie University, Sydney, NSW, Australia

OPEN ACCESS

Edited by:
Alessandra Savini,
University of Milano-Bicocca, Italy

Reviewed by:
Qing Li,
Qingdao Institute of Marine Geology (QIMG), China
Zhilei Sun,
Qingdao Institute of Marine Geology (QIMG), China

***Correspondence:**
Pibo Su
spb_525@sina.com

Specialty section:
This article was submitted to Marine Geoscience, a section of the journal Frontiers in Earth Science

Received: *15 February 2022*
Accepted: *19 April 2022*
Published: *03 May 2022*

Citation:
Bai C, Su P, Su X, Guo J, Cui H, Han S and Zhang G (2022) Sediment Microstructure in Gas Hydrate Reservoirs and its Association With Gas Hydrate Accumulation: A Case Study From the Northern South China Sea. Front. Earth Sci. 10:876134. doi: 10.3389/feart.2022.876134

Exploration and pilot production have confirmed that gas hydrates in the Shenhu area on the northern continental slope of the South China Sea have enormous resource potential. However, a meticulous depiction of gas hydrate reservoirs based on sediments is limited. The distributed low-flux gas hydrates are mainly deposited in the Shenhu area, and the gas hydrate saturation exhibits extreme vertical heterogeneity. In this study, we focused on the sediment microstructure of gas hydrate reservoirs. Based on the variation in gas hydrate saturation, the study interval was divided into non-gas hydrate (non-GH) as well as I-, II-, and III-gas hydrate reservoir layers. We analyzed the relationship between sediment microstructure and gas hydrate reservoirs based on computed tomography scans, specific surface area analysis, and scanning electron microscopy observations. The results showed that the sediment in gas hydrate reservoirs had three types of pores: 1) intergranular pores between coarse grains (CG-intergranular pores), 2) intergranular pores between fine grains (FG-intergranular pores), and 3) biologic grain pores (BG-pores). The CG- and FG-intergranular pores were mainly formed by the framework, which consisted of coarse minerals (such as quartz and feldspar) and clay minerals, respectively. The BG-pores were mainly formed by the coelomes of foraminifera. CG-intergranular pores and BG-pores can provide effective reservoir space and increase the permeability of sediment, which is conducive to gas hydrate accumulation. The FG-intergranular pores reduce permeability and are not conducive to gas hydrate accumulation. Clay minerals and calcareous ultramicrofossils with small grain sizes and complex microstructures fill the effective reservoir space and reduce the permeability of sediment; additionally, they improve the adsorption capacity of sediment to free gas or pore water, which is not conducive to gas hydrate formation and accumulation. The results of our study explicitly suggest that the microstructure of sediment is an important controlling factor for gas hydrate accumulation and reveals its underlying mechanism.

Keywords: sediments microstructure, gas hydrate reservoir, gas hydrate accumulation, shenhu area, south China sea

INTRODUCTION

Gas hydrates constitute a potential strategic energy resource for the future owing to their high-density energy and clean-burning features (Boswell and Collett, 2006; Tréhu et al., 2006; Boswell et al., 2012; Koh et al., 2012; Malagar et al., 2019). Globally, most gas hydrates occur in submarine sediments. In recent years, a series of scientific research, exploration, and gas hydrate production tests have been conducted in the Gulf of Mexico, Cascadia subduction zone, Nankai Trough in Japan, Ulleung Basin in Korea, Krishna-Godavari Basin in India, and the northern South China Sea (Pohlman et al., 2009; Boswell et al., 2012; Collett et al., 2012; Ryu et al., 2013; Ito et al., 2015; Zhang et al., 2015; Su et al., 2016; Boswell et al., 2019). Based on a large number of relevant previous studies, gas hydrate accumulation is significantly controlled by the gas hydrate stability zone, gas source, and gas migration channels (Collett, 2002; Lu and McMechan, 2002; Tréhu et al., 2006; Wu et al., 2007; Wang et al., 2014). However, as exemplified by many cases of gas hydrate drilling, the gas hydrate forms and saturation are significantly different among different sea areas, different sites in the same sea area, and even different layers at the same site (Colwell et al., 2004; Tréhu et al., 2006; Ryu et al., 2013; Boswell et al., 2019; Liang et al., 2019; Ye et al., 2019). Gas hydrate formation and saturation exhibit strong horizontal and vertical heterogeneity in the gas hydrate stability zone (Yang S. et al., 2017; Kang et al., 2020). The heterogeneity of gas hydrate accumulation is difficult to explain solely based on controlling factors, such as gas hydrate stability zone, gas source, or gas migration channels. Differences in gas hydrate reservoir properties may also play a key role in restricting gas hydrate accumulation.

For decades, research on gas hydrate reservoirs has mainly relied on geophysical methods. Many researchers have used seismic and logging while drilling (LWD) data to describe and characterize gas hydrate reservoirs (Chand et al., 2004; Collett et al., 2012; Wang et al., 2014; Liang et al., 2016; Haines et al., 2017; Yang J. et al., 2017). LWD data can be used to calculate the gas hydrate saturation and identify potential gas hydrate reservoirs (Chand et al., 2004; Collett et al., 2012; Liang et al., 2016; Yang J. et al., 2017). Seismic profiles can help describe and study the characteristics of gas hydrate-bearing deposits; by combining these with logging data, we can reveal the plane distribution of gas hydrate reservoirs (Popescu et al., 2006; Wang et al., 2014; Li et al., 2016; Su et al., 2017; Bai et al., 2019; Zhang et al., 2020). Most gas hydrate reservoir studies that rely on geophysical methods have been conducted on a large scale. Higher-resolution reservoir studies require more detailed and accurate information from sediment data. There has also been research on the properties of gas hydrate reservoir sediment. Some researchers have studied the effects of grain size parameters and biological components of sediments on gas hydrate reservoirs. They found that coarse grain size (Lu and McMechan, 2002; Colwell et al., 2004; Tréhu et al., 2006; Ito et al., 2015; Li et al., 2019), poor sorting (Waite et al., 2019; Yang et al., 2020), and some types of microfossils (e.g., foraminifera and diatoms) (Chen et al., 2013; Ryu et al., 2013; Zhang et al., 2015; Boswell et al., 2019) have potentially positive effects on gas hydrate accumulation. However, as gas hydrate exploration has increased, these rules cannot be applied to all research cases (Zhang et al., 2015; Yi et al., 2018; Boswell et al., 2019; Li et al., 2019; Su et al., 2021), indicating that the influence of sediment properties on gas hydrate accumulation is very complex.

Recent research has shown that sediment microstructure is also a controlling factor for gas hydrate accumulation (Jones et al., 2007; Ghosh and Ojha, 2021). Some researchers have used laboratory simulation methods to explore the formation process of gas hydrates in sediment and the variation in porosity and permeability properties and established the relationship between porosity and permeability parameters and gas hydrate saturation (Wang et al., 2020; Wu et al., 2020; Li et al., 2021). These laboratory simulations provide a reasonable basis for exploring the effect of the sediment microstructure on gas hydrate accumulation. However, the actual conditions for gas hydrate accumulation are complex. Thus, some researchers have used actual gas hydrate-bearing sediments for microstructural research. They considered that the mineral type and grain size determine the pore space and influence gas hydrate accumulation (Lee et al., 2013; Bian et al., 2020; Cai et al., 2020). Undoubtedly, the reservoir space is one of the key factors affecting gas hydrate accumulation. However, it is difficult to explain the gas hydrate accumulation rule in many research cases simply by emphasizing the control effect of sediment grain size and pore space, especially in gas hydrate reservoirs dominated by fine-grained sediments in the northern South China Sea (Zhang et al., 2015; Su et al., 2016; Li et al., 2019). Thus, the effect of sediment microstructure on gas hydrate accumulation requires further research.

Gas hydrates in the Shenhu area of the northern South China Sea (SCS) are typically dominated by diffused gas hydrates (Liang et al., 2016). Sediments in the Shenhu area have a more significant controlling effect on gas hydrate accumulation (Zhang et al., 2015; Li et al., 2019; Su et al., 2021). Therefore, the selection of gas hydrate-bearing sediment samples from the Shenhu area is more conducive to discussing the influence of the sediment microstructure on gas hydrate accumulation. In this study, scanning electron microscopy (SEM) and computed tomography (CT) were used to characterize the microstructure of gas hydrate-bearing sediments. Then, we combined the microstructural features of the sediment, specific surface area, and biological data to reveal the controlling effect of sediment microstructure on gas hydrate accumulation.

GEOLOGICAL SETTING

The SCS is 1,212 m deep on average, with a maximum depth of 5,377 m (Wu et al., 2007). The northeastern slope of the SCS is

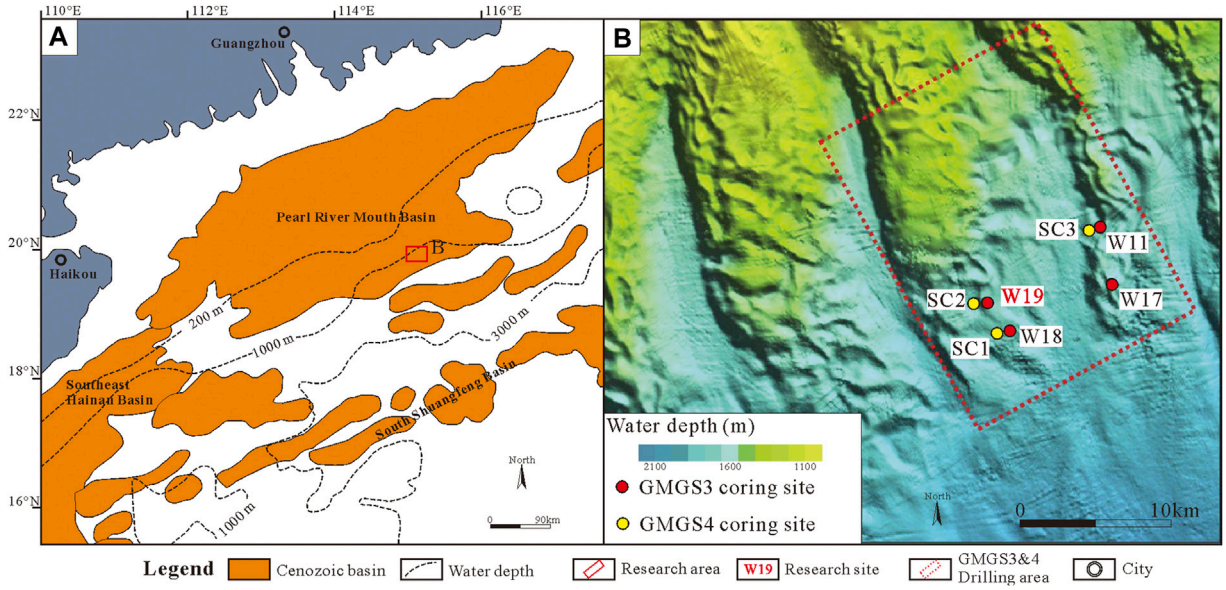

FIGURE 1 | The geological map of study area. **(A)** the geological map of northern slope of SCS, modified from Li et al. (2019); **(B)** enlarge the red box in figure **(A)**, the drilling area of GMGS3&4, modified from Zhang W. et al. (2019).

located in the transitional zone between quasi-passive and active continental margins. The northeastern slope of the SCS has a complex geological structure and covers a total area of approximately 2.3 × 10^5 km^2, with a length of 900 km and a width of 143–342 km (Shao et al., 2007; Wu et al., 2007; Bai et al., 2019; Li et al., 2019; Zhang W. et al., 2019). The western part of the northeastern slope of the SCS is the Pearl River Mouth Basin, which has an extensional setting (**Figure 1A**). During the Paleocene, the northeastern slope of the SCS was a rift basin, and numerous faults of different scales were formed (Shao et al., 2007; Bai et al., 2019; Li et al., 2019). After the Middle Miocene, the northeastern continental margin of the SCS entered a tectonic subsidence stage. During this stage, the regional sedimentary layer was dominated by marine sediments, with a very high deposition rate of approximately 520 m/Ma (Shao et al., 2007).

According to a series of exploratory drilling expeditions and two gas hydrate production tests conducted by the Guangzhou Marine Geological Survey (GMGS) in the past few years, the SCS is known worldwide as an attractive and potentially resource-rich area that contains gas hydrates (Liu et al., 2012; Li et al., 2018; Qin et al., 2020; Su et al., 2021). In the third gas hydrate exploratory drilling expeditions by GMGS (GMGS3), gas hydrates were obtained at sites W11, W17, W18, and W19 (**Figure 1B**). The sediment core, geophysical data, and geological background data of sites W11, W17, W18, and W19 were also obtained during the GMGS3 expedition. Site W19 is located on the western ridge of the GMGS3 drilling area and contains a favorable gas hydrate reservoir. The gas hydrates at site W19 occurred between 134 and 171 m below the seafloor (mbsf), at gas hydrate saturations as high as approximately 71% (Zhang et al., 2020). Site W19 was selected as the key site owing to its high hydrate saturation and thick reservoir.

MATERIALS AND METHODS

Core Samples, SEM Observations, and CT Scans

This study focused on the gas hydrate reservoir and adjacent layers of site W19 (114.4–171 mbsf) and 39 samples were obtained for SEM observations, CT scans, and specific surface area (SSA) analyses (**Table 1**; **Figure 3**). The gas hydrate in the core samples decomposed under changes in temperature and pressure conditions (**Figure 2A**). However, gas hydrate decomposition has a limited influence on the mineral and biological components and SSA in sediments (Zhang et al., 2016; Li et al., 2019; Waite et al., 2019). The microstructure of the core samples is not in the *in-situ* state with gas hydrates. However, the samples can represent the microstructural features of the sediment before gas hydrate formation, which is significant for gas hydrate accumulation analysis. The samples used for SEM observation and CT scans in this study were obtained using plastic square cubes (2 × 2 × 2 cm), which helped preserve the original microstructural features as much as possible (**Figure 2B**). The samples were stored on dry ice until the tests were conducted in the laboratory.

As the square cubes were made of plastic, which has no effect on the CT scan, the samples and square cubes were tested directly to obtain CT scan images and data. A total 12 samples were used for CT scan. The CT scan was performed by Nanjing Hongchuang Geological Exploration Technology Service Co., Ltd.

The samples used for the SEM observation were prepared as follows:

TABLE 1 | The sample list of Site W19.

Sample	Depth (mbsf)	Sample	Depth (mbsf)	Sample	Depth (mbsf)
W19-1	120.70	W19-14	136.35	W19-27	156.20
W19-2	122.50	W19-15	137.60	W19-28	156.55
W19-3	122.70	W19-16	138.60	W19-29	157.90
W19-4	122.90	W19-17	140.20	W19-30	158.30
W19-5	124.50	W19-18	141.40	W19-31	158.50
W19-6	126.60	W19-19	145.20	W19-32	161.20
W19-7	126.80	W19-20	146.20	W19-33	162.80
W19-8	127.80	W19-21	146.35	W19-34	163.20
W19-9	128.10	W19-22	146.50	W19-35	163.70
W19-10	130.15	W19-23	147.20	W19-36	164.20
W19-11	135.60	W19-24	148.70	W19-37	166.00
W19-12	135.90	W19-25	149.00	W19-38	166.50
W19-13	136.10	W19-26	154.90	W19-39	167.10

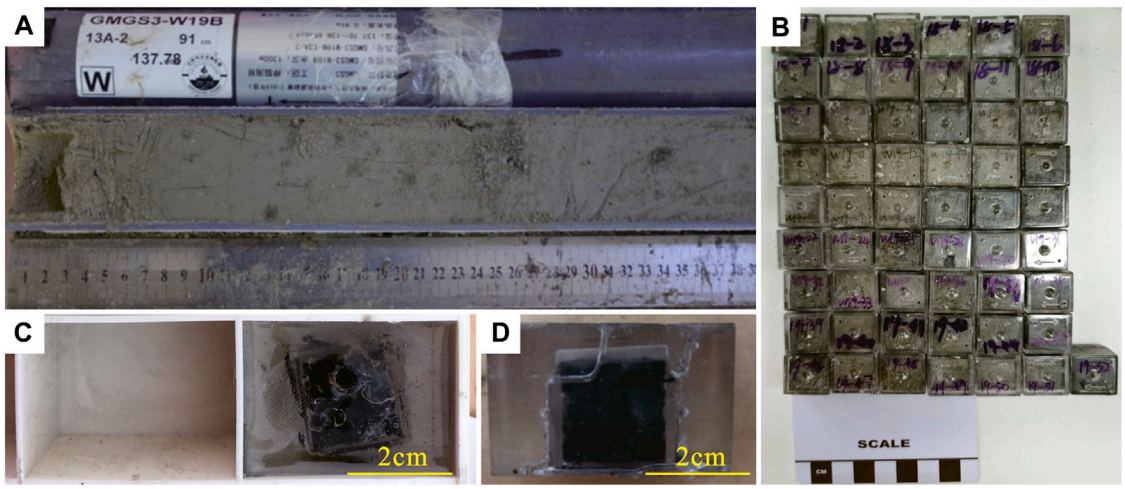

FIGURE 2 | The sampling method images. **(A)** the sediment cores of Site W19; **(B)** the sample cubes for microstructure analysis which sampling from sediment cores; **(C)** and **(D)** the images of sample preparation process.

(1) First, the epoxy resin and curing agent proportions were adjusted. We used more epoxy resin and less curing agent, which prolongs the curing time of epoxy resin and facilitates infiltration.
(2) Then, the samples were placed in a mold and wrapped with a mixture of epoxy resin and a curing agent (**Figure 2C**). The samples were then left at 25°C for curing (**Figure 2D**).
(3) Next, the samples were cut.
(4) The cut surface was reinfused with a mixture of epoxy resin and curing agent to ensure that the samples were completely cured.
(5) The cut surface of the samples was ground and the samples were placed on the slide and cut to 1–2 mm thickness.
(6) The samples were polished with 800- and 1200-mesh emery cloths to complete the preparation.

The samples for SEM observation were prepared at the Institute of Geology and Geophysics, Chinese Academy of Sciences.

Gas Hydrate Saturation

The analysis of gas hydrate saturation of site W19 was mainly based on the voyage report of GMGS3. In this study, resistivity log data, Cl^- anomalies of the pore water in sediment, and quantitative degassing of the pressure core were used to analyze the gas hydrate variation trend (Dvorkin et al., 1999; Qian et al., 2018; Ye et al., 2019).

Biological Statistics

Biological data were obtained from the voyage report of GMGS3 and were tested at the Test Center of the Guangzhou Marine Geological Survey.

Specific Surface Area

SSA analysis was conducted using Quantachrome Autosorb-1 and Quantachrome Nova Station A instruments at the Institute of Analysis and Testing, Beijing Academy of Science and Technology. Before the analysis, the samples were degassed at

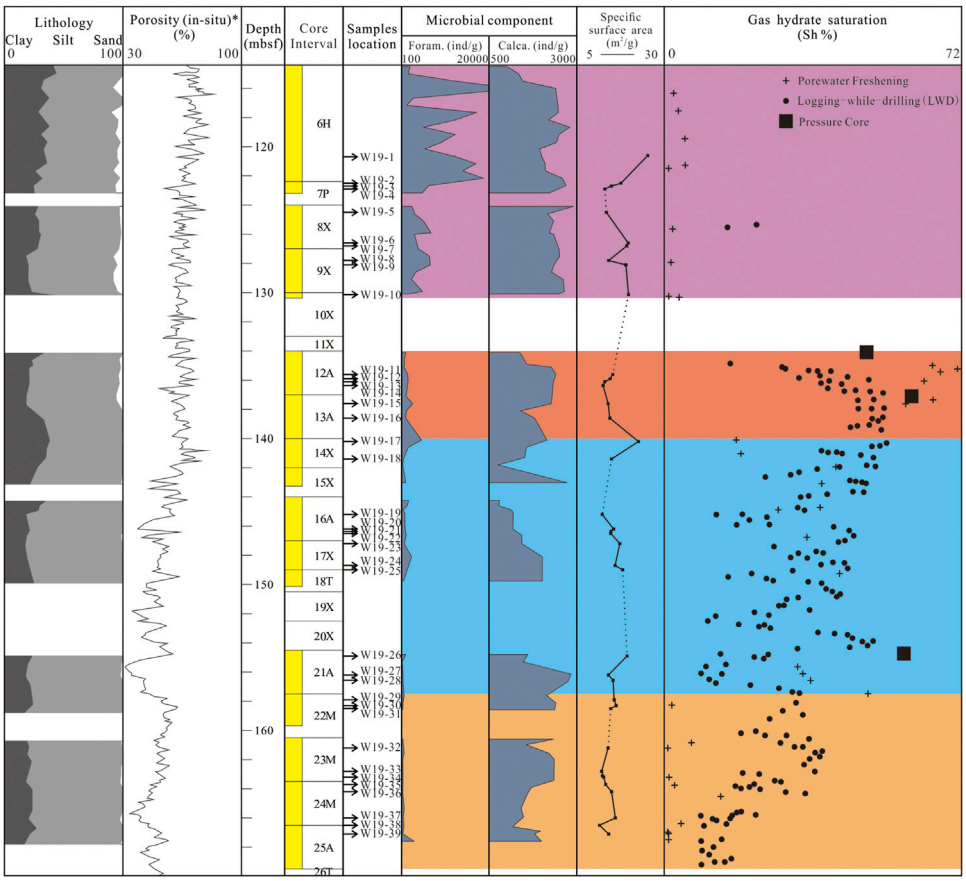

FIGURE 3 | The comprehensive column of Site W19. The lithology data are cited from voyage report of the GMGS3. Foram. and Calca. are short for foraminifera and calcareous ultra-microfossils, respectively. The purple, red, bule and orange shaded area indicate non-GH, I-, II-, and III-GHR layers, respectively. * The Porosity (*in-situ*) is calculated by LWD data.

approximately 383.15 K under vacuum for approximately 12 h to remove adsorbed moisture and residual volatiles. The N_2 sorption isotherms were determined at 77.35 K within a relative pressure (P/Po = absolute/saturation pressure) range of 0.009–0.995. The specific surface area was calculated using the Brunauer-Emmet-Teller equation (Brunauer et al., 1938).

RESULTS

Lithology

The lithological data of site W19 were collected from the voyage report of the GMGS3. In the study interval at site W19, the sediments were dominated by clayey silt and silt. The sand content of the sediments ranged from 0.12 to 10.85%, with an average of 3.34%. The silt content of the sediments ranged from 55.64 to 80.07%, with an average of 70.00%. The clay content of the sediments ranged from 17.21 to 44.19%, with an average of 26.66%. In the upper part of the study interval (114.4–145 mbsf), the sediments were dominated by clayey silt with only a few silt layers in the bottom part (**Figure 3**). In the lower part of the study interval (145–171 mbsf), the sediments were dominated by silt with several interbedded clayey silt layers (**Figure 3**). In Site W19, the sediments mainly consist of quartz, feldspar, calcite, and clay minerals, and a few dolomite, siderite, and anhydrite appear in some layers. The clay minerals were dominated by illite/smectite, illite, kaolinite, and chlorite.

Microstructural Features of Gas Hydrate-Bearing Sediment

Based on the SEM observations, the sediments at site W19 mainly consisted of quartz, feldspar, carbonates, and clay minerals (**Figure 4A**). The quartz mainly exhibited a granular shape with a diameter of 8–30 μm. The edge of the quartz was smooth and exhibited some abrasion (**Figure 4B**). The feldspar in the sediment could be classified into two categories, K-feldspar and plagioclase, which both have similar morphology. The diameter of the feldspar ranged from 10 to 30 μm, while its edge was smooth but indicated some traces of corrosion (**Figures 4A, C**). The carbonates in the sediment were mostly calcite, which appeared as fossils. Some fossils were calcareous ultramicrofossils with diameters of less than 2 μm (**Figure 4D**). Other fossils were foraminiferal shells, which

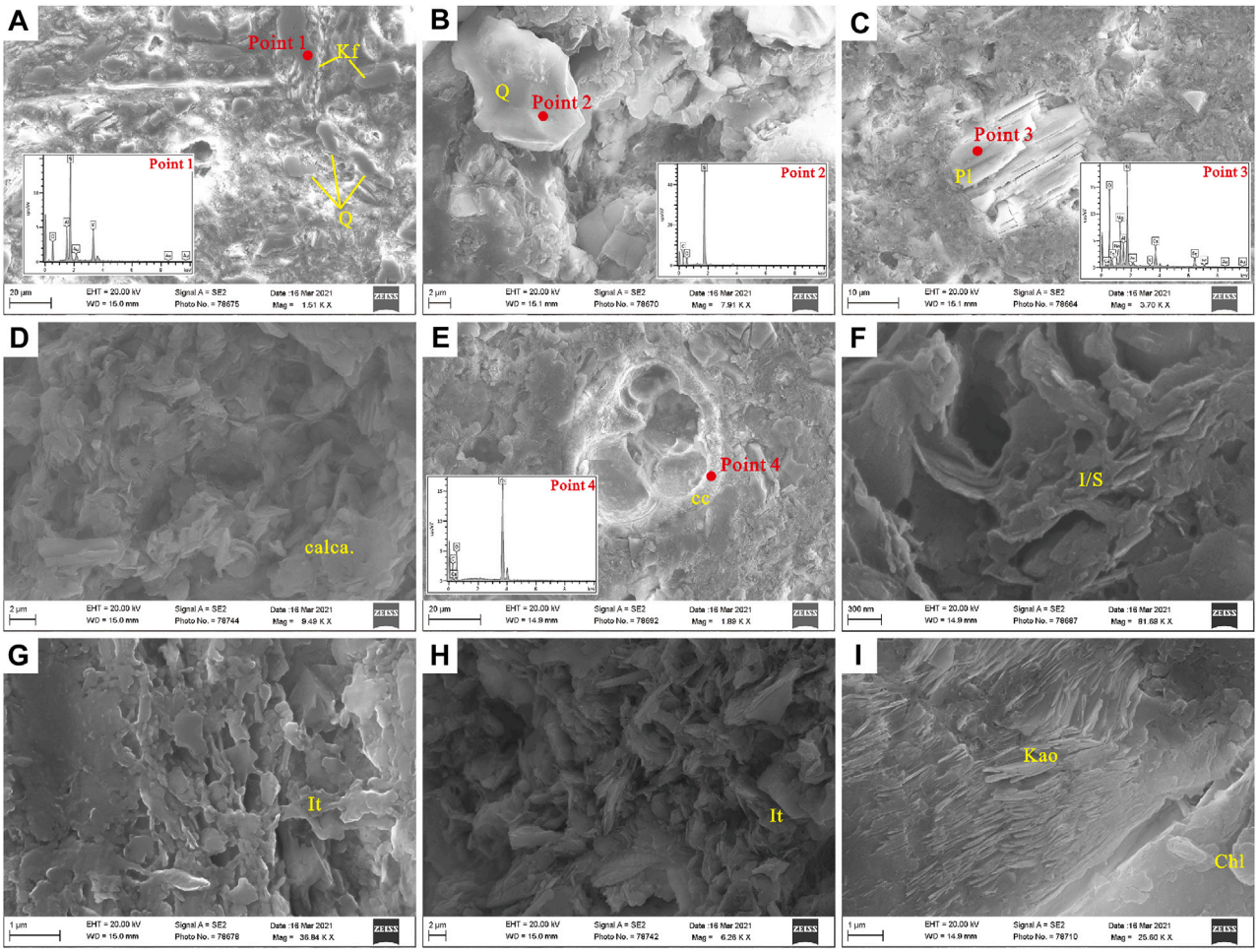

FIGURE 4 | The microstructure features of gas hydrate-bearing sediments. **(A)** Site W19, 126.60 mbsf, sediments consist of quartz, K-feldspar and clay minerals; **(B)** Site W19, 135.60 mbsf, the quartz in sediments; **(C)** Site W19, Site W19, 135.60 mbsf, the plagioclase in sediments; **(D)** Site W19, 127.80 mbsf, the calcareous ultramicrofossils in sediments; **(E)** Site W19, 135.90 mbsf, the foraminifera shell composed of calcite; **(F)** Site W19, 130.20 mbsf, the I/S in sediments; **(G)** Site W19, 136.1 mbsf, the filamentous ilite in sediments; **(H)** Site W19, 136.1 mbsf, the flaky ilite in sediments; **(I)** Site W19, 166.6 mbsf, the sheet-like kaolinite and flaky chlorite. Q, kf, Pl, calca, cc, I/S, It, Kao, and Chl are short for quartz, K-feldspar, plagioclase, calcareous ultramicrofossils, calcite, illite/semectite, illite, kaolinite and chlorite, respectively.

consisted of calcite. The calcite particles in the foraminiferal shells were fibrous with unclear edges. The diameter of the foraminiferal shells was >20 μm (**Figure 4E**). Many clay minerals in the sediment included filamentous or flaky illite/smectite (I/S) (**Figure 4F**), illite (**Figures 4G, H**), sheet-like kaolinite, and flaky chlorite (**Figure 4I**). The diameter of the clay mineral particles was less than 1 μm.

Gas Hydrate Saturation Data

In this study, gas hydrate saturation refers to resistivity log data, Cl^- anomalies of the pore water in the sediment, and quantitative degassing of the pressure core. The gas hydrate saturation ranged from 10 to 54% based on the resistivity log data (**Figure 3**). Based on the Cl^- anomalies of the pore water in the sediments, the gas hydrate saturation ranged from 0.21 to 70.90% (**Figure 3**). According to the voyage of GMGS3, only three pressure cores (12, 13, and 21A) were successfully obtained, from which we collected 234 L, 228 L, and 190 L, respectively, of methane gas. The gas hydrate saturation values calculated for the three pressure cores were 60, 58, and 49%, respectively (**Figure 3**).

Biological Statistics

The biological component mainly consisted of foraminifera and calcareous ultramicrofossils based on SEM observations. The abundance of the foraminifera in the study interval ranged from 238.8 ind/g to 39,014.4 ind/g, with an average of 3,214.5 ind/g. The abundance of calcareous ultramicrofossils ranged from 758 ind/g to 2,895 ind/g, with an average of 1,872.1 ind/g.

Specific Surface Area Data

The SSA data are presented in **Table 2**; **Figure 3**. The SSA of the sediments in the study interval ranged from 11.49 m^2/g to 24.86 m^2/g, with an average of 15.6 m^2/g.

TABLE 2 | The result of Specific surface area.

Sample	Depth (mbsf)	SSA (m^2/g)	Sample	Depth (mbsf)	SSA (m^2/g)	Sample	Depth (mbsf)	SSA (m^2/g)
W19-1	120.70	24.85	W19-14	136.35	12.53	W19-27	156.20	13.96
W19-2	122.50	17.56	W19-15	137.60	13.89	W19-28	156.55	15.32
W19-3	122.70	14.83	W19-16	138.60	14.39	W19-29	157.90	15.63
W19-4	122.90	13.01	W19-17	140.20	22.59	W19-30	158.30	16.23
W19-5	124.50	13.44	W19-18	141.40	14.90	W19-31	158.50	14.68
W19-6	126.60	19.64	W19-19	145.20	12.27	W19-32	161.20	13.92
W19-7	126.80	19.28	W19-20	146.20	15.53	W19-33	162.80	12.11
W19-8	127.80	14.10	W19-21	146.35	14.75	W19-34	163.20	12.69
W19-9	128.10	18.96	W19-22	146.50	14.63	W19-35	163.70	13.22
W19-10	130.15	19.75	W19-23	147.20	17.22	W19-36	164.20	14.89
W19-11	135.60	15.25	W19-24	148.70	15.89	W19-37	166.00	15.99
W19-12	135.90	14.46	W19-25	149.00	18.08	W19-38	166.50	11.49
W19-13	136.10	13.03	W19-26	154.90	19.30	W19-39	167.10	14.08

TABLE 3 | The statistics data of gas hydrate saturation data.

Intervals	Depth Range (mbsf)	Gas Hydrate Saturation (sh%)*		
		Average	Max	Min
Non-GH layer	114.4–130.39	2.53	4.89	0.97
I-GHR layer	134–140	64.84	70.90	58.48
II-GHR layer	140–157.5	33.95	49.27	17.27
III-GHR layer	157.5–169.5	1.88	6.44	0.21

**The saturation of gas hydrates is calculated from Cl^- anomalies in the pore water of gas hydrates-bearing sediments, and it cited from voyage report of GMGS3.*

DISCUSSION

Gas Hydrate Saturation Variation Rule

The quantitative degassing of the pressure core provides the most accurate gas hydrate saturation. However, owing to the high cost of obtaining a pressure core, data on gas hydrate saturation with quantitative degassing of the pressure core are scarce. It is difficult to indicate the variation in gas hydrate saturation. The gas hydrate saturation estimated by the resistivity logs was continuous and independent of the sediment samples. However, resistivity logs have multiple solutions (Chand et al., 2004; Collett et al., 2012; Wang et al., 2014). The gas hydrate saturation estimated by the Cl^- anomalies of pore water in sediment is relatively accurate and relatively continuous (Lu and McMechan, 2002; Su et al., 2021). Meanwhile, the study of microstructures depends on the sediment sample, and it can be well matched with the gas hydrate saturation estimated by the Cl^- anomalies of the pore water in the sediment.

The gas hydrate saturation was very low in the upper part of the study interval, highest in the middle part, decreased with fluctuation, and was lower in the bottom part (**Figure 3**). Combined with the methane gas migration direction, the study interval was divided into upper and lower sections with 134 mbsf as the boundary. The upper section was the non-gas hydrate layer (114.4–130.39 mbsf). Furthermore, the lower section was the gas hydrate reservoir layer, which was subdivided into three layers according to the gas hydrate saturation: 1) I-gas hydrate reservoir (I-GHR) layer, where the gas hydrate saturation ranged from 58.48 to 70.90%, with an average of 64.84% (**Table 3**); 2) II-gas hydrate reservoir (II-GHR) layer, where the gas hydrate saturation ranged from 17.27 to 49.27%, with an average of 33.95% (**Table 3**); 3) III- gas hydrate reservoir (III-GHR) layer, where the gas hydrate saturation ranged from 0.21 to 6.44%, with an average of 1.88% (**Table 3**).

Microstructure in Different Gas Hydrate Reservoir Layers

The study of the sediment microstructure relied on SEM observations and CT scans. CT scans can directly display the microstructural features of sediment, particularly the size and distribution of pores (Jones et al., 2007; Bian et al., 2020; Wu et al., 2020). SEM observations can reveal more details of microstructural features, such as more accurate size, morphology, and sediment composition of pores (Bohrmann et al., 2007; Klapp et al., 2010; Oshima et al., 2019; Cai et al., 2020).

The SEM observation and CT scan results indicate that there are 1) intergranular pores between coarse grains (CG-intergranular pores), 2) intergranular pores between fine grains (FG-intergranular pores), and 3) biologic grain pores (BG-pores) in the study interval sediments (**Figure 5A**).

CG-intergranular pores occur between coarse grains such as quartz, feldspar, or foraminiferal fossils and have irregular pore shapes. They have pore sizes between 10 and 100 μm (**Figure 5B**). FG-intergranular pores occur between coarse grains, such as clay minerals. Their pore shape varies with the morphology of the clay mineral, while their pore size is typically less than 1 μm (**Figure 5C**). BG-pores consist of coeloms of foraminifera. Their pore shape is either spherical or ellipsoidal, while the pore size is commonly greater than 50 μm (**Figure 5D**).

The microstructural features of the sediments among the non-GH, I-, II-, and III-GHR layers were significantly different. In the non-GH layer, the CT scan showed that the sediment had massive structures with many FG-intergranular pores and a few CG-intergranular pores (**Figures 6A–C**). The BG-pores in the non-GH layer were specific, and many FG-intergranular pore

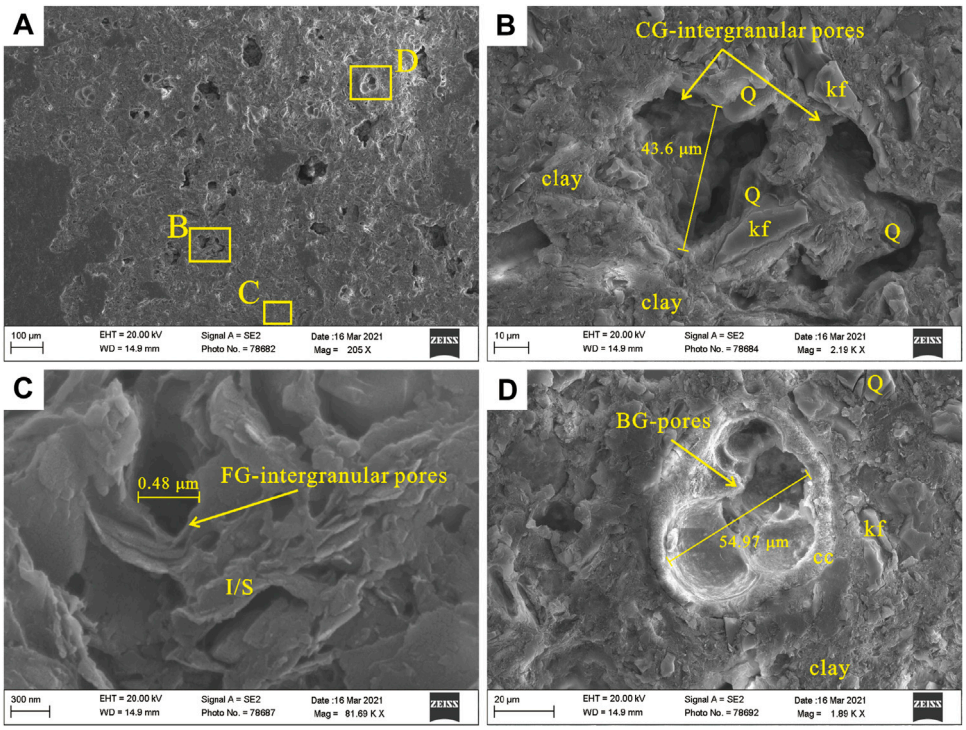

FIGURE 5 | Pores structure characteristics in gas hydrate reservoir. **(A)** Site W19, 136.10 mbsf, SEM image; **(B)**, **(C)**, and **(D)** enlarge the yellow box in figure **(A)**. Q, kf, cc, clay, and I/S are short for quartz, K-feldspar, calcite, clay minerals, and illite/semectite, respectively.

aggregates showed spherical BG-pore shapes visible in CT scan images (**Figures 6A–C**). The SEM observations confirmed that the BG-pores were filled with other components (**Figure 6D**).

In the I-GHR layer, the sediment microstructure was loose compared to the non-GH layer and had many CG-intergranular pores, BG-pores, and some FG-intergranular pores (**Figures 7A, B**). The SEM observations showed features similar to those observed in the CT scan (**Figures 7C, D**).

In the III-GHR layer, CG-intergranular pores and BG-pores were rare, while there were few FG-intergranular pores (**Figures 8A–C**). However, the clay fraction content in the III-GHR layer was not significantly different from those in the non-GH and I-GHR layers (**Figure 3**). This indicates that the structure of the clay minerals in the III-GHR layer was different from that in the non-GH and I-GHR layers.

In the II-GHR layer, some samples exhibited similar features to samples of the I-GHR layer (**Figures 9A, C**), while others exhibited similar features to those of the III-GHR layer (**Figures 9B, D**). Thus, the II-GHR layer acted as a transitional layer between the I-GHR and III-GHR layers, which is consistent with the wide range of gas hydrate saturation in the II-GHR layer (**Figure 3**).

Controlling Effects of Microstructure on Gas Hydrate Accumulation

The effect of the microstructure on gas hydrate accumulation is generally reflected in porosity and permeability (Jones et al., 2007; Klapp et al., 2010; Cai et al., 2020; Wang et al., 2020; Li et al., 2021). Previous studies have shown that large pores formed by coarser sediments are conducive to gas hydrate accumulation (Colwell et al., 2004; Boswell et al., 2009; Ito et al., 2015; Heeschen et al., 2016; Bian et al., 2020). The grain size of sediments does not affect the total porosity but may significantly affect the effective reservoir space and permeability (Wang et al., 2020). It may be difficult for extremely small pore spaces to form and accumulate gas hydrates owing to the migration ability of gas or pore water and capillary pressure (Brown and Ransom, 1996; Gamage et al., 2011; Li et al., 2021). Meanwhile, at the same porosity, more small pores lead to a significant decrease in sediment permeability (Brown and Ransom, 1996; Gamage et al., 2011; Oshima et al., 2019; Wu et al., 2020). Thus, a sediment layer with more CG-intergranular pores has more effective reservoir spaces and high permeability, which is beneficial for gas hydrate accumulation.

Many previous studies have shown that BG-pores consisting of foraminiferal coeloms can improve the quality of gas hydrate reservoirs, as foraminiferal coeloms are large and can thus provide additional effective reservoir space (Wang et al., 2011; Chen et al., 2013; Wang et al., 2014; Zhang et al., 2015; Li et al., 2019). In the I-, II-, and III-GHR layers, BG-pores gradually decreased, which is consistent with previous research results. However, according to **Figure 3**, the abundance of foraminifera was the highest in the non-GH layer, in contrast with previous research results. Meanwhile, BG-pore filling was verified both by SEM observations and CT scans (**Figure 6** and **Figure 10**). The filling components were clay minerals and many calcareous

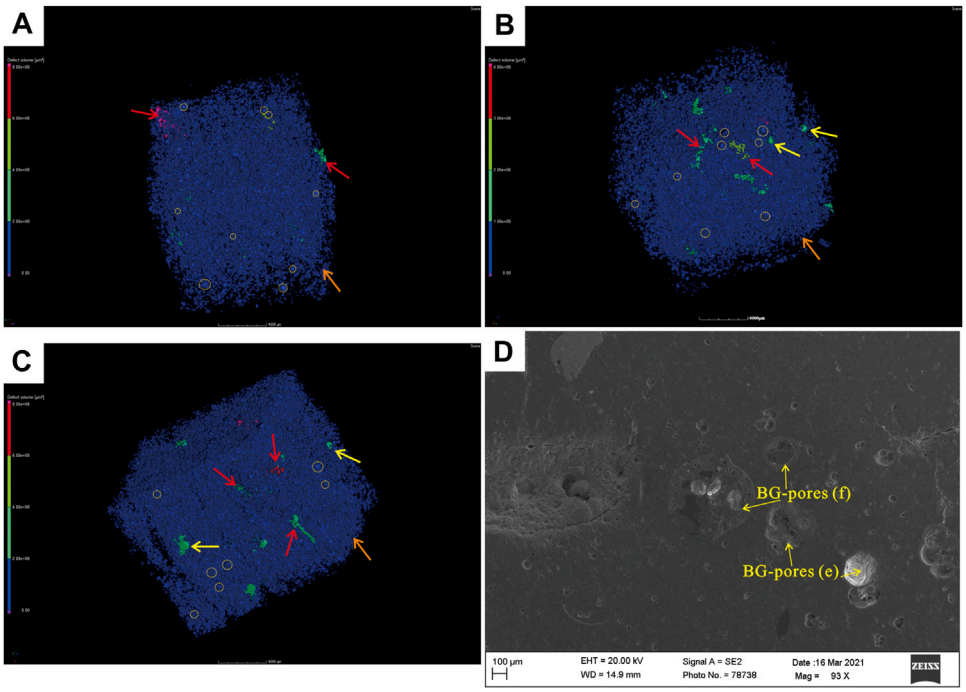

FIGURE 6 | Microstructure of sediments in the non-GH layer. **(A)** Site W19, 126.60 mbsf, CT scan image; **(B)** Site W19, 127.80 mbsf, CT scan image; **(C)** Site W19, 130.15 mbsf, CT scan image; **(D)** Site W19, 126.60 mbsf, SEM image; red arrows indicate CG-intergranular pores, yellow arrows indicate empty BG-pores (e), orange arrows indicate FG-intergranular pores; yellow dotted circle indicate filled BG-pores (f).

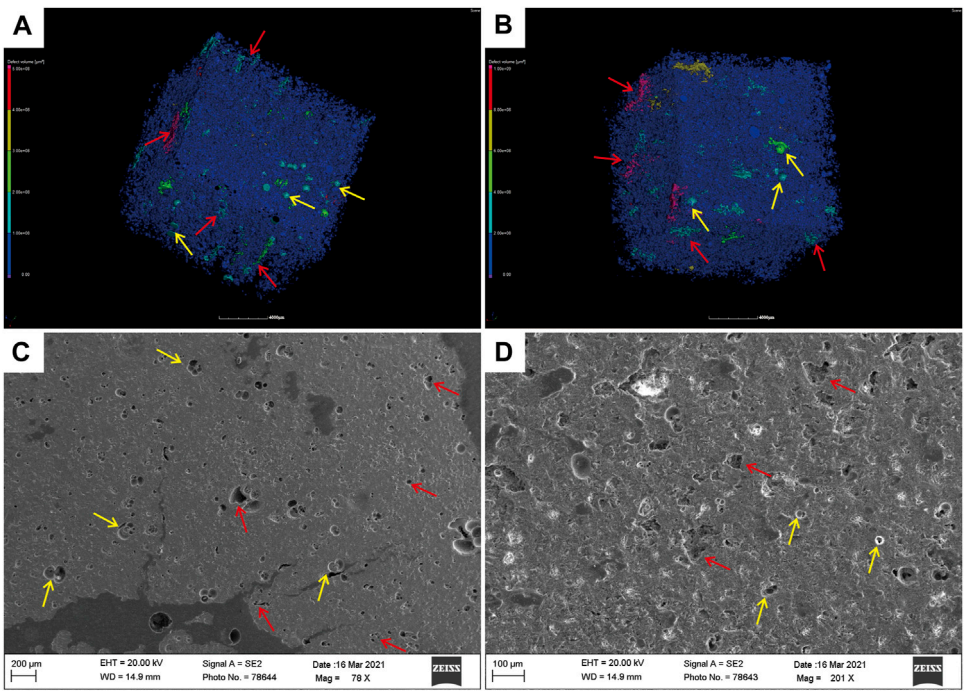

FIGURE 7 | Microstructure of sediments in the I-GHR layer. **(A)** Site W19, 137.60 mbsf, CT scan image; **(B)** Site W19, 138.60 mbsf, CT scan image; **(C)** Site W19, 130.70 mbsf, SEM image; **(D)** Site W19, 138.60 mbsf, SEM image; red arrows indicate CG-intergranular pores, yellow arrows indicate BG-pores.

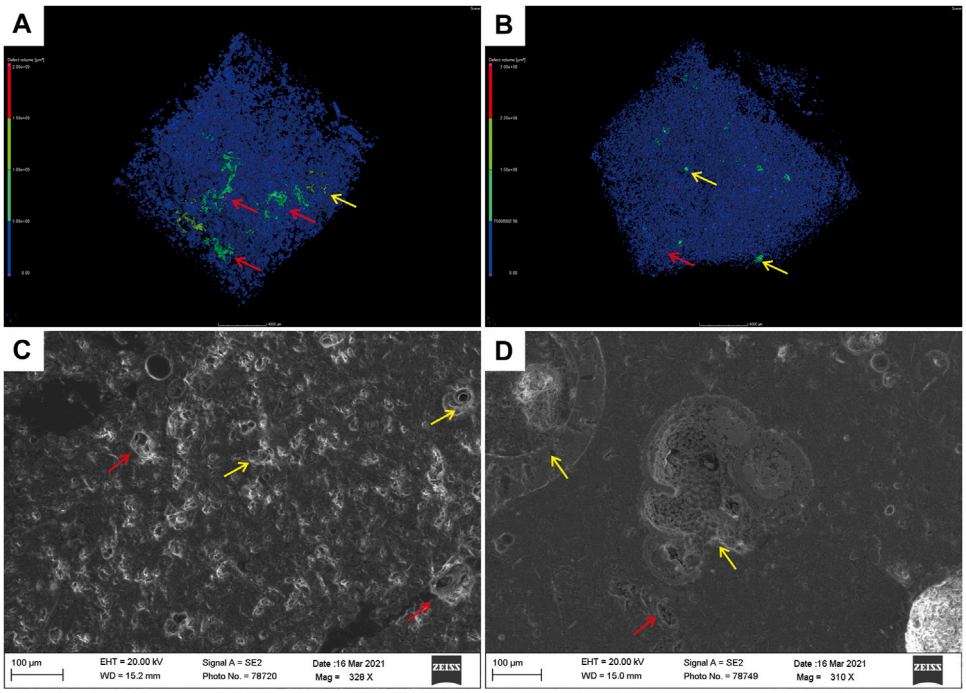

FIGURE 8 | (A) Site W19, 146.35 mbsf, CT scan image; **(B)** Site W19, 156.55 mbsf, CT scan image; **(C)** Site W19, 146.35 mbsf, SEM image; **(D)** Site W19, 156.55 mbsf, SEM image; red arrows indicate CG-intergranular pores, yellow arrows indicate BG-pores.

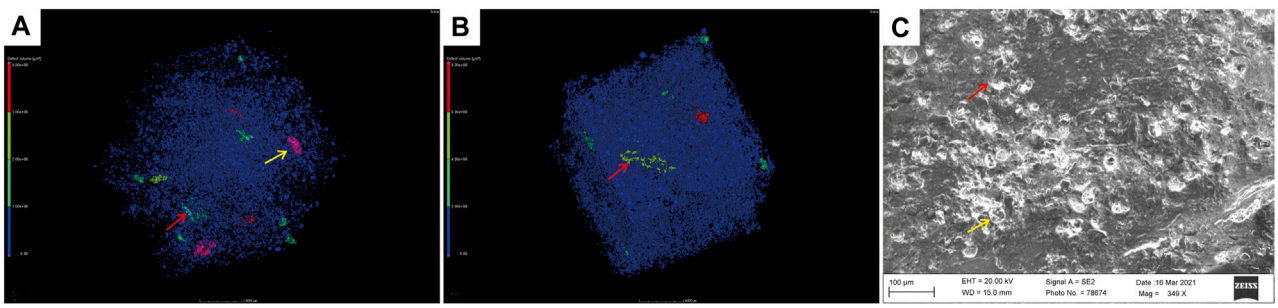

FIGURE 9 | (A) Site W19, 162.80 mbsf, CT scan image; **(B)** Site W19, 167.10 mbsf, CT scan image; **(C)** Site W19, 162.80 mbsf, SEM image; red arrows indicate CG-intergranular pores, yellow arrows indicate BG-pores.

ultramicrofossils (**Figure 10**). Calcareous ultramicrofossils have very small grain sizes (typically less than 2 μm) and clay fraction content. Thus, calcareous ultramicrofossils will reduce the effective reservoir space of the BG-pores and reduce the permeability of the sediment together with clay minerals.

The adsorption of methane by quartz and carbonates is significantly lower than that of clay minerals. The strong adsorption of methane by clay minerals is usually related to the complex structure and large SAA of clay minerals (Venaruzzo et al., 2002; Volzone et al., 2002; Ji et al., 2012). The SEM observations confirmed that the FG-intergranular pores were mainly clay minerals (**Figure 5C**). The microstructure of clay minerals controls the FG-intergranular pores. SSA is an effective parameter to characterize the microstructure of clay minerals (Dogan et al., 2006; Macht et al., 2011; Zhang Y. et al., 2019). Some studies have reported that the SSA is negatively correlated with gas hydrate saturation (Zhang et al., 2016; Zhang et al., 2017). The negative correlation between SSA and gas hydrate saturation may be determined by the clay mineral content and microstructure. The more complex microstructure of clay minerals leads to the formation of more FG-intergranular pores, affecting the permeability of sediment and the adsorption of free gas and pore water on sediments (Dogan et al., 2006; Gamage et al., 2011; Macht et al., 2011). The adsorption of free gas and pore water on sediments has potential significance for controlling gas hydrate formation. The weak adsorption capacity of sediments may make it difficult for free gas or pore water to remain in sediment and

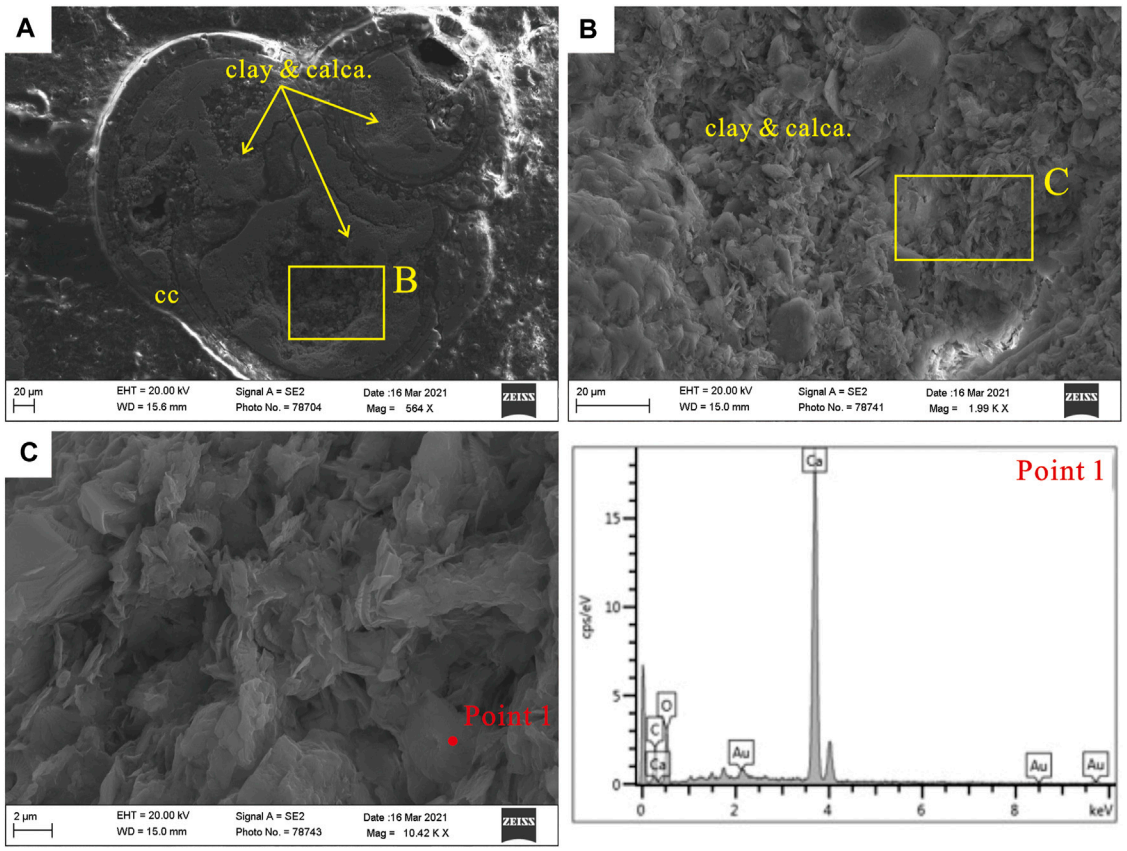

FIGURE 10 | Calcareous ultra-microfossils and clay minerals fill foraminifera coeloms. **(A)** Site W19, 126.60 mbsf, SEM image; **(B)** enlarge the yellow box in figure **(A)**; **(C)** enlarge the yellow box in figure **(B)**; cc and calca. are short for calcite and calcareous ultra-microfossils, respectively.

form gas hydrates. Conversely, the strong adsorption capacity of sediment may make it difficult for free gas or pore water to flow, thereby potentially acting as a sealing bed.

The *in-situ* porosity (calculated by LWD data) from the voyage report showed a sharp porosity drop in the I-GHR layer (**Figure 3**). The decreased porosity in the I-GHR layer is probably caused by gas hydrate enrichment. The porosity of the non-GH layer is not significantly higher than that of the underlying I-GHR layer. However, the abundance of the foraminifera in the non-GH layer is significantly higher than in the others. The high abundance of the foraminifera did not result in increased porosity. The saturation of gas hydrate in the non-GH layer is low (**Figure 3**) due to the BG-pores filling with calcareous ultramicrofossils and clay minerals. In the II- and III-GHR layers, the trend of porosity is consistent with that of gas hydrate saturation (**Figure 3**).

The CG-intergranular, FG-intergranular, and BG-pores were smaller in the III-GHR layer. The sediment in the III-GHR layer had low SSA. The reservoir space and adsorption capacity of the sediment were low and weak, respectively. After gas and water form and migrate to the III-GHR layer, it may be difficult to stay and no sufficient effective space to form the gas hydrate. The CT scan of samples shows FG-intergranular pores dominate the microstructure of the III-GHR layers (**Table 4**). The gas hydrate saturation of the CT scan samples in this layer is also very low (0.63–1.08%), indicating that the gas hydrate is not enriched. Hence, this layer may act as a gas migration channel (**Figure 11**). In the I-GHR layer, the sediments had many CG-intergranular pores and BG-pores (**Table 4**), indicating a more effective reservoir space and higher permeability (**Figure 11**). The CT scan samples" gas hydrate saturation in this layer is very high (58.48–62.89%). Thus, the gas hydrate had sufficient space and conditions to form and accumulate in the I-GHR layer. The II-GHR layer is a transition layer between the III- and I-GHR layers. The gas hydrate saturation of the CT scan samples in this layer (18.35–42.47%) is lower than in the I-GHR layer (**Figure 3** and **Table 4**). Sediments with microstructural features similar to the I-GHR layer are favorable for gas hydrate accumulation, and those similar to the III-GHR layer are unfavorable for gas hydrate accumulation (**Figure 11**). Although many BG-pores in the non-GH layer were filled, CG-intergranular pores were rare, making it difficult to form an effective reservoir space (**Figures 6**, **10**). Based on CT scan samples, the microstructure of sediments in the III-GHR layer is dominated by filled BG- and FG-intergranular pores (**Table 4**). The gas hydrate saturation of the CT scan samples in this layer is very low (1.45–3.41%). Meanwhile, the sediments in the non-GH layer had high SSA, which indicates that there were many FG-intergranular pores in

TABLE 4 | The microstructure types and gas hydrate saturation of samples.

Sample	Depth (mbsf)	Intervals	Dominated microstructure	Gas Hydrate Saturation (%)
W19-6	126.60	Non-GH layer	filled BG- and FG-intergranular pores	1.8
W19-8	127.80		filled BG- and FG-intergranular pores	1.45
W19-10	130.15		FG-intergranular pores	3.41
W19-14	136.35	I-GHR layer	CG-intergranular and BG-pores	62.89
W19-15	137.60		CG-intergranular and BG-pores	65.04
W19-16	138.60		CG-intergranular and BG-pores	58.48
W19-17	140.20	II-GHR layer	FG-intergranular pores	18.35
W19-21	146.35		FG- and CG-intergranular pores	34.4
W19-25	149.00		FG- and CG-intergranular pores	42.47
W19-28	156.35		FG- and CG-intergranular pores	33.45
W19-33	162.80	III-GHR layer	FG-intergranular pores	1.08
W19-39	167.10		FG-intergranular pores	0.63

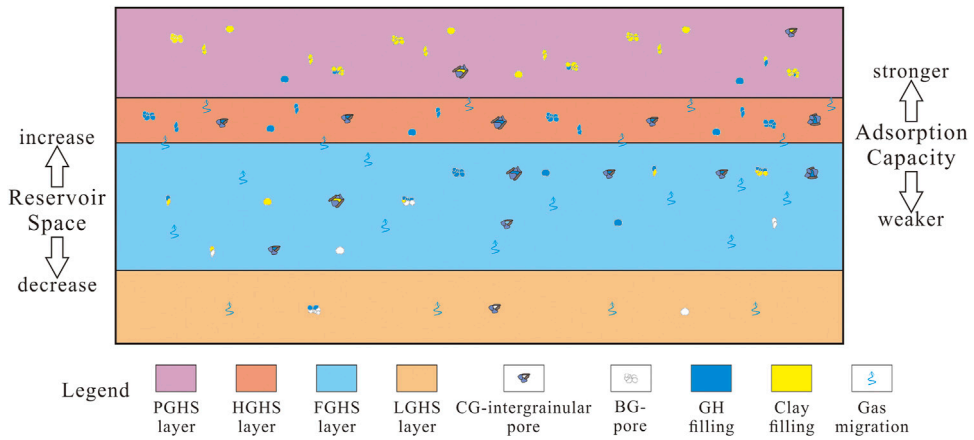

FIGURE 11 | Model of gas hydrate accumulation.

the sediment, thereby leading to low permeability and strong adsorption of the sediments and making free gas or pore water migration difficult (**Figure 11**). The sediment in the I- and III-GHR layers had the same low SSA, indicating a weak adsorption capacity for free gas or pore water. However, the non-GH layer overlying the I-GHR layer had strong adsorption capacity and lacked an effective reservoir space. Thus, free gas and pore water may accumulate in the I–GHR layer and form gas hydrates (**Figure 11**).

CONCLUSION

Based on the variation in gas hydrate saturation, the study interval was divided into non-GH, I-, II-, and III-GHR layers. Based on the SEM observations and CT scans, the study interval had three types of pores: CG-intergranular pores, FG-intergranular pores, and BG-pores.

The microstructure of the non-GH layer was dominated by FG-intergranular pores and had many filled BG-pores. The CG-intergranular and BG-pores dominated the microstructure of the I-GHR layer. All types of pores in the study interval were rare in the III-GHR layer; while the II-GHR layer represented a transition between the I-GHR and III-GHR layers.

The CG-intergranular and BG-pores can provide effective reservoir space and increase the permeability of sediment, which is conducive to gas hydrate accumulation. The FG-intergranular pores reduce permeability and are not conducive to gas hydrate accumulation. Clay minerals and calcareous ultramicrofossils with small grain sizes and complex microstructures fill the effective reservoir space and reduce the permeability of sediment. Clay minerals and calcareous ultramicrofossils improve the adsorption capacity of sediment to free gas or pore water, which is not conducive to gas hydrate formation and accumulation.

The non-GH layer sediment has strong absorption capacity and few effective pores, which inhibit the upward migration of free gas or pore water. The underlying I-GHR layer has high permeability and a more effective reservoir space. The superposition of the non-GH and I-GHR layers was conducive to the formation and accumulation of gas hydrates.

DATA AVAILABILITY STATEMENT

The original contributions presented in the study are included in the article/Supplementary Material, further inquiries can be directed to the corresponding author.

AUTHOR CONTRIBUTIONS

CB: complete work including theoretical development, editing and writing of the manuscript. PS: complete work including theoretical development, filed support, and modifying of the manuscript. XS: theoretical development and modifying of the manuscript. JG: samples preparation and analysis. HC: filed support and biological data analysis. SH: modifying of the manuscript. GZ: modifying of the manuscript.

FUNDING

Foundation of Hubei Key Laboratory of Marine Geological Resources (No. MGR202002). This works was supported by China Geological Survey Project (No. DD20190224), Chinese Fundamental Research Funds for the Central Universities (No. 2652019079) and Foundation of Hubei Key Laboratory of Marine Geological Resources (No. MGR202002).

ACKNOWLEDGMENTS

We would like to thank the Guangzhou Marine Geological Survey (GMGS) for allowing the data of this research to be shared. We wish to thank all those who contributed to the China National Gas Hydrate Program Expedition 3.

REFERENCES

Bai, C., Zhang, G., Lu, J. A., Liang, J., Yang, Z., Yan, W., et al. (2019). Deep-Water Sediment Waves as a Special Gas Hydrate Reservoirs in the Northeastern South China Sea. *Mar. Pet. Geol.* 101, 476–485. doi:10.1016/j.marpetgeo.2018.12.031

Bian, H., Xia, Y., Lu, C., Qin, X., Meng, Q., and Lu, H. (2020). Pore Structure Fractal Characterization and Permeability Simulation of Natural Gas Hydrate Reservoir Based on CT Images. *Geofluids* 2020, 1–9. doi:10.1155/2020/6934691

Bohrmann, G., Kuhs, W. F., Klapp, S. A., Techmer, K. S., Klein, H., Murshed, M. M., et al. (2007). Appearance and Preservation of Natural Gas Hydrate from Hydrate Ridge Sampled during ODP Leg 204 Drilling. *Mar. Geol.* 244, 1–14. doi:10.1016/j.margeo.2007.05.003

Boswell, R., and Collett, T. (2006). The Gas Hydrates Resource Pyramid: Fire in the Ice Newsletter. *U.S. DOE - office of Fossil Energy*, 5–7. Available at: https://www.researchgate.net/publication/240442367

Boswell, R., Frye, M., Shelander, D., Shedd, W., McConnell, D. R., and Cook, A. (2012). Architecture of Gas-Hydrate-Bearing Sands from Walker Ridge 313, Green Canyon 955, and Alaminos Canyon 21: Northern Deepwater Gulf of Mexico. *Mar. Petroleum Geol.* 34, 134–149. doi:10.1016/j.marpetgeo.2011.08.010

Boswell, R., Myshakin, E., Moridis, G., Konno, Y., Collett, T. S., Reagan, M., et al. (2019). India National Gas Hydrate Program Expedition 02 Summary of Scientific Results: Numerical Simulation of Reservoir Response to Depressurization. *Mar. Petroleum Geol.* 108, 154–166. doi:10.1016/j.marpetgeo.2018.09.026

Boswell, R., Shelander, D., Lee, M., Latham, T., Collett, T., Guerin, G., et al. (2009). Occurrence of Gas Hydrate in Oligocene Frio Sand: Alaminos Canyon Block 818: Northern Gulf of Mexico. *Mar. Petroleum Geol.* 26, 1499–1512. doi:10.1016/j.marpetgeo.2009.03.005

Brown, K. M., and Ransom, B. (1996). Porosity Corrections for Smectite-Rich Sediments: Impact on Studies of Compaction, Fluid Generation, and Tectonic History. *Geology* 24, 843. doi:10.1130/0091-7613(1996)024<0843:pcfsrs>2.3.co;2

Brunauer, S., Emmett, P. H., and Teller, E. (1938). Adsorption of Gases in Multimolecular Layers. *J. Am. Chem. Soc.* 60, 309–319. doi:10.1021/ja01269a023

Cai, J., Xia, Y., Lu, C., Bian, H., and Zou, S. (2020). Creeping Microstructure and Fractal Permeability Model of Natural Gas Hydrate Reservoir. *Mar. Petroleum Geol.* 115, 104282. doi:10.1016/j.marpetgeo.2020.104282

Chand, S., Minshull, T. A., Gei, D., and Carcione, J. M. (2004). Elastic Velocity Models for Gas-Hydrate-Bearing Sediments-A Comparison. *Geophys. J. Int.* 159, 573–590. doi:10.1111/j.1365-246X.2004.02387.x

Chen, F., Su, X., Lu, H., Zhou, Y., and Zhuang, C. (2013). Relations between Biogenic Component (Foraminifera) and Highly Saturated Gas Hydrates Distribution from Shenhu Area, Northern South China Sea. *Earth Sci.* 38, 907–915. (in Chinese with English abstract). doi:10.3799/dqkx.2013.089

Collett, T. S. (2002). Energy Resource Potential of Natural Gas Hydrates. *Bulletin* 86, 1971–1992. doi:10.1306/61EEDDD2-173E-11D7-8645000102C1865D

Collett, T. S., Lee, M. W., Zyrianova, M. V., Mrozewski, S. A., Guerin, G., Cook, A. E., et al. (2012). Gulf of Mexico Gas Hydrate Joint Industry Project Leg II Logging-While-Drilling Data Acquisition and Analysis. *Mar. Petroleum Geol.* 34, 41–61. doi:10.1016/j.marpetgeo.2011.08.003

Colwell, F., Matsumoto, R., and Reed, D. (2004). A Review of the Gas Hydrates, Geology, and Biology of the Nankai Trough. *Chem. Geol.* 205, 391–404. doi:10.1016/j.chemgeo.2003.12.023

Dogan, A. U., Dogan, M., Onal, M., Sarikaya, Y., Aburub, A., and Wurster, D. E. (2006). Baseline Studies of the Clay Minerals Society Source Clays: Specific Surface Area by the Brunauer Emmett Teller (BET) Method. *Clays Clay Min.* 54, 62–66. doi:10.1346/CCMN.2006.0540108

Dvorkin, J., Prasad, M., Sakai, A., and Lavoie, D. (1999). Elasticity of Marine Sediments: Rock Physics Modeling. *Geophys. Res. Lett.* 26, 1781–1784. doi:10.1029/1999GL900332

Gamage, K., Screaton, E., Bekins, B., and Aiello, I. (2011). Permeability-Porosity Relationships of Subduction Zone Sediments. *Mar. Geol.* 279, 19–36. doi:10.1016/j.margeo.2010.10.010

Ghosh, R., and Ojha, M. (2021). Amount of Gas Hydrate Estimated from Rock Physics Analysis Based on Morphology and Intrinsic Anisotropy in Area B, Krishna Godavari Offshore Basin, Expedition NGHP-02. *Mar. Petroleum Geol.* 124, 104856. doi:10.1016/j.marpetgeo.2020.104856

Haines, S. S., Hart, P. E., Collett, T. S., Shedd, W., Frye, M., Weimer, P., et al. (2017). High-Resolution Seismic Characterization of the Gas and Gas Hydrate System at Green Canyon 955, Gulf of Mexico, USA. *Mar. Petroleum Geol.* 82, 220–237. doi:10.1016/j.marpetgeo.2017.01.029

Heeschen, K. U., Schicks, J. M., and Oeltzschner, G. (2016). The Promoting Effect of Natural Sand on Methane Hydrate Formation: Grain Sizes and Mineral Composition. *Fuel* 181, 139–147. doi:10.1016/j.fuel.2016.04.017

Ito, T., Komatsu, Y., Fujii, T., Suzuki, K., Egawa, K., Nakatsuka, Y., et al. (2015). Lithological Features of Hydrate-Bearing Sediments and Their Relationship with Gas Hydrate Saturation in the Eastern Nankai Trough, Japan. *Mar. Petroleum Geol.* 66, 368–378. doi:10.1016/j.marpetgeo.2015.02.022

Ji, L., Zhang, T., Milliken, K. L., Qu, J., and Zhang, X. (2012). Experimental Investigation of Main Controls to Methane Adsorption in Clay-Rich Rocks. *Appl. Geochem.* 27, 2533–2545. doi:10.1016/j.apgeochem.2012.08.027

Jones, K. W., Kerkar, P. B., Mahajan, D., Lindquist, W. B., and Feng, H. (2007). Microstructure of Natural Hydrate Host Sediments. *Nucl. Instrum. Methods Phys. Res. Sect. B Beam Interact. Mater. Atoms* 261, 504–507. doi:10.1016/j.nimb.2007.03.032

Kang, D., Lu, J. a., Zhang, Z., Liang, J., Kuang, Z., Lu, C., et al. (2020). Fine-Grained Gas Hydrate Reservoir Properties Estimated from Well Logs and Lab Measurements at the Shenhu Gas Hydrate Production Test Site, the Northern Slope of the South China Sea. *Mar. Petroleum Geol.* 122, 104676. doi:10.1016/j.marpetgeo.2020.104676

Klapp, S. A., Bohrmann, G., Kuhs, W. F., Mangir Murshed, M., Pape, T., Klein, H., et al. (2010). Microstructures of Structure I and II Gas Hydrates from the Gulf of Mexico. *Mar. Petroleum Geol.* 27, 116–125. doi:10.1016/j.marpetgeo.2009.03.004

Koh, C. A., Sum, A. K., and Sloan, E. D. (2012). State of the Art: Natural Gas Hydrates as a Natural Resource. *J. Nat. Gas Sci. Eng.* 8, 132–138. doi:10.1016/j.jngse.2012.01.005

Lee, J.-S., Lee, J. Y., Kim, Y. M., and Lee, C. (2013). Stress-Dependent and Strength Properties of Gas Hydrate-Bearing Marine Sediments from the Ulleung Basin, East Sea, Korea. *Mar. Petroleum Geol.* 47, 66–76. doi:10.1016/j.marpetgeo.2013.04.006

Li, J.-F., Ye, J., Ye, J.-L., Qin, X.-W., Qiu, H.-J., Wu, N.-Y., et al. (2018). The First Offshore Natural Gas Hydrate Production Test in South China Sea. *China Geol.* 1, 5–16. doi:10.31035/cg2018003

Li, J., Lu, J. a., Kang, D., Ning, F., Lu, H., Kuang, Z., et al. (2019). Lithological Characteristics and Hydrocarbon Gas Sources of Gas Hydrate-Bearing Sediments in the Shenhu Area, South China Sea: Implications from the W01B and W02B Sites. *Mar. Geol.* 408, 36–47. doi:10.1016/j.margeo.2018.10.013

Li, X. S., Zhou, Q. J., Su, T. Y., Liu, L. J., Gao, S., and Zhou, S. W. (2016). Slope-Confined Submarine Canyons in the Baiyun Deep-Water Area, Northern South China Sea: Variation in Their Modern Morphology. *Mar. Geophys Res.* 37, 95–112. doi:10.1007/s11001-016-9269-0

Li, Y., Song, X., Wu, P., Sun, X., and Song, Y. (2021). Consolidation Deformation of Hydrate-Bearing Sediments: A Pore-Scale Computed Tomography Investigation. *J. Nat. Gas Sci. Eng.* 95, 104184. doi:10.1016/j.jngse.2021.104184

Liang, J., Zhang, G., Lu, J., Su, P., Sha, Z., Gong, Y., et al. (2016). Accumulation Characteristics and Genetic Models of Natural Gas Hydrate Reservoirs in the NE Slope of the South China Sea. *Nat. Gas. Ind.* 36, 157–162. (in Chinese with English abstract). doi:10.3787/j.issn.1000-0976.2016.10.020

Liang, J., Zhang, W., Lu, J. a., Wei, J., Kuang, Z., and He, Y. (2019). Geological Occurrence and Accumulation Mechanism of Natural Gas Hydrates in the Eastern Qiongdongnan Basin of the South China Sea: Insights from Site GMGS5-W9-2018. *Mar. Geol.* 418, 106042. doi:10.1016/j.margeo.2019.106042

Liu, C., Ye, Y., Meng, Q., He, X., Lu, H., Zhang, J., et al. (2012). The Characteristics of Gas Hydrates Recovered from Shenhu Area in the South China Sea. *Mar. Geol.* 307-310, 22–27. doi:10.1016/j.margeo.2012.03.004

Lu, S., and McMechan, G. A. (2002). Estimation of Gas Hydrate and Free Gas Saturation, Concentration, and Distribution from Seismic Data. *Geophysics* 67, 582–593. doi:10.1190/1.1468619

Macht, F., Eusterhues, K., Pronk, G. J., and Totsche, K. U. (2011). Specific Surface Area of Clay Minerals: Comparison between Atomic Force Microscopy Measurements and Bulk-Gas (N2) and -liquid (EGME) Adsorption Methods. *Appl. Clay Sci.* 53, 20–26. doi:10.1016/j.clay.2011.04.006

Malagar, B. R. C., Lijith, K. P., and Singh, D. N. (2019). Formation & Dissociation of Methane Gas Hydrates in Sediments: A Critical Review. *J. Nat. Gas Sci. Eng.* 65, 168–184. doi:10.1016/j.jngse.2019.03.005

Oshima, M., Suzuki, K., Yoneda, J., Kato, A., Kida, M., Konno, Y., et al. (2019). Lithological Properties of Natural Gas Hydrate-Bearing Sediments in Pressure-Cores Recovered from the Krishna-Godavari Basin. *Mar. Petroleum Geol.* 108, 439–470. doi:10.1016/j.marpetgeo.2019.01.015

Pohlman, J. W., Kaneko, M., Heuer, V. B., Coffin, R. B., and Whiticar, M. (2009). Methane Sources and Production in the Northern Cascadia Margin Gas Hydrate System. *Earth Planet. Sci. Lett.* 287, 504–512. doi:10.1016/j.epsl.2009.08.037

Popescu, I., De Batist, M., Lericolais, G., Nouzé, H., Poort, J., Panin, N., et al. (2006). Multiple Bottom-Simulating Reflections in the Black Sea: Potential Proxies of Past Climate Conditions. *Mar. Geol.* 227, 163–176. doi:10.1016/j.margeo.2005.12.006

Qian, J., Wang, X., Collett, T. S., Guo, Y., Kang, D., and Jin, J. (2018). Downhole Log Evidence for the Coexistence of Structure II Gas Hydrate and Free Gas below the Bottom Simulating Reflector in the South China Sea. *Mar. Petroleum Geol.* 98, 662–674. doi:10.1016/j.marpetgeo.2018.09.024

Qin, X., Liang, Q., Ye, J., Yang, L., Qiu, H., Xie, W., et al. (2020). The Response of Temperature and Pressure of Hydrate Reservoirs in the First Gas Hydrate Production Test in South China Sea. *Appl. Energy* 278, 115649. doi:10.1016/j.apenergy.2020.115649

Ryu, B.-J., Collett, T. S., Riedel, M., Kim, G. Y., Chun, J.-H., Bahk, J.-J., et al. (2013). Scientific Results of the Second Gas Hydrate Drilling Expedition in the Ulleung Basin (UBGH2). *Mar. Petroleum Geol.* 47, 1–20. doi:10.1016/j.marpetgeo.2013.07.007

Shao, L., Li, X., Geng, J., Pang, X., Lei, Y., Qiao, P., et al. (2007). Deep Water Bottom Current Deposition in the Northern South China Sea. *Sci. China Ser. D.* 50, 1060–1066. doi:10.1007/s11430-007-0015-y

Su, M., Luo, K., Fang, Y., Kuang, Z., Yang, C., Liang, J., et al. (2021). Grain-Size Characteristics of Fine-Grained Sediments and Association with Gas Hydrate Saturation in Shenhu Area, Northern South China Sea. *Ore Geol. Rev.* 129, 103889. doi:10.1016/j.oregeorev.2020.103889

Su, M., Sha, Z., Zhang, C., Wang, H., Wu, N., Yang, R., et al. (2017). Types, Characteristics and Significances of Migrating Pathways of Gas-bearing Fluids in the Shenhu Area, Northern Continental Slope of the South China Sea. *Acta Geol. Sin.* 91, 219–231. doi:10.1111/1755-6724.13073

Su, M., Yang, R., Wang, H., Sha, Z., Liang, J., Wu, N., et al. (2016). Gas Hydrates Distribution in the Shenhu Area, Northern South China Sea: Comparisons between the Eight Drilling Sites with Gas-Hydrate Petroleum System. *Geol. Acta* 14, 79–100. doi:10.1344/GeologicaActa2016.14.2.1

Tréhu, A., Ruppel, C., Holland, M., Dickens, G., Torres, M., Collett, T., et al. (2006). Gas Hydrates in Marine Sediments: Lessons from Scientific Ocean Drilling. *Oceanography* 19, 124–142. doi:10.5670/oceanog.2006.11

Venaruzzo, J. L., Volzone, C., Rueda, M. L., and Ortiga, J. (2002). Modified Bentonitic Clay Minerals as Adsorbents of CO, CO2 and SO2 Gases. *Microporous Mesoporous Mater.* 56, 73–80. doi:10.1016/S1387-1811(02)00443-2

Volzone, C., Rinaldi, J. O., and Ortiga, J. (2002). N2 and CO2 Adsorption by TMA- and HDP-Montmorillonites. *Mat. Res.* 5, 475–479. doi:10.1590/S1516-14392002000400013

Waite, W. F., Jang, J., Collett, T. S., and Kumar, P. (2019). Downhole Physical Property-Based Description of a Gas Hydrate Petroleum System in NGHP-02 Area C: A Channel, Levee, Fan Complex in the Krishna-Godavari Basin Offshore Eastern India. *Mar. Petroleum Geol.* 108, 272–295. doi:10.1016/j.marpetgeo.2018.05.021

Wang, J., Zhang, L., Ge, K., Zhao, J., and Song, Y. (2020). Characterizing Anisotropy Changes in the Permeability of Hydrate Sediment. *Energy* 205, 117997. doi:10.1016/j.energy.2020.117997

Wang, X., Collett, T. S., Lee, M. W., Yang, S., Guo, Y., and Wu, S. (2014). Geological Controls on the Occurrence of Gas Hydrate from Core, Downhole Log, and Seismic Data in the Shenhu Area, South China Sea. *Mar. Geol.* 357, 272–292. doi:10.1016/j.margeo.2014.09.040

Wang, X., Hutchinson, D. R., Wu, S., Yang, S., and Guo, Y. (2011). Elevated Gas Hydrate Saturation within Silt and Silty Clay Sediments in the Shenhu Area, South China Sea. *J. Geophys. Res.* 116, B05102. doi:10.1029/2010JB007944

Wu, P., Li, Y., Liu, W., Liu, Y., Wang, D., and Song, Y. (2020). Microstructure Evolution of Hydrate-Bearing Sands during Thermal Dissociation and Ensued Impacts on the Mechanical and Seepage Characteristics. *J. Geophys. Res. Solid Earth* 125, e2019JB019103. doi:10.1029/2019JB019103

Wu, S., Wang, X., Wong, H. K., and Zhang, G. (2007). Low-Amplitude BSRs and Gas Hydrate Concentration on the Northern Margin of the South China Sea. *Mar. Geophys Res.* 28, 127–138. doi:10.1007/s11001-007-9020-y

Yang, C., Lu, K., Liang, J., Lin, Z., Zhang, B., Liu, F., et al. (2020). Control Effect of Shallow-Burial Deepwater Deposits on Natural Gas Hydrate Accumulation in the Shenhu Sea Area of the Northern South China Sea. *Nat. Gas. Ind.* 40, 68–76. (in Chinese with English abstract). doi:10.3787/j.issn.1000-0976.2020.08.005

Yang, J., Wang, X., Jin, J., Li, Y., Li, J., Qian, J., et al. (2017). The Role of Fluid Migration in the Occurrence of Shallow Gas and Gas Hydrates in the South of the Pearl River Mouth Basin, South China Sea. *Interpretation* 5, SM1–SM11. doi:10.1190/INT-2016-0197.1

Yang, S., Liang, J., Lu, J., Qu, W., and Liu, B. (2017). New Understanding on the Characteristics and Controlling Factors of Gas Hydrate Reservoirs in the Shenhu Area on the Northern Slope of the South China Sea. *Earth Sci. Front.* 24 (4), 1–14. (in Chinese with English abstract). doi:10.13745/j.esf.yx.2016-12-43

Ye, J., Wei, J., Liang, J., Lu, J., Lu, H., and Zhang, W. (2019). Complex Gas Hydrate System in a Gas Chimney, South China Sea. *Mar. Petroleum Geol.* 104, 29–39. doi:10.1016/j.marpetgeo.2019.03.023

Yi, B. Y., Lee, G. H., Kang, N. K., Yoo, D. G., and Lee, J. Y. (2018). Deterministic Estimation of Gas-Hydrate Resource Volume in a Small Area of the Ulleung Basin, East Sea (Japan Sea) from Rock Physics Modeling and Pre-Stack Inversion. *Mar. Petroleum Geol.* 92, 597–608. doi:10.1016/j.marpetgeo.2017.11.023

Zhang, G., Liang, J., Lu, J. a., Yang, S., Zhang, M., Holland, M., et al. (2015). Geological Features, Controlling Factors and Potential Prospects of the Gas Hydrate Occurrence in the East Part of the Pearl River Mouth Basin, South China Sea. *Mar. Petroleum Geol.* 67, 356–367. doi:10.1016/j.marpetgeo.2015.05.021

Zhang, H., Lu, H., Liang, J., and Wu, N. (2016). The Methane Hydrate Accumulation Controlled Compellingly by Sediment Grain at Shenhu, Northern South China Sea. *Chin. Sci. Bull.* 61, 388–397. (in Chinese with English abstract). doi:10.1360/N972014-01395

Zhang, W., Liang, J., Lu, J. A., Wei, J., Su, P., Fang, Y., et al. (2017). Accumulation Features and Mechanisms of High Saturation Natural Gas Hydrate in Shenhu Area, Northern South China Sea. *Petroleum Explor. Dev.* 44, 708–719. doi:10.1016/S1876-3804(17)30082-4

Zhang, W., Liang, J., Wei, J., Lu, J. A., Su, P., Lin, L., et al. (2020). Geological and Geophysical Features of and Controls on Occurrence and Accumulation of Gas Hydrates in the First Offshore Gas-Hydrate Production Test Region in the Shenhu Area, Northern South China Sea. *Mar. Petroleum Geol.* 114, 104191. doi:10.1016/j.marpetgeo.2019.104191

Zhang, W., Liang, J., Wei, J., Su, P., Lin, L., and Huang, W. (2019a). Origin of Natural Gases and Associated Gas Hydrates in the Shenhu Area, Northern South China Sea: Results from the China Gas Hydrate Drilling Expeditions. *J. Asian Earth Sci.* 183, 103953. doi:10.1016/j.jseaes.2019.103953

Zhang, Y., Chen, T., Zhang, Y., and Ren, W. (2019b). Calculation Methods of Seepage Coefficient for Clay Based on the Permeation Mechanism. *Adv. Civ. Eng.* 2019, 1–9. doi:10.1155/2019/6034526

Conflict of Interest: The authors declare that the research was conducted in the absence of any commercial or financial relationships that could be construed as a potential conflict of interest.

Publisher's Note: All claims expressed in this article are solely those of the authors and do not necessarily represent those of their affiliated organizations, or those of the publisher, the editors and the reviewers. Any product that may be evaluated in this article, or claim that may be made by its manufacturer, is not guaranteed or endorsed by the publisher.

frontiers | Frontiers in Earth Science

BRIEF RESEARCH REPORT
published: 09 May 2022
doi: 10.3389/feart.2022.873615

Analysis of the Thermogenic Gas Source of Natural Gas Hydrates Over the Dongsha Waters in the Northern South China Sea

Changmao Feng, Guangjian Zhong*, Ming Sun, Zhenyu Lei, Hai Yi and Zhongquan Zhao*

Guangzhou Marine Geological Survey, Ministry of Natural Resources Key Laboratory of Mineral Resources, Guangzhou, China

Gas hydrates were newly discovered in the Dongsha Waters of the South China Sea by drilling in 2013 and 2019. The drilling results show that the hydrates consist of microbial gas and thermogenic gas, but the source layers of the thermogenic gas are not clear. The Chaoshan depression is the largest relict Mesozoic basin under the Dongsha Waters where thick T_3—K strata, up to 5000 m, have developed under thin Cenozoic sediments. The T_3—J_1 and J_3 bear the two main layers of hydrocarbon source rocks rich in II_2-III type organic matter, mainly in the western sag, the middle low bulge, and the eastern sag. The T_3—J_1 developed bathyal - neritic mud rocks, generally greater than 400 m in thickness. The J_3 mainly developed closed and semi-closed bay type mud, also II_2-III type. Nowadays these two layers are in their mature - over mature stages, thus potentially high-producing. There have developed deep faults cutting through the Mesozoic strata and distributing fractures within the Cenozoic sediments. Analysis of geochemical and geological samples dredged from the seabed indicates a significant oil and gas leakage activity well correlated spatially with the Mesozoic-associated faults. The association of fault-fractures can act as good channels for the thermogenic gas to move upward and diffuse into the temperature pressure stabilization zone of the hydrate. Thus, sufficient gas from the Mesozoic production layers is deemed the main source of thermogenic gas. The area where the Mesozoic faults are activated is the main leakage area of thermogenic gas, thus the main target for future hydrate exploration.

Keywords: chaoshan depression, the dongsha waters in the northern south china sea, mesozoic erathem, source of gas hydrate, gas channel by fault-fracture association

OPEN ACCESS

Edited by:
Zhifeng Wan,
Sun Yat-sen University, China

Reviewed by:
Yan Pin,
South China Sea Institute of Oceanology (CAS), China
Lijun Song,
Xi'an Shiyou University, China
HuiLiang Zhang,
PetroChina Hangzhou Research Institute of Geology, China

****Correspondence:***
Changmao Feng
fengchangm@163.com
Guangjian Zhong
2645078906@qq.com

Specialty section:
This article was submitted to Marine Geoscience, a section of the journal Frontiers in Earth Science

Received: *11 February 2022*
Accepted: *18 March 2022*
Published: *09 May 2022*

Citation:
Feng C, Zhong G, Sun M, Lei Z, Yi H and Zhao Z (2022) Analysis of the Thermogenic Gas Source of Natural Gas Hydrates Over the Dongsha Waters in the Northern South China Sea. Front. Earth Sci. 10:873615. doi: 10.3389/feart.2022.873615

INTRODUCTION

The northern part of the South China Sea has undergone more than 20 years of regional geological surveys. Rich hydrates have been discovered in the Shenhu and Dongsha survey areas, wholly in the Cenozoic Basins, in the northern South China Sea (Han et al., 2013; Su et al., 2014; Liang et al., 2016; Su et al., 2017; Zhang et al., 2017; Sha et al., 2019; He et al., 2020; Teng et al., 2020). Recently, hydrates (Zhong et al., 2020) have also been found in the Chaoshan depression, in a relict Mesozoic Basin in the Dongsha Waters, where the Cenozoic sequences are very thin while the Mesozoic strata is thick (Shao et al., 2007; Yang et al., 2008; Hao et al., 2009; Zhong et al., 2020). Although the hydrates found in the Dongsha Waters are similar in mixed biogenic and thermogenic compositions to the hydrates found elsewhere in the South China Sea, the

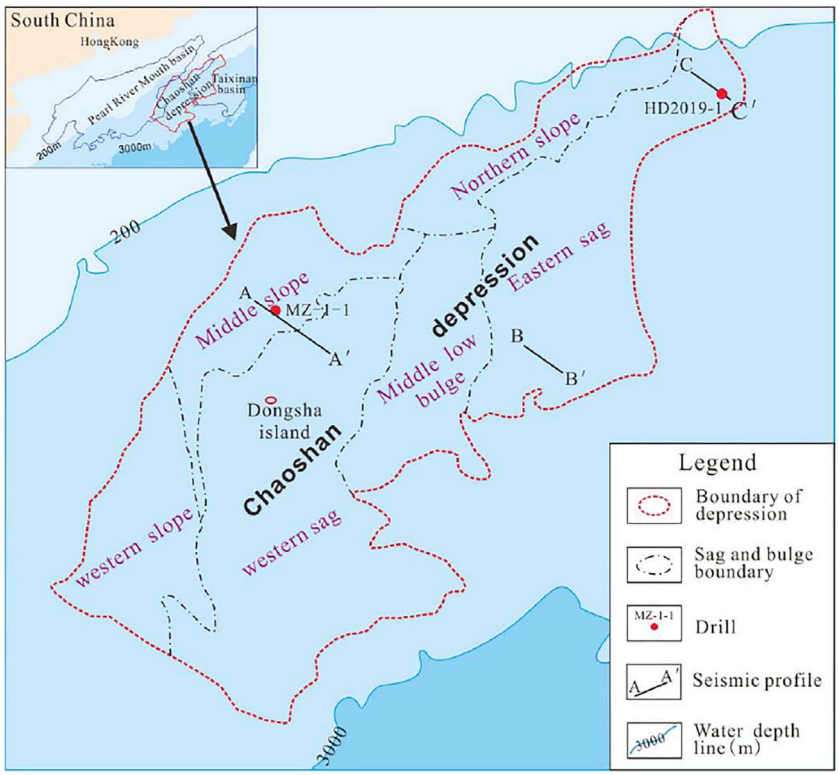

FIGURE 1 | Survey line location and tectonic division map of the Dongsha Waters in the northern South China Sea.

thermogenic gas in the lower part may not come from the Cenozoic layers as they are too thin (less than 1000 m) to produce enough thermogenic gas. With seismic and geochemical data, it is shown that the Mesozoic marine sedimentary layers are a potential source of the thermogenic gas. Hydrates and a high geochemical anomaly index indicate that gas seepage correlates well with the deep Mesozoic faults. Association of the deep fault in Mesozoic and shallow fracture in Cenozoic act as good transport passages. More hydrates can be expected from the Mesozoic source.

GEOLOGICAL OVERVIEW SETTING OF THE CHAOSHAN DEPRESSION

The Chaoshan depression is a Mesozoic Basin which lies in the Dongsha Waters in the northeast of the South China Sea, with an area of more than 37,000 km^2. The residual maximal thickness of Mesozoic sedimentary sequences is more than 5000 m (Zhong et al., 2020). It can be subdivided into six subordinate units, i.e., the eastern sag, the western sag, the middle low bulge, the northern slope, the middle slope, and the western slope (**Figure 1**). In September 2003, an exploration well (MZ-1-1) was drilled north of Dongsha Island. Although no hydrocarbon was shown, it confirmed the existence of thick Mesozoic sequences, including marine hydrocarbon source rocks and effective reservoir-cap combinations (Shao et al., 2007; Hao et al., 2009). The Chaoshan depression developed in the upper Triassic - lower Jurassic (T_3-J_1), middle Jurassic (J_2), upper Jurassic (J_3), and Cretaceous (K) (Qiang et al., 2018; Sun et al., 2018; Zhong et al., 2020). The T_3-J_1 is a set of neritic - bathyal depositions (Chen et al., 2005), the thickness is generally greater than 500 m, locally up to 3000 m. The J_2 is a set of neritic depositions, with thickness generally greater than 400 m, locally up to 1200 m. The J_3 is a set of neritic—bathyal depositions (Shao et al., 2007; Wu et al., 2007; Hao et al., 2009), 200–2500 m thick. The lower Cretaceous is a set of transitional facies depositions. The upper Cretaceous deposition has river-alluvial plain facies, lake facies to the north, and transitional facies to the south (Shao et al., 2007; Hao et al., 2009).

In 2013, the Guangzhou Marine Geological Survey (GMGS) conducted the first hydrate drilling exploration in the northeastern Chaoshan depression and obtained evidence of hydrates at 8 sites of the 13 drilling sites. The hydrates occur in various forms such as massive, lamellar, veined, and nodular and scattered (Zhang et al., 2015). In 2019, another well, HD 2019-1 (**Figure 1**), was successful again in drilling gas hydrates from 60 m below the seabed in the same area. The new sampled hydrates comprise rich thermogenic gas (Zhong et al., 2020). However, the details of the hydrates and the geology have been less reported. Given

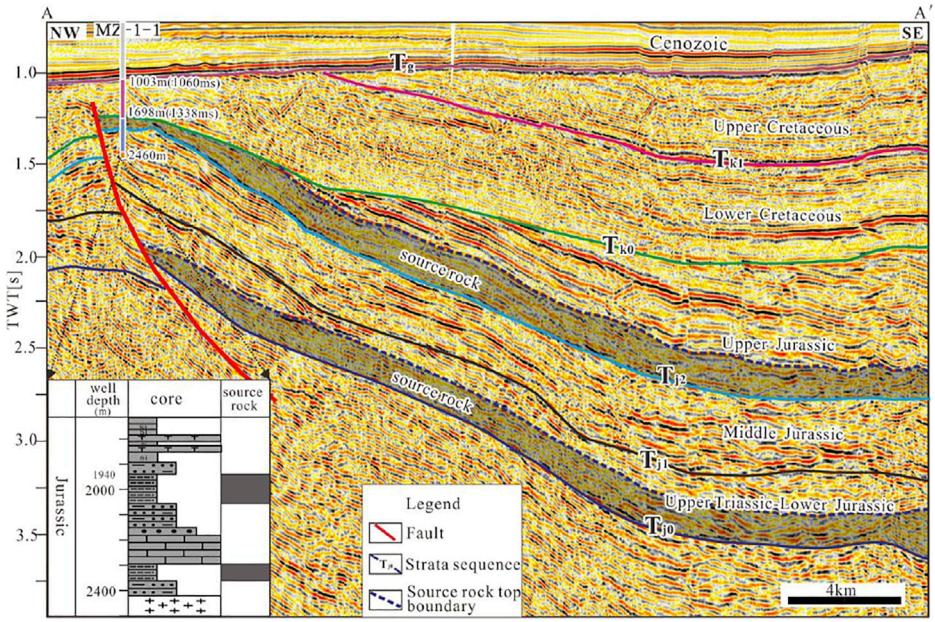

FIGURE 2 | (A,A′) Seismic section typical of the mud hydrocarbon source layers developed in the Chaoshan depression (see line position in **Figure 1**).

the thin Cenozoic sediments, the underlying thick Mesozoic is inferred as the potential gas source for the hydrates (Zhong et al., 2020). More than 20 years of geophysical and geochemical surveys enable analysis of the source.

DATA AND METHODS

GMGS has conducted extensive 2D multi-channel seismic and seafloor site sampling surveys over the Dongsha Waters. Up to now, the seismic grid density of the central and western parts of the Chaoshan depression has reached 16 km × 32 km, locally 2 km × 4 km, being coarser in the northeast boundary. The most-used 2D seismic streamer has 480 channels in 12.5 m spacing. The shooting spacing is 37.5 m using a source capacity of 5080 cubic inches. The coverage is up to 80 fold. The seismic profiles displayed later have been processed with routine industry procedures and pre-stacked time migration.

The seismic data were interpreted with the GeoFrame 2012 software platform. The formation is interpreted primarily based on correlation with the geologic exploration of the MZ-1-1 well (**Figure 2**) and seismic stratigraphic analysis. On this basis, combined with the reflection characteristics of productive mudstone on the seismic profile, data were traced by section, and time-depth-thickness was converted and mapped.

With the drill-seismic correlation, a basin simulation was carried out using IES Petromod software, and the distribution plan of the source rock Ro was mapped.

Site geochemical samples were collected in the central and southwestern Chaoshan depression with a grid of 8 km × 16 km. About 200 samples were selected for testing with items ranging from top air, top air heavy hydrocarbons, acid hydrolyzed hydrocarbons, acid hydrolyzed hydrocarbons, heavy hydrocarbons, fluorescence spectrum, altered carbonates, methane oxidizing bacteria, and butane oxidizing bacteria. The tests were carried out in Hefei Training and Testing Center of Sinopec Asset Management Co., Ltd. The indicators of the top air, top air heavy hydrocarbons, acid hydrolyzed hydrocarbons, altered carbonates, and methane oxidizing bacteria were selected and comprehensively analyzed. After normalization of these indicators, the Kriging and moving average methods were respectively used to map the comprehensive anomaly distribution of geochemical exploration.

RESULTS

Two Sets of Hydrocarbon Source Layers and Their Distributions

It was confirmed from the MZ-1-1 well that the Chaoshan depression had developed two sets of mainly hydrocarbon source rocks in the T_3-J_1 and bathyal—neritic and neritic facies in the J_3. The organic carbon content of the 1800–2000 m section of late Jurassic was 0.18–1.15%, the average was 0.67%, belonging to poor hydrocarbon source rock. The thickness of hydrocarbon source rock in the 2100 m–2400 m section of in the T_3-J_1 was 46.16 m, and the organic carbon content was 1.00–1.48%, with an average of 1.32%, belonging to medium hydrocarbon source rock. These two sets of hydrocarbon source rocks

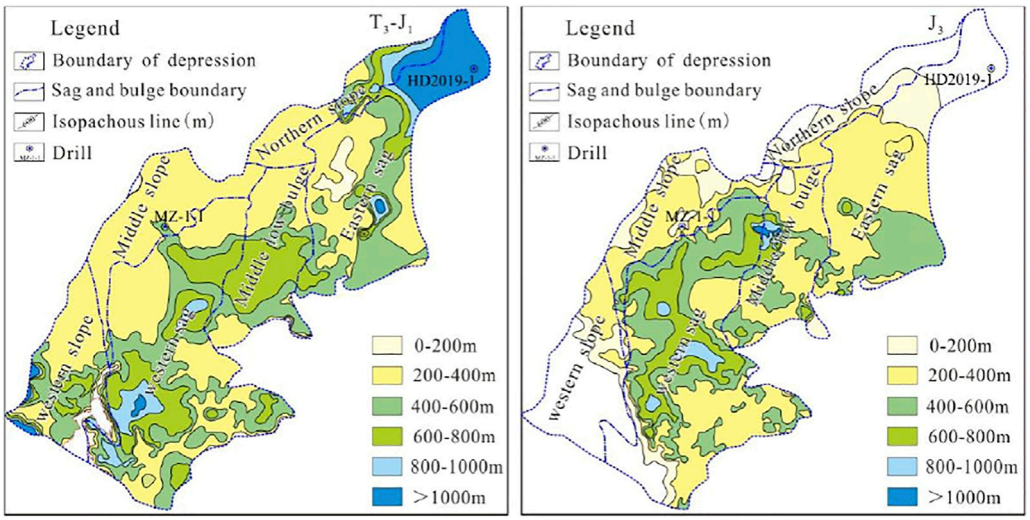

FIGURE 3 | Map of mud rock thickness of the two main hydrocarbon source layers in the Chaoshan depression.

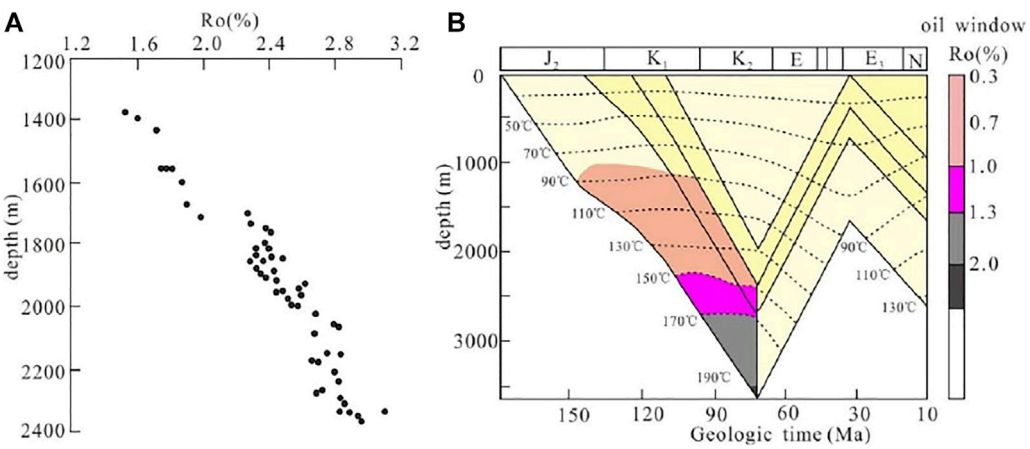

FIGURE 4 | Profile of the vitrinite reflectance and hydrocarbon generation history of the MZ-1-1 well (Yang et al., 2008). **(A)** Ro profile; **(B)** hydrocarbon generation history profile).

were of organic matter type II_2-III (Yang et al., 2008; Hao et al., 2009).

In the seismic section next to the MZ-1-1 well (**Figure 2**), the muddy rock layer featured medium-weak amplitude, weak continuous, and low—frequency or blank reflections. From interpretation of the seismic grid, both sets of source rocks thickened outward in various directions from the drilled high Mesozoic (**Figure 3**). The T_3-J_1 mudstone layer becomes much thick, larger than 1000 m to the northeast region of the eastern sag over where the HD2019-1 well was drilled. The J_3 mudstone layer also thickens, to generally 400–800 m, toward the middle low bulge and the western sag, prevailing in the NE-SW direction.

The mud hydrocarbon source rock of the J_3 mainly develops in the lower layer, its seismic facies characteristics are weak amplitude, medium-high frequency, medium-weak continuous, locally blank reflection, or chaotic reflection configuration (**Figure 2**), belonging to the bathyal-neritic deposition. This set of mud rock is distributed in the western sag, the middle low bulge, and the southern part of eastern sag, elongating in the NE-SW direction with stable thickness at about 400–800 m (**Figure 3**).

Maturity of Hydrocarbon Source Rock

Organic matter maturity is forwardly modeled based on seismic tying with the MZ-1-1 well where the hydrocarbon source rocks lie mostly below 1700 m. The maturity value, Ro, generally tends to increase sub-linearly with the formation depth from top to bottom (**Figure 4**), greater than 2.0% below 1700 m, and up to 3.0% at the bottom of the medium-upper

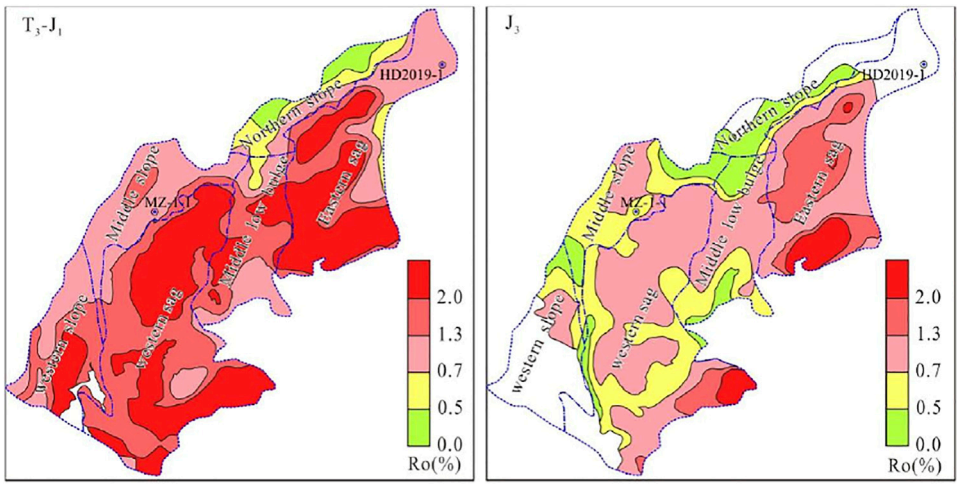

FIGURE 5 | Current Ro value distribution of the main hydrocarbon source rock of the Chaoshan depression.

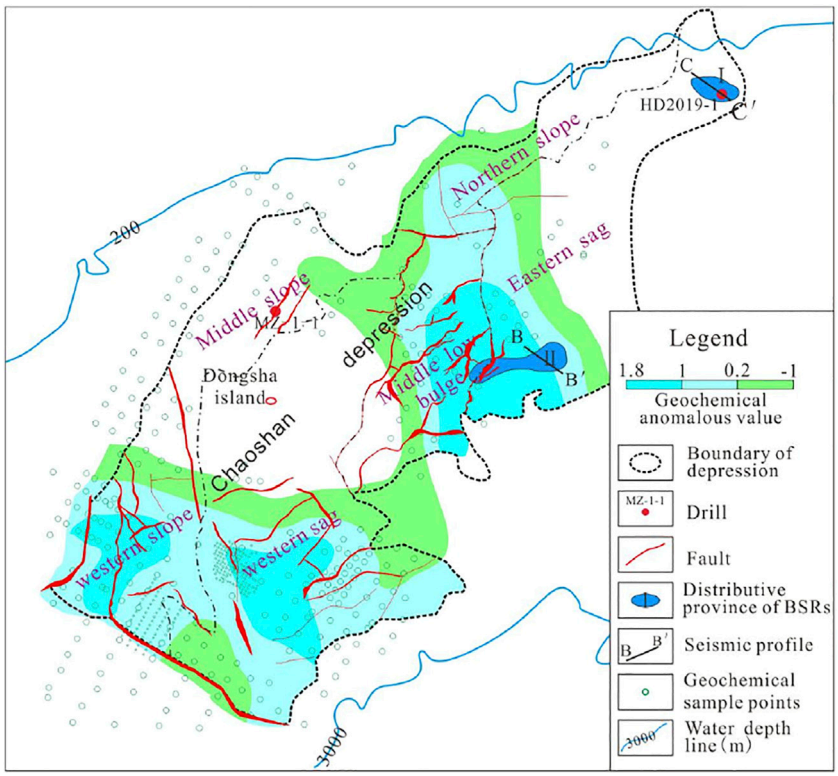

FIGURE 6 | Map of sample site and oil and gas geochemical anomalies, and Mesozoic faults in Chaoshan depression.

Jurassic (about 2400 m). The hydrocarbon source rock has entered the late phase of over mature (Yang et al., 2008). The middle-upper Jurassic source rock reached low maturity to the end of the late Jurassic period. The lower cretaceous reached the late hydrocarbon-generating stage in the middle of the late Cretaceous period (**Figure 4**).

On the plan view, the thickness of the T_3-J_1 hydrocarbon source rock increased with the formation deposition. Nowadays, except for the northern part of the northern slope and the eastern part of the eastern sag which are still in the immature-low mature stage (Ro<0.7%), the rest of the regions have entered the mature hydrocarbon-generating stage. Most of the western sag, the

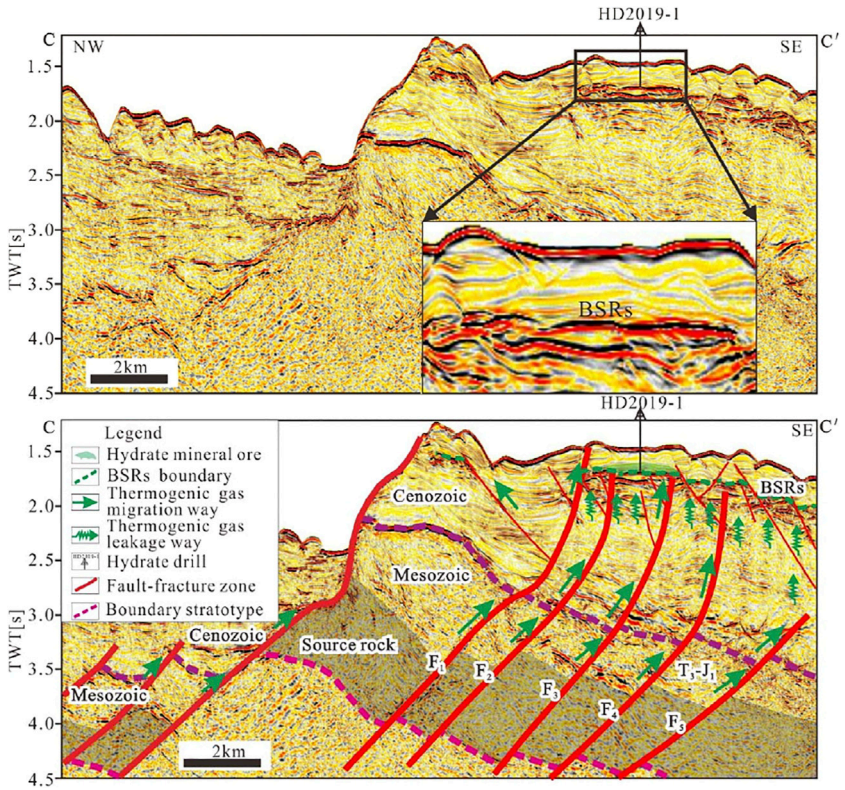

FIGURE 7 | (C,C′) profile hydrate accumulation pattern analysis graph (see line position in **Figure 1**).

southern part of the western slope, the southern-central part of the eastern sag, and the middle low bulge central regions are all entering the over mature stage (Ro>2.0%) (**Figure 5**).

Except in the western slope, J_3 hydrocarbon source rocks are in their immature stage in the middle slope, the northern slope, and the southern part of the middle low bulge; the low maturity-maturity stage is present in the other region. The central and southern part of the eastern sag and the southern part of the western sag enter into the gas generating stage (1.3% < Ro ≤ 2.0%), locally into the over mature stage (**Figure 5**). Therefore, the Chaoshan depression mainly developed two sets of hydrocarbon source rocks distributed in the NE-SW direction on the plane in T_3-J_1 and J_3. Most of the hydrocarbon source rocks are in their mature to over-mature stage nowadays. The potential for Mesozoic thermogenic gas generation is great.

Fault-Fracture Passage

The Mesozoic in the Chaoshan depression faulted mainly in three strikes: NE, near SN, and near EW (**Figure 6**). The faults can be recognized as two generations, one during the Mesozoic and another during the Cenozoic Era (**Figure 7**). The earlier one has offset the Mesozoic sequences, generally with small throws, resulting in fragmented, weak, and chaotic reflections of the Mesozoic sequences. While the young one has more distributed fractures with lasting activity from the Pliocene to the Quaternary, which leads to instability and blank reflections of the young sediments.

Widespread bottom simulating reflectors (BSRs) present the seismic profiles over the northeastern most corner of the Chaoshan depression, named as the NO. I BSR anomaly area, where the 2013 and 2019 drilling surveys were conducted with discoveries of hydrates. As an example, seismic profile C-C' (**Figure 7**) reveals that BSRs coincidently appeared above the fault-fracture zones, e.g., F_1, F_2, F_3, F_4, F_5, and others. The association of the fault deep into the Mesozoic and fractures within the shallow covering sediments form good channels for the thermogenic gas to migrate vertically upward and diffuse as a hydrate ore body as an expression of the BSRs.

Hydrocarbon Leakage

Submarine leakage of hydrocarbon leads to a geochemical anomaly on the seafloor. A quantified geochemical anomaly is calculated as described previously by normalization of five tested items over the sampled region. Its relative variation reflects the varying extent of hydrocarbon leakage.

Figure 6 shows that there are three obvious geochemical anomaly areas in the Chaoshan depression, i.e., in the western slope, the southern part of the western sag, and the junction area of the middle low bulge and the southern part of the eastern sag. They are potential areas of hydrocarbon leakage. Coincidently, these areas are distributed with numerous submarine mud

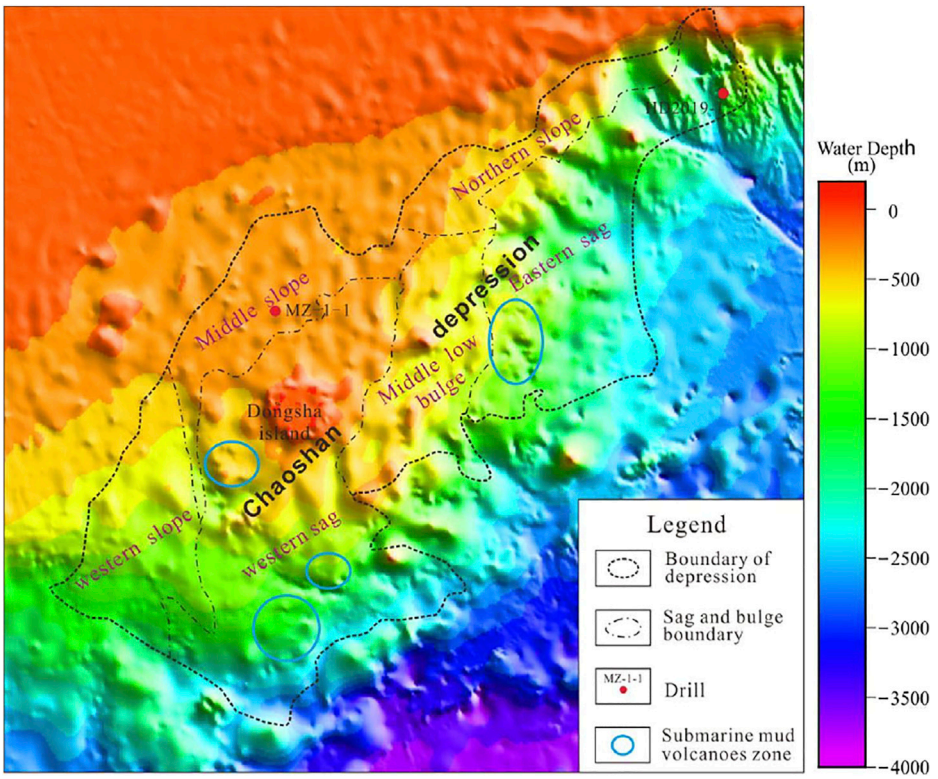

FIGURE 8 | Distribution map of the submarine mud volcanoes in the Dongsha Waters (mud volcanoes according to Yan et al., 2017; Yan et al., 2022).

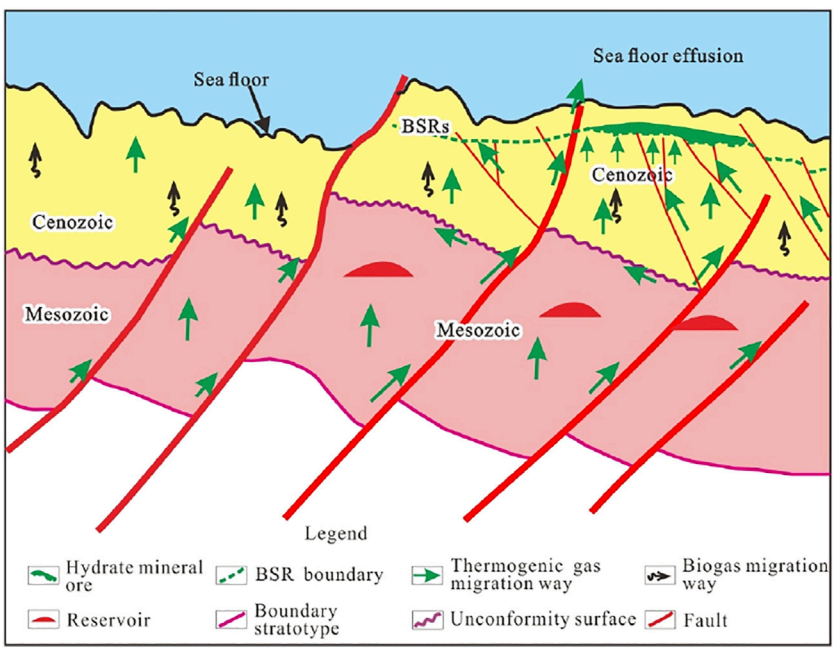

FIGURE 9 | The schematic model for gas hydrate accumulation in the Chaoshan depression.

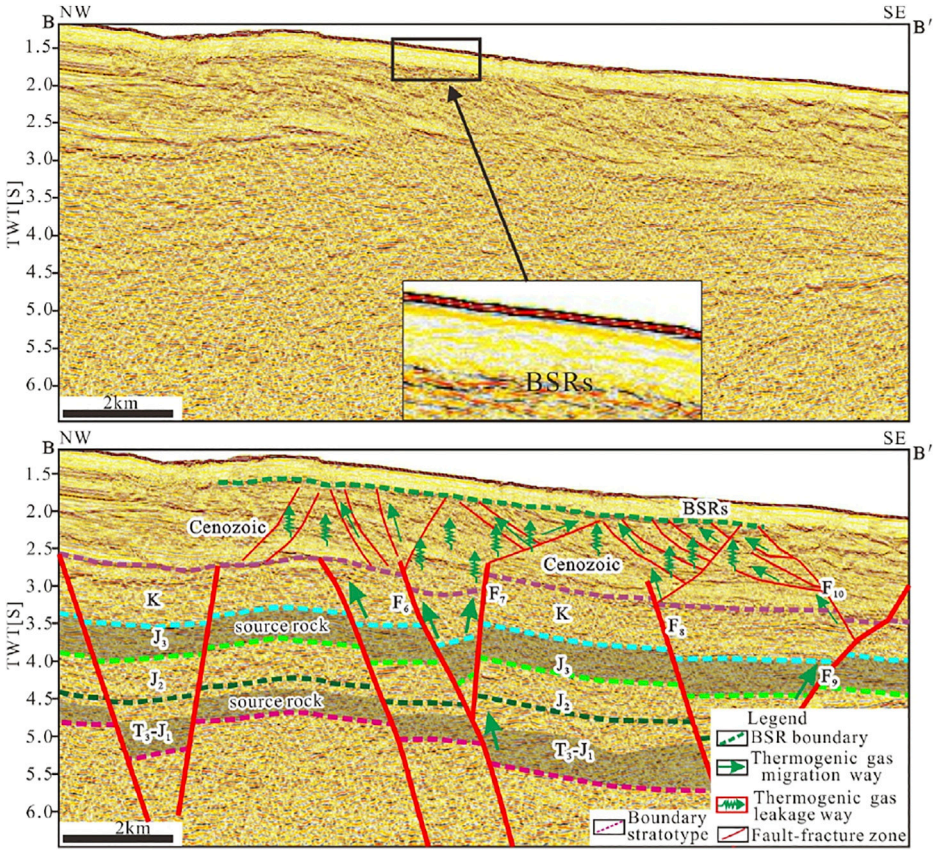

FIGURE 10 | (B,B′) profile hydrate accumulation pattern analysis graph (see line position in **Figure 1**).

volcanoes (**Figure 8**) which also usually indicates extensive leakage of oil and gas (Yan et al., 2017).

DISCUSSION

Accumulation Model of Hydrates Over the Dongsha Waters

The overlap map of the geochemical anomalous area and the Mesozoic fault distribution shows a clear correlation between them (**Figure 6**). The geochemical anomaly is often high over the fault zones.

Most of the mapped faults cut through the two sets of source rocks in the Mesozoic, and break to the Cenozoic. The Cenozoic in this area is thin, generally, less than 1000 m, and does not have the gas source foundation for the formation of thermogenic gas. Therefore, it can be concluded that the hydrate thermogenic gas in this area mainly comes from the Mesozoic.

The thermogenic gas in the lower part of the Chaoshan depression hydrate ore body in Dongsha Waters comes from the Mesozoic (**Figure 9**). The deep region's fault-fractures communicate the temperature and pressure stability region of the hydrate and the Mesozoic hydrocarbon source rock, and the deep thermogenic gas is migrated along the transport system to the overlying formation and mixed with the microbial gas, eventually forming hydrate. The fault plays a key role in the process of hydrate accumulation in the region. The Mesozoic fault development area is the main leakage area of thermogenic gas, and the gas source of thermogenic gas in this area is sufficient.

Prediction of Hydrate Development Area in the Dongsha Waters

Apart from the northeastern most corner of the Chaoshan depression, the junction area of the middle low bulge and the southern most part of the eastern sag (**Figure 6**) is also found with a large span of clearly visible BSRs (**Figure 10**) over where high organic carbon is seen from results of the geochemical survey (**Figure 6**). Here the Mesozoic sequences develop more completely, with the T_3- J_1, J_3 hydrocarbon source rock entering into a mature–over mature period. Similar fault-fractures, such as F_6, F_8, and F_9, cut deep to Mesozoic, and branch upward as F_7, F_{10}, and more fractures (**Figure 10**) connecting with them, forming well passages for the thermogenic gas to migrate upward to the Cenozoic. Moreover, abundant authigenic carbonate nodules and deep-water fauna, e.g., shells, coral, and sponges, are found from dredged samples over some of the mud volcanoes by the area, which implies vigorous leakage of hydrocarbon (Zhong et al., 2020; Yan et al., 2021). Given the gas leakage condition and appearance of BSRs, the junction area of the middle low bulge

and the southern most part of the eastern sag can be utilized as a future drilling target.

Implication of the Gas Source From Mesozoic

The oil and gas that leaked from the Mesozoic becomes the main source of thermogenic gas of the natural gas hydrate over the Dongsha Waters. The remaining hydrocarbon still can be traced through future exploration considering their wide distribution.

CONCLUSION

1) By regional correlation with previous drilling results of MZ-1-1, the Mesozoic source rocks are widely distributed over the Dongsha Waters, including the northeastern corner of the Chaoshan depression where hydrates were drilled. They source rocks are well matured to produce sufficient thermogenic gas contributing to hydrates.
2) Geochemical anomalies hinting at the micro-leakage of oil and gas from the deep are well correlated with zones of the Mesozoic fault-fractures which act as good transport channels for the thermogenic gas to leak and diffuse.
3) Enrichment of the Mesozoic thermogenic gas source in the gas hydrate is of great significance for hydrate and Mesozoic petroleum exploration.

DATA AVAILABILITY STATEMENT

The original contributions presented in the study are included in the article/Supplementary Material, further inquiries can be directed to the corresponding authors.

AUTHOR CONTRIBUTIONS

The author CF and GZ completed the main body of the paper. MS calculated the thickness map. Others participated in the preparation of the map.

ACKNOWLEDGMENTS

Three reviewers are thanked for their constructive comments and suggestions. This research was funded by the secondary project of China Geological Survey(DD20221860, DD20190212).

REFERENCES

Chen, B., Wang, J. L., Zhong, H. Z., and Hao, H. J. (2005). Geophysical Study of Pre-tertiary Basin Style of Chaoshan Sag in South China Sea. *J. Tongji Univ. (Natural Science)* 33, 1274–1280. Available at: https://kns.cnki.net/kcms/detail/detail.aspx?dbcode=CJFDanddbname=CJFD2005andfilename=TJDZ200509027andv=MTEyNDZZUzdEaDFUM3FUcldNMUZyQ1VSN2lmWStadUZ5bmhVcnJOTVNmUGRMRzRIdFRNcG85SFk0UjhlWDFMdXg=

Han, X. Q., Yang, K. H., and Huang, Y. Y. (2013). Origin and Nature of Cold Seep in Northeastern Dongsha Area, the South China Sea: Evidence from Chimney-like Seep Carbonates. *Chin. Sci. Bull.* 58, 1865–1873. doi:10.1007/s11434-013-5819-x

Hao, H. J., Lin, H. M., Yang, M. X., Xue, H. Y., and Chen, J. (2001). The Mesozoic in Chaoshan Depression: a New Domain of Petroleum Exploration. *China Offshore Oil and Gas* 15, 157–163. Available at: https://kns.cnki.net/kcms/detail/detail.aspx?dbcode=CJFDanddbname=CJFD2001andfilename=ZHSD200103000anduniplatform=NZKPTandv=zLQGLhpKClZwe3o6p34gwP_7lpX_oKnS1CUEXPkK4DgZnGtFENF231n3XTySl8PE

Hao, H. J., Shi, H. S., Zhang, X. T., Jiang, T. C., and Tang, S. L. (2009). Mesozoic Sediments and Their Petroleum Geology Conditions in Chaoshan Sag: a Discussion Based on Drilling Results from the Exploratory Well LF35-1-1. *China Offshore Oil and Gas* 21, 151–156. Available at: https://kns.cnki.net/kcms/detail/detail.aspx?dbcode=CJFDanddbname=CJFD2009andfilename=ZHSD200903001anduniplatform=NZKPTandv=9wmqc4yDGf7coDxOI3W_QlTzYls3Df4rmRD3rcgSXJ6mVS0tpm1c9YcwubOW7tUE

He, J. X., Yan, W., Zhu, Y. H., Zhang, W., Gong, F. X., Liu, S. L., et al. (2013). Biogenetic and Sub-biogenetic Gas Resource Potential and Genetic Types of Natural Gas Hydrates in the Northern Marginal Basins of South China Sea. *Nat. Gas Industry* 33, 121–134. doi:10.3787/j.issn.1000-0976.2013.06.023

He, J. X., Zhong, C. M., Yao, Y. J., Yan, P., Wang, Y. L., Wan, Z. F., et al. (2020). The Exploration and Production Test of Gas Hydrate and its Research Progress and Exploration prospect in the Northern South China Sea. *Mar. Geology. Front.* 36, 1–14. doi:10.16028/j.1009-2722.2020.127

Liang, J. Q., Zhang, G. X., Lu, J. A., Su, P. B., Sha, Z. B., Gong, Y. H., et al. (2016). Accumulation Characteristics and Genetic Models of Natural Gas Hydrate Reservoirs in the NE Slope of the South China Sea. *Nat. Gas Industry* 36, 157–162. doi:10.3787/j.issn.1000-0976.2016.10.020

Qiang, K. S., Zhang, G. X., Zhang, L., Lv, B. F., Zhong, G. J., Feng, C. M., et al. (2018). A Study of Depositional Characteristics of the Jurassic Strata in Chaoshan Sub-basin, Northern South China Sea, and its Control on Reservoir Beds. *Geology. China* 45, 48–58. doi:10.12029/gc20180105

Sha, Z. B., Xu, Z. Q., Fu, S. Y., Liang, J. Q., Zhang, W., Su, P. B., et al. (2019). Gas Sources and its Implications for Hydrate Accumulation in the Eastern Pearl River Mouth Basin. *Mar. Geology. Quat. Geology.* 39, 116–125. doi:10.16562/j.cnki.0256-1492.2019010902

Shao, L., You, H. Q., Hao, H. J., Wu, G. X., Qiao, P. J., and Lei, Y. C. (2007). Petrology and Depositional Environments of Mesozoic Strata in the Northeastern South China Sea. *Geol. Rev.* 53, 164–169. Available at: https://kns.cnki.net/kcms/detail/detail.aspx?dbcode=CJFDanddbname=CJFD2007andfilename=DZLP200702004anduniplatform=NZKPTandv=KltIONSOe0fHeETIqY1QtFzN1TPRFED6SFMbehBWY0zPARPbOucyyzYL0_ybZV6c

Su, P. B., Liang, J. Q., Fu, S. Y., Lv, W. J., and Gong, Y. H. (2017). Geological Background and Accumulation Models of Gas Hydrate Reservoir in Northern South China Sea. *Geology. China* 44, 415–427. doi:10.12029/gc20170301

Su, P. B., Sha, Z. B., Chang, S. Y., Liang, J. Q., and Fu, S. Y. (2014). Geological Models of Gas Hydrate Formation in the Eastern Sea Area of the Pearl River Mouth Basin. *Nat. Gas Industry* 34, 162–168. doi:10.3787/j.issn.1000-0976.2014.06.26

Sun, M., Ren, J. F., Zhong, G. J., and Yi, H. (2018). Fold Deformations of Mesozoic Strata and Their Genetic Mechanism in Southwestern Dongsha Waters of Northern South China Sea. *Geol. Rev.* 64, 828–842. doi:10.16509/j.georeview.2018.04.003

Teng, T. T., Su, X., Liu, H. D., Cui, H. P., Chen, F., Cheng, S. H., et al. (2020). Archaeal Diversity in Sediments of Core 973-5 from Deep-Sea Cold Seep, Dongsha Area in South China Sea. *Geoscience* 34, 104–116. doi:10.19657/j.geoscience.1000-8527.2019.009

Wu, G. X., Wang, R. J., Hao, H. J., and Shao, L. (2007). Microfossil Evidence for Development of Marine Mesozoic in the North of South China Sea. *Mar. Geology. Quat. Geology.* 27, 79–85. Available at: https://kns.cnki.net/kcms/detail/detail.aspx?dbcode=CJFDanddbname=CJFD2007andfilename=HYDZ200701014anduniplatform=NZKPTandv=scsCLrFrBHbYPzGMgb8QCrH1YG-7mzkQWmv96Wi81yBiPRhKLkUg3TlVwMTPPxI7

Yan, P., Wang, Y., Liu, J., Zhong, G., and Liu, X. (2017). Discovery of the Southwest Dongsha Island Mud Volcanoes amid the Northern Margin of the South China Sea. *Mar. Pet. Geology.* 88, 858–870. doi:10.1016/j.marpetgeo.2017.09.021

Yan, P., Wang, Y. L., Jin, Y. B., Zhao, M. X., and Zhong, G. J. (2021). Deep-water Coral of Multiple Benthal Strategies Discovered from mounds in the Dongsha

Waters in the South China Sea. *Earth Sci. Front.* doi:10.13745/j.esf.sf.2022.1.13

Yan, Y., Liao, J., Yu, J., Chen, C., Zhong, G., and Wang, Y. (2022). Velocity Structure Revealing a Likely Mud Volcano off the Dongsha Island, the Northern South China Sea. *Energies 15*, 195, 1–18 doi:10.3390/en15010195

Yang, S. C., Tong, Z. G., He, Q., and Hao, J. R. (2008). Mesozoic Hydrocarbon Generation History and Igneous Intrusion Impacts in Chaoshan Depression, South China Sea: a Case of LF35-1-1 Well. *China Offshore Oil and Gas* 20, 152–156. Available at: https://kns.cnki.net/kcms/detail/detail.aspx?dbcode=CJFDanddbname=CJFD2008andfilename=ZHSD200803002anduniplatform=NZKPTandv=PQDF9xpW_G1zCXbFA5lqpfH6NiGiKTabS1erksKv_rAVoUWu-zKPpXSC2LrtRUO3

Zhang, G., Liang, J., Lu, J. a., Yang, S., Zhang, M., Holland, M., et al. (2015). Geological Features, Controlling Factors and Potential Prospects of the Gas Hydrate Occurrence in the East Part of the Pearl River Mouth Basin, South China Sea. *Mar. Pet. Geology.* 67, 356–367. doi:10.1016/j.marpetgeo.2015.05.021

Zhang, W., Liang, J. Q., Lu, J. A., Wei, J. G., Su, P. B., Fang Y, X., et al. (2017). Accumulation Features and Mechanisms of High Saturation Natural Gas Hydrate in Shenhu Area, Northern South China Sea. *Pet. Exploration Develop.* 44, 670–680. doi:10.1016/s1876-3804(17)30082-4

Zhao, Z. Q., Sun, M., Wan, X. M., Chen, S. H., Zhao, J., Song, L. J., et al. (2020). The Application of Microbial Exploration Technology to the Oil and Gas Survey of Chaoshan Depression. *Geology. China* 47, 645–654. doi:10.12029/gc20200306

Zhong, G. J., Yan, P., Sun, M., Yu, J. H., Feng, C. M., Zhao, J., et al. (2020). Accumulation Model of Gas Hydrate in the Chaoshan Depression of South China Sea, China. *IOP Conf. Ser. Earth Environ. Sci.* 569, 1–12. doi:10.1088/1755-1315/569/1/012070

Conflict of Interest: The authors declare that the research was conducted in the absence of any commercial or financial relationships that could be construed as a potential conflict of interest.

Publisher's Note: All claims expressed in this article are solely those of the authors and do not necessarily represent those of their affiliated organizations, or those of the publisher, the editors and the reviewers. Any product that may be evaluated in this article, or claim that may be made by its manufacturer, is not guaranteed or endorsed by the publisher.

frontiers | Frontiers in Earth Science

ORIGINAL RESEARCH
published: 11 May 2022
doi: 10.3389/feart.2022.882701

Experimental Insights Into the *In Situ* Formation and Dissociation of Gas Hydrate in Sediments of Shenhu, South China Sea

Qian Zhang[1,2,3], *Xuwen Qin*[4,5], *Hong Zhang*[1,2,3], *Yanhui Dong*[1,2,3]*, *Cheng Lu*[4,5,6], *Shouding Li*[1,2,3], *Luokun Xiao*[1,2,3], *Chao Ma*[4,5] *and Hang Bian*[6,7]

[1]*Key Laboratory of Shale Gas and Geoengineering, Institute of Geology and Geophysics, Chinese Academy of Sciences, Beijing, China,* [2]*University of Chinese Academy of Sciences, Beijing, China,* [3]*Innovation Academy for Earth Science, Chinese Academy of Sciences, Beijing, China,* [4]*Guangzhou Marine Geological Survey, China Geological Survey, Guangzhou, China,* [5]*National Engineering Research Center of Gas Hydrate Exploration and Development, Guangzhou, China,* [6]*Center of Oil & Natural Gas Resource Exploration, China Geological Survey, Beijing, China,* [7]*School of Energy Resources, China University of Geosciences, Beijing, China*

Natural gas hydrates as sustainable energy resources are inherently affected by mineral surfaces and confined spaces in reservoirs. However, the habits of hydrates in geological sediments are still an open question. In this work, we systemically studied the process of hydrate formation and dissociation in sediments from the Shenhu area of the South China Sea to examine the evolution of hydrate saturation and permeability in sediments and their relationship. Characterization of samples indicates that sediments of the Shenhu area are mainly composed of clay and fine sand grains and provide a large number of nanopores for hydrate accumulation. For *in situ* observations enabled by low-field nuclear magnetic resonance methods, the formation of hydrates shows a different kinetic behavior with an induction time compared to hydrate dissociation. Estimated by variations of hydrate saturation (%) over time, the rate of hydrate formation is around 12%/min, while the dissociation rate increases to 3%/min with the higher temperature. With the presence of hydrates, pore space and thus permeability of sediments decreased obviously by one and three orders of magnitude when the hydrate saturation is 20 and 45%, respectively. Compared to models with the assumption of grain-coating and pore-filling hydrates, the tendency of permeability evolution from NMR measurements is between fitted lines from models. It highlights that the existing models considering a single pattern of hydrate growth cannot precisely describe the relationship between permeability and hydrate saturation. Hybrid hydrate habits coexist in sediments resulting from heterogeneous pore structures and thus complex gas–water distributions.

Keywords: gas hydrate, sediment, formation and dissociation, nuclear magnetic resonance, pore habit

OPEN ACCESS

Edited by:
Zhifeng Wan,
Sun Yat-sen University, China

Reviewed by:
Chao Fu,
China National Offshore Oil Corporation (China), China
Yanbin Yao,
China University of Geosciences, China

***Correspondence:**
Yanhui Dong
dongyh@mail.iggcas.ac.cn

Specialty section:
This article was submitted to Marine Geoscience, a section of the journal Frontiers in Earth Science

Received: *24 February 2022*
Accepted: *04 April 2022*
Published: *11 May 2022*

Citation:
Zhang Q, Qin X, Zhang H, Dong Y, Lu C, Li S, Xiao L, Ma C and Bian H (2022) Experimental Insights Into the In Situ Formation and Dissociation of Gas Hydrate in Sediments of Shenhu, South China Sea. Front. Earth Sci. 10:882701. doi: 10.3389/feart.2022.882701

INTRODUCTION

Gas hydrates are ice-like compounds composed of hydrogen-bound water molecules and low molecular weight gases that are stable at high pressure and low temperature. Natural gas hydrates (NGHs) are primarily distributed in permafrost and sediments and have attracted widespread attention as promising clean and sustainable energy resources (Sloan, 2003; Letcher, 2020). In

particular, the Shenhu area, located in the center of the northern continental slope of the South China Sea (SCS), has become a key target area for marine gas hydrate production with abundant NGH resources (Li et al., 2019).

The Shenhu area in the Pearl River Mouth Basin has sea knolls, submarine canyons, and erosion toughs, and obviously, seabed topography fluctuates with a water depth of 1000~1700 m (Wang et al., 2021). Previous studies indicate that the sea bottom of the Shenhu area has favorable conditions for hydrate formation with a temperature of 2~4°C, a pressure larger than 10 MPa, and the abundant thermogenic gas or biogenic gas for hydrate growth (Su et al., 2016; Liang et al., 2017; Li et al., 2019; Zhang et al., 2019). Moreover, geological bodies including slope fans, slumping blocks, and contour current sedimentation systems are conducive to the accumulation of hydrates. However, a comprehensive understanding of the reservoir characteristics and their impact on hydrate habits in this area is still an open question.

It is increasingly evident that properties of porous media play a critical role in the formation, dissociation, and occurrence of gas hydrates under natural conditions. Compared with homogeneous nucleation processes, hydrate formation can be promoted by the addition of porous media with regard to the lower activation energy, more nucleation sites, and the reduced potential barrier of nucleation (Prasad, 2015; Ghaedi et al., 2016; Andres-Garcia et al., 2019). Previous studies have paid attention to the particle size, distribution, composition of porous media, and their impacts on hydrate habits. In particular, the particle size is a key factor affecting mass transfer performance, hydrate phase equilibrium conditions, and thus the induction time of hydrate formation in geomaterials (Qin et al., 2021). Some scholars believed that the enhancement of heat and mass transfer in porous media with a large particle size facilitates the system to achieve supersaturation and nucleation, which results in a shorter induction time of hydrate (Kumar Saw et al., 2015; Liu et al., 2015). However, others believed that the reduction of induction time can be observed in systems with a smaller particle size because of the larger nucleation area, the greater variation in capillary pressure, and the stronger nucleation (Liu et al., 2015; Siangsai et al., 2015; Heeschen et al., 2016). To date, there is no uniform boundary between small and large particle size, and no consistent conclusion on the effect of the particle size on hydrate nucleation and growth (Qin et al., 2021). In marine sediments, different particle sizes and their ratio result in complex pore structures, which may complicate the processes of hydrate formation and dissociation. Therefore, further experimental investigation in terms of coupled factors regarding pore structural properties on hydrate habits is highly needed.

With the hydrate formation or dissociation, permeability in hydrate-bearing sediments varies subjected to pore structure evolution and has a profound impact on heat and mass transfer and the subsequent dynamics of hydrates (Wang, 2019; Li et al., 2020; Song et al., 2020). Previous studies have demonstrated that the evolution of permeability is highly controlled by sediment features and the saturation and pore habits of hydrate crystals (Ren et al., 2020; Wang et al., 2021; Lu et al., 2021a; 2021b). There are a lot of experimental results

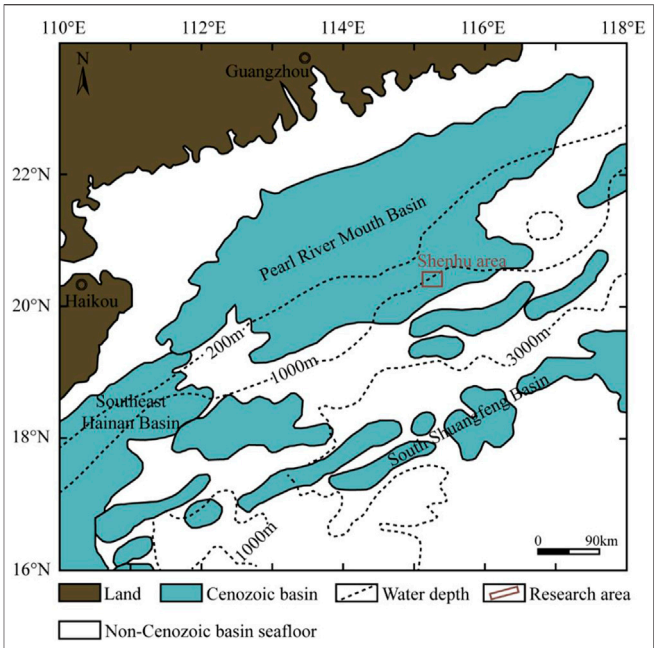

FIGURE 1 | Geological map of the Shenhu area and location of sites drilled. (Modified after Li et al., 2019; Wang et al, 2021).

about hydrate–saturation-dependent permeability in sediments, but the obvious discrepancy is observed as a result of differences in sample types, measurement methods, and experimental conditions (Kuang et al., 2020; Shen et al., 2020; Sun et al., 2021; Wen et al., 2021). Because of the absence of comparable experimental data, theoretical permeability models are developed to estimate the hydrate saturation and permeability relationship in sediments (Kleinberg, 2003; Mahabadi et al., 2016; Kossel et al., 2018). Most of the models are derived using simplified pore space, i.e., straight or tortuous capillary tubes, with the assumption of pore-filling or grain-coating hydrates in pores (Wang et al., 2021; Lei et al., 2022a). Apart from classic models, the hybrid model, modified Corey model, and cubic model are developed to address the hydrate-saturation-dependent permeability (Delli and Grozic, 2014; Lei et al., 2022a). Theoretical models usually include one or multiple uncertain parameters, which can be fitted by a variety of experimental results under different gas–water conditions. Various gas–water supply patterns complicate hydrate pore habits and limit the application of models for permeability prediction (Yin et al., 2018). In particular, gas hydrates mainly cement grain contacts under excess gas conditions, while tend to be as sediment frame components under excess water conditions (Delli and Grozic, 2014). Permeability usually decreases with increasing hydrate saturation; however, the permeability can vary several orders of magnitude regarding different sediment types and conditions even with identical hydrate saturation (Liang et al., 2011; Kang et al., 2016). A mechanistic understanding of permeability in hydrate-bearing sediments with regard to complex pore structure, gas–water conditions, and thus dynamic hydrate pore habits is still lacking.

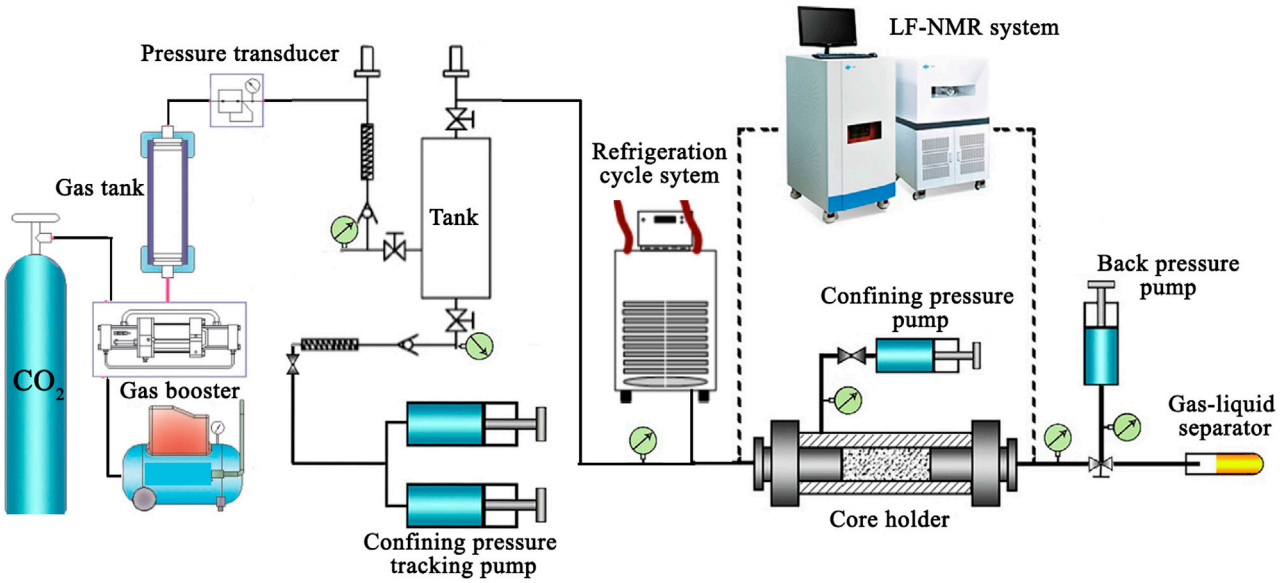

FIGURE 2 | Schematic diagram of the NMR experimental apparatus.

In this work, we focus on the dynamic properties of hydrates during the process of formation and dissociation in sediments of the Shenhu area to examine the hydrate pore habits in the complex porous system. The mineral composition, particle size, and pore size distribution of sediment samples were analyzed to reveal pore structure features. The *in situ* observations of hydrate dynamics were enabled by the low-field nuclear magnetic resonance (LF-NMR) method, which provides a fast and nondestructive way of detecting hydrogen-bearing fluids and has been widely used to measure the water saturation and permeability in hydrate-bearing sediments (Ji et al., 2019; Kuang et al., 2020; Wen et al., 2021). A comparison of permeability results from experiments and theoretical models was performed to examine the dynamic evolution of hydrate saturation and pore morphology in sediments of the Shenhu area. Further insights on favorable conditions for hydrate formation and model applicability are expected to provide.

MATERIALS AND METHODS

Samples

In this work, five representative sediment samples (i.e., W04-1 to W04-5) were acquired from the gas hydrate-bearing sediments in the Shenhu area (**Figure 1**). These samples were depressurized and stored after physical property measurements. For experiments on hydrate formation and dissociation, samples were initially evacuated and then saturated with distilled water at 12 MPa for 48 h.

Pore Structure Analysis of Samples

The characterization of mineral composition, particle size, and pore size was performed in this work. Mineralogical data were analyzed using the X-ray diffraction (XRD) method. The grain size analysis of sediment samples for the nano- or micrograins was performed using the Zetasizer Nano ZS90 particle size analyzer and HELOS-OASIS particle size analyzer, respectively. The ASAP 2460 instrument was used for N_2 adsorption measurements to determine pore size distributions of sediments.

In Situ Measurements of Gas Hydrates

Figure 2 shows a schematic of the LF-NMR monitoring apparatus, which was used to perform the *in situ* hydrate formation and dissociation experiments. The experimental apparatus system mainly comprises an LF-NMR analysis system, a core holder, a gas booster, a confining pressure tracking pump, a refrigeration cycle system, and the gas-liquid separator. The LF-NMR system is a Mini MR60 spectrometer with a magnetic field strength of 0.5 T and resonance frequency of 23 MHz. The confining pressure tracking pump is used to maintain certain confining pressure for CO_2 injection. The refrigeration cycle system contains a circulation pump for cooling the fluorocarbon oil to control the experimental temperature.

In experiments, all the sediment samples were enclosed with heat-shrink tubing as a core with a length of 3.9 cm and a diameter of 2.5 cm. They were saturated with distilled water in the core holder, and then the CO_2 was injected into the core holder with a constant flux until the water was displaced to specific content. The outlet valve of the core holder was then closed, and the CO_2 supplement was enabled by a high-pressure pump to maintain the pore pressure at 4 MPa. During the process, some gases dissolved in water across gas–water interfaces. *In situ* NMR measurements started with decreasing temperature. Temperature controlled by the refrigeration cycle system decreased at a speed of 0.01°C/min from room

temperature to 4°C and then kept stable until the end of hydrate formation. Then, the temperature increased at a speed of 0.02°C/min to 15°C for the hydrate dissociation. Gas permeability of the core was measured before and after the experiment. NMR measurements were performed using the Carr–Purcell–Meiboom–Gill (CPMG) pulse sequence during the experiment. Parameters of the CPMG pulse sequence included the echo number of 18,000, echo spacing of 0.15 ms, and waiting time of 1,000 ms.

Calculation of Hydrate Saturation and Permeability

The cumulative value of NMR signal intensity can quantify the water content and volume fraction in porous media, and the transverse relaxation time (T_2) of water, proportional to the surface-to-volume ratio (S/V), can be used to evaluate the pore structure (Ji et al., 2019). For CO_2 hydrate (CO_2·5.75 H_2O) formation and dissociation, the volume of CO_2 hydrate (V_h) can be calculated by water reduction as follows:

$$V_h = \frac{m_h}{\rho_h} = \frac{\frac{m_{wd}}{18 \times 5.75}(44 + 18 \times 5.75)}{\rho_h}, \quad (1)$$

where m_h is the mass of CO_2 hydrate, m_{wd} is the mass reduction of water, and ρ_h is the density of CO_2 hydrate. CO_2 hydrate saturation is the ratio of hydrate volume and pore volume.

The evolution of permeability subject to hydrate saturation is estimated by experimental data and theoretical models. The SDR method is usually used to calculate permeability from NMR data. It is based on the measured T_2 distribution being a pseudo-pore size distribution during hydrate formation or dissociation. **Eqn. 2** is described as follows:

$$K_{SDR} = C\varnothing^4 T_{2gm}^2, \quad (2)$$

where K is the permeability, Φ is the porosity (%), and T_{2gm} is the logarithmic mean of T_2 distribution (mD). The parameter C in the model is estimated by NMR measurements with known porosity and permeability of samples.

Theoretical permeability models differ from each other by using various assumptions of hydrate pore habits. The parallel capillary model, Kozeny grain model, and Masuda model are used in this paper.

1) Parallel capillary model (Kleinberg, 2003).

This model describing porous media as a bundle of straight, parallel cylindrical capillaries was developed by Kleinberg (2003). In this model, hydrate forms in the center of cylindrical pores, uniformly coating the walls of capillary. With the increase in hydrate saturation, an annular flow path is left for fluid. For the hydrate coating capillary walls model, the permeability can be calculated using **Eqn. 3**:

$$K(S_h) = K_0(1 - S_h)^2, \quad (3)$$

where K_0 is the permeability before hydrate formation and S_h is the hydrate saturation. If hydrate occurs in the center of the capillary model, **Eqn. 4** is used:

$$K(S_h) = K_0\left(1 - S_h^2 + \frac{2(1 - S_h)^2}{\ln(S_h)}\right). \quad (4)$$

2) Kozeny grain model (Spangenberg, 2001).

Spangberg (2001) assumed porous media as Kozeny grain models and hydrate distribution patterns of both coating the grains and occupying pore centers can be calculated. For the former pattern, the permeability is evaluated as shown in **Eqn. 5**:

$$K(S_h) = K_0(1 - S_h)^{n+1}, \quad (5)$$

where the saturation exponent n is 1.5 for $0 < S_h < 0.8$. When $S_h > 0.8$, the saturation exponent diverges. **Eqn. 6** is used to calculate the permeability when hydrate occupies the center of the pore, $n = 0.7S_h + 0.3$:

$$K(S_h) = K_0\frac{(1 - S_h)^{n+2}}{\left(1 + S_h^{0.5}\right)^2}. \quad (6)$$

3) Masuda model.

Masuda model (Masuda et al., 1997) is commonly applied to interpret the relationship between permeability and hydrate saturation as **Eqn. 7**:

$$K(S_h) = K_0(1 - S_h)^N, \quad (7)$$

where N with regard to pore structure is the permeability decreasing index and changes from 2 to 15 (Kumar et al., 2010).

PORE STRUCTURE CHARACTERISTICS OF SEDIMENTS

Mineral Composition Analysis

The XRD analysis of sediment samples shows that the predominant minerals are quartz (30.9%~37.0 wt. %), carbonate minerals (22.8%~30.8 wt. %), and mica (13.6~31.6 wt. %) and are followed by clay minerals. The lower contents of clay minerals were determined in this work compared to previous studies (Li et al., 2019; Wang et al., 2021), which reported the weight percent of clay minerals high to 40% for samples from the SCS.

Grain Size Analysis

The results of the grain size analysis show similar properties of particle size distributions for five sediment samples. The frequency curves of all the samples are unimodal (**Figure 3**) and negatively skewed, with peak values varying over a broad range of 20~40 um (**Figure 3B**). In particular, the median grain size of W04-1, W04-2, W04-3, W04-4, and W04-5 is 5.47, 18.57, 17.09, 11.84, and 17.48 um, respectively. It indicates that the sediments from the SCS mainly comprise clay (< 4 μm) and fine sand grains (4~64 μm). Particle size distributions of nanosized grains also highlight the grains of samples are very fine. The frequency curves are also unimodal with a range of 396~1,106 nm, and peak values of curves vary from 600 to 800 nm (**Figure 3A**).

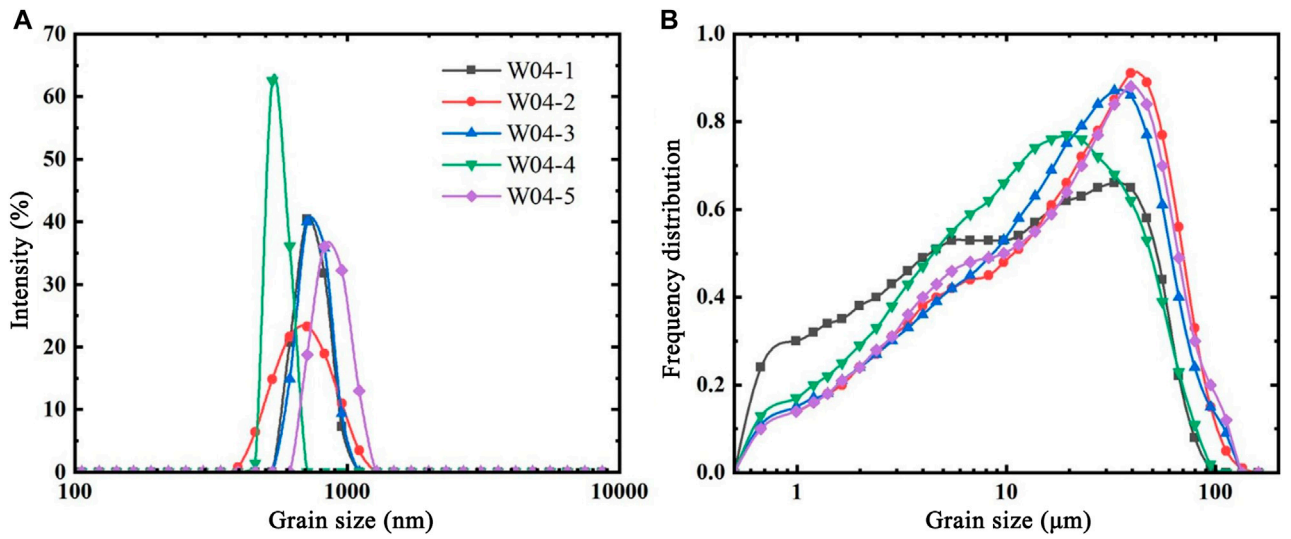

FIGURE 3 | Frequency distribution curves of the particle size of sediment samples.

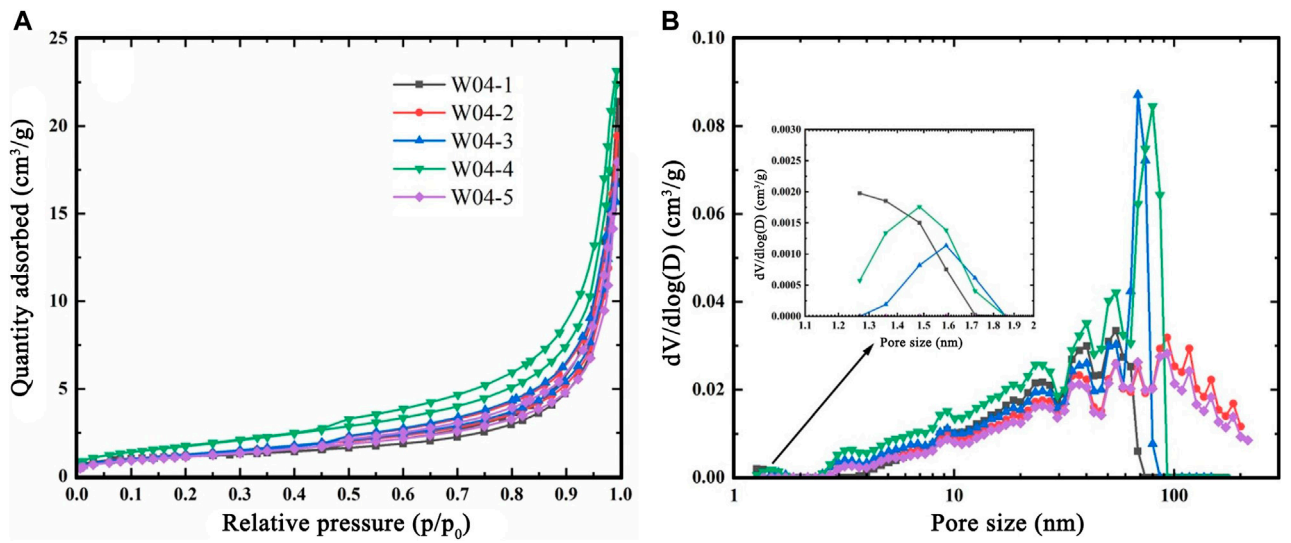

FIGURE 4 | Adsorption and desorption isotherms **(A)** and pore size distributions **(B)** of sediment samples from N_2 adsorption measurements.

Pore Size Analysis

The N_2 adsorption–desorption isotherms of five samples display similar patterns (**Figure 4A**). The adsorption isotherms increase slightly at a relative pressure (p/p_0) <0.45, followed by a sharp increase when p/p_0 is close to 1.0. The hysteresis loops of adsorption–desorption isotherms are indistinctive, which indicates the pore system of sediment samples is composed of cylindrical, wedge-shaped, or slit pores.

Figure 4B shows pore size distributions of W04-1 to W04-5. For W04-1, W04-3, and W04-4, results of pore size with the bimodal distribution mainly range from 1.3 to 80 nm. In particular, the first peak value is 1.27, 1.59, and 1.48 nm, and the second peak value is 54.42, 68.50, and 79.87 nm for W04-1, W04-3, and W04-4, respectively. The pore size curves are unimodal with a peak value of 93.13 nm for W04-2 and W04-5. Based on pore size analysis, a large number of nanopores in these sediments can provide considerable space for hydrate accumulation.

HYDRATE DYNAMICS ANALYSIS AND PERMEABILITY EVOLUTION

Results of NMR Measurements

Figure 5 shows the procedure of the experiments with an increase and then a decrease in the temperature. The whole process can be divided into several periods in terms of the variation of hydrate

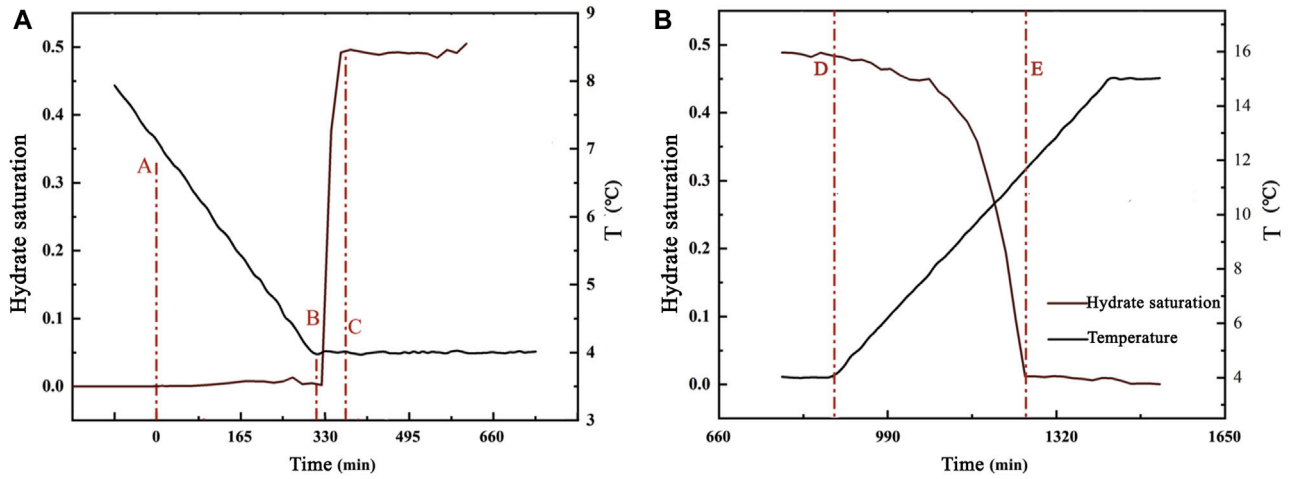

FIGURE 5 | Variations in hydrate saturation during the process of gas hydrate formation **(A)** and dissociation **(B).**

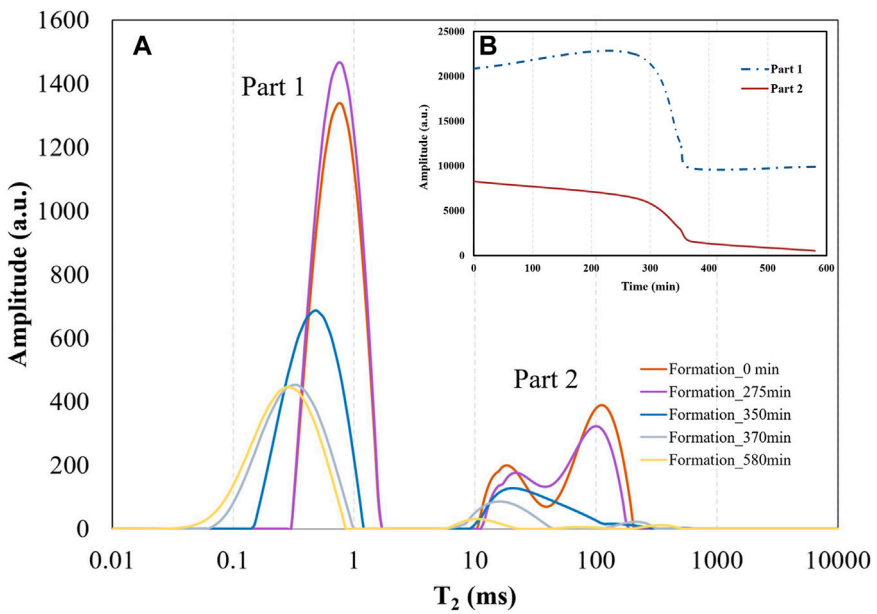

FIGURE 6 | T_2 distribution spectra of NMR **(A)** and cumulative signal of NMR **(B)** during gas hydrate formation.

saturation. For the period A-B, an induction time for hydrate formation is observed with the limited variation of hydrate. During period B-C, the pressure and temperature conditions are favorable for hydrate formation, and hydrate saturation increased rapidly up to 50%. The rate of hydrate formation is around 12%/min, estimated by variations of hydrate saturation (%) over time. The hydrate saturation is almost consistent within the period C-D resulting from the consumption of water and the limited contact between water and gas. After the D point, the temperature increases gradually and results in the dissociation of hydrates. During period D-E, the rate of dissociation gradually increases to 3%/min with the higher temperature. It is because the experimental condition is far away from the phase equilibrium condition, leading to a larger driving force for hydrate dissociation. At the end of the experiments, all the CO_2 hydrates dissociate, and the hydrate saturation decreases to 0.

Evolution of Pore Structure With Hydrate Dynamics

T_2 distribution spectra of NMR provide insights into the pore size distribution of sediments and the change of pore space subjected to the hydrate formation or dissociation. As shown in **Figure 6A**, there are two distinct parts for the initial signal of sediment samples, i.e., Part 1 (0.2~2 ms) and Part 2 (10~300 ms), representing the complex pore structure with mixed grains. At the early stage of

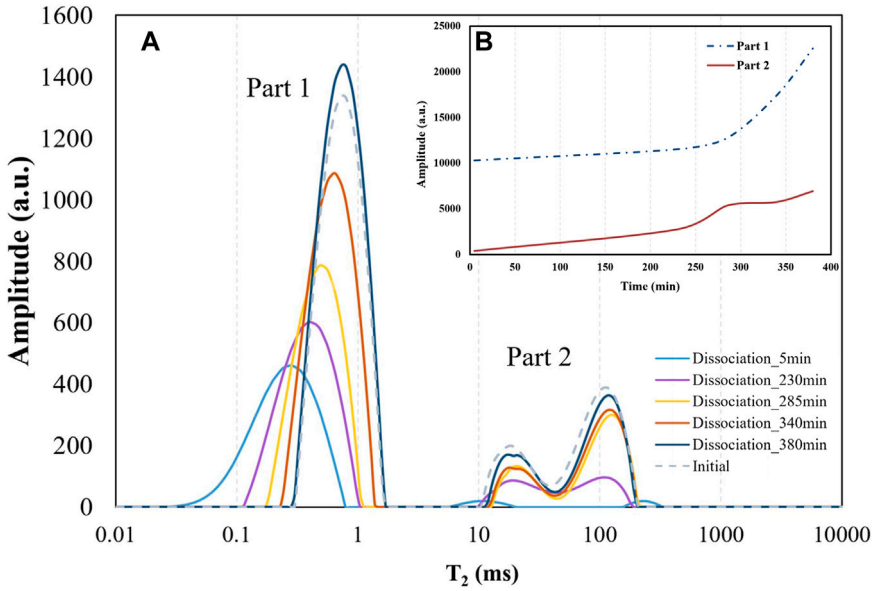

FIGURE 7 | T_2 distribution spectra of NMR **(A)** and cumulative signal of NMR **(B)** during gas hydrate dissociation.

hydrate formation, there is an obvious decrease in Part 2, whereas there is a slight increase in the peak of Part 1. It indicates that the pore space of Part 2 is occupied by the formation of hydrate and leads to a faster relaxation time of the NMR signal. The peak area of Part 2 decreases 40% from 275 to 350 min with a preferential formation of hydrate in larger pores. Some scholars believed that the enhanced performance of heat and mass transfer makes it easier for large pore spaces to achieve nucleation (Qin et al., 2021). With the continuous increase of hydrate saturation, Part 2 became vanished, while Part 1 was still with a low peak at the end of hydrate formation. The phenomenon shows the movement of fluid is quite limited with the presence of hydrates, and thus the local hydrate formation is restrained due to the lack of water or gas.

An opposite tendency of NMR signal variation can be observed in the process of hydrate dissociation (**Figure 7**). The value and width of peaks increase with the hydrate dissociation. Compared to the process of formation, the increase of Part 2 is slightly later than that of Part 1. The rate of hydrate dissociation gradually increases in both Part 1 and Part 2 over time confirmed by the cumulative intensity of the NMR signal. A noticeable difference is shown between the T_2 distribution spectra of the initial situation and the end of dissociation. Similar behaviors have been observed by Lei et al. (2022b). They analyzed microscopic pore characteristics and flowability of five samples from the Shenhu area, showing better connectivity in hydrate-bearing sediment samples after hydrate dissociation compared to samples from the underlying layer. It demonstrates that pore structure may be altered after the hydrate dynamics in both pore size and pore quantity.

Evolution of Permeability With Hydrate Dynamics

Hydrate saturation and permeability in the porous medium were determined by NMR measurements, and the tendency of permeability evolution subjected to the hydrate formation or dissociation is shown in **Figure 8**. With the increase of hydrate saturation, a remarkable decrease in permeability can be observed. It indicates that the permeability of porous media obviously decreases with occupying gas hydrates in pore spaces, and the evolution of permeability differs in terms of the hydrate quantity and distribution. In particular, an order of magnitude lower is in permeability with the hydrate saturation of 32%, while three orders of magnitude are lower with the hydrate saturation of 50% compared to the initial permeability.

By comparing permeability results obtained from experimental data and theory models, different tendencies of permeability evolution are shown in **Figure 8**. Generally, a sharper change of permeability is determined by experimental data at the early stage, while a gentler change at the middle stage is compared to other models. In particular, NMR results show a good agreement with the parallel capillary model (pore-filling) when the hydrate saturation is smaller than 0.1, indicating hydrates prefer to form in the pore central space. Compared to other patterns of hydrate distribution, e.g., a thin film of hydrate coating grain walls, the changes in the permeability are expected to be larger if hydrates occupy flow paths. When the hydrate saturation is larger than 0.3, permeability evolution can be especially captured by the Masuda model (n = 12). Some studies demonstrated that grain-coating hydrates appear to be more common than pore-filling ones with a low porosity and permeability (Lei et al., 2022a). Moreover, a drastic reduction in permeability may occur if formed hydrates plug the pore throats in addition to pore bodies, especially when a high hydrate saturation is in porous media. It is clear that the tendency of permeability evolution is differentiated induced by various patterns of hydrate growth in pores and is more complicated when hybrid patterns exist. In this work, most experimental

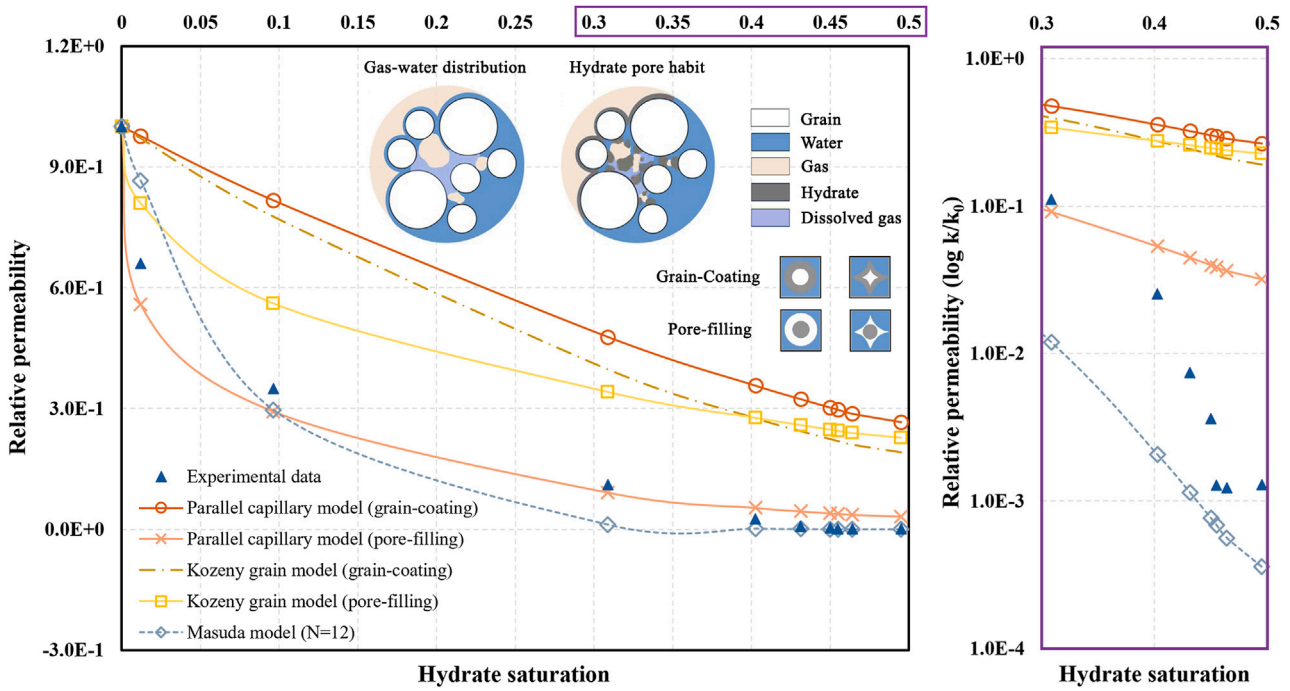

FIGURE 8 | Comparison of permeability evolution from experimental data and theory models.

permeability data points fall between fitted lines from different theoretical permeability models, i.e., the pore wall coating and pore center occupying models. It highlights that hybrid pore habits of hydrates affect the evolution of permeability in hydrate-bearing sediments of the Shenhu area, and a preponderant pattern of hydrate growth changes spatially and temporally.

During the process of hydrate formation and dissociation, pore structure characteristics of sediments influence the hydrate saturation and distribution, as well as gas–water conditions. Previous studies pointed out that various gas–water flow patterns result in excess-gas, excess-water, or dissolved-gas conditions for hydrate formation in sediments and have a profound impact on hydrate growth (Wang et al., 2021). In the excess-gas condition, a limited amount of water mainly cements hydrophilic grain surfaces or contacts, which results in grain-coating hydrates with gas diffusing into water layers. But when the ratio of gas to water is low, the formation of hydrate starts close to trapped gas bubbles or dissolved-gas regions, and gradually exhibits a pore-filling morphology. In this experiment, excess-gas, excess-water, and dissolved-gas conditions coexist in sediments, and gas–water ratios and distributions vary with hydrate dynamics (illustrated in **Figure 8**). Hydrates formed at gas–water interfaces can continuously grow to coat grains or occupy pore central spaces subjected to the specific gas–water condition. In this regard, a theoretical model assuming a single pattern of hydrate growth is expected to fail to predict the hydrate–saturation-dependent permeability in a geosystem in terms of heterogeneous pore structures and gas–water conditions.

CONCLUSIONS

Properties of porous media play a critical role in the formation, dissociation, and occurrence of gas hydrates under natural conditions. In a complex geological media, heterogeneous pore structure will largely complicate the scientific nature of hydrate dynamics during the process of formation and dissociation. This work performed *in situ* observations of pore structure evolution with regard to the changes in hydrate saturation by using LF-NMR measurements. The sediments from the Shenhu area of the SCS with the main components of quartz, calcite, and mica minerals, are composed of clay and fine grains. Nanopores with a range from several to tens of nanometers contribute to the pore space for hydrate growth and accumulation.

In such porous media, gas hydrates gradually form after an induction time; however, they immediately dissociate with an increasing temperature. Estimated by variations of hydrate saturation (%) over time, the rate of hydrate formation is around 12%/min, while the highest rate of dissociation is 3%/min. Because of the occupation of pore space with the hydrate growth, the permeability of sediments decreases obviously with an increase in hydrate saturation. However, the relationship between permeability and saturation is quite complex and cannot be described by theoretical models with a simple assumption of hydrate pore habits. When the saturation is from 20 to 45%, one to three orders of magnitude lower in permeability is determined by experiments, respectively. The tendency of permeability evolution compared to predicted outcomes from permeability models indicates coexistence of both pore-filling and grain-coating hydrate pore morphology

in sediments of the Shenhu area. Moreover, heterogeneous pore structure complicates gas–water conditions in sediments, which leads to spatial and temporal variations in hydrate pore habits. For the improved understanding and predictive capability of hydrate–saturation-dependent permeability, coupled effects of porous media properties and evolution conditions have to be addressed in hydrate-bearing sediments.

DATA AVAILABILITY STATEMENT

The original contributions presented in the study are included in the article/Supplementary Material, further inquiries can be directed to the corresponding author.

AUTHOR CONTRIBUTIONS

QZ, YD, and HZ contributed to the conception and design of the study. LX organized the database. XQ performed the statistical analysis. QZ and HZ wrote the first draft of the manuscript. CL, SL, CM, and HB wrote sections of the manuscript. All authors contributed to manuscript revision, read, and approved the submitted version.

FUNDING

This research was supported by the Key Research Program of the Institute of Geology & Geophysics, CAS (no. IGGCAS-201903), the National Natural Science Foundation of China (No. 51991365), Guangdong Major Project of Basic and Applied Basic Research (No. 2020B0301030003), and China Geological Survey Project (No. DD20211350).

ACKNOWLEDGMENTS

The authors are grateful to the Editor and two reviewers for their critical and constructive reviews.

REFERENCES

Andres-Garcia, E., Dikhtiarenko, A., Fauth, F., Silvestre-Albero, J., Ramos-Fernández, E. V., Gascon, J., et al. (2019). Methane Hydrates: Nucleation in Microporous Materials. *Chem. Eng. J.* 360, 569–576. doi:10.1016/j.cej.2018.11.216

Delli, M. L., and Grozic, J. L. H. (2014). Experimental Determination of Permeability of Porous media in the Presence of Gas Hydrates. *J. Pet. Sci. Eng.* 120, 1–9. doi:10.1016/j.petrol.2014.05.011

Ghaedi, H., Ayoub, M., Bhat, A. H., Mahmood, S. M., Akbari, S., and Murshid, G. (2016). The Effects of Salt, Particle and Pore Size on the Process of Carbon Dioxide Hydrate Formation: A Critical Review. *AIP Conf. Proc.* 1787, 060001. doi:10.1063/1.4968128

Heeschen, K. U., Schicks, J. M., and Oeltzschner, G. (2016). The Promoting Effect of Natural Sand on Methane Hydrate Formation: Grain Sizes and mineral Composition. *Fuel* 181, 139–147. doi:10.1016/j.fuel.2016.04.017

Ji, Y., Hou, J., Cui, G., Lu, N., Zhao, E., Liu, Y., et al. (2019). Experimental Study on Methane Hydrate Formation in a Partially Saturated sandstone Using Low-Field NMR Technique. *Fuel* 251, 82–90. doi:10.1016/j.fuel.2019.04.021

Kang, D. H., Yun, T. S., Kim, K. Y., and Jang, J. (2016). Effect of Hydrate Nucleation Mechanisms and Capillarity on Permeability Reduction in Granular Media. *Geophysical Research Letters* 43 (17), 9018–9025.

Kleinberg, R. L. (2003). Deep Sea NMR: Methane Hydrates Growth Habit in Porous media and its Relationship to Hydraulic Permeability, deposit Accumulation, and Submarine Slope Stability[J]. *J. Geophys. Res. Solid Earth* 108 (B10), 2508. doi:10.1029/2003jb002389

Kossel, E., Deusner, C., Bigalke, N., and Haeckel, M. (2018). The Dependence of Water Permeability in Quartz Sand on Gas Hydrate Saturation in the Pore Space. *J. Geophys. Res. Solid Earth* 123 (2), 1235–1251. doi:10.1002/2017jb014630

Kuang, Y., Zhang, L., Song, Y., Yang, L., and Zhao, J. (2020). Quantitative Determination of Pore-structure Change and Permeability Estimation under Hydrate Phase Transition by NMR. *AIChE J.* 66 (4), e16859. doi:10.1002/aic.16859

Kumar, A., Maini, B., Bishnoi, P. R., Clarke, M., Zatsepina, O., and Srinivasan, S. (2010). Experimental Determination of Permeability in the Presence of Hydrates and its Effect on the Dissociation Characteristics of Gas Hydrates in Porous Media[J]. *J. Pet. Sci. Eng.* 70 (1/2), 114–122. doi:10.1016/j.petrol.2009.10.005

Kumar Saw, V., Udayabhanu, G., Mandal, A., and Laik, S. (2015). Methane Hydrate Formation and Dissociation in the Presence of Silica Sand and Bentonite Clay. *Oil Gas Sci. Technol. - Rev. IFP Energies Nouvelles* 70, 1087–1099. doi:10.2516/ogst/2013200

Lei, X., Yao, Y., Luo, W., and Wen, Z. (2022a). Permeability Change in Hydrate Bearing Sediments as a Function of Hydrate Saturation: A Theoretical and Experimental Study. *J. Pet. Sci. Eng.* 208, 109449. doi:10.1016/j.petrol.2021.109449

Lei, X., Yao, Y., Qin, X., Lu, C., Luo, W., Wen, Z., et al. (2022b). Pore Structure Changes Induced by Hydrate Dissociation: An Example of the Unconsolidated Clayey-Silty Hydrate Bearing Sediment Reservoir in the South China Sea. *Mar. Geology.* 443, 106689. doi:10.1016/j.margeo.2021.106689

Letcher, M. T. (Editor) (2020). *Future Energy: Improved, Sustainable and Clean Options for Our planet[M]* (Amsterdam, Netherlands: Elsevier), 111–131.

Liang, H., Song, Y., Chen, Y., and Liu, Y. (2011). The Measurement of Permeability of Porous Media With Methane Hydrate. *Petroleum Science and Technology, 2011* 29, 79–87. doi:10.1016/j.margeo.2021.106689

Liang, J. Q., Wei, J. G., Bigalke, N., Roberts, J., Schultheiss, P., Holland, M., et al. (2017). "Laboratory Quantification of Geomechanical Properties of Hydrate-Bearing Sediments in the Shenhu Area of the South China Sea at *In-Situ* Conditions," in Proceedings of the 9th International Conference on Gas Hydrates, Denver, 30.

Li, J., Lu, J. a., Kang, D., Ning, F., Lu, H., Kuang, Z., et al. (2019). Lithological Characteristics and Hydrocarbon Gas Sources of Gas Hydrate-Bearing Sediments in the Shenhu Area, South China Sea: Implications from the W01B and W02B Sites. *Mar. Geology.* 408, 36–47. doi:10.1016/j.margeo.2018.10.013

Li, Z.-d., Tian, X., Li, Z., Xu, J.-z., Zhang, H.-x., and Wang, D.-j. (2020). Experimental Study on Growth Characteristics of Pore-Scale Methane Hydrate. *Energ. Rep.* 6, 933–943. doi:10.1016/j.egyr.2020.04.017

Liu, W., Wang, S., Yang, M., Song, Y., Wang, S., and Zhao, J. (2015). Investigation of the Induction Time for THF Hydrate Formation in Porous media. *J. Nat. Gas Sci. Eng.* 24, 357–364. doi:10.1016/j.jngse.2015.03.030

Lu, C., Qin, X., Mao, W., Ma, C., Geng, L., Yu, L., et al. (2021b). Experimental Study on the Propagation Characteristics of Hydraulic Fracture in Clayey-Silt Sediments. *Geofluids* 2021, 6698649. doi:10.1155/2021/6698649

Lu, C., Qin, X., Yu, L., Geng, L., Mao, W., Bian, H., et al. (2021a). The Characteristics of Gas-Water Two-phase Radial Flow in Clay-Silt Sediment and Effects on Hydrate Production. *Geofluids* 2021 (3), 1–14. doi:10.1155/2021/6623802

Masuda, Y. S., Naganawa, S., Ando, S., and Sato, K. (1997). "Numerical Calculation of Gas Production Performance From Reservoirs Containing Natural Gas Hydrates; Paper SPE 38291," in Proceedings, Western Regional Meeting, June, 25–27.

Prasad, P. S. R. (2015). Methane Hydrate Formation and Dissociation in the Presence of Hollow Silica. *J. Chem. Eng. Data* 60, 304–310. doi:10.1021/je500597r

Qin, Y., Pan, Z., Liu, Z., Shang, L., and Shang, L. (2021). Influence of the Particle Size of Porous Media on the Formation of Natural Gas Hydrate: A Review[J]. *Energy & Fuels* 35 (15), 11640. doi:10.1021/acs.energyfuels.1c00936

Ren, X., Guo, Z., Ning, F., and Ma, S. (2020). Permeability of Hydrate-Bearing Sediments. *Earth-Science Rev.* 202, 103100. doi:10.1016/j.earscirev.2020.103100

Shen, P., Li, G., Li, B., and Li, X. (2020). Coupling Effect of Porosity and Hydrate Saturation on the Permeability of Methane Hydrate-Bearing Sediments. *Fuel* 269, 117425. doi:10.1016/j.fuel.2020.117425

Siangsai, A., Rangsunvigit, P., Kitiyanan, B., Kulprathipanja, S., and Linga, P. (2015). Investigation on the Roles of Activated Carbon Particle Sizes on Methane Hydrate Formation and Dissociation . *Chemical Engineering Science* 126, 383–389.

Sloan, E. D. (2003). Fundamental Principles and Applications of Natural Gas Hydrates. *Nature* 426 (6964), 353–359. doi:10.1038/nature02135

Song, G., Li, Y., and Sum, A. K. (2020). Characterization of the Coupling between Gas Hydrate Formation and Multiphase Flow Conditions. *J. Nat. Gas Sci. Eng.* 83, 103567. doi:10.1016/j.jngse.2020.103567

Spangenberg, E. (2001). Modeling of the Influence of Gas Hydrate Content on the Electrical Properties of Porous Sediments. *J. Geophys. Res.* 106 (B4), 6535–6548. doi:10.1029/2000jb900434

Su, M., Yang, R., Wang, H., Sha, Z., Liang, J., Wu, N., et al. (2016). Gas Hydrates Distribution in the Shenhu Area, Northern South China Sea: Comparisons Between the Eight Drilling Sites With Gas-Hydrate Petroleum System. *Geol. Acta.* 14 (2), 79–100.

Sun, J., Dong, H., Arif, M., Yu, L., Zhang, Y., Golsanami, N., et al. (2021). Influence of Pore Structural Properties on Gas Hydrate Saturation and Permeability: a Coupled Pore-Scale Modelling and X-ray Computed Tomography Method. *J. Nat. Gas Sci. Eng.* 88, 103805. doi:10.1016/j.jngse.2021.103805

Wang, P. (2019). *Hydrate Formation Characteristic under Gas Migration in Porous medium[D]*. Dalian, China: Dalian University of Technology.

Wang, Q., Chen, X., Zhang, L., Wang, Z., Wang, D., and Dai, S. (2021). An Analytical Model for the Permeability in Hydrate-bearing Sediments Considering the Dynamic Evolution of Hydrate Saturation and Pore Morphology. *Geophys. Res. Lett.* 48 (8), e2021GL093397. doi:10.1029/2021gl093397

Wen, Z., Yao, Y., Luo, W., and Lei, X. (2021). Memory Effect of CO2-hydrate Formation in Porous media. *Fuel* 299, 120922. doi:10.1016/j.fuel.2021.120922

Yin, Z., Moridis, G., Chong, Z. R., Tan, H. K., and Linga, P. (2018). Numerical Analysis of Experimental Studies of Methane Hydrate Dissociation Induced by Depressurization in a sandy Porous Medium. *Appl. Energ.* 230, 444–459. doi:10.1016/j.apenergy.2018.08.115

Zhang, L., Sun, M., Sun, L., Yu, T., Song, Y., Zhao, J., et al. (2019). *In-situ* Observation for Natural Gas Hydrate in Porous Medium: Water Performance and Formation Characteristic. *Magn. Reson. Imaging* 65, 166–174. doi:10.1016/j.mri.2019.09.002

Conflict of Interest: The authors declare that the research was conducted in the absence of any commercial or financial relationships that could be construed as a potential conflict of interest.

Publisher's Note: All claims expressed in this article are solely those of the authors and do not necessarily represent those of their affiliated organizations or those of the publisher, the editors, and the reviewers. Any product that may be evaluated in this article, or claim that may be made by its manufacturer, is not guaranteed or endorsed by the publisher.

frontiers | Frontiers in Earth Science

ORIGINAL RESEARCH
published: 16 May 2022
doi: 10.3389/feart.2022.876913

Gas Hydrate Dissociation Events During LGM and Their Potential Trigger of Submarine Landslides: Foraminifera and Geochemical Records From Two Cores in the Northern South China Sea

Yi Huang[1,2], *Jun Cheng*[1,2,3], *Mingmin Wang*[1,2,3], *Shuhong Wang*[1,2]* *and Wen Yan*[1,2,3]

[1]Southern Marine Science and Engineering Guangdong Laboratory (Guangzhou), Guangzhou, China, [2]Key Laboratory of Ocean and Marginal Sea Geology, South China Sea Institute of Oceanology, Chinese Academy of Sciences, Guangzhou, China, [3]University of Chinese Academic of Sciences, Beijing, China

OPEN ACCESS

Edited by:
Lihua Zuo,
Texas A&M University Kingsville, United States

Reviewed by:
Luigi Jovane,
University of São Paulo, Brazil
Xianrong Zhang,
Qingdao Institute of Marine Geology (QIMG), China

***Correspondence:**
Shuhong Wang
wshds@scsio.ac.cn

Specialty section:
This article was submitted to Marine Geoscience, a section of the journal Frontiers in Earth Science

Received: 16 February 2022
Accepted: 28 April 2022
Published: 16 May 2022

Citation:
Huang Y, Cheng J, Wang M, Wang S and Yan W (2022) Gas Hydrate Dissociation Events During LGM and Their Potential Trigger of Submarine Landslides: Foraminifera and Geochemical Records From Two Cores in the Northern South China Sea.
Front. Earth Sci. 10:876913.
doi: 10.3389/feart.2022.876913

Although submarine slope failures and occurrence of gas hydrates are well known in the Dongsha area of the South China Sea the potential relationship between the aforementioned phenomena has not been clearly understood yet. Herein, we present carbon and oxygen isotope compositions of benthic foraminifera and sulfur isotopic composition of chromium reducible sulfur (CRS; $\delta^{34}S_{CRS}$) from two cores from the Dongsha slope, aiming at identifying gas hydrate dissociation events in geological history. The geochemical data indicated that a large amount of gas hydrate dissociated at the beginning of the Last Glacial Maximum (LGM). Meanwhile, disturbances in the sedimentary strata revealed that a submarine landslide occurred at the end of the Last Glacial Maximum. Moreover, the associated abrupt increase of benthic foraminifera abundance implies that the submarine landslide was probably caused by an intense methane releasing from gas hydrate dissociation. A smaller scale submarine landslide related to gas hydrate dissociation was also recorded in core 973-5, retrieved from the flat area at the base of the slope.

Keywords: gas hydrate, submarine landslide, benthic foraminifera, Dongsha area, South China Sea

INTRODUCTION

It is known that methane-rich fluids due to subsurface gas hydrate dissociation leak to the seafloor at specific sites on continental slopes the world over (Boetius and Wenzhoefer, 2013). In these systems, usually most of the methane and higher hydrocarbons are consumed by anaerobic oxidation of methane (AOM) coupled with sulfate reduction in the uppermost sedimentary layers (Boetius et al., 2000; Boetius and Wenzhoefer, 2013). This process leads to geochemical anomalies in the shallow surface sediment and porewater, favoring the precipitation of authigenic carbonates in the sulfate-methane transition zone (SMTZ) (Boetius and Wenzhoefer, 2013). Thus, AOM signals can be recorded by geochemical anomalies in authigenic carbonates, such as extremely negative $\delta^{13}C$ values (Roberts and Aharon, 1994; Peckmann and Thiel, 2004; Pierre et al., 2016). Authigenic carbonates are good archives to study methane seepage, but because of it is not continuous when precipating and

TABLE 1 | The location and length of the sample cores.

Core name	Longitude (E)	Latitude(N)	Water depth(m)	Length(m)
973-4	118°49.0818′	21°54.3247′	1,666	13.75
973-5	119°11.0066′	21°18.5586′	2,998	9.25

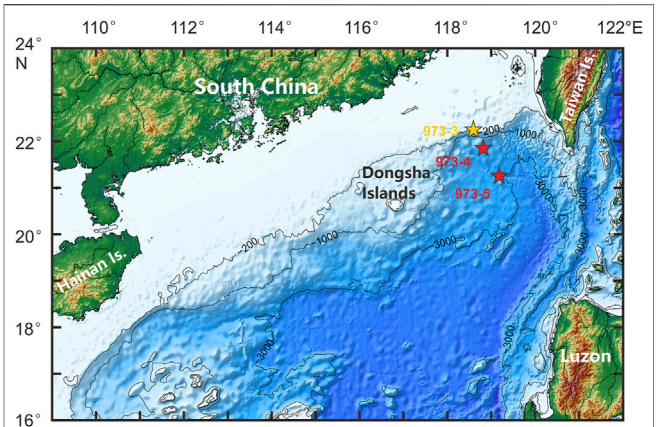

FIGURE 1 | Sampling stations in the Dongsha area of the northern SCS. Red stars represent the two sampling cores 973-4 and 973-5, and the yellow star represents the core 973-3 (Chen et al., 2014).

sometimes difficult to get proper samples, it is hard to reveal the evolution of the whole process of methane seepage. In contrast, sediment cores can serve as a potential archive to reconstruct the evolution of past methane seepage, especially when combined with age data (Bayon et al., 2015; Li et al., 2018). Specifically, $\delta^{34}S_{CRS}$ of sediments and $\delta^{13}C$ of foraminifera are the most commonly used research object in sediment cores. The $\delta^{34}S_{CRS}$ in the sediments is confirmed to be heavier in the SMTZ where the sulfate concentrations in the pore water has a rapid decrease, and consequently this value can be used to recognize paleo-SMTZs in the geological record (Peketi et al., 2012; Borowski et al., 2013; Gong et al., 2018). Benthic foraminifera near cold seep areas generally occur in large quantities, with wide areal distributions, short life cycles and stable shell preservation in the sediments after death. Thus, they are excellent for recording the effects of gas hydrate dissociation (Rathburn et al., 2000; Portilho-Ramos et al., 2018). Benthic foraminifera associations (Panieri, 2005) and the stable isotope composition of specific benthic foraminifera can therefore be used to record methane seepage activity in the geological record (Wefer et al., 1994; Stott et al., 2002; Herguera et al., 2014; Schneider et al., 2018). Although the fact that epigenetic carbonate precipitation plays a dominant role in the distinctly negative $\delta^{13}C$ record of benthic foraminifera is still controversial (Consolaro et al., 2015; Panieri et al., 2017), it is opportune to mention that the microstructure and geochemical characteristics of foraminifera influenced by post diagenesis can also trace the methane emissions in a geological period (Schneider et al., 2017). So AOM signals in cold seep environments are recorded in the foraminifera shells. It is well known that hydrate dissociation are likely to trigger intensive methane seepage (Chen et al., 2016), resulting in an abnormally high pore pressure and a reduction in the effective stress of continental slope sediments. When the amount of gas emission is massive enough or the continental slope with gas hydrate is steep, the fluidized decomposition zone will form a downward sliding surface. In this situation, any small perturbation of the stress, such as an earthquake, or the self-gravity of the sediments, may lead to slope failure (Kayen and Lee, 1991). Many submarine landslides are proved to be related to gas hydrate dissociation in the world, including the Storegga slide, off the coast of Norway, and Cape Fear, on the Atlantic continental slope (Leynaud et al., 2004; Solheim et al., 2005; Chaytor et al., 2009; Horozal et al., 2017). In the geological history, there are also some numerical simulation and sedimentary records that demonstrate the rapid changes of sedimentation affect the gas seepage activity, which also indicates the spatial and temporal charateristics of methane seepage (Karstens et al., 2018; Screaton et al., 2019). However, other researches argue that the destabilization of a hydrate system is a slow process and could be largely delayed by overpressure accumulation (Colin et al., 2020). Recently, climate-driven increase in temperature, especially during last deglacial (MIS5e), is proved to be a trigger factor of gas hydrate dissociation in SCS (Chen et al., 2019). Thus, the questions concerning the main cause of gas hydrate dissociation are still under debate, the subsequently methane seepage and its potential link to the submarine landslides are poorly documented. Many studies have identified the occurrence of fluidized decomposition zone by geophysical methods, such as seisetic reflection data (Eiger et al., 2017; Handwerger et al., 2017), little attention has been paid to the geochemical characteristics of gas hydrate and landslide deposits. The Dongsha area, which is located on the continental slope of the northeastern South China Sea (SCS), is an excellent area for such a study. The extensive development of gas chimneys, submarine landslides, mud diapirs, carbonate mounds and active cold seeps in this area (Chen et al., 2005; Yan et al., 2006; Yu et al., 2013; Feng and Chen, 2015; Wu et al., 2018), strongly suggests the occurrence of gas hydrate reservoirs (Chen et al., 2005; Li et al., 2011; Su et al., 2012). Here, by using the carbon-sulfate-benthic foraminifera system, two sediment cores in Dongsha slope are used to identify gas hydrate dissociation events and discuss the causal relationship between gas emissions and submarine landslides.

MATERIALS AND METHODS

Sediment cores 973-4 and 973-5 were collected from the middle of the slope and the flat area at the base of the Dongsha area, in the northern SCS, respectively, using a piston corer during the 973 cruise by the ship "R/V OceanVI" in 2011 (**Table 1**; **Figure 1**).

The core 973-4 is mostly made of grey and grey-green clay, with coarser-grain-size silt at the depth of 450–600 cm, in which foraminifera is abundant. Below 600 cm, there are black hydrogen sulfide disseminated plaque deposits with a distinct smell of rotten eggs. For the core 973-5, it is also mostly made of grey to grey-dark clay, the obvious foraminifera enriched silt layer occurred at around 250 ~300 cm there is an angular

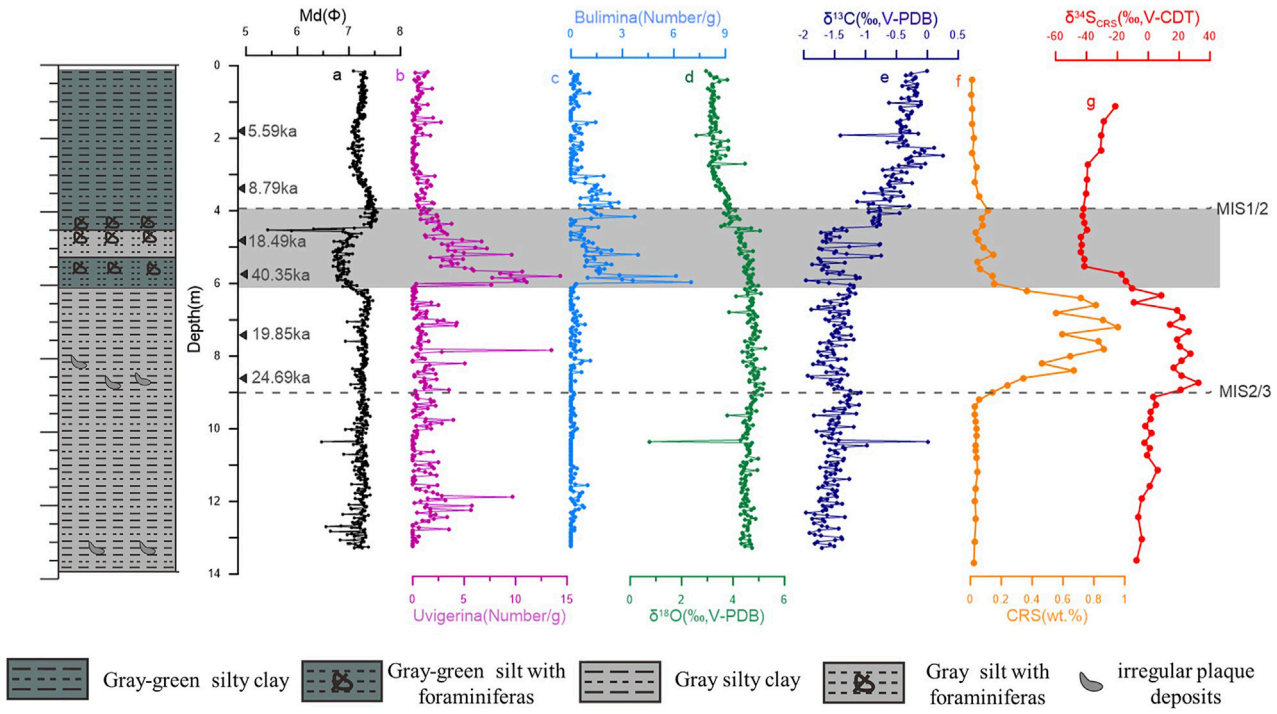

FIGURE 2 | Sediment particle size and geochemical records of core 973-4, lithostratigraphic picture (left) **(A)** Medium size, **(B)** quantity of *Uvigerina* spp., **(C)** quantity of *Bulimina* spp., **(D)** oxygen isotopes of *Uvigerina* spp., **(E)** carbon isotopes of *Uvigerina* spp., **(F)** CRS, **(G)** sulfur isotopic compositions. The triangles indicate the AMS^{14}C dating results (Zhang et al., 2018); the dashed lines indicate the demarcation lines of MIS1/MIS2 and MIS2/MIS3; and the shadowed horizon indicates horizons influenced by submarine landslides.

unconformity at around 460 cm. Sediment samples were collected every 2 cm from 15 cm bsf (below the seafloor) to the core bottom, except in the top 15 cm of each core, where only one sample was collected. Grain size measurements were carried out at the South China Sea Institution of Oceanology, Chinese Academic of Sciences, using a Mastersizer2000 Laser Particle Size Analyzer. The particle classification was 1Φ [Φ = $-\log_2 d$; d means particle diameter (mm)]. The detection limit was between 0.5 and 2000 μm, and the relative error was less than 3%. The benthic foraminifera *Uvigerina* spp. and *Bulimina* spp. were picked from the >200 μm-size fractions to calculate the assemblage density (number of individuals per gram of dry sediment) and perform the isotopic analysis (*Uvigerina* spp.). The $\delta^{13}C$ and $\delta^{18}O$ isotopes of foraminifera tests were measured on aMAT253 Stable Isotope Gas Mass Spectrometer in the South China Sea Institution of Oceanology, Chinese Academic of Sciences and calibrated to the VPDB standard. Analytical precision was estimated to be better than 0.03‰ for $\delta^{13}C$ and 0.08‰ for $\delta^{18}O$. CRS (chromium reducible sulfur, mainly FeS, FeS_2) in the bulk sediments were extracted following the method of Canfield (Canfield et al., 1986). two to five gcarbonate powder was digested in 6 mol/L HCl at 50°C for 6 h to release acid volatile sulfur under a continuous flow of N2 (g) and the residue (remain mainly as FeS and FeS_2) was analyzed for bulk carbonate CRS. CRS was extracted using 6 N HCl and 1M $CrCl_2$ for 3 h in 100% N2 atmosphere. The H2S evolved was driven via N2 carrier into 0.1 N $AgNO_3$ and trapped as Ag_2S for gravimetric and then isotopic measurements (Gong et al., 2018). The sulfur isotope analysis was performed at the Louisiana State University, using an Elemental Analyzer (EA) at 980°C, and subsequently with a Thermo-Electron Delta V Plus Advantage mass spectrometer. The standard deviation associated with $\delta^{34}S$ analysis was ±0.3‰, and reported relative to the VCDT (Vienna Canyon Diablo Troilite) standard.

RESULTS

Median Particle Size

Median particle size is commonly used to represent the average particle size of sediments (Hu et al., 2017; Li et al., 2018). The sediments in core 973-4 were fine-grained in most layers, but the grain size in the 4.3–6.0 m layer was significantly coarser (**Figure 2**). Core 973-5 contained fine-grained sediment in most layers, without any significant differences in the particle size being observed throughout the core; only a minor increase in coarser content was found in several layers (e.g., 1.3–2.7 m, 3.9–4.0 m, 5.9–6.0 m, 8.2–8.4 m, **Figure 3**).

Foraminifera Content

The foraminifera-rich layer (4.3–6.0 m) in core 973-4 is consistent with the high content of the sediment coarse fraction (**Figures 2B,C**). The numbers of the two species were almost always less than five per gram below 6 m bsf. This number

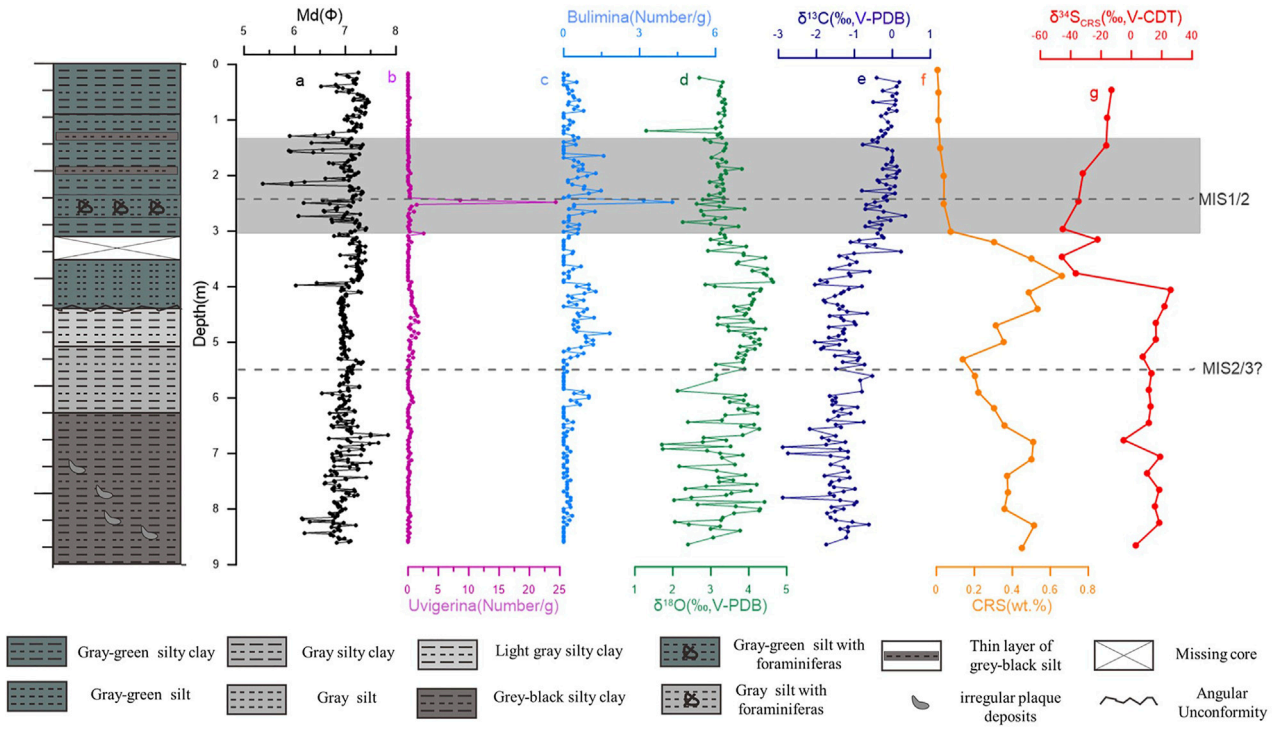

FIGURE 3 | Sediment particle size and geochemical records of core 973-5,lithostratigraphic picture (left) **(A)** Medium size, **(B)** quantity of *Uvigerina* spp., **(C)** quantity of *Bulimina* spp., **(D)** oxygen isotopes of *Uvigerina* spp., **(E)** carbon isotopes of *Uvigerina* spp., **(F)** CRS, **(G)** sulfur isotopic compositions, triangles indicate the AMS ^{14}C dating results (Wang, 2013); the dashed lines indicate the demarcation lines of MIS1/MIS2 and MIS2/MIS3; and the shadowed horizon indicates horizons influenced by submarine landslides.

increases abruptly to more than 10 per gram at about 6 m bsf and then gradually decreases upward until 4.3 mbsf. Low values are observed in the uppermost 4.3 m bsf of the core (**Figures 2B,C**). In core 973-5, the numbers of benthic foraminifera were far less than core in 973-4 and few foraminifera were seen in the whole core, except in a few layers (e.g., at depths of about 2.5 m, 4.0–5.5, and 6 m; **Figures 3B,C**).

Carbon and Oxygen Isotope Compositions of Uvigerina

The δ^{18}O composition of Uvigerina spp. in the core 973-4 varied from 2.57 to 5.26‰, with lighter δ^{18}O values in the upper part of the core (**Figure 2D**). The δ18O depletion fits well with the Deglaciation transition layer at about 4.3 m bsf and shows stable values in the uppermost core. In core 973-5, δ^{18}O values show a broad range of variation below 5.5 m bsf (**Figure 3D**), and values between 2.93 and 4.49‰ at the 3.3–3.6 m bsf layer, corresponding to the deglaciation transition. The δ^{13}C values for Uvigerina spp. in core 973-4 ranged from −1.97 to 0.25‰ with an average value of −1.15‰ (**Figure 2E**). The δ^{13}C values below 4.3 m bsf are obviously negative, with only small fluctuations; above this depth they become heavier until the surface. In core 973-5, the δ13C values were consistently negative below the depth of 3.3 m bsf and showed heavier trend from -2.9 to 0.18‰ in the upper part of the core (**Figure 3E**).

CRS and δ^{34}SCRS Values

In core 973-4, the CRS contents vary between 0.01 wt‰ and 0.95 wt‰. A high CRS content was observed in the interval 6.8–9.0 m (**Figure 2G**). The δ^{34}SCRS values show a wide variation, ranging from −43.8 to 32.6‰. The sulfate isotope compositions show extremely positive values at the CRS enrichment depth (6.8–9.0 m), and then are lower elsewhere, with a minimum value of −43.8‰ in the interval 2.8–5.6 m (**Figure 2F**). In core 973-5, high CRS contents and positive $\delta^{34}S_{CRS}$ values are observed below 4 m bsf (**Figure 3G**), and the $\delta^{34}S_{CRS}$ values above this depth become lighter, ranging from -46‰ to -15.7‰ (**Figure 3F**).

DISCUSSION

Radiocarbon- and δ^{18}O-derived age models (Zhang et al., 2018) suggested that two studied cores, 973-4 and 973-5, recorded sediment deposition since MIS3. Combined with the oxygen isotope change curve and previous research (Liu et al., 2018), we found that the 4.0–9.0 m bsf layer in core 973-4 records the sediment of MIS2, and the layer above 4.0 m corresponds to the sediment deposited since the Holocene. Interestingly, there was an age inversion around 5.8 m (40.35ka). The strata of MIS3 may be disturbed and MIS3 sediments have been reversed to MIS2. The age inversion intervals coincide with the foraminifera-rich

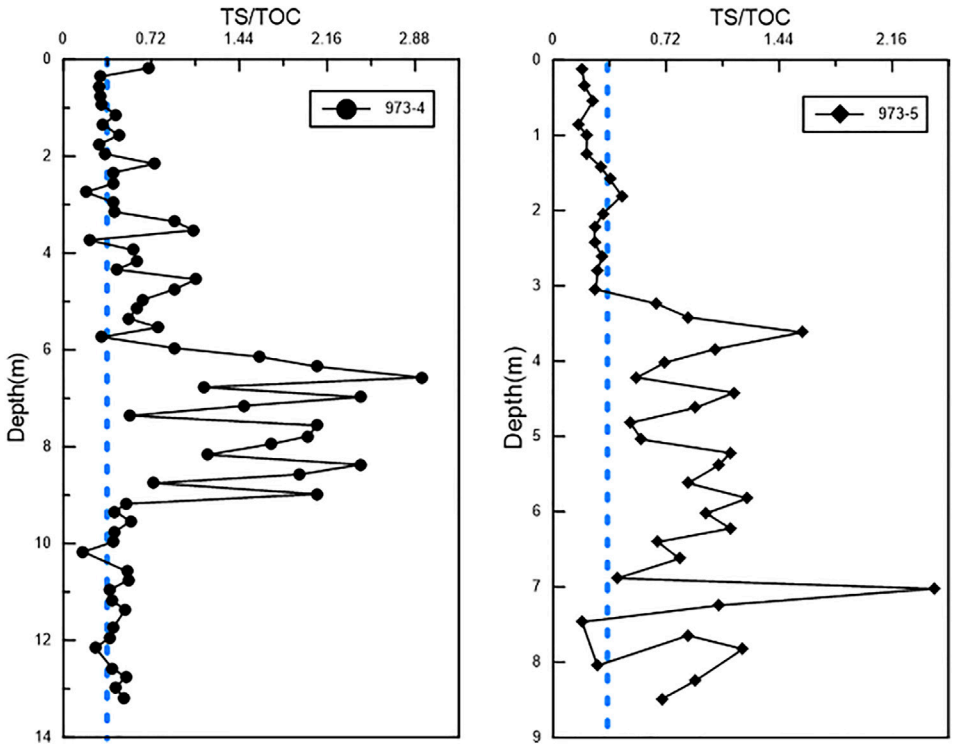

FIGURE 4 | TS/TOC ratios in the cores 973-4 and 973-5 (TS and TOC data cited from (Zhang et al., 2018); the blue dashed lines indicate the S/C ratio in normal marine sediment).

and sand content-rich layers (4.4–6.0 m), and possibly resulted from landslides or physical disturbance by intense seepage (Lin et al., 2016). In core 973-5, the demarcation lines of MIS1/2 and MIS2/3 are at the depths of 2.2 and 4.8 m bsf respectively; the age absence in 4.8 m bsf may also have been caused by a landslide.

Geochemical Records of Gas Hydrate Dissociation Events

In the typically anoxic subseafloor marine sediments, the consumption of porewater sulfate is controlled by two microbially mediated processes: 1) organo clastic sulfate reduction (OSR) (Berner, 1982); and 2) anaerobic oxidation of methane (AOM) (Boetius et al., 2000). The two net reactions are expressed stoichiometrically as follows: $2CH_2O + SO_4^{2-} \rightarrow 2HCO_3^- + H_2S$ 1) $CH_4 + SO_4^{2-} \rightarrow HCO_3^- + HS^- + H_2O$ 2) However, these two different processes always result in different average S/C ratio in sediments. In oxic and suboxic marine sediments (OSR dominate), the reduced sulfur and total organic carbon (TOC) contents typically show a positive correlation with an average S/C ratio of 0.36 (Berner, 1982). In our studied cores, the TOC content was typically low (Zhang et al., 2018), and the S/C ratios at 6.0–9.0 m bsf (973-4) and below 4.0 m bsf (973-5) were higher than 0.36 (**Figure 4**). These situations were referred to an organically-limited and methane-rich environment, in which AOM was the dominant process, contributed to a significant fraction of sulfides (Kaneko et al., 2010; Lim et al., 2011; Sato et al., 2012) and may have significantly increased the S/C ratios of sediments. This AOM origin for sulfides explains why there was no correlations between the CRS and TOC contents in the sediments of both cores (**Figure 5**).

Positive $\delta^{34}S$ (up to 32.6‰) values of sulfide minerals could represent a present- or paleo-SMTZ (sulfate-methane transition zone) where AOM process occurred strongly (Aharon and Fu, 2003; Jorgensen et al., 2004; Borowski et al., 2013; Zhu et al., 2013). In the studied cores, the $\delta^{34}S_{CRS}$ values below 6.0 m bsf in core 973-4 and below 4.0 m bsf in the core 973-5 are positive. Especially in the 6.0–9.0 m bsf layer of core 973-4, a wide SMTZ with positive sulfur isotope compositions up to 20‰ represents a sustained and stable methane flux. As shown in the **Figure 2G**, at the end of the LGM period (4.0–6.0 m) with a low sea-level stage, the $\delta^{34}S_{CRS}$ became highly negative (−43.8‰ to −39.4‰). The low $\delta^{34}S$ values in seep-impacted sediments may be attributed to iron limitation caused by low sedimentation rates (Formolo and Lyons, 2013) or disproportionation of microbial sulfur occurring close to the sediment-water interface (Canfield and Thamdrup, 1994; Borowski et al., 2013). Because the sedimentation rate of our study area is typically high at low sea level stands (Zhang et al., 2018), disproportionation of microbial sulfur instead of iron limitation might be the reason for the low $\delta^{34}S_{CRS}$ values.

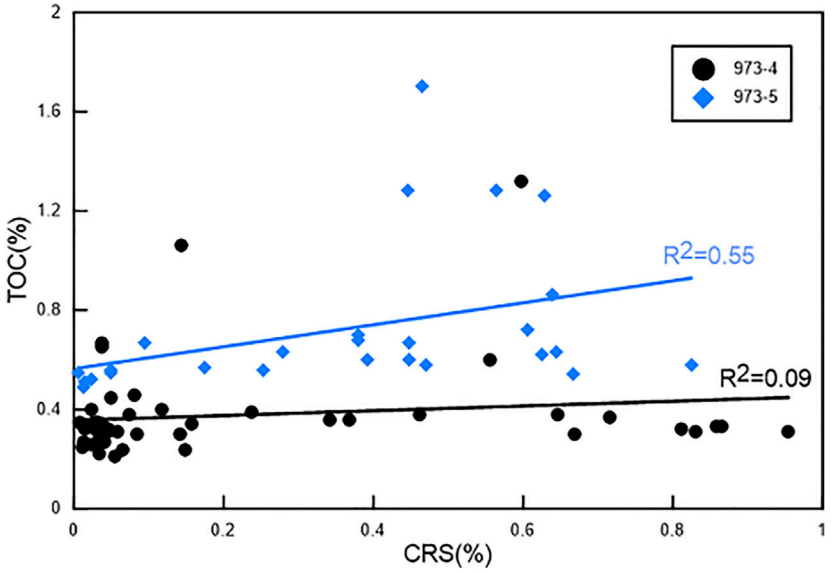

FIGURE 5 | The correlations between TOC and CRS in cores 973-4 and 973-5 (Zhang et al., 2018).

Generally, disproportionation of microbial sulfur happen in an open system, which can be caused by intense methane flux (Li et al., 2018). Herein, we suppose the low $\delta^{34}S$ values might be also caused by this phenomenon in this period.

Response of Specific Benthic Foraminifera to Gas Hydrate Dissociation Events

According to previous research, the $\delta^{13}C$ values of *Uvigerina* spp. in normal seawater range from −0.1 to 1.0‰ (Rathburn et al., 2003; Schmiedl et al., 2004; Fontanier et al., 2006). However, in our studied cores, the $\delta^{13}C$ values of benthic foraminifera below 3.9 m bsf in core 973-4 and 2.5 m bsf in core 973-5 (corresponding to the end of the Last Glacial period) were almost all lower than -1.0‰, showing an obvious negative carbon bias. Although some researchers considered that the $\delta^{13}C$ values in the Glacial period were more negative than that in Deglacial period (Wei et al., 2006), the $\delta^{13}C$ values of benthic foraminifera in the northern SCS always vary from about -0.6 to 0.2‰ (range variation of approximately 0.8‰ in the past 90 ka) under the influence of climate change (Wei et al., 2006). These indicate that such wide range of the carbon negative bias (e.g.,1.9‰ in core 973-4) in our study area was not caused by climate change and seem to be caused by AOM reaction. In addition, when recording methane seepage activity, a wide range of $\delta^{13}C$ values of benthic foraminifera are more appropriate than absolute negative values (Rathburn et al., 2003). Thus, the carbon negative bias can be attributed to methane seepage in the studied cores. Because ^{18}O is higher in cold seep fluids, and the heavier $\delta^{18}O$ values were thought to be another evident of gas hydrate dissociation or cold seep activity (Uchida et al., 2004). In core 973-4 and 973-5, the $\delta^{18}O$ values were obviously heavier during the Glacial period in both cores, which is consistent with the $\delta^{13}C$ results. Thus we can tentatively deduce the methane seepage activities in the core 973-4 by analyzing the $\delta^{13}C$ and $\delta^{18}O$ values change. **Figure 2E** shows negative carbon isotope compositions in MIS2 (4.0–9.0 m), indicating a sustained methane seepage during this period. Furthermore, other reports have suggested that cold seeps were particularly active at low sea-level stands due to a hydrostatic pressure reduction in the SCS (Tong et al., 2013; Han et al., 2014), hence it supports our hypothesis that an intense methane seepage happened during LGM (4.0–6.0 m). Since the end of the LGM (above 4.0 m), the $\delta^{13}C$ values in core 973-4 were quite stable and comparable to normal sea-water values typical of non-seep environments. This implies that the gas hydrate dissociation events gradually weakened in this core since the Holocene. As the temperature rose gradually in the Deglaciation periods, the changes in global ice volume and bottom water temperature were not the dominant factors for hydrate decomposition. Instead, as the sea level and the hydrostatic pressure on the sediment have gradually increased since the Last Glacial, the gas hydrate stability zone has thickened, thus causing a weakening of gas hydrate dissociation and methane seepage. *Uvigerina* spp. and *Bulimina* spp. are considered as specific endophytic benthic foraminifera that can adapt to the modern cold seep environments with high TOC and low oxygen content (Abu-Zied et al., 2008), and they were the two dominant species of benthic foraminifera in cores 973-4 and 973-5. Moreover, as shown in **Figures 2B,C**, their numbers increased to different extents during the Last Glacial period (4.0–9.0 m of core 973-4), which may be under the influence of the methane flux related to the gas hydrate dissociation during that time (Chen et al., 2007). However, previous research indicated that normal cold seep activity cannot significantly change the total abundance of benthic foraminifera (Panieri et al., 2009). Therefore, the large increases in the number of benthic foraminifera at the end of the LGM period (4.0–6.0 m of core 973-4), especially the abrupt increase in the layer

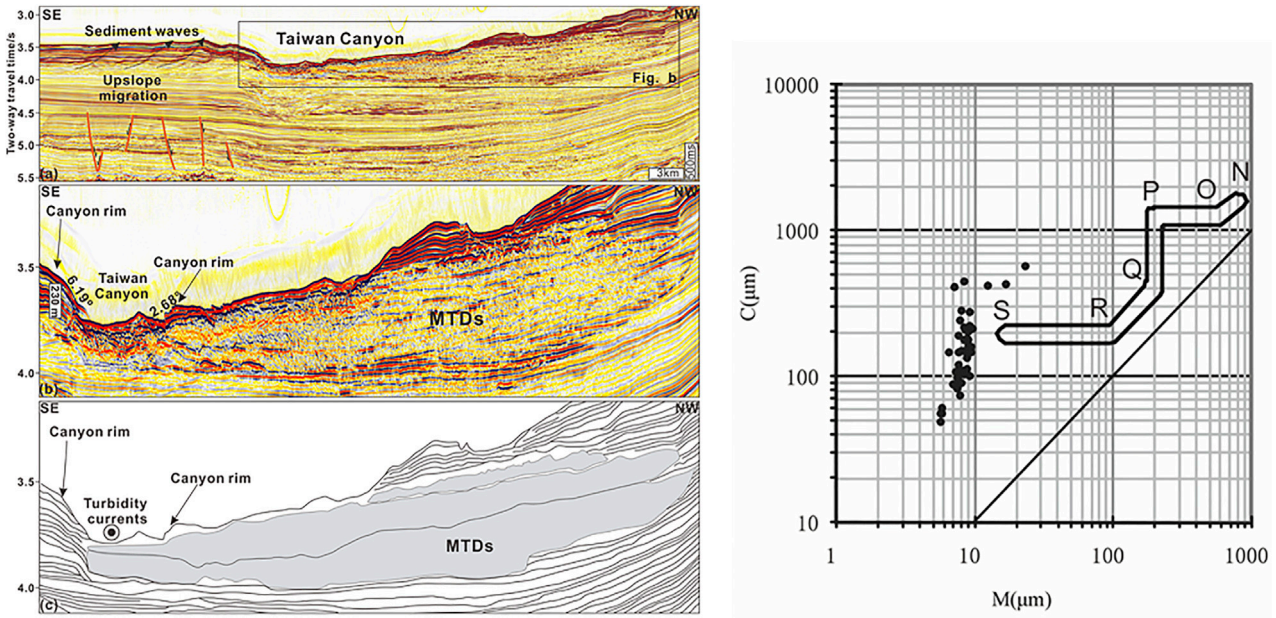

FIGURE 6 | The seismic profile of the D2 survey line (from Li, 2020, left) and Passega C-M diagram (Passega, 1964, right). C = maximum (D99; first percentile) grain size of 973-4, M = median grain size. The dots represent the interval (4–6 m) with coarser grain content. **(A)** Two-dimensional (2D) seismic profile of the Taiwan Canyon highlighting the morphological differences in canyon banks. **(B)** The mass transport deposits (MTDs) are characterized by chaotic amplitude reflections. **(C)** Line drawn interpretation of **(B)** illustrating the presence of widespread MTDs in the north-east of Taiwan Canyon.

at about 6 m bsf in core 973-4, is more likely associated with geological events rather than to large quantities of methane fluid. Sustained methane seepage can provide a rich food source for benthic foraminifera (Schonfeld, 2001), and *Bulimina* spp. can adapt well to a low oxygen and high sulfide cold seep environment, even in shallow waters (Panieri, 2006). The high density of this species related to methane seepage lead to another increase above the layer in which gas hydrate dissociated.

Triggering Mechanism for the Submarine Landslides in the Dongsha Area

Gravity flows such as submarine landslides and turbidity currents are ubiquitous in Dongsha area (Li et al., 2020). And these gravity flows are proved to be able to drive erosion and deposition in Taiwan submarine canyons. As shown on the bathymetric and seismic profiles close to the research areas. Recurrent MTDs are identified in the slope, which indicate Dongsha slope might be eroded by slope failures. And Li et al. (2020) concluded that a combined action of recurrent slope instability and turbidity currents drive the erosion and deposition of submarine asymmetry in our studying area. But from the C-M plot (**Figure 6**) (Passega, 1964), a common method to identify the force of deposition using the sediment size. The grain size distribution in the 4.4–6.0 m bsf layer in core 973-4 is not parallel to the RQ line in the, which indicated that sedimentation was not impacted by turbidity currents. Thus we contribute the gravity flows recorded in our sediment cores to submarine landslides.

The sediment particle size results in the three cores, 973-3 (Chen et al., 2014), 973-4 and 973-5, which were located at the top, middle and bottom of the Dongsha area continental slope, were comprehensively investigated. The submarine landslides in this study area mainly developed at the top of the continental slope, with lower intensity in the middle slope, and only landslide deposits were present at the bottom of the slope. Furthermore, the age reversal interval (**Figure 2**) coincided with the high foraminifera and sand content in layer 4.4–6.0 m bsf in core 973-4, which is consistent with frequent submarine landslides influencing this area (Zhong et al., 2015; Lin et al., 2016; Wu et al., 2018).

Based on a comprehensive analysis of geochemical and sediment records, gas hydrate dissociation events and submarine landslides were recognized in two cores. We take 973-4 for analyzing (**Figure 7**). There was sustained and stable methane seepage during the beginning of MIS2 (6.0–9.0 m, **Figure 7A**) and the methane flux was relatively low. Therefore, iron sulfides with high $\delta^{34}S_{CRS}$ and benthic foraminifera with negative $\delta^{13}C$ were found in the sediment layer (**Figure 7A**). At the end of MIS2, responding to the LGM period (4.0–6.0 m), the methane flux was very high and the SMTZ was near the seafloor (**Figure 7B**). In this case, the enrichment of TOC might be due to the lower rates of AOM and higher methane flux into the water column (Consolaro et al., 2015). More importantly, the massive decomposition of gas hydrate during the low-stand sea level period reduced slope stability (Sultan et al., 2010; Kwon et al., 2011), and herein led to the formation of the submarine landslides and sediment transportation from the top to the flat area of the slope (**Figure 7B**). The abrupt increase in benthic foraminifera quantity also verify this geological activity. Because methane diffused into the atmosphere before it had completely reacted, the $\delta^{34}S_{CRS}$ values of iron sulfides were low but the $\delta^{13}C$ values of benthic foraminifera showed negative anomalies (**Figure 7B**). Since the Last Glacial period (above 4.0 m), rising sea level has prevented the decomposition of gas hydrates and gradually

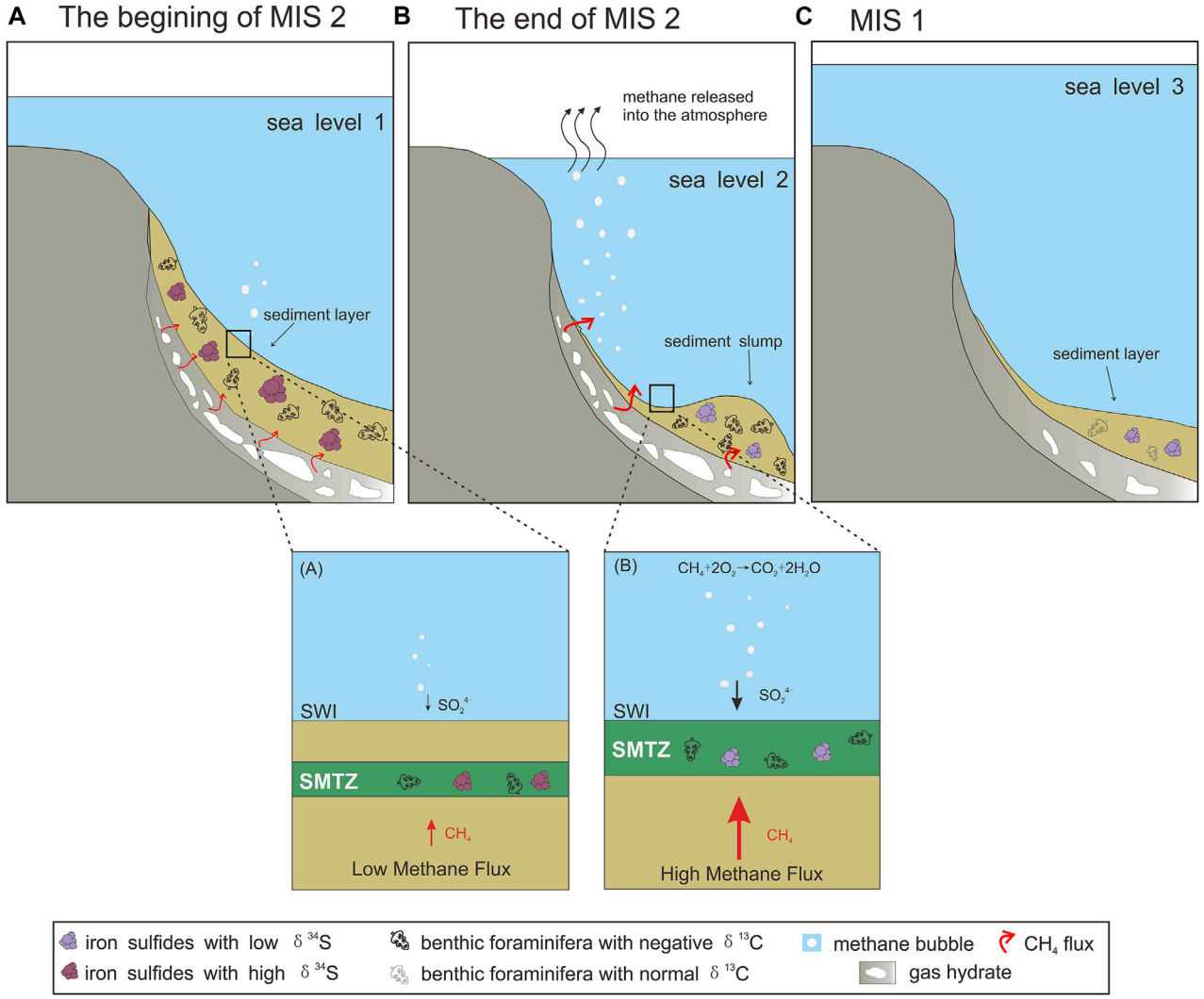

FIGURE 7 | Relationship between gas hydrate decomposition and submarine landslides (SWI: sea water interface).

weakened cold seep activity. Thus, the geochemical and benthic foraminifera records showed no further anomalies (**Figure 7C**).

CONCLUSION

Two sediment cores from the Dongsha slope in the SCS were used to identify gas hydrate dissociation events and subsequently the potential trigger of submarine landslides. The distinctly negative $\delta^{13}C$ values and positive $\delta^{18}O$ values along with extremely positive $\delta^{34}S_{CRS}$ values in both cores at the end of the LGM period suggested that there were persistent gas hydrate dissociation events in the Dongsha area during this period. In core 973-4, obvious submarine landslide deposits only occurred at the 4.4–6.0 m interval (end of LGM), and the numbers of *Uvigerina* spp. and *Bulimina* spp. sharply increased in this horizon. These results implied that the submarine landslides were probably caused by intense methane release events during this period. More importantly, as shown here, a novel strategy with geochemical methods were used to investigate the relationship between submarine landslides and gas hydrate dissociation events. Further studies of numerical methods are needed to quantitatively illustrate the casual relationship between them.

DATA AVAILABILITY STATEMENT

The raw data supporting the conclusion of this article will be made available by the authors, without undue reservation.

AUTHOR CONTRIBUTIONS

Formal analysis and writing—original draft preparation, YH; writing—review and editing, JC, MW, SW, and WY; All

authors have read and agreed to the published version of the manuscript.

FUNDING

Our work is supported by Key Special Project for Introduced Talents Team of Southern Marine Science and Engineering Guangdong Laboratory (Guangzhou) (GML2019ZD0104), the Innovation Development Fund of South China Sea Eco-Environmental Engineering Innovation Institute of the Chinese Academy of Sciences (ISEE2018PY02), the National Natural Science Foundation of China (41576035).

ACKNOWLEDGMENTS

We would like to thank all the crew members of the R/V Ocean VI of the 2011 Guangzhou Marine Geological Survey cruise. We acknowledge Dr. Peng for measuring sulfur isotopic compositions.

REFERENCES

Abu-Zied, R. H., Rohling, E. J., Jorissen, F. J., Fontanier, C., Casford, J. S. L., and Cooke, S. (2008). Benthic Foraminiferal Response to Changes in Bottom-Water Oxygenation and Organic Carbon Flux in the Eastern Mediterranean during LGM to Recent Times. *Mar. Micropaleontol.* 67 (1-2), 46–68. doi:10.1016/j.marmicro.2007.08.006

Aharon, P., and Fu, B. S. (2003). Sulfur and Oxygen Isotopes of Coeval Sulfate-Sulfide in Pore Fluids of Cold Seep Sediments with Sharp Redox Gradients. *Chem. Geol.* 195 (1-4), 201–218. doi:10.1016/s0009-2541(02)00395-9

Bayon, G., Henderson, G. M., Etoubleau, J., Caprais, J.-C., Ruffine, L., Marsset, T., et al. (2015). U-Th Isotope Constraints on Gas Hydrate and Pockmark Dynamics at the Niger Delta Margin. *Mar. Geol.* 370, 87–98. doi:10.1016/j.margeo.2015.10.012

Berner, R. A. (1982). Burial of Organic Carbon and Pyrite Sulfur in the Modern Ocean; its Geochemical and Environmental Significance. *Am. J. Sci.* 282 (4), 451–473. doi:10.2475/ajs.282.4.451

Boetius, A., Ravenschlag, K., Schubert, C. J., Rickert, D., Widdel, F., Gieseke, A., et al. (2000). A Marine Microbial Consortium Apparently Mediating Anaerobic Oxidation of Methane. *Nature* 407 (6804), 623–626. doi:10.1038/35036572

Boetius, A., and Wenzhöfer, F. (2013). Seafloor Oxygen Consumption Fuelled by Methane from Cold Seeps. *Nat. Geosci.* 6 (9), 725–734. doi:10.1038/ngeo1926

Borowski, W. S., Rodriguez, N. M., Paull, C. K., and Ussler, W. (2013). Are 34S-Enriched Authigenic Sulfide Minerals a Proxy for Elevated Methane Flux and Gas Hydrates in the Geologic Record? *Mar. Petroleum Geol.* 43, 381–395. doi:10.1016/j.marpetgeo.2012.12.009

Canfield, D. E., Raiswell, R., Westrich, J. T., Reaves, C. M., and Berner, R. A. (1986). The Use of Chromium Reduction in the Analysis of Reduced Inorganic Sulfur in Sediments and Shales. *Chem. Geol.* 54 (1-2), 149–155. doi:10.1016/0009-2541(86)90078-1

Canfield, D. E., and Thamdrup, B. (1994). The Production of 34 S-Depleted Sulfide during Bacterial Disproportionation of Elemental Sulfur. *Science* 266 (5193), 1973–1975. doi:10.1126/science.11540246

Chaytor, J. D., ten Brink, U. S., Solow, A. R., and Andrews, B. D. (2009). Size Distribution of Submarine Landslides along the US Atlantic Margin. *Mar. Geol.* 264 (1-2), 16–27. doi:10.1016/j.margeo.2008.08.007

Chen, D. F., Huang, Y. Y., Yuan, X. L., and Cathles, L. M. (2005). Seep Carbonates and Preserved Methane Oxidizing Archaea and Sulfate Reducing Bacteria Fossils Suggest Recent Gas Venting on the Seafloor in the Northeastern South China Sea. *Mar. Petroleum Geol.* 22 (5), 613–621. doi:10.1016/j.marpetgeo.2005.05.002

Chen, F., Hu, Y., Feng, D., Zhang, X., Cheng, S., Cao, J., et al. (2016). Evidence of Intense Methane Seepages from Molybdenum Enrichments in Gas Hydrate-Bearing Sediments of the Northern South China Sea. *Chem. Geol.* 443, 173–181. doi:10.1016/j.chemgeo.2016.09.029

Chen, F., Wang, X., Li, N., Cao, G., and Peckmann, J. (2019). Gas Hydrate Dissociation during Sea-Level Highstand Inferred from U/Th Dating of Seep Carbonate from the South China Sea. *Geophys. Res. Lett.* 46, 13928–13938. doi:10.1029/2019GL085643

Chen, F., Xin, S. U., Hongfeng, L. U., Chaoyun, C., Yang, Z., Sihai, C., et al. (2007). Carbon Stable Isotopic Composition of Benthic Foraminifers from the Northern of the South China Sea: Indicator of Methane-Rich Environment. *Mar. Geol. Quat. Geol.* 27 (4), 1–7.

Chen, F., Zhuang, C., Zhang, G., Lu, H., Duan, X., Zhou, Y., et al. (2014). Abnormal Sedimentary Events and Gas Hydrate Dissociation in Dongsha Area of the South China Sea during Last Glacial Period. *Earth Sci.-J. China U. Geosci.* 39 (11), 1517–1526. doi:10.3799/dqkx.2014.144

Colin, F., Ker, S., Riboulot, V., and Sultan, N. (2020). Irregular BSR: Evidence of an Ongoing Reequilibrium of a Gas Hydrate System. *Geophys. Res. Lett.* 47, 20. doi:10.1029/2020GL089906

Consolaro, C., Rasmussen, T. L., Panieri, G., Mienert, J., Bünz, S., and Sztybor, K. (2015). Carbon Isotope (δ¹³C) Excursions Suggest Times of Major Methane Release during the Last 14 Kyr in Fram Strait, the Deep-Water Gateway to the Arctic. *Clim. Past.* 11 (4), 669–685. doi:10.5194/cp-11-669-2015

Eiger, J., Berndt, C., Krastel, S., Piper, D. J. W., Gross, F., and Geissler, W. H. (2017). Chronology of the Fram Slide Complex Offshore NW Svalbard and its Implications for Local and Regional Slope Stability. *Mar. Geol.* 393, 141–155. doi:10.1016/j.margeo.2016.11.003

Feng, D., and Chen, D. (2015). Authigenic Carbonates from an Active Cold Seep of the Northern South China Sea: New Insights into Fluid Sources and Past Seepage Activity. *Deep Sea Res. Part II Top. Stud. Oceanogr.* 122, 74–83. doi:10.1016/j.dsr2.2015.02.003

Fontanier, C., Mackensen, A., Jorissen, F. J., Anschutz, P., Licari, L., and Griveaud, C. (2006). Stable Oxygen and Carbon Isotopes of Live Benthic Foraminifera from the Bay of Biscay: Microhabitat Impact and Seasonal Variability. *Mar. Micropaleontol.* 58 (3), 159–183. doi:10.1016/j.marmicro.2005.09.004

Formolo, M. J., and Lyons, T. W. (2013). Sulfur Biogeochemistry of Cold Seeps in the Green Canyon Region of the Gulf of Mexico. *Geochimica Cosmochimica Acta* 119, 264–285. doi:10.1016/j.gca.2013.05.017

Gong, S., Hu, Y., Li, N., Feng, D., Liang, Q., Tong, H., et al. (2018). Environmental Controls on Sulfur Isotopic Compositions of Sulfide Minerals in Seep Carbonates from the South China Sea. *J. Asian Earth Sci.* 168, 96–105. doi:10.1016/j.jseaes.2018.04.037

Han, X., Suess, E., Liebetrau, V., Eisenhauer, A., and Huang, Y. (2014). Past Methane Release Events and Environmental Conditions at the Upper Continental Slope of the South China Sea: Constraints by Seep Carbonates. *Int. J. Earth Sci. Geol. Rundsch* 103 (7), 1873–1887. doi:10.1007/s00531-014-1018-5

Handwerger, A. L., Rempel, A. W., and Skarbek, R. M. (2017). Submarine Landslides Triggered by Destabilization of High-Saturation Hydrate Anomalies. *Geochem. Geophys. Geosyst.* 18 (7), 2429–2445. doi:10.1002/2016gc006706

Herguera, J. C., Paull, C. K., Perez, E., Ussler, W., III, and Peltzer, E. (2014). Limits to the Sensitivity of Living Benthic Foraminifera to Pore Water Carbon Isotope Anomalies in Methane Vent Environments. *Paleoceanography* 29 (3), 273–289. doi:10.1002/2013pa002457

Horozal, S., Bahk, J.-J., Urgeles, R., Kim, G. Y., Cukur, D., Kim, S.-P., et al. (2017). Mapping Gas Hydrate and Fluid Flow Indicators and Modeling Gas Hydrate Stability Zone (GHSZ) in the Ulleung Basin, East (Japan) Sea: Potential Linkage between the Occurrence of Mass Failures and Gas Hydrate Dissociation. *Mar. Petroleum Geol.* 80, 171–191. doi:10.1016/j.marpetgeo.2016.12.001

Hu, Y., Chen, L., Feng, D., Liang, Q., Xia, Z., and Chen, D. (2017). Geochemical Record of Methane Seepage in Authigenic Carbonates and Surrounding Host Sediments: A Case Study from the South China Sea. *J. Asian Earth Sci.* 138, 51–61. doi:10.1016/j.jseaes.2017.02.004

Jorgensen, B. B., Bottcher, M. E., Luschen, H., Neretin, L. N., and Volkov, I., II (2004). Anaerobic Methane Oxidation and a Deep H2S Sink Generate Isotopically Heavy Sulfides in Black Sea Sediments. *Geochim. Cosmochim. Ac.* 68 (9), 2095–2118. doi:10.1016/j.gca.2003.07.017

Kaneko, M., Shingai, H., Pohlman, J. W., and Naraoka, H. (2010). Chemical and Isotopic Signature of Bulk Organic Matter and Hydrocarbon Biomarkers within Mid-slope Accretionary Sediments of the Northern Cascadia Margin Gas Hydrate System. *Mar. Geol.* 275 (1-4), 166–177. doi:10.1016/j.margeo.2010.05.010

Karstens, J., Haflidason, H., Becker, L. W. M., Berndt, C., Rüpke, L., Planke, S., et al. (2018). Glacigenic Sedimentation Pulses Triggered Post-glacial Gas Hydrate Dissociation. *Nat. Commun.* 9, 635. doi:10.1038/s41467-018-03043-z

Kayen, R. E., and Lee, H. J. (1991). Pleistocene Slope Instability of Gas Hydrate-Laden Sediment on the Beaufort Sea Margin. *Mar. Geotec.* 10 (1-2), 125–141. doi:10.1080/10641199109379886

Kwon, T.-H., Lee, K.-R., Cho, G.-C., and Lee, J. Y. (2011). Geotechnical Properties of Deep Oceanic Sediments Recovered from the Hydrate Occurrence Regions in the Ulleung Basin, East Sea, Offshore Korea. *Mar. Petroleum Geol.* 28 (10), 1870–1883. doi:10.1016/j.marpetgeo.2011.02.003

Leynaud, D., Mienert, J., and Nadim, F. (2004). Slope Stability Assessment of the Helland Hansen Area Offshore the Mid-Norwegian Margin. *Mar. Geol.* 213 (1-4), 457–480. doi:10.1016/j.margeo.2004.10.019

Li, G., Moridis, G. J., Zhang, K., and Li, X.-S. (2011). The Use of Huff and Puff Method in a Single Horizontal Well in Gas Production from Marine Gas Hydrate Deposits in the Shenhu Area of South China Sea. *J. Petroleum Sci. Eng.* 77 (1), 49–68. doi:10.1016/j.petrol.2011.02.009

Li, N., Yang, X., Peng, J., Zhou, Q., and Chen, D. (2018). Paleo-cold Seep Activity in the Southern South China Sea: Evidence from the Geochemical and Geophysical Records of Sediments. *J. Asian Earth Sci.* 168, 106–111. doi:10.1016/j.jseaes.2017.10.022

Li, W., Li, S., Alves, T. M., Rebesco, M., and Feng, Y. (2021). The Role of Sediment Gravity Flows on The Morphological Development of A Large Submarine Canyon (Taiwan Canyon), North-East South China Sea. *Sedimentology* 68, 1091–1108. doi:10.1111/sed.12818

Lim, Y. C., Lin, S., Yang, T. F., Chen, Y.-G., and Liu, C.-S. (2011). Variations of Methane Induced Pyrite Formation in the Accretionary Wedge Sediments Offshore Southwestern Taiwan. *Mar. Petroleum Geol.* 28 (10), 1829–1837. doi:10.1016/j.marpetgeo.2011.04.004

Lin, Q., Wang, J., Taladay, K., Lu, H., Hu, G., Sun, F., et al. (2016). Coupled Pyrite Concentration and Sulfur Isotopic Insight into the Paleo Sulfate-Methane Transition Zone (SMTZ) in the Northern South China Sea. *J. Asian Earth Sci.* 115, 547–556. doi:10.1016/j.jseaes.2015.11.001

Liu, J., Izon, G., Wang, J., Antler, G., Wang, Z., Zhao, J., et al. (2018). Vivianite Formation in Methane-Rich Deep-Sea Sediments from the South China Sea. *Biogeo. Discuss.* 15, 6329–6348. doi:10.5194/bg-15-6329-2018

Panieri, G. (2005). Benthic Foraminifera Associated with a Hydrocarbon Seep in the Rockall Trough (NE Atlantic). *Geobios* 38 (2), 247–255. doi:10.1016/j.geobios.2003.10.004

Panieri, G., Camerlenghi, A., Conti, S., Pini, G. A., and Cacho, I. (2009). Methane Seepages Recorded in Benthic Foraminifera from Miocene Seep Carbonates, Northern Apennines (Italy). *Palaeogeogr. Palaeocl.* 284 (3-4), 271–282. doi:10.1016/j.palaeo.2009.10.006

Panieri, G. (2006). Foraminiferal Response to an Active Methane Seep Environment: A Case Study from the Adriatic Sea. *Mar. Micropaleontol.* 61 (1-3), 116–130. doi:10.1016/j.marmicro.2006.05.008

Panieri, G., Lepland, A., Whitehouse, M. J., Wirth, R., Raanes, M. P., James, R. H., et al. (2017). Diagenetic Mg-Calcite Overgrowths on Foraminiferal Tests in the Vicinity of Methane Seeps. *Earth Planet. Sci. Lett.* 458, 203–212. doi:10.1016/j.epsl.2016.10.024

Passega, R. (1964). Grain Size Representation by CM Patterns as a Geologic Tool. *J. Sediment. Res.* 34 (4), 830–847. doi:10.1306/74d711a4-2b21-11d7-8648000102c1865d

Peckmann, J., and Thiel, V. (2004). Carbon Cycling at Ancient Methane-Seeps. *Chem. Geol.* 205 (3-4), 443–467. doi:10.1016/j.chemgeo.2003.12.025

Peketi, A., Mazumdar, A., Joshi, R. K., Patil, D. J., Srinivas, P. L., and Dayal, A. M. (2012). Tracing the Paleo Sulfate-Methane Transition Zones and H2S Seepage Events in Marine Sediments: An Application of C-S-Mo Systematics. *Geochem. Geophy. Geosy.* 13 (10), 1–11. doi:10.1029/2012gc004288

Pierre, C., Blanc-Valleron, M.-M., Caquineau, S., März, C., Ravelo, A. C., Takahashi, K., et al. (2016). Mineralogical, Geochemical and Isotopic Characterization of Authigenic Carbonates from the Methane-Bearing Sediments of the Bering Sea Continental Margin (IODP Expedition 323, Sites U1343-U1345). *Deep Sea Res. Part II Top. Stud. Oceanogr.* 125-126, 133–144. doi:10.1016/j.dsr2.2014.03.011

Portilho-Ramos, R. C., Cruz, A. P. S., Barbosa, C. F., Rathburn, A. E., Mulitza, S., Venancio, I. M., et al. (2018). Methane Release from the Southern Brazilian Margin during the Last Glacial. *Sci. Rep.* 8, 5948. doi:10.1038/s41598-018-24420-0

Rathburn, A. E., Levin, L. A., Held, Z., and Lohmann, K. C. (2000). Benthic Foraminifera Associated with Cold Methane Seeps on the Northern California Margin: Ecology and Stable Isotopic Composition. *Mar. Micropaleontol.* 38 (3-4), 247–266. doi:10.1016/s0377-8398(00)00005-0

Rathburn, A. E., Perez, M. E., Martin, J. B., Day, S. A., Mahn, C., Gieskes, J., et al. (2003). Relationships between the Distribution and Stable Isotopic Composition of Living Benthic Foraminifera and Cold Methane Seep Biogeochemistry in Monterey Bay, California. *Geochem. Geophy. Geosy.* 4, 1106. doi:10.1029/2003gc000595

Roberts, H. H., and Aharon, P. (1994). Hydrocarbon-derived Carbonate Buildups of the Northern Gulf-Of- Mexico Continental Slope- a Review of Submersible Investigations. *Geo-Mar. Lett.* 14 (2-3), 135–148. doi:10.1007/bf01203725

Sato, H., Hayashi, K.-I., Ogawa, Y., and Kawamura, K. (2012). Geochemistry of Deep Sea Sediments at Cold Seep Sites in the Nankai Trough: Insights into the Effect of Anaerobic Oxidation of Methane. *Mar. Geol.* 323-325, 47–55. doi:10.1016/j.margeo.2012.07.013

Schmiedl, G., Pfeilsticker, M., Hemleben, C., and Mackensen, A. (2004). Environmental and Biological Effects on the Stable Isotope Composition of Recent Deep-Sea Benthic Foraminifera, from the Western Mediterranean Sea. *Mar. Micropaleontol.* 51 (1-2), 129–152. doi:10.1016/j.marmicro.2003.10.001

Schneider, A., Crémière, A., Panieri, G., Lepland, A., and Knies, J. (2017). Diagenetic Alteration of Benthic Foraminifera from a Methane Seep Site on Vestnesa Ridge (NW Svalbard). *Deep Sea Res. Part I Oceanogr. Res. Pap.* 123, 22–34. doi:10.1016/j.dsr.2017.03.001

Schneider, A., Panieri, G., Lepland, A., Consolaro, C., Crémière, A., Forwick, M., et al. (2018). Methane Seepage at Vestnesa Ridge (NW Svalbard) since the Last Glacial Maximum. *Quat. Sci. Rev.* 193, 98–117. doi:10.1016/j.quascirev.2018.06.006

Schonfeld, J. (2001). Benthic Foraminifera and Pore-Water Oxygen Profiles: A Re-assessment of Species Boundary Conditions at the Western Iberian Margin. *J. Foraminifer. Res.* 31 (2), 86–107. doi:10.2113/0310086

Screaton, E. J., Torres, M. E., Dugan, B., Heeschen, K. U., Mountjoy, J. J., Ayres, C., et al. (2019). Sedimentation Controls on Methane-Hydrate Dynamics Across Glacial/Interglacial Stages: An Example From International Ocean Discovery Program Site U1517, Hikurangi Margin. *Geochem. Geophys. Geosyst.* 20, 4906–4921. doi:10.1029/2019GC008603

Solheim, A., Berg, K., Forsberg, C. F., and Bryn, P. (2005). The Storegga Slide Complex: Repetitive Large Scale Sliding with Similar Cause and Development. *Mar. Pet. Geol.* 22 (1-2), 97–107. doi:10.1016/b978-0-08-044694-3.50012-3

Stott, L. D., Bunn, T., Prokopenko, M., Mahn, C., Gieskes, J., and Bernhard, J. M. (2002). Does the Oxidation of Methane Leave an Isotopic Fingerprint in the Geologic Record? *Geochem. Geophy. Geosy.* 3 (2), 1–16. doi:10.1029/2001gc000196

Su, Z., He, Y., Wu, N., Zhang, K., and Moridis, G. J. (2012). Evaluation on Gas Production Potential from Laminar Hydrate Deposits in Shenhu Area of South China Sea through Depressurization Using Vertical Wells. *J. Petroleum Sci. Eng.* 86-87, 87–98. doi:10.1016/j.petrol.2012.03.008

Sultan, N., Marsset, B., Ker, S., Marsset, T., Voisset, M., Vernant, A. M., et al. (2010). Hydrate Dissolution as a Potential Mechanism for Pockmark Formation in the Niger Delta. *J. Geophys. Res.* 115, 1–33. doi:10.1029/2010jb007453

Tong, H., Feng, D., Cheng, H., Yang, S., Wang, H., Min, A. G., et al. (2013). Authigenic Carbonates from Seeps on the Northern Continental Slope of the

South China Sea: New Insights into Fluid Sources and Geochronology. *Mar. Petroleum Geol.* 43, 260–271. doi:10.1016/j.marpetgeo.2013.01.011

Uchida, M., Shibata, Y., Ohkushi, K., Ahagon, N., and Hoshiba, M. (2004). Episodic Methane Release Events from Last Glacial Marginal Sediments in the Western North Pacific. *Geochem. Geophy. Geosy* 5 (8), 1–14. doi:10.1029/2004gc000699

Wang, C. (2013). *The Magnetic Parameters and its Environmental Implications in Sediments since Late Pleistocene from Dongsha Area, South China Sea*. Beijing: China University of Geosciences, 1–45.

Wefer, G., Heinze, P.-M., and Berger, W. H. (1994). Clues to Ancient Methane Release. *Nature* 369 (6478), 282. doi:10.1038/369282a0

Wei, G.-J., Huang, C.-Y., Wang, C.-C., Lee, M.-Y., and Wei, K.-Y. (2006). High-resolution Benthic Foraminifer Delta C-13 Records in the South China Sea during the Last 150 Ka. *Mar. Geol.* 232 (3-4), 227–235. doi:10.1016/j.margeo.2006.08.005

Wu, X., Liang, Q., Ma, Y., Shi, Y., Xia, Z., Liu, L., et al. (2018). Submarine Landslides and Their Distribution in the Gas Hydrate Area on the North Slope of the South China Sea. *Energies* 11, 3481. doi:10.3390/en11123481

Yan, P., Deng, H., and Liu, H. (2006). The Geological Structure and Prospect of Gas Hydrate over the Dongsha Slope, South China Sea. *Terr. Atmos. Ocean. Sci.* 17 (4), 645–658. doi:10.3319/tao.2006.17.4.645(gh)

Yu, X., Wang, J., Li, S., Fang, J., Jiang, L., Cong, X., et al. (2013). The Relationship between Tectonic Subsidence and BSR of Upper Neogene in the Deep-Water Area of the Northern Continental Slope, South China Sea. *Acta Geol. sin-engl.* 87 (3), 804–818.

Zhang, B., Pan, M., Wu, D., and Wu, N. (2018). Distribution and Isotopic Composition of Foraminifera at Cold-Seep Site 973-4 in the Dongsha Area, Northeastern South China Sea. *J. Aaian Earth Sci.* 168, 14–154. doi:10.1016/j.jseaes.2018.05.007

Zhong, G., Cartigny, M. J. B., Kuang, Z., and Wang, L. (2015). Cyclic Steps along the South Taiwan Shoal and West Penghu Submarine Canyons on the Northeastern Continental Slope of the South China Sea. Geol. Sos. *Am. Bull.* 127 (5-6), 804–824. doi:10.1130/b31003.1

Zhu, M.-X., Shi, X.-N., Yang, G.-P., and Hao, X.-C. (2013). Formation and Burial of Pyrite and Organic Sulfur in Mud Sediments of the East China Sea Inner Shelf: Constraints from Solid-phase Sulfur Speciation and Stable Sulfur Isotope. *Cont. Shelf Res.* 54, 24–36. doi:10.1016/j.csr.2013.01.002

Conflict of Interest: The authors declare that the research was conducted in the absence of any commercial or financial relationships that could be construed as a potential conflict of interest.

frontiers | Frontiers in Earth Science

ORIGINAL RESEARCH
published: 26 May 2022
doi: 10.3389/feart.2022.882080

The Controlling Factors of the Natural Gas Hydrate Accumulation in the Songnan Low Uplift, Qiongdongnan Basin, China

Yang Wei[1,2,3,4], Kuang Zenggui[3,4], Ren Jinfeng[3,4], Liang Jinqiang[3,4], Lu Hong[2], Ning Zijie[3,4], Xu Chenlu[3,4], Lai Hongfei[3,4], Chen Rui[4], Zhao Bin[4], Chen Jing[3,4], Zhang Xi[3,4] and Liu Lei[5]*

[1]Southern Marine Science and Engineering Guangdong Laboratory (Guangzhou), Guangzhou, China, [2]State Key Laboratory of Organic Geochemistry, Guangzhou Institute of Geochemistry, Chinese Academy of Sciences, Guangzhou, China, [3]National Engineering Research Center of Gas Hydrate Exploration and Development, Guangzhou, China, [4]Guangzhou Marine Geology Survey, China Geological Survey, Guangzhou, China, [5]Beijing International Engineering Consulting Co., Ltd., Beijing, China

OPEN ACCESS

Edited by:
Lihua Zuo,
Texas A&M University Kingsville, United States

Reviewed by:
Taohua He,
China University of Petroleum, Huadong, China
Qilin Xiao,
Yangtze University, China
Wei Zhou,
Southern Marine Science and Engineering Guangdong Laboratory (Zhuhai), China

***Correspondence:**
Ren Jinfeng
jf_ren@163.com

Specialty section:
This article was submitted to Marine Geoscience, a section of the journal Frontiers in Earth Science

Received: 23 February 2022
Accepted: 11 April 2022
Published: 26 May 2022

Citation:
Wei Y, Zenggui K, Jinfeng R, Jinqiang L, Hong L, Zijie N, Chenlu X, Hongfei L, Rui C, Bin Z, Jing C, Xi Z and Lei L (2022) The Controlling Factors of the Natural Gas Hydrate Accumulation in the Songnan Low Uplift, Qiongdongnan Basin, China. Front. Earth Sci. 10:882080. doi: 10.3389/feart.2022.882080

Hydrocarbon charging stages and natural gas hydrate accumulation models were established in the Songnan Low Uplift, Qiongdongnan Basin (QDNB), China. Detailed geochemical analysis, paleotemperature and paleopressure analyses, seismic interpretation, and hydrocarbon charging characterization were conducted to investigate the controlling factors of natural gas hydrate accumulation. The Yacheng and Lingshui formations in the Lingshui Sag were identified as effective source rocks. The $\delta^{13}C_1$ values of the gas hydrates vary from –35.97‰ to –59.50‰, following a direction from the Sag Center to the Low Uplift, indicating that $\delta^{13}C_1$ values became relatively lighter during gas migration. Seismic data evidence revealed that large-scale faults, laterally distributed sandstones, and gas chimneys were comprehensive, however efficient hydrocarbon migration pathways. Systematic overpressure was developed in the Yacheng and Huangliu formations, which offer sufficient hydrocarbon migration impetus. Hydrocarbon-bearing aqueous inclusions and their coexisting aqueous inclusions were observed in the Huangliu Formation in the Lingshui Sag, indicating four stages of hydrocarbon charging in the QDNB. Based on the comprehensive analysis in this research, two gas hydrate accumulation models were proposed in the Songnan Low Uplift, QDNB, as follows: 1) a mixture of gas migrated by large-scale faults and a thermogenic-biogenic mixed gas model and 2) gas hydrates from laterally distributed sandstones sealed by MTDs.

Keywords: migration pathway, paleopressure characteristics, hydrocarbon charging stages, gas hydrate accumulation, the Songnan Low Uplift

INTRODUCTION

The Qiongdongnan Basin (QDNB) is located in the northwestern continental margin of the South China Sea, which is a petroliferous Cenozoic basin with strong overpressure being widely developed (Huang et al., 2003; Hao et al., 2007; Zhu et al., 2009; Huang et al., 2012; Huang et al., 2016). A series of large gas fields, including LS25-1, LS17-2, LS18-1, and YL8 gas fields, were discovered in the Neogene Huangliu and Yinggehai formations in the west of the QDNB in the last few decades, with

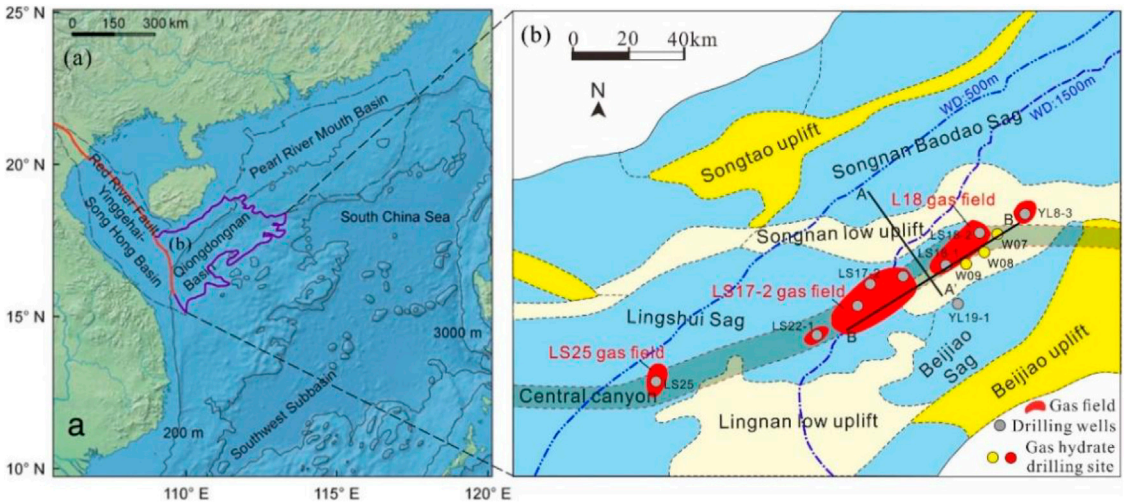

FIGURE 1 | (A) Location of the Qiongdongnan Basin (QDNB) with purple color in the northwestern South China Sea. **(B)** Structural sketch of the western QDNB (modified after He et al., 2021) with gas fields and drilling wells being labeled. WD, water depth.

the main source rocks of the Paleogene Yacheng and Lingshui formations being deposited in a coastal plain or littoral to a neritic environment (Huang et al., 2012; Zhang et al., 2014; Huang et al., 2016; Su et al., 2017; Zhu et al., 2018; Xie et al., 2019; Zhang et al., 2019a, Zhang et al., 2019b, Zhang et al., 2019c; Su et al., 2021). The Yacheng and Lingshui formations of the LS25-1 and LS17-2 gas fields in the Lingshui Sag were overpressured, while the main gas-bearing layers, the Mesozoic granite Yacheng reservoirs of the YL8-1 and YL8-3 gas fields in the Songnan Low Uplift, were normal pressured (Wang et al., 2016; Gan et al., 2019; Shi et al., 2019; Yang et al., 2021).

A clean and efficient energy resource natural gas hydrate has been widely discovered in the QDNB (Zhang et al., 2018; Fang et al., 2019; Liang et al., 2019; Wei et al., 2019; Ye et al., 2019), showing significant exploration potentials in this area. In addition, a number of typical and representative gas hydrates were discovered and are being sampled at sites GMGS5, W07, W08, and W09 by the Guangzhou Marine Geological Survey (GMGS) in 2018, which were identified as typical gas hydrate sites in the Songnan Low Uplift. Stable carbon isotope analysis of the hydrated gas indicated a mixed microbial and thermogenic origin for their formation (Liang et al., 2019; Wei et al., 2019; Ye et al., 2019; Zhang et al., 2020; Lai et al., 2021).

Numerous research studies on the geological, geochemical, and geophysical characteristics of the gas hydrate system have been conducted in the QDNB (Zhang et al., 2018; Liang et al., 2019; Wei et al., 2019; Ye et al., 2019; Deng et al., 2021); however, natural gas hydrate accumulation mechanisms, reservoir characterization, and production trials need further research, especially on the influences of hydrocarbon charge on natural gas hydrate accumulation. The Yacheng and Lingshui formations are the most important source rocks in the Lingshui Sag, which have entered the dry gas window. The overpressured source rock intervals and preferential migration pathways offer continuous gas sources into the hydrate-bearing reservoirs. As a result, source rock maturations, migration pathways, overpressure, and hydrate-bearing reservoir characteristics co-contribute to natural gas hydrate accumulation.

Aims of this research are to

(1) investigate the migration pathways and overpressure characteristics of natural gas hydrates in the QDNB;
(2) clarify the influence of hydrocarbon charge on gas hydrate accumulation;
(3) understand origins of gas forming the gas hydrates; and
(4) establish natural gas hydrate accumulation models.

GEOLOGICAL SETTING

The Lingshui Sag is located in the west of the deep-water area of the QDNB (**Figure 1**). The LS25 gas field is located in the west of the Lingshui Sag, adjacent to the Ledong Sag, and the LS17-2 and LS18 gas fields are located in the eastern slope of the Lingshui Sag (**Figure 1B**, Yao et al., 2015; Zhang et al., 2016; Huang et al., 2017; Li et al., 2017; Zhang et al., 2019c). Tectonic evolution of the QDNB comprises two stages: rifting from Eocene to Oligocene and a depression stage from Miocene to Quaternary (Hu et al., 2013). The QDNB experienced multi-stage tectonic movements, including Shenhu, Zhujiang, Nanhai, and Dongsha tectonic movements (Wang et al., 2021). Tectonic evolution of the Lingshui Sag is consistent with that of the QDNB, leading to the deposition of 6,000–12,000 m Cenozoic strata (**Figure 2**), which are divided into eight formations, including the Oligocene Yacheng and Lingshui formations (36~30 Ma and 30~21 Ma), the Miocene Sanya, Meishan, and Huangliu formations (21~15.5 Ma, 15.5~10.5 Ma, and 10.5~5.5 Ma), and the Pliocene Yinggehai Formation (5.5~1.9 Ma) (**Figure 2**) (Su et al., 2018).

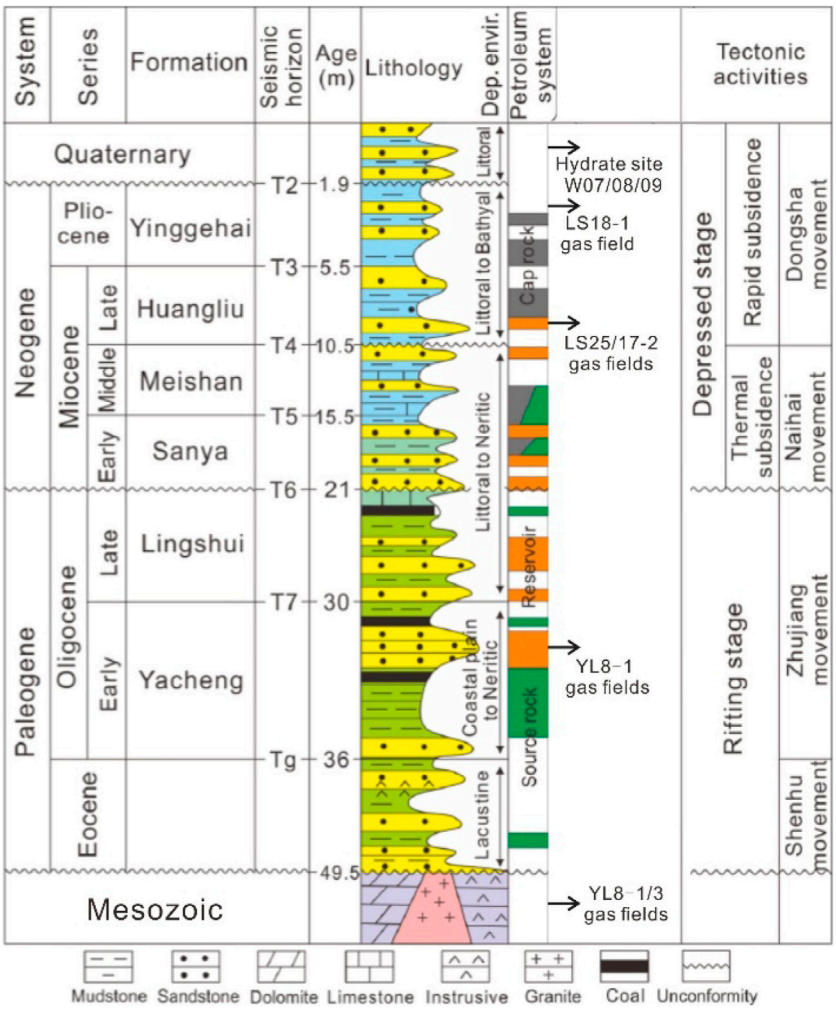

FIGURE 2 | Simplified stratigraphic column of the QDNB (modified after Su et al., 2018; Lai et al., 2021). Dep. Envir., depositional environment.

The Songnan Low Uplift—which is bounded by the Lingshui Sag, the Songnan-Baodao sags, the Changchang Sag, and the Beijiao Sag (**Figure 1B**)—comprises the main targeted areas for natural gas hydrate exploration. Discoveries of the YL8 and YL1 gas fields indicated that the Songnan Low Uplift is an area of natural gas accumulation (Shi et al., 2019; Zhang et al., 2019c; Yang et al., 2021), which is also subject to gas hydrate accumulation. Gas-bearing formations of the YL8-1/3, LS25/17-2, and LS18-1 gas fields are mainly the Huangliu, Yinggehai, and Yacheng formations, and the hydrate-bearing formation in the GMGS5-W07/W08/W09 sites are mainly in the Quaternary formation (**Figure 2**).

RESULTS AND DISCUSSION

Gas Source

TOC contents and Rock-Eval parameters were effective to characterize hydrocarbon generation potentials of source rocks (He et al., 2018; He et al., 2022). TOC contents of the analyzed mudstones, carbonaceous mudstones, and coal samples in the Yacheng and Lingshui formations range from 0.13 wt.% to 96.51 wt.% (**Figure 3A**). Rock-Eval data reveal hydrocarbon generation potentials of free hydrocarbon (S_1) and generative hydrocarbon potential (S_2) of the analyzed samples ranging from 0.02 mg HC/g TOC to 154.05 mg HC/g TOC (**Figure 3A**), which are identified as the main source rocks forming the discovered gas fields. Most of the analyzed samples were characterized as fair to very good source rocks, with carbonaceous mudstones and coal samples being identified as excellent source rocks, indicating great hydrocarbon generation potential for the source rock formations (**Figure 3A**).

Maximum temperature (T_{max}) and hydrogen index (I_H) values show close-set distribution, with T_{max} values ranging from 408 to 482°C and I_H values ranging from 11 mg HC/g TOC to 462 mg HC/g TOC, respectively (**Figure 3B**). The average T_{max} reaches 444°C, and the average I_H value is 101 mg HC/g TOC, indicating

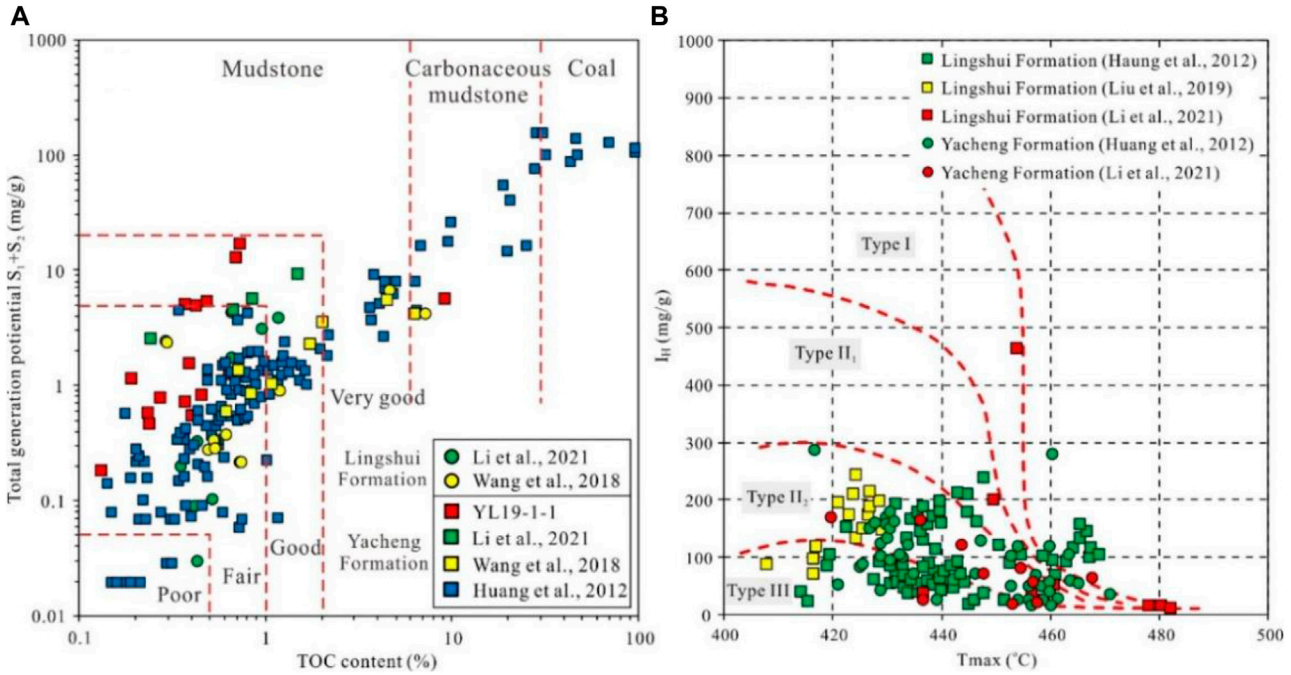

FIGURE 3 | (A) Hydrocarbon generation potential evaluation and **(B)** organic matter types of the Yacheng and Lingshui formations in the QDNB.

TABLE 1 | Thermal maturity of source rocks, namely, Meishan, Lingshui, and Yacheng formations, in the Sag Center and Low Uplift in the QDNB.

Area	Well	Formation	Tmax (oC)	Ro (%)	Data source
Sag Center	L25-2	Yacheng	/	>2.0	Zhang et al. (2019c)
	L25-1	Meishan	/	0.80	
Low Uplift	LS33-1	Lingshui	/	0.79	Wang et al. (2018)
	YL19	Lingshui	422	0.51	
	LS33	Lingshui	424	0.49	He, (2020)
	YL19	Yacheng	474	1.14	
	YL8	Yacheng	/	1.52~1.70	Li et al. (2020)

that source rocks of the Yacheng and Lingshui formations are sufficiently mature to generate dry gas. In the T_{max} versus I_H plots (**Figure 3B**), most of the analyzed samples were considered to be Type II_2 and III kerogens, with a smaller number of analyzed samples being characterized as Type II_1 kerogen (**Figure 3B**).

Vitrinite reflectance (R_o%) was measured to assess thermal maturities of the source rocks in this research. R_o% values of the samples in the Yacheng Formation are >2.0% in the Lingshui Sag, a higher value than that of the samples in the Low Uplift (**Table 1**). The results indicate that the Yacheng and Lingshui formations in the QDNB are highly matured to over-matured.

Natural gas compositions in the LS25, LS17-2, LS18-1, YL8-1, and YL8-3 gas fields and the GMGS5-W08 hydrate site are dominated by hydrocarbon gas, accounting for 76.38~99.79% of the total gas volumes (**Table 2**). Methane (CH_4) contents of the gas fields and the GMGS5-W08 gas hydrate site range from 75.48 to 96.14% and 79.16 to 97.69%, respectively (**Table 2**). Wet gas (C_2+) contents vary from 0.85 to 8.44% for the gas fields and from 2.10 to 19.55% for the gas hydrate samples (**Table 2**). Dryness coefficients ($C_1/C_{1\text{-}5}$ by volume) were in the range of 0.91–0.95 (**Table 2**). The $\delta^{13}C_1$, $\delta^{13}C_2$, and $\delta^{13}C_3$ values of all gas fields and W08 range from −59.5 to 35.97‰, −28.40 to 22.40‰, and −27.80‰ to −20.20‰, respectively. The $\delta^{13}C$ values of the CO_2 samples vary from −20.70‰ to −2.70‰ in the gas fields (**Table 2**).

Previous studies suggested that $\delta^{13}C_1$ and $\delta^{13}C_2$ threshold values to distinguish thermogenic and microbial origins of CH_4 and C_2H_6 are −55‰ and −42‰, respectively, (Milkov, 2005). Thermogenic gas can be subdivided into coal-type and oil-type gas by $\delta^{13}C_2$ and $\delta^{13}C_3$ threshold values of −28‰ and −25‰, respectively (Xu and Shen, 1996; Huang et al., 2016; Liu Q. et al., 2019; Lai et al., 2021). A plot of the $\delta^{13}C_1$ values versus the $\delta^{13}C_2$ values of the analyzed gas samples shows that methane (CH_4) in both the gas hydrates and gas fields was composed of thermo-

TABLE 2 | Gas composition and isotopic composition of the LS25, LS17-2, LS18-1, YL8-1, and YL8-3 large gas fields and hydrate-related gas at site GMGS-W08 in the QDNB. (Data were collected from Liang et al., 2015; Zhang et al., 2019a; Zhang et al., 2019b; Li et al., 2020; Lai et al., 2021; Yang et al., 2021; Zhu et al., 2021).

Well	Depth (m)	Formation	Gas compositions (%)				C1/(C1~C5)	δ13C (‰)			
			C1	C2+	CO2	N2		C1	C2	C3	CO2
LS25 gas field											
LS25-1	3,760.8	Huangliu	87.31	7.83	3.08	1.79	0.92	−39.37	−25.39	−23.30	−8.97
	3,920.0~890.0		85.17	7.77	6.08	0.97	0.92	−38.30	−25.15	−23.71	−3.68
LS25-2	4,094.0		81.38	8.07	8.89	1.33	0.91	−35.97	−25.57	−23.13	−4.53
LS17-2 gas field											
LS17-1	3,306.0	Huangliu	90.04	5.94	0.9	2.97	0.94	−36.93	−23.63	−22.09	−16.42
	3,366.4		91.05	5.75	0.68	2.37	0.94	−37.30	−23.62	−21.89	−16.39
LS17-2	3,331.3		91.55	5.93	0.07	2.17	0.94	−37.55	−24.09	−22.96	−18.03
LS22-1-1	3,339.0		91.16	7.98	0.31	0.55	0.92	−39.20	−26.20	−23.80	/
	3,352.5		91.37	7.75	0.32	0.57	0.93	−38.80	−26.00	−23.70	/
	3,391.0		91.53	7.59	0.32	0.55	0.93	−39.20	−26.00	−24.10	/
LS17-2-1	3,306.0		92.51	6.38	0.45	0.68	0.94	−36.81	−23.51	−21.97	/
	3,324.0		93.25	5.93	0.21	0.62	0.94	−36.78	−23.62	−22.17	/
	3,366.4		92.69	6.21	0.46	0.63	0.94	−37.25	−23.77	−21.87	/
	3,468.5		92.56	6.31	0.52	0.61	0.94	−36.83	−24.09	−21.58	/
LS1728N1	3,305.2		/	/	/	/	/	−40.15	−25.94	/	/
LS1728N2	3,406.5		/	/	/	/	/	−38.89	−25.95	/	/
LS1727N3	3,477.0		/	/	/	/	/	−46.46	−26.12	/	/
LS1724N4	3,251.0		/	/	/	/	/	−39.07	−25.37	/	/
LS1724N6	3,355.0		/	/	/	/	/	−39.15	−23.61	/	/
LS1724N7	3,445.0		/	/	/	/	/	−38.36	−24.57	/	/
L17-B	3,228.5		91.68	5.90	0.70	1.66	0.94	−38.20	−23.80	−21.80	−20.70
L17-A	3,321.0~3,351.0		93.00	5.97	0.62	0.26	0.94	−37.30	−24.10	−22.20	−9.20
L17-G	3,477.0		83.38	8.44	0.30	5.87	0.91	−46.50	−26.10	−24.00	−15.70
LS18-1 gas field											
LS18-1	2,819.9~2,846.7	Yinggehai	93.17	6.27	0.05	0.51	0.94	−40.46	−25.17	−23.82	/
LS18-A	2,819.9~2,846.7		92.89	6.24	0.04	0.64	0.94	−40.20	−25.30	−24.00	/
YL8-1 gas field											
YL8-1	/	Yacheng	/	/	/	/	0.97	−45.20	−28.40	−27.80	/
	/	Pre-tertiary	/	/	/	/	0.97	−44.90	−27.40	−27.70	/
YL8-1	/	Sanya	/	/	/	/	0.98	−45.50	−27.50	−27.60	/
	/	Yacheng	/	/	/	/	0.98	−44.00	−27.10	−27.80	/
	/	Pre-tertiary	/	/	/	/	0.99	−42.70	−26.90	/	/
YL8-1-A	2,956.7	Mesozoic	94.50	2.97	0.60	1.80	0.98	−45.00	−27.50	−27.60	−16.00
YL8-1-A	2,988.2		94.60	3.05	0.50	1.70	0.98	−44.20	−27.20	−27.40	−17.20
YL8-1-B	3,070.0		84.02	0.85	14.08	1.03	0.99	−43.80	−26.90	/	−8.90
YL8-1-B	3,354.0		75.48	0.90	19.07	4.55	0.99	−42.40	−26.80	/	−8.90
YL8-3 gas field											
YL8-3	/	Pre-tertiary	/	/	/	/	0.97	−43.20	−26.80	−26.50	/
YL8-3	/	Yacheng	/	/	/	/	0.97	−43.30	−26.70	−26.50	/
	/	Pre-tertiary	/	/	/	/	0.97	−43.40	−26.70	−26.40	/
YL8-3-A	2,828.8~2,936.0	Mesozoic	95.67	3.22	0.83	0.19	0.97	−42.70	−26.60	−26.60	−2.70
YL8-3-B	2,894.0	Yacheng	95.68	3.08	0.37	0.85	0.97	−43.30	−27.00	−26.80	−16.40
YL8-3-B	2,905.0	Yacheng	90.36	2.94	0.32	6.39	0.97	−43.70	−26.30	−26.70	−17.60
YL8-3-B	2,911.0	Yacheng	96.14	3.19	0.22	0.44	0.97	−43.30	−27.00	−26.50	−17.60
GMGS5-W08 gas hydrate drilling site											
GH-1	8.0	Quaternary	97.69	2.10	/	/	/	−59.50	−26.00	−22.40	/
PCS-1	32.9		94.94	4.81	/	/	/	−54.40	−25.50	−22.90	/
GH-2	62.9		81.21	17.46	/	/	/	−56.30	−26.90	−22.70	/
PCS-2	79.0		95.75	4.08	/	/	/	−58.60	−25.10	−21.60	/
PCS-3	80.9		95.73	4.04	/	/	/	−48.80	−22.40	−20.20	/
PCS-4	112.3		96.46	3.32	/	/	/	−53.80	−23.30	−20.70	/
PCS-5	145.7		83.49	15.54	/	/	/	−49.30	−27.50	−23.00	/
GH-3	148.4		79.16	19.55	/	/	/	−50.40	−26.50	−22.80	/
PCS-6	158.0		84.17	14.89	/	/	/	−50.40	−26.90	−22.20	/
PCS-7	187.1		92.82	6.63	/	/	/	−50.40	−26.70	−23.20	/

microbial methane (CH_4) and thermogenic methane (CH_4). Ethanes (C_2H_6) were derived solely from coal-type thermogenic gas with $\delta^{13}C_2$ values > −28‰ (**Figure 4A**).

A notable phenomenon is that the $\delta^{13}C_1$ values decreased from −35.97‰ to −59.5‰ along gas migration pathways (from LS25 to W08 or from the Sag Center to the Low Uplift),

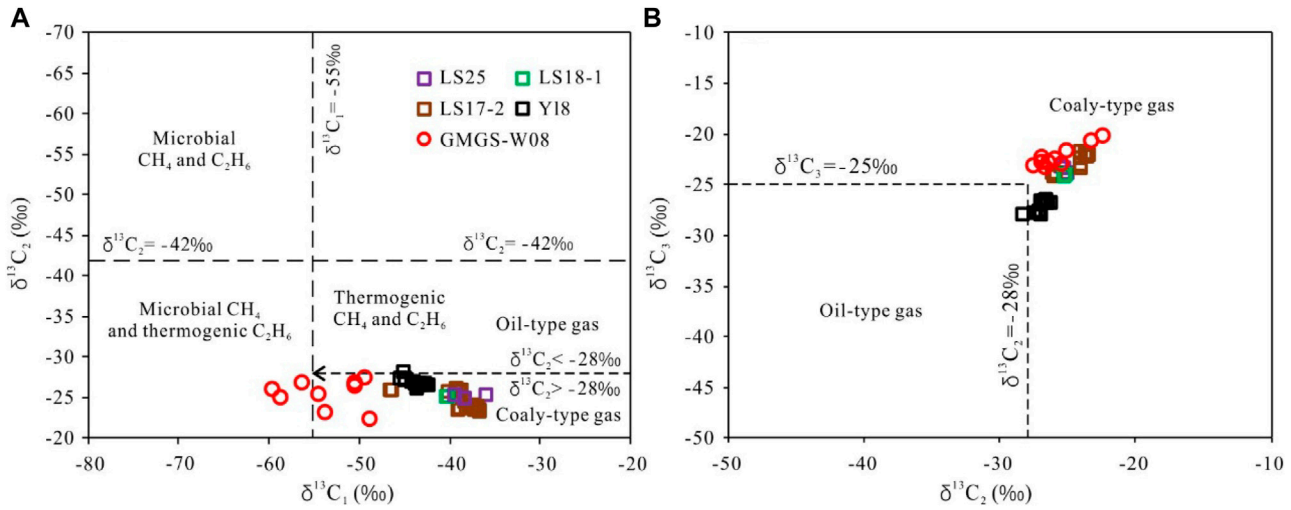

FIGURE 4 | (A) Genetic diagram of $\delta^{13}C_1$ versus $\delta^{13}C_2$ showing a thermogenic and microbial mixed gas of the natural gas hydrate (modified from Milkov, 2005). **(B)** Genetic diagram of $\delta^{13}C_2$ versus $\delta^{13}C_3$ (Modified from Liu S. Y. et al., 2019) showing a coal-type gas of the natural gas hydrate. All data were collected from the LS25, LS17-2, LS18-1, YL18, and GMGS5-W08 gas fields (**Table 2**).

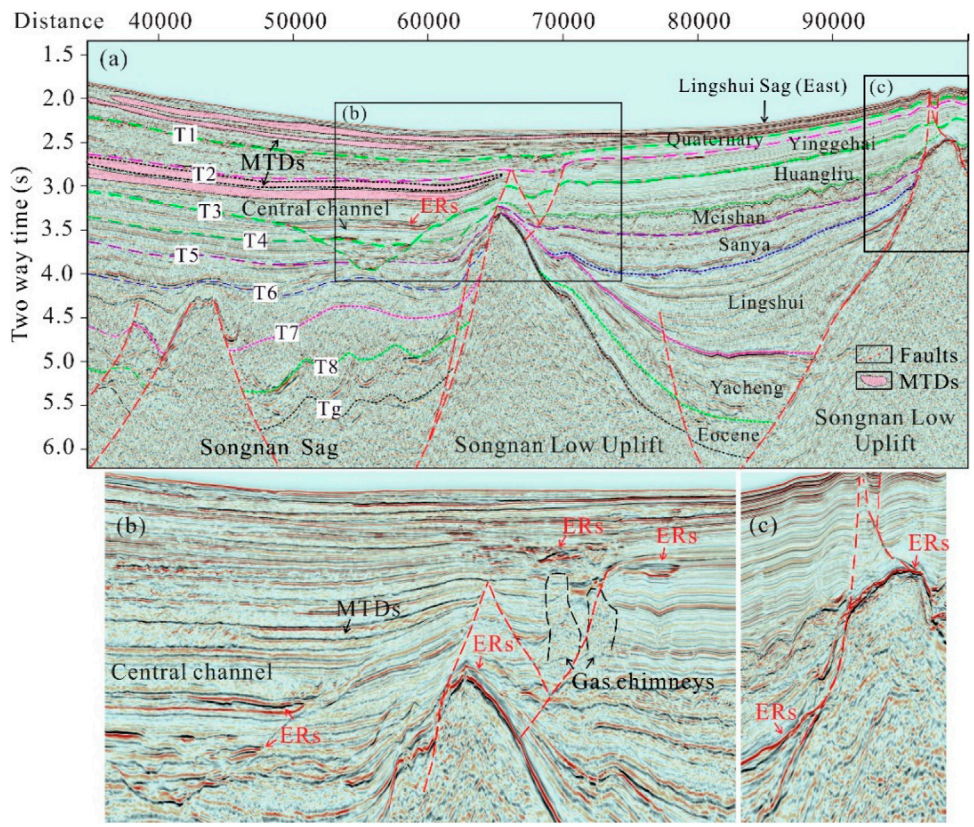

FIGURE 5 | (A) Representative seismic profiles of the Songnan Low Uplift. **(B,C)** Partial enlarged details for the geological characteristics of the Songnan Low Uplift.

indicating lighter $\delta^{13}C_1$ values due to fraction effects of secondary migration and increased contents of biogenic gas. The C_2+ hydrocarbon gas in the hydrate was mainly derived from the deeply buried coal-type source rocks, and methane (CH_4) often has a mixed thermogenic and microbial origin.

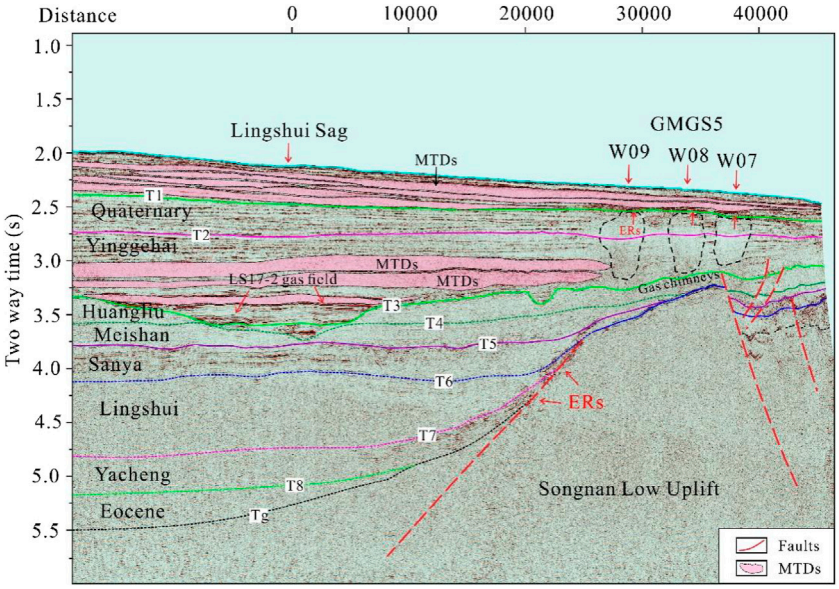

FIGURE 6 | Seismic reflection features of the bottom simulating reflector (BSR), diapirs, gas chimneys, and faults in the QDNB, showing the accumulation process of the hydrate-related gas at the site GMGS5-W08.

Migration Pathways

Natural gas hydrate accumulation, which is similar to the conventional oil and gas reservoirs, is often associated with faults, gas chimneys, and diapirism. Faults that fail to reach the gas hydrate stability zone (GHSZ) directly are not efficient pathways for hydrate accumulation that some large-scale faults, however, are often connected with gas chimneys to form efficient fluid migration pathway systems. Normal faults are identified in the study area, which extend from the source rocks to the Quaternary strata or connected with gas chimneys at shallower burial depths (**Figure 5A**), a characteristic indicating intense fluid migration from deep areas to the seafloor or shallow traps through the fault-chimney pathways. In parallel, enhanced reflections (ERs) were widely developed on the top of or at the flanks of the gas chimneys, faults, and central channel (**Figures 5B,C**), indicating significant fluid flow in the study area (Cartwright et al., 2007; Horozal et al., 2009; Petersen et al., 2010; Karstens & Berndt, 2015; Kang et al., 2016).

Gas chimneys were developed mainly in the Low Uplift, exhibiting vertical columnar or finger shapes (**Figure 5B** and **Figure 6**). The GMGS5 W07, W08, and W09 gas hydrate sites are located directly on the top of three large gas chimneys (**Figure 6**). Diameters of the gas chimneys vary from 3 to 5 km, and the top of the chimneys terminates at the T1 interface, ~150 m from the seafloor (**Figure 6**). Gas chimneys are characterized by mushroom-shaped acoustic blanking zones, with weak internal push-down reflections being interpreted (**Figure 6**). The high-amplitude reflections at the edge or within the gas chimneys were identified as high-velocity gas hydrate in the soft sediments (**Figure 6**). Normal faults were interpreted within the gas chimneys, with invisible faults and/or fractures beyond seismic resolution being widely developed in the interior of the gas chimneys. With widely distributed enhanced reflections (ERs) on the top of or at the flanks of the gas chimneys (**Figure 6**), fluid charging should occur constantly in the study area.

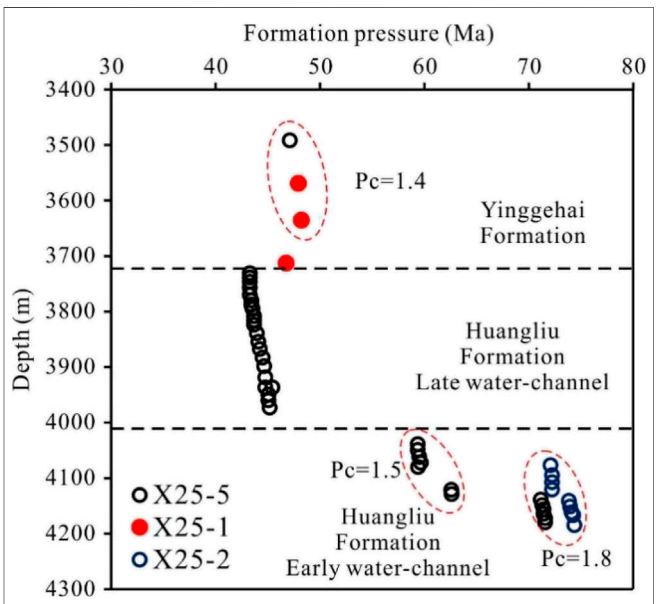

FIGURE 7 | Pressure distribution of LS25 gas fields in the Lingshui Sag (Li et al., 2021).

Overpressures

Pressure and temperature, especially overpressure, are important driving forces for sub-surface fluid flow, and understanding their

TABLE 3 | Homogenization temperatures (Ths) of coexisting aqueous inclusions and hydrocarbon charging time (HCT) of the large gas fields in the Lingshui Sag.

Location	Formation	Inclusion type	Th (°C)	HCT (Ma)	Reference
Well W-6 (LS17)	Huangliu	Hydrocarbon-bearing	100~240 peak value 160~180	0.4~0.6	Xu et al. (2014)
LS17 gas field	Huangliu	Aqueous	Stage I: 78~90.2	2~0	He, (2020)
LS25 gas field			Stage II: 99.7~101.2	2~0	
X17 gas field (LS17)	Huangliu	Hydrocarbon-bearing	Stage I: 87.2	0.3	Gan et al. (2019)
			Stage II: 110~120	0.2	
			Stage III: 140~160	0.0	

origins and evolution is the key aspect to understand oil and gas migration and accumulation mechanisms.

In the LS25 gas field of the QDNB, two separate overpressure systems were identified (**Figure 7**, Gan et al., 2019). The lower overpressure system is mainly formed by hydrocarbon generation, with a maximum pressure coefficient (Pc) > 1.8, which extends up to the bottom of the Huangliu Formation. The upper overpressure system is in the second member of the Yinggehai Formation, which was subject to rapid subsidence and disequilibrium compaction of the shallow marine mudstones, with a pressure coefficient (Pc) of c. 1.4. Gas accumulation in the Huangliu Formation (from 1.8 Ma to the present) is relatively later than that in the second member of the Yinggehai overpressured interval, indicating that gas accumulation in the late Huangliu channel system occurred between the formation of the two high-pressure systems since 1.8 Ma, a timing with large-scale hydrocarbon generation and migration. Two thick gas layers in the early and late phases of channel depositions have pressure coefficients of 1.5 and 1.0, respectively. Sandstone intervals deposited early in the channel have a pressure coefficient (Pc) up to 1.8, a characteristic indicating poor gas preservation conditions of upper units of the channel due to the development of intense fractures.

Gas generated source rocks were accumulated in the distinct reservoirs of the channel system by overpressure and buoyancy, with continuous upward migration into the second member of the Yinggehai Formation being hindered by the existence of the upper overpressure system. However, the fluid can be migrated laterally along the porous sandstones in the channels which were proved by the discovery of the LS18 gas field, east of the Central Canyon.

Hydrocarbon-Charging Stages

Fluid inclusion can be applied to confirm phases of oil and gas accumulation, which record important information on fluid properties, trapping temperatures, and pressures under *in situ* conditions. Hydrocarbon-bearing aqueous inclusions and aqueous inclusions were widely developed in the Huangliu Formation in the LS25 and LS17-2 gas fields in the Lingshui Sag (Xu et al., 2014; Gan et al., 2018; He, 2020). Homogenization temperatures (Ths) of the hydrocarbon-bearing aqueous inclusions are >120°C, ranging from 130 to 160°C. The Ths of the aqueous inclusions range from 78 to 90.2°C and from 99.7 to 101.2°C in wells LS17-2-7 and LS25-3-1, respectively, which is significantly lower than that of the hydrocarbon-bearing aqueous inclusions (He, 2020).

At least three hydrocarbon charging stages were identified in the study area according to the Ths of the hydrocarbon-bearing aqueous inclusions in the Huangliu Formation of the LS17 gas field, corresponding to Ths of 87.2°C, 110~120°C, and 140~160°C, respectively (Gan et al., 2019; **Table 3**). Timing for hydrocarbon charging is estimated to be c. 0.3 Ma at a temperature of 87.2°C. Some of the Ths of the hydrocarbon-bearing aqueous inclusions are relatively higher than the current strata temperature (approximately 100°C), indicating the influence of deep thermal fluids/gas in the Central Canyon gas fields in the Lingshui Sag, which were driven by the deep high-pressure/temperature fluid systems.

In addition, hydrocarbon-bearing aqueous inclusions and the coexisting aqueous inclusions were commonly developed in the target formation, indicating multi-stages of fluid migration in the QDNB. The Ths of the coexisting aqueous inclusions range from 78 to 90.2°C and from 99.7 to 101.2°C in wells LS17 and LS25 in the Lingshui Sag, matching a trapping time of 2~0 Ma (**Table 3**).

The previous study indicates four stages of hydrocarbon and fluid migration stages in the QDNB, with charging times from 17.5 to 13 Ma (Stage I), 10 to 5.5 Ma (Stage II), 4 to 2 Ma (Stage III), and 2 to 0 Ma (Stage VI), respectively (**Figure 8**) (Liu and Chen, 2011; Huang et al., 2012; Xu et al., 2014; Su et al., 2016a, 2016b; Xu et al., 2017; Gan et al., 2018; Zhong et al., 2019; He, 2020).

Natural Gas Hydrate Accumulation Mechanism

Based on the geochemical analysis, paleotemperature/pressure and hydrocarbon charging analyses, and the structural characteristics of the QDNB, preliminary accumulation models for natural gas hydrates were proposed in the Songnan Low Uplift (**Figure 9**).

Prior to the accumulation processes forming gas hydrates, favorable hydrocarbon generation conditions, efficient migration pathways, and sufficient driving forces are key aspects to form gas hydrates. TOC contents and Rock-Eval results indicate good hydrocarbon generation potential of the Yacheng and Lingshui source rock formations, which are highly matured or over-matured. Effective hydrocarbon migration systems in the study area mainly comprise faults, laterally distributed extended channel sandstones, and gas chimneys. Faults that extend from the source rock intervals up to the Quaternary strata or gas chimneys provide efficient hydrocarbon migration pathways. In the LS25 gas field, late deposition in the channel of the Huangliu Formation has a Pc value of 1.0, and the early deposited intervals in the channel have Pc values of 1.5~1.8, which are significantly higher. Some of the Pc

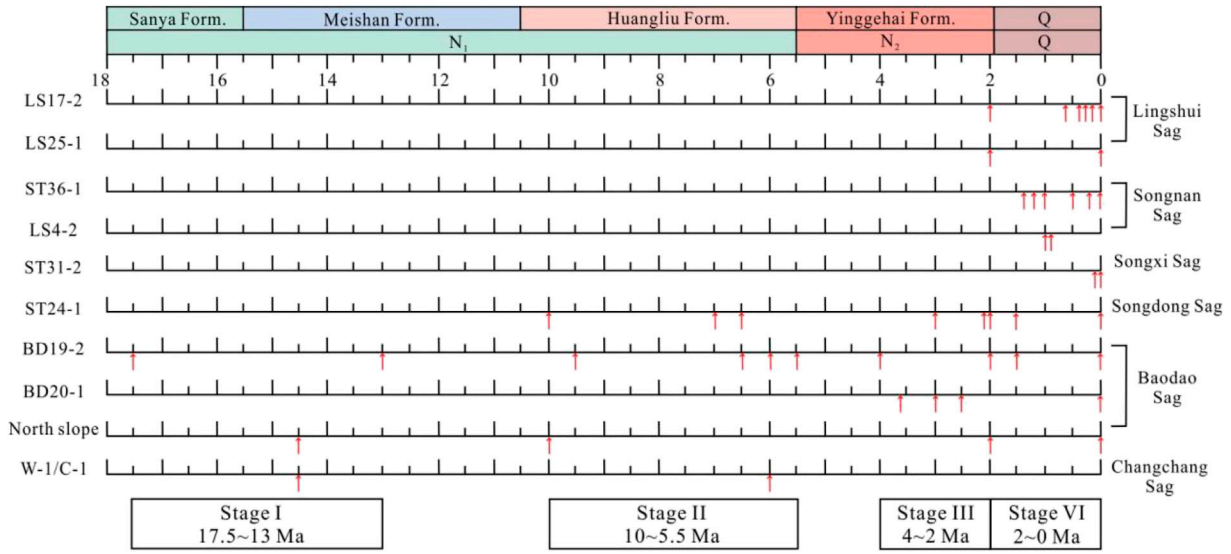

FIGURE 8 | Hydrocarbon-charging orders and times in the eastern part of the QDNB.

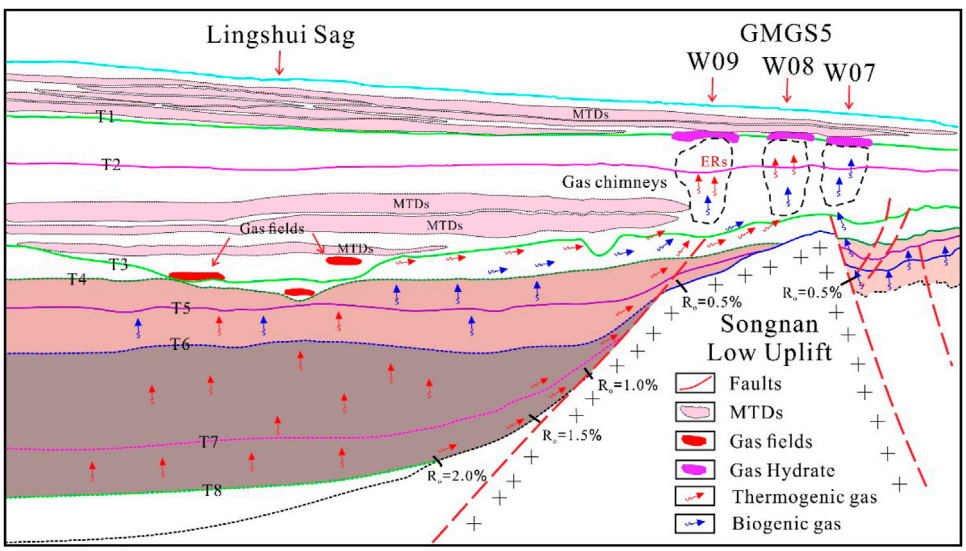

FIGURE 9 | Hydrocarbon-charging and gas hydrate accumulation model of the Songnan Low Uplift in the QDNB.

values in the Yacheng Formation can even reach 2.1 (Zhang et al., 2016), indicating that strong overpressure at depth can provide sufficient impetus for hydrocarbon migration.

With our analysis, high-overmatured thermogenic gas was postulated to be derived from mudstone or coal-bearing strata of the Oligocene Yacheng and Lingshui formations. Gases in the Lingshui Sag could migrate upward through faults. Meanwhile, natural gas was also migrated through laterally distributed sandstone due to the sealing effect of the MTDs (**Figure 9**). Furthermore, migration of gas was mixed with shallow biogenic gas, thus forming the gas hydrate, such as the cases of the W09 and W08 gas hydrates (**Figure 9**). Biogenic gas derived from immature or low mature source rocks of the shallow Sanya and Meishan formations can also migrate through faults to form gas hydrates in the study area, such as the W07 gas hydrates (**Figure 9**). A mixture of biogenic gas in the study area can also be the result of diffusion through interbedded microcracks and pore networks in the shallower strata.

CONCLUSION

Detailed geochemical analysis, paleotemperature and paleopressure analyses, seismic interpretation, and hydrocarbon charging characterization were conducted to

investigate the controlling factors of natural gas hydrate accumulation. Our research reaches the following conclusions.

(1) The Yacheng and Lingshui formations with high-overmatured source rocks are effective to generate thermogenic gas, and the Meishan and Sanya formations with immature to low matured source rocks can provide abundant biogenic gas.
(2) Large-displacement faults, laterally distributed sandstones, and overpressure are the main driving force and migration pathways for the formation of gas hydrates at shallow burial depths.
(3) Four stages of fluid migration occurred in the QDNB, with stage IV (2~0 Ma) hydrocarbon migration as the main stage of gas hydrate formation.
(4) The natural gas hydrate accumulation model was subscribed into two types: large-scale fault migration and lateral migration of thermogenetic gases to form the hydrate in shallow sediments.

DATA AVAILABILITY STATEMENT

The original contributions presented in the study are included in the article/Supplementary Material, further inquiries can be directed to the corresponding author.

AUTHOR CONTRIBUTIONS

YW and RJ wrote the whole manuscript and provided all figures. NZ, XC, and LH gathered and prepared data. CR provided all tables. KZ, LJ, and LH contributed to the discussion and outline. ZB, CJ, ZX, and LL imporved the grammar of writing.

FUNDING

This article was granted by the Key Special Project for Introduced Talents Team of Southern Marine Science and Engineering Guangdong Laboratory (Guangzhou) (Grant No. GML2019ZD0102), the State Key Laboratory of Organic Geochemistry, GIGCAS (Grant No. SKLOG 2020**), and the Guangdong Basic and Applied Basic Research Foundation (No. 2020A1515110405).

ACKNOWLEDGMENTS

The authors are grateful to all participants of the fifth China National Gas Hydrate Drilling Expedition (GMGS5) during the preparation of this manuscript.

REFERENCES

Cartwright, J., Huuse, M., and Aplin, A. (2007). Seal Bypass Systems. *Bulletin* 91, 1141–1166. doi:10.1306/04090705181

Deng, W., Liang, J., Zhang, W., Kuang, Z., and He, Y. (2021). Typical Characteristics of Fracture-Filling Hydrate-Charged Reservoirs Caused by Heterogeneous Fluid Flow in the Qiongdongnan Basin, Northern South China Sea. *Mar. Pet. Geology.* 124, 104810. doi:10.1016/j.marpetgeo.2020.104810

Fang, Y., Wei, J., Lu, H., Liang, J., Lu, J. a., Fu, J., et al. (2019). Chemical and Structural Characteristics of Gas Hydrates from the Haima Cold Seeps in the Qiongdongnan Basin of the South China Sea. *J. Asian Earth Sci.* 182, 103924. doi:10.1016/j.jseaes.2019.103924

Gan, J., Wu, D., Zhang, Y., Liu, S., Guo, M., Li, X., et al. (2019). Distribution Pattern of Present-Day Formation Temperature in the Qiongdongnan Basin: Implications for Hydrocarbon Generation and Preservation. *Acta Metallurgica Sinica* 25 (6), 952–960. doi:10.16108/j.issn.1006-7493.2019053

Gan, J., Zhang, Y. Z., and Liang, G. (2018). On Accumulation Process and Dynamic Mechanism of Natural Gas in the Deep-Water Area of Central Canyon, Qiongdongnan Basin. *Acta Geol. Sin.* 92 (11), 2359–2362. doi:10.3969/j.issn.0001-5717.2018.11.011

Hao, F., Zou, H., Gong, Z., Yang, S., and Zeng, Z. (2007). Hierarchies of Overpressure Retardation of Organic Matter Maturation: Case Studies from Petroleum Basins in China. *Bulletin* 91 (10), 1467–1498. doi:10.1306/05210705161

He, C., Gan, J., Liang, G., Li, X., Wang, X., Li, T., et al. (2021). Characteristics of the Organic Carbon Isotope of Oligocene Source Rocks in deepwater Area of the Qiongdongnan Basin and its Main Controlling Factors. *Geochemical* 50 (2), 175–184. PhD thesis.

He, C. M. (2020). *Geochemistry and Hydrocarbon Generation of Source Rocks and Origins of Natural Gases in the deepwater Area of the Qiongdongnan Basin*. [PhD thesis]. Guangzhou: Guangzhou institute of Geochemistry, Chinese Academy of Science.

He, T., Li, W., Lu, S., Pan, W., Ying, J., Zhu, P., et al. (2022). Mechanism and Geological Significance of Anomalous Negative δ13Ckerogen in the Lower Cambrian, NW Tarim Basin, China. *J. Pet. Sci. Eng.* 208, 109384. doi:10.1016/j.petrol.2021.109384

He, T., Lu, S., Li, W., Tan, Z., and Zhang, X. (2018). Effect of Salinity on Source Rock Formation and its Control on the Oil Content in Shales in the Hetaoyuan Formation from the Biyang Depression, Nanxiang Basin, Central China. *Energy Fuels* 32, 6698–6707. doi:10.1021/acs.energyfuels.8b01075

Horozal, S., Lee, G. H., Yi, B. Y., Yoo, D. G., Park, K. P., Lee, H. Y., et al. (2009). Seismic Indicators of Gas Hydrate and Associated Gas in the Ulleung Basin, East Sea (Japan Sea) and Implications of Heat Flows Derived from Depths of the Bottom-Simulating Reflector. *Mar. Geology.* 258, 126–138. doi:10.1016/j.margeo.2008.12.004

Hu, B., Wang, L., Yan, W., Liu, S., Cai, D., Zhang, G., et al. (2013). The Tectonic Evolution of the Qiongdongnan Basin in the Northern Margin of the South China Sea. *J. Asian Earth Sci.* 77, 163–182. doi:10.1016/j.jseaes.2013.08.022

Huang, B., Li, L., and Huang, H. (2012). Origin and Accumulation Mechanism of Shallow Gases in the North Baodao Slope, Qiongdongnan Basin, South China Sea. *Pet. Exploration Develop.* 39, 567–573. doi:10.1016/s1876-3804(12)60077-9

Huang, B., Tian, H., Li, X., Wang, Z., and Xiao, X. (2016). Geochemistry, Origin and Accumulation of Natural Gases in the deepwater Area of the Qiongdongnan Basin, South China Sea. *Mar. Pet. Geology.* 72, 254–267. doi:10.1016/j.marpetgeo.2016.02.007

Huang, B., Xiao, X., and Li, X. (2003). Geochemistry and Origins of Natural Gases in the Yinggehai and Qiongdongnan Basins, Offshore South China Sea. *Org. Geochem.* 34, 1009–1025. doi:10.1016/s0146-6380(03)00036-6

Huang, H. T., Huang, B. J., Huang, Y. W., Li, X., and Tian, H. (2017). Condensate Origin and Hydrocarbon Accumulation Mechanism of the Deepwater Giant Gas Field in Western South China Sea: a Case Study of Lingshui 17-2 Gas Filed in Qiongdongnan Basin, South China Sea. *Pet. Exploration Develop.* 44 (3), 380–388. doi:10.1016/s1876-3804(17)30047-2

Kang, N.-k., Yoo, D.-g., Yi, B.-y., and Park, S.-c. (2016). Distribution and Origin of Seismic Chimneys Associated with Gas Hydrate Using 2D Multi-Channel Seismic Reflection and Well Log Data in the Ulleung Basin, East Sea. *Quat. Int.* 392, 99–111. doi:10.1016/j.quaint.2015.08.002

Karstens, J., and Berndt, C. (2015). Seismic Chimneys in the Southern Viking Graben - Implications for Palaeo Fluid Migration and Overpressure Evolution. *Earth Planet. Sci. Lett.* 412, 88–100. doi:10.1016/j.epsl.2014.12.017

Lai, H., Fang, Y., Kuang, Z., Ren, J., Liang, J., Lu, J. a., et al. (2021). Geochemistry, Origin and Accumulation of Natural Gas Hydrates in the Qiongdongnan Basin, South China Sea: Implications from Site GMGS5-W08. *Mar. Pet. Geology.* 123, 104774. doi:10.1016/j.marpetgeo.2020.104774

Li, J. S., Li, X. Q., Wang, Y., Wang, G., Xu, X. D., and Liu, H. Y. (2021). Geochemical Characteristics and Hydrocarbon Generation Potential Evaluation of Source Rocks in Deep-Water Area of Qiongdongnan Basin. *J. Mining Sci. Technol.* 6 (2), 166–175. doi:10.19606/j.cnki.jmst.2021.02.004

Li, X., Gan, J., Yang, X., Laing, G., and Wang, Z. L. (2020). Characterization of Natural Gas Migration in the Ancient Buried hill, East Deep-Water Area of Qiongdongnan Basin. *Nat. Gas Geosci.* 31 (7), 970–979. doi:10.11764/j.issn.1672-1926.2020.02.007

Li, X. S., Zhang, Y. C., Yang, X. B., Xu, X. F., Zhang, J. X., and Man, X. (2017). New Understanding and Progress of Natural Gas Exploration in Yinggehai-Qiongdongnan Basin. *China Offshore Oil and Gas* 29 (6), 5–15. doi:10.11935/j.issn.1673-1506.2017.06.001

Liang, G., Gang, J., and Li, X. (2015). Genetic Types and Origin of Natural Gas in Lingshui Sag, Qiongdongnan Basin. *China Offshore Oil Gas* 27, 47–53. (In Chinese with English abstract). doi:10.11935/j.issn.1673-1506.2015.04.006

Liang, J., Zhang, W., Lu, J. a., Wei, J., and Kuang, Z. (2019). Geological Occurrence and Accumulation Mechanism of Natural Gas Hydrates in the Eastern Qiongdongnan basin of the South China Sea: Insights from Site GMGS5-W9-2018. *Mar. Geology.* 418, 106042. doi:10.1016/j.margeo.2019.106042

Liu, Q., Wu, X., Wang, X., Jin, Z., Zhu, D., Meng, Q., et al. (2019). Carbon and Hydrogen Isotopes of Methane, Ethane, and Propane: a Review of Genetic Identification of Natural Gas. *Earth-Science Rev.* 190, 247–272. doi:10.1016/j.earscirev.2018.11.017

Liu, S. Y., Chen, H. Y., Li, D. Y., Sun, W. Y., and Li, C. Y. (2019). Sedimentary Characteristics and Source Rock Development Model of the Oligocene Lingshui Formation in Lingshui Sag, Qiongdongnan Basin. *Mar. Origin Pet. Geology.* 24 (01), 63–70. doi:10.3969/j.issn.1672-9854.2019.01.008

Liu, Z., and Chen, H. (2011). Hydrocarbon Charging Orders and Times in the Eastern Area of Qiongdongnan Basin. *Geoscience* 25 (2), 279–288. doi:10.1007/s12182-011-0123-3

Milkov, A. V. (2005). Molecular and Stable Isotope Compositions of Natural Gas Hydrates: a Revised Global Dataset and Basic Interpretations in the Context of Geological Settings. *Org. Geochem.* 36, 681–702. doi:10.1016/j.orggeochem.2005.01.010

Petersen, G. J., Bünz, S., Hustoft, S., Mienert, J., and Klaeschen, D. (2010). High-resolution P-Cable 3D Seismic Imaging of Gas Chimney Structures in Gas Hydrated Sediments of an Arctic Sediment Drift. *Mar. Pet. Geology.* 27 (9), 1981–1994. doi:10.1016/j.marpetgeo.2010.06.006

Shi, H. S., Yang, J. H., Zhang, Y. Z., Gan, J., and Yang, J. H. (2019). Geological Understanding Innovation and Major Breakthrough to Natural Gas Exploration in Deep Water in Qiongdongnan Basin. *China Pet. Exploration* 24 (6), 691–698. doi:10.3969/j.issn.1672-7703.2019.06.001

Su, A., Chen, H., Chen, X., Liu, H., Liu, Y., and Lei, M. (2018). New Insight into Origin, Accumulation and Escape of Natural Gas in the Songdong and Baodao Regions in the Eastern Qiongdongnan basin, South China Sea. *J. Nat. Gas Sci. Eng.* 52, 467–483. doi:10.1016/j.jngse.2018.01.026

Su, A., Chen, H., He, C., Lei, M., and Liu, Y. (2017). Complex Accumulation and Leakage of YC21-1 Gas Bearing Structure in Yanan Sag, Qiongdongnan Basin, South China Sea. *Mar. Pet. Geology.* 88, 798–813. doi:10.1016/j.marpetgeo.2017.09.020

Su, A., Chen, H. H., He, C., Zhai, P. Q., Liu, Y. H., and Lei, M. Z. (2016b). The Characteristic of Fluid Activities and Diagenetic Responses of the Pressure Discharging Zone in Yacheng Area, Qiongdongnan Basin, South China Sea. *Acta Petrolei sinica* 37 (10), 1216–1230. doi:10.7623/syxb201610002

Su, A., Chen, H., Yang, W., Feng, Y. X., Zhao, J. X., and Lei, M. Z. (2021). Hydrocarbon Gas Leakage from High-Pressure System in the Yanan Sag, Qiongdongnan Basin, South China Sea. *Geol. J.* 56, 5094–5108. doi:10.1002/gj.4225

Su, A., Du, J. M., Chen, H. H., Yu, Y., and Lei, M. Z. (2016a). Diagenetic Fluid Type and Activity History of Controlling the Development of Abnormal Pore Zone: Taking the north Margin of Baodao Sag, Qiongdongnan Basin as an Example. *Nat. Gas Geosci.* 27 (10), 1837–1847. doi:10.11764/j.issn.1672-1926.2016.10.1837

Wang, P., Li, S., Suo, Y., Guo, L., Santosh, M., Li, X. Y., et al. (2021). Structural and Kinematic Analysis of Cenozoic Rift Basins in South China Sea: A Synthesis. *Earth-Science Rev.* 216 (2), 103522. doi:10.1016/j.earscirev.2021.103522

Wang, Y., Li, X. Q., Liang, W. L., Sun, K. X., Zhang, M., Xu, X. D., et al. (2018). Characteristics of Saturated Hydrocarbon Biomarkers and the Biogenetic Composition of Source Rocks in the Qiongdongnan Basin. *J. Mining Sci. Technol.* 3 (3), 209–218. doi:10.19606/j.cnki.jmst.2018.03.001

Wang, Z., Sun, Z., Zhang, Y., Guo, M., Zhu, J., Huang, B., et al. (2016). Distribution and Hydrocarbon Accumulation Mechanism of the Giant deepwater central canyon Gas Field in Qiongdongnan basin, Northern South China Sea. *China Pet. Exploration* 21 (4), 1–12. doi:10.3969/j.issn.1672-7703.2016.04.006

Wei, J., Liang, J., Lu, J., Zhang, W., and He, Y. (2019). Characteristics and Dynamics of Gas Hydrate Systems in the Northwestern South China Sea - Results of the Fifth Gas Hydrate Drilling Expedition. *Mar. Pet. Geology.* 110, 287–298. doi:10.1016/j.marpetgeo.2019.07.028

Xie, Y., Zhang, G., Sun, Z., Zeng, Q., Zhao, Z., and Guo, S. (2019). Reservoir Forming Conditions and Key Exploration Technologies of Lingshui 17-2 Giant Gas Field in deepwater Area of Qiongdongnan Basin. *Pet. Res.* 4, 1–18. doi:10.1016/j.ptlrs.2019.01.004

Xu, H. Z., Zhang, Y. Z., Lin, C. M., Pei, J. X., and Liu, Y. Z. (2014). Characteristics and Key Controlling Factors of Natural Gas Accumulation in the central Submarine canyon, Qiongdongnan Basin. *Acta Geol. Sinica* 88 (9), 1741–1751. doi:10.3969/j.issn.0001-5717.2014.09.010

Xu, X. D., Zhang, Y. Z., Xiong, X. F., Gan, J., and Liang, G. (2017). Genesis, Accumulation and Distribution of CO2 in the Yinggehai-Qiongdongnan Basin, North South China Sea. *Mar. Geology. Front.* 33 (7), 45–54. doi:10.16028/j.1009-2722.2017.07005

Xu, Y., and Shen, P. (1996). A Study of Natural Gas Origins in China. *AAPG Bull.* 80, 1604–1614. doi:10.1306/64eda0c8-1724-11d7-8645000102c1865d

Yang, X. B., Zhou, J., Yang, J. H., He, X. H., Wu, H., Gan, J., et al. (2021). Natural Gas Source and Accumulation Model of Mesozoic Buried hill in the Eastern Deep Water Area of Qiongdongnan Basin. *Acta Petrolei Sinica* 42 (3), 283–292. doi:10.7623/syxb202103002

Yao, Z., Wang, Z. F., Zuo, Q. M., Sun, Z. P., Dang, Y. Y., Mao, X. L., et al. (2015). Critical Factors for the Formation of Large-Scale deepwater Gas Field in Central Canyon System of Southeast Hainan Basin and its Exploration Potential. *Acta Petrolei Sinica* 36 (11), 1358–1366. doi:10.7623/syxb201511005

Ye, J., Wei, J., Liang, J., Lu, J., Lu, H., and Zhang, W. (2019). Complex Gas Hydrate System in a Gas Chimney, South China Sea. *Mar. Pet. Geology.* 104, 29–39. doi:10.1016/j.marpetgeo.2019.03.023

Zhang, G. C., Zeng, Q. B., Su, L., Yang, H. Z., Chen, Y., Yang, D. S., et al. (2016). Accumulation Mechanism of LS 17-2 Deep Water Giant Gas Field in Qiongdongnan Basin. *Acta Petrolei Sinica* 37 (S1), 34–46. doi:10.7623/syxb2016S1004

Zhang, G., Zhang, Y., Shen, H., and He, Y. (2014). An Analysis of Natural Gas Exploration Potential in the Qiongdongnan Basin by Use of the Theory of "Joint Control of Source Rocks and Geothermal Heat". *Nat. Gas Industry B* 1, 41–50. doi:10.1016/j.ngib.2014.10.005

Zhang, W., Liang, J. Q., Lu, J. A., Meng, M. M., He, Y. L., Deng, W., et al. (2020). Characteristics and Controlling Mechanism of Typical Leakage Gas Hydrate Reservoir Forming System in the Qiongdongnan Basin, Northern South China Sea. *Nat. Gas Industry* 40 (8), 90–99. doi:10.3787/j.issn.1000-0976.2020.08.007

Zhang, W., Liang, J. Q., Su, P. B., Wei, J. G., Sha, Z. B., Lin, L., et al. (2018). Migrating Pathways of Hydrocarbons and Their Controlling Effects Associated with High Saturation Gas Hydrate in Shenhu Area, Northern South China Sea. *Geology. China* 45 (1), 1–14. doi:10.12029/gc20180101

Zhang, Y. Z., Gan, J., Xu, X. D., Liang, G., and Li, X. (2019c). The Source and Natural Gas Lateral Migration Accumulation Model of Y8-1 Gas Bearing Structure, East Deep Water in the Qiongdongnan Basin. *Earth Sci.* 44 (8), 2609–2618. doi:10.3799/dqkx.2019.159

Zhang, Y. Z., Li, X. S., Xu, X. D., Gan, J., Yang, X. B., Liang, G., et al. (2019b). Genesis, Origin, and Accumulation Process of the Natural Gas of L25 Gas Field in the Western deepwater Area, Qiongdongnan Basin. *Mar. Origin Pet. Geology.* 24 (3), 73–82. doi:10.3969/j.issn.1672-9854.2019.03.009

Zhang, Y. Z., Xu, X. D., Gan, J., Yang, X. B., Zhu, J. T., Yang, J. H., et al. (2019a). Formation Condition and Accumulation of Pliocene Strata-Trapped Gas Field L18 in the deepwater Area of the Qiongdongnan Basin. *Haiyang Xuebao* 41 (3), 121–133. doi:10.3969/j.issn.0253-4193.2019.03.012

Zhong, J., Yang, X., Zhu, P., Xu, S., Deng, X., Tuo, L., et al. (2019). Porosity Evolution Differences of the Lingshui Formation Reservoir between Baodao

and Changchang Sag, Qiongdongnan Basin. *Earth Sci.* 44 (8), 2665–2676. doi:10.3969/j.issn.0253-4193.2019.03.012

Zhu, W. L., Huang, B. J., Mi, L., Wilkins, R. W. T., Fu, N., and Xiao, X. M. (2009). Geochemistry, Origin, and Deep-Water Exploration Potential of Natural Gases in the Pearl River Mouth and Qiongdongnan Basins, South China Sea. *AAPG Bull.* 93, 741–761. doi:10.1306/02170908099

Zhu, W., Shi, H., Huang, B., Zhong, K., and Huang, Y. (2021). Geology and Geochemistry of Large Gas fields in the deepwater Areas, continental Margin Basins of Northern South China Sea. *Mar. Pet. Geology.* 126, 104901. doi:10.1016/j.marpetgeo.2021.104901

Zhu, Y., Sun, L., Hao, F., and Tuo, L. (2018). Geochemical Composition and Origin of Tertiary Oils in the Yinggehai and Qiongdongnan Basins, Offshore South China Sea. *Mar. Pet. Geology.* 96, 139–153. doi:10.1016/j.marpetgeo.2018.05.029

Conflict of Interest: Author LL was employed by the company Beijing International Engineering Consulting Co., Ltd.

The remaining authors declare that the research was conducted in the absence of any commercial or financial relationships that could be construed as a potential conflict of interest.

Publisher's Note: All claims expressed in this article are solely those of the authors and do not necessarily represent those of their affiliated organizations, or those of the publisher, the editors, and the reviewers. Any product that may be evaluated in this article, or claim that may be made by its manufacturer, is not guaranteed or endorsed by the publisher.

frontiers | Frontiers in Earth Science

ORIGINAL RESEARCH
published: 02 June 2022
doi: 10.3389/feart.2022.902517

Distribution Characteristics of Quaternary Channel Systems and Their Controlling Factors in the Qiongdongnan Basin, South China Sea

Miaomiao Meng[1,2,3]*, *Jinqiang Liang*[1,2,3], *Zenggui Kuang*[1,2,3], *Jinfeng Ren*[1,2,3], *Yulin He*[1,2,3]*, *Wei Deng*[1,2,3] and *Yuehua Gong*[1,2,3]

[1]Guangzhou Marine Geological Survey, China Geological Survey, Guangzhou, China, [2]Southern Marine Science and Engineering Guangdong Laboratory (Guangzhou), Guangzhou, China, [3]National Engineering Research Center of Gas Hydrate Exploration and Development, Guangzhou, China

OPEN ACCESS

Edited by:
Jinan Guan,
Guangzhou Institute of Energy Conversion (CAS), China

Reviewed by:
Junjie Liu,
Guangzhou Institute of Geochemistry (CAS), China
Xiaoqun Yang,
Institute of Geology and Geophysics (CAS), China

***Correspondence:**
Miaomiao Meng
18811309981@126.com
Yulin He
heyulin200910@163.com

Specialty section:
This article was submitted to Sedimentology, Stratigraphy and Diagenesis, a section of the journal Frontiers in Earth Science

Received: 23 March 2022
Accepted: 05 May 2022
Published: 02 June 2022

Citation:
Meng M, Liang J, Kuang Z, Ren J, He Y, Deng W and Gong Y (2022) Distribution Characteristics of Quaternary Channel Systems and Their Controlling Factors in the Qiongdongnan Basin, South China Sea. Front. Earth Sci. 10:902517. doi: 10.3389/feart.2022.902517

The study of deepwater channels is important for the understanding of the sedimentary evolution mechanism and the sedimentary process of the marginal sea. In 2019, thick pore-filling gas hydrate with high saturation was firstly discovered in the Quaternary sands of the Qiongdongnan Basin (QDNB), which expanded the reservoir types of gas hydrates in the South China Sea. However, the distribution of sand-related channels is not well characterized, which limits the ability to predict sand reservoirs with gas hydrate. Using integrated 2D/3D seismic, multi-beam, well logging, and coring data, the current study documents the distribution characteristics of channel systems in the Quaternary strata and discusses their controlling factors. The integrated analysis shows that the channel-related sedimentary facies include channel-filling facies, levee facies, crevasse splay facies, and lobes facies. A total of six periods of channel systems is identified in the Quaternary strata. There are obvious distribution differences between the Channel 1 and Channel 3 systems when comparing the western, middle, and eastern sections: the channels in the western and eastern sections are mainly dominated by near straight V-shaped channels, while the middle section mainly consists of large braided channels, where channel-levee sedimentary facies developed. Compared with the distribution of the Central Canyon that developed in the Miocene, the Channel 1 and Channel 3 systems in the western section show southward migration since the Miocene. The distribution and evolution of Quaternary channels were likely collectively controlled by seafloor morphology, tectonic movement, sea-level fluctuations, and provenance supply. Tectonic movement controls seafloor morphology, which directly controls the flow of channels and their distribution characteristics; provenance supply determines the scale and sedimentary characteristics of each channel. The periodic changes in sea-level determine the evolution of multi-stage channel systems. This study has implications for the prediction of gas hydrate–bearing sands in the Quaternary QDNB and deepens our understanding of the Quaternary tectonic and sedimentary evolution in the QDNB.

Keywords: channel system, Quaternary, sedimentary characteristic, Qiongdongnan Basin, gas hydrates

1 INTRODUCTION

Gas hydrates are crystalline compounds of water and gas molecules, mainly methane, which form under stable high-pressure and low-temperature conditions (Sloan, 2003), and are regarded as a promising new clean energy resource (Moridis et al., 2013; Collett, 2014; Chong et al., 2016). Being able to find highly saturated gas hydrate ore is a crucial link in the gas hydrate exploration and development process. Of the total quantity of gas hydrate resources available globally, 97% is mainly distributed in the deep-water sedimentary system, such as mass transport deposits, deep-water turbidity fans, and channel-levee facies (Yu and Zhang, 2005; Behseresht and Bryant, 2012; Liang et al., 2018; Santra et al., 2020). Theoretically, the high deposition rate of coarse grain deposits not only provides a good fluid transport pathway for the formation of gas hydrates, but also acts as the perfect reservoir for its accumulation (Sha et al., 2009; Egawa et al., 2015). For gas hydrate production, coarse grain reservoirs have good porosity, high permeability, and high stability. This reservoir type is the priority target for mining, as was the case with the great breakthroughs in sandstone gas hydrate exploration in the Mallik delta and Alaska continental slope. Many countries, such as Japan, the United States, Canada, South Korea, and India, are targeting coarse grain reservoirs for gas hydrate test production. Reservoirs of gas hydrate drilling areas with high investigation and research levels, such as the Nankai Trough and the Gulf of Mexico basin (Alaminos Canyon area, Walker Ridge area, and Green Canyon area) are located in the channel-levee facies or turbidity deposits (Uchida and Tsuji, 2004; Boswell et al., 2009; 2012; Scholz et al., 2012; Waite et al., 2019). Therefore, one of the important tasks for gas hydrate exploration is to find dominant sedimentary facies that might provide favorable reservoirs.

High saturation diffusion gas hydrates in the Quaternary sandy sediments were found for the first time during the gas hydrate drilling expedition of the Qiongdongnan Basin (hereinafter referred to as QDNB) in 2019. This tremendous breakthrough enriched the reservoir types of gas hydrate exploration in China. Finding potential high-quality sandy reservoirs requires the ability to better predict the distribution characteristics of sand bodies. Through the interpretation of high-resolution 3D seismic data of the drilling area in QDNB in 2019, it has been concluded that sand bodies with highly saturated gas hydrate belong to channel-levee facies deposition (Meng et al., 2021). At present, the study of Quaternary sediments in the QDNB is limited to the submarine shallow surface, because of its high scientific value in the study of monsoon evolution and events causing abrupt climate change (Xu et al., 2010; Wang et al., 2014; Huang et al., 2013; Hu et al., 2014; Liu et al., 2010; Wang et al., 2014; Yan et al., 2016). With the discovery of hydrate in the QDNB, the distribution, development, and formation mechanism of mass transported deposits (hereinafter referred to as MTDs) and their relationship with gas hydrate have also been studied (Meng et al., 2021; Cheng et al., 2021). The deepwater channel system is the main mode of sand transport, and controls the distribution of sand bodies. Unfortunately, the identification, controlling factors of sinuous channel in the Pleistocene strata of the limited 3D area in the southwest margin slope area of the QDNB has rarely been studied (Yuan et al., 2009; Yuan et al., 2010a, b; Wang et al., 2015), there has been no research on the distribution and evolutionary mechanism of channels in the Quaternary strata of the QDNB.

In addition, deep-sea sediments are the most precious carrier of information regarding the evolution of the Earth system. The QDNB in the northern part of the South China Sea (SCS) is a typical marginal sea basin, and its sediments record the dynamic processes of climate change, tectonic uplift, and sea-level change, as well as the sedimentary archives of the dynamic processes of the deep continental margin lithosphere (Covault et al., 2010; Lin, et al., 2015; Gong et al., 2016; Romans et al., 2016). Therefore, the study of Quaternary channel systems in the QDNB will not only provide guidance for the prediction of sand distribution, which is important for the prediction of highly saturated gas hydrate occurrences, but also deepen our current understanding of the sedimentary processes and evolution mechanism of the marginal sea (e.g., Matenco et al., 2013; Gong et al., 2016, Gong et al., 2018; Walsh et al., 2016).

Channel systems can develop on the slope, at the base of slope, and on the basin floor. channels tend to be shallower and exhibit a sinuous and distributary pattern on the basin floor (Weimer et al., 2006). Side-scan sonar image, bathymetry map, and 3D seismic data are often used to study the morphologies of channel systems on the seabed surface (Kenyon and Millington, 1995; Mitchum and Wach, 2002; Fildani and Normark, 2004). Amplitude extraction map and coherence map from 3D seismic are used to identify the channel shape and size (Saller et al., 2004). Most of previous work pay more attention to the channel morphologies, internal sedimentary characteristic, depositional model, sedimentary processes within sinuous channels, however, few work was done on the channel system evolution on basin level. This is one of the purposes of our study, hoping to bring some inspiration to similar basins or areas globally.

Therefore, the objectives of this study are to 1) identify the characteristics of Quaternary channels, 2) clarify the lateral distribution characteristics and evolution of channel systems in different periods, and 3) discuss the factors controlling the distribution of channel systems.

2 GEOLOGICAL SETTING

The QDNB is located in the northwestern slope of the SCS (**Figure 1A**). This basin is adjacent to the Yinggehai Basin to the northwest, the slope of Hainan Island to the north, the Pearl River Mouth Basin to the northeast, and the Yongle Uplift to the south (**Figure 1B**). The QDNB mainly consists of five first-order tectonic units: the Northern Depression, the Northern Uplift, the Central Depression, the Southern Low Uplift, and the Southern Depression. The Quaternary channel systems in our study are mainly located in the Central Depression.

The QDNB is a Cenozoic passive continental marginal basin, with a water depth ranging from 300 to 2,600 m and an area of about 8.3×10^4 km^2. The QDNB mainly underwent two stages of tectonic evolution, the Eocene–Oligocene rifting stage and the

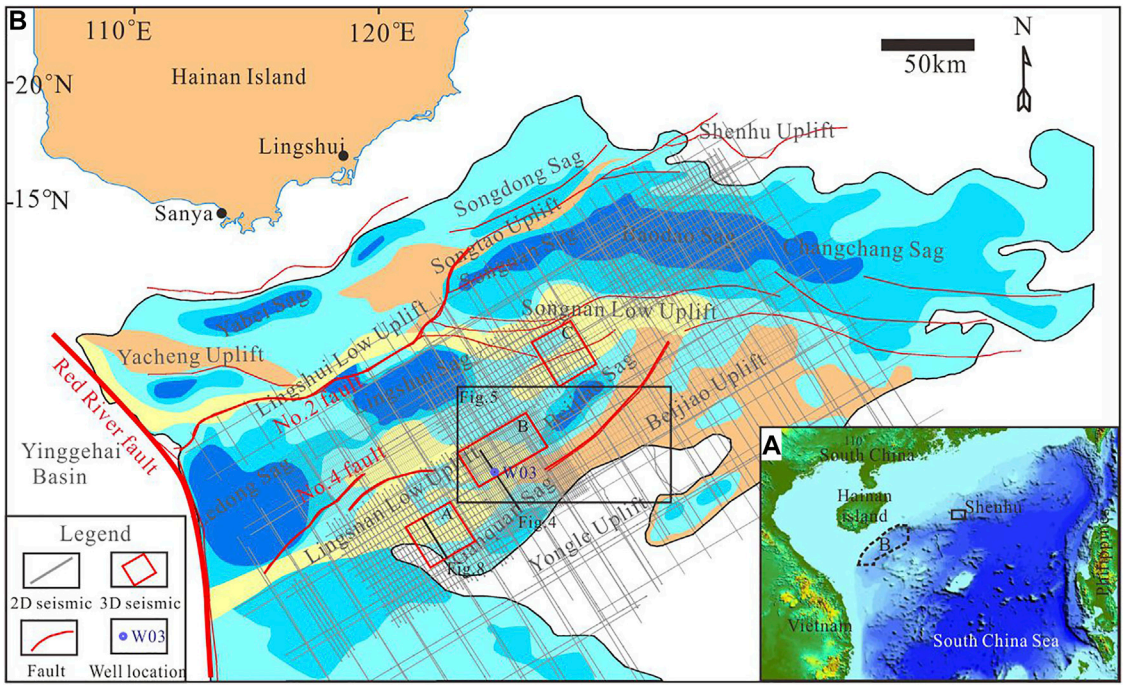

FIGURE 1 | (A) The location of the QDNB. **(B)** The tectonic units of the QDNB. The gray lines denote 2D seismic lines, and the red rectangles denote 3D seismic areas.

Early Miocene-Quaternary thermal subsidence stage (Zhao et al., 2015). The filling sequences in the basin are mainly composed of Paleocene, Neogene, and Quaternary strata. From bottom to top, the Paleocene mainly contains Eocene and Oligocene strata (the Yacheng and Lingshui formations); the Neogene strata include Miocene (the Sanya, Meishan, and Huangliu formations) and Pliocene (the Yinggehai Formation) strata; and the Quaternary strata include the Ledong Formation (**Figure 2**). The Early Oligocene Yacheng Formation consists of marsh to coastal plain facies; the lower Lingshui Formation consists of fan delta facies; the upper Lingshui–Meishan formations consist of littoral to neritic facies; and the Huangliu–Ledong formations mainly consist of bathyal to abyssal facies.

Since the Middle Miocene, this basin as a whole entered the rapid subsidence stage, and the continental slope system began to form in the northern margin of the basin under the action of the depression. In the Late Miocene, the northern margin of the basin showed obvious shelf-slope break and entered the stage of rapid subsidence. The northwestern provenance was sufficient, and the continental slope moved forward rapidly due to the influence of high-speed sediments. The channel that developed along the shelf margin reflects the enhancement of sediment transport capacity to the sea during this period.

From the Pleistocene to the present, the QDNB has been in a period of highstand systems tract since the sea-level began to decline gradually. In addition to the large-scale delta depositional system that developed in the northwest shelf-slope break, the whole area is in a semi-bathyal sedimentary environment, which is mainly composed of fine-grained argillaceous rocks. The last stage of the prograding reflector pushed seaward more than the previous stages, indicating that the range of sea-level decline was small and frequent during the late Pleistocene to the late Holocene, and the range of sea-level decline was large at the end of the Holocene.

3 DATA AND METHODS

2D/3D seismic, coring, well logging, and multi-beam data were comprehensively used to study the Quaternary channel systems in the QDNB. A total of 34,000 km^2 of 2D seismic data and 1,900 km^2 of 3D seismic data were acquired by the Guangzhou Marine Geological Survey from 2005 to 2021 (**Figure 1**). 3D seismic data in areas A, B, and C offer a range of visualization and attribute analysis that can provide specific information on the development of channel systems. 2D seismic data that cover the whole basin were used to track the distribution of the channel system in the QDNB. Two drilling expeditions in 2019 and 2021 acquired a large quantity of well logging and coring data, which provide a lot of geological information that is closely related to gas hydrates. One typical drilling well (W03) and its coring samples were used to study the vertical channel evolution.

A total of 57,300 km^2 of multi-beam data that nearly cover the entire QDNB were used to identify the seabed channels and the variation in seabed morphology.

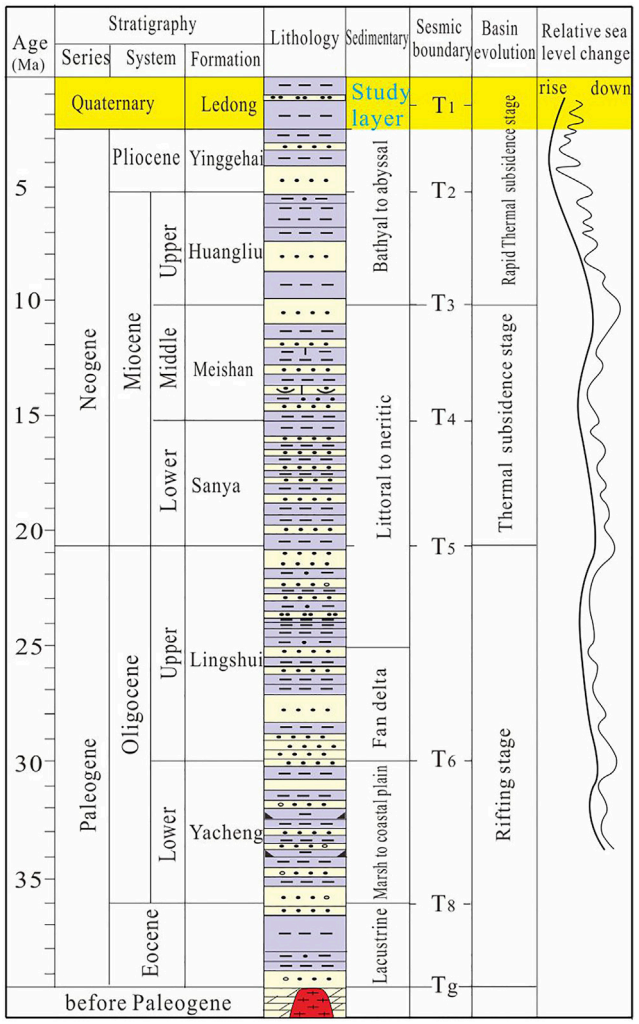

FIGURE 2 | Tectono-stratigraphic column of the QDNB. Note: the yellow areas show the Quaternary strata.

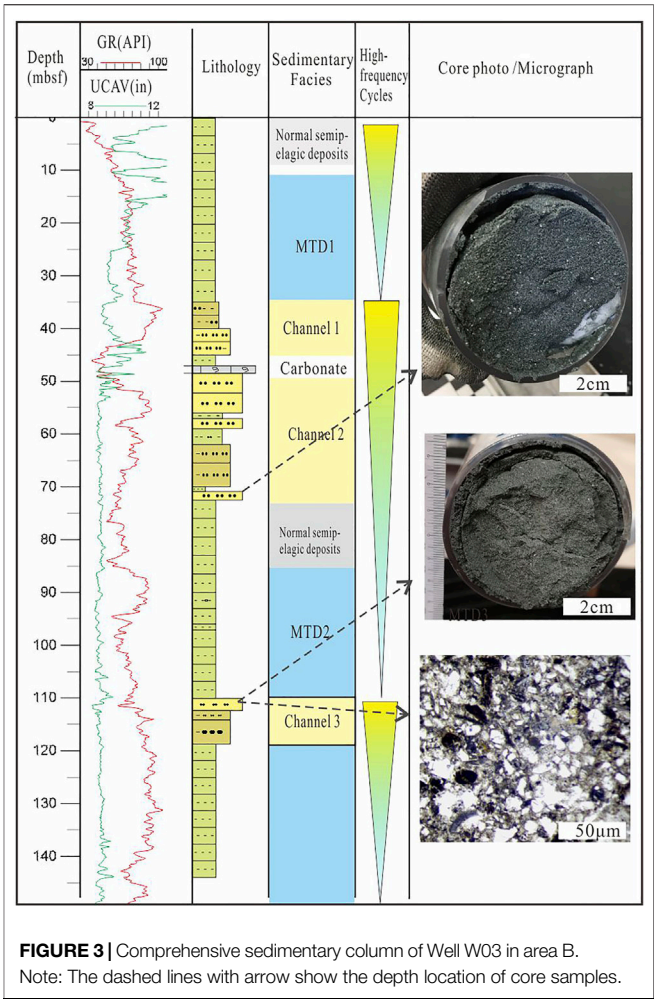

FIGURE 3 | Comprehensive sedimentary column of Well W03 in area B. Note: The dashed lines with arrow show the depth location of core samples.

Well-seismic correlation was carried out to establish the corresponding relationship between the lithology of Well W03 and the plane characteristics of seismic attributes. Core calibration and seismic attribute analysis were used to identify channels and to study channel-related sedimentary facies. Multi-layer high-resolution seismic sedimentology research was used to establish the evolution history of channel systems.

4 RESULTS

4.1 Evidence of Quaternary Channel Systems

Gas hydrate–bearing sands were found for the first time during gas hydrate drilling in area B of the QDNB. Three sets of sand layers were drilled, and the lithology of the sand layer is mainly silt. The sedimentary facies is characterized by the interactive deposition of channel-levee facies and MTDs. Three-stage sedimentary high-frequency cycles were identified, with muds at the bottom and sands as the top in each cycle (**Figure 3**), The cycles show the repetition of sedimentary facies association (MTD and channel-levee facies). MTD represents the beginning of an event deposition, while channel -levee facies represents the relative termination of the event deposition. The three-stage channels and MTDs were clearly identified in the seismic profile that crosses Well W03 and these have a good corresponding relationship with the three sets of sand layers and MTDs that were encountered in the drilling cores (**Figure 4**). Therefore, the comprehensive calibration of seismic drilling and the cores not only confirms the existence of the Quaternary channels, but also well identifies the channel stages near the seabed. At least in area B, the three channel stages exhibit southeast migration (**Figure 4**). Because the drilling did not extend through the Quaternary strata, the 2D/3D seismic data are the only data that can be used to identify channels deep beneath the seabed. Through the interpretation of a large quantity of seismic data in the QDNB, a total of six channel stages were identified, which are described in detail later.

Several discontinuity seabed channels were observed clearly from the multi-beam data in the deep-sea area of the central

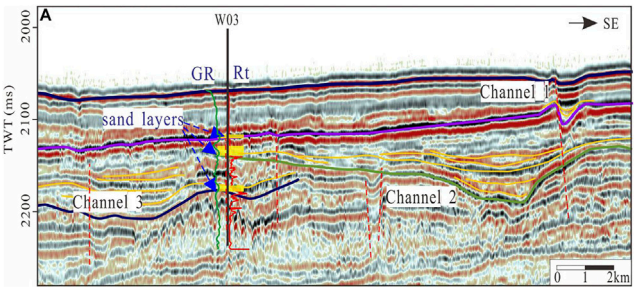

FIGURE 4 | 2D seismic profile that crosses Well W03 in area B. Three channels are shown in seismic profiles and three sand layers are verified from Well W03. Note: The location of seismic profile in **Figure 1B**.

QDNB. Combined with the change in topography, the main direction of channel flow is concluded to be from SE to NE. Theoretically, the channel should be continuous, however, most of the area is flat with deep-sea mud, and only a few parts of remnant channels can be seen from the multi-beam data (**Figure 5**). Therefore, the channels are in the extinction stage, which is the latest period of the channel system in the QDNB.

4.2 Channel-Related Seismic Facies and Sedimentary Facies Identification

4.2.1 Channel-Related Seismic Facies

The most intuitive seismic facies in the Quaternary QDNB is the channel-filling seismic facies, which is flat at the top and has a bulge at the bottom, and its bottom boundary is generally U-shaped or V-shaped, and the adjacent underlying strata are usually truncated to varying degrees. A V-shaped bottom boundary represents high turbidity current scour and rapid deposition of the channel, while a U-shaped bottom boundary represents low turbidity current scour and slow deposition of the channel. The channel-filling seismic facies is mainly characterized by strong amplitude and low frequency, with parallel or subparallel internal structures, and with both sides or one side having in-phase axis overlap above the boundary of the underlying concave filling boundary.

Based on the internal stacking patterns within the channel, four filling seismic facies were identified. These facies types were used to assist in interpreting the extent of the channel facies and its lateral, upper, and lower boundaries.

1) Parallel filling facies: The internal reflection of the in-phase axis generally has a parallel or subparallel structure (**Figure 6**). This is a typical case of a local erosive channel, usually indicating submarine canyon or turbidite channel-filling.
2) Progradation filling facies: The internal reflection is parallel to the underlying denudation reflection, and there is obvious onlap to the upward-dip direction and truncation to the downward-dip direction (**Figure 6**). The internal reflection wave is inclined with weak accretion, which is similar to the underwater delta fan.

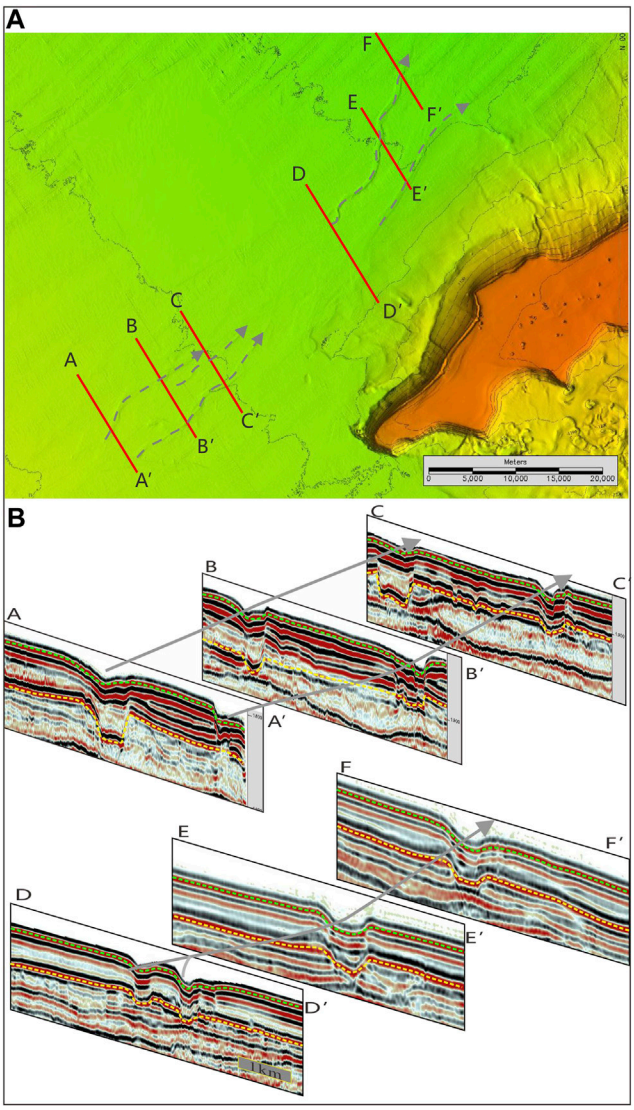

FIGURE 5 | (A) The seabed channels identified from multi-beam data and seismic data in the QDNB. Note: The red lines show the location of seismic profile in **(B)**, and the grey arrow lines shows the distribution of remnant seabed channels; **(B)** The seismic profiles present the channel-filling process. Note: The gray arrows show the direction of seabed channels, the yellow dashed lines show the sequence interface during the formation of the latest channel, the green dashed lines show the sequence interface of seabed.

3) Onlap filling facies: The external shape is similar to that of the parallel filling facies, and the internal reflection is uniform, parallel to the gently divergent structure, with high continuity and variable amplitude at both ends, and slightly higher than that of the underlying strata (**Figure 6**). This represents the late development stage of the channel.
4) Multistage filling facies: The seismic profile is characterized by multiple filling facies in the same period and vertical superposition or migration in different periods (**Figure 6**), indicating the development of multiple channels and multi-stage channels.

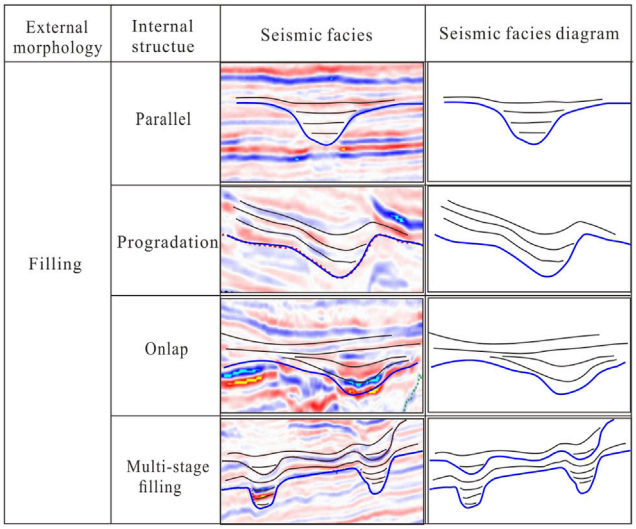

FIGURE 6 | Seismic facies characteristics classification of channels in the Quaternary QDNB.

4.2.2 Sedimentary Facies Identification

Based on the division of seismic facies, through the comprehensive interpretation of geological setting, sea-level changes, drilling data, and seismic attributes, the hydrodynamic condition, sedimentary environment, and its specific sedimentation were analyzed, and then the corresponding sedimentary facies were determined.

Channels with scales greater than the seismic resolution are easier to identify; for example, the Central Canyon developed in the Miocene of the QDNB. However, in addition to some regions or periods where the channel scale is relatively large and be identified from seismic profiles, many channels are small in scale that cannot be identified easily from seismic profiles, and their transverse distribution characteristics are more difficult to determine. Combined with the identification of sand layers from drilling, interpretation of seismic data, and 3D seismic horizon attribute analysis, the distribution characteristics of channels where the sand layer is located can be well explained. Through the tracing of channels by 2D/3D data, the sedimentary facies, distribution characteristics, and scale of Channel 3 system were identified in areas A, B, and C, respectively (**Figure 7**).

A mostly channel-levee sedimentary system (**Figure 7**) developed in the Quaternary QDNB, which is composed of channel-filling facies, levee facies, crevasse splay facies, and channel terminal lobes facies. Channels usually maintain turbidity current deposition, which represents long-term and long-distance sediment transport. The levee is formed by gravity flow out of channel edge and extends laterally, due to the rapid decrease in gravity flow velocity, the levee near the channel is very thick, and thin far away from the channel. Crevasse splay and channel terminal lobes were found in Channel 3 system of area C (**Figure 7**).

4.3 The Distribution of Multi-Stage Channels

Through the analysis and comparison of the seismic phase axis contact relationship and seismic attribute characteristics of areas A, B, and C, it was determined that the Quaternary strata can be divided into seven sub-sequences (S_1–S_7) (**Figure 8**). The seismic interpretation and attribute analysis found that the distribution of channels is clearly shown in S_1–S_6 (**Figure 9**). The corresponding channel system for each sequence is named Channel 1 system, Channel 2 system, and so on. Considering that gas hydrate–bearing sands are mainly developed in the Channel 3 system, and multi-beam data can provide sufficient information for the study of near seabed channels (Channel 1 system), the Channel 3 system and Channel 1 system were used to study the distribution characteristics of channel systems in the Quaternary QDNB.

Combined with 2D seismic data, the distribution of channels in the QDNB was tracked, and the distribution characteristics of the Channel 3 and Channel 1 systems in the whole QDNB were obtained. It can be seen that the channel-levee sedimentary system is widely developed (**Figures 7**, **8**), especially in the middle of the central depression zone of the QDNB.

There are obvious distribution differences on the Channel 3 and Channel 1 systems between the western, middle, and eastern sections (**Figure 10**).

4.3.1 Distribution Characteristics of the Channel 3 System

One nearly straight channel, showing a V-shape in the seismic profile, is developed in the western section of the central depression of the QDNB. The channel is located at the lower part of the continental slope. Therefore, the channel in this area mainly erodes the continental shelf. The superposition mode is mainly in the lateral order superposition, reflecting the obvious lateral accumulation due to the directional action of the bottom current. The downcutting effect of the channel is slightly weakened eastward, and the restraining effect of the channel is gradually weakened. Therefore, the channel formed several branches in the southeast direction (**Figure 10**).

The channel system in the central section has many branches and meanders to the east, showing the characteristics of a large braided channel system. Far extending levees were developed on both sides of the channel, and the north side was mainly developed in large areas. The channels in the middle section are located in the submarine plain, and the erosion of downcutting is weakened. The single channel identified from the seismic profile is mainly of a wide U-type, with obvious levees developed on its flanks. The channel-levee system is mainly superimposed by vertical disordered superposition. As the restriction of the channel is further reduced, channels in this area show vertical disordered superposition erosion or accretion.

Several branch channels in the eastern section converge into one. There are still deposits of levees, lobes, and crevasses in area C. Drilling confirms that the thickness of levees is 6–8 m. As the eastern part of the central depression zone of the QDNB is close to the northwest sub-basin, the seafloor terrain becomes steeper. It inherits the topographic characteristics of the Central Canyon development period; therefore, multiple channels converge into one channel. The channel here presents a V-shaped straight channel.

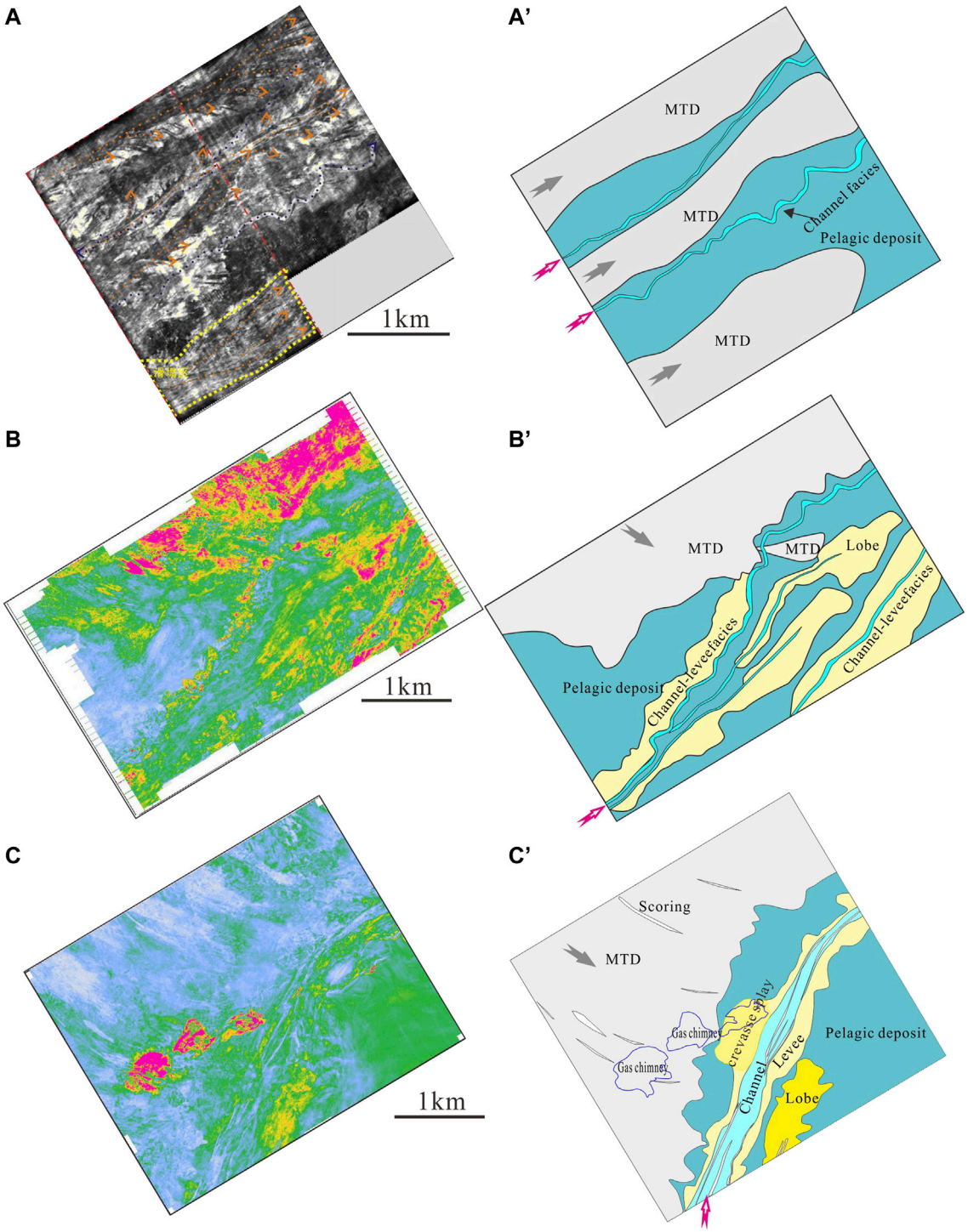

FIGURE 7 | Attributes and sedimentary facies of the Channel 3 system in areas A, B, and C of the QDNB. **(A)** Minimum amplitude attribute map of the Channel 3 system in area A; **(A′)** Sedimentary facies map of Channel 3 system in area A; **(B)** RMS amplitude attribute map of the Channel 3 system in area B; **(B′)** Sedimentary facies map of Channel 3 system in area B; **(C)** RMS amplitude attribute map of the Channel 3 system in area C; **(C′)** Sedimentary facies map of Channel 3 system in area C. Note: The red arrows show the flow direction of channels, and the gray arrows shows the direction of MTDs.

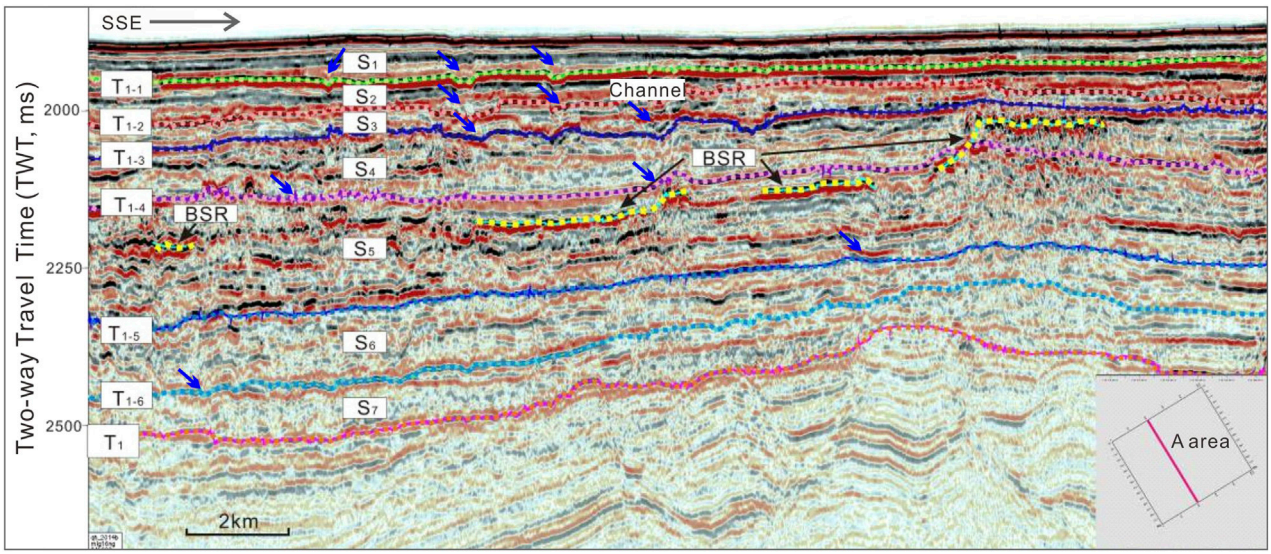

FIGURE 8 | Sequence stratigraphy and 6 periods of channel systems of the Quaternary strata in area A. Note: The blue arrows show the locations of channels. The location of this seismic profile is in **Figure 1B**.

4.3.2 Distribution Characteristics of the Channel 1 System

Similar to the Channel 3 system, three near straight channels are also apparent in the western section of the Channel 1 system, and a large braided channel system in the middle section that converges into a straight channel again in the western section.

The Channel 1 system differs from the Channel 3 system in the following ways: 1) In the western section, Channel 1 system has three near straight channels and locates more to the south; 2) In the middle section, there are fewer branch channels, with two main channels in the north and south, and a large submarine fan in area B; 3) In the eastern section, the channel system is similar to Channel 3, but almost devoid of sandy deposits.

5 DISCUSSION

5.1 What are the Controlling Factors on the Distribution of Quaternary Channel Systems?

The direct factors affecting the morphology, evolution, and sedimentary characteristics of deep-water channels include submarine topographic slope, sedimentary hydrodynamic conditions, and sediment grain size. Indirect factors include tectonic movement, sea-level change, and provenance supply. The possible controlling factors on channel distributions in the Quaternary QDNB are discussed below in detail.

5.1.1 Seafloor Morphology

Topography is a prerequisite for the formation of channels, which determines and influences the location and morphology of channel development (Armitage, 2009). A profile (Line 1) of multi-beam data was extracted where the latest period channels (Channel 1 system) of the QDNB is located (**Figure 11A**), and the variations in seabed elevation and slope were obtained. It was found that the seabed elevation gradually decreases from SW to NE, with an elevation difference of 1,411 m (**Figure 11B**). There are significant slope differences between the western, middle, and eastern sections. The slope of the western section varies greatly, ranging from 0.6° to 0.3°; the slope of the middle section is generally about 0.2°, which is relatively flat; while in the eastern section, the slope becomes steeper again (**Figure 11C**).

Combined with the above distribution characteristics of the Channel 1 system, it was found that there is a good correlation between slope variation and the development of the channel system.

In the western section, the slope is steep and the channels are near straight. With the descending of the slope, the channels form branches, but are still dominated by near straight form, and the erosion is mainly below the channel. The sediments are mostly passing deposits, and the levee-overflow deposits are not developed, and the channel is completely filled by argillaceous deposits in the later period (**Figure 5**).

In the middle section, the slope is relatively gentle, and with weakened downcutting and strengthened flooding of the deepwater channel, the curved channel develops, and a large lobe deposit is developed near the east.

In the eastern section, the slope becomes steeper again, and the two channels converge into one, and the channel morphology inherits the characteristics of the Central Canyon; with insufficient provenance supply, the channel is mainly covered by thin layers of pelagic sediment.

5.1.2 Tectonic Movement

The Central Canyon runs across the QDNB from east to west, which is about 570 km long and 9–39 km wide. The main body of

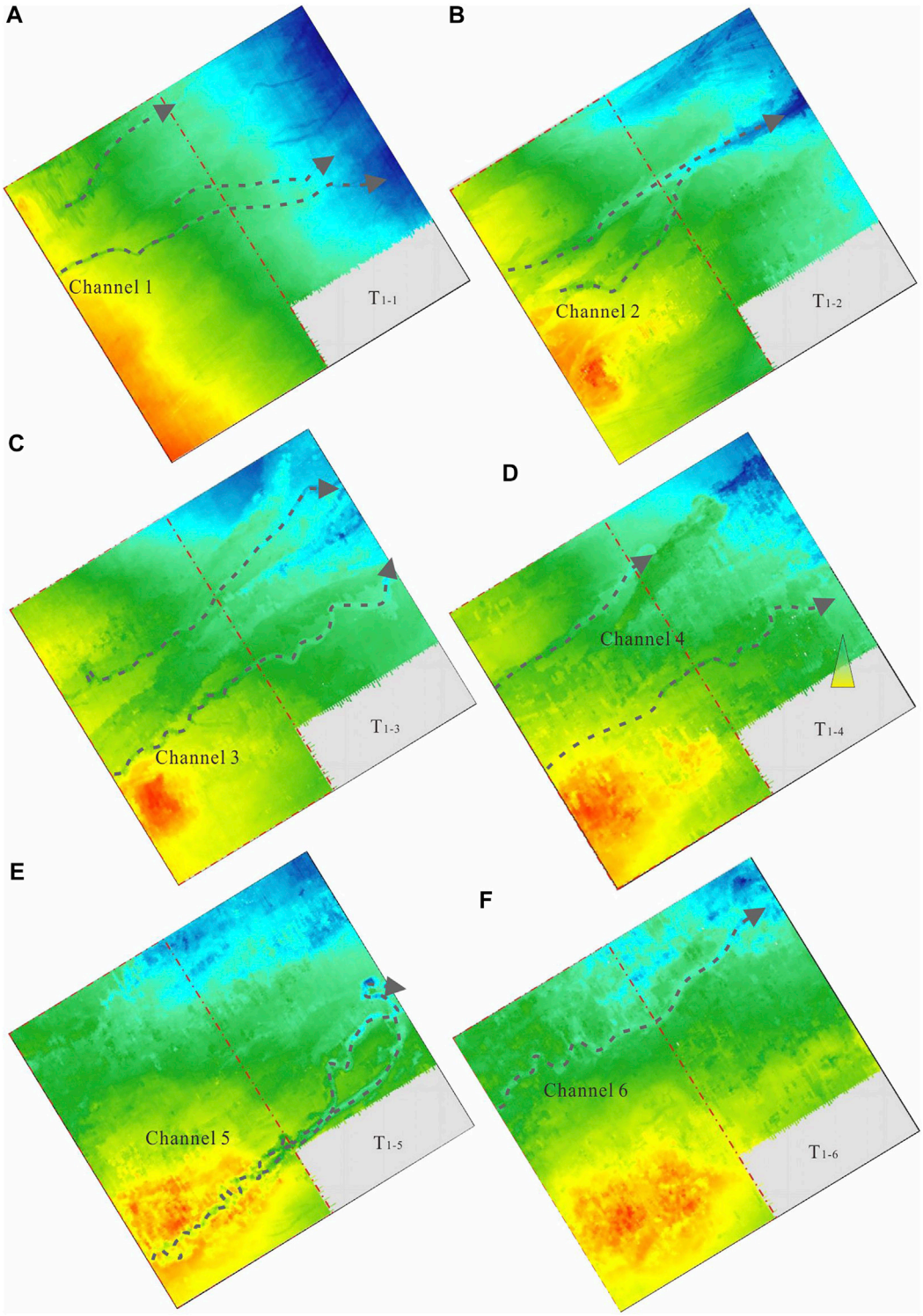

FIGURE 9 | Sequence boundary structure maps of the Quaternary strata in area A **(A)** Structure map of T_{1-1} sequence boundary; **(B)** Structure map of T_{1-2} sequence boundary; **(C)** Structure map of T_{1-3} sequence boundary; **(D)** Structure map of T_{1-4} sequence boundary; **(E)** Structure map of T_{1-5} sequence boundary; **(F)** Structure map of T_{1-6} sequence boundary. Note: The grey dash lines show the channel systems, and the arrows indicate the channel flow directions.

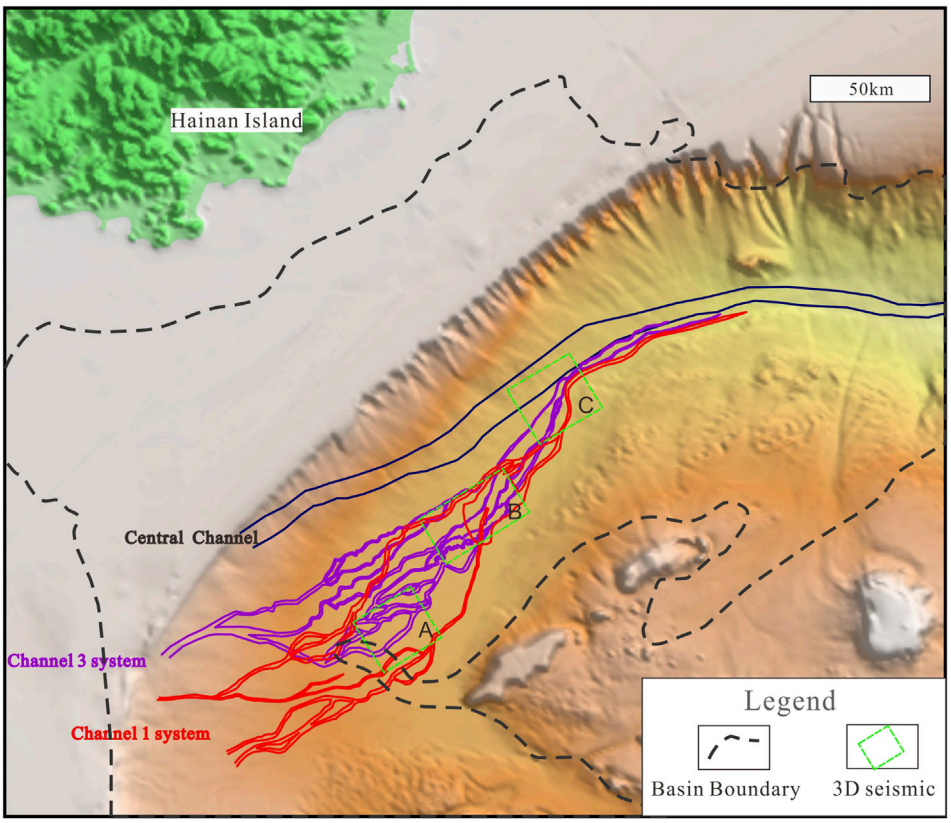

FIGURE 10 | The distribution of the Channel 1 and 3 systems and the Central channel in the QDNB. Note: The purple solid line shows the distribution of Channel 3 system traced from quaternary hydrate-bearing sands in C area; the read solid line shows the distribution Channel 1 system near seabed, which is the latest period of the Quaternary channel systems; the blue solid line shows the distribution of the Central channel that developed at the Pliocene strata; the black dashed line shows the boundary of the QDNB.

the canyon began to develop in the Late Miocene (10 Ma) and ended in the Pliocene. It is not only an important pathway for transporting sediments from shallow water to deep water, but also a site for the deposition of detrital materials. The Central Canyon plays a pivotal role in the tectonic sedimentary evolution of the QDNB, and is closely related to hydrocarbon accumulation (Wang, 2012), so the degree of research on its architecture, sedimentation process, provenance sources, and controlling factors is relatively high (Gong et al., 2011; Su et al., 2014; Wang et al., 2016).

The distribution of the Central Canyon in the Miocene is also depicted in the distribution map of the Quaternary channel system in the QDNB (**Figure 10**). The Quaternary channels in the eastern section are almost superposed with the Central Canyon, which can be clearly seen in the seismic profile. However, in the western section, the development of the Quaternary channel systems show southward migration, and the migration amplitude increases westward, up to more than 100 km. This indicates the southward migration of the provenance system from the Central Canyon and Quaternary channel system. The question is why was there such a great migration distance since 10.5 Ma? The immediate factor is most likely the relative topographic decline to the south, and the southward migration of the subsidence center. The main factor that can change the regional subsidence center could be tectonic movement.

The large faults in the west of the QDNB mainly include the Red River fault and No. 2 fault. A great deal of research has been conducted on the tectonic activity of the Red River fault and its control on the tectonic and sedimentary evolution of the Yinggehai Basin and QDNB (Xie et al., 2006; Lei et al., 2021; Xie et al., 2021), with one of the big discoveries being the late Miocene strike-slip reversal (Sun et al., 2003; Wang et al., 2016; Zhu et al., 2009). The Red River fault in the western QDNB shifted from sinistral strike-slip to dextral movement at about 5.5 Ma (**Figure 1**). The dextral strike-slip movement may have continued into the Quaternary period, which resulted in the faster subsidence in the southwest of the QDNB compared with the northwest, and the subsidence center moved southward. At the same time, the slope-subparallel basement faults (No.4 fault) shifted to dextral slip (Graham, 2016). In addition, the No. 2 fault may have also been active, and all of these slight tectonic activity contributions have changed the morphology since the Miocene, as exemplified by the greater subsidence in the south compared to the north, and the greater subsidence in the east compared to the west. Finally, these contributed to the southward migration of the

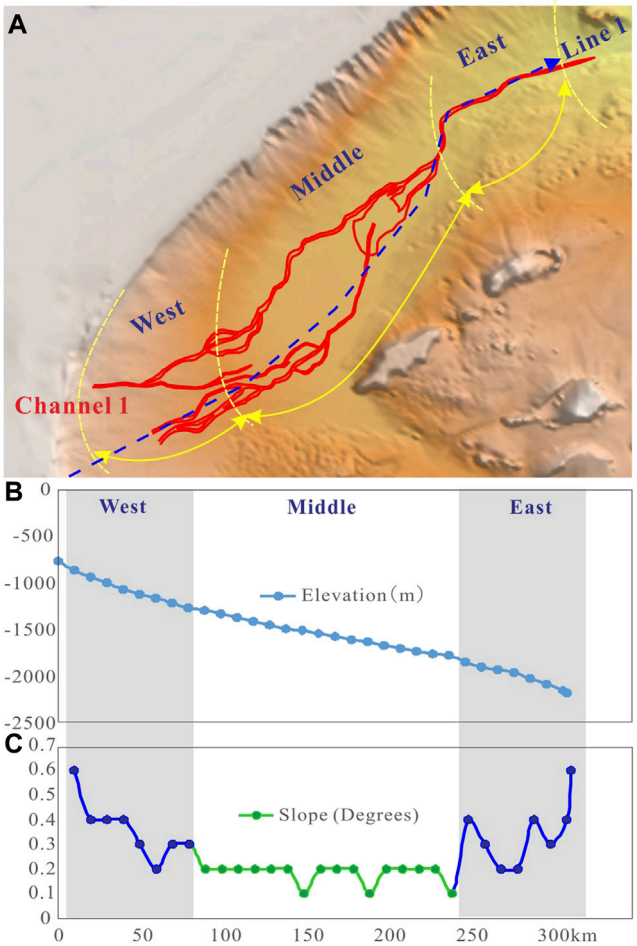

FIGURE 11 | (A) The distribution characteristics of the Channel 1 system and seabed multi-beam data. Note: line 1 is the plan position of elevation and slope variation maps in **(B,C)**. **(B)** The elevation variation of line 1 from SW to NE; **(C)** The slope variation of line 1 from SW to NW.

channel provenance in the QDNB from the Miocene to the present (**Figure 8**). The southward migration of channels represents the southward migration of the subsidence center, while the southward migration of the subsidence center is the joint geological response of the dextral rotation of the Red River strike-slip fault, No. 4 fault, and No. 2 fault (**Figure 1**). Due to the southward migration of subsidence center, as well as the rapid southward migration of passive continental margin (Gong et al., 2019; Chen et al., 2020), the northwest provenance continued to prograde from north to south, and result to the southward migration of low terrain and channel systems. Therefore, the southward migration of channel systems can be considered as the result of the combined action of tectonic and sedimentation.

5.1.3 Sea-level Fluctuations

Frequent sea-level changes can affect provenance supply and lead to the development of multi-stage channels. The six stages of Quaternary channels in the QDNB are often inter-deposited with MTDs (**Figure 3**), which may have a good relationship with sea-level changes. The periodic sea-level change in the QDNB is controlled by the combined effect of global sea-level change and regional crustal subsidence (especially thermal subsidence), therefore, the sea-level change in the QDNB is different from the global sea-level rise and fall cycle (Haq et al., 1987; Hao et al., 2000). At present, there is a lack of information regarding the continuous period and amplitude of Quaternary sea-level change in the QDNB (Bintanja et al., 2005; Yu and Chen, 2009), but the basic consensus is that there are multiple periods of sea-level change and the overall sea-level is declining (Chen et al., 2020). However, the multi-stage channel development can also provide some enlightenment for the study of Quaternary sea-level change in the QDNB.

5.1.4 Provenance Supply

The flow direction of channels in the Quaternary QDNB is from west to east, which is basically consistent with that of the Central Canyon. Therefore, the provenance of Quaternary channels can be compared with that of the Central Canyon. Most scholars believe that the provenance of the Central Canyon mainly came from the Red River system (Lin et al., 2001; Su et al., 2019; Lyu et al., 2021) and the Red River submarine fan in the Yinggehai Basin, which is considered to be the direct source supplying the Central Canyon (Wang et al., 2011; Xie, 2020; Xu et al., 2020). However, some researchers believe that it originated from central and northern Vietnam (Zhang et al., 2017; Su et al., 2019) and the provenance of Hainan Island (Lin et al., 2001; Cao et al., 2013).

It should be noted that the western part of the Quaternary channel system migrated about 100 km southward compared with the Central Canyon (**Figure 8**), so the provenance of the Quaternary may be less contributed by the Red River system and more influenced by the Vietnamese river system. In addition, although the channel length of the Quaternary is similar to that of the Central Canyon, the channel width is significantly narrower than that of the Central Canyon (**Figure 8**), which also indicates a significant decrease in sediment transport, and could indirectly reflect a significant decrease in sediment supply in the provenance area. The decrease of provenance supply is the result of the interaction of Himalayan movement, sea-level and climate changes. As for how these factors affect the provenance supply, it is a complex and synergistic mechanism that has not been solved yet, but it reflects the disappearance of the channel systems to some extent. That, in turn, could shed light on tectonic movement, sea-level and climate changes.

The development of the Quaternary channel system in the QDNB is the result of multi-factor synthesis: the tectonic movement controls seafloor morphology, which directly controls the flow of channels and their distribution characteristics, and the provenance supply determines the scale of each channel and the sedimentary characteristics. The periodic changes in sea-level determine the evolution of the multi-stage channel systems.

5.2 The Prediction of Gas Hydrate-Bearing Sand Reservoirs

Deepwater channel system is an important transport pathway for sand sediments. Sand bodies can be deposited by channel-filling deposits, levee deposits, crevasse splay and lobes, which are often regarded as favorable oil and gas reservoirs (Morris, and Busby-Spera, 1990; Babonneau et al., 2002; Wynn et al., 2002; Abreu et al., 2003; Beaubouef, 2004).

Under the limit of low temperature and high pressure, the gas hydrate can only occur in shallow sediments under the seabed. Taken the QDNB as a case, the lower limit of gas hydrate occurrence depth confirmed by drilling is about 200 mbsf. Therefore, it is necessary to study the characteristics of shallow channel systems. Based on our study, the Quaternary channels in the QDNB are branching from southwest and gradually converging toward east. In the western section, few coarse grain sands may exist in channel-filling facies; in the middle section, the sea floor morphology is flat and the braided channel becomes dense. It is speculated that there are both channel-filling, levees and crevasse splay deposits, with the possibility of multi-stage superposition of sand bodies. Therefore, the favorable shallow sand bodies (mainly belonging to channel-filling deposits, levees, crevasse splay deposits and lobes deposits) in the QDNB may be developed in the middle section where channel developed. This study can provide sedimentological basis for the prediction of gas hydrate-bearing sand reservoirs in the QDNB, and more 3D seismic, drilling and logging data are necessary to better predict sand reservoirs in the future. In addition, the identification and prediction of high saturated gas hydrates in sand reservoirs also needs comprehensive analysis of gas hydrate stability zone, sufficient gas source and favorable structure pathway.

6 CONCLUSION

Using the integrated 2D/3D seismic, multi-beam, well logging, and coring data, the current study documents the distribution characteristics of the channel system and its controlling factors in the Quaternary strata of the QDNB. The integrated analysis shows the following observation that:

1) The channel-related sedimentary facies include the channel-filling facies, levee facies, crevasse splay facies, and lobes facies; six periods of channel systems are identified in the Quaternary strata.
2) There are obvious distribution differences in the Channel 1 and Channel 3 systems between the western, middle, and eastern sections: the channels in the western and eastern sections are mainly dominated by near straight V-shaped channels, while the middle section mainly consists of large braided channels, where a channel-levee sedimentary system developed.
3) Compared with the distribution of the Central Canyon, the channels in the western section show southward migration since the Miocene.
4) The distribution and evolution of the Quaternary channels were likely collectively controlled by the seafloor morphology, tectonic movement, sea-level fluctuations, and provenance supply. Tectonic movement controls seafloor morphology, which directly controls the flow of channels and their distribution characteristics, and the provenance supply determines the scale of each channel and their sedimentary characteristics. The periodic changes in sea-level determine the evolution of multi-stage channel systems.
5) It is predicted that the favorable shallow sand bodies (mainly belonging to channel-filling deposits, levees, crevasse splay deposits and lobes deposits) in the QDNB may be developed in the middle section where channel developed.

DATA AVAILABILITY STATEMENT

The original contributions presented in the study are included in the article/Supplementary Material, further inquiries can be directed to the corresponding author.

AUTHOR CONTRIBUTIONS

MM: Conceptualization, Writing—Original Draft, JL: Supervision, ZK: Review, JR: Data collection, YH: Redrafted and Figure drawing, WD: Software, YG: Suggestion. All authors contributed to manuscript revision, read and approved the submitted version.

FUNDING

This work was supported by the National Natural Science Foundation of China (grant numbers 42102144; 42176215), Key Special Project for Introduced Talents Team of Southern Marine Science and Engineering Guangdong Laboratory (Guangzhou) (grant number GML2019ZD0102), and the China Geological Survey Project (grant number DD20221705).

ACKNOWLEDGMENTS

The authors wish to thanks to those who contributed to the success of the China National Gas Hydrate Program Expeditions 6 (GMGS6) and all personnel involved in seismic data acquisition and processing. Editor Jinan Guan and two reviewers for their insightful and helpful reviews are greatly appreciated. We thank LetPub for its linguistic assistance during the preparation of this manuscript.

REFERENCES

Abreu, V., Sullivan, M., Pirmez, C., and Mohrig, D. (2003). Lateral Accretion Packages (LAPs): An Important Reservoir Element in Deep Water Sinuous Channels. *Mar. Petroleum Geol.* 20, 631–648. doi:10.1016/j.marpetgeo.2003.08.003

Armitage, D. A. (2009). *High-Resolution Architectural Evolution of Depositional Elements in Deep-Marine Slope Environments: The Quaternary Niger Delta slope, Quaternary southwest Grand Banks slope, Canada, and Cretaceous Tres Pasos Formation*. Doctoral dissertation, Chile: Stanford University

Babonneau, N., Savoye, B., Cremer, M., and Klein, B. (2002). Morphology and Architecture of the Present Canyon and Channel System of the Zaire Deep-Sea Fan. *Mar. Petroleum Geol.* 19, 445–467. doi:10.1016/s0264-8172(02)00009-0

Beaubouef, R. T. (2004). Deep-water Leveed-Channel Complexes of the Cerro Toro Formation, Upper Cretaceous, Southern Chile. *Bulletin* 88, 1471–1500. doi:10.1306/06210403130

Behseresht, J., and Bryant, S. L. (2012). Sedimentological Control on Saturation Distribution in Arctic Gas-Hydrate-Bearing Sands. *Earth Planet. Sci. Lett.* 341-344, 114–127. doi:10.1016/j.epsl.2012.06.019

Bintanja, R., van de Wal, R. S. W., and Oerlemans, J. (2005). Modelled Atmospheric Temperatures and Global Sea Levels over the Past Million Years. *Nature* 437 (7055), 125–128. doi:10.1038/nature03975

Boswell, R., Collett, T. S., Frye, M., Shedd, W., McConnell, D. R., and Shelander, D. (2012). Subsurface Gas Hydrates in the Northern Gulf of Mexico. *Mar. Petroleum Geol.* 34, 4–30. doi:10.1016/j.marpetgeo.2011.10.003

Boswell, R., Shelander, D., Lee, M., Latham, T., Collett, T., Guerin, G., et al. (2009). Occurrence of Gas Hydrate in Oligocene Frio Sand: Alaminos Canyon Block 818: Northern Gulf of Mexico. *Mar. Petroleum Geol.* 26, 1499–1512. doi:10.1016/j.marpetgeo.2009.03.005

Cao, L., Jiang, T., Wang, Z., Zhang, D., and Sun, H. (2013). Characteristics of Heavy Minerals and Their Implications for Neogene Provenances Evolution in Qiongdongnan Basin. *J. Central South Univ. Sci. Technol.* 44 (5), 230–240. (In Chinese with English abstract).

Chen, S., Steel, R., Wang, H., Zhao, R., and Olariu, C. (2020). Clinoform Growth and Sediment Flux into Late Cenozoic Qiongdongnan Shelf Margin, South china Sea. *Basin Res.* 32 (1), 302–319. doi:10.1111/bre.12400

Cheng, C., Jiang, T., Kuang, Z., Ren, J., Liang, J., Lai, H., et al. (2021). Seismic Characteristics and Distributions of Quaternary Mass Transport Deposits in the Qiongdongnan Basin, Northern South China Sea. *Mar. Petroleum Geol.* 129, 105–118. doi:10.1016/j.marpetgeo.2021.105118

Chong, Z. R., Yang, S. H. B., Babu, P., Linga, P., and Li, X.-S. (2016). Review of Natural Gas Hydrates as an Energy Resource: Prospects and Challenges. *Appl. Energy* 162, 1633–1652. doi:10.1016/j.apenergy.2014.12.061

Collett, T. S. (2014). Gas Hydrates as a Future Energy Resource. *Geotimes* 49, 24–27.

Covault, J. A., Romans, B. W., Fildani, A., McGann, M., and Graham, S. A. (2010). Rapid Climatic Signal Propagation from Source to Sink in a Southern California Sediment-Routing System. *J. Geol.* 118, 247–259. doi:10.1086/651539

Egawa, K., Nishimura, O., Izumi, S., Fukami, E., Jin, Y., Kida, M., et al. (2015). Bulk Sediment Mineralogy of Gas Hydrate Reservoir at the East Nankai Offshore Production Test Site. *Mar. Petroleum Geol.* 66, 379–387. doi:10.1016/j.marpetgeo.2015.02.039

Fildani, A., and Normark, W. R. (2004). Late Quaternary Evolution of Channel and Lobe of Monterey Fan[J]. *Mar. Geol.* 206 (1). doi:10.1016/j.margeo.2004.03.001

Gong, C., Blum, M. D., Wang, Y., Lin, C., and Xu, Q. (2018). Can Climatic Signals Be Discerned in a Deep-Water Sink?: An Answer from the Pearl River Source-To-Sink Sediment-Routing System. *GSA Bull.* 130, 661–677. doi:10.1130/b31578.1

Gong, C., Qi, K., Ma, Y., Li, D., and Xu, H. (2019). Tight Coupling Between the Cyclicity of Deep-Water Systems and Rising-Then-Flat Shelf-Edge Pairs Along the Submarine Segment of the Qiongdongnan Sediment-Routing System. *J. Sediment. Res.* 89 (10), 956–975. doi:10.2110/jsr.2019.47

Gong, C., Steel, R. J., Wang, Y., Lin, C., and Olariu, C. (2016). Shelf-margin Architecture Variability and its Role in Sediment-Budget Partitioning into Deep-Water Areas. *Earth-Science Rev.* 154, 72–101. doi:10.1016/j.earscirev.2015.12.003

Gong, C., Wang, Y., Zhu, W., Li, W., Xu, Q., and Zhang, J. (2011). The Central Submarine Canyon in the Qiongdongnan Basin, Northwestern South China Sea: Architecture, Sequence Stratigraphy, and Depositional Processes. *Mar. Petroleum Geol.* 28 (9), 1690–1702. doi:10.1016/j.marpetgeo.2011.06.005

Graham, S. (2016). *3-D Seismic Characterization of Submarine Landslides on a Pliocene-Pleistocene Siliciclastic Continental Slope*. South China Sea.

Hao, Y., Chen, P., and Wan, X. (2000). Late Tertiary Sequence Stratigraphy and Sea Level Changes in Yinggehai-Qiongdongnan Basin. *Geoscience* 14 (3), 237–245.

Haq, B. U., Hardenbol, J., and Vail, P. R. (1987). Chronology of Fluctuating Sea Levels since the Triassic. *Science* 235, 1156–1167. doi:10.1126/science.235.4793.1156

Hu, B., Li, J., Cui, R., Wei, H., Zhao, J., Li, G., et al. (2014). Clay Mineralogy of the Riverine Sediments of Hainan Island, South China Sea: Implications for Weathering and Provenance. *J. Asian Earth Sci.* 96, 84–92. doi:10.1016/j.jseaes.2014.08.036

Hu, B., Wang, L., Yan, W., Liu, S., Cai, D., Zhang, G., et al. (2013). The Tectonic Evolution of the Qiongdongnan Basin in the Northern Margin of the South China Sea. *J. Asian Earth Sci.* 77, 163–182. doi:10.1016/j.jseaes.2013.08.022

Huang, D., Du, J., Deng, B., and Zhang, J. (2013). Distribution Patterns of Particle-Reactive Radionuclides in Sediments off Eastern Hainan Island, China: Implications for Source and Transport Pathways. *Cont. Shelf Res.* 57, 10–17. doi:10.1016/j.csr.2012.04.019

Kenyon, N. H., and Millington, J. (1995). "Contrasting Deep-Sea Depositional Systems in the Bering Sea," *Atlas of Deep Water Environments: Architectural Style in Turbidite Systems*. K. T. Pickering, R. N. Hiscott, N. H. Kenyon, F. R. Lucchi, and R. Smith (London: Chapman & Hall), 196–202. doi:10.1007/978-94-011-1234-5_28

Lei, C., Ren, J., Pei, J., Liu, B., Zuo, X., Liu, J., et al. (2021). Tectonics of the Offshore Red River Fault Recorded in the Junction of the Yinggehai and Qiongdongnan Basins. *Sci. China Earth Sci.* 64 (11), 1893–1908. (In Chinese with English abstract. doi:10.1007/s11430-020-9796-2

Liang, J., Wang, H., and Su, P. (2018). *Study on Controlling Factors of Natural Gas Hydrate Accumulation*. Beijing: Geological publishing house.

Lin, C., Liu, J., Cai, S., Zhang, Y., Lv, M., and Li, J. (2001). Sedimentary Composition and Development Background of Large-Scale Incised Valley and Submarine Gravity Flow System in Yinggehai-Qiongdongnan Basin. *Sci. China* 46 (1), 69–72. (in Chinese with English abstract). doi:10.3321/j.issn:0023-074X.2001.01.018

Lin, C., Xia, Q., Shi, H., and Zhou, X. (2015). Geomorphological Evolution, Source to Sink System and Basin Analysis. *Earth Sci. Front.* 22 (1), 9–20. (In Chinese with English abstract). doi:10.13745/j.esf.2015.01.002

Liu, Z., Colin, C., Li, X., Zhao, Y., Tuo, S., Chen, Z., et al. (2010). Clay Mineral Distribution in Surface Sediments of the Northeastern South China Sea and Surrounding Fluvial Drainage Basins: Source and Transport. *Mar. Geol.* 277, 48–60. doi:10.1016/j.margeo.2010.08.010

Matenco, L., Andriessen, P., and the Network, S. S. (2013). Quantifying the Mass Transfer from Mountain Ranges to Deposition in Sedimentary Basins: Source to Sink Studies in the Danube Basin-Black Sea System. *Glob. Planet. Change* 103, 1–18. doi:10.1016/j.gloplacha.2013.01.003

Meng, M., Liang, J., Lu, J. a., Zhang, W., Kuang, Z., Fang, Y., et al. (2021). Quaternary Deep-Water Sedimentary Characteristics and Their Relationship with the Gas Hydrate Accumulations in the Qiongdongnan Basin, Northwest South China Sea. *Deep Sea Res. Part I Oceanogr. Res. Pap.* 177, 103628. doi:10.1016/j.dsr.2021.103628

Mitchum, R. M., and Wach, G. D. (2002). *Niger Delta Pleistocene Leveed-Channel Fans: Models for Offshore Reservoirs [M]*.

Moridis, G. J., Collett, T. S., Boswell, R., Hancock, S., Rutqvist, J., Santamarina, C., et al. (2013). Gas Hydrates as a Potential Energy Source: State of Knowledge and Challenges. *Advanced Biofuels and Bioproducts*. 1. 977–1033. doi:10.1007/978-1-4614-3348-4_37

Morris, W., and Busby-Spera, C. (1990). A Submarine-Fan Valley-Levee Complex in the Upper Cretaceous Rosario Formation: Implication for Turbidite Facies Models. *GSA Bull.* 102, 900–914. doi:10.1130/0016-7606(1990)102<0900:asfvlc>2.3.co;2

Romans, B. W., Castelltort, S., Covault, J. A., Fildani, A., and Walsh, J. P. (2016). Environmental Signal Propagation in Sedimentary Systems across Timescales. *Earth-Science Rev.* 153, 7–29. doi:10.1016/j.earscirev.2015.07.012

Saller, A. H., Noah, J. T., Ruzuar, A. P., and Schneider, R. (2004). Linked Lowstand Delta to Basin-Floor Fan Deposition, Offshore Indonesia: An Analog for Deep-Water Reservoir Systems. *Bulletin* 88, 21–46. doi:10.1306/09030303003

Santra, M., Flemings, P. B., Scott, E., and Meazell, P. K. (2020). Evolution of Gas Hydrate-Bearing Deep-Water Channel-Levee System in Abyssal Gulf of Mexico: Levee Growth and Deformation. *Bulletin* 104 (9), 1921–1944. doi:10.1306/04251918177

Scholz, N. A., Riedel, M., Bahk, J.-J., Yoo, D.-G., and Ryu, B.-J. (2012). Mass Transport Deposits and Gas Hydrate Occurrences in the Ulleung Basin, East Sea - Part 1: Mapping Sedimentation Patterns Using Seismic Coherency. *Mar. Petroleum Geol.* 35 (1), 91–104. doi:10.1016/j.marpetgeo.2012.03.004

Sha, Z., Guo, Y., Yang, M., Liang, J., and Wang, L. (2009). Relation between Sedimentation and Gas Hydrate Reservoirs in the Northern Slope of South china Sea. *Mar. Geol. Quat. Geol.* 29 (5), 89–98.

Sloan, E. D. (2003). Fundamental Principles and Applications of Natural Gas Hydrates. *Nature* 426, 353–359. doi:10.1038/nature02135

Su, M., Wu, C., Chen, H., Li, D., Jiang, T., Xie, X., et al. (2019). Late Miocene Provenance Evolution at the Head of Central Canyon in the Qiongdongnan Basin, Northern South China Sea. *Mar. Petroleum Geol.* 110, 787–796. doi:10.1016/j.marpetgeo.2019.07.053

Su, M., Xie, X., Xie, Y., Wang, Z., Zhang, C., Jiang, T., et al. (2014). The Segmentations and the Significances of the Central Canyon System in the Qiongdongnan Basin, Northern South china Sea. *J. Asian Earth Sci.*, 79(pt.A), 552–563.doi:10.1016/j.jseaes.2012.12.038

Sun, Z., Zhong, Z., Zhou, D., Qiu, X., and Wu, S. (2003). Deformation Mechanism of Red River Fault Zone during Cenozoic and Experimental Evidences Related to Yinggehai Basin Formation. *J. Trop. Oceanogr.* 22, 1–9. (In Chinese with English abstract)

Uchida, T., and Tsuji, T. (2004). Petrophysical Properties of Natural Gas Hydrates-Bearing Sands and Their Sedimentology in the Nankai Trough. *Resour. Geol.* 54 (1), 79–87. doi:10.1111/j.1751-3928.2004.tb00189.x

Waite, W. F., Jang, J., Collett, T. S., and Kumar, P., (2019). Downhole Physical Property-Based Description of a Gas Hydrate Petroleum System in NGHP-02 Area C: A Channel, Levee, Fan Complex in the Krishna-Godavari Basin Offshore Eastern India. *Mar. Petroleum Geol.* 108, 272–295. doi:10.1016/j.marpetgeo.2018.05.021

Walsh, J. P., Wiberg, P. L., Aalto, R., Nittrouer, C. A., and Kuehl, S. A. (2016). Source-to-sink Research: Economy of the Earth's Surface and its Strata. *Earth-Science Rev.* 153, 1–6. doi:10.1016/j.earscirev.2015.11.010

Wang, D., Wang, Y., Yao, G., Wu, S., and Qin, Z. (2015). Deep-water Sediment Cycles in the Qiongdongnan Basin. *Chin. Sci. Bull.* 60 (10), 933–943. (In Chinese with English Abstract. doi:10.1360/n972014-00477

Wang, S., Zhang, N., Chen, H., Li, L., and Yan, W. (2014). The Surface Sediment Types and Their Rare Earth Element Characteristics from the Continental Shelf of the Northern South China Sea. *Cont. Shelf Res.* 88, 185–202. doi:10.1016/j.csr.2014.08.005

Wang, Y., Xu, Q., Li, D., Han, J., Lv, M., Wang, Y., et al. (2011). Late Miocene Red River Submarine Fan, Northwestern South China Sea. *Chin. Sci. Bull.* 56, 781–787. (In Chinese with English abstract). doi:10.1007/s11434-011-4441-z

Wang, Y., Zhang, D., Zhao, P., Yang, C., Huang, C., and Su, C. (2016). A New Consideration on the Genetic Mechanism of the Central Canyon in the Qiongdonnan Basin, the Northern South China Sea. *Haiyang Xuebao* 38 (11), 97–104. (In Chinese with English abstract). doi:10.3969/j.issn.0253-4193.2016.11.009

Wang, Z. (2012). Important Deepwater Hydrocarbon Reservoirs: The Central Canyon System in the Qiongdongnan Basin. *Acta Sedimentol. Sin.* 30 (4), 646–653. (In Chinese with English abstract). doi:10.14027/j.cnki.cjxb.2012.04.002

Weimer, P., Slatt, R. M., Bouroullec, R., Fillon, R., and Tari, G., (2006). *Introduction to the Petroleum Geology of Deepwater Setting[M].* American Association of Petroleum Geologists.

Wynn, R., Kenyon, N. H., and Masson, D. G., (2002). Characterization and Recognition of Deep-Water Channel-Lobe Transition Zones. *AAPG Bull.* 86, 1441–1462. doi:10.1306/61eedcc4-173e-11d7-8645000102c1865d

Xie, H., Zhou, D., Shi, H., Li, Y., and Kong, D., (2021). Comparative Study on the Cenozoic Tectonic and Sedimentary Evolution in the Deep-Water Areas of the Zhujiang River Estuary Basin and the Qiongdongnan Basin. *Haiyang Xuebao* 43 (3), 48–61. (In Chinese with English abstract). doi:10.12284/hyxb2021055

Xie, X., Müller, R. D., Li, S., Gong, Z., and Steinberger, B. (2006). Origin of Anomalous Subsidence along the Northern South China Sea Margin and its Relationship to Dynamic Topography. *Mar. Petroleum Geol.* 23 (7), 745–765. doi:10.1016/j.marpetgeo.2006.03.004

Xie, Y. (2020). Sedimentary Characteristics and Hydrocarbon Exploration Potential of the Upstream of the Central Canyon in the Yinggehai and Qiongdongnan Basin. *Bull. Geol. Sci. Technol.* 39 (5), 69–78. (In Chinese with English abstract). doi:10.19509/j.cnli.dzkq.2020.0601

Xu, F., Chen, S., Cao, Y., Chen, M., Li, A., and Xiao, S. (2010). Geochemical Records and Geological Significance of the Continental Shelf Sediments in the Northern South China Sea since 4400a. *Acta Sedimentol. Sin.* 28 (6), 1198–1205. doi:10.14027/j.cnki.cjxb.2010.06.007

Xu, Q., Li, D., Zhu, W., and Wang, Y. (2020). SHRIMP U-Pb Ages of Detrital Zircons: Discussions on Provenance Control and the Red River Capture Event. *Sediment. Geol. Tethyan Geol.* 40 (3), 20–30. (In Chinese with English abstract). doi:10.19826/j.cnki.1009-3850.2020.07009

Yan, H., Tian, X., Xu, F., Hu, B., and Liu, Z. (2016). Sediment Provenance of Offshore Mud Area of the Eastern Hainan Island in South China Seas in the Mid-holocene. *Haiyang Xuebao* 38 (7), 97–106. (In Chinese with English abstract). doi:10.3969/j.jssn.0253-4193.2016.07.009

Yu, K., and Chen, T. (2009). Beach Sediments from Northern South China Sea Suggest High and Oscillating Sea Levels during the Late Holocene. *Earth Sci. Front.* 16 (6), 138–145. doi:10.1016/s1872-5791(08)60110-4

Yu, X., and Zhang, Z. (2005). Characteristics of Neogene Depositional Systems on the Northern continentalSlope of the South China Sea and Their Relationships with Gas Hydrate. *Geol. China* 32 (3), 470–476. (In Chinese with English abstract).

Yuan, S., Cao, F., and Wu, S. (2010a). Architecture and Origin of Deepwater Sinuous Channel on the Slope of Nortern South China Sea. *Acta Sedimentol. Sin.* 28 (1), 68–75.

Yuan, S., Wu, S., Thomas, L., Yao, G., Lv, F., Cao, F., et al. (2009). Fine-grained Pleistocene Deepwater Turbidite Channel System on the Slope of Qiongdongnan Basin, Northern South china Sea. *Mar. Petroleum Geol.* 26 (8), 1441–1451. doi:10.1016/j.marpetgeo.2009.03.007

Yuan, S., Wu, S., and Yao, G. (2010b). The Controlling Factors Analysis of Qiongdongnan Slope Deepwater Channels and its Significance to the Hydrocarbon Exploration. *Mar. Geol. Quat. Geol.* 30 (2), 61–66. doi:10.3724/sp.j.1140.2010.02061

Zhang, D., Zhang, Y., Shao, L., Liu, X., Wang, Y., He, X., et al. (2017). Sedimentary Provenance in the Central Canyon of Qiongdongnan Basin in the Northern South China Sea. *Nat. Gas. Geosci.* 28 (10), 1574–1581. (In Chinese with English abstract). doi:10.11764/j.issn.1672-1926.2017.08.012

Zhao, Z., Sun, Z., Wang, Z., Sun, Z., and Zhang, C. (2015). The High Resolution Sedimentary Filling in Qiongdongnan Basin, Northern South China Sea. *Mar. Geol.* 361, 11–24. doi:10.1016/j.margeo.2015.01.002

Zhu, M., Graham, S., and McHargue, T. (2009). The Red River Fault Zone in the Yinggehai Basin, South China Sea. *Tectonophysics* 476, 397–417. doi:10.1016/j.tecto.2009.06.015

Conflict of Interest: The authors declare that the research was conducted in the absence of any commercial or financial relationships that could be construed as a potential conflict of interest.

Publisher's Note: All claims expressed in this article are solely those of the authors and do not necessarily represent those of their affiliated organizations, or those of the publisher, the editors and the reviewers. Any product that may be evaluated in this article, or claim that may be made by its manufacturer, is not guaranteed or endorsed by the publisher.

frontiers | Frontiers in Earth Science

ORIGINAL RESEARCH
published: 17 June 2022
doi: 10.3389/feart.2022.902469

Gas Hydrate Accumulation Related to Pockmarks and Faults in the Zhongjiannan Basin, South China Sea

Guangxu Zhang[1,2], Xiujuan Wang[2,3], Lin Li[4]*, Luyi Sun[1,2], Yiqun Guo[5], Yintao Lu[4], Wei Li[6], Zhaoqi Wang[4], Jin Qian[1,2], Taotao Yang[4] and Wenlong Wang[1,2]*

[1]Center for Ocean Mega-Science and Key Laboratory of Marine Geology and Environment, Institute of Oceanology, Chinese Academy of Sciences, Qingdao, China, [2]Laboratory for Marine Mineral Resources, Qingdao National Laboratory for Marine Science and Technology, Qingdao, China, [3]Frontiers Science Center for Deep Ocean Multispheres and Earth System, Key Lab of Submarine Geosciences and Prospecting Techniques, MOE and College of Marine Geosciences, Ocean University of China, Qingdao, China, [4]Petrochina Hangzhou Research Institute of Geology, Hangzhou, China, [5]Haikou Marine Geological Survey Center of China Geological Survey, Haikou, China, [6]CAS Key Laboratory of Ocean and Marginal Sea Geology, South China Sea Institute of Oceanology, Chinese Academy of Sciences, Guangzhou, China

OPEN ACCESS

Edited by:
Pibo Su,
Guangzhou Marine Geological Survey, China

Reviewed by:
Jiangxin Chen,
Qingdao Institute of Marine Geology (QIMG), China
Ming Su,
Sun Yat-sen University, China
Jinxiu Yang,
China University of Petroleum, China

***Correspondence:**
Xiujuan Wang
wangxiujuan@ouc.edu.cn
Lin Li
lilin_hz@petrochina.com.cn

Specialty section:
This article was submitted to Marine Geoscience, a section of the journal Frontiers in Earth Science

Received: *23 March 2022*
Accepted: *02 May 2022*
Published: *17 June 2022*

Citation:
Zhang G, Wang X, Li L, Sun L, Guo Y, Lu Y, Li W, Wang Z, Qian J, Yang T and Wang W (2022) Gas Hydrate Accumulation Related to Pockmarks and Faults in the Zhongjiannan Basin, South China Sea. Front. Earth Sci. 10:902469. doi: 10.3389/feart.2022.902469

The amplitude and coherence attributes of three-dimensional (3D) seismic data are used to confirm gas hydrate occurrence and to delineate its distribution in the Zhongjiannan basin, South China Sea. High amplitude anomalies (HAAs) are distributed above or below the regional base of gas hydrate stability zone (BGHSZ), which intersect with the bottom simulating reflectors (BSRs) or are interrupted by different types of pockmarks. The maximum amplitude attribute extracted along T1 (5.5 Ma) horizon is controlled by the widely distributed faults. The layer-bound polygonal faults (PFs) show networks of small normal faults, and the dominant orientations of PFs are similar or orthogonal to the regional tectonic faults, which provide the fluid migration pathways for gas and fluids to form HAAs. BSR shows the strong amplitude and continuous reflection where the faults or PFs can reach the BGHSZ without the influence of the pockmarks. Most of the pockmarks are related to the reactivation of faults and magmation, and some pockmarks are caused by the dissociation of gas hydrate. Around the matured pockmark, the BSR is discontinuous, and HAAs locally appear within the pockmarks. The inverted acoustic impedance profile shows obviously high values of HAAs except in pockmark zones. Partial HAAs occur above BGHSZ, and the continuity is interrupted by the pockmarks with only high values around the pockmarks. We propose that BSR, HAAs, pockmarks, and different types of faults are closely related to the occurrence and distribution of gas hydrates in the study area. This work allows us to understand the relationship between gas hydrate occurrence and accumulation with pockmarks, faults, and magmatic activities.

Keywords: gas hydrate, high amplitude anomalies, polygonal fault, pockmarks, Zhongjiannan basin

INTRODUCTION

The occurrences of gas hydrates with different morphologies have been confirmed in the northern slope of South China Sea by Guangzhou Marine Geological Survey (GMGS) drilling expeditions since 2007 (e.g., Zhang et al., 2007; Zhang et al., 2014; Yang et al., 2015; Zhang et al., 2015; Yang et al., 2017; Jiangong Wei et al., 2019; Liang et al., 2019; Ye et al., 2019; Zhang et al., 2019; Zhang et al.,

2020a; Zhang et al., 2020b). Pore-filling gas hydrates with different thicknesses and saturation were found just above the base of the gas hydrate stability zone in the Pearl River Mouth Basin (PRMB) (Yang et al., 2017; Wang et al., 2011; Wang et al., 2014a; Wang et al., 2022; Zhang et al., 2020a; Zhang et al., 2020b). The gas hydrate-bearing layer shows high amplitude anomalies (HAAs) with the same polarity to the seafloor reflection above BSR showing on the seismic profile (Wang et al., 2016; Zhang et al., 2020a; Wang et al., 2022). The reservoir of gas hydrates in PRMB is mainly clay silt with abundant foraminifera and calcareous debris (Chen et al., 2013; Kang et al., 2018; Li et al., 2018). Moreover, the gas hydrate production test was also conducted in this area where the gas hydrate target is a three-layer structure of a hydrate layer, a mixed layer of hydrate and free gas, and a free gas layer (Li et al., 2018; Qian et al., 2018; Qin et al., 2020). Recently, gas hydrate drilling expeditions in the Qiongdongnan Basin (QDNB) have found that the morphologies of gas hydrates and the seismic anomalies for gas hydrate-bearing layers are quite different from those found in the PRMB. The gas source in the QDNB is mainly thermogenic gas, while that of PRMB is a mixed source or mainly biogenic gas (Wu et al., 2009; Wu et al., 2010; Wang et al., 2014a; Liang et al., 2019; Ye et al., 2019; Zhang et al., 2020b; Lai et al., 2021). Gas hydrates with veins, nodules, massive, and fracture-filled were found from the pressure core samples, and the three dimensional (3D) seismic profiles show chimney-like structures extended to different layers with pull-up reflections and weak amplitude, while it shows the seismic anomalies as acoustic blanking reflection in the two-dimensional seismic profile (e.g., Liang et al., 2019; Ye et al., 2019; Zhang et al., 2019; Wang et al., 2021; Wang et al., 2022). The BSR is approximately parallel to the seafloor, with a discontinuous distribution, obviously different from that observed in the QDNB that is influenced by the widely distributed mass transport depositions. Many studies have shown that the accumulation of gas hydrates is closely related to gas chimneys and faults, which provide upward migration pathways of deep thermogenic gas (Wu et al., 2009; Liang et al., 2019; Ye et al., 2019; Zhang et al., 2020a; Su et al., 2020).

Fluid migration and reservoir are important factors for gas hydrate accumulation in fine-grained sediments. Biogenic gas and thermogenic gas can form gas hydrates. The fluid can migrate upward through diffusion, convection, and gas phase to form gas hydrates within the gas hydrate stability zone (Collett et al., 2009). The biogenesis gases generated in the fine-grained sediments can migrate to the coarse-grained sediments in a short distance by diffusion to form gas hydrates, and they may transport for a long distance along coarse-grained or permeable strata by convection in a gas phase or dissolved gas together with water, which can accumulate in the favorable reservoir to form gas hydrates (Li et al., 2019). Pockmarks with bowl-shaped negative topography on the seabed are formed at the seafloor or buried below the seafloor caused by fluid seepage (e.g., Berndt et al., 2003; Svensen et al., 2004; Hovland et al., 2005; Gay et al., 2006; Cartwright et al., 2007; Prunelé et al., 2016). Faults can serve as migration conduits for hydrocarbon gas and fluids, thereby which can affect the formation and distribution of gas hydrates (Berndt et al., 2003; Cartwrighty et al., 2003; Hustoft et al., 2007; Sun et al., 2010; Laurent et al., 2012; Ostanin et al., 2012). Widely distributed BSRs have been found in the Zhongjiannan Basin (ZJNB), which are related to pockmarks and polygonal faults (Lu et al., 2017; Liu et al., 2019; Lu et al., 2021). The previous study showed that BSRs are not parallel to the seafloor and have variable depths from the seafloor ranging from 184 to 263 m (Lu et al., 2017). However, the controlling factors of gas hydrate distribution, saturation, and thickness are not well known. In this study, we reprocessed the 3D seismic data together with broadband inversion and attribute analysis to reveal the occurrence and controlling factors for gas hydrate. We summarized the relationship between gas hydrate, polygonal faults, normal faults, and pockmarks and their controlling on gas hydrate occurrence and accumulation in the study area.

GEOLOGICAL SETTING

The South China Sea (SCS) is one of the largest continental margin basins in the Western Pacific. The Zhongjiannan basin is located at the Western margin of the SCS, and it is near the Qiongdongnan basin, Xisha Island, and Zhongsha Island (**Figure 1**). The tectonic evolution of the Zhongjiannan basin can be divided into two stages: rift extension and post-rift thermal subsidence by the boundary of 23.3 Ma (Xie et al., 2006). During the rifting period, tectonic activities were relatively active, and multiple groups of the northeast and near east-west oriented faults were developed (Xie et al., 2008). During the post-rift period, the tectonic activity was relatively weak in the Early-Middle Miocene (Zhou et al., 1995), while the neotectonics movement has been active since the late Miocene due to the collision between Taiwan and the Chinese mainland continent (Lüdmann and KinWong, 1999). Widespread magmatic activities, uplifts, and fluid flow systems occurred due to the left-lateral transgression and the right-lateral wrenching along the East Vietnam boundary fault zone since 5.5 Ma (Morley, 2002; Li et al., 2013; Chen et al., 2015). Abundant polygonal faults were developed during the stage of stable thermal subsidence in the post-rift period. Faults and volcanoes were reactivated due to tectonic activity, which can serve as vertical pathways for deep thermogenic gas migration and are beneficial to gas hydrate accumulation (Sun et al., 2011; Sun et al., 2013; Chen et al., 2015; Lu et al., 2017; Chen et al., 2018; Yang et al., 2020).

The stratigraphic sequences in the shallow sediments are quite different since 10.5 Ma (T2) due to lack of well data. We interpreted eight seismic horizons to study the tectonic activity, and its influence on fluid flow and gas hydrate formation, namely, the Seafloor, T1 (5.02 Ma), T2 (10.5 Ma), T3 (16.5 Ma), T4 (23.3 Ma), T5 (28.0 Ma), T6 (35.4), and Tg (56.5 Ma), bounded the intervals named Yinggehai, Huangliu, Meishan, Sanya, Lingshui, Yacheng, and Lingtou Formation, respectively. Based on the sequence stratigraphy analysis and seismic interpretation from core samples, the reflector T1 is the boundary of the Miocene and Pliocene. The thickness of this layer ranges from 300 to

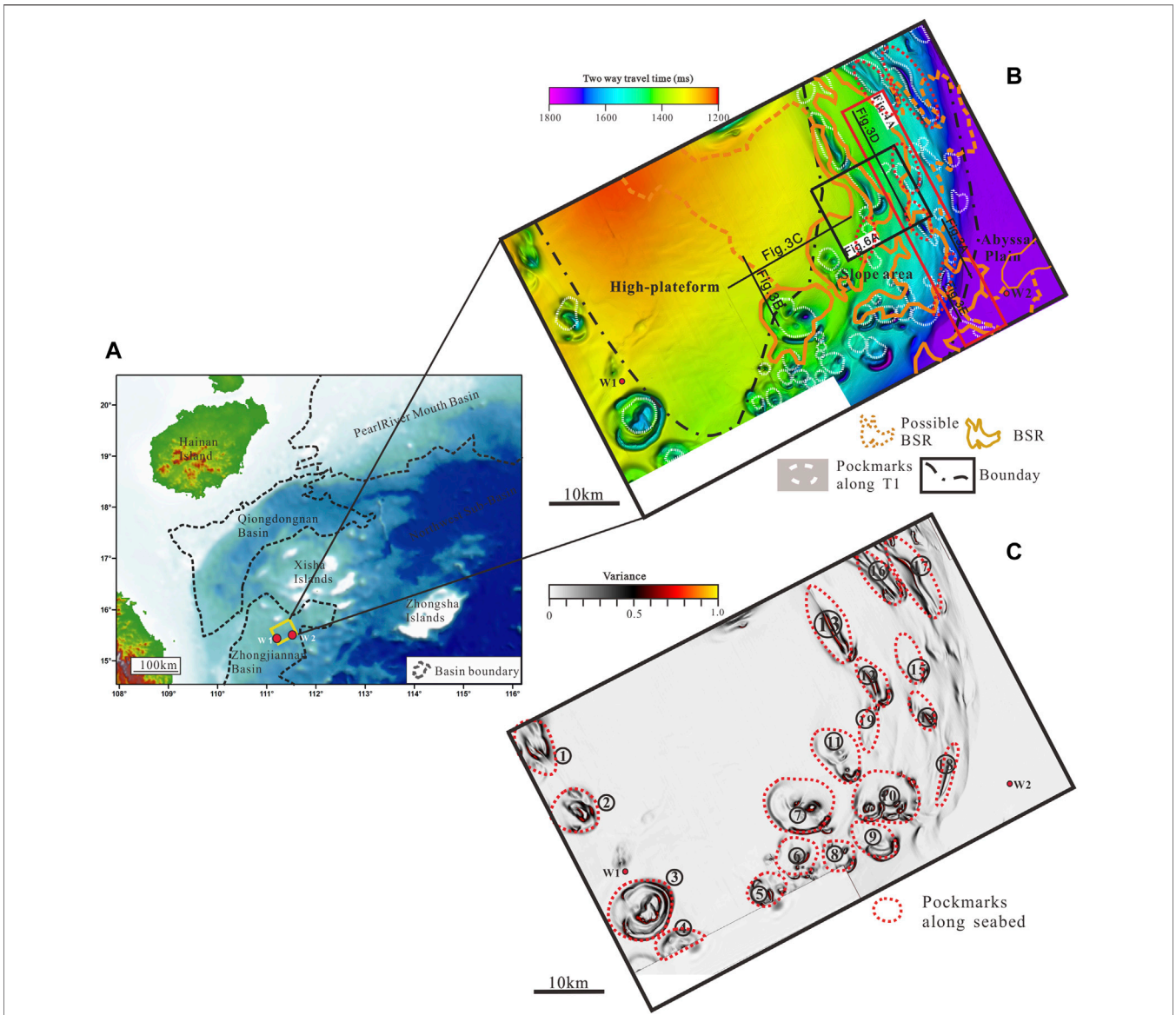

FIGURE 1 | (A) The location of Zhongjiannan basin is to the south of Qiongdongnan basin, the northern slope of South China Sea. **(B)** The water depth of seafloor interpreted from 3D seismic data showing the pockmarks and different types of BSRs. The white break line represents the pockmarks identified along with horizon T1. The black rectangle marks the location of the reprocessed 3D seismic data boundary. **(C)** The variance slice along the seabed showing the pockmarks. The red break line represents the pockmarks identified along with the horizon seabed.

750 ms two-way travel time showing high amplitude reflections in the study area (**Figure 2**). The water depths range from 800 to 1400m, and two sites were drilled in 2014 in the study area. The geothermal gradient measured at Sites W1 and W2 are about 54.1°C/km and 5.02°C/km, respectively, and the seafloor surface temperature is about 5°C (Li et al., 2022). The calculated methane hydrate stability zone is about 160–240 m using the phase equilibrium curve (Sloan and Koh, 2007). The Miocene and upper strata have low organic matter maturity (Ro<0.5%) and are in the immature stage (Liu et al., 2019), which is the primary strata of biogenic gas.

DATA AND METHOD

Seismic Data

High-resolution 3D seismic data were acquired by WesternGeco Geophysics using eight parallel cables and 960-channel streamers in 2011. The trace interval is 3.25 m, and the time sampling is 2 ms, with a bin spacing of 12.5 and 25 m of the inline and crossline, respectively. Conventional processed 3D seismic data are used to identify deeper structures in the middle and deep strata. BSR was identified from the seismic data in this basin with an area of about 350 km^2 (Lu et al., 2017; Li et al., 2022). To study the properties of gas hydrate accumulation and distribution, 100 km^2 3D seismic data

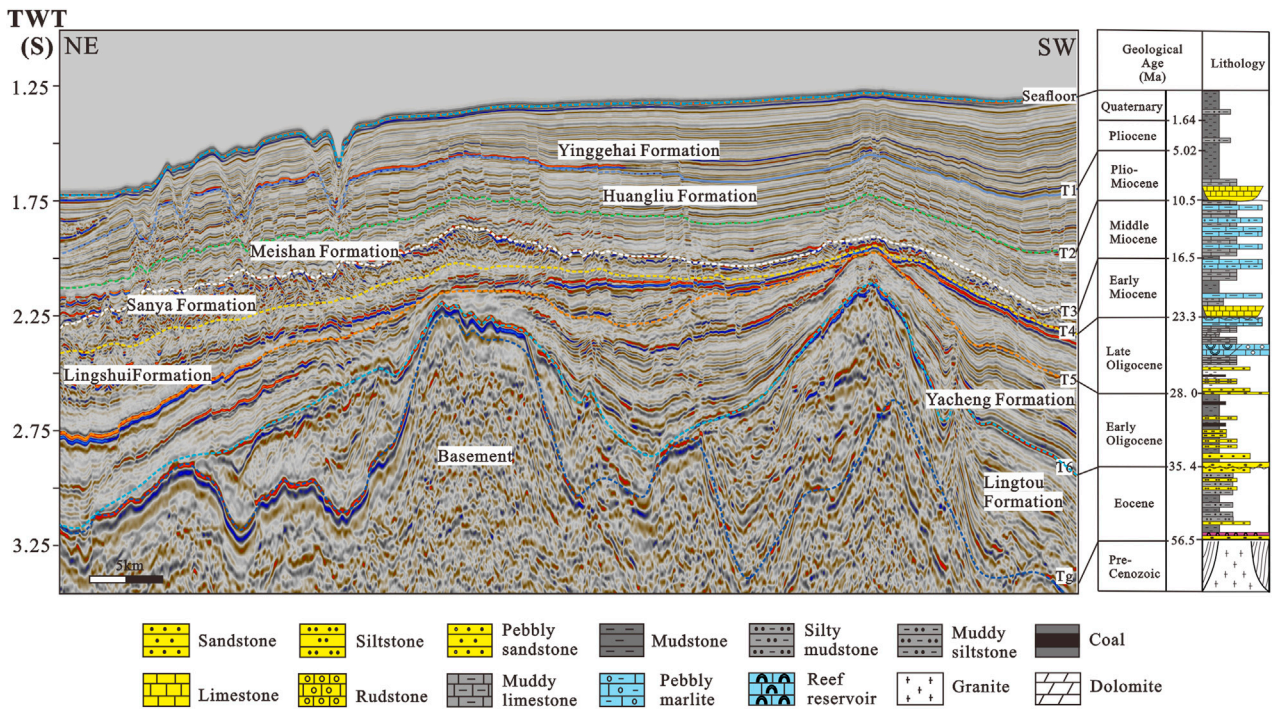

FIGURE 2 | Schematic stratigraphic sequences in the Zhongjiannan basin and the main seismic horizons (modifed after Xie et al., 2006; Lu et al., 2017).

were reprocessed to improve the signal-to-noise ratio, protect low frequencies, and broaden the frequency bandwidth by suppressing ghost waves. For high-resolution interpretation, horizons T1, T2, T3, T4, T5, and T6 were picked every 20 lines and traces. In some areas of pockmarks and volcanoes, in lines and traces were picked every two to five lines. To understand how polygonal faults and faults have interacted with HAAs and fluid flow in this area, the following attributes of 3D seismic data were extracted: 1) the maximum amplitude along horizon T1 and BGHSZ with different time windows and 2) the coherence slice along T0, T1, T2, and T5 using Petrel E&P are used to describe the lateral amplitude discontinuities and to enhance the faults and fractures. Manual interpretation of fault strikes was carried out from coherence slices. Extracted fault strikes from individual fault segments are then plotted on bidirectional rose diagrams for further structural analysis with the Grapher software. 3) The root mean square (RMS) amplitude attribute along T1 with a 50 ms time window above along the picked horizon are generated to show the sedimentary environment.

Broadband Inversion of Acoustic Impedance

The constrained sparse spike inversion (CSSI) of broadband full-stack seismic data was carried out to obtain the acoustic impedance profile. The input data include the time-migrated seismic data, the average seismic wavelet, horizons, and the low-frequency impedance model. The wavelets are estimated by creating pseudo-wells at different positions. Since the target layer is buried in a shallow depth, the wavelets estimated by different pseudo-wells are relatively stable. Therefore, a zero-phase average wavelet is used to invert acoustic impedance. The low-frequency model is established by combining the compaction trend with the stack velocity due to the lack of gas hydrate logging data in the study area. The frequency range of the compaction trend is about 0–1 Hz, and the frequency range of the velocity field is 0–2 Hz. The compaction trend of the low-frequency model is used to correct the trend of the velocity field model. Gas hydrate saturations have been estimated from the P-wave well log data, inverted seismic velocity or impedance data and rock physics modeling to provide spatial distribution of gas hydrate occurrences (e.g., Helgerud et al., 1999; Lee and Collett, 2009; Lee and Waite, 2008; Lu and Mcmechan, 2002, Lu and McMechan, 2004; Shelander et al., 2012; Riedel and Shankar, 2012; Wang et al., 2011; Wang et al., 2014a, Wang et al., 2016; Wang et al., 2021). Lithology and porosity are essential factors for affecting the estimated gas hydrate saturation.

Till now, no gas hydrate drilling well has been conducted in the area. We used the well logs at the adjacent area with similar sedimentary environments and two oil exploration wells in this basin to get the porosity profile (Li et al., 2022). We used the same method to invert the porosity data in this basin. The inverted acoustic impedance data were used to calculate gas hydrate saturation using the sand/clay or carbonate/clay rock physics models in the Shenhu area (Wang et al., 2016). The main mineralogical compositions are assumed of 40% clay+60% sand and 100% carbonate, respectively. The RMS and maximum value of gas hydrate saturations are extracted along

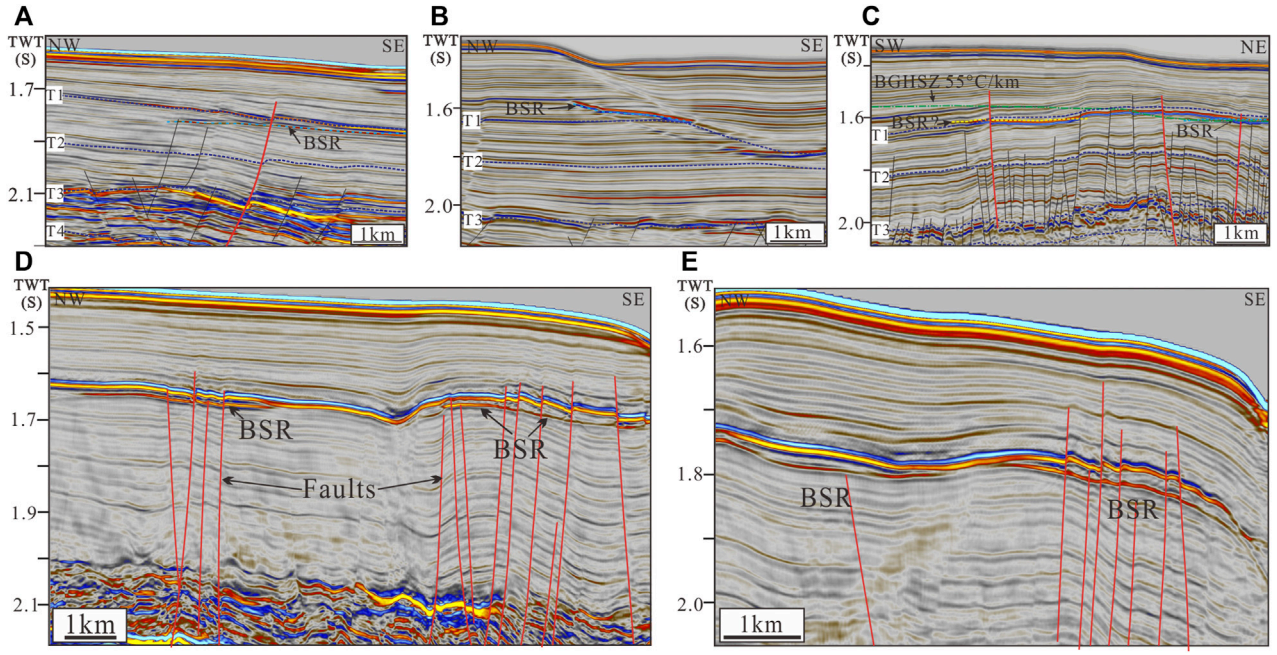

FIGURE 3 | (A)–(E) The seismic characteristics of BSR and high amplitude anomalies at different locations and their relationship with faults, pockmarks, and the base of the gas hydrate stability zone calculated from 55°C/km (location shown in **Figure 1B**).

BGHSZ to show the distribution of gas hydrate in the reprocessed seismic data. We can compare gas hydrate identified from reprocessed data to seismic attributes from conventional seismic data in the study area to show the distribution.

RESULTS

Characteristics of BSR and High Amplitude Anomaly Features

BSRs are delineated using the high-resolution and reprocessed 3D seismic data to show the spatial distribution (**Figure 3**). The BSRs show a weak amplitude in the conventional processed 3D seismic data (**Figure 3A–C**), while the reprocessed seismic data show continuous BSR and high amplitude reflection indicating the occurrence of gas hydrate (**Figure 3E,F**, **Figure 4D**). The seismic response of the gas hydrate layer has a strong amplitude reflection with the revered polarity of the seafloor (Lu et al., 2017; Li et al., 2022). The BSRs show the variations of amplitude, continuity, and spatial distribution at the platform, platform margin, and abyssal plain, including three different geological environments (**Figure 3**): 1) fault-controlled BSRs and HAAs. Most BSRs and HAAs are related to faults, especially where BSR and HAAs are separated by a low saturation gas hydrate-bearing layer (**Figure 3A, C–E**); 2) pockmark-influenced BSR. BSR is occurred within or at the edge of pockmarks, which shows the discontinuous, weak-medium amplitude and shallower depth (**Figure 3B**); and 3) BSR and HAA overlap BGHSZ. BSR is located at the BGHSZ with HAA, and BSR and BGHSZ are consistent (**Figure 3D,E**).

The BSR shows relatively weak amplitude compared to HAAs seen from the reprocessed seismic profile (**Figure 4D**). The BSR and HAA are easy to distinguish when gas hydrate-bearing sediments are thicker. However, when the BSR, HAA, and BGHSZ match each other, the seismic amplitude is strong. The inverted acoustic impedance shows high acoustic impedance value for the HAA layer, which is continuous and slightly changes. The depths to the seafloor of HAA vary laterally due to the influence of the sedimentary environment.

Characteristics of Acoustic Impedance and Gas Hydrate Saturations

Gas hydrate saturations are estimated using an effective medium model and the inverted acoustic impedance (Li et al., 2022). The estimated gas hydrate saturation using the clay/sand model (with 40% clay and 60% sand) is about 10–50% of the pore space. Due to the lack of drilling data, we are not sure about the lithology of the HAA layer, and we consider the lithology influence on the inverted acoustic impedance. In the fine-grained sediments with high gas hydrate-bearing sediments, calcite content is up to 60% at Site GMGS3-W18 (Kang et al., 2018). We assume that the gas hydrate-bearing sediment with a content of 100% calcite under this extreme condition, and the calculated gas hydrate saturation is significantly reduced, but the average saturation of the HAA layer can reach 20%, and the partial region with gas hydrate saturation is up to 40% (**Figure 4E**). The thickness of the gas hydrate-bearing layer ranges from 10 to 57 m (Li et al., 2022).

The maximum values of the inverted acoustic impedance are extracted along BGHSZ with time windows of 50 ms to show the

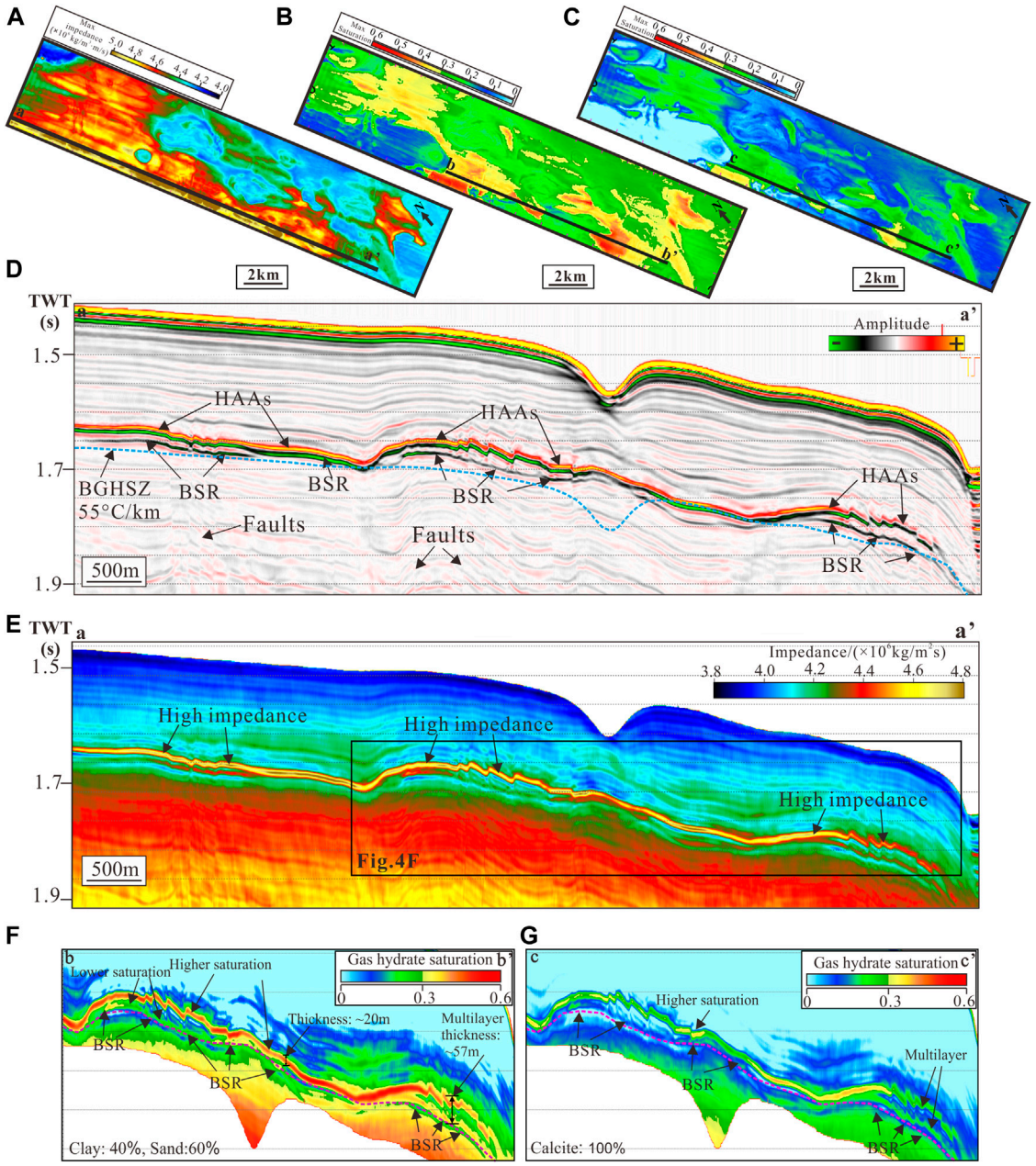

FIGURE 4 | (A) Maximum value extracted from the acoustic impedance along BGHSZ with 50 ms spanning windows, showing the distribution of the acoustic impedance. **(B)** Maximum value of the estimated gas hydrate saturations using the clay/sand model along BGHSZ with a 50 ms search window. **(C)** Maximum value of the estimated gas hydrate saturation using a model with 100% calcite, showing the distribution of gas hydrate saturation. **(D)** The reprocessed broadband seismic profile shows BSR and high amplitude anomalies (HAAs). **(E)** The inverted acoustic impedance profile shows high acoustic impedance of the HAA layer **(F)–(G)** Gas hydrate saturation profiles estimated from iterative inversion using the lithologies of 40% clay and 60% sand, and carbonate, respectively.

distribution of gas hydrate (**Figure 4A**). The inverted acoustic impedance show similar changes except at the edge of pockmarks. However, the maximum attributes of estimated gas hydrate saturations extracted along BGHSZ with a time window of 50 ms show obviously different features (**Figure 4B**). Gas hydrate saturations estimated using the clay/sand model are higher than that estimated from the calcite model (**Figure 4F,G**). There are no gas hydrates around the pockmarks.

Characteristics of Polygonal Faults

Small and "non-tectonic" extensional faults affect about 1000 m of sediments and show the polygonal pattern in plain view, which show small offsets ranging from 10 to 50 ms two-way travel time and a spacing ranging from 100 m to 2 km. The coherency attribute slices are used to show the detailed lateral distribution of polygonal fault discontinuities (**Figure 5B–D**). The polygonal faults are confined to the stratigraphic intervals

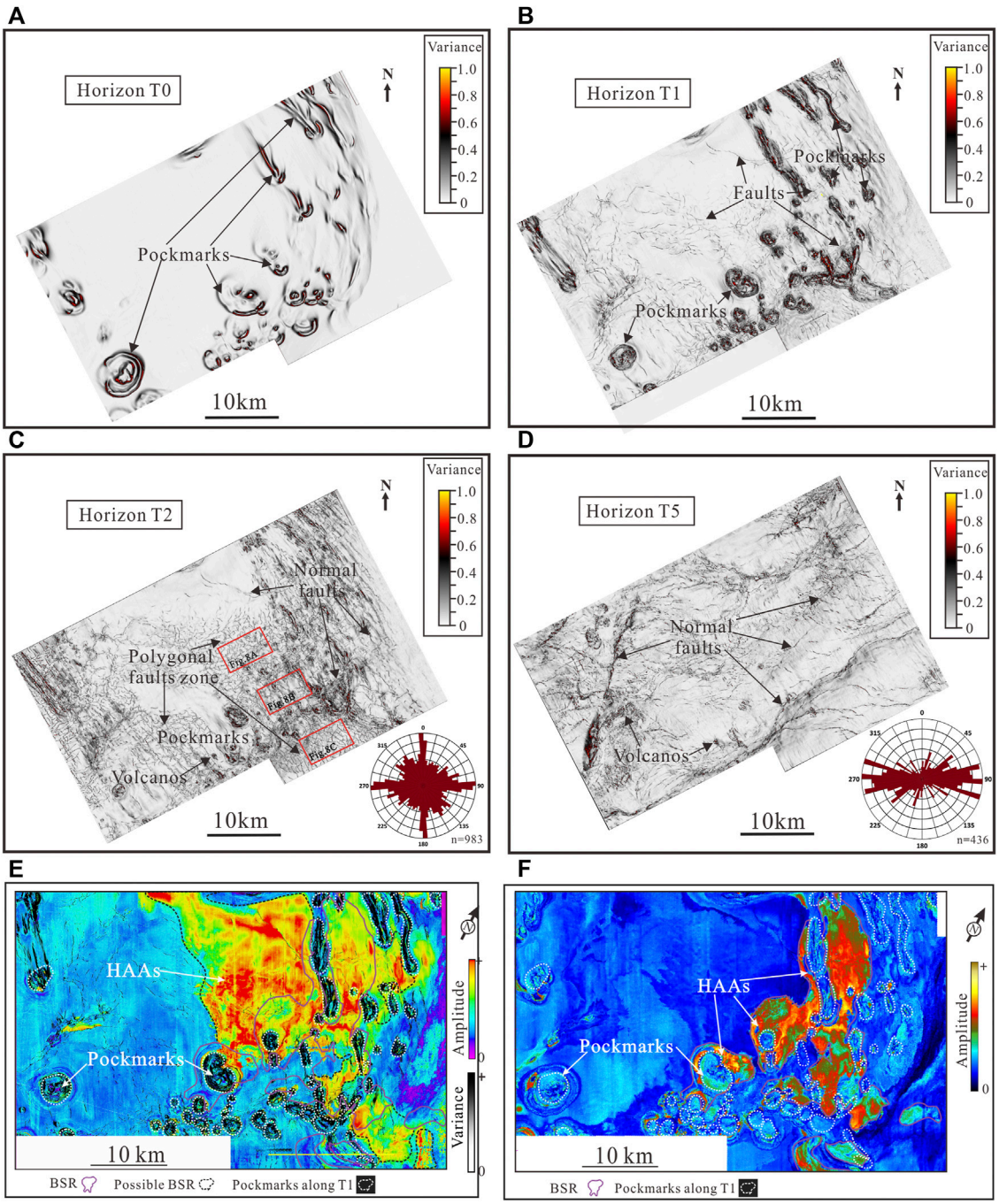

FIGURE 5 | (A)–(D) The time slices of the coherence attribute along horizons T0, T1, T2, and T5, respectively. The maps show the variations of polygonal faults and fault systems in the study area. The inset rose diagrams of horizons T2 and T5 showing the strikes of faults, respectively. **(E)** Maximum amplitude attribute map extracted along T1 with a time window 60 ms above this layer, which overlays on the fault probability volume obtained from variance slice along horizon T1, showing the relationship between HAAs, faults, and pockmarks. **(F)** Maximum amplitude attribute map extracted along BGHSZ with a time window of 60 ms above and the pockmarks found in the horizon T1 showing the relationship between the distribution of the HAAs and the pockmarks.

from T1 to T4, and the maximum displacement values range from several meters to over 100 m seen from the coherence attribute. The polygonal faults are found in the middle of the platform and southeast parts of the study area and rarely developed in the west part, showing the irregular polygonal map geometry (**Figures 5**, **6**). A high density of polygonal faults is encountered in the platform and slope region. The polygonal faults are orthogonally linked to the adjacent tectonic faults (**Figure 5**). The seismic section represents discontinuous and sinuous seismic events in the polygonal

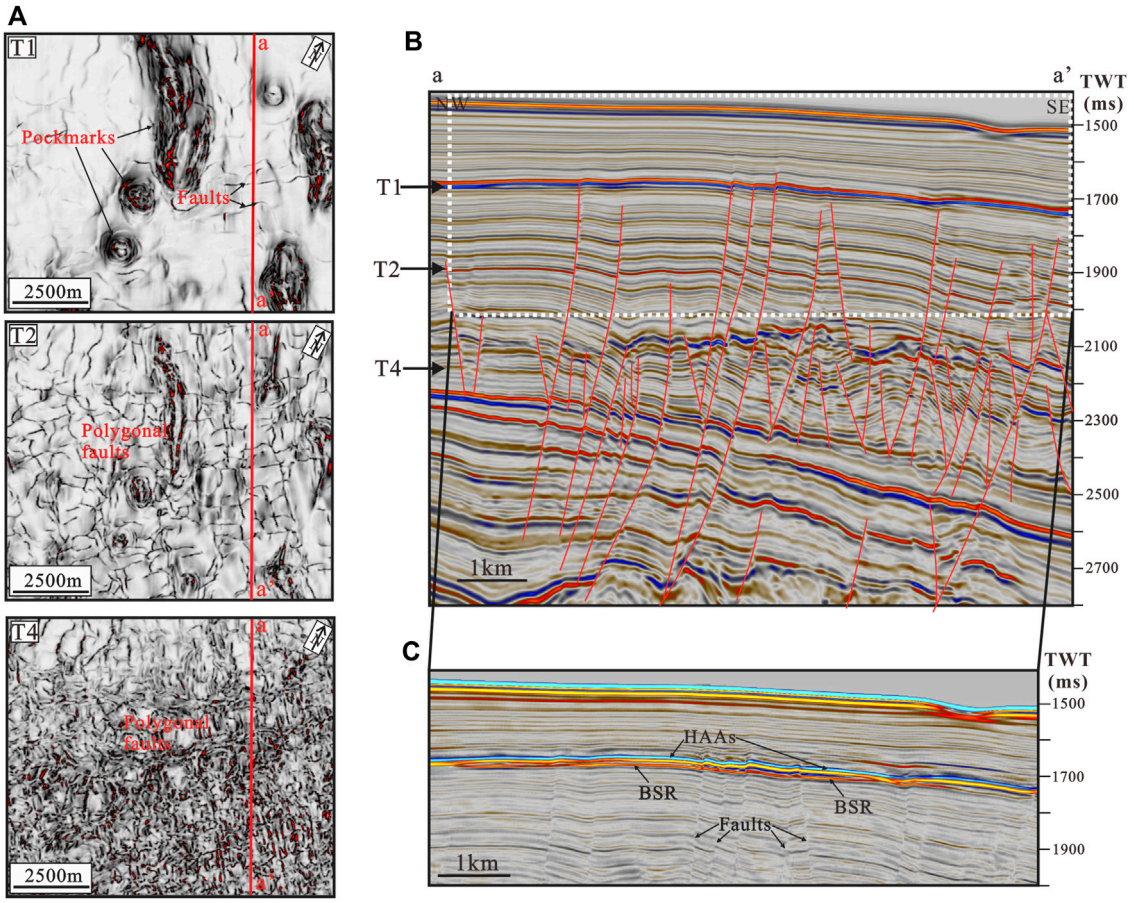

FIGURE 6 | Three-dimensionality of polygonal fault geometry. **(A)** Three coherence slices extracted from horizons T1, T2, and T4, respectively, show polygonal faults' variations at different depths. **(B)** Seismic profile showing the position of three coherence slices showing complex tier, with few master faults transecting the full thickness reaching the BSR and HAA and with many other smaller faults **(C)**. The reprocessed seismic profile showing the relationship between BSR, HAAs, and faults.

fault's interval. Partial polygonal faults can cut through BSRs and HAA layer (**Figures 3**, **6**).

A representative area for the polygonal fault network block was analyzed to compare the relation between the fault strike and polygonal strike. Faults found from the T5 horizon are mainly tectonic faults with the strike of NE-SW (**Figure 5D**). In contrast, the coherence attribute slice of the T2 horizon shows that polygonal faults and tectonic faults are widely distributed, and the strikes are N-S and NE-SW (**Figure 5C**), respectively. By comparing the strikes identified from T2 and T5 horizons, we find that some polygonal faults have similar strikes to tectonic faults and some polygonal faults have quite different strikes. In general, the idealized polygonal planform is a classical hexagonal pattern in which the faults intersect at angles of 60° or so, and faults are almost equal in strike length. This classical pattern is found in the regional area (**Figure 5C**). At different layers, distinct fault planform patterns are found from three horizons of T1, T2, and T4, showing the significant variations in the fault pattern and connectivity at different depths (**Figure 6**). The seismic profile shows the positions of the three coherence slices, which is a complex tier. There are few "master" faults that can penetrate through the overlying strata to the BSR and HAA. Many other smaller faults are generated in the local strata and fill in the space between the larger faults intersecting with them at different levels within the tier. The distribution of these faults is very important for the upward migration of fluid flow, which can transport plenty of fluids from deeper sediments to the BGHSZ to form gas hydrate.

Morphological Characteristics of Pockmarks

Pockmarks generally indicate upward migration of gas and fluid with a subsurface deformation feature. Different types of pockmarks have been described using the seismic data and multibeam bathymetry map in the study area (Sun et al., 2011; Sun et al., 2013; Chen et al., 2015; Lu et al., 2017), which are associated with various fluid flow features and structures. The seismic reflection data and the coherence attributes along the seafloor suggest that more than 19 pockmarks are developed with different geometric shapes, including the circular, elliptical, crescents, elongated, or composite types with different

TABLE 1 | Summary of morphometrics of the studied pockmarks.

Pockmark number	Long axis diameter (km)	Short axis diameter (km)	Ratio of long and short axis	Water depth range (m)	Maximum depth of pit (m)	Shape
PM 1	6.24	4.48	1.39	1350–1500	180	Ellipse
PM 2	4.79	4.25	1.13	1320–1550	236	Circle
PM 3	6.45	6.07	1.06	1330–1620	289	Circle
PM 4	3.8	3.2	1.19	1400–1520	90	Circle
PM 5	4.2	3.7	1.14	1400–1560	140	Circle
PM 6	4.1	3.9	1.05	1400–1620	202	Circle
PM 7	6.3	5.7	1.11	1350–1620	252	Circle
PM 8	3.58	3.32	1.10	1420–1700	226	Circle
PM 9	5.46	2.91	1.88	1470–1650	180	Ellipse
PM 10	6.63	6.61	1.01	1500–1720	180	Circle
PM 11	6.61	2.72	2.43	1380–1620	175	Ellipse
PM 12	5.81	2.18	2.67	1450–1620	168	Crescent
PM 13	9.12	3.19	2.86	1350–1540	216	Crescent
PM 14	4.62	2.07	2.23	1530–1660	130	Crescent
PM 15	5.52	2.58	2.24	1490–1640	110	Crescent
PM 16	7.10	2.39	2.97	1470–1620	100	Crescent
PM 17	10.08	2.31	4.36	1480–1680	96	Crescent
PM 18	6.94	0.88	7.89	1650–1700	38	Crescent
PM 19	4.75	1.56	3.05	1420–1460	40	Crescent

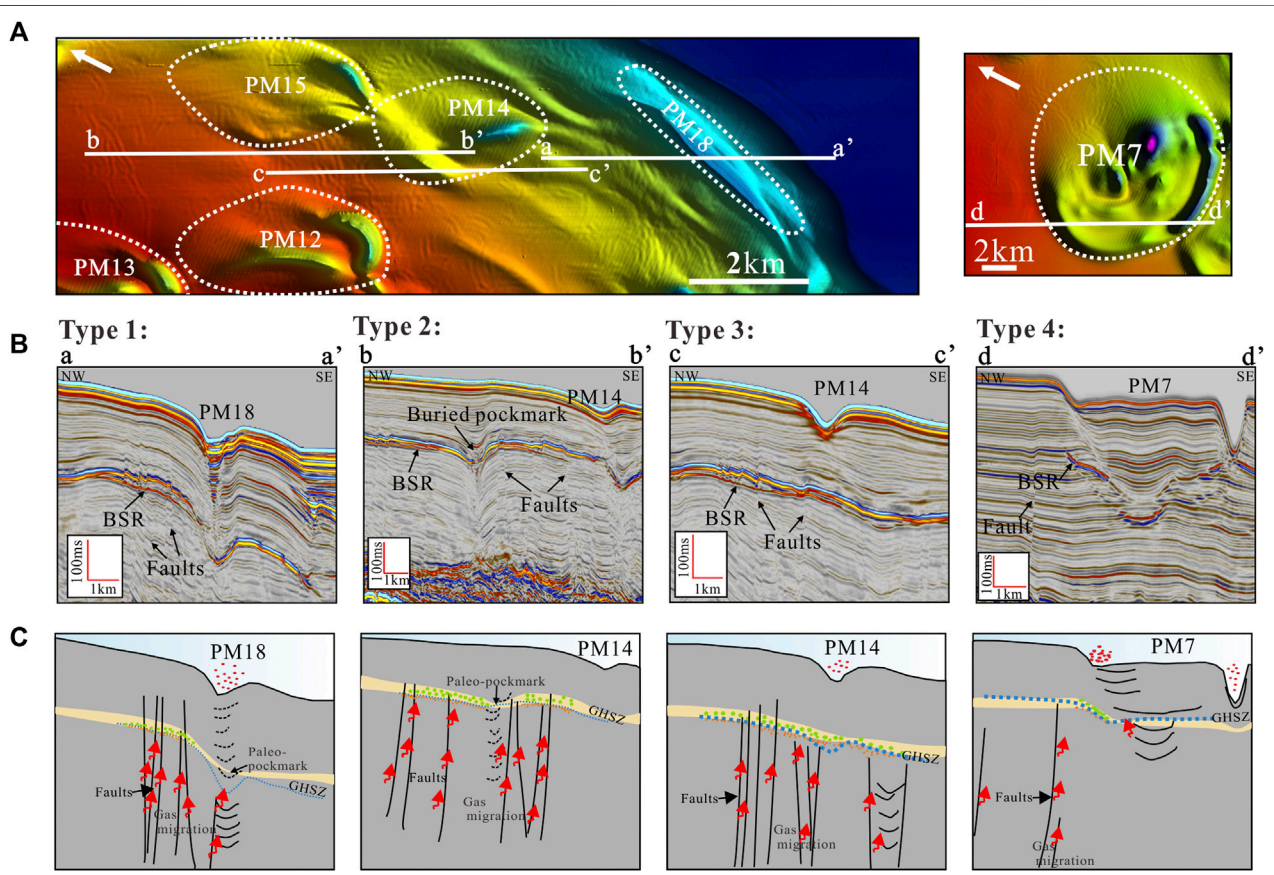

FIGURE 7 | (A) Detailed map of the represented pockmarks. **(B)–(C)** The seismic sections and conceptual view of the four types of pockmarks in the 3D study area, showing the relationship between the pockmarks, faults, and gas hydrate.

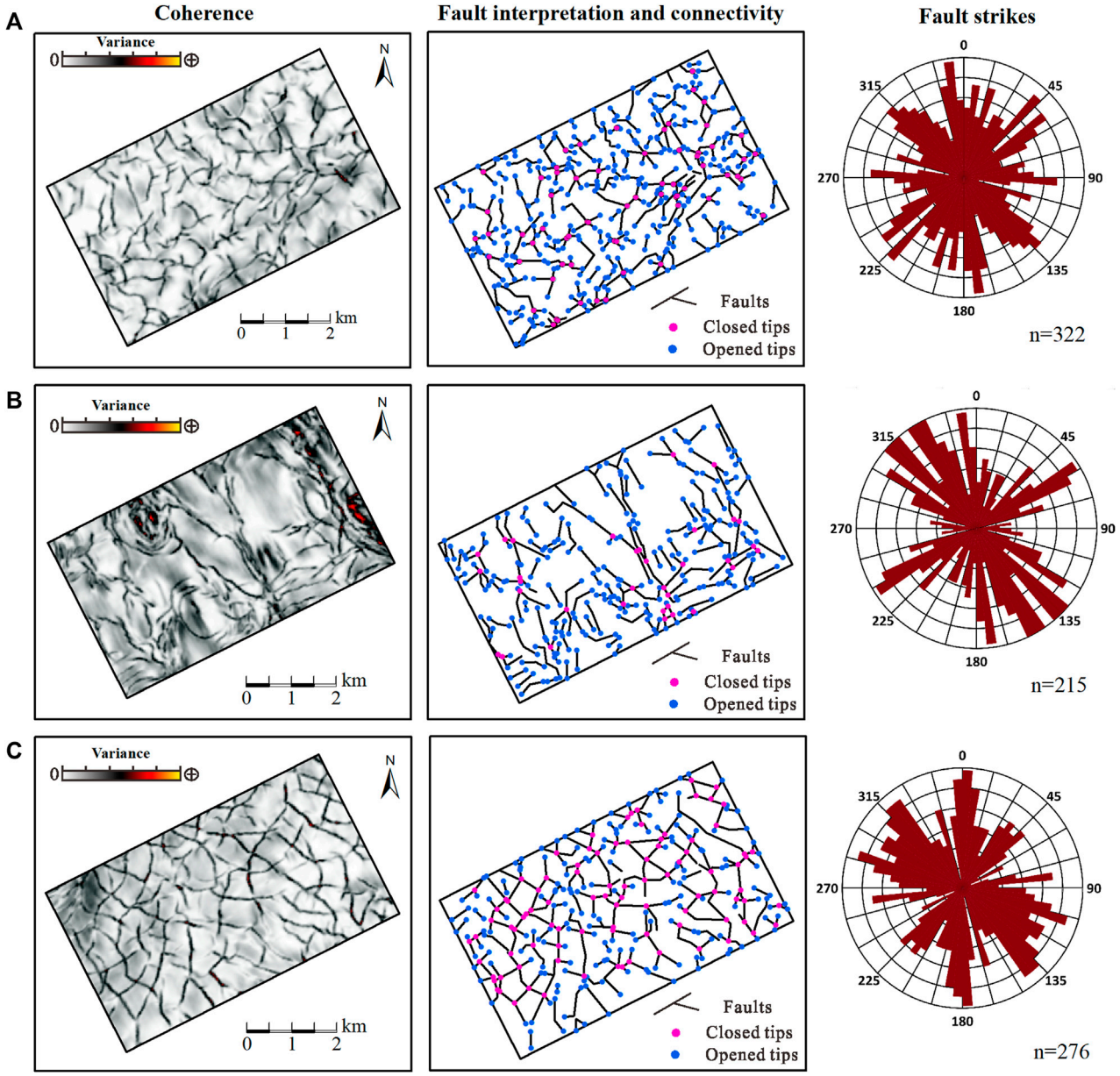

FIGURE 8 | (A)–(C) The coherence slices along horizons T2, fault interpretation and connectivity, rose diagram of the fault strikes for areas A, B, and C, respectively. The locations are shown in **Figure 5C**. The coherence slices showing the fault system. In the fault interpretation and connectivity map: The pink solid dots mark the closed tips of the faults, the blue solid dots mark the opened tips of the faults, the degree of maturity refers to the number of 'open' versus 'closed' or restricted lateral tips.

diameters and depths (**Figures 1**, **5A**; **Table 1**). Most of the pockmarks are asymmetrical in plain view. The long axis diameters of the pockmarks range from 3.5 to 10 km, and the short axis diameters range from 0.9 to 6.6 km, with a maximum diameter in excess of 10 km and a depth up to 289 m, lying on the seafloor with V- and U-shaped structures on the seismic profiles. The ratio of long and short axis ranges from 1 to 7.8, pockmarks with large ratio located around the slope belt. In addition, the average water depth of the pockmark-developed area is around 1400 m.

The coherence slices along horizons can illustrate the pockmarks better than coherence slices with a specific time. The coherence slices along the seafloor and horizon T1 are extracted, respectively (**Figures 5**, **6**), which indicate that the modern seafloor pockmarks can be traced back to the T1 layer, and most of the pockmarks have an obvious inheritance. Based on the morphological characteristics and the relationship with BSR and faults, which can be classified into four categories (**Figure 7**): Type 1 is the paleo-pockmarks developed on the T1 layer, which have continuity with the seafloor pockmarks.

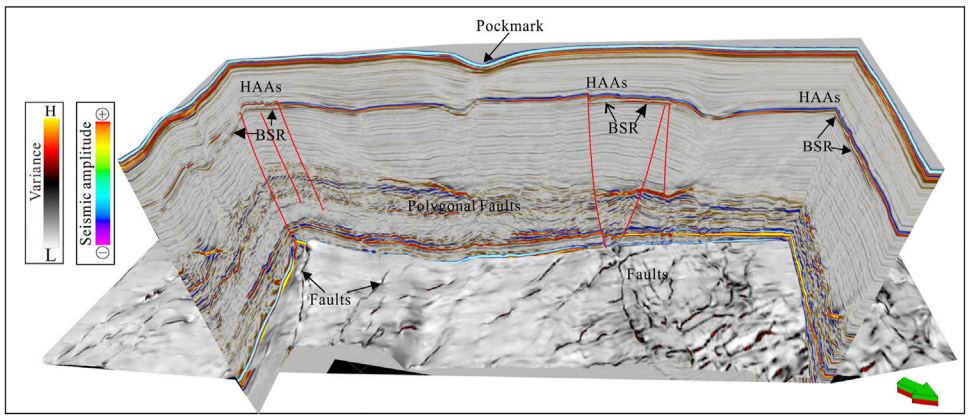

FIGURE 9 | 3D perspective view of the coherence slice map of the T5 horizon shows the normal fault formed by tectonics combined with the cross-sections. The BSRs and high amplitude anomalies (HAAs) have been identified.

High amplitude reflections can be observed within the pockmarks, indicating the gas release along pockmarks. The HAAs show the pull-down reflection, and the faults are developed. BSRs are continuous and have a strong amplitude. There is no BSR under the pockmarks, but there are apparent HAAs and BSR reflections at the adjacent strata around the pockmarks; Type 2 is the buried pockmarks formed at horizon T1, and it is difficult to identify the pockmark at the seafloor. The pull-down reflections are very clear due to fluids migrated along the polygonal faults and faults developed in the deep sediments. The pockmark may be caused by the fluids due to the formation of polygonal faults and cause the dissociation of gas hydrate; Type 3 is that the seismic sections suggest that the pockmarks occur at the seafloor and are not formed along with horizon T1. It is the boundary of the crescent pockmark. The scale of the pockmark is significantly larger than the paleo-pockmarks generated at horizon T1, and the seismic section cannot cover the overall perspective of the pockmark, which is consistent with Type 1; Type 4 is matured larger pockmarks associated with BSRs and HAAs developed at the flank of the pockmark. The formation of pockmarks may be related to the activity of faults and volcanoes. HAAs can be seen inside the pockmark, and partial collapse and deformation are also observed due to subsidence.

Interplay of Gas Hydrate, Pockmarks, Volcanoes, and Faults

Widely developed polygonal faults have been found from the coherence slices of 3D seismic data that were mainly formed in Miocene and Pliocene strata (**Figure 5**). Several tectonic faults can affect the layer containing polygonal faults, but the polygonal faults of the entire region show the variable strikes and different maturity of the fault networks (**Figure 8**). The planform geometry of polygonal faults may be influenced by the local stress anisotropy, local structures, or changes in lithology (Cartwright, 2011).

We choose three representative areas to show the differences of the strikes, maturity, and the role on fluid flow (**Figure 8**). The strikes of zone 1 are complex and have several directions, and those of zone 3 focus on two main directions. The maturity of zone 1 is 0.16, which is lower than that of zone 3 with a value of 0.33 due to the differences in lithology, temperature, compaction, and consolidation processes during burial, which indicates that the polygonal faults have plenty of space to grow. The strikes and geometry in zone 2 changed significantly due to the pockmark formation indicating that the orthogonality is reduced. The formations of pockmarks changed the slope gradient, which can influence the directionality of polygonal faults. The strikes of polygonal faults are changed into a ring or radial planform array surrounding the pockmarks. The HAAs show continuous reflection in lateral except at the pockmarks with weak and pull-down reflections. Moreover, HAAs show a high value where some faults are terminated below the HAAs (**Figure 9**). The pockmarks show irregular and distorted shapes due to the dissociation of gas hydrate formed in T1 horizon, especially at the small-scale pockmarks or buried pockmarks.

Volcanoes have been identified from the seismic sections, coherence, and amplitude slice attributes of the seismic data in the study area (**Figures 5**, **10**). The pockmarks show a low coherence value and chaotic, low, or medium amplitude anomalies, with cone or subcone shape in seismic sections. The features of the volcano intensely reconstruct and penetrate the overlying sediments, and partial volcanoes are located beneath the pockmarks (**Figure 10B**). The diameter of the volcanoes could reach more than 1 km, and their roots could be reached to very deep intervals, and some pockmarks are rooted on them (**Figure 10**).

The spatial distributions of HAAs, pockmarks, polygonal faults, tectonic faults associated with uplift, and volcanism show the spatial relationship between them (**Figure 10A,B**). Some faults are formed above the volcano, which can arrive at HAAs (**Figure 10C**). Several volcanoes or pipes are found around or the edge of pockmarks in the study area, which are important

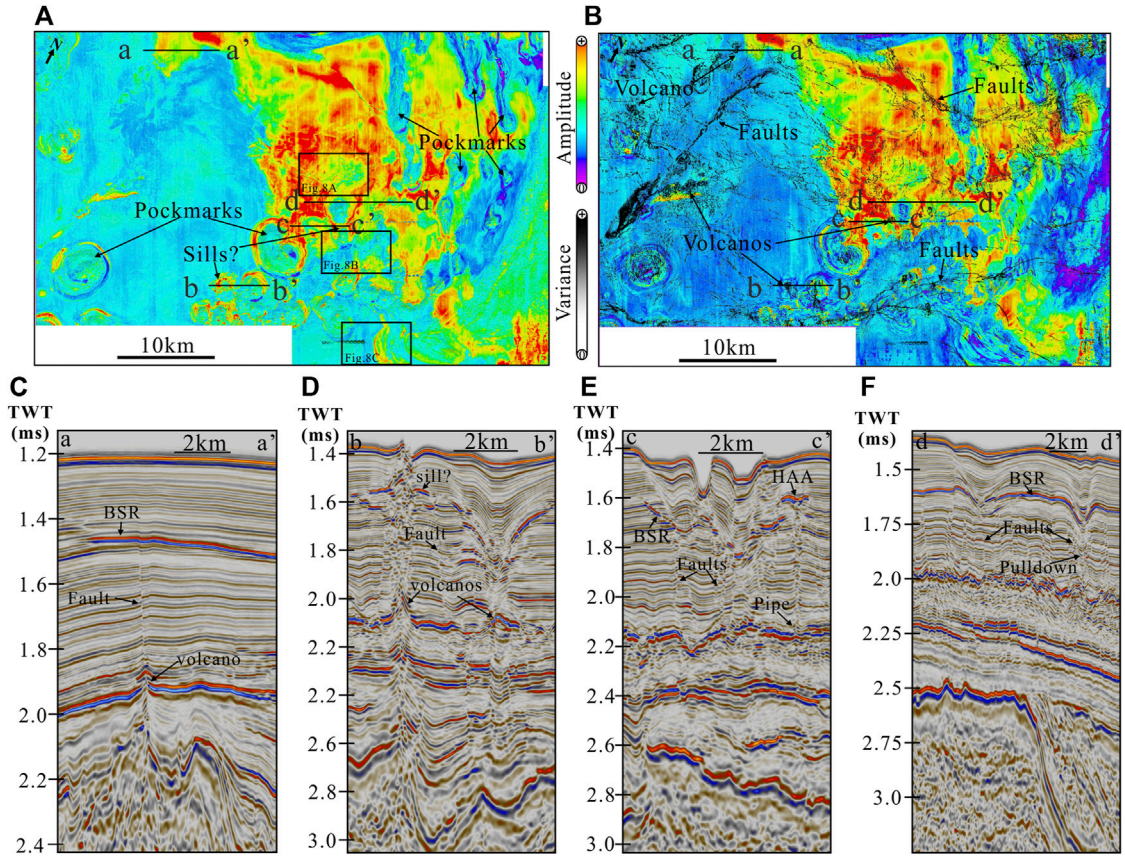

FIGURE 10 | (A) Maximum amplitude attribute maps extracted from horizon T1 with a time window of 50 ms showing variations of amplitude. **(B)** The overlay map of maximum amplitude attribute extracted along horizon T1 within a time window of 50 ms and coherence slice along horizon T5, showing the distribution of the HAAs and deeper faults. **(C–F)** Showing seismic profiles of a-a′, b-b′, c-c′, and d-d′, respectively, and the seismic characteristics of BSR, faults, and volcanoes have been indicated at each section.

focused fluid flow pathways for the expulsion of liquid, gas, and sediment to the shallow deposition. The obvious pull-up and chaotic, weak reflections are found in the deeper layers and high amplitude at the shallow layer (**Figure 10D**). At large-scale or circle pockmarks, the HAAs are observed around or internal the pockmarks seen from the maximum amplitude attribute along with T1 (**Figure 10D–F**). Therefore, polygonal faults, tectonic faults, volcanoes, and pipes originating from deeper layers provide fluid pathways for deep gas upward migration into the upper sedimentary layer to form gas hydrate.

DISCUSSION

Variations of BSR and High Amplitude Anomalies

Gas hydrates related to BSRs are widely distributed in the Zhongjiannan basin (Lu et al., 2017; Li et al., 2022). The BSR shows the continuous, moderate, and extensive distribution on the platform and patches and high amplitude interrupted by pockmarks at the edge of the platform (**Figure 10**). High amplitude reflection just above the BGHSZ is an indicator of the elevated gas hydrate-bearing layer, which is similar to that found in the Shenhu area, South China Sea (Wang et al., 2016; Wang et al., 2021). However, the characteristics of the gas hydrate-bearing layer in the Zhongjiannan basin is quite different from that found in the Pearl River Mouth Basin. The gas hydrate layer in the study area is more continuous and larger, showing that lithology controls HAAs except for the pockmark area. The gas hydrate layer can extend tens of kilometers without being interrupted (**Figures 3**, **4**). Moreover, the gas hydrate layer varies from the seafloor depth, and the shallow water area has a greater depth, which indicates that the occurrence of gas hydrate is not only controlled by the temperature–pressure condition. Gas hydrate distribution found in other basins, and SCS has poor spatial continuity and appears to be patched due to the influence of reservoir, fluid flow, and other factors. The gas hydrate-related BSR is usually characterized by strong amplitude, negative polarity, roughly parallel to the seafloor, and a cross-cutting seismic reflector. However, the diagenesis-related BSRs result from the positive acoustic impedance contrast between silicate rich sediments of different diagenetic stages opal A, opal CT, and quartz conversions, and the temperature is about 35–50°C (Hein et al., 1978; Hein et al., 2010) or 45–50°C (Kastner et al., 1977;

Keller and Isaacs, 1985) triggered by different factors (e.g., Cartwright, 2011; Davies and Ireland, 2011), which have been widely found in the mid-Norwegian margin (Berndt et al., 2005), southern South Korea Plateau, East Sea (Lee et al., 2003), and South China Sea (Wang et al., 2010; Han et al., 2016; Lu et al., 2017). The geothermal gradient in this area is about 55°C/km; the BSR depth is about 220 m by assuming an average P-wave velocity of 1700 m/s, and the temperature is about 17°C, which indicates that the temperature at the interpreted BSR is difficult to cause the transition between opal A/opal CT. Therefore, the depth range of the BSR is within the temperature–pressure condition and supports gas hydrate-related BSR.

The inverted acoustic impedance profile also shows high values in the HAA area, and the maximum values occur at different intervals (**Figure 4**). Some appear just above the BSR and some at a distance above the BSR, which is interrupted by the occurrence of pockmarks. We found that most of pockmarks are related to HAA and HAA are related to lithology change. However, sand-rich coarse-grained reservoirs developed in the deepwater marine depositional system also showed HAAs, which are easily to form gas hydrates, such as in the Gulf of Mexico (Boswell et al., 2012; Collett and Boswell, 2012), Nankai Trough (Fujii et al., 2015; Suzuki et al., 2015; Yamamoto, 2015), Ulleung basin (Bahk et al., 2011; Kim et al., 2011), Krishna-Godavari basin (Kumar et al., 2016), and South China Sea (e.g., Wang et al., 2014b; Zhong et al., 2017; Kang et al., 2018; Li et al., 2019). Even if the lithology of carbonates is assumed, the calculated gas hydrate saturation still comes to 20–40% of the pore space. The fine-grained sediments more than a kilometer thick below BGHSZ are the biogenic gas zone. The widely distributed polygonal faults identified from coherence slices are just located below the BGHSZ with different offsets and maturity, which act as the fluid migration pathways from deeper sediments. Therefore, the gas hydrate-bearing layer is controlled by faults and lithology, indicating the contribution of gas migrated from deeper sediments below BGHSZ.

The maximum amplitude and RMS amplitude attributes extracted from horizon T1 and BGHSZ within a 50 ms time window show the distributions of HAAs associated with gas hydrate (**Figure 10**). The distribution of high amplitude values identified from BGHSZ is smaller than that extracted from the T1 horizon (**Figure 10**). Many reasons can cause this phenomenon, such as structure II gas hydrate (Sloan and Koh, 2007; Kida et al., 2006; Lu et al., 2007; Bourry et al., 2009; Kida et al., 2009; Klapp et al., 2010), rapid sedimentation (Hornbach et al., 2008; Zander et al., 2018; Han et al., 2021), and hot fluid. At the same geological condition, the base of the structure II hydrate stability zone will be deeper than that of BGHSZ (Sloan and Koh, 2007). The seismic profile shows that HAA is deeper on the platform, where water depth is slightly shallower than that of the edge of the platform. The tectonic faults extend to the HAA layer, which can transport thermogenic gas from deeper sediment to BGHSZ (**Figure 10B**). Rapid sedimentation will cause the thicker BGHSZ, which has been found in the Black Sea (Zander et al., 2018), Hikurangi margin (Pecher et al., 2017; Han et al., 2021), and Blake Ridge (Hornbach et al., 2008). The sedimentation at the platform is thicker than that of the edge of the platform, where many pockmarks are formed. The formation of pockmarks also indicates the variation of fluid activity, which can cause slightly shallower BGHSZ. Therefore, the variations of HAAs are caused by the occurrence of gas hydrate showing the difference of gas hydrate saturation and the changes of the geological environment. In the future, gas hydrate drilling expedition should be conducted to confirm the distribution and the controlling factors.

Gas Hydrate Accumulation Influenced by Fluid Migration and Pockmarks

Evidence about geological controls on gas hydrate accumulation was summarized through a combination of the fluid migration pathways from coherence slice, the reservoir from RMS amplitude attributes, and pressure–temperature. **Figure 11** is a 3D display showing the occurrence of gas hydrate, the faults identified from T2 and T5 horizons, and the basement structural form interpreted from 3D seismic data. Previous studies have shown that the polygonal faults, normal faults, and volcanic activity contribute to the formation of gas hydrate, which provides the fluid migration pathways (Xia et al., 2022). Our study supports this founding about fluid migration. However, we also found that the coupling of lithology and timing of hydrocarbon gas release is very important for the widely distributed gas hydrate in the study area. The tectonic faults rooted from basement uplift provide the pathways for thermogenic gas, while the polygonal faults developed in the strata between T5 and T1 not only increase the permeability of fine-grained sediments but also act as hydrocarbon gas pathways for the vertical migration. Cases of polygonal faults transporting fluids have been applied in the Lower Congo Basin (Gay et al., 2006), Norway continental margin (Berndt et al., 2003; Hustoft et al., 2007), and Scotian slope of the eastern Canada continental margin (Cullen et al., 2008). The RMS and maximum amplitude attributes clearly show the relationship between the BSRs, pockmarks, and different types of faults developed in this area (**Figures 9**, **10**). The development density of faults is directly related to the BSR amplitude strength. From the gas hydrate saturation profile (**Figure 4**), the relative enrichment gas hydrate-bearing layer is controlled by faults. Even if the gas hydrate layer is above the BGHSZ, the gas hydrate saturation is still higher due to the influence of faults. It can play a crucial role in migrating upward fluids from the deep strata to the shallow favorable gas hydrate-bearing layer. The detailed seismic data interpretation shows that the fluid migration pathways mainly include normal faults, polygonal faults, regional unconformity, and pockmarks (**Figures 10**, **11**).

Based on the comprehensive analysis of coherence, amplitude, and acoustic impedance attributes, we propose a schematic model to explain the accumulations and occurrence of gas hydrates and their relationship with pockmarks and different faults (**Figure 12**). Different types of pockmarks have been found by previous studies, which indicate the fluids' seep in the Zhongjiannan basin (Sun et al., 2011; Sun et al., 2013; Lu et al., 2017; Chen et al., 2018). There are various mechanisms triggered by fluid advection, salt-tectonic faulting, and gas hydrate dynamics. Even though pockmarks have different patterns, we found that almost all of the pockmarks

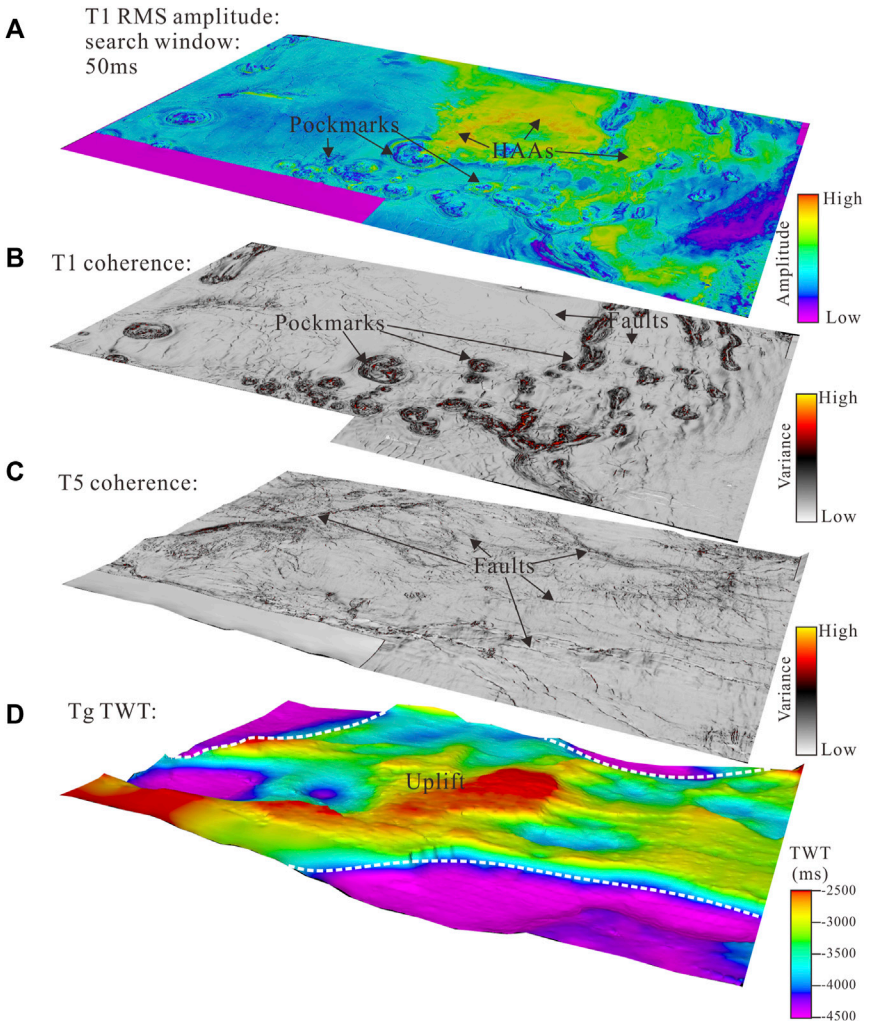

FIGURE 11 | (A) RMS amplitude map extracted from horizon T1 with a time window of 50 ms. **(B)** Coherence slice extracted along horizon T1 showing the distribution of faults and pockmarks. **(C)** Coherence slice along the horizon T5 showing the distribution of normal faults originated from the basement **(D)** The isochronal map of horizon Tg showing the lower uplift.

originate from just below the T1 horizon or below the BSR. The widely distributed BSRs are interrupted by the presence of pockmarks. There are two types of pockmarks triggered by different reasons. Type 1 pockmarks such as Pockmark number six are relatively mature, larger circle pockmarks that are related to the magmatic intrusion or the fault reactivation due to tectonic activity (**Figure 10**). The extensional role due to the pull-up caused by magmatic activities can produce faults and slumps. The fluids can migrate to seafloor along pathways of faults and volcanoes and form pockmarks. When volcanic activity stops, the strata cool and the crater area collapses downward, which will make the formation of pockmarks. Partial HAAs are found around or within the pockmarks. Type 2 pockmarks are triggered due to the dissociation of gas hydrate caused by tectonic activity. Gas hydrates with elevated saturation are formed at the T1 horizon due to plenty of gas migrated along polygonal faults and tectonic faults and new sedimentation. However, the equilibrium conditions, such as temperature and pressure, for gas hydrate formation may be destroyed due to hot fluids migrated along faults, which will cause the dissociation of gas hydrate, with seafloor subsidence in matured Type 4 pockmarks. BGHSZ shifts upward and becomes shallower under new temperature and pressure balance conditions. The gas generated from deep thermogenic gas and gas hydrate dissociation continues to migrate. Hydrate-related BSRs and HAAs will gradually develop and intersect with the normal sedimentary formation. The BSR will be discontinuous due to gas hydrate dissociation, and the dissociated gas will release to the seafloor along the pockmarks (**Figure 12**). Therefore, we suggest that thermogenic gas generated in the deeper sediments can migrate to the shallower sediments along faults, volcanoes, and pipes. The biogenic gas generated in Miocene and Pliocene strata can migrate to shallower sediments along these pathways and polygonal faults. The mixed gas sources contribute to the accumulation of gas hydrate at the favorable reservoir.

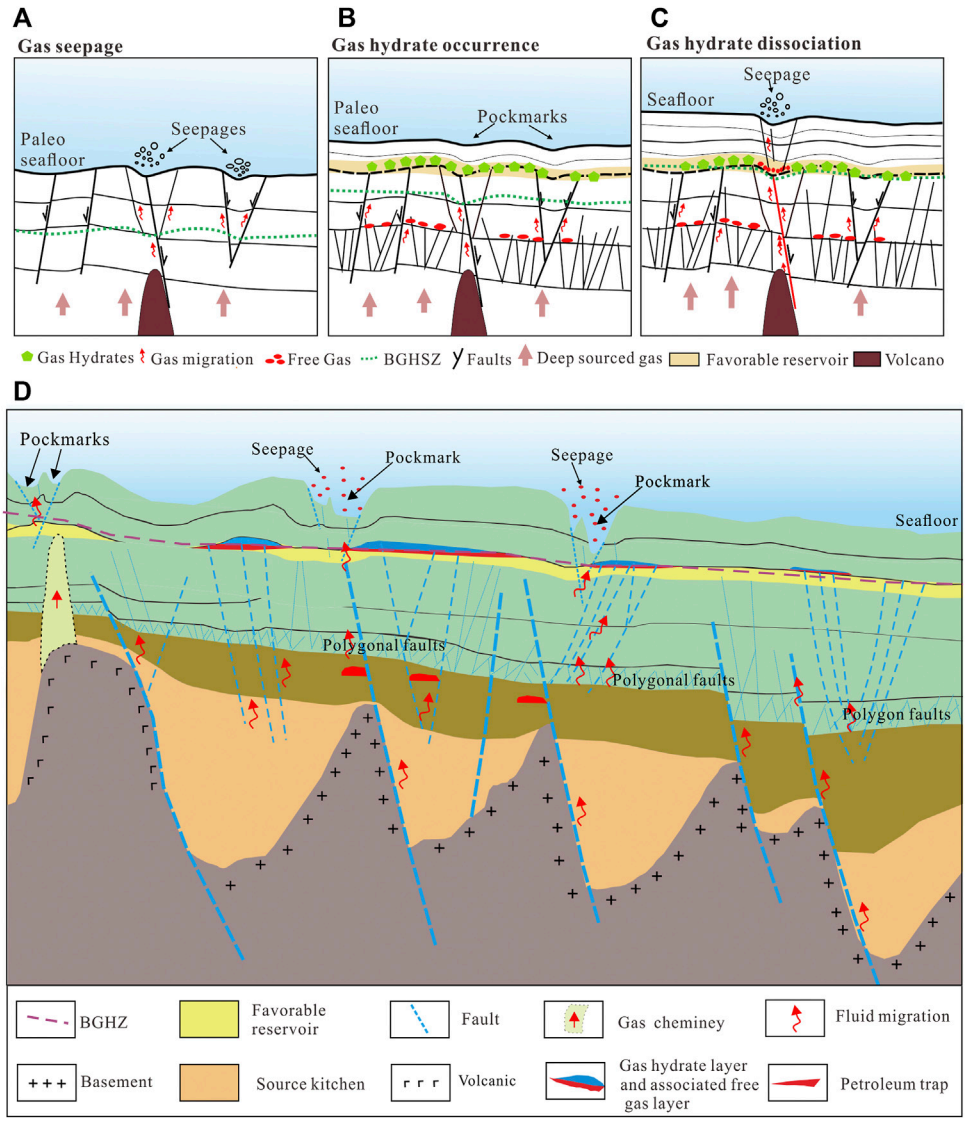

FIGURE 12 | (A)–(C) Conceptual model of development of pockmarks controlled by magmatic activity and gas hydrate dissociation below gas hydrate stability throughout heat flux or fault reactivation from the deep. The scenario is composed of three phases **(A,B,C)**. **(D)**Schematic model map in the study area of the Zhongjiannan basin showing the relationship among gas reservoir, polygonal faults, shallow gas accumulations, BSR, pockmarks, volcano, gas hydrates, and associated free gas.

CONCLUSION

We use the reprocessed, high-resolution 3D seismic data and seismic attributes to reveal the widely distributed BSRs, HAAs, and pockmarks in the Zhongjiannan basin. The wide and continuous distributions of HAAs are caused by the elevated gas hydrate saturation occurred above the BGHSZ. Since the Miocene, the sediments in the Zhongjiannan basin have been dominated by the fine-grained deposits. Abundance polygonal faults are triggered thermally due to magmatic activity and sedimentation, which can serve as the fluid migration pathways and change the reservoir properties. Fluids with hydrocarbon gas can migrate upward along faults, polygonal faults, and volcanoes to BGHSZ. The HAAs with high acoustic impedance varies from the seafloor depth, and the BSR controlled by faults and sedimentary layer shows gas hydrate occurrence. The HAAs are widely distributed and laterally continuous near the base of gas hydrate stability with a thickness ranging from 20 m to more than 50 m. Faults control the thicker gas hydrate layer, and the continuity is interrupted by the occurrence of pockmarks. Moreover, some pockmarks may be triggered by the dissociation of gas hydrate dissociation. Gas hydrate accumulation is related to magmatic activities, faults, and structural uplift. In the future, gas hydrate drilling expedition should be conducted to confirm the widely, continuous distributed gas hydrate.

DATA AVAILABILITY STATEMENT

The original contributions presented in the study are included in the article/supplementary material; further inquiries can be directed to the corresponding authors.

AUTHOR CONTRIBUTIONS

GZ and XW contributed to the conception and design of the work and write the drafted manuscript. LL, YG, and YL contributed to the data acquisition and interpretation. LS, WL, JQ, WW, and TY contributed to data analysis and interpretation. ZW and JQ processed the seismic data, and XW inverted the acoustic impedance data for the manuscript. All authors contributed to review and improve the article and approved the submitted version.

FUNDING

This research was jointly supported by the Shandong Special Fund of Pilot National Laboratory for Marine Science and Technology (Qingdao) (No.2021QNLM020002) and the National Natural Science Foundation of China (Grant No. 42076219), the China Academy of Petroleum Exploration and Development (2019B-4909) and WL is funded by the CAS Pioneer Hundred Talents Program.

REFERENCES

Bahk, J.-J., Um, I.-K., and Holland, M. (2011). Core Lithologies and Their Constraints on Gas-Hydrate Occurrence in the East Sea, Offshore Korea: Results from the Site UBGH1-9. *Mar. Petroleum Geol.* 28, 1943–1952. doi:10.1016/j.marpetgeo.2010.12.003

Berndt, C., Bünz, S., and Mienert, J. (2003). Polygonal Fault Systems on the Mid-Norwegian Margin: a Long-Term Source for Fluid Flow. *Geol. Soc. Lond. Spec. Publ.* 216, 283–290. doi:10.1144/GSL.SP.2003.216.01.18

Berndt, C., Mienert, J., Vanneste, M., and Bünz, S. (2005). in *Gas Hydrate Dissociation and Sea-Floor Collapse in the Wake of the Storegga Slide, Norway*. Editors B. T. G. Wandås, J. P. Nystuen, E. Eide, and F. Gradstein (Amsterdam: Elsevier), 285–292. Norwegian Petroleum Society (NPF) Special Publication, 12. doi:10.1016/S0928-8937(05)80055-4

Boswell, R., Collett, T. S., Frye, M., Shedd, W., Mcconnell, D. R., and Shelander, D. (2012). Subsurface Gas Hydrates in the Northern Gulf of Mexico. *Mar. Petroleum Geol.* 34, 4–30. doi:10.1016/j.marpetgeo.2011.10.003

Bourry, C., Chazallon, B., Charlou, J. L., Pierre Donval, J., Ruffine, L., Henry, P., et al. (2009). Free Gas and Gas Hydrates from the Sea of Marmara, Turkey. *Chem. Geol.* 264, 197–206. doi:10.1016/j.chemgeo.2009.03.007

Cartwright, J. (2011). Diagenetically Induced Shear Failure of Fine-Grained Sediments and the Development of Polygonal Fault Systems. *Mar. Petroleum Geol.* 28, 1593–1610. doi:10.1016/j.marpetgeo.2011.06.004

Cartwright, J., Huuse, M., and Aplin, A. (2007). Seal Bypass Systems. *Bulletin* 91, 1141–1166. doi:10.1306/04090705181

Cartwright, J., James, D., and Bolton, A. (2003). The Genesis of Polygonal Fault Systems: a Review. *Geol. Soc. Lond. Spec. Publ.* 216, 223–243. doi:10.1144/gsl.sp.2003.216.01.15

Chen, F., Su, X., Lu, H., Zhou, Y., and Zhuang, C. (2013). Relations between Biogenic Component (Foraminifera) and Highly Saturated Gas Hydrates Distribution from Shenhu Area, Northern South China Sea. *Earth Sci. China Univ. Geosci.* 38, 907–915. doi:10.3799/dqkx.2013.089

Chen, J., Song, H., Guan, Y., Yang, S., Pinheiro, L. M., Bai, Y., et al. (2015). Morphologies, Classification and Genesis of Pockmarks, Mud Volcanoes and Associated Fluid Escape Features in the Northern Zhongjiannan Basin, South China Sea. *Deep Sea Res. Part II Top. Stud. Oceanogr.* 122, 106–117. doi:10.1016/j.dsr2.2015.11.007

Chen, J., Song, H., Guan, Y., Pinheiro, L. M., and Geng, M. (2018). Geological and Oceanographic Controls on Seabed Fluid Escape Structures in the Northern Zhongjiannan Basin, South China Sea. *J. Asian Earth Sci.* 168, 38–47. doi:10.1016/j.jseaes.2018.04.027

Collett, T. S., and Boswell, R. (2012). Resource and Hazard Implications of Gas Hydrates in the Northern Gulf of Mexico: Results of the 2009 Joint Industry Project Leg II Drilling Expedition. *Mar. Petroleum Geol.* 34, 1–3. doi:10.1016/j.marpetgeo.2012.01.002002

Collett, T. S., Johnson, A. H., Knapp, C. C., Boswell, R., Energy, N., and Virginia, W. (2009). Natural Gas Hydrates: A Review. *AAPG Mem.* 89, 146–219. doi:10.1306/13201101M891602

Cullen, J., Mosher, D. C., and Louden, K. (2008). "The Mohican Channel Gas Hydrate Zone , Scotian Slope : Geophysical Structure," in Proceedings of the 6th International Conference on Gas Hydrates (ICGH 2008), Vancouver, British Columbia, CANADA, July 2008.

Davies, R. J., and Ireland, M. T. (2011). Initiation and Propagation of Polygonal Fault Arrays by Thermally Triggered Volume Reduction Reactions in Siliceous Sediment. *Mar. Geol.* 289, 150–158. doi:10.1016/j.margeo.2011.05.005

de Prunelé, A., Ruffine, L., Riboulot, V., Peters, C. A., Croguennec, C., Guyader, V., et al. (2017). Focused Hydrocarbon-Migration in Shallow Sediments of a Pockmark Cluster in the Niger Delta (Off Nigeria). *Geochem. Geophys. Geosyst.* 18, 93–112. doi:10.1002/2016GC006554

Fujii, T., Suzuki, K., Takayama, T., Tamaki, M., Komatsu, Y., Konno, Y., et al. (2015). Geological Setting and Characterization of a Methane Hydrate Reservoir Distributed at the First Offshore Production Test Site on the Daini-Atsumi Knoll in the Eastern Nankai Trough, Japan. *Mar. Petroleum Geol.* 66, 310–322. doi:10.1016/j.marpetgeo.2015.02.037

Gay, A., Lopez, M., Cochonat, P., Séranne, M., Levaché, D., and Sermondadaz, G. (2006). Isolated Seafloor Pockmarks Linked to BSRs, Fluid Chimneys, Polygonal Faults and Stacked Oligocene-Miocene Turbiditic Palaeochannels in the Lower Congo Basin. *Mar. Geol.* 226, 25–40. doi:10.1016/j.margeo.2005.09.018

Han, J., Leng, J., and Wang, Y. (2016). Characteristics and Genesis of the Polygonal Fault System in Southern Slope of the Qiongdongnan Basin, South China Sea. *Mar. Petroleum Geol.* 70, 163–174. doi:10.1016/j.marpetgeo.2015.11.022

Han, S., Bangs, N. L., Hornbach, M. J., Pecher, I. A., Tobin, H. J., and Silver, E. A. (2021). The Many Double BSRs across the Northern Hikurangi Margin and Their Implications for Subduction Processes. *Earth Planet. Sci. Lett.* 558, 116743. doi:10.1016/j.epsl.2021.116743

Hein, J. R., Scholl, D. W., Barron, J. A., Jones, M. G., and Miller, J. (1978). Diagenesis of Late Cenozoic Diatomaceous Deposits and Formation of the Bottom Simulating Reflector in the Southern Bering Sea*. *Sedimentology* 25, 155–181. doi:10.1111/j.1365-3091.1978.tb00307.x

Hein, J. R., Scholl, D. W., Barron, J. A., Jones, M. G., and Miller, J. (2010). Diagenesis of Late Cenozoic Diatomaceous Deposits and Formation of the Bottom Simulating Reflector in the Southern Bering Sea. *Sedimentology* 25, 155–181. doi:10.1111/j.1365-3091.1978.tb00307.x

Helgerud, M. B., Dvorkin, J., Nur, A., Sakai, A., and Collett, T. (1999). Elastic-wave Velocity in Marine Sediments with Gas Hydrates: Effective Medium Modeling. *Geophys. Res. Lett.* 26, 2021–2024. doi:10.1029/1999GL900421

Hornbach, M. J., Saffer, D. M., Holbrook, W. S., Van Avendonk, H. J. A., and Gorman, A. R. (2008). Three-dimensional Seismic Imaging of the Blake Ridge Methane Hydrate Province: Evidence for Large, Concentrated Zones of Gas Hydrate and Morphologically Driven Advection. *J. Geophys. Res.* 113, 1–15. doi:10.1029/2007JB005392

Hovland, M., Svensen, H., Forsberg, C. F., Johansen, H., Fichler, C., Fosså, J. H., et al. (2005). Complex Pockmarks with Carbonate-Ridges off mid-Norway: Products of Sediment Degassing. *Mar. Geol.* 218, 191–206. doi:10.1016/j.margeo.2005.04.005

Hustoft, S., Mienert, J., Bünz, S., and Nouzé, H. (2007). High-resolution 3D-Seismic Data Indicate Focussed Fluid Migration Pathways above Polygonal Fault Systems of the Mid-Norwegian Margin. *Mar. Geol.* 245, 89–106. doi:10.1016/j.margeo.2007.07.004

Jiangong Wei, J., Liang, J., Lu, J., Zhang, W., and He, Y. (2019). Characteristics and Dynamics of Gas Hydrate Systems in the Northwestern South China Sea - Results of the Fifth Gas Hydrate Drilling Expedition. *Mar. Petroleum Geol.* 110, 287–298. doi:10.1016/j.marpetgeo.2019.07.028

Kang, D., Liang, J., Kuang, Z., Lu, J., Guo, Y., Liang, J., et al. (2018). Application of Elemental Capture Spectroscopy Logging in Hydrate Reservoir Evaluation in the Shenhu Sea Area. *Nat. Gas. Ind.* 38, 54–60. doi:10.3787/j.issn.1000-0976.2018.12.006

Kastner, M., Keene, J. B., and Gieskes, J. M. (1977). Diagenesis of Siliceous Oozes-I. Chemical Controls on the Rate of Opal-A to Opal-CT Transformation-An Experimental Study. *Geochim. Cosmochim. Acta* 41, 1041–1059. doi:10.1016/0016-7037(77)90099-0

Keller, M. A., and Isaacs, C. M. (1985). An Evaluation of Temperature Scales for Silica Diagenesis in Diatomaceous Sequences Including a New Approach Based on the Miocene Monterey Formation, California. *Geo-Marine Lett.* 5, 31–35. doi:10.1007/BF02629794

Kida, M., Khlystov, O., Zemskaya, T., Takahashi, N., Minami, H., Sakagami, H., et al. (2006). Coexistence of Structure I and II Gas Hydrates in Lake Baikal Suggesting Gas Sources from Microbial and Thermogenic Origin. *Geophys. Res. Lett.* 33, 10–13. doi:10.1029/2006GL028296

Kida, M., Suzuki, K., Kawamura, T., Oyama, H., Nagao, J., Ebinuma, T., et al. (2009). Characteristics of Natural Gas Hydrates Occurring in Pore-Spaces of Marine Sediments Collected from the Eastern Nankai Trough, off Japan. *Energy fuels.*. 23, 5580–5586. doi:10.1021/ef900612f

Kim, G. Y., Yi, B. Y., Yoo, D. G., Ryu, B. J., and Riedel, M. (2011). Evidence of Gas Hydrate from Downhole Logging Data in the Ulleung Basin, East Sea. *Mar. Petroleum Geol.* 28, 1979–1985. doi:10.1016/j.marpetgeo.2011.01.011

Klapp, S. A., Murshed, M. M., Pape, T., Klein, H., Bohrmann, G., Brewer, P. G., et al. (2010). Mixed Gas Hydrate Structures at the Chapopote Knoll, Southern Gulf of Mexico. *Earth Planet. Sci. Lett.* 299, 207–217. doi:10.1016/j.epsl.2010.09.001

Kumar, P., Collett, T. S., Vishwanath, K., Shukla, K. M., Nagalingam, J., Lall, M. V., et al. (2016). Gas Hydrate-Bearing S and Reservoir Systems in the Offshore of India : Results of the India National Gas Hydrate Program Expedition 02. *Fire Ice* 16, 1–8.

Lai, H., Fang, Y., Kuang, Z., Ren, J., Liang, J., Lu, J. a., et al. (2021). Geochemistry, Origin and Accumulation of Natural Gas Hydrates in the Qiongdongnan Basin, South China Sea: Implications from Site GMGS5-W08. *Mar. Petroleum Geol.* 123, 104774. doi:10.1016/j.marpetgeo.2020.104774

Laurent, D., Gay, A., Baudon, C., Berndt, C., Soliva, R., Planke, S., et al. (2012). High-resolution Architecture of a Polygonal Fault Interval Inferred from Geomodel Applied to 3D Seismic Data from the Gjallar Ridge, Vøring Basin, Offshore Norway. *Mar. Geol.* 332-334, 134–151. doi:10.1016/j.margeo.2012.07.016

Lee, G. H., Kim, H.-J., Jou, H.-T., and Cho, H.-M. (2003). Opal-A/opal-CT Phase Boundary Inferred from Bottom-Simulating Reflectors in the Southern South Korea Plateau, East Sea (Sea of Japan). *Geophys. Res. Lett.* 30, 1–4. doi:10.1029/2003GL018670

Lee, M. W., and Collett, T. S. (2009). Gas Hydrate Saturations Estimated from Fractured Reservoir at Site NGHP-01-10, Krishna-Godavari Basin, India. *J. Geophys. Res.* 114, 1–13. doi:10.1029/2008JB006237

Lee, M. W., and Waite, W. F. (2008). Estimating Pore-Space Gas Hydrate Saturations from Well Log Acoustic Data. *Geochem. Geophys. Geosyst.* 9, a–n. doi:10.1029/2008GC002081

Li, S., Suo, Y., Liu, X., Dai, L., Yu, S., Zhao, S., et al. (2013). Basic Strcutural Pattern and Tectonic Models of the South China Sea: Problems, Advances and Controversies. *Mar. Geol. Quat. Geol.* 32, 35–53. doi:10.3724/sp.j.1140.2012.06035

Li, J.-f., Ye, J., Qin, X.-w., Qiu, H.-j., Wu, N.-y., Lu, H.-l., et al. (2018). The First Offshore Natural Gas Hydrate Production Test in South China Sea. *China Geol.* 1, 5–16. doi:10.31035/cg2018003

Li, J., Lu, J. a., Kang, D., Ning, F., Lu, H., Kuang, Z., et al. (2019). Lithological Characteristics and Hydrocarbon Gas Sources of Gas Hydrate-Bearing Sediments in the Shenhu Area, South China Sea: Implications from the W01B and W02B Sites. *Mar. Geol.* 408, 36–47. doi:10.1016/j.margeo.2018.10.013

Li, L., Wang, B., Sun, L., Wang, Z., Lu, Y., Yang, T., et al. (2022). The Characteristic and Controlling Factors of the Concentrated Gas Hydrate Occurrence in the Zhongjian Basin, South China Sea. *Earth Sci.* 46, 72. doi:10.3799/dqkx.2022.072

Li, W., Cook, A., Daigle, H., Malinverno, A., Nole, M., and You, K. (2019). Factors Controlling Short-Range Methane Migration of Gas Hydrate Accumulations in Thin Coarse-Grained Layers. *Geochem. Geophys. Geosyst.* 20, 3985–4000. doi:10.1029/2019GC008405

Liang, J., Zhang, W., Lu, J. a., Wei, J., Kuang, Z., He, Y., et al. (2019). Geological Occurrence and Accumulation Mechanism of Natural Gas Hydrates in the Eastern Qiongdongnan Basin of the South China Sea: Insights from Site GMGS5-W9-2018. *Mar. Geol.* 418, 106042. doi:10.1016/j.margeo.2019.106042

Liu, J., Yang, R., Zhang, J., Wei, W., and Wu, D. (2019). Gas Hydrate Accumulation Conditions in the Huaguang Depression of Qiongdongnan Basin and Prediction of Favorable Zones. *Mar. Geol. Quat. Geol.* 39, 134–142. doi:10.16562/j.cnki.0256-1492.2018072701

Lu, S., and Mcmechan, G. A. (2002). Estimation of Gas Hydrate and Free Gas Saturation, Concentration, and Distribution from Seismic Data. *Geophysics* 67, 582–593. doi:10.1190/1.1468619

Lu, S., and McMechan, G. A. (2004). Elastic Impedance Inversion of Multichannel Seismic Data from Unconsolidated Sediments Containing Gas Hydrate and Free Gas. *Geophysics* 69, 164–179. doi:10.1190/1.1649385

Lu, H., Seo, Y.-t., Lee, J.-w., Moudrakovski, I., Ripmeester, J. A., Chapman, N. R., et al. (2007). Complex Gas Hydrate from the Cascadia Margin. *Nature* 445, 303–306. doi:10.1038/nature05463

Lu, Y., Luan, X., Lyu, F., Wang, B., Yang, Z., Yang, T., et al. (2017). Seismic Evidence and Formation Mechanism of Gas Hydrates in the Zhongjiannan Basin, Western Margin of the South China Sea. *Mar. Petroleum Geol.* 84, 274–288. doi:10.1016/j.marpetgeo.2017.04.005

Lu, Y., Xu, X., Luan, X., Jiang, S., Ran, W., Yang, T., et al. (2021). Morphology, Internal Architectures, and Formation Mechanisms of Mega-Pockmarks on the Northwestern South China Sea Margin. *Interpretation* 9, T1039–T1054. doi:10.1190/INT-2020-0175.1

Lüdmann, T., and KinWong, H. (1999). Neotectonic Regime on the Passive Continental Margin of the Northern South China Sea. *Tectonics* 311, 113–138. doi:10.1016/S0040-1951(99)00155-9

Morley, C. K. (2002). A Tectonic Model for the Tertiary Evolution of Strike-Slip Faults and Rift Basins in SE Asia. *Tectonophysics* 347, 189–215. doi:10.1016/S0040-1951(02)00061-6

Ostanin, I., Anka, Z., di Primio, R., and Bernal, A. (2012). Identification of a Large Upper Cretaceous Polygonal Fault Network in the Hammerfest Basin: Implications on the Reactivation of Regional Faulting and Gas Leakage Dynamics, SW Barents Sea. *Mar. Geol.* 332-334, 109–125. doi:10.1016/j.margeo.2012.03.005

Pecher, I. A., Villinger, H., Kaul, N., Crutchley, G. J., Mountjoy, J. J., Huhn, K., et al. (2017). A Fluid Pulse on the Hikurangi Subduction Margin: Evidence from a Heat Flux Transect across the Upper Limit of Gas Hydrate Stability. *Geophys. Res. Lett.* 44, 12385–12395. doi:10.1002/2017GL076368

Qian, J., Wang, X., Collett, T. S., Guo, Y., Kang, D., and Jin, J. (2018). Downhole Log Evidence for the Coexistence of Structure II Gas Hydrate and Free Gas below the Bottom Simulating Reflector in the South China Sea. *Mar. Petroleum Geol.* 98, 662–674. doi:10.1016/j.marpetgeo.2018.09.024

Qin, X. W., Lu, J. A., Lu, H. L., Qiu, H. J., Liang, J. Q., Kang, D. J., et al. (2020). Coexistence of Natural Gas Hydrate, Free Gas and Water in the Gas Hydrate System in the Shenhu Area, South China Sea. *China Geol.* 3, 210–220. doi:10.31035/cg2020038

Riedel, M., and Shankar, U. (2012). Combining Impedance Inversion and Seismic Similarity for Robust Gas Hydrate Concentration Assessments - A Case Study from the Krishna-Godavari Basin, East Coast of India. *Mar. Petroleum Geol.* 36, 35–49. doi:10.1016/j.marpetgeo.2012.06.006

Shelander, D., Dai, J., Bunge, G., Singh, S., Eissa, M., and Fisher, K. (2012). Estimating Saturation of Gas Hydrates Using Conventional 3D Seismic Data, Gulf of Mexico Joint Industry Project Leg II. *Mar. Petroleum Geol.* 34, 96–110. doi:10.1016/j.marpetgeo.2011.09.006

Sloan, E. D., and Koh, C. A. (2007). *Clathrate Hydrates of Natural Gases (third ed)* CRC Press, Boca Raton, America, 10–18. doi:10.1201/9781420008494

Su, P., Liang, J., Zhang, W., Liu, F., Wang, F., Li, T., et al. (2020). Natural Gas Hydrate Accumulation System in the Shenhu Sea Area of the Northern South China Sea. *Nat. Gas. Ind.* 40, 77–89. doi:10.3787/j.issn.1000-0976.2020.08.006

Sun, Q., Wu, S., Lü, F., and Yuan, S. (2010). Polygonal Faults and Their Implications for Hydrocarbon Reservoirs in the Southern Qiongdongnan Basin, South China Sea. *J. Asian Earth Sci.* 39, 470–479. doi:10.1016/j.jseaes.2010.04.002

Sun, Q., Wu, S., Hovland, M., Luo, P., Lu, Y., and Qu, T. (2011). The Morphologies and Genesis of Mega-Pockmarks Near the Xisha Uplift, South China Sea. *Mar. Petroleum Geol.* 28, 1146–1156. doi:10.1016/j.marpetgeo.2011.03.003

Sun, Q., Wu, S., Cartwright, J., Lüdmann, T., and Yao, G. (2013). Focused Fluid Flow Systems of the Zhongjiannan Basin and Guangle Uplift, South China Sea. *Basin Res.* 25, 97–111. doi:10.1111/j.1365-2117.2012.00551.x

Suzuki, K., Schultheiss, P., Nakatsuka, Y., Ito, T., Egawa, K., Holland, M., et al. (2015). Physical Properties and Sedimentological Features of Hydrate-Bearing Samples Recovered from the First Gas Hydrate Production Test Site on Daini-Atsumi Knoll Around Eastern Nankai Trough. *Mar. Petroleum Geol.* 66, 346–357. doi:10.1016/j.marpetgeo.2015.02.025

Svensen, H., Planke, S., Malthe-Sørenssen, A., Jamtveit, B., Myklebust, R., Rasmussen Eidem, T., et al. (2004). Release of Methane from a Volcanic Basin as a Mechanism for Initial Eocene Global Warming. *Nature* 429, 542–545. doi:10.1038/nature02575.110.1038/nature02566

Wang, X., Wu, S., Yuan, S., Wang, D., Ma, Y., Yao, G., et al. (2010). Geophysical Signatures Associated with Fluid Flow and Gas Hydrate Occurrence in a Tectonically Quiescent Sequence, Qiongdongnan Basin, South China Sea. *Geofluids* 10, 351–368. doi:10.1111/j.1468-8123.2010.00292.x

Wang, X., Hutchinson, D. R., Wu, S., Yang, S., and Guo, Y. (2011). Elevated Gas Hydrate Saturation within Silt and Silty Clay Sediments in the Shenhu Area, South China Sea. *J. Geophys. Res.* 116, B05102. doi:10.1029/2010JB007944

Wang, X., Lee, M., Collett, T., Yang, S., Guo, Y., and Wu, S. (2014a). Gas Hydrate Identified in Sand-Rich Inferred Sedimentary Section Using Downhole Logging and Seismic Data in Shenhu Area, South China Sea. *Mar. Petroleum Geol.* 51, 298–306. doi:10.1016/j.marpetgeo.2014.01.002

Wang, X., Collett, T. S., Lee, M. W., Yang, S., Guo, Y., and Wu, S. (2014b). Geological Controls on the Occurrence of Gas Hydrate from Core, Downhole Log, and Seismic Data in the Shenhu Area, South China Sea. *Mar. Geol.* 357, 272–292. doi:10.1016/j.margeo.2014.09.040

Wang, X., Qian, J., Collett, T. S., Shi, H., Yang, S., Yan, C., et al. (2016). Characterization of Gas Hydrate Distribution Using Conventional 3D Seismic Data in the Pearl River Mouth Basin, South China Sea. *Interpretation* 4, SA25–SA37. doi:10.1190/INT-2015-0020.1

Wang, X., Jin, J., Guo, Y., Li, J., Li, Y., Qian, J., et al. (2021). The Characteristics of Gas Hydrate Accumulation and Quantitative Estimation in the North Slope of South China Sea. *Earth Sci.* 46, 1038–1057. doi:10.3799/dqkx.2020.321

Wang, X., Zhou, J., Li, L., Jin, J., Li, J., Guo, Y., et al. (2022). "Bottom Simulating Reflections in the South China Sea BT - World Atlas of Submarine Gas Hydrates in Continental Margins," in (Springer International Publishing), 163–172. doi:10.1007/978-3-030-81186-0_13

Wu, N., Yang, S., Wang, H., Liang, J., Gong, Y., Lu, Z., et al. (2009). Gas-bearing Fluid Influx Sub-system for Gas Hydrate Geological System in Shenhu Area, Northern South China Sea. *Chin. J. Geophys. Ed.* 52, 1641–1650. doi:10.3969/j.issn.0001-5733.2009.06.027

Wu, N., Yang, S., Zhang, H., Liang, J., Wang, H., and Lu, J. a. (2010). Gas Hydrate System of Shenhu Area, Northern South China Sea:Wire-Line Logging, Geochemical Results and Preliminary Resources Estimates. *Proc. Annu. Offshore Technol. Conf.* 1, 654–666. doi:10.4043/20485-ms

Xia, Y., Yang, J., Chen, Y., Lu, S., Wang, M., Deng, S., et al. (2022). A Review of the Global Polygonal Faults: Are They Playing a Big Role in Fluid Migration? *Front. Earth Sci.* 9, 1–16. doi:10.3389/feart.2021.786915

Xie, X., Müller, R. D., Li, S., Gong, Z., and Steinberger, B. (2006). Origin of Anomalous Subsidence along the Northern South China Sea Margin and its Relationship to Dynamic Topography. *Mar. Petroleum Geol.* 23, 745–765. doi:10.1016/j.marpetgeo.2006.03.004

Xie, X., Müller, R. D., Ren, J., Jiang, T., and Zhang, C. (2008). Stratigraphic Architecture and Evolution of the Continental Slope System in Offshore Hainan, Northern South China Sea. *Mar. Geol.* 247, 129–144. doi:10.1016/j.margeo.2007.08.005

Yamamoto, K. (2015). Overview and Introduction: Pressure Core-Sampling and Analyses in the 2012-2013 MH21 Offshore Test of Gas Production from Methane Hydrates in the Eastern Nankai Trough. *Mar. Petroleum Geol.* 66, 296–309. doi:10.1016/j.marpetgeo.2015.02.024

Yang, S., Zhang, M., Liang, J. Q., Lu, J., Zhang, Z. J., Holland, M., et al. (2015). Preliminary Results of China's Third Gas Hydrate Drilling Expedition: a Critical Step from Discovery to Development in the South China Sea. *Cent. Nat. Gas. Oil* 412, 386–7614.

Yang, S., Liang, J., Lu, J., Qu, C., and Liu, B. (2017). New Understandings on the Characteristics and Controlling Factors of Gas Hydrate Reservoirs in the Shenhu Area on the Northern Slope of the South China Sea. *Earth Sci. Front.* 24, 1–14. doi:10.13745/j.esf.yx.2016-12-43

Yang, Z., Wang, B., Li, L., Li, D., Zhang, Y., and Sun, G. (2020). Characteristics of Pockmarks and Their Genesis Zhongjian Offshore Area, South China Sea. *Mar. Geol. Front.* 36, 42–49. doi:10.16028/j.1009-2722.2018.025

Ye, J., Wei, J., Liang, J., Lu, J., Lu, H., Zhang, W., et al. (2019). Complex Gas Hydrate System in a Gas Chimney, South China Sea. *Mar. Petroleum Geol.* 104, 29–39. doi:10.1016/j.marpetgeo.2019.03.023

Zander, T., Choi, J. C., Vanneste, M., Berndt, C., Dannowski, A., Carlton, B., et al. (2018). Potential Impacts of Gas Hydrate Exploitation on Slope Stability in the Danube Deep-Sea Fan, Black Sea. *Mar. Petroleum Geol.* 92, 1056–1068. doi:10.1016/j.marpetgeo.2017.08.010

Zhang, H. Q., Yang, S. X., Wu, N. Y., Su, X., Holland, M., Schultheiss, P., et al. (2007). Successful and Surprising Results for China's First Gas Hydrate Drilling Expedition. *Fire Ice Methane Hydrate Newsl.* 7, 6–9.

Zhang, G. X., Yang, S. X., Zhang, M., Liang, J. Q., Lu, J., Holland, M., et al. (2014). GMGS2 Expedition Investigates Rich and Complex Gas Hydrate Environment in the South China Sea. *Fire Ice* 14, 1–5.

Zhang, G., Liang, J., Lu, J. a., Yang, S., Zhang, M., Holland, M., et al. (2015). Geological Features, Controlling Factors and Potential Prospects of the Gas Hydrate Occurrence in the East Part of the Pearl River Mouth Basin, South China Sea. *Mar. Petroleum Geol.* 67, 356–367. doi:10.1016/j.marpetgeo.2015.05.021

Zhang, W., Liang, J., Su, P., Wei, J., Gong, Y., Lin, L., et al. (2019). Distribution and Characteristics of Mud Diapirs, Gas Chimneys, and Bottom Simulating Reflectors Associated with Hydrocarbon Migration and Gas Hydrate Accumulation in the Qiongdongnan Basin , Northern Slope of the South China Sea. *Geol. J.* 54, 3556–3573. doi:10.1002/gj.3351

Zhang, W., Liang, J., Wan, Z., Su, P., Huang, W., Wang, L., et al. (2020a). Dynamic Accumulation of Gas Hydrates Associated with the Channel-Levee System in the Shenhu Area, Northern South China Sea. *Mar. Petroleum Geol.* 117, 104354. doi:10.1016/j.marpetgeo.2020.104354

Zhang, W., Liang, J., Wei, J., Lu, J. a., Su, P., Lin, L., et al. (2020b). Geological and Geophysical Features of and Controls on Occurrence and Accumulation of Gas Hydrates in the First Offshore Gas-Hydrate Production Test Region in the Shenhu Area, Northern South China Sea. *Mar. Petroleum Geol.* 114, 104191. doi:10.1016/j.marpetgeo.2019.104191

Zhong, G., Liang, J., Guo, Y., Kuang, Z., Su, P., and Lin, L. (2017). Integrated Core-Log Facies Analysis and Depositional Model of the Gas Hydrate-Bearing Sediments in the Northeastern Continental Slope, South China Sea. *Mar. Petroleum Geol.* 86, 1159–1172. doi:10.1016/j.marpetgeo.2017.07.012

Zhou, D., Ru, K., and Chen, H.-z. (1995). Kinematics of Cenozoic Extension on the South China Sea Continental Margin and its Implications for the Tectonic Evolution of the Region. *Tectonophysics* 251, 161–177. doi:10.1016/0040-1951(95)00018-6

Conflict of Interest: The authors declare that the research was conducted in the absence of any commercial or financial relationships that could be construed as a potential conflict of interest.

frontiers | Frontiers in Earth Science

ORIGINAL RESEARCH
published: 23 June 2022
doi: 10.3389/feart.2022.884375

Two-Phase Modeling Technology and Subsection Modeling Method of Natural Gas Hydrate: A Case Study in the Shenhu Sea Area

Fang Liu[1,2], *Jinqiang Liang*[1,2]*, *Hongfei Lai*[1,2], *Lei Han*[3], *Xiaoxue Wang*[1,2], *Tingwei Li*[1,2] and *Feifei Wang*[1,2]

[1]Guangzhou Marine Geological Survey, Guangzhou, China, [2]Southern Marine Science and Engineering Guangdong Laboratory (Guangzhou), Guangzhou, China, [3]Sinopec Petroleum Exploration and Production Research Institute, Beijing, China

It is found that natural gas hydrate is not only a pore-filling material but also exists in the reservoir in the form of rock skeleton particles. Therefore, the traditional petrophysical simulation method cannot well describe the physical properties of natural gas hydrate reservoir. At the same time, the physical properties of the hydrate layer and its associated free gas layer are quite different, so it is difficult to fit the physical properties of the two media using traditional modeling methods. The two-phase modeling technology used in this paper is the equivalent medium modeling technology based on BK solid substitution theory and Gassmann fluid substitution theory, which simulates hydrate particles in rock skeleton and hydrate filling in pores, respectively. The forward simulation results show that the two-phase simulation technology of natural gas hydrate can well fit the P-wave and S-wave velocity information of the medium. At the same time, the equivalent medium model of the free gas reservoir is established by using only Gassmann fluid substitution theory. The practical application shows that the subsection modeling method can well solve the problem of the too large difference between the two sets of reservoir physical properties and make the calibration results of forward modeling synthetic records more accurate.

Keywords: gas hydrate, two-phase petrophysical modeling, segmented modeling method, Shenhu area, Gassmann fluid substitution

OPEN ACCESS

Edited by:
Jinan Guan,
Guangzhou Institute of Energy Conversion (CAS), China

Reviewed by:
Jiaxin Sun,
China University of Geosciences Wuhan, China
Bo Liu,
Hebei University of Engineering, China
Haiteng Zhuo,
Sun Yat-sen University, China

***Correspondence:**
Jinqiang Liang
ljinqiang@petalmail.com

Specialty section:
This article was submitted to Economic Geology, a section of the journal Frontiers in Earth Science

Received: *26 February 2022*
Accepted: *09 May 2022*
Published: *23 June 2022*

Citation:
Liu F, Liang J, Lai H, Han L, Wang X, Li T and Wang F (2022) Two-Phase Modeling Technology and Subsection Modeling Method of Natural Gas Hydrate: A Case Study in the Shenhu Sea Area. Front. Earth Sci. 10:884375. doi: 10.3389/feart.2022.884375

1 INTRODUCTION

Natural gas hydrate is a new type of clean energy that has been paid attention to since the 20th century. It is widely distributed in the continental shelf, deep-water basin, and permafrost area and has the characteristics of extremely rich resources. In the 1990s (Paull and Matsumoto, 2000; Wood and Ruppel, 2000; Boswell R et al., 2012; Yamamoto K, 2014), China gradually carried out the investigation of natural gas hydrate and completed the leap from exploration to experimental exploitation in more than 20 years (Zhang H Q et al., 2007; Wang X J et al., 2014; Yang et al., 2015; Yang et al., 2017a). Especially in the South China Sea, a large number of natural gas hydrate investigations and two rounds of experimental exploitation have been carried out (Li et al., 2018; Sha et al., 2019; Zhang et al., 2017; Zhang et al., 2018; Zhang et al., 2020a; Zhang et al., 2020b; Su et al., 2020; Yang et al., 2017b; Yang et al., 2020). At present, the investigation method of natural gas hydrate is still dominated by the seismic method, but the seismic exploration method can only

describe the possible range and spatial distribution of ore body and cannot quantitatively characterize the distribution characteristics of hydrate saturation in the ore body. It is necessary to establish the mathematical expression relationship between P-wave, S-wave velocity, density, and other physical parameters obtained by seismic data inversion and saturation through the method of petrophysical modeling. In this way, the 1-dimensional gas hydrate physical parameters obtained from logging data are extended to 2-dimensional and 3-dimensional space to complete the prediction of gas hydrate saturation (Worthington, 2008; Huang et al., 2012; Pan et al., 2019; Dong et al., 2020; Liu et al., 2020; Betlem et al., 2021; Yang et al., 2021).

With the development of natural gas hydrate, many petrophysical models suitable for natural gas hydrate have been developed.

Natural gas hydrate in sediments shows the properties of both fluid and solid skeleton, which have been found in laboratory research (Buffett and Zatsepina, 2000). With the efforts of many scholars, a variety of petrophysical theories suitable for simulating hydrate deposition have been proposed, including the weighted empirical formula (Lee et al., 1996), equivalent medium theory (Zhang and Toksoz, 2012), three-phase Biot type theory (Lee 2008), modified Biot Gassmann theory (Lee 2002), etc. The three-phase Biot type equation proposed by Carcione and Tinivella (2000) assumes that the formation is composed of three phases of sediment, hydrate, and pore fluid to calculate the elastic wave velocity in the hydrate stability zone. Lee (2008) introduces parameters to describe pore filling and contact behavior on the basis of the three-phase Biot type; The equivalent medium theory and modified Biot Gassmann theory are essentially pore-filling models for the simulation of natural gas hydrate bearing sediments. Zhang Yuwen et al. (2004) based on Biot's two-phase medium theory and aiming at the three hydrate deposition models proposed by Ecker, studied the variation law of the velocity and attenuation of fast P-wave, slow P-wave, and S-wave with frequency in hydrate bearing strata with and without dissipation. According to the research results of Dai et al. (2008); Zhang et al. (2011) summarized the hydrate petrophysical models based on equivalent media into five categories, and quantitatively analyzed the relationship between reservoir wave velocity and Poisson's ratio with hydrate saturation. Gao et al. (2012) used the improved Biot Gassmann (bgtl) model proposed by Lee to estimate the saturation of gas hydrate in well A by using P-wave velocity for the unconsolidated deep-water sedimentary strata with high porosity and silty clay in Shenhu sea area of the South China Sea. Pan et al. (2014) compared the saturation predicted by the effective medium model, the improved boit Gassmann model, and the simplified three-phase equation under the same occurrence state. It is found that the hydrate saturation predicted by the effective medium model and the improved Biot Gassmann model is more reasonable than that predicted by the simple three-phase equation (stpe).

Based on BK solid replacement theory and Gassmann fluid replacement theory, this paper establishes the equivalent medium two-phase modeling technology to characterize the two phase states of fluid filling and rock skeleton of natural gas hydrate respectively. This technology is applied to the natural gas hydrate work area in the Shenhu sea area of the South China Sea. At the same time, the subsection modeling method is used to fit the natural gas hydrate layer and free gas layer. The test shows that this method and technology has good applicability to the petrophysical modeling of natural gas hydrate in the Shenhu sea area, can well characterize the physical properties of natural gas hydrate and free gas reservoir in this work area, and can provide strong support for the quantitative study of natural gas hydrate saturation.

2 TRADITIONAL ROCK PHYSICAL MODELING METHODS

There are many types of hydrate petrophysical models. According to the previous research results and the actual situation of the study area, this study attempts to implement the existing model and analyzes the applicability of the existing model according to the actual data.

2.1 Empirical Formula Class (Three-Phase Weight Equation)

Pearson et al. (1983)applied the three-phase time-average equation (**Eq. 1**) to hydrate bearing rocks and qualitatively explained the acoustic properties of hydrate bearing strata in the consolidation medium:

$$\frac{1}{V_p} = \frac{\phi(1-S)}{V_w} + \frac{\phi S}{V_h} + \frac{(1-\phi)}{V_m}. \tag{1}$$

In **Formula 1**, V_p is the P-wave velocity of hydrate bearing formation. V_h is the P-wave velocity of pure hydrate. V_w is the P-wave velocity of the fluid; V_m is the P-wave velocity of the matrix. Φ is porosity; S is the saturation of the hydrate.

Similar to the three-phase time-average equation given by Pearson (1983), the three-phase equation Wood and Stoffa Pand Shipley (1994) of hydrate bearing sediments can be defined as

$$\frac{1}{\rho V_p^2} = \frac{\phi(1-S)}{\rho_w V_w^2} + \frac{\phi S}{\rho_h V_h^2} + \frac{(1-\phi)}{\rho_m V_m^2}. \tag{2}$$

In **Formula 2**, ρ_h is the density of pure hydrate, ρ_w is the density of the fluid, ρ_m is the density of the matrix, and the volume density of the formation

$$\rho = (1-\phi)\rho_m + (1-S)\phi\rho_w + S\phi\rho_h. \tag{3}$$

In 1996, M.W. Lee et al. used the weight method of the three-phase time-average equation and the three-phase Wood equation used by Nobes et al. (1986)to estimate the velocity of deep-sea hydrate bearing sediments, and the three-phase weight equation was written as

$$\frac{1}{V_p} = \frac{W\phi(1-S)^n}{V_{p1}} + \frac{1-W\phi(1-S)^n}{V_{p2}}. \tag{4}$$

In **Formula 3**, V_{p1} is the P-wave velocity calculated by Wood's equation; V_{p2} is the P-wave velocity calculated by the time-

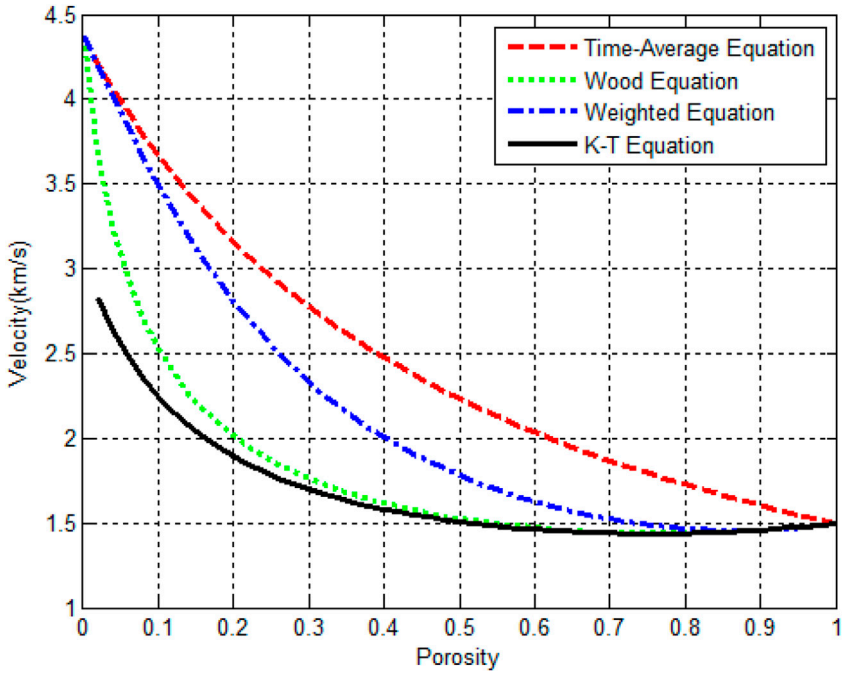

FIGURE 1 | Relationship between formation velocity and porosity without hydrate.

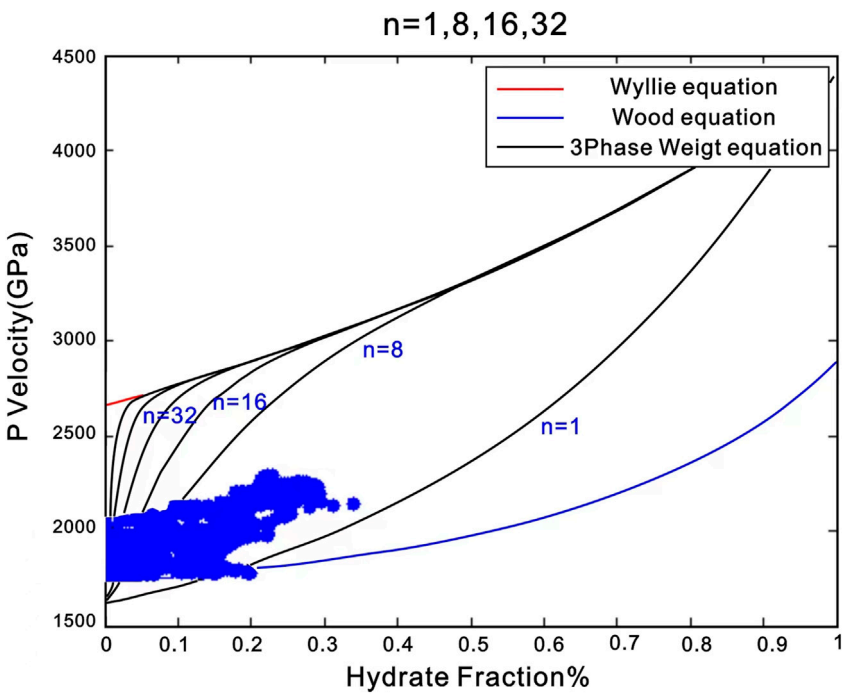

FIGURE 2 | Relation between the velocity obtained from the three-phase weight equation and hydrate saturation.

average equation. W is the weighting factor; n is the constant that simulates the variation of diagenesis with hydrate saturation.

The higher rock velocities estimated by time-average equations require the artificially lower matrix velocities. Based on the matrix velocity of 4.37 km/s and the assumption that hydrate is not present, the relationship between formation velocity and porosity is obtained by using the three-phase time-average equation, three-phase Wood equation, and three-

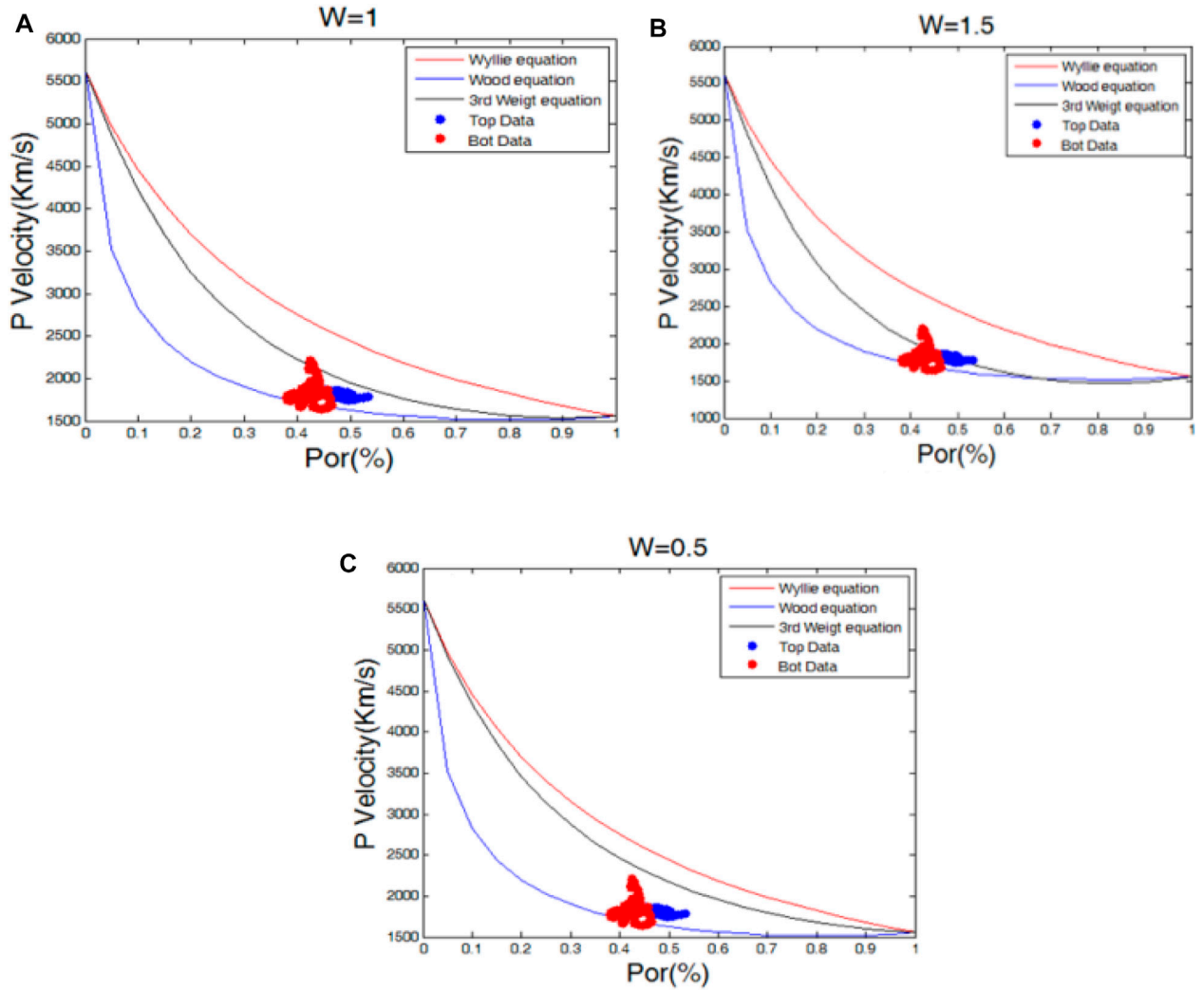

FIGURE 3 | Selection of formation consolidation factor W for three-phase weighting equation.

phase weight equation respectively, as shown in **Figure 1**. The curve obtained by the weighted equation is located between the time-average equation and the Wood equation.

When the hydrate saturation is 0, when W > 1, the weighting equation is inclined to Wood's equation, and when W < 1, the weighting equation is inclined to the time-average equation. Since (1-s)≤1, the weighting equation rapidly approaches the time-average equation as n increases (as shown in **Figure 2**). Therefore, when applying the three-phase weighting equation, a flexible method is provided by using the weighting factor and the exponential term, which is more suitable for consolidation (the time-average equation is more suitable) or suspension conditions (Wood's equation is more suitable). The blue dots in **Figure 3** are the actual data of a well in the study area. By changing the size of N, different data in different depth sections can be fitted.

The consolidation factor W, which controls the degree of consolidation, is determined by using the formation data without hydrate and fitting with the forward curve. By comparing the data from Well A, it can be seen that the fitting effect is best when W = 1.5.

Finally, using the W and N obtained by analysis, the P-wave velocity in the study area can be forward modeled, as shown in **Figure 4**. Among them, the blue curve is the measured curve, and the red curve is the forecast curve. The overall trend is generally consistent, but the prediction error of the free gas layer is large, so further stratified modeling may be needed.

2.2 Equivalent Medium Model (Five Classical Hydrate Models)

As shown above, the most popular hydrate rock physical models are based on the six models proposed by Zhang (2012) (**Figure 5**). The six models refer to the contact

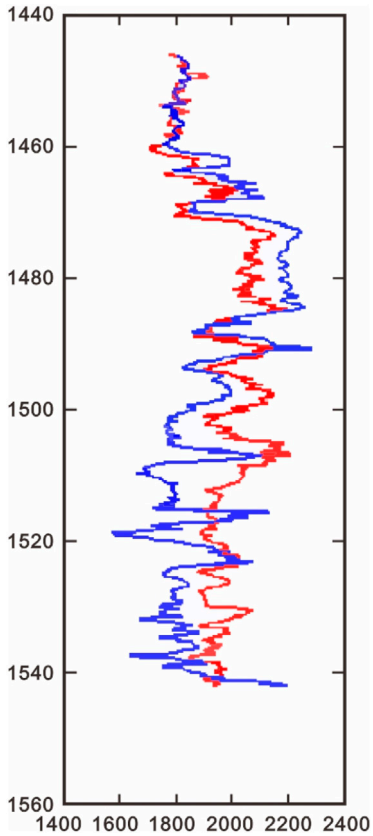

FIGURE 4 | P-wave velocity prediction results of well A.

cementation model, particle-enfolded model, skeleton particle support model, pore filling model, nodules fracture filling model, and fracture filling model respectively. In the contact cementation model, rock grains are regarded as freely accumulated spheres, and the hydrates bond the spheres together in contact. In the model of particle-enfolded, the rock particles are regarded as freely accumulated spheres, and the hydrate grows around the particles, acting as cement. In the skeleton particle support model, the hydrate is regarded as the bearing particles on the framework. In the pore filling model, hydrates are treated as particles or fluids to fill pores. In the nodular fissure filling mode, hydrate is deposited or filled in the fissure as nodules, which belongs to uneven distribution. The doping mode is to treat the hydrate as evenly distributed in the rock matrix, similar to the ice layer of the tundra. The filling mode of nodule fracture is to deposit hydrate as a nodule or fill it in the fracture, which belongs to a kind of heterogeneous distribution. However, the fracture filling model is not common in this work area, so the follow-up content has not carried out research on this model.

According to the analysis of mineral composition and porosity data of several Wells in the study area, the mineral composition in the study area is relatively single, mainly concentrated in clay (illite), quartz, and calcite. As shown in the multi-well histogram analysis (**Figure 6**), the porosity ranges from 30% to 55%, illite from 10% to 45%, quartz from 10% to 40%, and calcite from 0% to 15%.

Based on the mineral analysis results, we constructed measurement plates of five classical rock physical models and compared them with the actual data (**Figure 7**).

According to the rock physics template analysis, the hydrate enrichment form in this study area is the most consistent with the trend of the third type (skeleton particle support type) and the fourth type (pore filling type), which confirms the hydrate enrichment form in this area from the side. However, the measured values of longitudinal and S-wave velocity in the

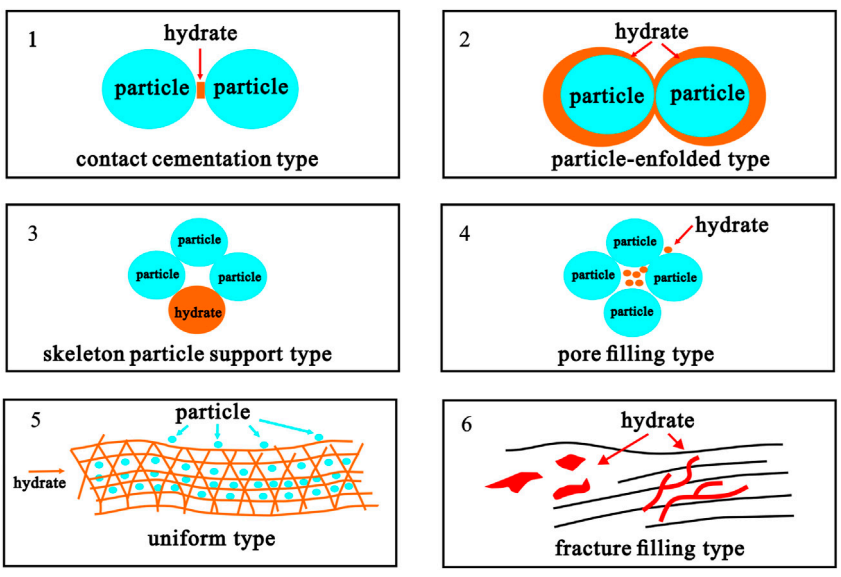

FIGURE 5 | Enrichment diagram of five classical hydrate models.

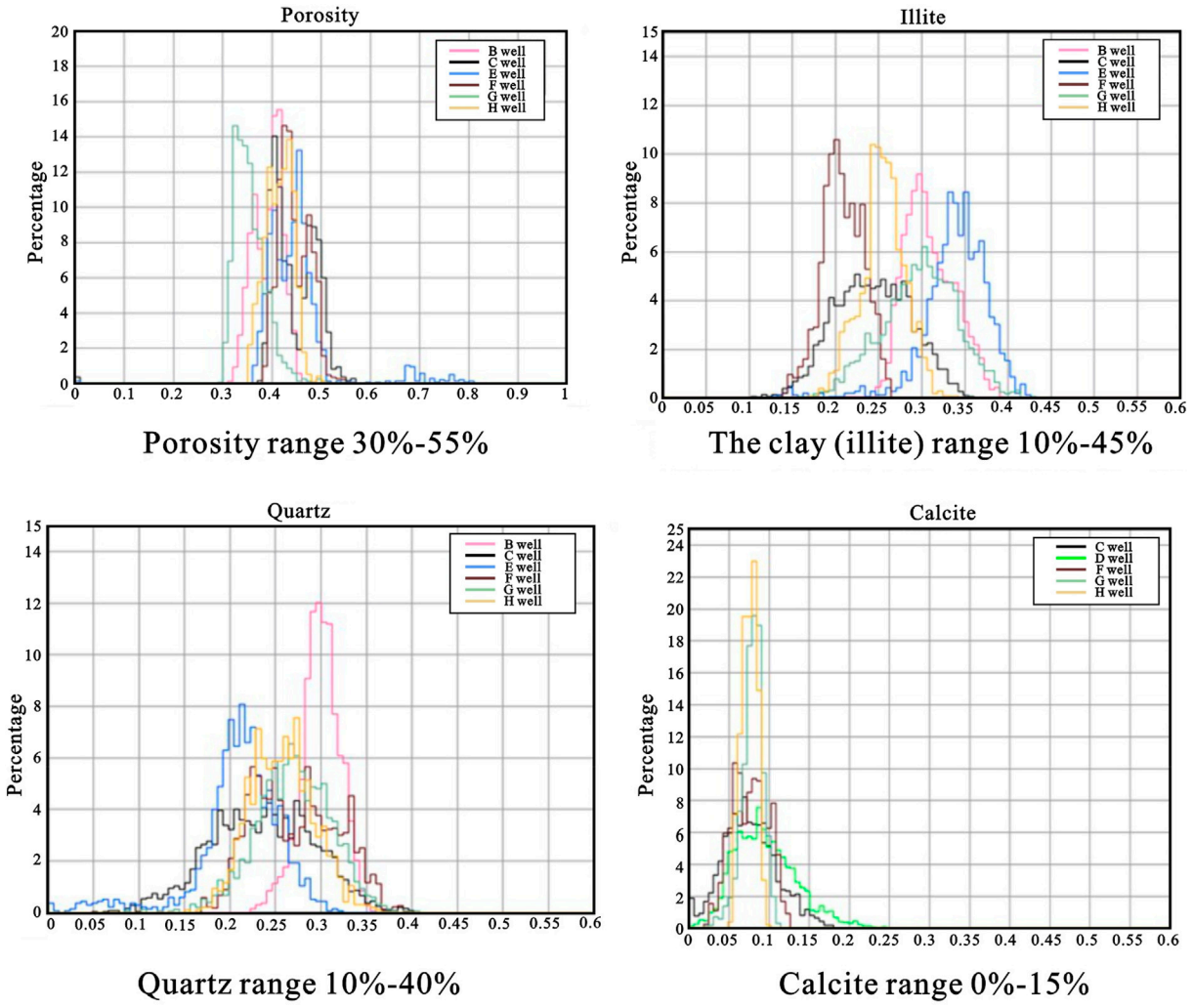

FIGURE 6 | Histogram of mineral composition and porosity distribution of multiple Wells in the study area.

study area are slightly lower than the template curve, which may be caused by the incorrect elastic parameters of mineral components.

3 TWO-PHASE MODELING TECHNOLOGY AND SEGMENTED MODELING METHOD

3.1 Petrophysical Modeling of Dual-Phase Hydrate

According to the previous study, most of the existing petrophysical models can be divided into two categories: one category regards hydrate as pore fluid, and the other category regards hydrate as skeleton mineral. Neither of the two models can well simulate the hydrate enrichment in the study area.

Through inductive analysis, we think that the two kinds of modeling ideas have some disadvantages. When hydrate is completely used as pore fluid, the modeling process uses Gassmann's theory for fluid replacement, which results in the S-wave velocity of such models not changing with the hydrate content (as shown in Model 4). However, through statistical analysis, the shear modulus of hydrate is 2.57 MPa. It is precise because the shear modulus of hydrate is non-zero that its content must affect the S-wave velocity of the mixture. For the other types of models (for example, Model 3 and Model 5), which treat hydrate as skeleton minerals, the relationship between hydrate and pore fluid is ignored, resulting in an equal proportion of S-wave velocity with the increase of hydrate content. According to the template analysis, the correlation between hydrate saturation and velocity in this study area is between the above two categories. The S-wave velocity increases with the increase of hydrate content, but the increase rate is lower than that of the template of Model three and Model 4. Therefore, the existing hydrate models cannot meet the needs of hydrate modeling in this study area, and how to choose an appropriate equivalent medium theory to simulate hydrate is the core and key of modeling in this study area.

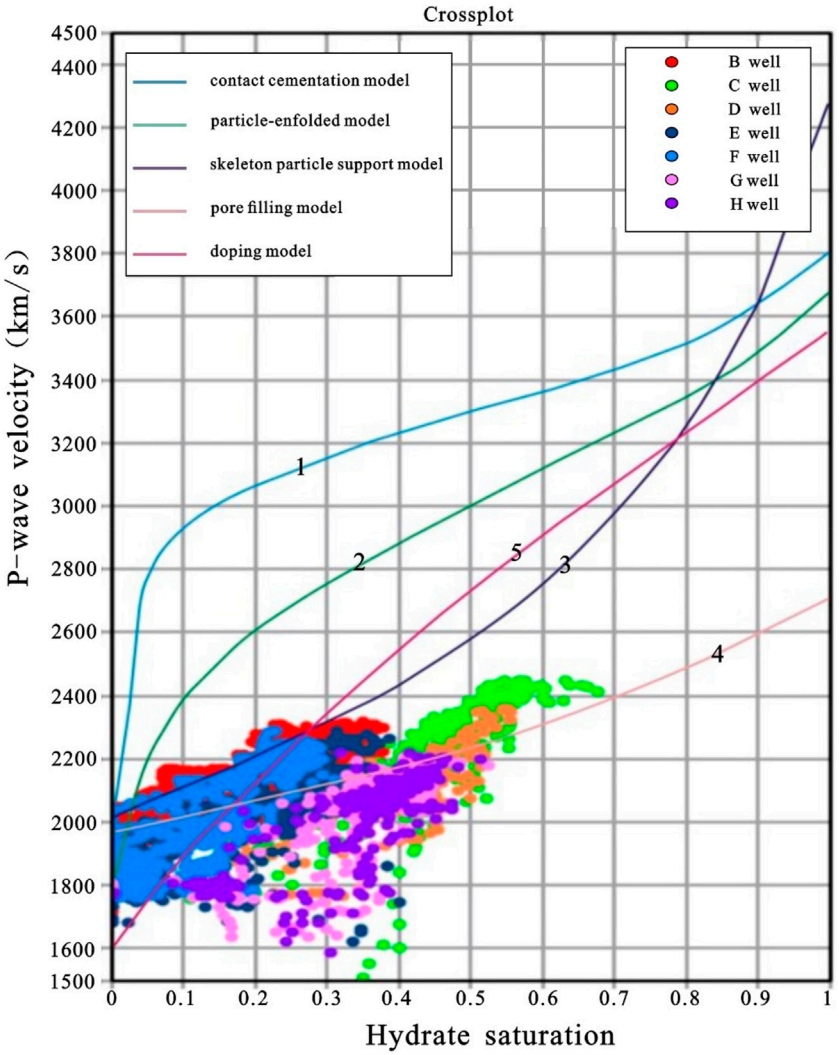

FIGURE 7 | Rock physics template for five classic hydrate models.

As shown in **Figure 8**, the two-phase modeling idea constructed in this study is between the existing pore-filled model and the skeleton supported model, which means that part of hydrate exists in the skeleton form, while the other part is enriched in the form of pore fluid. Based on the above ideas, the two-phase rock physical model we constructed is shown in **Figure 9**. As shown in the virtual frame in the figure, we divided the hydrate into two parts: the skeleton that plays a supporting role and the fluid in the pore. The hydrate, which acts as the skeleton, is combined with calcite, quartz, and illite to form the skeleton of the model, and they are fused by VRH averaging theory to obtain the dry rock skeleton. The hydrates enriched in the pores, together with water and gas, are added to the dry rock skeleton as pore fluid. Based on the above analysis, since the shear modulus of hydrate is non-zero, we use the BK solid substitution theory to simulate hydrate in pores. BK theory has been widely used in the simulation of rock physical model of unconventional shale in recent years, which is used to simulate the kerogen with non-zero shear modulus. In this study, we apply this idea to hydrate simulation. Gas and water are replaced by conventional Gassmann's theory, and the equivalent hydrate mixture is finally obtained.

Based on the rock physical model of the two-phase hydrate constructed above, we carried out S-wave velocity prediction on Well E in the study area to test the feasibility of the model. The results are shown in **Figure 10**. The curve in the figure on the left is the S-wave velocity, the curve on the right is the P-wave velocity, the red curve represents the measured curve, and the blue curve represents the predicted curve. The error between the predicted velocity curve and the measured velocity curve is small, which proves that the rock physical model of double phase hydrate is available.

The main petrophysical model formulas used in this model are as follows:

3.1.1 Voigt–Reuss–Hill Boundary

Voigt–Reuss–Hill boundary is composed of Voigt upper bound, Reuss lower bound, and hill average. Voigt boundary is the upper

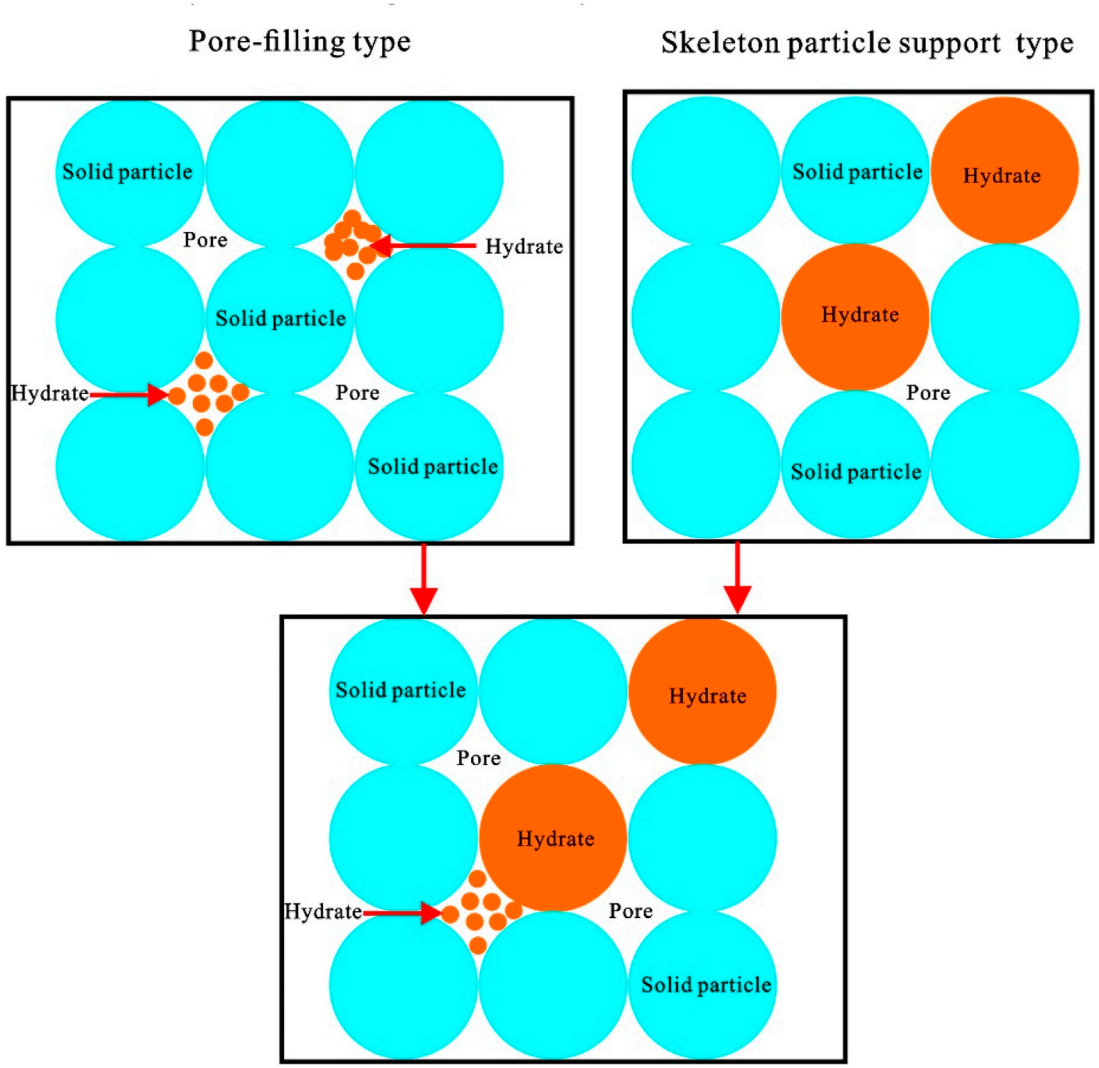

FIGURE 8 | Two-phase hydrate modeling diagram.

limit of the VRH boundary, also known as equal strain average. Its results describe the average stress-strain relationship when each phase of the mixture is assumed to have equal strain. The specific formula is as follows:

$$M_V = \sum_{i=1}^{N} \phi_i M_i. \tag{5}$$

In the formula, M_V and M_i are the elastic modulus of the mixture and phase i, respectively, ϕ_i is the volume fraction of phase i.

Reuss average is the lower bound of the VRH average, also known as the equal stress average, which assumes that each phase has the same stress. The specific formula is as follows:

$$\frac{1}{M_R} = \sum_{i=1}^{N} \frac{\phi_i}{M_i}. \tag{6}$$

The meaning of each parameter in the formula is the same as that of the Voigt formula.

Hill pointed out that the arithmetic weighting of Voigt and Reuss can be used to predict the equivalent modulus of rock. The specific formula is as follows:

$$M_{VRH} = \frac{M_V + M_R}{2}. \tag{7}$$

It can be seen that the Voigt upper limit is the arithmetic weight of the elastic parameters of each phase, and the Reuss average is the arithmetic average of the reciprocal of the elastic parameters of each phase. Hill average is to average the equivalent results of the two. This averaging is based on the assumption of stress averaging or strain averaging. Therefore, when applying Voigt–Reuss–Hill upper and lower limits, it is necessary to assume that each component of the mixture is identical and the rock is linear and elastic.

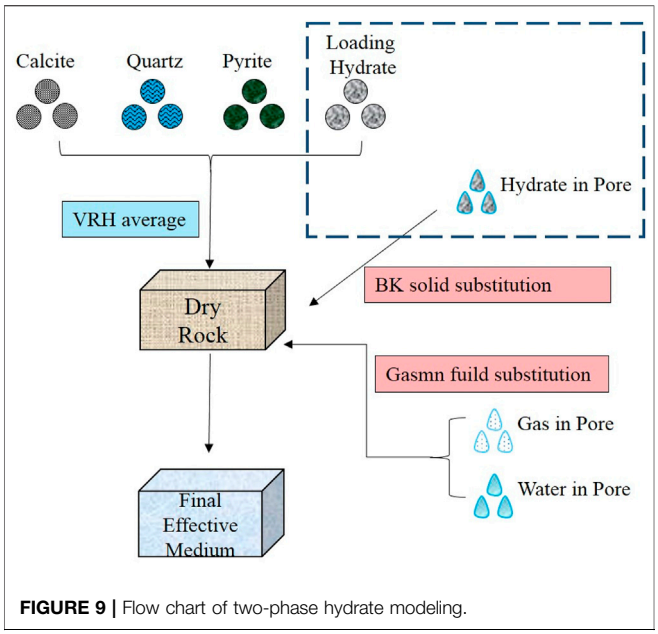

FIGURE 9 | Flow chart of two-phase hydrate modeling.

3.1.2 Gassmann Equation

Gassmann's theory describes the propagation of seismic waves in porous media with saturated fluid, which belongs to the low-frequency model. The equation constructs the relationship between seismic wave velocity, pore fluid, and mineral skeleton. Gassmann formula is widely used to calculate the change of elastic modulus caused by the change of fluid in pores (i.e. fluid substitution).

The relationship between the elastic modulus of rock skeleton and the elastic modulus between porosity and matrix is as follows:

$$\frac{1}{K_{dry}} = \frac{1}{K_m} + \frac{\phi}{K_\phi}. \tag{8}$$

In the formula, K_{dry}, K_m, K_ϕ They are the equivalent elastic modulus of dry rock skeleton, matrix, and rock with pore space. ϕ is the porosity. Under low-frequency conditions, the relationship between the rock equivalent elastic modulus of fully saturated fluid and porosity is as follows:

$$\frac{1}{K_{sat}} = \frac{1}{K_m} + \frac{\phi}{K'_\phi}. \tag{9}$$

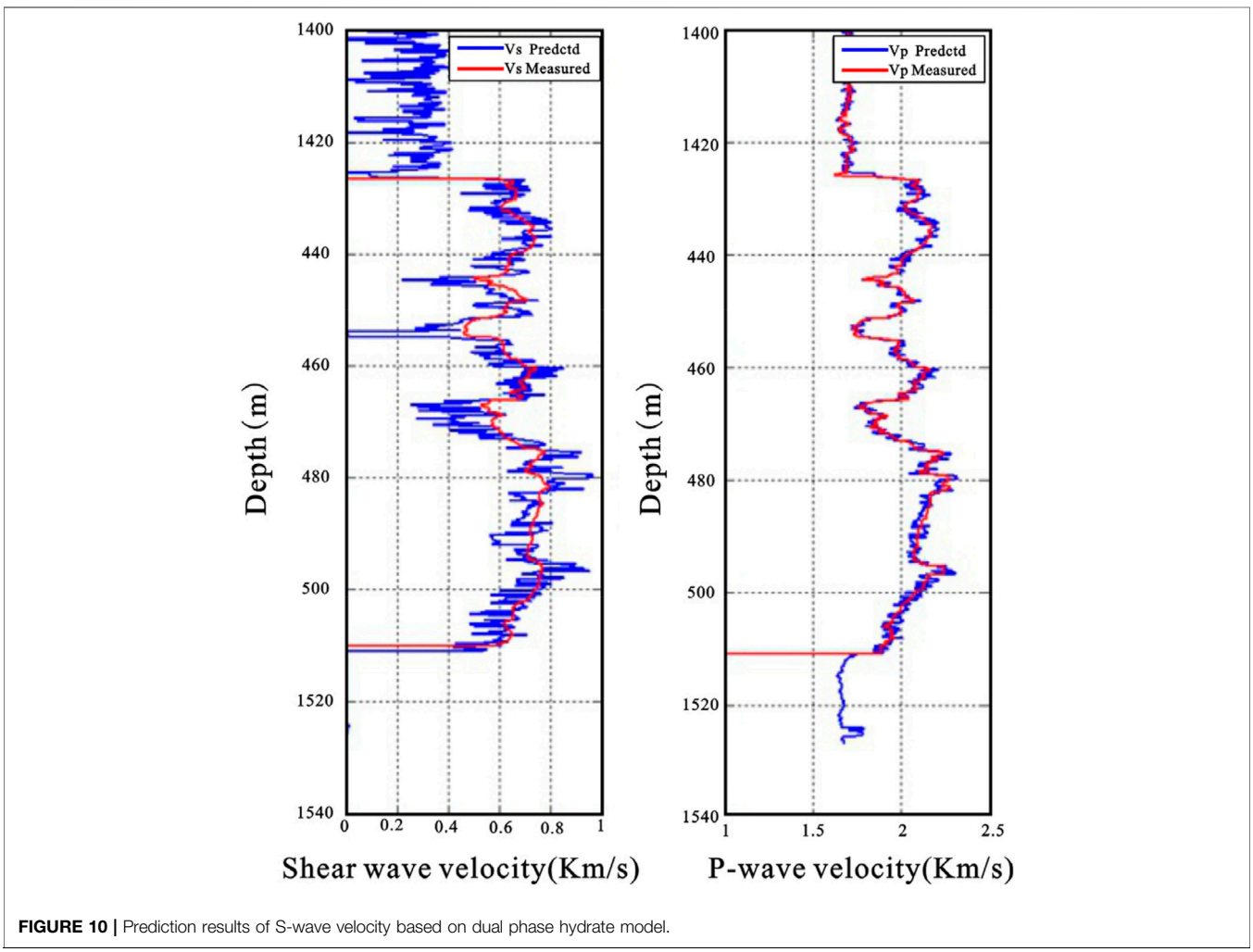

FIGURE 10 | Prediction results of S-wave velocity based on dual phase hydrate model.

In the formula, K_{sat} is the equivalent elastic modulus of rock in saturated fluid, $K_{\phi}^{'}$ can be expressed as

$$K_{\phi}^{'} = K_{\phi} + \frac{K_m K_{fl}}{K_m - K_{fl}} \approx K_{\phi} + K_{fl}. \tag{10}$$

In the formula, K_{fl} is the elastic modulus of the fluid. Simultaneously from the abovementioned formula, eliminating $K_{\phi}^{'}$ can yield

$$\frac{K_{sat}}{K_m - K_{sat}} = \frac{K_{dry}}{K_m - K_{dry}} + \frac{K_{fl}}{\phi\left(K_m - K_{fl}\right)}, \tag{11}$$

which is the basic form of the Gassmann equation. Based on the basic equation, Xu and White (1995) changed the abovementioned formula to

$$K_{sat} = K_{dry} + \frac{\left(1 - K_{dry}/K_m\right)^2}{\frac{\phi}{K_{fl}} + \frac{1-\phi}{K_m} - \frac{K_{dry}}{K_m^2}}. \tag{12}$$

Gassmann equation assumes that the change of pore fluid does not affect the equivalent shear modulus of rock (μ_{sat}), that is, the equivalent shear modulus of saturated fluid rock is equal to the shear modulus of rock skeleton (μ_{dry}), as shown in the following formula:

$$\frac{1}{\mu_{sat}} = \frac{1}{\mu_{dry}}. \tag{13}$$

Using the abovementioned formula, the equivalent elastic modulus of saturated fluid rock can be calculated, and when combined with the density equation, the P-wave velocity and the S-wave velocity of rock can be obtained.

$$\rho = (1 - \phi)\rho_m + \phi\rho_f. \tag{14}$$

$$v_p = \sqrt{\frac{K + \frac{4}{3}\mu}{\rho}}, v_s = \sqrt{\frac{\mu}{\rho}}. \tag{15}$$

The assumptions that Gassmann's theory needs to meet are as follows:

1) The rock skeleton is homogeneous and isotropic
2) All pores in the rock are interconnected, and there is no chemical reaction between pore fluid and skeleton; that is, fluid and skeleton are two independent systems
3) The model needs to meet the low-frequency assumption; that is, the pore fluid (without viscosity) can flow fully at the half wavelength of seismic wave, and the pore pressure is always in equilibrium
4) The fluid is completely saturated

3.1.3 Brown–Korringa Replacement Model

Gassmann's equation is based on an isotropic assumption, which can not meet the needs of anisotropic shale petrophysical modeling. Brown and Korringa derived the Gassmann equation in anisotropic form. The Brown–Korringa formula can be used to describe the theoretical relationship of the equivalent modulus of an anisotropic rock skeleton when it is saturated with fluid. The specific formula is as follows:

$$S_{ijkl}^{dry} - S_{ijkl}^{sat} = \frac{\left(S_{ij\alpha\alpha}^{dry} - S_{ij\alpha\alpha}^{0}\right)\left(S_{kl\alpha\alpha}^{dry} - S_{kl\alpha\alpha}^{0}\right)}{\left(S_{\alpha\alpha\beta\beta}^{dry} - S_{i\alpha\alpha\beta\beta}^{0}\right) + \left(\beta_{fl} - \beta_0\right)\phi}, \tag{16}$$

where S_{ijkl}^{dry} is the equivalent elastic flexibility tensor of rock skeleton, S_{ijkl}^{sat} is the equivalent elastic flexibility tensor of saturated fluid rock, $S_{ij\alpha\alpha}^{0}$ is the equivalent elastic flexibility tensor of constituent minerals, β_{fl} and β_0 compressibility of pore fluid and mineral, ϕ is the porosity.

Based on the constructed model, we have carried out shear wave velocity prediction for well E in the work area, as shown in **Figure 10**. The left side is the shear wave velocity, the right side is the longitudinal wave velocity, the red curve is the measured curve, and the blue curve is the predicted curve. The error between the predicted results and the measured results is small, which proves the feasibility of the model.

3.2 Segmented Modeling Method

Then we applied the previously proposed two-phase hydrate petrophysical model to other Wells in the study area, as shown in **Figure 11**. The predicted S-wave velocities are shown in the figure on the left, with the red curve representing the measured S-wave velocities and the blue curve representing the predicted S-wave velocities. The results show that the fitting effect of the model is good when the target well contains only a hydrate layer. However, when the target well contains not only the hydrate layer but also the free gas layer, the fitting effect of the model is still good for the hydrate layer, but poor for the free gas layer.

According to the analysis, the petrophysical model of double phase hydrate mainly focuses on the modeling of hydrate and does not consider the enrichment form of free gas too much. As shown in **Figure 12**, the longitudinal and S-wave velocity relationship between the hydrate layer and free gas layer was calculated. Red represents the hydrate layer and blue represents the free gas layer. As can be seen from the figure, the S-wave velocities at different depths in the hydrate layer are different, while the S-wave velocities at different depths in the free gas layer have almost no difference. It is verified from the side that hydrate saturation has a direct effect on the S-wave velocity due to its non-zero shear modulus, while free gas saturation has little effect on the S-wave velocity. Therefore, for the free gas layer, we need to build a targeted rock physical model of the free gas layer to improve the prediction accuracy of S-wave velocity.

Since the physical properties of the free gas layer and hydrate layer are quite different, it is difficult to simulate the characteristics of both by using the same petrophysical model. Therefore, we construct the idea of a segmented modeling method of hydrate + free gas. For the hydrate layer, we also use the rock physical model of double phase hydrate proposed above, while for the free gas layer, we build a new modeling idea. Since the free gas layer does not contain hydrate, we do not need to consider hydrate simulation. The specific idea is as follows: first, the main skeleton minerals such as calcite, quartz, and illite were fused with the VRH average theory to obtain a solid mixture. Then, the empty pores are added to the solid mixture background based on DEM theory. Finally, the Gassmann fluid substitution

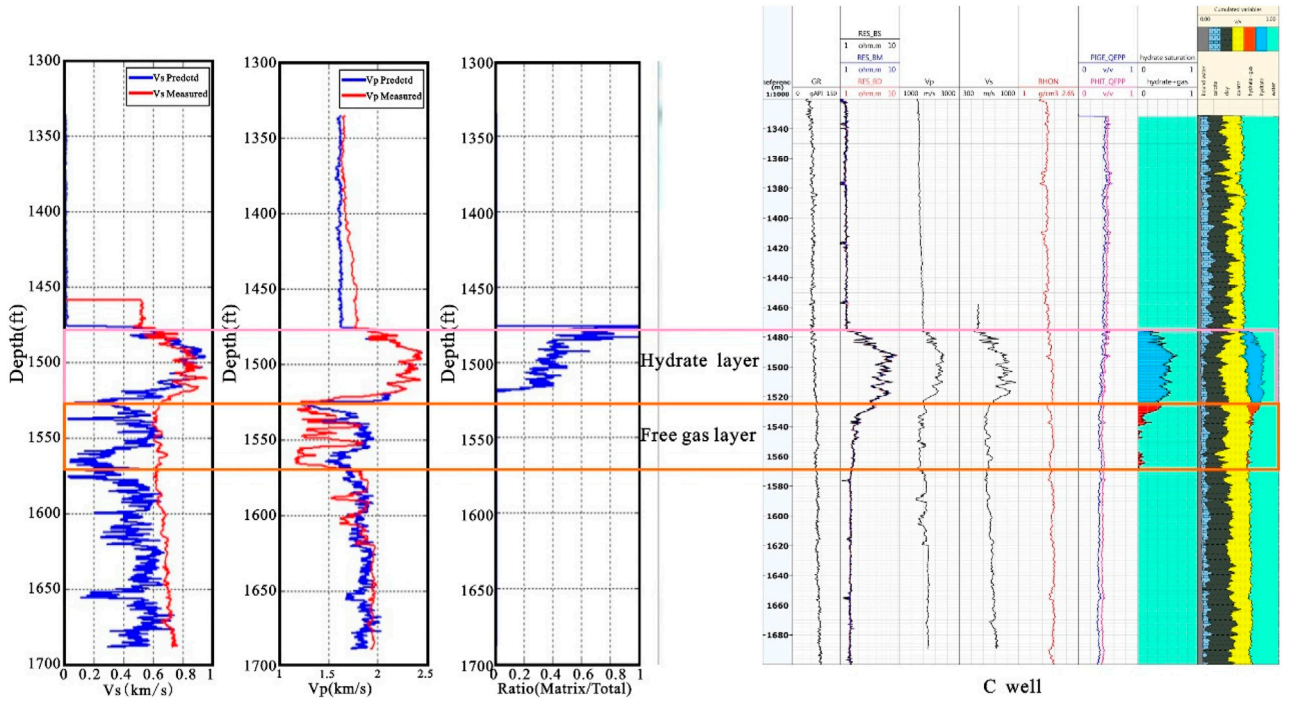

FIGURE 11 | S-wave velocity prediction results of well C based on dual phase hydrate petrophysical model.

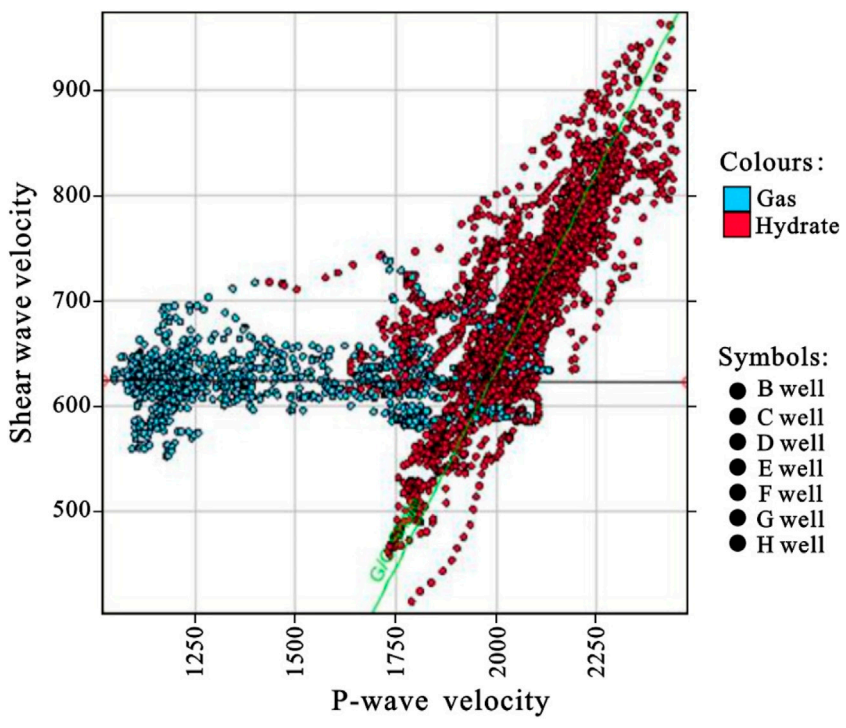

FIGURE 12 | Relationship of longitudinal and S-wave velocity between hydrate layer and free gas layer.

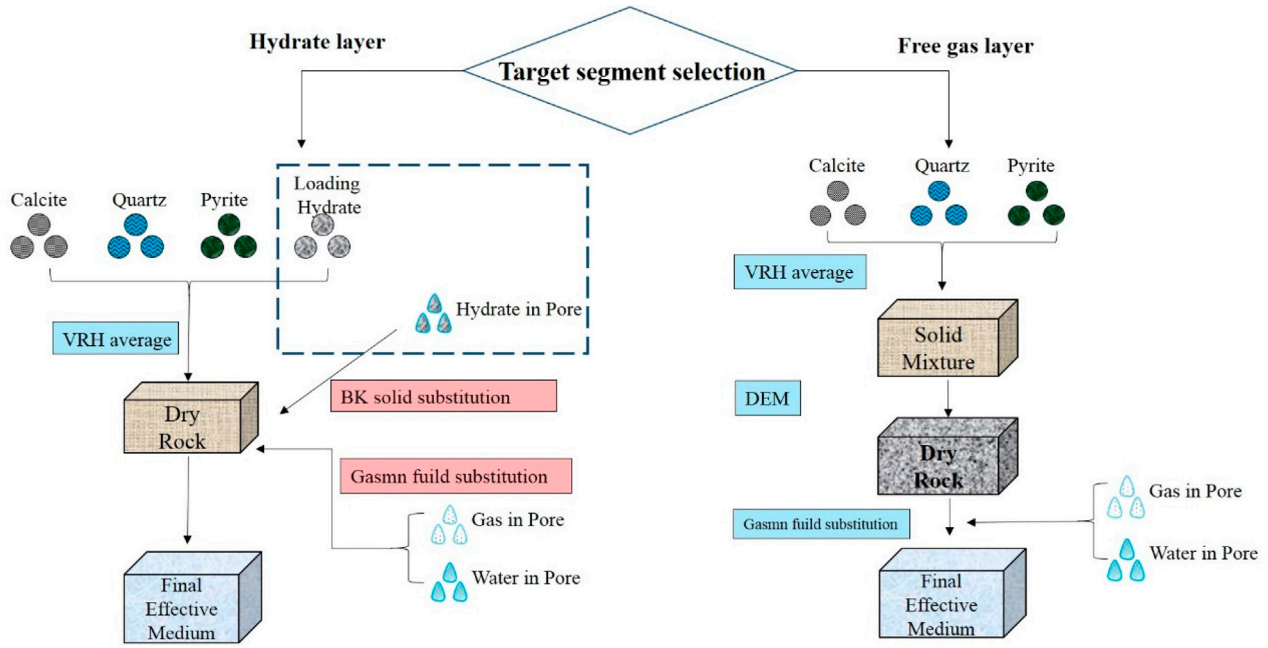

FIGURE 13 | Segmental petrophysical modeling process of hydrate and free gas layers.

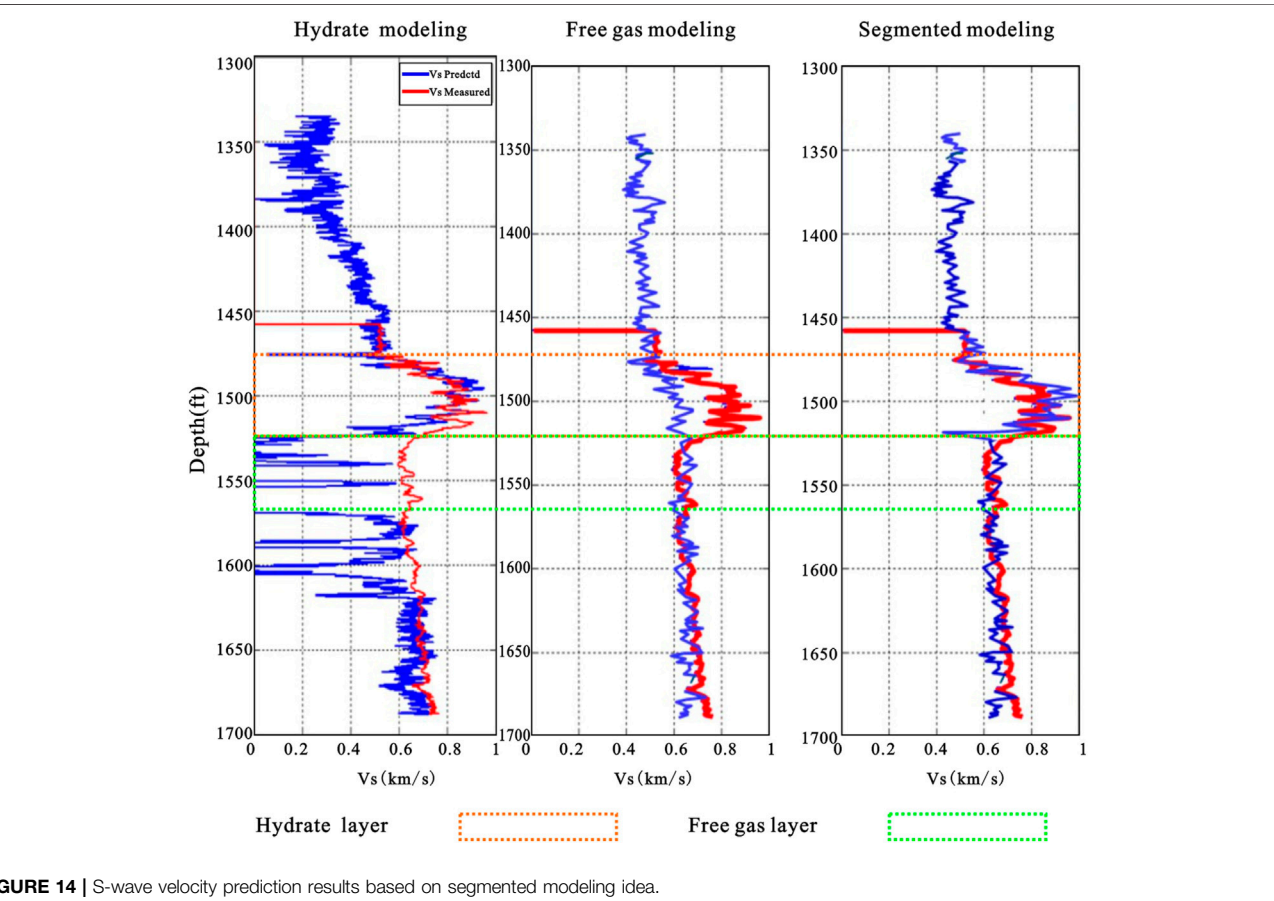

FIGURE 14 | S-wave velocity prediction results based on segmented modeling idea.

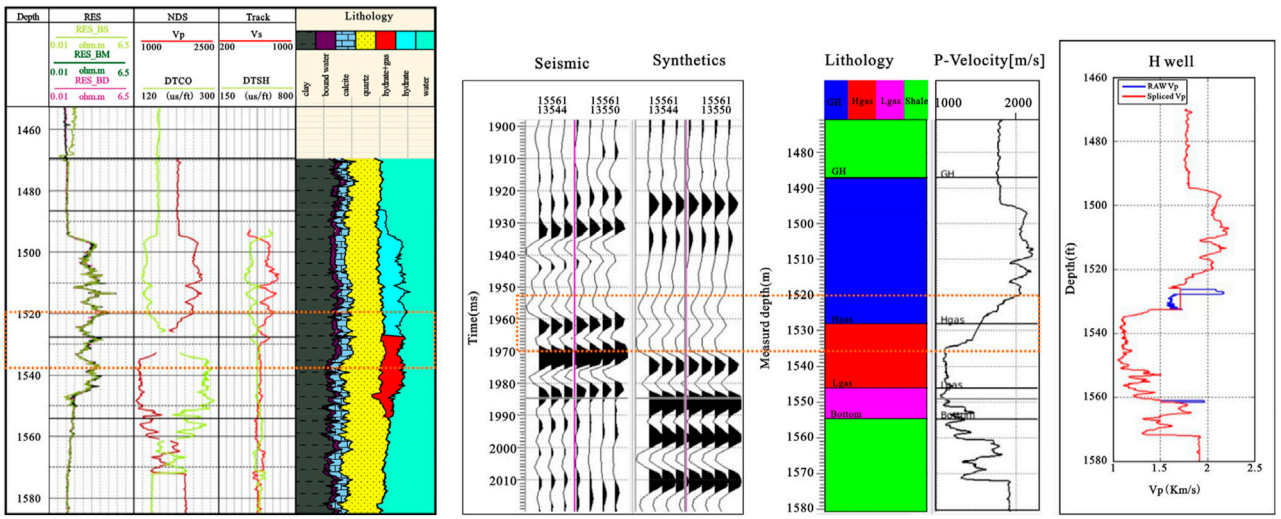

FIGURE 15 | Diagram of calibrating downhole seismic in Well H (before optimization).

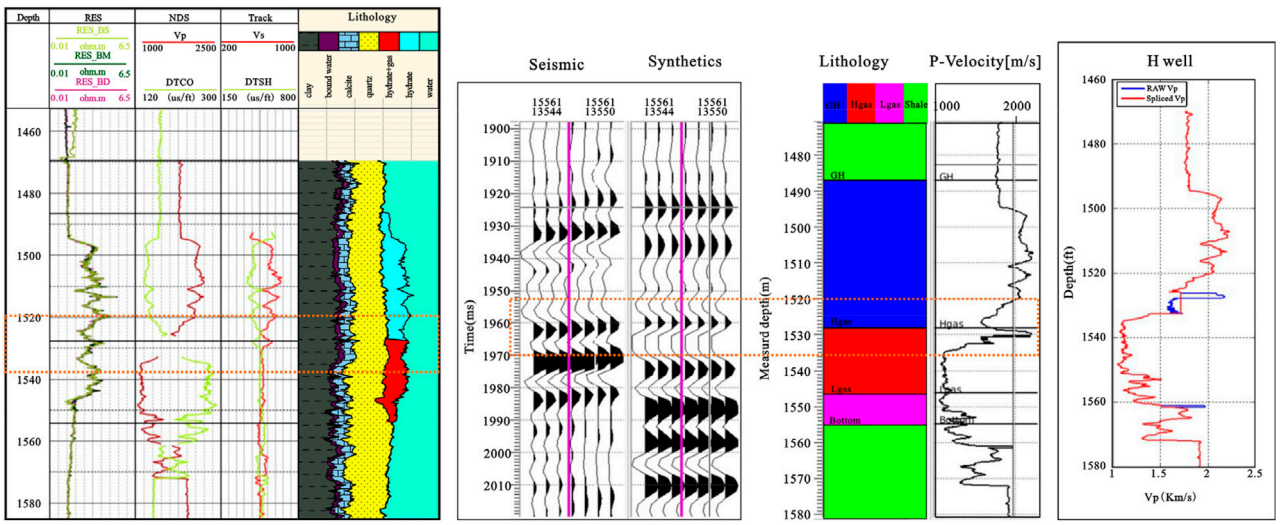

FIGURE 16 | Diagram of calibrating downhole seismic in Well H (after optimization).

theory is used to add water and free gas to the dry rock skeleton to obtain the final equivalent medium **Figure 13**.

Based on the idea of piecewise modeling, we used different petrophysical models to predict the S-wave velocity for hydrate and free gas respectively, and then combined the prediction results of different intervals. The prediction results are shown in **Figure 14**. In the figure, the predicted S-wave curve based on the rock physical model of two-phase hydrate is shown on the left side, and the predicted S-wave curve based on the modeling method for free gas is shown in the middle. The red represents the measured curve, and the blue represents the predicted curve. It can be found that the prediction result of the free gas layer S-wave has been significantly improved by using the segmented modeling method, and the predicted curve is basically consistent with the measured curve.

4 OPTIMIZATION OF CALIBRATING DOWNHOLE SEISMIC BASED ON MODELING

Through analysis, it is found that the P-wave velocity of some Wells in the study area is discontinuous. In order to solve this problem, conventional commercial software is used to complete the missing velocity value through the interpolation method, but the prediction accuracy of velocity value based on the interpolation method cannot be guaranteed. Therefore, we

tried to use the constructed rock physical model to improve the accuracy of velocity prediction and finally improve the effect of calibrating downhole seismic.

As shown in **Figure 15**, the logging curve in the left figure shows the absence of P-wave velocity at the boundary between the hydrate and free gas layers. The missing velocity is simply interpolated by commercial software, and the forward trace is calculated based on the interpolation velocity. However, there are some differences between the forward trace and seismic data, which may be caused by inaccurate velocity prediction. On the right of **Figure 16** are the P-wave velocities calculated based on the model proposed in this study. Blue represents the predicted velocity and red represents the measured velocity. The synthetic records are obtained by using the velocities calculated by the rock physical model. It can be seen from the figure that in the P-wave velocity missing section, the forward modeling record has been significantly improved, and the reflection interface between the hydrate layer and the free gas layer has been clearly displayed. On the whole, the S-wave velocity prediction based on the rock physical model can improve the incomplete forward logging profile caused by the lack of velocity curve to some extent, and finally improve the precision of calibrating downhole seismic.

5 CONCLUSION

Through the application of actual data, two conclusions can be drawn:

1) The two-phase modeling technology based on BK solid substitution theory and Gassmann fluid substitution theory can take into account both the existing forms of hydrate as rock skeleton particle and pore-filling material. The equivalent medium model obtained by this technology can be used to fit more accurate longitudinal and S-wave velocities.
2) The physical properties of the gas hydrate layer and its associated free gas layer are very different, so the same modeling idea cannot be used. The segmenting modeling method can fully consider the physical properties of the two layers, which can greatly improve the effect of forward synthesis record calibration.

DATA AVAILABILITY STATEMENT

The original contributions presented in the study are included in the article/Supplementary Materials; further inquiries can be directed to the corresponding author.

AUTHOR CONTRIBUTIONS

FL: Investigation, Formal analysis, Writing—original draft. JL: Review and editing. HL: Supervision. LH: Geophysical interpretation. XW: Investigation and seismic analysis. TL: Logging analysis. FW: Figure drawing.

FUNDING

This study was funded by the Key Special Project for Introduced Talents Team of Southern Marine Science and Engineering Guangdong Laboratory (Guangzhou) (No. GML2019ZD0102), the Guangdong Province Marine Economic Development (Six Major Marine Industries) Special Fund Project (No. (2021) No. 58), the China National Hydrate Project(DD20190224), and the Open Fund Project of Hubei Key Laboratory of Marine Geological Resources (MGR202002).

ACKNOWLEDGMENTS

The authors are grateful for the linguistic assistance from LetPub (www.letpub.com) during the preparation of this manuscript. In addition, they appreciate the valuable comments and suggestions from Editor Jinan Guan, other editors, and reviewers.

REFERENCES

Betlem, P., Roy, S., Birchall, T., Hodson, A., Noormets, R., Römer, M., et al. (2021). Modelling of the Gas Hydrate Potential in Svalbard's Fjords. *J. Nat. Gas Sci. Eng.* 94, 104127. doi:10.1016/j.jngse.2021.104127

Boswell, R., Frye, M., Shelander, D., Shedd, W., McConnell, D. R., and Cook, A., and (2012). Architecture of Gas-Hydrate-Bearing Sands from Walker Ridge 313, Green Canyon 955, and Alaminos Canyon 21: Northern Deepwater Gulf of Mexico. *Mar. Petroleum Geol. Petrol Geol.* 34 (1), 134–149. doi:10.1016/j.marpetgeo.2011.08.010

Buffett, B. A., and Zatsepina, O. Y. (2000). Formation of Gas Hydrate from Dissolved Gas in Natural Porous Media. *Mar. Geol.* 164 (1-2), 69–77. doi:10.1016/s0025-3227(99)00127-9

Carcione, J. M., and Tinivella, U. (2000). Bottom-simulating Reflectors: Seismic Velocities and AVO Effects. *Geophysics* 65 (1), 54–67. doi:10.1190/1.1444725

Dai, J., Snyder, F., Gillespie, D., Koesoemadinata, A., and Dutta, N. (2008). Exploration for Gas Hydrates in the Deepwater, Northern Gulf of Mexico: Part I A Seismic Approach Based on Geologic Model, Inversion, and Rock Physics Principles. *Mar. Petroleum Geol.* 25 (9), 830–844. doi:10.1016/j.marpetgeo.2008.02.006

Dong, H., Sun, J., Arif, M., Golsanami, N., Yan, W., and Zhang, Y. (2020). A Novel Hybrid Method for Gas Hydrate Filling Modes Identification via Digital Rock. *Mar. Petroleum Geol.* 115, 104255. doi:10.1016/j.marpetgeo.2020.104255

Gao, H. Y., Zhong, G. F., Liang, J. Q., and Guo, Y. Q. (2012). Estimation of Gas Hydrate Saturation with Modified Biot-Gassmann Theory: a Case from Northern South China Sea. *Mar. Geol. Quat. Geol.* 32 (4), 83-89. doi:10.3724/sp.j.1140.2012.04083

Huang, J.-W., Bellefleur, G., and Milkereit, B. (2012). Application of Conditional Simulation of Heterogeneous Rock Properties to Seismic Scattering and Attenuation Analysis in Gas Hydrate Reservoirs. *J. Appl. Geophys.* 77, 83–96. doi:10.1016/j.jappgeo.2011.12.002

Lee, M. W.(2008). Models for Gas Hydrate-Bearing Sediments Inferred from Hydraulic Permeability and Elastic Velocities. U. S. Geophysical Survey Scientific Investigations. Report 2008-5219.

Lee, M. W. (2002). Modified Biot-Gassmann Theory for Calculating Elastic Velocities for Unconsolidated and Consolidated Sediments. *Mar. Geophys. Res.* 23 (5-6), 403–412. doi:10.1023/b:mari.0000018195.75858.12

Lee, M. W., Hutchinson, D. R., Collett, T. S., and Dillon, W. P. (1996). Seismic Velocities for Hydrate-Bearing Sediments Using Weighted Equation. *J. Geophys. Res.* 101 (9), 20347–20358. doi:10.1029/96jb01886

Li, J.-f., Ye, J. L., Ye, J.-l., Qin, X.-w., Qiu, H.-j., Wu, N.-y., et al. (2018). The First Offshore Natural Gas Hydrate Production Test in South China Sea. *China Geol.* 1 (1), 5–16. doi:10.31035/cg2018003

Liu, X. Q., Liu, H. S., Xing, L., Qin, Z. L., Ma, B. J., and Wang, M. (2020). Sensitivity Analysis of Petrophysical Parameters for Estimating Hydrate Saturation in the Shenhu Area. *Appl. Geophys.* 17 (5), 649–659. doi:10.1007/s11770-018-0718-1

Nobes, D. C., Villinger, H., Davis, E. E., and Law, L. K. (1986). Estimation of Marine Sediment Bulk Physical Properties at Depth from Seafloor Geophysical Measurements. *J. Geophys. Res.* 91 (B14), 14033–14043. doi:10.1029/jb091ib14p14033

Pan, H. J., Liu, T. Y., Wu, L., Wang, H. T., and Xue, M. M. (2014). Morphology Identification and Saturation Estimation of Gas Hydrate. *Prog. Geophys.* 29 (4), 1735–1740. doi:10.6038/pg20150666

Pan, H., Li, H. B., Li, H., Zhang, Y., Chen, J., Cai, S., et al. (2019). Joint Interpretation of Elastic and Electrical Data for Petrophysical Properties of Gas-Hydrate-Bearing Sediments Using Inverse Rock Physics Modeling Method. *Petro S Journ.* 60 (6), 854–871. doi:10.30632/pjv60n6-2019a9

Paull, C. K., and Matsumoto, R.(2000). Leg 164 Overview[C], Proceedings of the Ocean Drilling Program:Scientific Resultsollege Station, Ocean Drilling Program, TX, 164

Pearson, C. F., Halleck, P. M., Mcguire, P. L., Hermes, R., and Mathews, M. (1983). Natural Gas Hydrate Deposits: a Review of *In Situ* Properties. *J. Phys. Chem.* 87 (21), 4180–4185. doi:10.1021/j100244a041

Sha, Z. B., Xu, Z. Q., Fu, S. Y., Liang, J. Q., Zhang, W., Su, P. B., et al. (2019). Gas Sources and its Implications for Hydrate Accumulation in the Eastern Pearl River Mouth Basin. *Mar. Geol. Quat. Geol.* 39 (4), 116–125. doi:10.16562/j.cnki.0256-1492.2019010902

Su, P. B., Liang, J. Q., Zhang, W., Liu, F., Wang, F. F., Li, T. W., et al. (2020). Natural Gas Hydrate Accumulation System in the Shenhu Sea Area of the Northern South China Sea. *Nat. Gas. Ind.* 40 (8), 77–89. doi:10.3787/j.issn.1000-0976.2020.08.006

Wang, X., Collett, T. S., Lee, M. W., Yang, S., Guo, Y., and Wu, S. (2014). Geological Controls on the Occurrence of Gas Hydrate from Core, Downhole Log, and Seismic Data in the Shenhu Area, South China Sea. *Mar. Geol.* 357, 272–292. doi:10.1016/j.margeo.2014.09.040

Wood, W., and Stoffa Pand Shipley, T. (1994). Quantitative Detection of Methane Hydrate through High-Resolution Seismic Velocity Analysis. *J. Geophys. Res.* 99 (5), 9681–9695. doi:10.1029/94jb00238

Wood, W. T., and Ruppel, C.(2000). Seismic and Thermal Investigations of the Blake Ridge Gas Hydrate Area:a Synthesis[C], Proceedings of the Ocean Drilling Program:Scientific Results College Station, Ocean Drilling Program, TX 164:253 - 264

Worthington, P.(2008). Petrophysical Evaluation of Gas Hydrate Formations. International Petroleum Technology Conference, Kuala Lumpur, Malaysia, December 03 2008. doi:10.3997/2214-4609-pdb.148.iptc12610

Xu, S., and White, R. E. (1995). A New Velocity Model for Clay-sand Mixtures 1. *Geophys. Prospect.* 43, 91–118. doi:10.1111/j.1365-2478.1995.tb00126.x

Yamamoto, K. (2014). Methane Hydrate Offshore Production Test in the Eastern Nankai Trough; A Milestone on the Path to Real Energy Resource. Proceedings of the 8th International Conference on Gas Hydrates (ICGH 2014), Beijing, ICGH. T3–T153

Yang, C. Z., Luo, K. W., Liang, J. Q., Lin, Z. X., Zhang, B. D., Liu, F., et al. (2020). Control Effect of Shallow-Burial Deepwater Deposits on Natural Gas Hydrate Accumulation in the Shenhu Sea Area of the Northern South China Sea. *Nat. Gas. Ind.* 40 (8), 68–76.

Yang, S. X., Lei, Y., and Liang, J. Q. (2017a). Concentrated Gas Hydrate in the Shenhu Area, South China Sea: Results from Drilling Expeditions GMGS3 & GMGS4[C], Proceedings of 9th International Conference on Gas Hydrates, Denver, Colorado, USA, June 25 – 30, 2017

Yang, S. X., Liang, J. Q., Liu, C. L., and Sha, Z. B. (2017b). Progresses of Gas Hydrate Resources Exploration in Sea Area. *Geol. Surv. China.* 4 (2), 1–8. doi:10.19388/j.zgdzdc.2017.02.01

Yang, S. X., Zhang, M., and Liang, J. Q. (2015). Preliminary Results of China's Third Gas Hydrate Drilling Expedition: A Critical Step from Discovery to Development in the South China Sea. *Fire Ice.* 15 (2), 1–21.

Yang, W. Q., Zong, Z. Y., Jiang, M., and Liu, X. X. (2021). Rock Physics Modeling Method of Natural Gas Hydrate Based on Equivalent Medium Theory. *Oil Geophys. Prospect.* 56 (3), 528–535. doi:10.13810/j.cnki.issn.1000-7210.2021.03.011

Zhang, H. Q., Yang, S. X., and Wu, N. Y. (2007). Successful and Surprising Results for China's First Gas Hydrate Drilling Expedition. Fire in the Ice. *Methane hydrate Newsl. Natl. Energy Technol. Laboratory, U. S. Dep. Energy.*, 6–9.

Zhang, W. D., Wang, R. H., Ren, S. R., Ma, Q. T., and Li, Y. (2011). A Study on Physical Models of Gas Hydrate Reservoirs. *ACTA Pet. Sin.* 5, 866–871.

Zhang, W., Liang, J. Q., He, J. X., Cong, X. R., Su, P. B., Lin, L., et al. (2018). Differences in Natural Gas Hydrate Migration and Accumulation between GMGS1 and GMGS3 Drilling Areas in the Shenhu Area, Northern South China Sea. *Nat. Gas. Ind.* 38 (3), 138–149. doi:10.3787/j.issn.1000-0976.2018.03.017

Zhang, W., Liang, J. Q., Lu, J. A., Wei, J. G., Su, P. B., Fang, Y. X., et al. (2017). Accumulation Features and Mechanisms of High Saturation Natural Gas Hydrate in Shenhu Area, Northern South China Sea. *Petroleum Explor. Dev.* 44 (5), 670–680. doi:10.1016/s1876-3804(17)30082-4

Zhang, W., Liang, J. Q., Lu, J. A., Meng, M. M., He, Y. L., Deng, W., et al. (2020a). Characteristics and Controlling Mechanism of Typical Leakage Gas Hydrate Reservoir Forming System in the Qiongdongnan Basin, Northern South China Sea. *Nat. Gas. Ind.* 40 (8), 90–99. doi:10.3787/j.issn.1000-0976.2020.08.007

Zhang, W., Liang, J., Wei, J., Lu, J. a., Su, P., Lin, L., et al. (2020b). Geological and Geophysical Features of and Controls on Occurrence and Accumulation of Gas Hydrates in the First Offshore Gas-Hydrate Production Test Region in the Shenhu Area, Northern South China Sea. *Mar. Petroleum Geol.* 114, 104191. doi:10.1016/j.marpetgeo.2019.104191

Zhang, Y. W., Liu, X. W., and Jin, Y. J. (2004). Study of Velocity and Attenuation for Gas-Bearing Hydrate Formation. *Oil Geophys. Prospect.* 39 (2), 205–214.

Zhang, Y., and Toksöz, M. N. (2012). Computation of Dynamic Seismic Responses to Viscous Fluid of Digitized Three-Dimensional Berea Sandstones with a Coupled Finite-Difference Method. *J. Acoust. Soc. Am.* 132 (2), 630–640. doi:10.1121/1.4733545

Conflict of Interest: The authors declare that the research was conducted in the absence of any commercial or financial relationships that could be construed as a potential conflict of interest.

Publisher's Note: All claims expressed in this article are solely those of the authors and do not necessarily represent those of their affiliated organizations, or those of the publisher, the editors, and the reviewers. Any product that may be evaluated in this article, or claim that may be made by its manufacturer, is not guaranteed or endorsed by the publisher.

frontiers | Frontiers in Earth Science

ORIGINAL RESEARCH
published: 14 July 2022
doi: 10.3389/feart.2022.882207

Pore-Water Geochemical Gradients of Sulfate, Calcium, Magnesium, and Iodide Correlated With Underlying Gas Hydrate Potential: A Case Study of the Shenhu Area, South China Sea

Xinyu Ai[1], *Rihuan Zha*[1], *Yijun Lai*[1], *Tao Yang*[1]* *and Pibo Su*[2]

[1]School of Earth Sciences and Engineering, Nanjing University, Nanjing, China, [2]Guangzhou Marine Geological Survey Guangzhou, China

Geochemical profiles in pore water of marine sediments have been considered as, important indicators of gas hydrate occurrence. In the gas hydrate area around the world, the decrease of sulfate, calcium, and magnesium concentrations with depth mainly results directly or indirectly from the anaerobic oxidation of methane (AOM). The ubiquitous abnormally high concentration gradients of iodide in the research area reflect the large methane-generating potential of the area. Thus, we explore the feasibility of using gradients of sulfate, iodide, and authigenic carbonate precipitation as indicators for gas hydrate in the regional exploration of gas hydrate formation. We test the criterion in the gas hydrate zone in the South China Sea (SCS) for the recognition of gas hydrate by using the gradients of sulfate, calcium plus magnesium, and iodide. Contour maps of pore-water gradients from expeditions in the study area are used to correlate the key gradients to underlying gas hydrate occurrence. The results show that the largest potential gas hydrate indicated by the contour maps of the indicators are well consistent with the discovery of GMGS1 and GMGS3 expedition. It implies the possible applicability of this geochemical method in gas hydrate exploration. Also, we identify a promising area in the South China Sea for future gas hydrate investigations. It is the first collective application of the gradients of sulfate, calcium plus magnesium, and iodide to a gas hydrate terrane, especially to a large area of the SCS. We believe that the result of this research will benefit the future exploration of gas hydrate and will arouse a lot of interest from other researchers.

Keywords: Pore water, gas hydrate, geochemistry, South China Sea, sulfate, calcium, magnesium, iodide

OPEN ACCESS

Edited by:
Zhifeng Wan,
Sun Yat-sen University, China

Reviewed by:
Junxi Feng,
Guangzhou Marine Geological Survey, China
Chao Cao,
Third Institute of Oceanography, Ministry of Natural Resources, China

***Correspondence:**
Tao Yang
yangtao@nju.edu.cn

Specialty section:
This article was submitted to Marine Geoscience, a section of the journal Frontiers in Earth Science

Received: *23 February 2022*
Accepted: *16 June 2022*
Published: *14 July 2022*

Citation:
Ai X, Zha R, Lai Y, Yang T and Su P (2022) Pore-Water Geochemical Gradients of Sulfate, Calcium, Magnesium, and Iodide Correlated With Underlying Gas Hydrate Potential: A Case Study of the Shenhu Area, South China Sea. Front. Earth Sci. 10:882207. doi: 10.3389/feart.2022.882207

HIGHLIGHTS

1. We link sulfate, calcium, magnesium, and iodide pore-water gradients to the occurrence of underlying gas hydrates.
2. We support this hypothesis using data from recognized gas hydrate occurrences globally.
3. We identify a promising area in the South China Sea for future gas hydrate investigations.

1 INTRODUCTION

The gas hydrate is an ice-like substance consisting of water and gas (most is CH_4) that forms under conditions of low temperature, high pressure, and adequate gas concentration (Sloan, 1990). An accepted estimation of gas hydrate resources is about 3,000 trillion cubic meters (TCM), which is enormous when compared with the conventional gas resources (~404 TCM) and shale gas (204-456 TCM) (Chong et al., 2016). Due to its considerable reserves and clean combustion products, gas hydrate may become a promising energy resource (Collett, 2002; Hesse, 2003; Makogon et al., 2007; Boswell and Collett, 2011; Chong et al., 2016). The methane contained within gas hydrates is a kind of potential greenhouse gas, 20 times more effective as a greenhouse gas than carbon dioxide (CO_2) (Mitchell, 1989; Ruppel, 2011). Therefore, any release of methane from gas hydrate decomposing due to temperature or pressure changes can cause a positive feedback cycle for atmospheric warming, thus impacting climate change (Borowski et al., 1996; Haq, 2000; Wallmann et al., 2014; Brown et al., 2016; Reay et al., 2018). Accordingly, the abundance, nature, and distribution of gas hydrate are of great importance and have been arousing a lot of research interests of many researchers.

Geophysical methods are widely applied to the study of gas hydrate distribution and abundance. Bottom-simulating reflectors (BSRs) are often coincident with gas hydrate occurrences at depth because dissociating gas hydrate produces in situ gaseous methane that causes an acoustic impedance contrast that generates its strong seismic reflector (Miller et al., 1991; Hornbach et al., 2012). However, a BSR is not necessarily associated with, or completely consistent with, the presence of gas hydrate (Kvenvolden et al., 1993; Le et al., 2015; Dumke et al., 2016). Thus, we try to improve the setup of regional gas hydrate exploration by employing some geochemical indicators. Geochemical methods have already been tried to confirm potential gas hydrate-bearing areas through the geochemical studies of pore water in sediment (Borowski et al., 1996; Dickens, 2001; Bhatnagar et al., 2008; Wu et al., 2013; Pogodaeva et al., 2020). One of the most commonly used geochemical tools for hydrate recognition in drill cores is the presence of freshening chloride anomalies coupled with $\delta^{18}O$ increase in pore water (Hesse, 2003; Luo et al., 2014). Nevertheless, the cores need to penetrate through the hydrate occurrence zone (often hundreds of meters below the seafloor) for the recognition of these anomalies, which is an economic disadvantage for large-scale exploration projects. Alternatively, the profiles of other pore water species (e.g., SO_4^{2-}, I^-) that record early diagenetic reactions in shallow sediments can serve as a powerful tool in gas hydrate exploration (Schulz, 2006). Some reactions associated with methane could be employed to indicate the existence of gas hydrate because a large amount of methane may occur in the gas hydrate occurrence zone. Within the sulfate reduction zone, normally, sulfate is consumed by organoclastic sulfate reduction (OSR) (Berner, 1980; Gieskes et al., 1981):

$$2CH_2O + SO_4^{2-} \rightarrow H_2S + 2HCO_3^- \quad (1)$$

However, in the sulfate-methane transition zone (SMTZ, or SMI for sulfate–methane interface) where methane upwells from deep sediments, sulfate supplied from seawater will be exhausted by the anaerobic oxidation of methane (AOM) reaction (Barnes and Goldberg, 1976),

$$SO_4^{2-} + CH_4 \rightarrow HS^- + 2HCO_3^- + H_2O \quad (2)$$

Substantial depletion of sulfate through AOM causes the SMTZ to become shallower (Blair and Aller, 1995; Borowski et al., 1996; Dickens, 2001). Some researchers accordingly proposed that the linearity of sulfate gradients and the shallow depth of SMTZ could be used to indicate the existence of gas hydrate-bearing areas (Borowski et al., 1999;

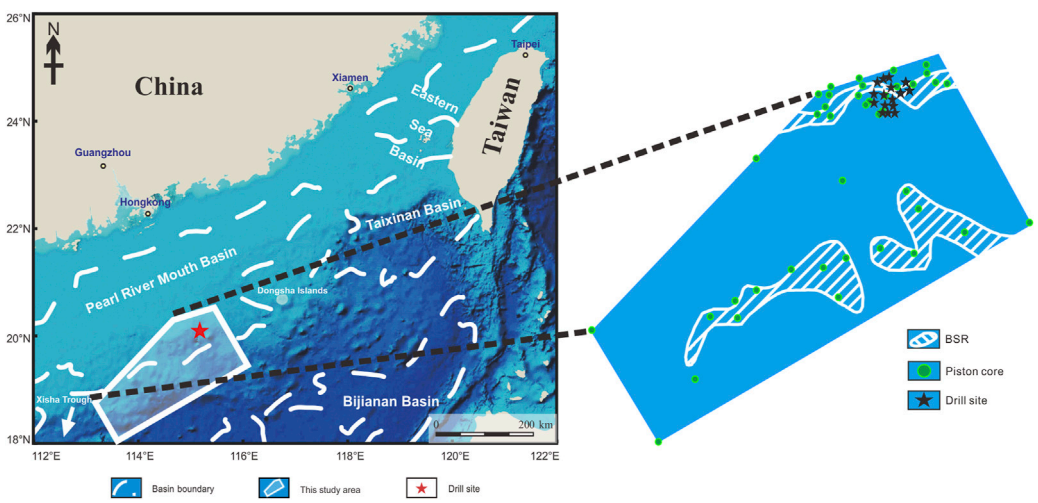

FIGURE 1 | Major basins of the South China Sea and the location of the study area (Modified from Ye et al., 2016). The right part exhibits the detailed situation of the research region, including the information of piston cores we used in the article.

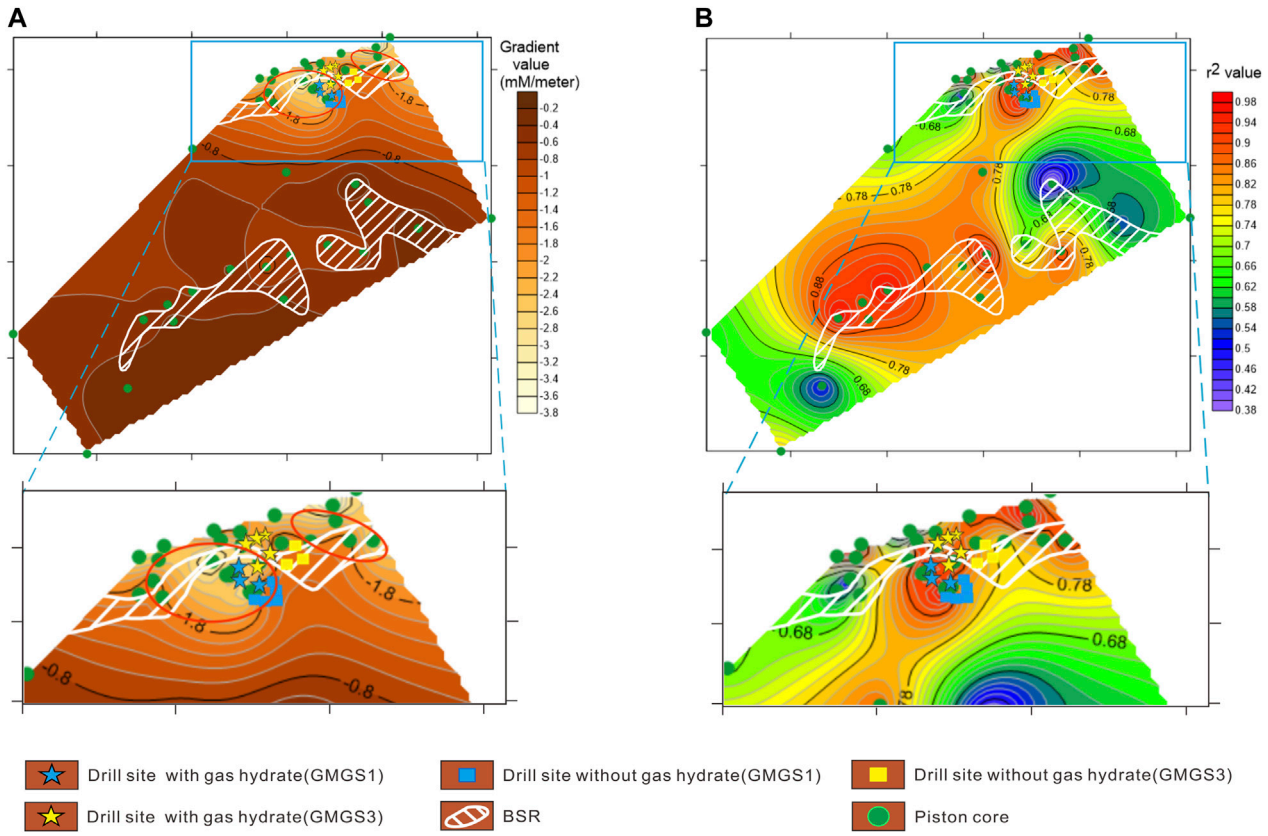

FIGURE 2 | Contour maps of sulfate gradient in units of mM/meter **(A)** and corresponding r2 values **(B)** in the research area. Note the location of cores identified by green-filled circles and BSR outlines (white, from GMGS reports). The stars represent the drill sites, in which gas hydrates were recovered (blue stars represent GMGS1, yellow stars represent GMGS3). The squares represent the drill sites which has no gas hydrates recovered. In 6A, the lighter color indicates a larger gradient, which indicates a higher possibility of gas hydrate existence. In 6B, warmer colors (red) indicate a sulfate gradient that is closer to linearity, usually representing a larger portion of sulfate depletion due to AOM. Based on the gradient and r2, the most promising area is inferred which are marked by red circles in 6A.

Kim et al., 2020). What's more, the calcium concentration of pore water is also sensitive to the AOM process (Rodriguez et al., 2000). It declines with depth due to the enhanced authigenic carbonate precipitation. At the SMTZ where intense AOM reactions occur, the sharp increase in pore water alkalinity may cause the rapid decrease in calcium concentration (Raiswell, 1988; Boetius et al., 2000; Rodriguez et al., 2000). Besides, concentrated iodine anomaly is also commonly observed in gas hydrate-bearing areas (Fehn et al., 2003; Fehn et al., 2006; Muramatsu et al., 2007). The abnormally high concentration of iodide in pore water is related to the decomposition of massive sedimentary organic matter, which represents a large potential gas source. As a result, the concentrated iodide concentration of pore water could also reflect the possible occurrence of gas hydrate. Based on previous research we mentioned above, we try to explore the feasibility of using gradients of sulfate, iodide, and authigenic carbonate precipitation as indicators for gas hydrate in the regional exploration of gas hydrate formation.

Many gas hydrate-bearing areas around the world have been identified and investigated including the Blake Ridge (Paull et al., 1996; Paull and Matsumoto, 2000), Hydrate Ridge (Milkov et al., 2003; Torres et al., 2004), Gulf of Mexico (Boswell et al., 2009), Nankai Trough (Kastner et al., 1993) and Ulleung Basin (Park et al., 2008). In China, several geophysical and geochemical explorations of gas hydrate have been carried out on the northern slope of the South China Sea (SCS) since the 1990s (Zhang et al., 2002; Wu et al., 2004; Jiang et al., 2008; Wu et al., 2011; Zhang et al., 2012; Zhang et al., 2015; Jin et al., 2020; Wang et al., 2021). Numerous data from piston cores and drill sites have been accumulated, which allows us to make a regional comparison of hydrate distribution. The existence of gas hydrate in the northern SCS has been confirmed by geological, geophysical, and geochemical evidence including the occurrence of well-developed BSRs, methane-derived carbonate and shallow SMTZ depth (Liu et al., 2006; Song et al., 2007; Wang et al., 2011; Wu et al., 2011; Li et al., 2012; Li et al., 2015; Zhang et al., 2015; Chen et al., 2016; Jin et al., 2020). During the Sino-German Cooperative Project in early 2004, methane seepages in the SCS were verified for the first time by the discovery of Jiulong Methane Reef (Han et al., 2008). Three years later, natural gas hydrate samples were first recovered in a gas hydrate drilling expedition (GMGS1) which was initiated by Guangzhou Marine Geological Survey in the Shenhu area, northern SCS (Zhang et al., 2007; Wu

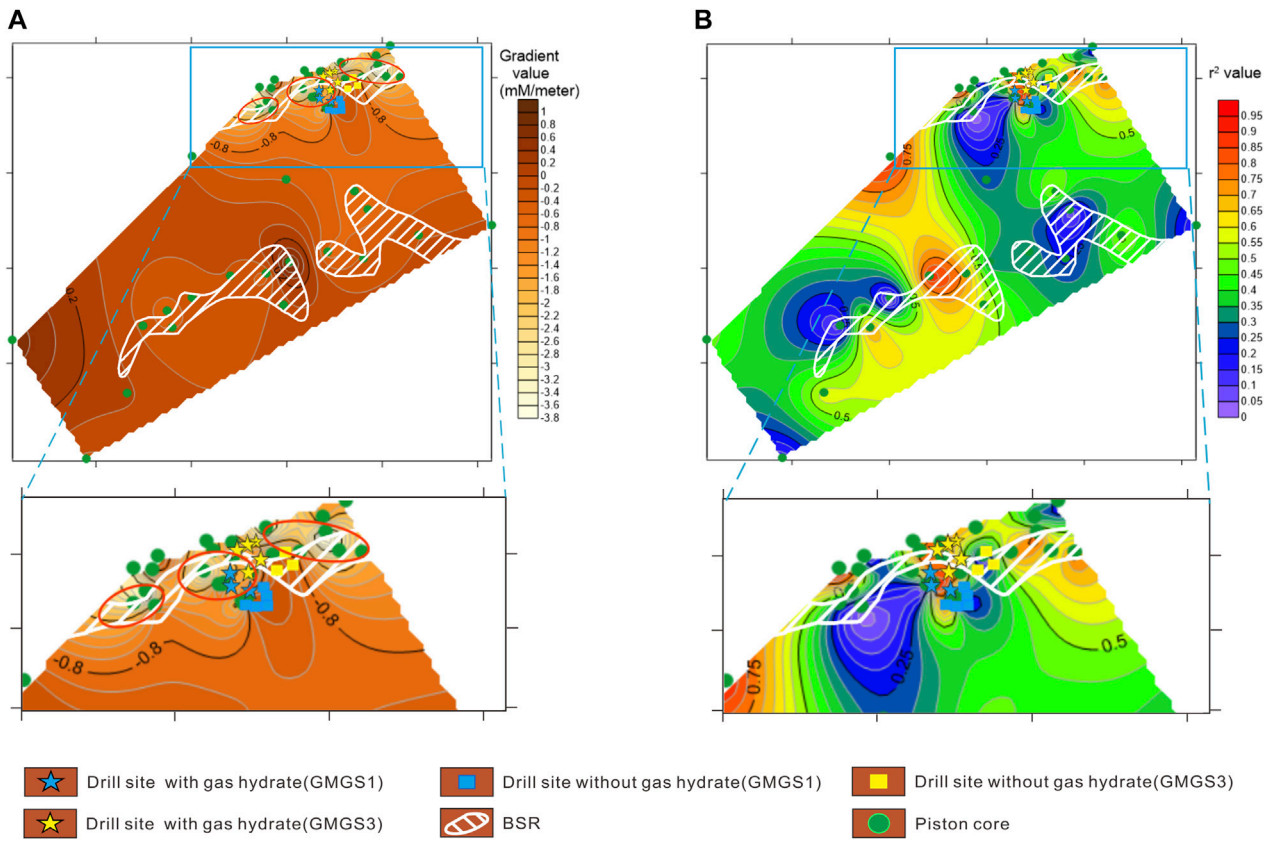

FIGURE 3 | Contour maps of gradients of authigenic carbonate precipitation intensity in units of mM/meter **(A)** and corresponding r^2 values **(B)** in the research area. Note the location of cores identified by green-filled circles and BSR outlines (white, from GMGS reports). The stars represent the drill site, in which gas hydrates were recovered (blue stars represent GMGS1, yellow stars represent GMGS3). The squares represent the drill site that has no gas hydrates recovered. In 7A, the lighter color indicates a larger gradient, which indicates a higher possibility of gas hydrate existence. In 7B, warmer colors (red) indicate that the corresponding gradient is closer to linearity. Based on the gradient and r^2, the most promising area is inferred which are marked by red circles in 7A.

et al., 2011). In 2013, GMGS2 was conducted in the east of Pearl River Mouth Basin of SCS, and massive gas hydrates were successfully recovered (Zhang et al., 2015). Recently, several visible gas hydrates were recovered in the Shenhu area again during the expedition GMGS3, which further constrain the gas hydrate reserves of the SCS (Yang et al., 2015). In 2016, GMGS4 was conducted in Shenhu area, and the new gas hydrates were found (Yang et al., 2017). In 2018, GMGS5 was conducted in QiongDongNan area of SCS, and massive gas hydrates were sampled (Ye et al., 2019).

Based on previous gas hydrate research, we correlate comprehensive geochemical indicators, the gradients of sulfate, calcium plus magnesium, and iodide, to the occurrence of underlying gas hydrate in marine sediments. The approach is based on the influence of the occurrence of gas hydrate on the geochemical characteristics of shallow pore water and was tested by correlating the collective gradients to known areas of gas hydrate. This result is compared with the hydrate detection results of GMGS1 and GMGS3. Based on this geochemical criterion, we also predict another promising area for future gas hydrate exploration in the northern SCS through the geographic information system. We believe that this research will benefit the future exploration of gas hydrate and will arouse a lot of interest from other researchers.

2 GEOLOGICAL SETTING AND METHODS

The South China Sea, tectonically controlled by interactions of Eurasian Plate, Pacific Plate, and Indo-Australian Plate, is one of the largest marginal basins in the western Pacific Ocean (Li, et al., 2012; Wang et al., 2013). A series of sedimentary basins (e.g., the Taixinan Basin, the Pearl River Mouth Basin, and the Qiongdongnan Basin) in the northern SCS are filled with Mesozoic and Cenozoic sediments, whose largest thickness is over 10 km. The thick sediments provide ideal methane sources for gas hydrate formation (Lüdmann and Wong, 1999). Moreover, the northern slope of the SCS has a water depth of 200~3400 m and a bottom water temperature of 2~5 °C, these temperature and pressure conditions are suitable for gas hydrate formation (Yao, 2001).

The study region, the Shenhu area, is situated in the middle of the northern slope of SCS (between the Xisha Trough and the Dongsha Islands) (**Figure 1**). In this area, quantities of

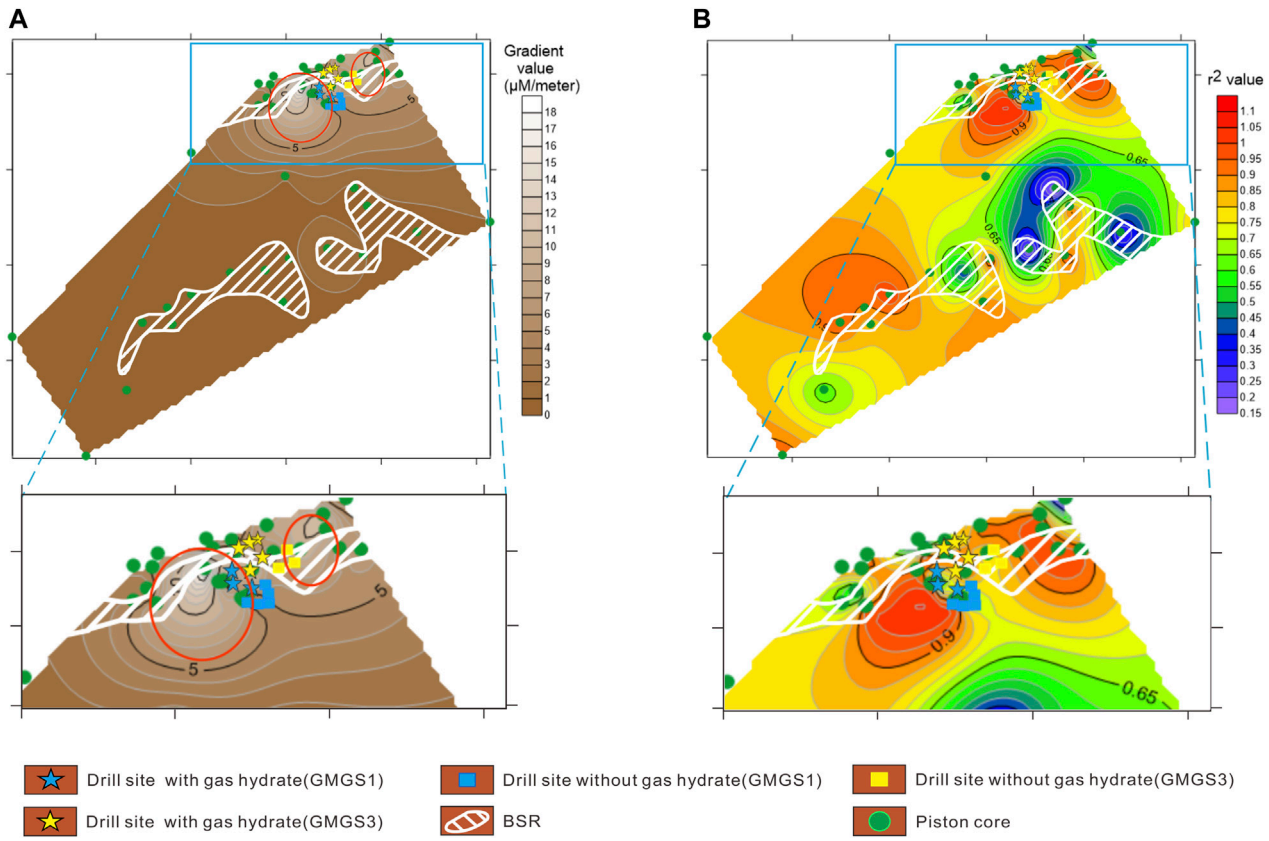

FIGURE 4 | Contour maps of iodine gradient in units of μM/meter **(A)** and corresponding r^2 values **(B)** in the research area. Note the location of cores identified by green-filled circles and BSR outlines (white, from GMGS reports). The stars represent the drill site, in which gas hydrates were recovered (blue stars represent GMGS1, yellow stars represent GMGS3). The squares represent the drill site that has no gas hydrates recovered. In 8A, the lighter color indicates the larger gradient, which indicates a higher possibility of gas hydrate existence. In 8B, warmer colors (red) indicate that the corresponding gradient is closer to linearity. Based on the gradient and r^2, the most promising area is inferred which are marked by red circles in 8A.

deepwater sedimentary fan have developed since Neogene, with average sedimentation rates of 110, 38, 27 m Ma^{-1} for Pleistocene, Pliocene, Miocene respectively (Wu et al., 2011). A series of high-angle faults and vertical fracture systems cut the sedimentary section since Pliocene. A series of central diapiric areas such as gas chimneys are well developed in the Shenhu area, providing favorable geological environments and structures for gas hydrate formation (Lüdmann et al., 2001; Wu et al., 2004). High-resolution seismic investigations show that most of BSRs are 150-350 m below the seafloor (Wu et al., 2013). In order to detect the occurrences and determine the distribution of gas hydrates, some surveys have been carried out by Guangzhou Marine Geological Survey since the 1990s. Hundreds of piston cores were recovered by research vessels of the Guangzhou Marine Geological Survey in recent years.

All the geochemical data were measured at the state key laboratory for mineral deposits research, Nanjing University. The anions and cations of pore water except iodide were measured by an ion chromatography (Metrohm 790-1, Metrosep A Supp 4-250/Metrosep C 2-150). Anions were eluted by 1.8 mM Na_2CO_3 + 1.7 mM $NaHCO_3$. For cation system, ions were eluted by 4 mM dihydroxysuccinic acid + 0.75 mM pyridinedicarboxylic acid. In both systems, the flow rate of eluent was set at 1.0 mL/min, and the relative standard deviation of the measurement results was less than 3%. Iodide was measured using an inductive couple plasma mass spectrometry (ICP-MS) (Element II, ThermoFisher), and the analytical precisions were estimated to be <2%. Samples for iodide measurement was prepared by diluting in 1‰ aqua ammonia with 10 ppb of Rh as an internal standard.

The gradients of indicators are calculated by least-squares fitting, generating a correlation coefficient (r^2) used to access the linearity of geochemical profiles. Detailed data of core sites are shown in **Table 1**. The r^2 value ranges from 0-1, which represents a strong correlation at value 1, a decoupling correlation at value 0. Both the gradient and corresponding r^2 values are mapped over the study area using Surfer® software.

3 RESULTS

We analyzed 246 pore water samples from 23 piston cores in Shenhu area (**Figure 1**). Due to the space limitation and since the

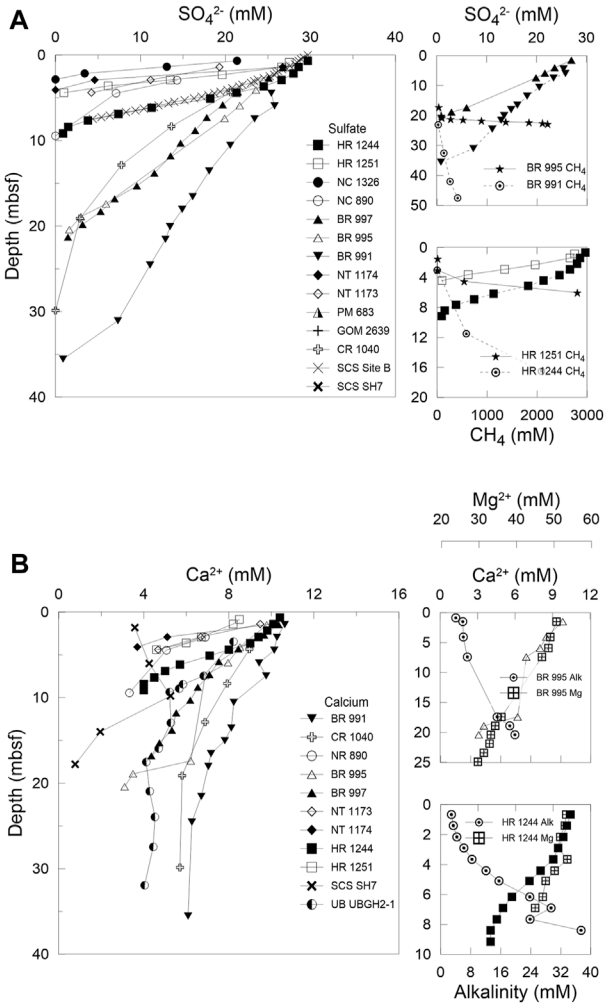

FIGURE 5 | Profiles of sulfate **(A)** and calcium **(B)** with depth in gas hydrate-bearing areas worldwide. Data are selected from Hydrate Ridge (HR) (Milkov et al., 2003; Torres et al., 2004), Blake Ridge (BR) (Borowski et al., 1996; Rodriguez et al., 2000; Dickens, 2001), Nankai Trough (NT) (Kastner et al., 1993; Newberry et al., 2004), Peru Margin (PM) (Kastner et al., 1990; Kvenvolden and Kastner, 1990), North Cascadia (NC) (Lu et al., 2008), Gulf of Mexico (GOM) (Aharon and Fu, 2000), Costa Rica (CR) (Teichert et al., 2009), South China Sea (SCS) (Wu et al., 2011; Ye et al., 2016) and Ulleung Basin (UB) (Kim et al., 2007; Kim et al., 2011).

gradient redox is what we mainly discuss, in this paper we only show the gradient and r^2 calculated from sulfate, iodide and calcium plus magnesium concentration profiles (**Table 1**).

The downward concentration gradients of sulfate, calcium plus magnesium ions and iodide vary from -0.2 to -3.72, from 0.94 to -3.15 and from 0.13 to 11.3, respectively.

HS428PC has the steepest decreasing gradient of sulfate and the steepest increasing gradient of iodide. HS251PC has the lowest sulfate decreasing gradient and HS60PC has the lowest iodide increasing gradient. For calcium plus magnesium, the downward gradient values exhibit both negative and positive. The highest downward increasing gradient of calcium plus magnesium occurs in HS08-6PC and the highest downward decreasing gradient is in HS296PC. Almost all the sites with relatively high absolute gradient values have the r^2 values close to 1.

The absolute values of sulfate and iodide downward gradient have a positive relationship, which means that when sulfate decreasing trend is steeper, the iodide has a steeper increasing trend. The calcium plus magnesium concentration gradient is more complicated, but in general, the absolute values exhibit a positive relationship with sulfate and iodide.

The sites with highest absolute gradient values of sulfate, iodide or authigenic carbonate intensity [i.e., the depletion of (Ca^{2+}) + (Mg^{2+})] are invariably distributed in the northeast region of the study area (in red circles from **Figure 2A**, **Figure 3A** and **Figure 4A**) where the r^2 values are also high. The absolute gradient values gradually decrease from the northeast corner to the rest of the study area, with most of study area showing low absolute values except the northeast region. In addition, it has to be noticed that high r^2 values also exist in other regions except for the northeast area.

4 DISCUSSION

4.1 Geochemical Anomalies Associated With Gas Hydrate

4.1.1 AOM Process

In the gas hydrate-bearing areas, AOM is usually strong due to the enrichment of methane. Methane flux from below causes a significant portion of the interstitial sulfate pool to be consumed through AOM and deplete sulfate more rapidly than OSR alone (Borowski et al., 1996; Borowski et al., 2000). Under the correct condition, intense AOM can result in the linear depletion of sulfate, while OSR leads to a convex curve of the sulfate gradient. (Borowski et al., 1996; Niewöhner et al., 1998; Dickens, 2001; Joye et al., 2004). Thus, under the condition where AOM is intense due to the upward methane flux from below in the methane seepage area of the gas hydrate zone, the curve of sulfate gradient is impacted mainly by AOM rather than OSR. As shown in **Figure 5A**, the rapid consumption of sulfate with depth is common in gas hydrate-bearing sites all over the world. Despite the general downtrend, there are some differences in sulfate gradients among different regions due to the various tectonic and sedimentary environments. For the same region, larger methane flux usually leads to steeper sulfate gradients, as clearly shown in **Figure 5A**. For example, in Black Ridge, the methane flux of Site 995 is larger than Site 991, and the sulfate gradient of Site 995 is steeper. A similar situation occurs in Hydrate Ridge where the sulfate gradient of Site 1,251 is steeper than that of Site 1,244 perhaps due to the larger methane flux of Site 1,251.

Increased consumption of sulfate through AOM also can result in increases in alkalinity near the SMTZ, producing a diagenetic environment beneficial to the precipitation of dissolved calcium and magnesium to form authigenic carbonate cement:

$$\text{For dolomite}: Ca^{2+} + Mg^{2+} + 4HCO_3^- \rightarrow CaMg(CO_3)_2 + 2CO_2 + 2H_2O. \quad (3-1)$$

$$\text{For calcite}: Ca^{2+} + 2HCO_3^- \rightarrow CaCO_3 + CO_2 + H_2O. \quad (3-2)$$

Concentrations of calcium and magnesium ions usually decrease with depth (Raiswell, 1988; Blair and Aller, 1995; Rodriguez et al., 2000; Tong et al., 2013). As the result of authigenic carbonate precipitation, Ca^{2+} exhibits a similar downward trend to that of sulfate in these gas hydrate-bearing sites (**Figure 5B**). The concentrations of calcium and magnesium ions decrease as the alkalinity rises with depth. The alkalinity often reaches its maximum in the SMTZ, as exemplified in both Blake Ridge and Hydrate Ridge (**Figure 5B**). It shows that AOM has a great effect on calcium and magnesium ions. Consequently, strong authigenic carbonate precipitation could occur in the gas hydrate-bearing areas.

4.1.2 Decomposition of Organic Matter

The gas source that is necessary for hydrate formation, thermogenic or biogenic, ultimately originates from the decomposition of organic matter (Kvenvolden and McMenamin, 1980; Kvenvolden, 1998; Clennell et al., 1999; Wallmann et al., 2006). Biophilic elements such as iodine are

TABLE 1 | The detailed data of core sites, which are used to draw contour maps.

Core site	BSR present?	Water Depth	Sulfate gradient (mM/m)	r^2 value	Ca + Mg gradient (mM/m)	r^2 value	Iodide gradient (μM/m)	r^2 value
HS23PC	Yes	1301	-2.79	0.92	-0.49	0.78	6.98	0.98
HS57PC	Yes	2930	-0.31	0.91	-0.20	0.35	0.18	0.81
60PC	Yes	2314	-0.92	0.8	0.30	0.73	0.13	0.38
HS217PC	Yes	1204	-1.85	0.75	-0.18	0.71	10.08	0.89
HS219PC	Yes	1266	-1.62	0.82	-2.68	0.54	5.17	0.99
HS243PC	Yes	2072	-0.69	0.65	-0.85	0.36	1.75	0.13
HS247PC	Yes	2505	-0.66	0.49	-0.69	0.24	1.07	0.96
HS251PC	Yes	2282	-0.2	0.37	-0.18	0.52	0.54	0.12
HS253PC	Yes	2453	-0.53	0.69	-1.81	0.06	0.78	0.94
HS260PC	Yes	2794	-0.22	0.55	-1.25	0.29	0.31	0.25
HS296PC	Yes	1094	-1.77	0.72	-3.15	0.04	8.29	0.99
HS359PC	Yes	940	-2.56	0.77	-1.88	0.67	10.35	0.93
HS08-5PC	Yes	2140	-0.58	0.99	0.71	0.06	0.84	0.95
HS08-6PC	Yes	2385	-0.53	0.9	0.94	0.46	0.5	0.88
HS08-7PC	Yes	2660	-0.65	0.98	-1.48	0.01	0.93	0.99
HS08-14PC	Yes	3320	-0.39	0.83	0.54	0.01	0.43	0.88
HS389PC	No	1380	-1.48	0.83	-1.64	0.01	3.17	0.62
HS396PC	No	1210	-2.76	0.94	-1.62	0.78	10.75	0.93
HS412PC	No	740	-2.65	0.91	-2.85	0.67	8.23	0.94
HS428PC	No	766	-3.72	0.98	-2.12	0.27	11.3	0.99
HS446PC	No	710	-2.47	0.75	-1.11	0.4	3.04	0.19
HS08-8PC	No	1960	-0.36	0.87	-1.76	0.34	0.38	0.79
HS08-11PC	No	2178	-0.63	0.98	-1.02	0.16	0.8	0.99

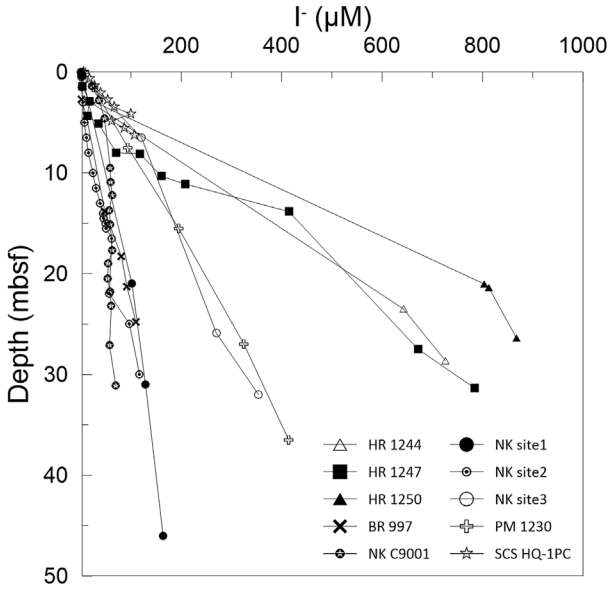

FIGURE 6 | Profile of iodide concentration with depth in pore water worldwide. Data are selected from Nankai Trough (NK) (Fehn et al., 2003; Muramatsu et al., 2007), Hydrate Ridge (HR) (Torres et al., 2004; Fehn et al., 2005; Lu et al., 2008), Blake Ridge (BR) (Egeberg and Dickens, 1999), South China Sea (SCS) (Yang et al., 2010) and Peru Margin (PM) (Martin et al., 1993).

also released in the process of organic matter decomposition, contributing dissolved iodide (I^-) to pore waters:

$$2CH_2O(I^-)_\kappa \rightarrow CO_2 + CH_4 + 2\kappa I^-. \quad (4)$$

Where κ represents the molar fraction of iodide in organic matter.

Within sulfate reduction zone, the organic matters are reduced by sulfate, and also release the iodide:

$$2CH_2O(I^-)_\kappa + SO_4^{2-} \rightarrow H_2S + 2HCO_3^- + 2\kappa I^-. \quad (5)$$

Where κ also represents the molar fraction of iodide in organic matter. High iodide gradient implies a high organic matter decomposition rate, no matter in gas source region below SMTZ or sulfate reduction zone, which will cause a high reaction rate of both methanogenesis and OSR. Therefore, high methane flux can still be indicated by high iodide gradient although the OSR rate can be high. In addition, the iodide migrates from gas source can elevate the iodide gradient to several magnitude high (e.g., HS428PC relative to 60PC), which is much more significant than the iodide released from OSR.

As a result, iodide exhibits abnormally high concentration in gas hydrate-bearing areas (Kastner et al., 1993; Martin et al., 1993; Egeberg and Dickens, 1999; Fehn et al., 2003; Fehn et al., 2006; Yang et al., 2010). As shown in **Figure 6** in gas hydrate-bearing areas, the iodide concentration of pore water ($[I^-]_{porewater}$) increases to several hundred times that of the seawater value ($[I^-]_{seawater}$). There is also a regional variation in iodide gradient because the types and activity of organic matter that have a regional difference could affect the process of decomposition. The organic matter of large activity is liable to decomposition.It is noteworthy that the abnormally high concentration of iodide is

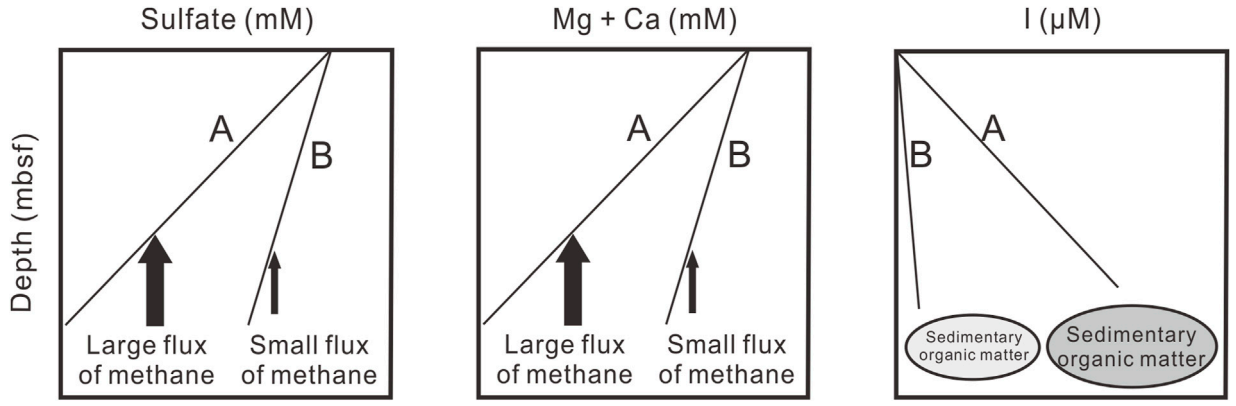

FIGURE 7 | The definition of the gradients of sulfate, Mg^{2+}+Ca^{2+}, and iodide. For all these indicators, the gradient of line A is larger than that of line B.

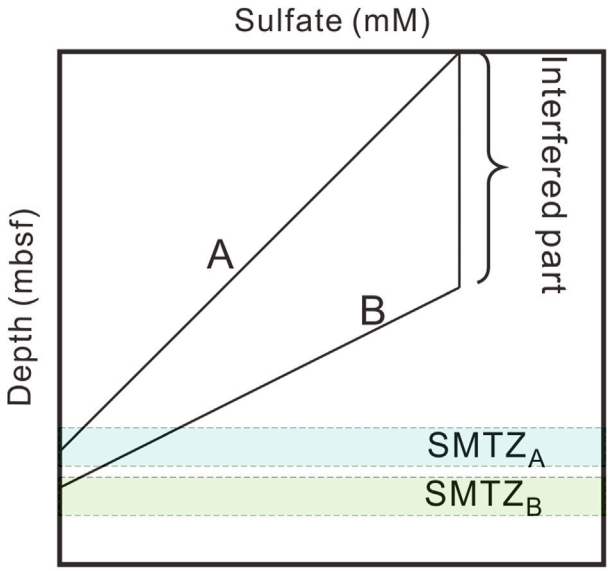

FIGURE 8 | Alteration of depth to the sulfate-methane transition zone (SMTZ) by various processes such as irrigation, bioturbation, and submarine sediment slides. Note that the SMTZ depth of A is shallower than that of B and possesses a different gradient.

not only supplied by the decomposition of local organic matter but may also be influenced by other sources (Fehn et al., 2006; Lu et al., 2008). Fehn et al. (2006) proposed that a large fraction of the iodine is derived from another source that was located to the east (40 km) of Hydrate Ridge through the iodine isotopic dating of pore water. Because of the similar diffusion coefficients between iodide and methane, external fluids from organic matter decomposition simultaneously transport iodine and methane to this site, which promotes the gas hydrate formation by offering a major fraction of methane in the Oregon Hydrate Ridge. To conclude, the high concentration of iodide would reflect massive organic matter decomposition, no matter from internal or external sources, which is helpful to the formation of gas hydrate.

4.2 Definition of Anomaly Indicators

In gas hydrate-bearing areas, the upward methane flux usually exists due to the more likely methane seepage, which may lead to steep sulfate gradients and carbonate precipitation. What's more, the enrichment of iodide may also indicate the existence of the regional methane source because the iodine and methane may be derived from the same source. Accordingly, we use three pore-water geochemical indicators – sulfate gradients, calcium plus magnesium gradients (a proxy for authigenic carbonate formation), and iodide gradient to recognize potential gas hydrate occurrence in underlying sediments. In each case, the higher the gradient, the greater the possibility of gas hydrate formation (**Figure 7**).

As mentioned above, magnesium and calcium are sensitive to the flux of methane, and iodine reflects the potentiality of the gas source. The indicator proposed here has several advantages over the SMTZ depth proxy. One major shortcoming of using the SMTZ depth as the indicator for hydrate recognition is that the SMTZ depth is liable to be altered by environmental factors such as irrigation, bioturbation, and submarine slide displacement (Fossing et al., 2000; Zabel and Schulz, 2001; Croguennec et al., 2016). As shown in **Figure 8**, the SMTZ of Site A is shallower than that of Site B, which nevertheless contains an interfered part. In this case, using the SMTZ depth as the indicator for hydrate recognition may result in erroneous results. However, by using the gradient of sulfate as the indicator, the correct conclusion can be obtained.

4.3 The Contour Maps of three Indicators and Corresponding r^2 Value in the Shenhu Area

We have accumulated sizeable piston-coring data in the study area during the past decade, which provides us with an ideal chance to test the robustness of this new criterion. The gradients of the three indicators (i.e., sulfate, Mg^{2+}+Ca^{2+}, and iodine) of all the core sites in the research area are presented in the form of contour maps. For each indicator, the r^2 values are also given in the corresponding contour map to characterize the shape and linearity of the concentration profile and further assess its relationship to AOM and underlying gas hydrate. The distribution of BSRs on contour maps is acquired from Guangzhou Marine Geological Survey reports.

4.3.1 Sulfate Gradient

Mapping results of sulfate gradients are shown in **Figure 2A**. In **Figure 2A**, the lighter the color is, the larger the sulfate gradient is (see **Figure 7** for the definition), which corresponds to a larger possibility of hydrate existence. The lightest colors can be found mainly in the northeast of the study area and are roughly divided into two parts. Both two parts (red circles) are the most promising areas for gas hydrate occurrence. The yellow stars and blue stars in

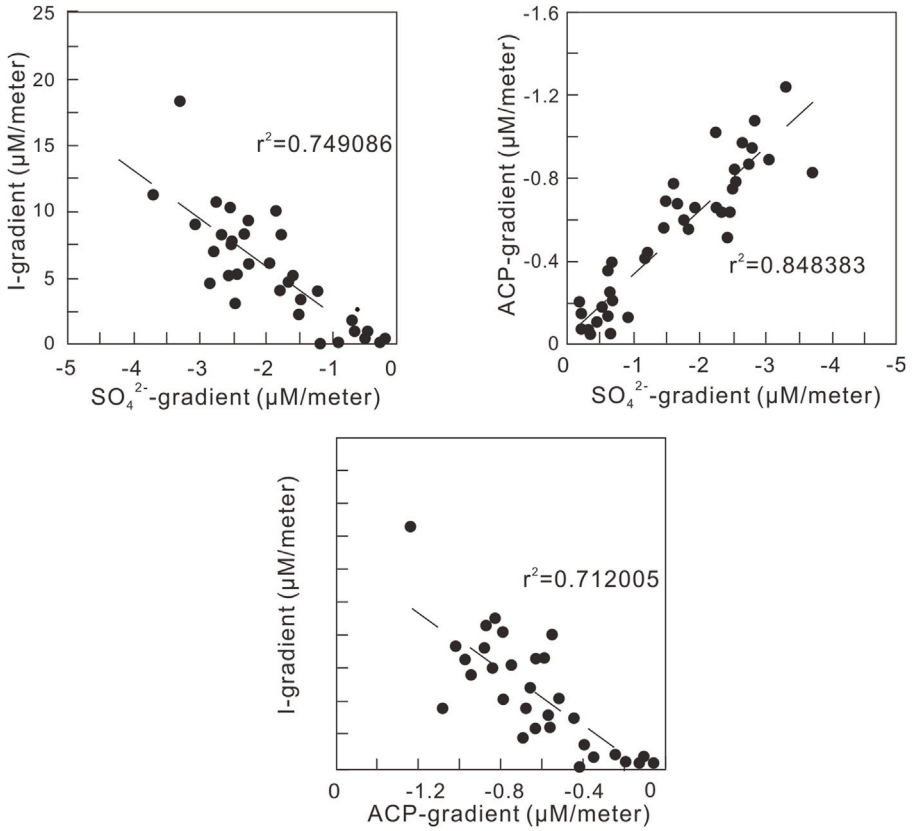

FIGURE 9 | Correlation of authigenic carbonate precipitation intensity (denoted as ACP), sulfate, and iodide gradients in the study area. The relation of these three gradients shows a good correlation (r^2 is 0.75, 0.85, 0.71 respectively). It indicates that the gradients of sulfate, Ca + Mg, and iodide is influenced by the same factors (AOM, methane flux, and the decomposition of organic matter)

Figure 2 are drill sites where gas hydrate samples have been collected in GMGS1 and GMGS3 expedition (yellow represents GMGS1, blue represents GMGS3), including the first gas hydrate sample of China, recovered during the GMGS1 expedition, 2007 (Wu et al., 2013). The yellow squares and blue squares in **Figure 2** represent drill sites that have no gas hydrate samples recovered. It is shown in **Figure 2A** that the stars locate mostly in one of the red circles, while squares locate mainly out of the red circles. It indicates that the gradient of the sulfate is related to the occurrence of gas hydrate to some extent. Corresponding r^2 values of stars are also high (close to 1) in the contour map of r^2 (**Figure 2B**). The other red circle is the promising area predicted by this criterion for gas hydrate occurrence and it needs to be tested by future exploration.

4.3.2 Authigenic Carbonate Precipitation Intensity

The contour map of the intensity of authigenic carbonate precipitation exhibits a similar result to that of sulfate gradients (**Figure 3A**). It also suggests that the northeastern part of the study area, which however could be roughly divided into three small parts, is the most promising area of gas hydrate occurrence. The stars are located in the middle red circle, which is coherent with the mapping result of the criterion. Also, the other two red circles are promising areas for gas hydrate occurrence. In **Figure 3B**, the corresponding r^2 values in the red circles are high (close to 1), which ensures the reliability of the gradient estimation.

4.3.3 Iodide Gradient

As for iodide, in the contour map (**Figure 4**), the lighter (white area) the color is, the larger the gradient is. In **Figure 4A**, two promising areas (red circles) for gas hydrate occurrence are identified. For the third time, the stars are located in one of the red circles, which is again coherent with the mapping result of the criterion. The other circle is a promising area for the existence of gas hydrate. The r^2 values in the red circles are also close to 1, which again supports the reliability of the gradient values.

4.4 The Correlation of Anomaly Indicators

Through the correlation diagrams of authigenic carbonate precipitation intensity, sulfate, and iodine gradients of the study area, there is some correlation among them (**Figure 9**). It suggests that all of them are controlled by similar factors, i.e., the decomposition of organic matter and methane production. On the one hand, the organic matter fermentation and disintegration (both biological and thermal decomposition) could release methane and iodide, so the increase in methane and iodide are coupled to some degree. On the other hand, an increased flux of

methane would strengthen the AOM process, which fuels the sulfate reduction and the precipitation of calcium and magnesium. Thus, we propose that these three indicators could be used together as powerful tools in the exploration of gas hydrates.

5 CONCLUSION

We investigated the concentration profiles of sulfate, calcium, magnesium and iodide in pore water from worldwide main gas hydrate-bearing sites. Each kind of ion has a similar trend in different sites, but shows different downward gradients.

The gradients of sulfate concentration, calcium plus magnesium concentration and authigenic carbonate precipitation intensity can indicate the rate of AOM, which is mainly influenced by the flux of methane. Iodide concentration is strongly affected by the decomposition of organic matter from gas source, and can indicate the methane flux from below or other sources. Thus, the higher the values of these indicators are, the more likely gas hydrate exists in the deep. Also, in some cases where irrigation, bioturbation or submarine slide displacement occurs, the depth of SMTZ is not accurate to indicate the flux of methane, and the sulfate gradient can be a more accurate one.

According to the response of pore water composition in shallow sediment to the high flux of methane in gas hydrate-bearing areas, we proposed that the gradients of sulfate, authigenic carbonate precipitation, and iodide together could be comprehensively employed as the indicators in the exploration of gas hydrate. These indicators were applied to the Shenhu area, SCS, and the results were presented in the form of contour maps. Satisfactory, the most promising area for hydrate occurrence predicted in the three contour maps is consistent with the discovery of GMGS1 and GMGS3 expeditions, which indicates the availability of this criterion. According to the criterion, a new promising area for the existence of gas hydrate was identified, though it needs to be tested by future exploration. We believe that this new geochemical criterion will benefit the exploration of gas hydrate in the future.

DATA AVAILABILITY STATEMENT

The raw data supporting the conclusions of this article will be made available by the authors, without undue reservation.

AUTHOR CONTRIBUTIONS

TY provided the main idea and financial support. XA wrote the main part of the manuscript. RZ checked the English and finished the manuscript. YL finished the experiments in the manuscript. PS gave some important suggestions about manuscript revision.

FUNDING

This study was supported by National Natural Science Foundation of China (41873011) and National Key Scientific Project organized by the China Geological Survey (Grant No. GZH201200305-06-03).

REFERENCES

Aharon, P., and Fu, B. (2000). Microbial Sulfate Reduction Rates and Sulfur and Oxygen Isotope Fractionations at Oil and Gas Seeps in Deepwater Gulf of Mexico. *Geochimica Cosmochimica Acta* 64 (2), 233–246. doi:10.1016/s0016-7037(99)00292-6

Barnes, R. O., and Goldberg, E. D. (1976). Methane Production and Consumption in Anoxic Marine Sediments. *Geol* 4 (5), 297–300. doi:10.1130/0091-7613(1976)4<297:mpacia>2.0.co;2

Berner, R. A. (1980). *Early Diagenesis: A Theoretical Approach*. New Jersey, United States: Princeton University Press.

Bhatnagar, G., Chapman, W. G., Dickens, G. R., Dugan, B., and Hirasaki, G. J. (2008). Sulfate-methane Transition as a Proxy for Average Methane Hydrate Saturation in Marine Sediments. *Geophys. Res. Lett.* 35 (3), L03611. doi:10.1029/2007gl032500

Blair, N. E., and Aller, R. C. (1995). Anaerobic Methane Oxidation on the Amazon Shelf. *Geochimica Cosmochimica Acta* 59 (18), 3707–3715. doi:10.1016/0016-7037(95)00277-7

Boetius, A., Ravenschlag, K., Schubert, C. J., Rickert, D., Widdel, F., Gieseke, A., et al. (2000). A Marine Microbial Consortium Apparently Mediating Anaerobic Oxidation of Methane. *Nature* 407 (6804), 623–626. doi:10.1038/35036572

Borowski, W. S., Hoehler, T. M., Alperin, M. J., Rodriguez, N. M., and Paull, C. K. (2000). Significance of Anaerobic Methane Oxidation in Methane-Rich Sediments Overlying the Blake Ridge Gas Hydrates. *Proc. ocean Drill. program, Sci. results* 164, 87–99. doi:10.2973/odp.proc.sr.164.214.2000

Borowski, W. S., Paull, C. K., and Ussler, W. (1999). Global and Local Variations of Interstitial Sulfate Gradients in Deep-Water, Continental Margin Sediments: Sensitivity to Underlying Methane and Gas Hydrates. *Mar. Geol.* 159 (1), 131–154. doi:10.1016/s0025-3227(99)00004-3

Borowski, W. S., Paull, C. K., and Ussler, W. (1996). Marine Pore-Water Sulfate Profiles Indicate In Situ Methane Flux from Underlying Gas Hydrate. *Geol* 24 (7), 655–658. doi:10.1130/0091-7613(1996)024<0655:mpwspi>2.3.co;2

Boswell, R., and Collett, T. S. (2011). Current Perspectives on Gas Hydrate Resources. *Energy Environ. Sci.* 4 (4), 1206–1215. doi:10.1039/c0ee00203h

Boswell, R., Shelander, D., Lee, M., Latham, T., Collett, T., Guerin, G., et al. (2009). Occurrence of Gas Hydrate in Oligocene Frio Sand: Alaminos Canyon Block 818: Northern Gulf of Mexico. *Mar. Petroleum Geol.* 26 (8), 1499–1512. doi:10.1016/j.marpetgeo.2009.03.005

Brown, P. J., Sanders, R., McDonagh, E., Henson, S., Best, A. I., Poulton, A. J., et al. (2016). "Impacts and Effects of Ocean Warming on Carbon Management Including Methane Hydrates," in *Explaining Ocean Warming, Causes, Scale, Effects and Consequence*. Editors D. Laffoley and J. M. Baster (IUCN), 380–384. doi:10.2305/IUCN.CH.2016.08.en

Chen, D., Wang, X., Völker, D., Wu, S., Wang, L., Li, W., et al. (2016). Three Dimensional Seismic Studies of Deep-Water Hazard-Related Features on the Northern Slope of South China Sea. *Mar. Petroleum Geol.* 77, 1125–1139. doi:10.1016/j.marpetgeo.2016.08.012

Chong, Z. R., Yang, S. H. B., Babu, P., Linga, P., and Li, X.-S. (2016). Review of Natural Gas Hydrates as an Energy Resource: Prospects and Challenges. *Appl. Energy* 162, 1633–1652. doi:10.1016/j.apenergy.2014.12.061

Clennell, M. B., Hovland, M., Booth, J. S., Henry, P., and Winters, W. J. (1999). Formation of Natural Gas Hydrates in Marine Sediments: 1. Conceptual Model of Gas Hydrate Growth Conditioned by Host Sediment Properties. *J. Geophys. Res.* 104 (B10), 22985–23003. doi:10.1029/1999jb900175

Collett, T. S. (2002). Energy Resource Potential of Natural Gas Hydrates. *AAPG Bull.* 86 (11), 1971–1992. doi:10.1306/61eeddd2-173e-11d7-8645000102c1865d

Croguennec, C., Ruffine, L., Dennielou, B., Baudin, F., Caprais, J.-C., Guyader, V., et al. (2016). Evidence and Age Estimation of Mass Wasting at the Distal Lobe of the Congo Deep-Sea Fan. *Deep Sea Res. Part II Top. Stud. Oceanogr.* 142, 50–63. doi:10.1016/j.dsr2.2016.12.013

Dickens, G. R. (2001). Sulfate Profiles and Barium Fronts in Sediment on the Blake Ridge: Present and Past Methane Fluxes through a Large Gas Hydrate Reservoir. *Geochimica Cosmochimica Acta* 65 (4), 529–543. doi:10.1016/s0016-7037(00)00556-1

Dumke, I., Burwicz, E. B., Berndt, C., Klaeschen, D., Feseker, T., Geissler, W. H., et al. (2016). Gas Hydrate Distribution and Hydrocarbon Maturation North of the Knipovich Ridge, Western Svalbard Margin. *J. Geophys. Res. Solid Earth* 121, 1405–1424. doi:10.1002/2015jb012083

Egeberg, P. K., and Dickens, G. R. (1999). Thermodynamic and Pore Water Halogen Constraints on Gas Hydrate Distribution at ODP Site 997 (Blake Ridge). *Chem. Geol.* 153 (1), 53–79. doi:10.1016/s0009-2541(98)00152-1

Fehn, U., Lu, Z., and Tomaru, H. (2005). Data from. 129 I/I Ratios and Halogen Concentrations in Pore Waters of the Hydrate Ridge: Relevance for the Origin of Gas Hydrates in ODP Leg 204. Proceedings of the Ocean Drilling Program: Scientific Results 204

Fehn, U., Lu, Z., and Tomaru, H. (2006). Data Report: 129I/I Ratios and Halogen Concentrations in Pore Water of Hydrate Ridge and Their Relevance for the Origin of Gas Hydrates: A Progress Report. *Proc. Ocean Drill. Program Sci. Results* 204. doi:10.2973/odp.proc.sr.204.107.2006

Fehn, U., Snyder, G. T., Matsumoto, R., Muramatsu, Y., and Tomaru, H. (2003). Iodine Dating of Pore Waters Associated with Gas Hydrates in the Nankai Area, Japan. *Geol* 31 (6), 521–524. doi:10.1130/0091-7613(2003)031<0521:idopwa>2.0.co;2

Fossing, H., Ferdelman, T. G., and Berg, P. (2000). Sulfate Reduction and Methane Oxidation in Continental Margin Sediments Influenced by Irrigation (South-East Atlantic off Namibia). *Geochimica Cosmochimica Acta* 64 (5), 897–910. doi:10.1016/s0016-7037(99)00349-x

Gieskes, J. M., Warme, J. E., Douglas, R. G., and Winterer, E. L. (1981). "Deep-Sea Drilling Interstitial Water Studies: Implications for Chemical Alteration of the Oceanic Crust, Layers I and II," in *The Deep Sea Drilling Project: A Decade of Progress* (United States: SEPM Society for Sedimentary Geology). doi:10.2110/pec.81.32.0149

Han, X., Suess, E., Huang, Y., Wu, N., Bohrmann, G., Su, X., et al. (2008). Jiulong Methane Reef: Microbial Mediation of Seep Carbonates in the South China Sea. *Mar. Geol.* 249 (3), 243–256. doi:10.1016/j.margeo.2007.11.012

Haq, B. U. (2000). "Climatic Impact of Natural Gas Hydrate," in *Natural Gas Hydrate* (Berlin, Germany: Springer), 137–148.

Hesse, R. (2003). Pore Water Anomalies of Submarine Gas-Hydrate Zones as Tool to Assess Hydrate Abundance and Distribution in the Subsurface: What Have We Learned in the Past Decade? *Earth-Science Rev.* 61 (1), 149–179. doi:10.1016/s0012-8252(02)00117-4

Hornbach, M. J., Bangs, N. L., and Berndt, C. (2012). Detecting Hydrate and Fluid Flow from Bottom Simulating Reflector Depth Anomalies. *Geology* 40 (3), 227–230. doi:10.1130/g32635.1

Jiang, S.-Y., Yang, T., Ge, L., Yang, J.-H., Wu, N.-Y., Liu, J., et al. (2008). "Geochemical Anomaly of Pore Waters and Implications for Gas Hydrate Occurence in the South China Sea", in: Proceedings of the 6th International Conference on Gas Hydrates (ICGH 2008). British Columbia, CANADA, July 6–10, 2008.

Jin, J., Wang, X., Guo, Y., Li, J., Li, Y., Zhang, X., et al. (2020). Geological Controls on the Occurrence of Recently Formed Highly Concentrated Gas Hydrate Accumulations in the Shenhu Area, South China Sea. *Mar. Petroleum Geol.* 116, 104294. doi:10.1016/j.marpetgeo.2020.104294

Joye, S. B., Boetius, A., Orcutt, B. N., Montoya, J. P., Schulz, H. N., Erickson, M. J., et al. (2004). The Anaerobic Oxidation of Methane and Sulfate Reduction in Sediments from Gulf of Mexico Cold Seeps. *Chem. Geol.* 205 (3), 219–238. doi:10.1016/j.chemgeo.2003.12.019

Kamath, V. A., Jr. (1990). Clatrate Hydrates of Natural gases. By E. Dendy Sloan, Jr., Marcel Dekker, Inc., New York, 1990, 664 pp.,$125.00(U.S. and Canada),$150.00(other countries). *AIChE J.* 36 (12), 1931–1932. doi:10.1002/aic.690361223

Kastner, M., Elderfield, H., Jenkins, W. J., Gieskes, J. M., Gamo, T., Hill, I., et al. (1993). Geochemical and isotopic evidence for fluid flow in the western Nankai subduction zone, Japan. *Proc. Ocean Drill. Program Sci. Results* 131, 397–413. doi:10.2973/odp.proc.sr.131.143.1993

Kastner, M., Elderfield, H., Martin, J. B., Suess, E., Kvenvolden, K. A., and Garrison, R. E. (1990). Diagenesis and interstitial-water chemistry at the Peruvian continental margin—major constituents and strontium isotopes. *Proc. Ocean Drill. Program Sci. Results* 112, 413–440.

Kim, G. Y., Yi, B. Y., Yoo, D. G., Ryu, B. J., and Riedel, M. (2011). Evidence of gas hydrate from downhole logging data in the Ulleung Basin, East Sea. *Mar. Petroleum Geol.* 28 (10), 1979–1985. doi:10.1016/j.marpetgeo.2011.01.011

Kim, J.-H., Hachikubo, A., Kida, M., Minami, H., Lee, D.-H., Jin, Y. K., et al. (2020). Upwarding gas source and postgenetic processes in the shallow sediments from the ARAON Mounds, Chukchi Sea. *J. Nat. Gas Sci. Eng.* 76, 103223. doi:10.1016/j.jngse.2020.103223

Kim, J.-H., Park, M.-H., Tsunogai, U., Cheong, T.-J., Ryu, B.-J., Lee, Y.-J., et al. (2007). Geochemical characterization of the organic matter, pore water constituents and shallow methane gas in the eastern part of the Ulleung Basin, East Sea (Japan Sea). *Isl. Arc* 16 (1), 93–104. doi:10.1111/j.1440-1738.2007.00560.x

Kvenvolden, K. A. (1998). A primer on the geological occurrence of gas hydrate. *Geol. Soc. Lond. Spec. Publ.* 137 (1), 9–30. doi:10.1144/gsl.sp.1998.137.01.02

Kvenvolden, K. A., Ginsburg, G. D., and Soloviev, V. A. (1993). Worldwide distribution of subaquatic gas hydrates. *Geo-Marine Lett.* 13 (1), 32–40. doi:10.1007/bf01204390

Kvenvolden, K. A., and Kaster, M. (1990). Gas hydrates of the Peruvian outer continental margin. *Proc. Ocean Drill. Program Sci. Results* 112, 517–526. doi:10.2973/odp.proc.sr.112.147.1990

Kvenvolden, K. A., and McMenamin, M. A. (1980). Hydrates of natural gas; a review of their geologic occurrence. *U. S. Geol. Surv. Rep.* doi:10.3133/cir825

Le, A. N., Huuse, M., Redfern, J., Gawthorpe, R. L., and Irving, D. (2015). Seismic characterization of a Bottom Simulating Reflection (BSR) and plumbing system of the Cameroon margin, offshore West Africa. *Mar. Petroleum Geol.* 68, 629–647. doi:10.1016/j.marpetgeo.2014.12.006

Li, L., Lei, X., Zhang, X., and Zhang, G. (2012). Heat flow derived from BSR and its implications for gas hydrate stability zone in Shenhu Area of northern South China Sea. *Mar. Geophys Res.* 33 (1), 77–87. doi:10.1007/s11001-012-9147-3

Li, L., Liu, H., Zhang, X., Lei, X., and Sha, Z. (2015). BSRs, estimated heat flow, hydrate-related gas volume and their implications for methane seepage and gas hydrate in the Dongsha region, northern South China Sea. *Mar. Petroleum Geol.* 67, 785–794. doi:10.1016/j.marpetgeo.2015.07.008

Liu, C.-S., Schnurle, P., Wang, Y., Chung, S.-H., Chen, S.-C., and Hsiuan, T.-H. (2006). Distribution and characters of gas hydrate offshore of southwestern Taiwan. *Terr. Atmos. Ocean. Sci.* 17 (4), 615. doi:10.3319/tao.2006.17.4.615(gh)

Lu, Z., Tomaru, H., and Fehn, U. (2008). Iodine ages of pore waters at Hydrate Ridge (ODP Leg 204), Cascadia Margin: Implications for sources of methane in gas hydrates. *Earth Planet. Sci. Lett.* 267 (3), 654–665. doi:10.1016/j.epsl.2007.12.015

Lüdmann, T., and Wong, H. K. (1999). Neotectonic regime on the passive continental margin of the northern South China Sea. *Tectonophysics* 311 (1), 113–138.

Lüdmann, T., Wong, H. K., and Wang, P. (2001). Plio–Quaternary sedimentation processes and neotectonics of the northern continental margin of the South China Sea. *Mar. Geol.* 172 (3), 331–358. doi:10.1016/S0025-3227(00)00129-8

Luo, M., Chen, L., Tong, H., Yan, W., and Chen, D. (2014). Gas Hydrate Occurrence Inferred from Dissolved Cl− Concentrations and δ18O Values of Pore Water and Dissolved Sulfate in the Shallow Sediments of the Pockmark Field in Southwestern Xisha Uplift, Northern South China Sea. *Energies* 7 (6), 3886–3899. doi:10.3390/en7063886

Makogon, Y., Holditch, S., and Makogon, T. (2007). Natural gas-hydrates—A potential energy source for the 21st Century. *J. Petroleum Sci. Eng.* 56 (1), 14–31. doi:10.1016/j.petrol.2005.10.009

Martin, J. B., Gieskes, J. M., Torres, M., and Kastner, M. (1993). Bromine and iodine in Peru margin sediments and pore fluids: implications for fluid origins. *Geochimica Cosmochimica Acta* 57 (18), 4377–4389. doi:10.1016/0016-7037(93)90489-j

Milkov, A. V., Claypool, G. E., Lee, Y.-J., Xu, W., Dickens, G. R., Borowski, W. S., et al. (2003). In Situ methane concentrations at Hydrate Ridge, offshore Oregon: New constraints on the global gas hydrate inventory from an active margin. *Geology* 31 (10), 833–836. doi:10.1130/g19689.1

Miller, J. J., Lee, M. W., and von Huene, R. (1991). An Analysis of a Seismic Reflection from the Base of a Gas Hydrate Zone, Offshore Peru (1). *Aapg Bull.* 75 (5), 910–924. doi:10.1306/0c9b288f-1710-11d7-8645000102c1865d

Mitchell, J. F. B. (1989). The "greenhouse" effect and climate change. *Rev. Geophys.* 27 (1), 115–139. doi:10.1029/rg027i001p00115

Muramatsu, Y., Doi, T., Tomaru, H., Fehn, U., Takeuchi, R., and Matsumoto, R. (2007). Halogen concentrations in pore waters and sediments of the Nankai Trough, Japan: implications for the origin of gas hydrates. *Appl. Geochem.* 22 (3), 534–556. doi:10.1016/j.apgeochem.2006.12.015

Newberry, C. J., Webster, G., Cragg, B. A., Parkes, R. J., Weightman, A. J., and Fry, J. C. (2004). Diversity of prokaryotes and methanogenesis in deep subsurface sediments from the Nankai Trough, Ocean Drilling Program Leg 190. *Environ. Microbiol.* 6 (3), 274–287. doi:10.1111/j.1462-2920.2004.00568.x

Niewöhner, C., Hensen, C., Kasten, S., Zabel, M., and Schulz, H. (1998). Deep sulfate reduction completely mediated by anaerobic methane oxidation in sediments of the upwelling area off Namibia. *Geochimica Cosmochimica Acta* 62 (3), 455–464.

Park, K.-P., Bahk, J.-J., Kwon, Y., Kim, G.-Y., Riedel, M., Holland, M., et al. (2008). Korean national Program expedition confirms rich gas hydrate deposit in the Ulleung Basin, East Sea. *Fire Ice Methane Hydrate Newsl.* 8 (2), 6–9.

Paull, C. K., and Matsumoto, R. (2000). 1. Leg 164 overview. *Proc. ocean Drill. program. Sci. Results* 164, 3–10. doi:10.2973/odp.proc.sr.164.204.2000

Paull, C., Matsumoto, R., Wallace, P., Black, N., Borowski, W., Collett, T., et al. (1996). "Proceedings of the Ocean Drilling Program,". Initial Reports 164, 241–275.

Pogodaeva, T. V., Poort, J., Aloisi, G., Bataillard, L., Makarov, M. M., Khabuev, A. V., et al. (2020). Fluid migrations at the Krasny Yar methane seep of Lake Baikal according to geochemical data. *J. Gt. Lakes. Res.* 46 (1), 123–131. doi:10.1016/j.jglr.2019.08.003

Raiswell, R. (1988). Chemical model for the origin of minor limestone-shale cycles by anaerobic methane oxidation. *Geol* 16 (7), 641–644. doi:10.1130/0091-7613(1988)016<0641:cmftoo>2.3.co;2

Reay, D. S., Smith, P., Christensen, T. R., James, R. H., and Clark, H. (2018). Methane and Global Environmental Change. *Annu. Rev. Environ. Resour.* 43 (1), 165–192. doi:10.1146/annurev-environ-102017-030154

Rodriguez, N., Paull, C., and Borowski, W. (2000). 30. Zonation of authigenic carbonates within gas hydrate-bearing sedimentary sections on the Blake Ridge: offshore southeastern north America. *Proc. Ocean Drill. Program, Sci. Results* 164, 30. doi:10.2973/odp.proc.sr.164.227.2000

Ruppel, C. (2011). Methane hydrates and contemporary climate change. *Nat. Educ. Knowl.* 3 (10), 29.

Schulz, H. D. (2006). "Quantification of early diagenesis: Dissolved constituents in pore water and signals in the solid phase," in *Marine Geochemistry*. Editors H. D. Schulz and M. Zabel (Berlin,Germany: Springer), 73–124.

Song, H.-B., Wu, S.-G., and Jiang, W.-W. (2007). The Characteristics of BSRs and Their Derived Heat Flow on the Profile 973 in the Northeastern South China Sea. *Chin. J. Geophys.* 50 (5), 1321–1331. doi:10.1002/cjg2.1151

Teichert, B. M., Gussone, N., and Torres, M. E. (2009). Controls on calcium isotope fractionation in sedimentary porewaters. *Earth Planet. Sci. Lett.* 279 (3), 373–382. doi:10.1016/j.epsl.2009.01.011

Tong, H., Feng, D., Cheng, H., Yang, S., Wang, H., Min, A. G., et al. (2013). Authigenic carbonates from seeps on the northern continental slope of the South China Sea: new insights into fluid sources and geochronology. *Mar. Petroleum Geol.* 43, 260–271. doi:10.1016/j.marpetgeo.2013.01.011

Torres, M., Wallmann, K., Tréhu, A., Bohrmann, G., Borowski, W., and Tomaru, H. (2004). Gas hydrate growth, methane transport, and chloride enrichment at the southern summit of Hydrate Ridge, Cascadia margin off Oregon. *Earth Planet. Sci. Lett.* 226 (1), 225–241. doi:10.1016/j.epsl.2004.07.029

Wallmann, K., Aloisi, G., Haeckel, M., Obzhirov, A., Pavlova, G., and Tishchenko, P. (2006). Kinetics of organic matter degradation, microbial methane generation, and gas hydrate formation in anoxic marine sediments. *Geochimica Cosmochimica Acta* 70 (15), 3905–3927. doi:10.1016/j.gca.2006.06.003

Wallmann, K. J., Dallimore, S., Biastoch, A., Westbrook, G., Shakova, N., Severinghaus, J., et al. (2014). *Assessment of the Sensitivity and Response of Methane Gas Hydrate to Global Climate Change*. Nairobi, Kenya: UNEP.

Wang, L., Sun, X., Shen, S., Wu, P., Liu, T., Liu, W., et al. (2021). Undrained triaxial tests on water-saturated methane hydrate-bearing clayey-silty sediments of the South China Sea. *Can. Geotech. J.* 58 (3), 351–366. doi:10.1139/cgj-2019-0711

Wang, P., Li, Q., Tian, J., Jian, Z., Liu, C., Li, L., et al. (2013). Long-Term Cycles in the Carbon Reservoir of the Quaternary Ocean: A Perspective From the South China Sea. *Nat. Sci. Rev.* 1 (1), 119–143. doi:10.1093/nsr/nwt028

Wang, X., Wu, S., Lee, M., Guo, Y., Yang, S., and Liang, J. (2011). Gas hydrate saturation from acoustic impedance and resistivity logs in the Shenhu area, South China Sea. *Mar. Petroleum Geol.* 28 (9), 1625–1633. doi:10.1016/j.marpetgeo.2011.07.002

Wu, L., Yang, S., Liang, J., Su, X., Fu, S., Sha, Z., et al. (2013). Variations of pore water sulfate gradients in sediments as indicator for underlying gas hydrate in Shenhu Area, the South China Sea. *Sci. China Earth Sci.* 56 (4), 530–540. doi:10.1007/s11430-012-4545-6

Wu, N., Zhang, H., Yang, S., Zhang, G., Liang, J., Lu, J. a., et al. (2011). Gas hydrate system of Shenhu area, northern South China Sea: geochemical results. *J. Geol. Res.* 2011, 370298. doi:10.1155/2011/370298

Wu, S., Zhang, G., Guo, C., Huang, Y., and Zhong, S. (2004). Geological constraint on the distribution of gas hydrate in the Dongsha continental slope of South China Sea. *Acta Pet. Sin.* 25, 7–12. doi:10.7623/syxb200404002

Yang, S., Ming, Z., Liang, J., Lu, J., Zijiang, Z., Holland, M., et al. (2015). Preliminary results of China's third gas hydrate drilling expedition: A critical step from discovery to development in the South China Sea. *Fire Ice* 15 (2), 1–5.

Yang, S. X., Liang, J. Q., and Lei, Y. (2017). GMGS4 gas hydrate drilling expedition in the South China Sea. *Fire Ice* 17 (1), 7–11.

Yang, T., Jiang, S., Ge, L., Yang, J., Wu, N., Zhang, G., et al. (2010). Geochemical characteristics of pore water in shallow sediments from Shenhu area of South China Sea and their significance for gas hydrate occurrence. *Chin. Sci. Bull.* 55 (8), 752–760. doi:10.1007/s11434-009-0312-2

Yao, B. (2001). The gas hydrate in the South China Sea. *J. Trop. Oceanogr.* 20 (2), 20–28. doi:10.3969/j.issn.1009-5470.2001.02.004

Ye, H., Yang, T., Zhu, G., Jiang, S., and Wu, L. (2016). Pore water geochemistry in shallow sediments from the northeastern continental slope of the South China sea. *Mar. Petroleum Geol.* 75, 68–82. doi:10.1016/j.marpetgeo.2016.03.010

Ye, J., Wei, J., Liang, J., Lu, J., Lu, H., and Zhang, W. (2019). Complex gas hydrate system in a gas chimney, South China Sea. *Mar. Petroleum Geol.* 104, 29–39. doi:10.1016/j.marpetgeo.2019.03.023

Zabel, M., and Schulz, H. D. (2001). Importance of submarine landslides for non-steady state conditions in pore water systems—lower Zaire (Congo) deep-sea fan. *Mar. Geol.* 176 (1), 87–99. doi:10.1016/s0025-3227(01)00164-5

Zhang, G.-x., Huang, Y.-y., Zhu, Y.-h., and Wu, B.-h. (2002). Prospect of gas hydrate resources in the South China Sea. *Mar. Geol. Quat. Geol.* 22 (1), 75–82. doi:10.3724/SP.J.1140.2013.02097

Zhang, G., Chen, F., Yang, S., Su, X., Sha, Z., Wang, H., et al. (2012). Accumulation and exploration of gas hydrate in deep-sea sediments of northern South China Sea. *Chin. J. Ocean. Limnol.* 30, 876–888. doi:10.1007/s00343-012-1313-6

Zhang, G., Liang, J., Lu, J. a., Yang, S., Zhang, M., Holland, M., et al. (2015). Geological features, controlling factors and potential prospects of the gas hydrate occurrence in the east part of the Pearl River Mouth Basin, South China Sea. *Mar. Petroleum Geol.* 67, 356–367. doi:10.1016/j.marpetgeo.2015.05.021

Zhang, H., Yang, S., Wu, N., Su, X., Holland, M., Schultheiss, P., et al. (2007). Successful and surprising results for China's first gas hydrate drilling expedition. *Fire Ice Methane Hydrate Newsl.* 7 (3), 6–9.

Conflict of Interest: The authors declare that the research was conducted in the absence of any commercial or financial relationships that could be construed as a potential conflict of interest.

Publisher's Note: All claims expressed in this article are solely those of the authors and do not necessarily represent those of their affiliated organizations, or those of the publisher, the editors and the reviewers. Any product that may be evaluated in this article, or claim that may be made by its manufacturer, is not guaranteed or endorsed by the publisher.

Frontiers in
Earth Science

Investigates the processes operating within the major spheres of our planet

Advances our understanding across the earth sciences, providing a theoretical background for better use of our planet's resources and equipping us to face major environmental challenges.

Discover the latest Research Topics

See more →

Frontiers

Avenue du Tribunal-Fédéral 34
1005 Lausanne, Switzerland
frontiersin.org

Contact us

+41 (0)21 510 17 00
frontiersin.org/about/contact